EDITED and PUBLISHED quarterly at the offices of The American Society of Mechanical Engineers, United Engineering Center, 345 E. 47th St., New York, N. Y. 10017. Cable address, "Mechaneer," New York. Second-class postage paid at New York, N. Y., and at additional mailing offices.
CHANGES OF ADDRESS must be received at Society headquarters seven weeks before they are to be effective. Please send old label and new address.
PRICES: To members, $25.00, annually; to nonmembers, $50.00. Single copies, $15.00 each. Add $1.50 for postage to countries outside the United States and Canada.
STATEMENT from By-Laws. The Society shall not be responsible for statements or opinions advanced in papers or . . . printed in its publications (B 13, Par. 4).

INDEXED by the Engineering Index, Inc.

transactions of the ASME

Published Quarterly by
The American Society of
Mechanical Engineers
Volume 99 • Series C • Number 1
FEBRUARY 1977

journal of heat transfer

TECHNICAL NOTES

(Contents continued on page 159)

DISCUSSION

E. M. Sparrow
B. R. Baliga
S. V. Patankar

Department of Mechanical Engineering,
University of Minnesota,
Minneapolis, Minn.

Heat Transfer and Fluid Flow Analysis of Interrupted-Wall Channels, With Application to Heat Exchangers

An analysis has been made of laminar flow and heat transfer in channels whose walls are interrupted periodically along the streamwise direction. Such channels are frequently employed in high-performance compact heat exchangers. Numerical solutions of the mass, momentum, and energy conservation equations yielded local heat transfer and pressure drop results. These results were obtained for a range of Reynolds numbers and for several values of a dimensionless geometrical parameter characterizing the streamwise length L of the individual plate segments which make up the interrupted walls. The Prandtl number was fixed at 0.7 for all the calculations. The basic heat transfer and pressure drop results were employed to investigate whether an interrupted-wall channel experiences an augmented heat transfer rate compared with that for a parallel plate channel. For conditions of equal heat transfer surface area and equal pumping power, appreciably higher heat transfer rates prevailed in the interrupted-wall channel for a wide range of operating conditions. The augmentation was especially marked for relatively short channels and high Reynolds numbers. The results also demonstrated the existence of a new type of fully developed regime, one that is periodic. At sufficiently large downstream distances, the velocity and temperature profiles repeat their values at successive axial stations separated by a distance 2L and, in addition, the average heat transfer coefficient for a plate segment takes on a constant value.

Introduction

It is well known that the heat transfer coefficients in the entrance region of a duct are substantially larger than those at locations farther downstream. This is because the entrance region is characterized by thin thermal boundary layers, whereas in the downstream region transport of heat occurs across the entire duct cross section. The fact that higher heat transfer coefficients are attainable in the entrance region has motivated the design of heat exchangers having flow passages which consist, in effect, of a succession of entrance regions. The walls of such passages are interrupted periodically along the streamwise direction. Each interruption enables the velocity and temperature distributions to become more cross-sectionally homogeneous and a new boundary layer is restarted when the passage wall is resumed downstream of the interruption.

Along with the augmentation of the heat transfer coefficient, there is an increase in pressure drop due to the higher skin friction associated with the successive boundary layer restartings. Therefore, the evaluation of the overall performance of a heat exchanger having interrupted wall passages should take account of pressure drop and pumping power as well as of the enhanced heat transfer coefficients. These matters will be discussed more fully later in the paper.

In the research to be described here, an analysis is performed for fluid flow and heat transfer in a heat exchanger made up of interrupted-wall passages as shown schematically on the left-hand side of Fig. 1. The available literature on heat exchangers of this general type (i.e., offset plate transfer surfaces) has very recently been reviewed by Wieting [1].[1] This survey indicated a complete absence of

Contributed by the Heat Transfer Division for publication in the JOURNAL OF HEAT TRANSFER. Manuscript received by the Heat Transfer Division August 6, 1976.

[1] Numbers in brackets designate References at end of paper.

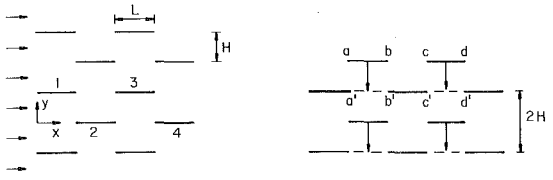

Fig. 1 Schematic diagram of an array of interrupted-wall passages

analytical work and that only a modest amount of experimental data are available. A substantial portion of the data have Reynolds numbers below 1000, and this range was characterized by Wieting as being "primarily laminar." There is, therefore, ample motivation for pursuing a laminar analysis of the flow and heat transfer, as will be carried out here. On the other hand, owing to fabrication irregularities such as burred or bent (or "scarfed" [2]) edges at the upstream and downstream ends of the surface interruptions, the results of a laminar analysis represent an ideal which can only be approximated in practice.

The array pictured in Fig. 1 can be envisioned as a stack of interrupted-wall channels. For example, one such channel has an upper wall which consists of plates 1, 3, 5, . . . and a lower wall which consists of plates 2, 4, 6, ... The streamwise length of each plate is L, and the streamwise length of the interruption between successive plates is also L. The transverse spacing between the interrupted channel walls is H. To enable the analysis to be performed on a two-dimensional basis, it is assumed that the span of the plate segments, normal to the plane of the page, is large compared with H. In addition, to facilitate the solution, the plates are assumed to have negligible thickness.

The flow enters the array from the left with uniform profiles of velocity and temperature. Velocity and thermal boundary layers develop on the first rank of plates, typified by plate 1. The effect of this boundary layer development is mitigated, at least in part, in the gap downstream of plate 1 where diffusion and convection tend to restore the velocity and temperature to their bulk values. This enables new boundary layers to be restarted on the third rank of plates, typified by plate 3, and so on and so forth. A similar sequence of boundary layer restartings occurs on the plates of the second, fourth, sixth, . . . ranks.

The entering fluid temperature is T_i, whereas the plate segments are taken to be isothermal at temperature T_w. The plates can be envisioned to be fins of high conductivity or highly flattened tubes carrying an essentially isothermal fluid.

It is relevant to establish the relationship between an interrupted-wall channel and a conventional parallel plate channel. To this end, reference may be made to the right-hand diagram of Fig. 1. Here, the interrupted channel is illustrated once again. Suppose that the plates in the second rank are translated downward by a distance H so that, for example, segment ab now occupies the position $a'b'$. Similarly, imagine the plates of the fourth rank to be moved downward so that cd occupies $c'd'$; and so forth and so on. Clearly, by such a rearrangement, the array of interrupted-wall channels has become an array of parallel plate channels, each of height $2H$. The array of parallel plate channels has the same heat transfer surface area and the same frontal area as the array of interrupted channels. Therefore, it is natural to compare the heat transfer and flow characteristics of the two systems. Such comparisons will be performed later in the paper.

The interrupted-wall heat exchanger of Fig. 1 encompasses complex fluid flow and heat transfer processes activated by the repetitive interaction of wakes and boundary layers. The solution of the problem requires a numerical approach as will be described shortly. There are three parameters whose numerical values have to be specified as a prelude to each solution. These include the Reynolds number, the ratio of plate length L to transverse spacing H, and the Prandtl number. The Reynolds number was evaluated by employing the Kays-London definition [2]

$$\mathrm{Re} = (4H)\bar{u}/\nu \tag{1}$$

where $4H$ is the hydraulic diameter. The solutions encompassed the Reynolds number range from 200 to 1600 for values of L/H of 0.2, 0.5, 1, 2, and 5. The Prandtl number was fixed at 0.7 (air) for all of the solutions.

The basic results obtained from the solutions are the dimensionless distributions of fluid bulk temperature and pressure drop as a function of position along the length of the heat exchanger. These results can be employed as input to obtain all quantities of interest with respect to both heat transfer and fluid flow. We have employed these results to evaluate the heat transfer augmentation (relative to a parallel plate channel) caused by the periodic interruption of the passage walls.

Two findings of the present research are especially worthy of note. The first is with regard to the augmentation brought about by the interruption of the walls. For the conditions of equal pumping power and equal heat transfer surface area, heat transfer augmentations of up to 80 percent relative to the parallel plate channel were encountered. The present analytically based augmentation calculations are unusual in that the augmentation information available in the literature is generally based on experiments.

The other finding has to do with the concepts of fully developed flow and heat transfer. These concepts are well understood for conventional duct flows, where the velocity profile eventually becomes independent of the streamwise coordinate x and the heat transfer coefficient may also become independent of x [3]. On the other hand, for an interrupted-wall passage, the periodic restarting of the boundary layer precludes the attainment of fully developed conditions characterized by an x-independent velocity profile and heat transfer coefficient. Rather, as will be demonstrated later, fully developed conditions occur periodically for interrupted-wall passages such as those of Fig. 1. Specifically, at sufficiently large downstream distances, the velocity profiles at stations x, $(x + 2L)$, $(x + 4L)$, . . . will be identical, as will the values of the local heat transfer coefficients.

Analysis

From an examination of the left-hand diagram of Fig. 1, it is evident that the fluid flow and heat transfer processes that occur in any one channel are repeated in all of the channels which make up the array. Therefore, it is sufficient to confine the analysis to a single channel. For concreteness, we deal with the channel whose upper boundary consists of plates 1, 3, 5, . . . together with the intervening interruption segments at $y = H$ and $L < x < 2L$, $3L < x < 4L$. . . . . Similarly, the

Nomenclature

c_p = specific heat
H = transverse spacing between plates
k = thermal conductivity
$\mathcal{L}$ = overall length of channel
L = length of plate segment
$\dot{m}$ = mass flow rate per unit span
Pr = Prandtl number
p = pressure
p_i = inlet pressure
Q = surface-integrated heat transfer rate
$Q_{\max}$ = maximum value of Q, $\dot{m}c_p(T_w - T_i)$
Re = Reynolds number, $(4H)\bar{u}/\nu$
T = temperature
T_b = local bulk temperature
T_i = inlet temperature
T_w = wall temperature
u, v = velocity components
$\bar{u}$ = mean velocity
x, y = coordinates
α = thermal diffusivity
Δp = pressure difference, $(p - p_i)$
ν = kinematic viscosity
ρ = density

Subscripts

0 = parallel plate channel
P = equal pumping power

lower boundary is made up of plates 2, 4, 6, . . . and their intervening interruption segments. It may be noted that each interruption segment is a symmetry line so that

$$v = 0, \quad \partial u/\partial y = \partial T/\partial y = 0 \tag{1}$$

This is in contrast to the plate surfaces, where

$$u = v = 0, \quad T = T_w \tag{2}$$

The conservation equations which serve as the basis of the finite difference formulation are those that are commonly employed for hydrodynamically and thermally developing duct flows. These equations are identical to the well-known boundary layer equations for external flows in that streamwise second derivatives are omitted and the pressure is regarded as a function only of the streamwise coordinate (which eliminates further consideration of the cross-stream momentum equation). For constant fluid properties and for negligible viscous dissipation and compression work, the momentum, mass, and energy equations become

$$u(\partial u/\partial x) + v(\partial u/\partial y) = -(dp/dx)/\rho + \nu(\partial^2 u/\partial y^2) \tag{3}$$

$$\partial u/\partial x + \partial v/\partial y = 0 \tag{4}$$

$$u(\partial T/\partial x) + v(\partial T/\partial y) = \alpha(\partial^2 T/\partial y^2) \tag{5}$$

where the x and y coordinates are shown in Fig. 1 and the symbols are defined in the Nomenclature.

The major difference between the analysis of external boundary layers and of duct flows is that whereas the pressure gradient dp/dx is a known input in the former, it is an unknown in the latter. What is known in a duct flow is that a given mass flow passes through a specified cross-sectional geometry. This information is employed in determining the pressure gradient.

The general structure of the finite difference formulation follows that of Patankar and Spalding [4], with x and ω (a dimensionless stream function ranging from zero to one) being used as the coordinates instead of x and y. However, the procedure described in [4] for dealing with the pressure gradient involves some arbitrariness; therefore, a new procedure was devised, the essential features of which are outlined in the Appendix. This procedure enables an initial estimate of dp/dx to be corrected so that the true value is obtained.

The grid was laid out with a total of 31 points in the transformed cross-stream coordinate ω, with a higher concentration of grid points near the channel boundaries $\omega = 0$ and $\omega = 1$. The deployment pattern of the grid points in the streamwise direction was investigated via auxiliary computational experiments. It was found advantageous to employ a layout which started with a very small step size at the leading edge of each plate, with the sizes of the successive steps increasing in accordance with the relation $\Delta x_{i+1} = 1.5\,\Delta x_i$ and remaining constant

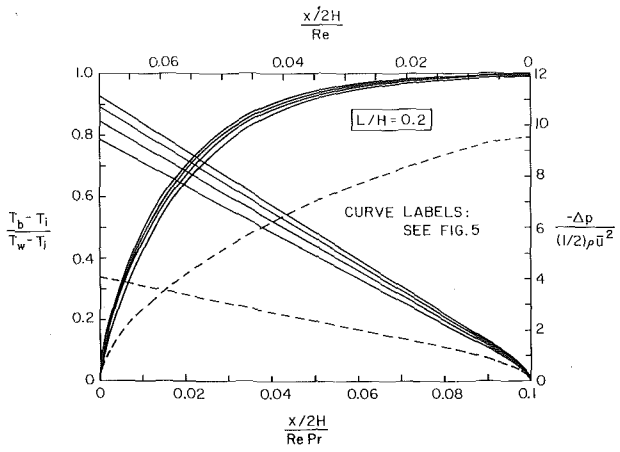

Fig. 2 Distributions of bulk temperature and of pressure along the length of an interrupted-wall channel, $L/H = 0.2$

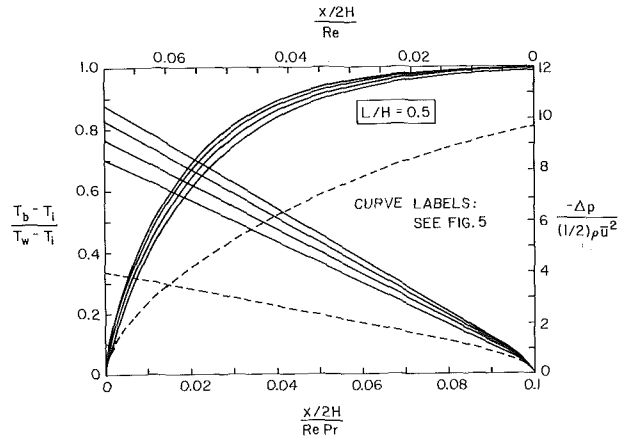

Fig. 3 Distributions of bulk temperature and of pressure along the length of an interrupted-wall channel, $L/H = 0.5$

once a value Δx_{max} had been attained. The initial step size Δx_1 was proportional to the Reynolds number. This pattern was repeated for each of the plates along the length of the channel.

Aside from the accuracy tests involved with the step size studies, comparisons were made with published analytical information for related problems, the parallel plate channel being the most relevant. A comparison of local Nusselt numbers obtained from the present procedure with those of Mercer, Pearce, and Hitchcock [5] showed excellent agreement.

To supplement the foregoing statement of the governing equations and boundary conditions, it is relevant to list those facets of the analytical model which may reflect departures from conditions in operational heat exchangers.

1 Uniform entering flow, without free stream turbulence and free of other disturbances (which might be caused by supports and grilles).

2 Plane plates of negligible thickness whose leading and trailing edges are neither bent nor burred.

3 Isothermal plate surfaces.

4 Steady, separation-free flow in the wakes of the plates for which the boundary layer equations provide an adequate description.

5 Two-dimensional flow and heat transfer with negligible influence of spanwise variations.

Results and Discussion

Heat Transfer and Pressure Drop Results. There is a variety of dimensionless groups currently in use for the presentation of heat transfer results for heat exchangers, for example, Nusselt number, Stanton number, j-factor, effectiveness, etc. These groups are variously employed in the LMTD (log-mean temperature difference) and NTU (number of transfer units) approaches to heat exchanger design. For the presentation of the results obtained here, it appeared reasonable to employ a grouping from which all other groups could be readily deduced and which would facilitate a broad range of performance calculations. On this basis, the dimensionless local bulk temperature, $(T_b - T_i)/(T_w - T_i)$, was selected as the presentation variable for the heat transfer results.

The heat transfer and pressure drop results for the interrupted-wall channel are presented as solid lines in Figs. 2–6 as a function of position along the length of the channel. The successive figures correspond to ratios of plate length to tranverse spacing L/H equal to 0.2, 0.5, 1, 2, and 5. In each figure, the bulk temperature distributions are referred to the left-hand ordinate, where the group $(T_b - T_i)/(T_w - T_i)$ ranges from zero to one, and to the lower abscissa, where the streamwise coordinate x is incorporated into the dimensionless parameter $(x/2H)$RePr. The inclusion of Re in the abscissa variable helps to bring together the results for the various Reynolds numbers, although a residual dependence on Re remains. Pr is included to help

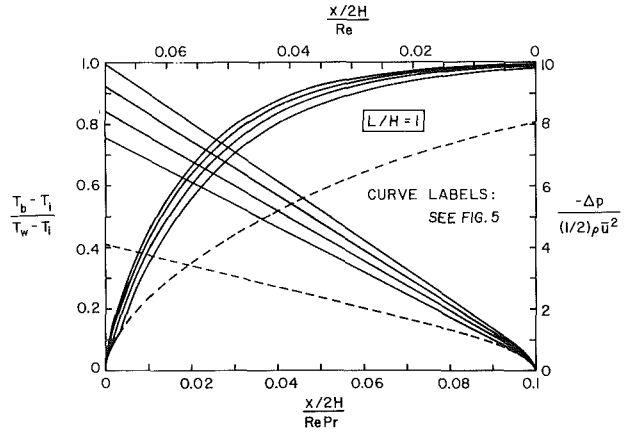

Fig. 4 Distributions of bulk temperature and of pressure along the length of an interrupted-wall channel, $L/H = 1$

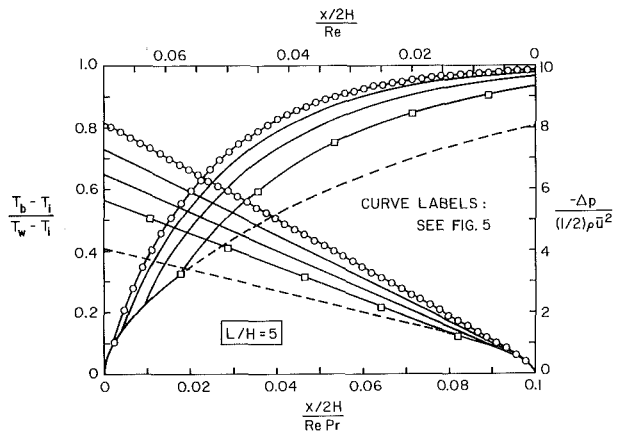

Fig. 6 Distributions of bulk temperature and of pressure along the length of an interrupted-wall channel, $L/H = 5$

generalize the results to Prandtl numbers other than the value 0.7 for which the solutions were obtained.

The pressure distribution along the channel is expressed as the difference between the local pressure p at x and the pressure p_i at the inlet cross section. The pressure difference $-\Delta p = (p_i - p)$ is made dimensionless by $\frac{1}{2}\rho\bar{u}^2$, so that the pressure drop is measured in terms of the velocity head. The dimensionless pressure distributions are referred to the right-hand ordinate and to the upper abscissa.

Also included in the figures are dashed lines which represent the results for a parallel plate channel of height $2H$. As was discussed in the Introduction in connection with the right-hand diagram of Fig. 1, an array of such parallel plate channels has the same heat transfer surface area and the same frontal area as the array of interrupted-wall channels. When plotted against $(x/2H)\mathrm{Re}$, the bulk temperature and static pressure distributions for the parallel plate channel are independent of the Reynolds number. Furthermore, since the parallel plate channel is in no way influenced by the L/H ratio, the dashed lines which appear in each of the successive figures are identical.

The dimensionless bulk temperature distributions of Figs. 2–6 can also be interpreted as a heat transfer ratio. For fluid passing through a channel whose walls are at T_w, the maximum rate of heat transfer corresponding to an inlet temperature T_i and a mass flow rate $\dot{m}$ is $Q_{\max} = \dot{m}c_p(T_w - T_i)$. The attainment of $Q_{\max}$ requires that the channel be very long. For a finite length of channel between $x = 0$ and $x = x$, the surface-integrated heat transfer rate may be denoted by Q and the bulk temperature at x by T_b such that $Q = \dot{m}c_p(T_b - T_i)$. Therefore,

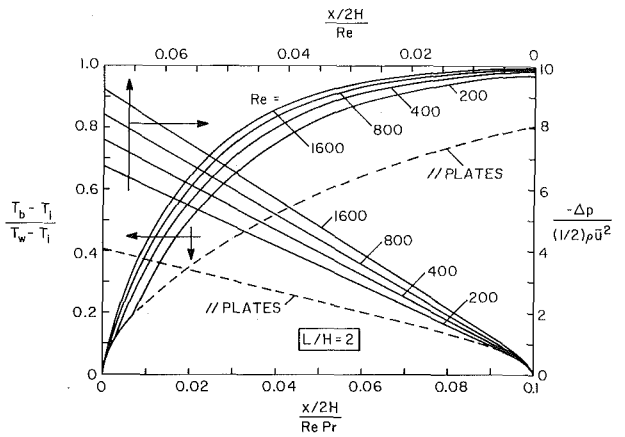

Fig. 5 Distributions of bulk temperature and of pressure along the length of an interrupted-wall channel, $L/H = 2$

$$Q/Q_{\max} = (T_b - T_i)/(T_w - T_i) \tag{6}$$

Thus, the larger the ordinate value of the dimensionless bulk temperature distribution, the greater is the surface-integrated heat transfer rate. Since the latter necessarily increases with increasing downstream distance, the distribution curves rise as x increases, ultimately leveling off as $Q_{\max}$ is approached for sufficiently large x.

Attention will now be turned to the trends evidenced by the results of Figs. 2–6. In each figure, the relative heat transfer performance of the interrupted-wall and parallel plate channels can be identified by comparing the ordinates of the solid and dashed curves. If the corresponding ordinates are compared at a given value of the abscissa, the implied conditions of the comparison are equality of the channel lengths and equality of the mass flows. The equality of mass flows is one of many possible constraints that may be considered, as is discussed more fully in the next section.

For the aforementioned conditions of comparison, the heat transfer performance of the interrupted-wall channel is clearly superior to that of a parallel plate channel. The widening of the spread between the solid and dashed curves as L/H decreases is indicative of a relatively better performance of the interrupted-wall channel. Also, the spread between the solid and dashed curves is accentuated at higher Reynolds numbers, especially when the plate segments are relatively long (i.e., large L/H).

Thus, the foregoing findings corroborate the a priori expectations of comparisons made at equal mass flows and equal heat transfer surface areas. That is, the interrupted-wall channel yields superior heat transfer performance, which is especially marked when the plate segments are short and the Reynolds number is high.

Unfortunately, a comparison of pressure drops for the interrupted-wall and parallel plate channels under the same set of constraints shows that a toll in higher pressure drop is being paid for the heat transfer augmentation. This toll is greater when the plate segments are short and the Reynolds number is high. In addition, the increase in pressure drop owing to the wall interruptions has a special impact in long channels. As is evident from Figs. 2–6, the heat transfer augmentation for long ducts diminishes with increasing downstream distance since Q is bounded by $Q_{\max}$ for both the interrupted-wall and parallel plate channels. On the other hand, the pressure drop penalty is still exacted without abatement. Therefore, on a constant mass flow basis, the use of interrupted plates appears to be less attractive for long channels than for intermediate length channels.

The foregoing discussion is based on an interpretation of the results within the context of the presentation variables used in Figs. 2–6. Other interpretations are possible, as will be seen later.

Heat transfer coefficients and Nusselt numbers can readily be de-

duced from Figs. 2–6, if desired. Various definitions may be employed depending on the choice of the thermal driving force. For example

$$h_1 = (Q/A)/(T_w - T_i), \quad h_2 = (Q/A)/(\text{LMTD}) \tag{7}$$

where LMTD is the log-mean temperature difference involving $(T_w - T_i)$ and $(T_w - T_b)$. Q is the overall rate of heat transfer per channel, and A is the surface area, which is equal to x (per unit span). If ϕ_b is used to denote the dimensionless bulk temperature ordinate of Figs. 2–6, then

$$\frac{h_1(4H)}{k} = \frac{\phi_b}{2(x/2H)/\text{RePr}} \tag{8a}$$

$$\frac{h_2(4H)}{k} = \frac{-\ln(1-\phi_b)}{2(x/2H)/\text{RePr}} \tag{8b}$$

Stanton numbers and Colburn j-factors can be obtained directly from equations (8a) and (8b).

As a final matter with respect to Figs. 2–6, the data symbols appearing in Fig. 6 will now discussed. These symbols are intended to indicate positions at which $x = nL$, where $n = 1, 2, 3, \ldots$. Thus, each symbol corresponds to the terminal point of plate n and to the beginning of plate $(n + 1)$. Except for $x < \text{L}$, the curves were drawn by smoothly connecting the points plotted as $x = nL$, without consideration of the results at the intervening points. A corresponding presentation for all the curves in Figs. 2–6 would have made the plotting and drafting too arduous.

Augmentation. The question of whether an alternative surface configuration gives rise to heat transfer augmentation relative to a standard surface depends on the constraints under which the comparison is made [6]. In the foregoing section of the paper, comparisons were made at equal mass flow and equal surface area because these constraints arose naturally from the presentation variables. Now, augmentation will be examined for constraints which appear to be more commonly accepted in the literature [7, 8].

Specifically, we wish to compare the rate of heat transfer Q for an array of interrupted-wall channels (plate length L, transverse spacing H) with the rate of heat transfer Q_0 for an array of parallel plate channels (channel height $2H$) under the following simultaneous constraints:

(a) equal heat transfer surface area;

(b) equal pumping power, $(\dot{m}/\rho)\Delta p$.

In view of the pressure drop characteristics presented in Figs. 2–6, the equal pumping power constraint requires that the rate of flow through the interrupted-wall channels be lower than that in the parallel plate channels. The Reynolds numbers will, therefore, be different so that Figs. 2–6 cannot be employed directly for the comparison.

The computational procedure for determining Q/Q_0 subject to the aforementioned constraints will be outlined briefly. First, the heat transfer surface area is fixed by selecting the streamwise length of the heat exchanger $\mathcal{L}/H$. Then, a graph of dimensionless pumping power versus Reynolds number is prepared for the parallel plate channel using the dashed pressure drop curve in any of Figs. 2–6. Next, the geometry of the interrupted channel is chosen by fixing L/H. A Reynolds number Re for this channel is selected and the corresponding dimensionless pumping power is evaluated. With this pumping power, one returns to the pumping power—Reynolds number graph for the parallel plate channel and reads out the Reynolds number Re_0.

With the values of Re and Re_0 (along with $\mathcal{L}/H$ and Pr), the abscissa variable in the appropriate figure among Figs. 2–6 is then evaluated for both of the channels, and the $(T_b - T_i)/(T_w - T_i)$ are read out. Then, since

$$Q = \dot{m}c_p(T_b - T_i), \quad Q_0 = \dot{m}_0 c_p(T_b - T_i)_0 \tag{9}$$

It follows that

$$\left(\frac{Q}{Q_0}\right)_P = \frac{\text{Re}(T_b - T_i)/(T_w - T_i)}{\text{Re}_0(T_b - T_i)_0/(T_w - T_i)} \tag{10}$$

The subscript P has been appended to the Q/Q_0 ratio to identify the constant pumping power constraint.

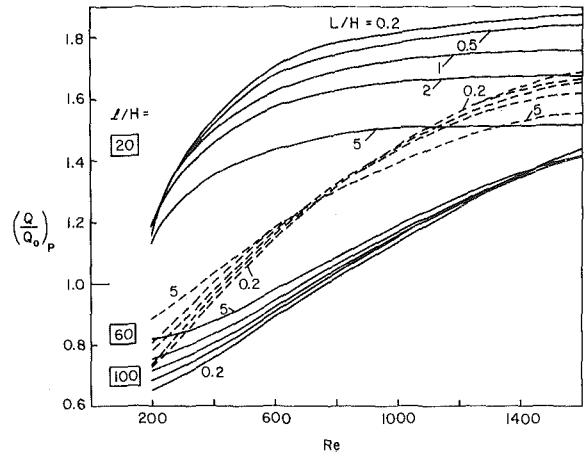

Fig. 7 Ratio of heat transfer in interrupted-wall and parallel plate channels for equal pumping power and equal surface area

The $(Q/Q_0)_P$ ratio has been evaluated for three heat exchanger lengths, $\mathcal{L}/H = 20$, 60, and 100, and for interrupted-wall channels with L/H values of 0.2, 0.5, 1, 2, and 5. For each of these cases, the Reynolds number Re of the interrupted-wall channel was varied from 200 to 1600. The results of these computations are presented in Fig. 7, where $(Q/Q_0)_P$ is plotted as a function of Re. As seen in the figure, the results separate themselves into three groups depending on the heat exchanger length $\mathcal{L}/H$. Within each group, the curves are parameterized by the plate length to spacing ratio L/H.

The successful attainment of heat transfer augmentation is signaled by values of $(Q/Q_0)_P$ greater than one. From Fig. 7, it is seen that for interrupted-wall channels, augmentation can be achieved over a broad spectrum of operating conditions. The augmentation is greatest for relatively short heat exchanger lengths and at higher Reynolds numbers. Thus, for a heat exchanger characterized by $\mathcal{L}/H = 20$, values of $(Q/Q_0)_P$ of 1.5 and greater are attained over a wide range of Reynolds numbers. On the other hand, for $\mathcal{L}/H = 100$, heat transfer augmentation is achieved only for $\text{Re} > \sim 700$.

The attainment of augmentation for relatively short channels and high Reynolds numbers is related to the fact that the local wall-to-bulk temperature differences tend to be relatively large for either of these conditions. Consequently, the higher heat transfer coefficients that are present in an interrupted-wall channel are able to serve with good effect in increasing the rates of heat transfer. On the other hand, when the local wall-to-bulk temperature differences are small (long channels and/or low Reynolds numbers), the high heat transfer coefficients are not very effective.

The plate length to spacing ratio L/H has only a modest effect on the $(Q/Q_0)_P$ results, except for short channels. This is because for intermediate and long channels, the number of plates $N = (\mathcal{L}/H)(H/L)$ is appreciable for all the L/H values considered. However, for a relatively short channel such as $\mathcal{L}/H = 20$, the number of plates ranges from 4 to 100 as L/H is varied from 5 to 0.2. It is plausible that such a difference in the number of plates should affect the results.

As a note of qualification, it should be reiterated that the numerical results of Fig. 7 were evaluated from solutions for isothermal plate segments. The extent to which the results will be altered by other thermal boundary conditions is uncertain.

Fully Developed Flow and Heat Transfer. In conventional ducts, fully developed flow and heat transfer are, respectively, defined by the conditions

$$u \neq \text{function of } x \tag{11}$$

$$(T - T_w)/(T_b - T_w) \neq \text{function of } x \tag{12}$$

As corollaries to equations (11) and (12), the friction factor and the heat transfer coefficient are independent of x.

Table 1 Fully developed Nusselt numbers (equation (14))

$\mathrm{RePr}/(L/H)$	28	70	140	280	560	1400	2800	5600
$\overline{\mathrm{Nu}}_p$	13.91	17.49	19.69	21.72	23.48	25.38	26.54	27.54

In an interrupted-wall channel, fully developed conditions as defined by equations (11) and (12) do not exist. The boundary layer development that occurs on each plate of the array gives rise to x-dependent velocity and temperature fields which violate these definitions. Instead, as will now be illustrated, a different type of fully developed regime is encountered at sufficiently large downstream distances in an interrupted-wall channel. Specifically, at streamwise locations x, $(x + 2L)$, $(x + 4L)$, ... in the fully developed regime, identical velocity profiles are encountered. Similarly, the distributions of $(T - T_w)/(T_b - T_w)$ are the same at x, $(x + 2L)$, $(x + 4L)$, ... Furthermore, the average heat transfer coefficient $\overline{h}_p$ per plate segment is constant for all plates in the fully developed regime.

With respect to $\overline{h}_p$, let Q_p denote the rate of heat transfer per plate and let $(T_w - T_b)'$ and $(T_w - T_b)''$, respectively, represent the wall-to-bulk temperature differences at the beginning and end of the plate. Then,

$$\overline{h}_p = \frac{Q_p/A}{\text{LMTD of } (T_w - T_b)' \text{ and } (T_w - T_b)''} \tag{13}$$

where LMTD is the log-mean temperature difference. With this definition, it can be shown that the Nusselt number is expressible as

$$\overline{\mathrm{Nu}}_p = \frac{\overline{h}_p(4H)}{k} = \frac{\mathrm{RePr}}{L/H} \ln \frac{(T_w - T_b)'}{(T_w - T_b)''} \tag{14}$$

From the numerical evaluation of equation (14), it was found that the fully developed Nusselt number depends on the group $\mathrm{Re}/(L/H)$ rather than separately on Re and (L/H). Table 1 gives representative values of the Nusselt number for the range of $\mathrm{RePr}/(L/H)$ of the solutions (which were performed for $\mathrm{Pr} = 0.7$). The tabulated results are substantially higher than the value of 7.54 for a parallel plate channel.

The attainment of fully developed velocity and temperature profiles is illustrated in Figs. 8 and 9 for an interrupted-wall channel with $L/H = 1$. The figures correspond to $\mathrm{Re} = 1600$ and 200, respectively. In the lower part of each figure, there is a pair of graphs (placed side by side) showing the development of the velocity distribution $u/\bar{u}$. The pair of graphs in the upper part of each figure depicts the corresponding development of the dimensionless temperature distribution $(T - T_w)/(T_b - T_w)$. The curves in the left-hand graphs are for $x/L = 0$, 2, 4, ... and correspond to the trailing edges of plates 2, 4, ... Those in the right-hand graph are for $x/L = 1$, 3, 5, ... and correspond to the trailing edges of plates 1, 3, 5, ...

Inspection of Fig. 8 shows that the profiles at x/L, $(x/L + 2)$, $(x/L + 4)$, ... undergo a development in the initial portion of the channel and ultimately attain a shape which is independent of x. This indicates the existence of a periodic fully developed regime. We have verified that a fully developed regime of this type exists at all stations between the leading and trailing edges of the plates, with fully developed profiles that are specific to each station. Fig. 9 confirms the findings of Fig. 8 and also illustrates the significant effect of the Reynolds number. By comparing these figures, it is seen that the development length is markedly decreased as the Reynolds number decreases.

These figures also enable an assessment of the readjustment of profiles which occurs due to the interruption of the channel wall. As an example, consider the $u/\bar{u}$ profile for $x/L = 1$ shown at the lower right of Fig. 8 and note that the velocities near $y/H = 1$ are very small. On the other hand, in the $u/\bar{u}$ profile for $x/L = 2$, the velocities near $y/H = 1$ are quite large, thereby reflecting the readjustment that has taken place owing to the interruption of the wall between plates 1 and 3. The revitalized velocity field near $y/H = 1$ drives the boundary layer development on plate 3.

Concluding Remarks and Comparisons With Experiment

The results of the present investigation, as given in Figs. 2–6, enable the evaluation of the heat transfer and fluid flow performance of laminar heat exchangers made up of interrupted-wall channels. These results were employed to compare the heat transfer rates in heat exchangers composed either of interrupted-wall channels or of parallel plate channels. For conditions of equal heat transfer surface area and equal pumping power, appreciably higher transfer rates prevailed in the interrupted-wall heat exchanger for a wide range of operating conditions. The heat transfer augmentation was especially marked for relatively short heat exchanger channels and at higher Reynolds numbers.

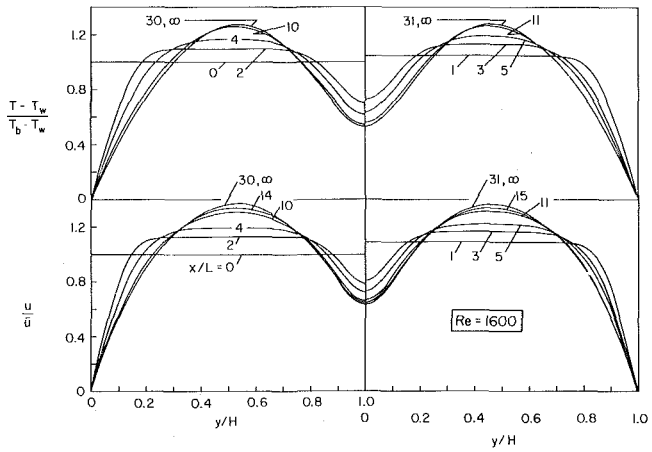

Fig. 8 Developing and fully developed velocity and temperature profiles, $L/H = 1$ and $\mathrm{Re} = 1600$

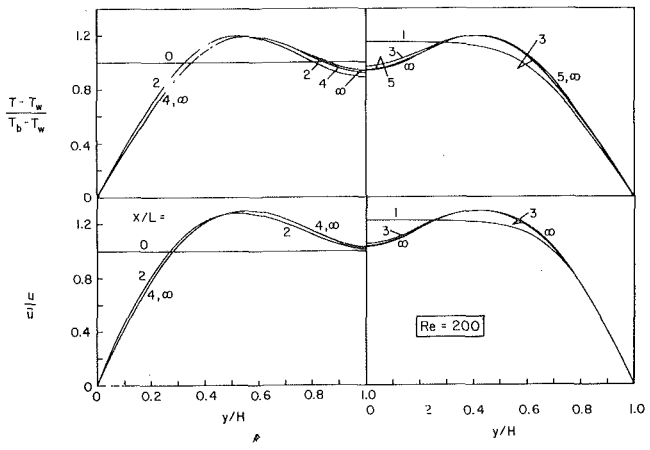

Fig. 9 Developing and fully developed velocity and temperature profiles, $L/H = 1$ and $\mathrm{Re} = 200$

The results also demonstrated the existence of a new type of fully developed regime. At sufficiently large downstream distances, the velocity profiles at x, $(x + 2L)$, $(x + 4L)$, . . . are identical, as are the dimensionless temperature profiles $(T - T_w)/(T_b - T_w)$. In addition, the average heat transfer coefficient per plate is constant for all plates in the fully developed regime.

It is relevant to compare the present analytical predictions with representative experimental results. For this comparison, the literature was searched for experiments where the span of the plates (normal to the plane of Fig. 1) was on the order of (or greater than) ten times the transverse spacing H. Three cases were found which fulfilled this criterion. Of these, the tests of London and Shah's core 103 [9] extended to lower Reynolds numbers than the others, and this case was, therefore, chosen for the comparison.

In Fig. 5 of [9], the overall heat transfer and pressure drop results for core 103, respectively, expressed as the Colburn factor j and the friction factor f, are plotted on log-log paper as a function of a hydraulic-diameter Reynolds number N_R. The low Reynolds number results are well represented by straight lines, from which the data begin to deviate at about $N_R = 900$. The predictions of the present analysis for the overall heat transfer and pressure drop corresponding to the geometrical parameters of core 103 were recast in terms of j and f versus N_R (the heat transfer coefficient is based on the log-mean temperature difference). These analytical results are well represented by $j = 3.92\, N_R{}^{-0.792}$ and $f = 9.60\, N_R{}^{-0.792}$.

When these lines are plotted in Fig. 5 of [9], it is seen that in the range of N_R up to 900, the present heat transfer predictions lie above the data by 20–35 percent, whereas the f predictions lie below the data by 10–20 percent. This finding suggests that the bent and scarfed edges of the plates may have taken a toll in pressure drop while the heat transfer is reduced owing to the disturbance of the thin laminar boundary layers that are responsible for the augmentation. Another relevant factor in the deviations between analysis and experiment is the finite plate thickness, which can cause flow separation at the trailing edge and, perhaps, also at the leading edge.

Acknowledgment

This research was performed under the auspices of NSF Grant ENG-7518141.

References

1 Wieting, A. R., "Empirical Correlations for Heat Transfer and Flow Friction Characteristics of Rectangular Offset-Fin Plate-Fin Heat Exchangers," JOURNAL OF HEAT TRANSFER, TRANS. ASME, Series C, Vol. 97, 1975, pp. 488–490.

2 Kays, W. M., and London, A. L., *Compact Heat Exchangers,* Second ed., McGraw-Hill, New York, 1964.

3 Kays, W. M., *Convective Heat and Mass Transfer,* McGraw-Hill, New York, 1966.

4 Patankar, S. V., and Spalding, D. B., *Heat and Mass Transfer in Boundary Layers,* Second ed., Intertext Books, London, 1970.

5 Mercer, W. E., Pearce, W. M., and Hitchcock, J. E., "Laminar Forced Convection in the Entrance Region Between Parallel Flat Plates," JOURNAL OF HEAT TRANSFER, TRANS. ASME, Series C, Vol. 89, 1967, pp. 251–257.

6 Bergles, A. E., Junkhan, G. H., and Bunn, R. L., "Performance Criteria for Cooling Systems on Agricultural and Industrial Machines," Report HTL-6, Department of Mechanical Engineering, Iowa State University, Ames, Iowa, Dec., 1974.

7 Bergles, A. E., "Survey and Evaluation of Techniques to Augment Convective Heat and Mass Transfer," in *Progress in Heat and Mass Transfer,* Vol. 1, Pergamon Press, Oxford, 1969, pp. 331–424.

8 Bergles, A. E., "Recent Developments in Convective Heat Transfer Augmentation," *Applied Mechanics Reviews,* Vol. 26, 1973, pp. 675–682.

9 London, A. L., and Shah, R. K., "Offset Rectangular Plate-Fin Surfaces—Heat Transfer and Flow Friction Characteristics," *Journal of Engineering for Power,* TRANS. ASME, Series A, Vol. 90, 1968, pp. 218–228.

APPENDIX

Treatment of the Pressure Gradient dp/dx

The unknown pressure gradient dp/dx appears in the x-direction momentum equation. The implicit finite difference form of this equation can be written as

$$a_i u_i = b_i u_{i+1} + c_i u_{i-1} + d_i + e_i (dp/dx) \tag{A-1}$$

for $i = 1, 2, 3, \ldots N$, with $c_1 = 0$ and $b_N = 0$.

Here, the subscript i denotes a grid location in the cross-stream direction; each value of i corresponds to a fixed value of ω, the dimensionless stream function. From the definition of ω, we can deduce that

$$(\psi_E - \psi_I) \int_0^1 (\rho u)^{-1} d\omega = y_E - y_I \tag{A-2}$$

where the subscripts I and E denote the two edges of the boundary layer, $(\psi_E - \psi_I)$ is the stream function difference across the layer, and $y_E - y_I$ is the thickness of the layer. (Here, we have, for convenience, restricted our attention to a plane flow. The extension of the method to axisymmetric situations is straightforward.)

For a confined flow in a known geometry, the value of $(y_E - y_I)$ at a given value of x is known. Then, equation (A-2) represents an additional constraint on the values of u and enables us to arrive at the appropriate value of dp/dx. The discretized form of equation (A-2) can be expressed as

$$\sum_{i=1}^{N} f_i/u_i = M \tag{A-3}$$

where f_i contains the ω increment and the local value of ρ, while M is the known quantity $(y_E - y_I)/(\psi_E - \psi_I)$.

The calculation procedure outlined below is an iterative solution of equations (A-1) and (A-3) for the u's and dp/dx as unknowns. The iteration algorithm can be interpreted as an adaptation of the Newton-Raphson procedure. The convergence has been found to be very rapid; within two or three iterations, the values of u cease to change for at least six significant figures. This procedure eliminates the arbitrariness and the resultant inaccuracy of the confined-flow procedure described in [4].

We manipulate equation (A-1) along the lines of the tri-diagonal-matrix algorithm. We first seek the transformation

$$u_i = P_i u_{i+1} + Q_i + R_i (dp/dx) \tag{A-4}$$

where P_i, Q_i, and R_i are given by the recurrence relations

$$\left.\begin{aligned} P_i &= b_i/(a_i - c_i P_{i-1}) \\ Q_i &= (d_i + c_i Q_{i-1})/(a_i - c_i P_{i-1}) \\ R_i &= (e_i + c_i R_{i-1})/(a_i - c_i P_{i-1}) \end{aligned}\right\} \tag{A-5}$$

The recurrence procedure is started using

$$P_1 = b_1/a_1, \quad Q_1 = d_1/a_1, \quad R_1 = e_1/a_1 \tag{A-6}$$

Since $b_N = 0$, it follows that $P_N = 0$, and this leads us to the second transformation

$$u_i = A_i + B_i (dp/dx) \tag{A-7}$$

where

$$A_N = Q_N, \quad \text{and } B_N = R_N \tag{A-8}$$

and the other A's and B's are given by the recurrence relations

$$\left.\begin{aligned} A_i &= Q_i + P_i A_{i+1} \\ B_i &= R_i + P_i B_{i+1} \end{aligned}\right\} \tag{A-9}$$

Equation (A-7) expresses u_i in terms of dp/dx. If we substitute this relation into equation (A-3), we get an equation with dp/dx as the only unknown. This equation is not linear and is, therefore, solved by the following iteration algorithm.

$$\left.\begin{aligned} (dp/dx)_{\text{new}} &= (dp/dx)_{\text{old}} + (S_I - M)/S_{II} \\ \text{where} \\ S_I &\equiv \sum_{i=1}^{N} f_i/(A_i + B_i (dp/dx)_{\text{old}}) \end{aligned}\right\}$$

and

$$S_{II} = \sum_{i=1}^{N} f_i B_i / (A_i + B_i (dp/dx)_{\text{old}})^2 \qquad \text{(A-10)}$$

Summary of the Procedure

(i) Calculate the coefficients a_i, b_i, c_i, d_i, and e_i in the momentum equation (A-1).

(ii) Obtain P_i, Q_i, R_i using equations (A-6) and (A-5).

(iii) Finally, calculate A_i, B_i using equations (A-8) and (A-9).

(iv) Starting with a guess value of (dp/dx) (such as the value of dp/dx in the last forward step), use the iteration algorithm (A-10) until satisfactory convergence.

(v) Use equation (A-7) to find the values of u_i.

T. M. Kuzay
Technical Staff Member,
Argonne National Laboratory,
Argonne, Ill.
Mem. ASME

C. J. Scott
Assoc. Professor,
Mechanical Engineering Department,
University of Minnesota,
Minneapolis, Minn.
Mem. ASME

Turbulent Heat Transfer Studies in Annulus With Inner Cylinder Rotation

Experimental investigations of turbulent heat transfer are made in a large-gap annulus with both rotating and nonrotating inner cylinder. The vertical annular channel has an electrically heated outer wall; the inner wall is thermally and electrically insulated. The axial air flow is allowed to develop before rotation and heating are imparted. The resulting temperature fields are investigated using thermocouple probes located near the channel exit. The wall heat flux, wall axial temperature development, and radial temperature profiles are measured. For each axial Reynolds number, three heat flux rates are used. Excellent correlation is established between rotational and nonrotational Nusselt number. The proper correlation parameter is a physical quantity characterizing the flow helix. This parameter is the inverse of the ratio of axial travel of the flow helix in terms of hydraulic diameter, per half revolution of the spinning wall.

Introduction

Several forms of rotating flows present themselves in chemical and mechanical mixing and separation devices, electrical and turbomachinery, combustion chambers, pollution control devices, swirl nozzles, rocketry, fusion reactors, and in atmospheric and geophysical phenomena. Rotation of the flow in these examples can be induced through boundary motion, as an initial swirl, or through the action of a body force field. The basic aim of this study has been to obtain reliable experimental data on heat transfer in a well-controlled, boundary-induced, helical flow field. For this purpose, a concentric, vertical, annular geometry was chosen. The flow geometry is shown in Fig. 1. The adiabatic inner cylinder was rotated and the outer, stationary boundary was heated with a uniform heat flux. The air flow in the test section attained full development in both velocity and temperature after certain lengths.

The governing equations for the rotational flow in the annulus are examined and nondimensionalized in order to identify the pertinent parameters. It is through this process that the appropriate physical parameter was found that unifies the axial and tangential swirl flow case (mixed mode) Nusselt numbers along with the case of pure axial flow.

Contributed by the Heat Transfer Division and presented at the Winter Annual Meeting, Houston, Texas, November 30–December 5, 1975, of THE AMERICAN SOCIETY OF MECHANICAL ENGINEERS. Revised manuscript received by the Heat Transfer Division, September 21, 1976. Paper No. 75-WA/HT-55.

The governing time-averaged equations for mass conservation, for the three momentum equations and finally for the energy balance in cylindrical polar coordinates are written in the following for axial-symmetry and with five additional assumptions. These assumptions are:

1 Density fluctuations caused by pressure differences, or else by thermal expansion or its cross correlations are assumed to be negligible.

2 μ, k, C_p property fluctuations are negligible.

3 Pressure fluctuations are negligible.

4 Body forces acting on fluid particles are negligible except the centrifugal force.

5 Variations in the axial direction of mean values are assumed to be small compared with the corresponding variations in the radial direction.

The governing equations are nondimensionalized using the following definitions:

$$\bar{r} = \frac{r}{R} \qquad \bar{p} = \frac{p}{\rho V_T{}^2} \qquad \bar{z} = \frac{z}{L} \qquad \bar{T} = T/T_R$$

$$\bar{u} = \frac{u}{V_T} \qquad \bar{u}' = \frac{u'}{V_T} \qquad \bar{v} = \frac{v}{V_T} \qquad \bar{v}' = \frac{v'}{V_T}$$

$$\bar{w} = \frac{w}{U_M} \qquad \bar{w}' = \frac{w'}{U_M} \tag{1}$$

The surface velocity of the rotating shaft is chosen for the normalization of the mean and fluctuating components of the radial velocity, as well as for the static pressure. This choice is proper because

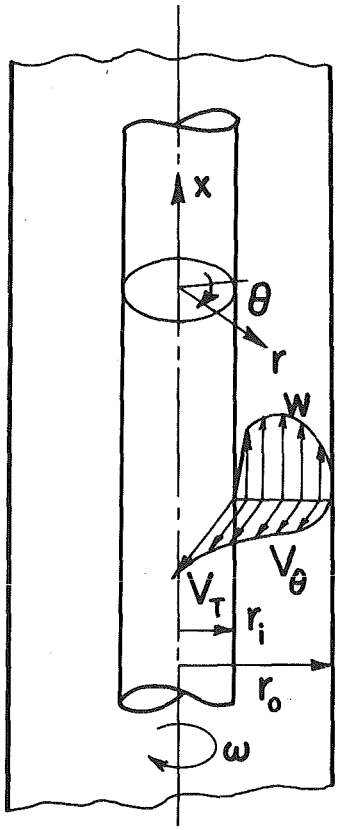

Fig. 1 The coordinate system

of the resulting helical flow in the test section with inner shaft rotation.

The resulting expressions are written out in the following. Dimensionless parameters are arranged in groups and bars are omitted from the nondimensional quantities for convenience.

Continuity Equation.

$$\frac{1}{r}\frac{\partial}{\partial r}(ru) + \frac{R}{L}\frac{U_M}{V_T}\left(\frac{\partial w}{\partial z}\right) = 0 \tag{2}$$

Radial Momentum Equation.

$$\frac{\rho v^2}{r} = \rho\frac{\partial p}{\partial r} \tag{3}$$

Tangential Momentum Equation.

$$u\frac{\partial v}{\partial r} + \frac{R}{L}\frac{U_M}{V_T}w\frac{\partial v}{\partial z} + \frac{uv}{r} = \frac{1}{RV_T}\frac{1}{r^2}\frac{\partial}{\partial r}\left[\nu r^3\frac{\partial}{\partial r}\left(\frac{v}{r}\right)\right] - \frac{1}{r^2}\frac{\partial}{\partial r}(r^2\overline{u'v'}) \tag{4}$$

Axial Momentum Equation.

$$u\frac{\partial w}{\partial r} + \frac{RU_M}{LV_T}w\frac{\partial w}{\partial z} = \frac{U_M R}{V_T L}\left(\frac{V_T}{U_M}\right)^2\frac{\partial p}{\partial z} + \frac{1}{V_T R}\frac{1}{r}\frac{\partial}{\partial r}[\nu r\overline{u'w'}] - \frac{1}{r}\frac{\partial}{\partial r}[r\overline{u'w'}] \tag{5}$$

Energy Equation.

$$u\frac{\partial T}{\partial r} + \frac{RU_M}{LV_T}w\frac{\partial T}{\partial z} = \frac{\nu}{RV_T}\frac{1}{r}\frac{\partial}{\partial r}\left(\frac{1}{\mathrm{Pr}}r\frac{\partial T}{\partial r}\right) + \frac{1}{(V_T L/\nu)\mathrm{Pr}}\frac{\partial^2 T}{\partial^2 Z} - \frac{1}{r}\frac{\partial}{\partial r}(r\overline{u'T'}) + \frac{U_M{}^2}{C_p T_R}\frac{\nu}{V_T R}\left[\left(\frac{V_T}{U_M}\right)^2\left[r\frac{\partial}{\partial r}\left(\frac{v}{r}\right)\right]^2 + \left(\frac{\partial w}{\partial r}\right)^2\right] + \frac{V_T{}^2}{C_p R}\left[u\frac{\partial p}{\partial r} + \left(\frac{R}{L}\frac{U_M}{V_T}\right)w\frac{\partial p}{\partial z}\right] + \text{more terms of dissipation} \tag{6}$$

Two new nondimensional groups in the equations are defined. For the mixed flow cases, the strength of rotation is identified by the ratio of tangential velocity on the surface of the rotating shaft to the mean axial velocity. This ratio (V_T/U_M) is called "the rotation ratio." The rotation parameter is the name given to the group

$$\frac{L}{R}\left(\frac{V_T}{U_M}\right) \tag{7}$$

Here, (L) and (R) are the unspecified characteristic dimensions of the test section. (L) is related to the peripheral velocity and (R) to the axial velocity. This reasoning is due to the fact that the tangential velocity initiates a helical flow in the test section. (L) is typically the pitch of the flow helix; (R) is typically the hydraulic diameter of the annulus. Therefore, the L/R ratio is a factor relating the characteristic

Nomenclature

b = gap ratio of annulus $(R_o - R_i)/R_i$
C_p = specific heat of air at constant pressure
D = test section tube diameter
D_H = hydraulic diameter = $D_o - D_i$
h = heat transfer coefficient
k = thermal conductivity of air
L = characteristic axial dimension of the annular channel in equations (2) through (6)
N = rpm of the rotating inner cylinder
Nu = Nusselt number = hD_H/k
Pr = molecular Prandtl number
p = pressure
q'' = heat flux
$r = r(r, \theta, z)$ the cylindrical coordinate system
R = radius, also reference radial dimension
Re = Reynolds number = $U_M D_H/\nu$
$S = R_i/R_o = D_i/D_o$ radius ratio of annulus
t = time in equation (9)
T = temperature
U_M = mean axial velocity
x = axial coordinate from the beginning of heating
u, v, w = radial, tangential, and axial velocity components
V_T = peripheral velocity of the rotating inner cylinder
α = rotation parameter $\frac{2}{\pi}\left(\frac{D_H}{D_i}\right)\left(\frac{V_T}{U_M}\right)$
ρ = density
$\zeta = V_T/U_M$, the rotation ratio; ratio of the tangential velocity on the inner cylinder and the mean axial flow; the velocity ratio
$\lambda = 1 + \alpha^2$, a function of the rotation parameter
ω = angular velocity of rotation
Φ = dissipation terms
θ = nondimensional temperature = $\frac{T - T_{ent}}{q_{ow}'' D_H/k}$
μ = molecular viscosity

Subscripts and Superscripts

b = bulk
ent = entrance
fd = fully developed
i = inner
io, oo = inner and outer diameters of the outer tube
iw, ow = inner and outer wall
l = laminar
M = mean
o = outer, also straight flow case
r = radial direction
R = reference
T = total
θ = in tangential direction
ϕ = mixed mode flow case to include axial and tangential motion
$(')$ = fluctuating turbulent components

dimensions of the flow helix in the annulus. In the following, the $L/R(V_T/U_M)$ ratio is identified through a physical interpretation of this helical flow.

The characteristic dimension of an annulus in straight flow is its hydraulic diameter which comes from the following arbitrary, but well-accepted definition

$$D_H = \frac{4 \times \text{Area}}{\text{wetted perimeter}} = D_o - D_i \tag{8}$$

With rotation, the characteristic dimension changes since the flow is in a helical form and the wetted perimeter increases in direct proportion to the number of times the flow helix wraps around the walls. The straight flow case can be regarded as a limiting case of the helical flow, where the helical pitch is infinite since the flow helix tightness is zero. In the other extreme, in a circular flow, the helix pitch is zero and helix tightness is infinite. Between these extreme cases, the effect of flow helix can be accounted for by considering the number of hydraulic diameters the flow requires per half revolution of the rotating surface. Here, one half of a revolution is taken since it is more representative of the helix pitch than the full revolution. This is calculated as follows

$$\gamma = t\frac{U_M}{D_H} \tag{9}$$

Here, t is the time for the inner pipe to rotate one half revolution ($t = 60/2N$ s). Since $N = 60/2\pi\ V_T/R_i$, equation (9) becomes

$$\gamma = \pi\frac{R_i}{D_H}\frac{U_M}{V_T} \tag{10}$$

The rotation parameter α is inverse of this ratio which is indicative of the tightness of the flow helix. Indeed, both the friction factor[1] and the Nu with rotation were successfully correlated with "the rotation parameter."

Previous Work. The straight axial flow with no boundary rotation and the inner cylinder rotation with no axial flow constitute the two limiting cases of annular flow heat transfer studies. There exists a large body of work in the literature associated with both categories. A representative list of the former category includes references [1–4].[2] The last one, authored by Kays and Leung is perhaps the most comprehensive treatment of the straight annular flow heat transfer. In that work, the authors presented an analytic solution complemented by extensive experimental data. Also, an empirical relationship in the form $\text{Nu} = 0.022\ \text{Re}^{0.8}\ \text{Pr}^{0.5}$ is proposed to fit the experimental data.

Heat transfer in an annulus with inner cylinder rotation but in the absence of an axial "carrier" was studied in references [5–8]. These studies established the various possible flow regimes in the annulus and their stability limits as a function of the rotational Taylor number. Four flow regimes were recognized: laminar, laminar with Taylor vortices, turbulent with Taylor vortices and a fully turbulent regime. The heat transfer studies referenced previously spanned all four regimes. For the fully turbulent case the Nu is correlated with the rotational Taylor number as follows [7]:

$$\text{Nu} = 0.409\ (\text{Ta})_m{}^{0.241} \tag{11}$$

Here Ta is a modified Taylor number, the conventional rotational Taylor number divided by a complicated radius ratio geometric factor [5].

The mixed mode case with inner cylinder rotation in the presence of axial flow was first studied by Luke [9] in connection with the cooling of the electric motors. This work was later expanded by Gazley [10] who inferred from his data and those of Luke's, the form $\text{Nu} \sim (\text{Re})_{eff}{}^{0.8}$. In this relationship, the effective Re was constructed by an effective velocity defined as

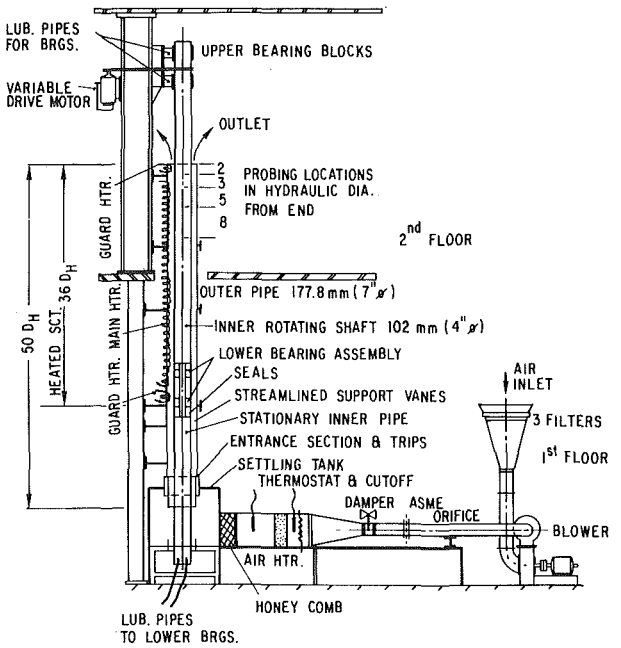

Fig. 2 Schematic of test setup for annular flow with rotating inner boundary

$$v_{eff} = \left[U_M{}^2 + \left(\frac{V_T}{2}\right)^2\right]^{1/2} \tag{12}$$

Tachibana and Fukui [11] did similar work to Gazley's and, again, using Gazley's effective velocity for the narrow gap annulus offered a heat transfer correlation in the form:

$$\text{Nu} = 0.015\left(1 + 2.3\frac{D_H}{L}\right)(D_o/D_i)^{0.45}(\text{Re})_{eff}{}^{0.8}\text{Pr}^{1/3} \tag{13}$$

In this equation L is the test section length and the short test section used in the experiments warranted inclusion of the entrance effects.

Molozhen and Polyak [12] reviewed the work of references [9–11] along with Kosterin and Finatev's [13]. They proposed a lengthy expression for Nusselt number which spans the two limiting cases of pure-rotational and pure-axial, fully turbulent heat transfer in annuli with arbitrary gap ratio.

The present work [15] attempts to fill a gap in the annular flow heat transfer. This is the case of a wide-gap, long annular channel with moderate radius ratio for fully developed turbulent axial flow in the presence of inner cylinder rotation. The rotational speed is varied from zero to several times the mean axial velocity.

The Experimental Apparatus

A primary experimental objective was to produce a simple, ultimately predictable, temperature profile. This was achieved through uniform heating from one wall and insulating the outer wall. Then, the developed temperature profile has a linear axial dependence.

The rotating inner pipe in the annulus was balanced dynamically to 3300 rpm. All of the experiments were conducted at two specific shaft speeds of 1500 and 2000 rpm. Therefore, the tangential velocity in the test section was preset and the rotation ratio could be changed by varying the axial Re. For the Re range mentioned previously, the rotation ratio varied from 0 to 2.8.

The overall design of the experimental setup is shown schematically in Fig. 2. The apparatus consists of a tall structure of two concentric pipes, accommodated between two floors of the Mechanical Engineering Department at the University of Minnesota. The lower floor houses the air intake, blower, ASME metering orifice, ducting, the plenum chamber, the nonrotating initial section of the annulus, the

[1] To be reported separately.

[2] Numbers in brackets designate References at end of paper.

support tower, and the lubrication circuit for the lower bearing assembly of the rotating shaft. The upper room houses the actual measuring section, the drive shaft with a variable speed motor, lubrication circuit for the drive shaft bearing blocks, and a heavy supporting structure to hold the assembly.

Test Section. The test section consists of two vertically mounted concentric tubes. The outer one is made up in four sections, each 91.4-cm long. The first section of the 4-piece outer tube is made of thick-walled steel pipe. It was honed inside to 177.9-mm ID and a 193.7-mm OD. This section is different in material and wall thickness from the remaining three upper brass tube sections because this inlet section is not heated and it supports the weight of the upper three-piece assembly.

Near the upper end of the steel tube, four holes of 3.2-mm dia were drilled on 90-deg centers. These holes were used to accommodate pins for four concentricity vane spacers inserted between the nonrotating 101.6-mm OD inner pipe and the 177.8-mm ID outer pipe. At the upper end of the pipe, the annulus concentricity is held within ±0.123 mm over the nominal 177.8-mm ID. The remaining upper three sections of the outer tube were all cut from a 366-cm long brass tube with 177.8-mm nominal ID and 3.12-mm nominal wall thickness. Care was taken to assure a smooth and continuous outer wall. To this end the matching junctions were honed in assembly.

The outer wall is fully instrumented with thermocouples, wall pressure taps, probe holes, heaters and miscellaneous items for the heater circuit.

The substructure of the shaft was a 76.2-mm OD and 60.3-mm ID carbon steel pipe. It was round to within ±0.076 mm. The shaft was lined on the outside with 1.23-cm thick insulating Textolite sleeve over the lower 274.5 cm of its length.

Main Heater Construction. Uniform electrical heating is applied to the top three sections of the outer wall. Heat flux applied to such a thick wall tube with high thermal conductivity averages out within the tube wall. The primary heater was a 22.9-mm wide and 0.15-mm thick continuous stainless steel strip wound around the outer tube in a spiral, over an electrically insulating tape. The heater spiral was wound with 2.5-mm gap between the successive helixes. In reference [14] an analysis is given on the effect of heater spacing on the uniformity of heating. The 2.5-mm spacing is well within the allowable range in order not to disturb uniformity of the heating on the flow side of the thick-walled tube.

A 25.4-mm wide fiberglass self-adhesive tape was wound around the bare tubes without any overlap so that structural, as well as thermal uniformity was maintained. Finally, the stainless steel heater strip was laid over the fiberglass tape, expoxied in place, and covered with another layer of the same tape. The outer tube had 7.6-cm wide guard heaters at each end. Each guard heater had 13½ revolutions of 3.2-mm wide heater strip again with the same gap as the main heaters.

The measurement technique for power input to the main and guard heaters was the same. d-c electric current was read over calibrated shunts. The main heater shunt was read on Leeds Northrup K-3 Model Potentiometer.

Thermocouple Circuit. Thermocouples in the test section are all 30 WG copper-constantan. A total of 82 thermocouples were placed in between the heater strips. When the thermocouples are attached to the outside of the tube, the inner wall temperature may be calculated from the following formula:

$$T_{io} = T_{oo} - q_w'' R_{oo/k} Ln(R_{oo}/R_{io}) \tag{14}$$

With the present configuration, this temperature difference is negligible (~0.5°C).

Temperature Traverses. There are four probe access ports on the test section (Fig. 2). These are located 2, 3, 5, and 8 D_H from the flow exit plane. Surveys of the velocity were made at the uppermost two ports. No significant difference was observed between these measurements. All subsequent data were taken at the 3 D_H port.

The spherical temperature probe tip was made of a 0.25-mm dia copper constantan thermocouple. The tip diameter was 0.83 mm.

Flow and Temperature Development Length. There is general agreement among researchers that tripped turbulent, straight flow in an annulus will develop within 15–30 hydraulic dia. With mixed-mode flows there is no available information. The overall test section length is 51 D_H. A three D_H length is provided by the plexiglass entrance sleeve and 15 D_H is occupied by the nonrotating lower section. The flow is tripped 51 mm inside the entrance by a 7-mm thick, 4-mm hexagonal aluminum honeycomb.

The rotating portion of the annular test section begins after the stationary 15 D_H long flow passage. The rotational portion is also the heated part of the test section. Consequently, the temperature and the tangential velocity profiles have 36 D_H for their development lengths, while the axial flow has a total of 51 D_H.

Experimental Procedure

One complete set of temperature tests required three runs: pure axial flow and the rotational cases of 1500 and 2000 rpm. In special cases, runs were also taken at additional rpm, such as 1750, 2200, and 2400.

In each set of tests, air mass flow and the heating rate were held constant (three heating rates were applied for each axial Reynolds number). Generally speaking, in these tests, the "high," "medium," and "low" heating rates imply a bulk temperature rise of 12.8–15, 7.2–8.9, and 2.8–4.5°C, respectively.

Data Reduction for the Temperature Measurements. The overall method of data reduction in the tests is as follows:

1 Identify the thermocouples along the same generatrix of the outer tube and fit least square curves, up to second degree, to their data.

2 Calculate mass flow rate, Re and the rotation ratio. Test section temperature for Re calculations was taken to be the bulk temperature calculated from:

$$T_b = T_{ent} + \left(\frac{dT}{dx}\right)_{fd} x \tag{15}$$

$(dT/dx)_{fd}$ is the gradient calculated from curve fits to the wall axial temperature data computed.

3 In the heater resistor calculations, the resistance of each loop of the heater helix was evaluated from the calibration using the local temperature computed from the curve fit to the axial wall temperature distribution. Then, the average heat flux was determined as follows:

$$q_{\text{wall, average}} = \frac{I^2 \Sigma R_{\text{Loop}}}{\text{Area}} \tag{16}$$

Area is the outer wall surface area under the main heater, I is the electric current read over the calibrated shunt circuit.

4 Compute bulk temperature rise by overall energy balance.

$$Q'' \text{ Total} = \pi(D_o{}^2 - D_i{}^2)\rho U_M C_p (T_b - T_{ent})/4 \tag{17}$$

$$\frac{dT}{dx} = \left(\frac{dT}{dx}\right)_b = \frac{T_b - T_{ent}}{L} \tag{18}$$

The bulk temperature gradient obtained in this manner is superior to the method described previously in item 2 due to the inevitable scatter in the wall measured temperature data as exemplified in Fig. 3.

5 Evaluate the net wall heat flux by estimating the heat losses. For heat losses directed inward the conduction heat transfer is negligible for the experimental range of the Reynolds numbers. Radiation exchange was 3–5 percent of the wall heat flux. For the lowest Reynolds numbers, the local free convection heat loss amounts to maximum 8 percent of the wall heat flux in the test section.

Combined conduction heat losses to outside and the convection-radiation heat losses to inside vary from a low of 5 percent to a high of 25 percent. For the majority of runs they fall between 12 and 14 percent. This loss is due mainly to a conduction heat loss through the 2.5 cm-thick fiberglass insulation.

6 Obtain local (h), and local (Nu) through their definitions. Nondimensionalize the test section and the wall temperatures using the definition

$$\theta = \frac{T - T_{ent}}{q''_{ow} \dfrac{D_H}{k}} \tag{19}$$

This form of nondimensionalizing of the temperature is appropriate for the constant heat flux boundary condition. The entrance temperature and the heat flux are the two primary experimental variables controlled during the tests. The form of the normalized temperatures eliminate these two variables as separate parameters to be considered.

Results and Discussion

Wall Temperature Distribution. Some sample results for the test section inner wall temperature distribution are plotted in Fig. 3.[3] The outer wall of the test section was heated electrically with a uniform heat flux. With this kind of heating, wall temperature attains a linear rise upon full development. The initial region has a parabolic rise. This character is well demonstrated in the following graphs; particularly in the pure axial flow cases. Results are plotted for the readings by 45 thermocouples located along the same generatrix of the outer cylinder.

The shape of the wall temperature curve for the pure axial flow shows that the test section attained full thermal development for all the heat flux rates studied. With imposition of rotation, wall temperature diminishes. As ζ decreases, rotational curves approach the nonrotational curve although the effect is still noticeable in the plots where ζ is as low as 0.56.

When ζ is large (around 2 or more) initially a local peaking occurs in the axial wall temperature distribution. The axial location of the peak is 6–8 D_H from the beginning of heating and rotation. The reason for the peak and subsequent dip is unknown. The peaking may be due to final development of the velocity field following rotation imparted on it at $x/D_H = 0$. If this is so, the flow field with rotation becomes developed in about 16 hydraulic dia. This figure is inferred from observations of the wall temperature curves with rotation. Finally, rotation caused an upward wiggle in the axial temperature profile near the end of the test section. This is particularly noticeable at higher ζs. This is an exit effect where the flow field is modified due to exit. The upward turn of the curve indicates a weakened rotational effect near the exit. An annular jet of air expands at the exit with the result that the rotation decays are felt upstream of the exit.

Radial Temperature Profiles. Samples of the measured radial temperature profiles are presented in Figs. 4 and 5. Radial temperatures are normalized using the same form as equation (19). The outer wall temperature shown in the plots are the computed inner wall temperature of the test section outer wall. The temperature profiles are very smooth. The curves are aligned in an orderly manner in passing from the uniform heat flux outer boundary to the adiabatic inner boundary. There is a large decrease of temperature near the outer wall. The profiles are strongly modified with inner cylinder rotation. The outer wall temperature drops sharply; then the profile continues toward the adiabatic inner wall with a slope gentler than the nonrotating case. The rotating profiles are appreciably flattened. With increased rotation, the inner boundary temperature increases. However, this "temperature recovery-like" effect does not change the nature of the inner boundary condition which is still an adiabatic wall.

The enhanced mixing due to flow rotation is suspected to be mainly responsible for the overall changes of the radial temperature profile in the test section. Near the inner wall, dissipation and increased turbulent mixing are both valid mechanisms to influence the profiles.

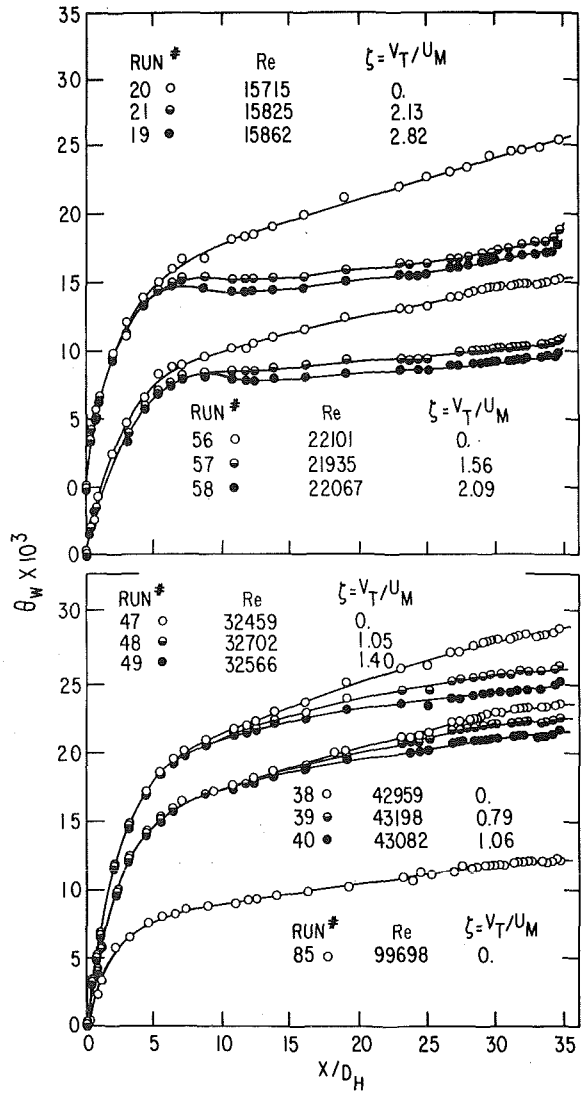

Fig. 3 Axial wall temperature profiles

Unfortunately, we do not have, as yet, turbulence data to assess the magnitudes of the velocity and temperature cross-correlations near the boundaries to understand the transfer mechanism involved.

The cross-over point of the radial temperature profiles in the test section also raises an interesting point. The cross-over point for the profiles is near the region of maximum axial velocity. This can be observed in most of the Figs. 4 and 5. A possible explanation may again be due to the $\overline{u'T'}$ correlations under the influence of the centrifugal forces of rotation.

Axial Nusselt Number Distribution. Plots of axial Nusselt numbers are relevant since they provide an additional check on the attainment of thermal development in the test section. Axial Nusselt numbers are presented in Figs. 6 and 7 for the pure axial flow and 2000 rpm mixed-mode cases. Nusselt number plots verify that there is complete thermal development in the test section. In fact, thermal development was attained within 18 to 20 D_H when the local Nu was within 5 percent of the asymptotic value.

Fully Developed Nusselt Numbers. Experimental data for Nu_o are shown in Fig. 8. Measurements of four other investigators are also shown on the same graph. There is reasonable agreement among all these results. Although air is used as the working fluid in all these experiments, the radius ratios of the test setups are not identical. Also shown in this figure is the conventional empirical relationship for Nu-Re.

[3] At this point it is appropriate to assert that in the graphical representation of the data for the mixed flow cases, the rotation ratio ζ rather than the rotation parameter α, is preferred to indicate the relative strength of the rotation. First, the two parameters differ only by a constant factor (α = constant · ζ). Second, and more importantly, ζ is more directly indicative of the relative strength of the rotation i.e., the inner cylinder peripheral velocity being significantly higher or lower than the mean axial velocity in the annulus.

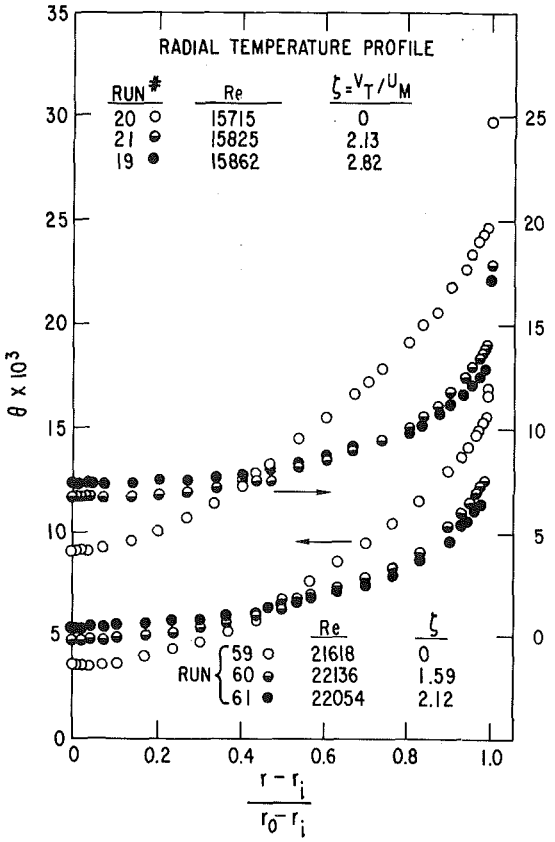

Fig. 4 Radial temperature profiles

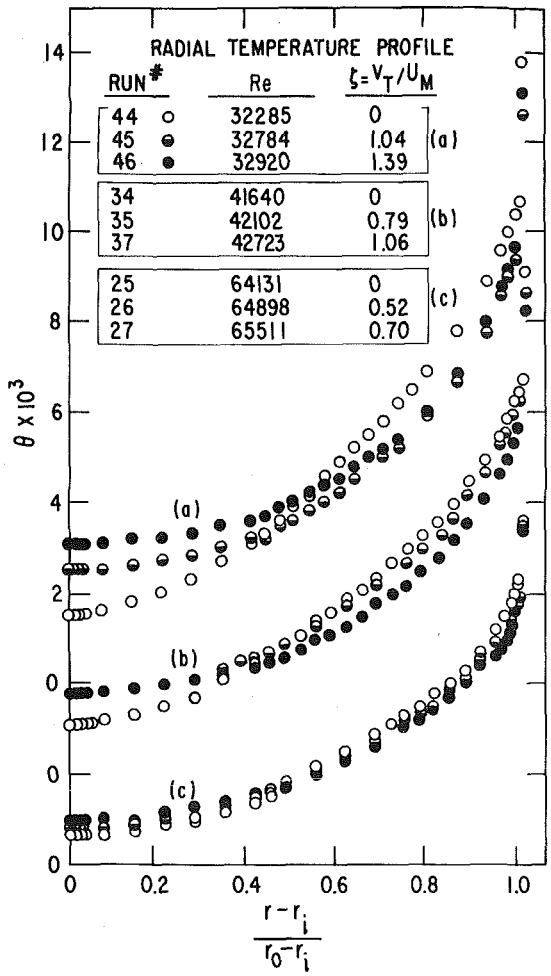

Fig. 5 Radial temperature profiles

In Fig. 9 the mixed-mode, fully developed Nu numbers are nondimensionalized with respect to pure axial flow Nusselt numbers (Nu_o). In the figure the high, medium, and low heat fluxes correspond to three runs at the same axial Re. Fig. 9 demonstrates the increased heat transfer from the outer wall in the mixed-mode flow cases. The trend is a nearly parabolic rise of Nu with ζ. In Fig. 10 all Nu data are replotted against Re to demonstrate effect of rotation in another manner. Open circles are the data points corresponding to mixed mode case. At a fixed Re, Nu increases with increasing ζ. Effect of ζ on the Nu is particularly strong at lower Reynolds numbers. Effect becomes negligible above Re = 50,000 for the highest rotation used in the present tests. The same experimental points are compared with the limited available data from other experimenters in Fig. 11. Apart from the effect of different radius ratio of the annuli, there is substantial agreement in the measurements. (Luke and Gazley's studies are for heat transfer from the inner cylinder.) An interesting point revealed in Fig. 11 is that rotation of the inner cylinder does not significantly affect Nu until the rotation ratio reaches a value about $\zeta = 0.8$. This may be the reason why investigators [11] chose to separate their heat transfer data in two regions: $\zeta \leq 1.1$ and $\zeta > 1.1$ for the heated helical flow in a narrow gap annulus.

A single correlation developed in reference [15] is (Fig. 12).

$$\frac{Nu_\phi}{Nu_o} = [(1 + \alpha^2)]^{0.8714} \tag{17}$$

The data deviate from this correlation curve by a maximum of 11 percent. Of the 44 total data points used in correlations, there are only 4 points with deviations over 10 percent. Most points deviate under ±5 percent.

Conclusions

Inner pipe rotation in annular flow produces significant effects on turbulent temperature field. These effects are easier to detect and measure when the rotation ratio $\zeta = V_T/U_M$ is larger than unity. In this study the rotation ratio varied between 0 and 2.80.

With inner cylinder rotation the temperature profile attained full development within the available 36 hydraulic dia length (possibly as short as 25 D_H) following the start of rotation and heating.

The primary effect of inner cylinder rotation was a flattening of the

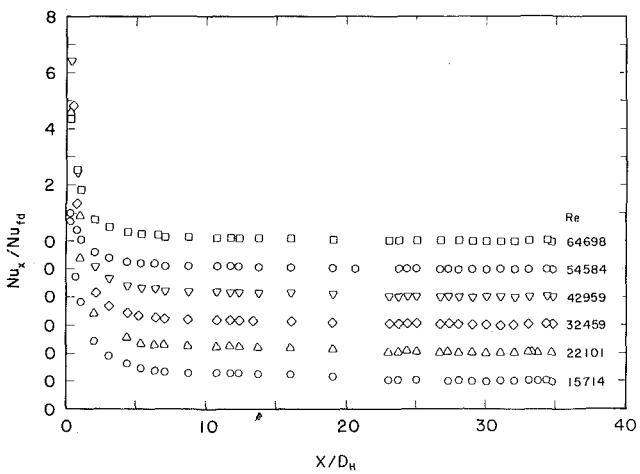

Fig. 6 Local Nusselt number variation for pure axial flow

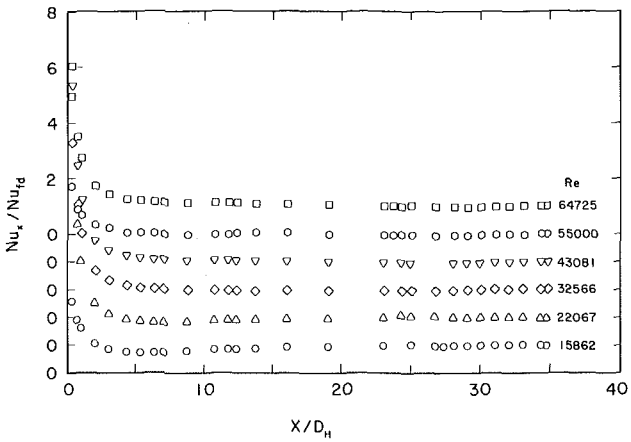

Fig. 7 Local Nusselt number variation in mixed flow at 2000 rpm

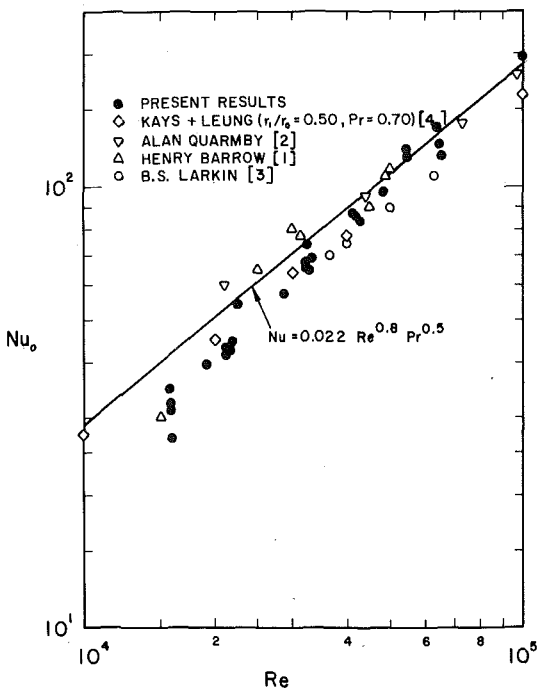

Fig. 8 Pure axial flow fully developed Nusselt number results

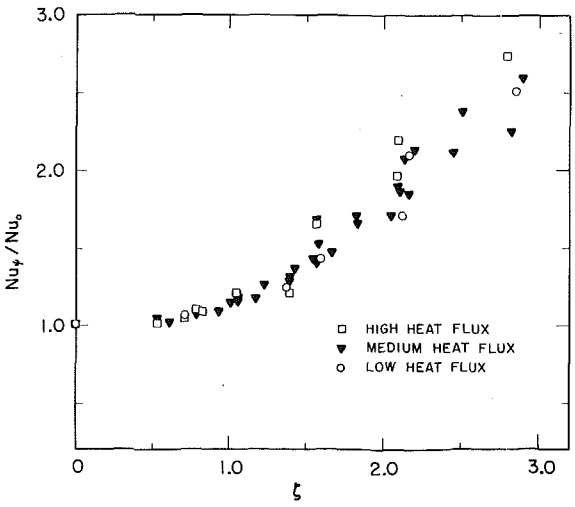

Fig. 9 Fully developed Nusselt number results versus rotation ratio for mixed flow

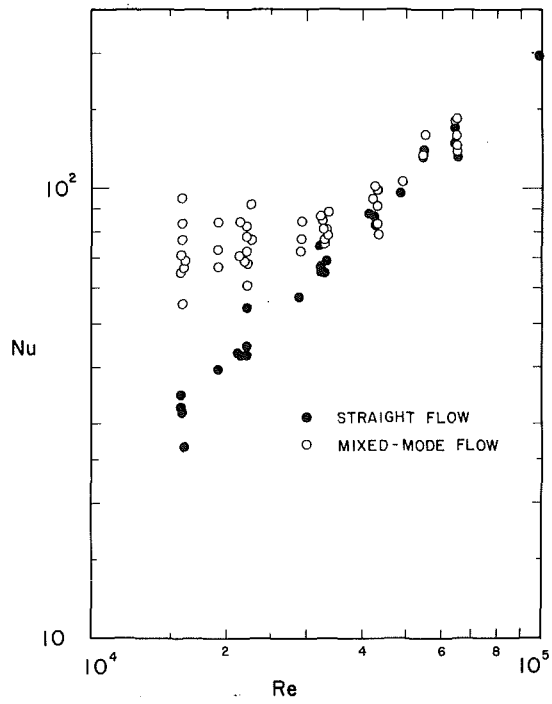

Fig. 10 Fully developed Nusselt number results versus Reynolds number; rotation ratio is the variable at fixed axial Reynolds number

radial temperature profiles over a large portion of the cross section. The temperature profile changed in the following manner: near the outer wall, which was a uniform heat flux boundary, temperatures were decreased resulting in steeper gradients; near the inner wall, which was an adiabatic boundary, the temperature profile still preserved its adiabatic character except that temperatures were increased, showing a temperature recovery-like effect.

A physical parameter was adopted that correlates the mixed-mode friction coefficient and Nusselt number data using the normal pure axial flow relations. This parameter is $2/\pi\ D_H/D_i\ V_T/U_M$ which is called the rotation parameter. It corresponds to inverse of the axial travel of the flow helix in terms of significant dimension of the flow

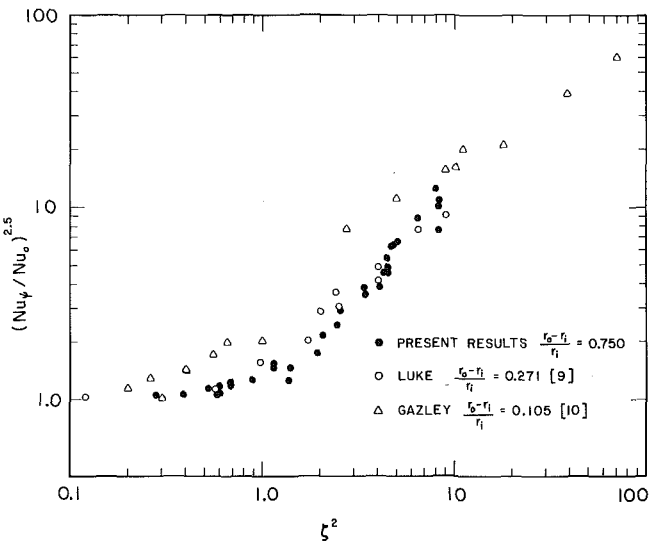

Fig. 11 Comparison of the fully developed Nusselt number results with other experiments

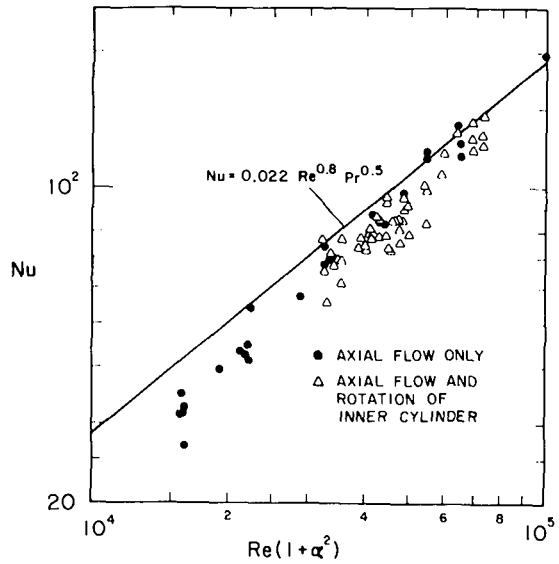

Fig. 12 Correlation of the fully developed Nusselt number with rotation parameter

geometry (D_H) per half revolution of the inner cylinder. With this parameter, the correlated form of the Nusselt number is as follows:

$$\frac{\mathrm{Nu}_\phi}{\mathrm{Nu}_o} = \left[1 + \left(\frac{2}{\pi}\frac{D_H}{D_i}\frac{V_T}{U_M}\right)^2\right]^{0.8714}$$

Acknowledgments

This research was partially supported by the U. S. Army Research Office-Durham, under contract number DAHCO4-67-C-0021.

References

1 Barrow, H., "Fluid Flow and Heat Transfer in an Annulus With a Heated Core Tube," *Proceedings of the Institution of Mechanical Engineers*, Vol. 169, 1955, pp. 1113–1123.

2 Quarmby, A., and Anand, R. K., "Turbulent Heat Transfer in the Thermal Entrance Region of Concentric Annuli With Uniform Wall Heat Flux," *International Journal of Heat and Mass Transfer*, Vol. 13, 1970, pp. 395–411.

3 Larkin, B. S., "Experimental Measurement of the Effect of Heat Flux on Local Heat Transfer Coefficient and Friction Coefficient in an Annulus," *Journal of Mechanical Engineering Science*, Vol. 7, No. 3, 1965, pp. 300 305.

4 Kays, W. M., and Leung, E. Y., "Heat Transfer in Annular Passages-Hydrodynamically Developed Turbulent Flow With Arbitrarily Prescribed Heat Flux," *International Journal of Heat and Mass Transfer*, Vol. 6, 1963, pp. 537 557.

5 Kaye, J., and Elgar, E. G., "Modes of Adiabatic and Diabatic Fluid Flow in an Annulus With an Inner Rotating Cylinder," JOURNAL OF HEAT TRANSFER TRANS. ASME, Vol. 80, No. 3, 1958, p. 753.

6 Bjorklund, J. S., and Kays, W. M., "The Heat Transfer Between Concentric Rotating Cylinders," JOURNAL OF HEAT TRANSFER, TRANS. ASME, Series C, Vol. 81, 1959, pp. 175 -186.

7 Becker, K. M., and Kaye, J., "The Influence of a Radial Temperature Gradient on the Instability of Flow in an Annulus With a Rotating Inner Cylinder," TRANS. ASME, May 1962, pp. 106–110.

8 Becker, K. M., and Kaye, J., "Measurement of Diabatic Flow in an Annulus With an Inner Rotating Cylinder," JOURNAL OF HEAT TRANSFER, TRANS. ASME, Series C, Vol. 84, May 1962, pp. 97–105.

9 G. E. Luke, "The Cooling of Electric Machines," TRANS. ASME, Vol. 42, 1923, p. 646.

10 Gazley, C., "Heat Transfer Characteristics of the Rotational Axial Flow between Concentric Cylinders," TRANS. ASME, Vol. 80, No. 1, 1958.

11 Tachibana, F., and Fukui, S., "Convective Heat Transfer of the Rotational and Axial Flow Between Two Concentric Cylinders," *Bull. of JSME*, Vol. 7, No. 26, 1964.

12 Zysina-Molozhen, L. M., and Polyak, M. P., "Heat Transfer in an Annulus Between Stationary and Rotating Coaxial Cylinders," *Teploenergetika*, Vol. 6, 1970, pp. 46 50.

13 Kosterin, S. I., Finatev, and Yu, P., Inzh-Fiz. Zh. 1963 (10) (was unavailable for review).

14 Hennecke, D. K., "Flow and Heat Transfer in a Rotating Cavity With Axial Throughflow," PhD thesis, University of Minnesota, July 1970.

15 Kuzay, T. M., "Turbulent Heat and Momentum Transfer Studies in an Annulus With Rotating Inner Cylinder," PhD thesis, University of Minnesota, Dec. 1973.

A. A. Shibani
Mechanical Engineering Department,
University of Alfaateh,
Tripoli, Libya

M. N. Özişik
Mechanical and Aerospace Engineering
Department, North Carolina State University,
Raleigh, N. C.

A Solution of Freezing of Liquids of Low Prandtl Number in Turbulent Flow Between Parallel Plates

The steady-state freezing of liquids of low Prandtl number in turbulent flow between parallel plates, the walls of which are kept at uniform temperature lower than the freezing temperature of the liquid, is solved by matched asymptotic technique. The location of the liquid-solid interface and the heat transfer rate are established as a function of the axial position along the channel.

Introduction

Only a limited amount of research has been done on the subject of phase change involving freezing of liquids flowing inside ducts; this is due to the difficulty arising from the influence of the flow field on the thermal behavior of the liquid phase. Therefore, various approximate procedures have appeared in the literature in recent years. The first significant work on this subject was reported by Zerkle and Sunderland [1][1] for the case of steady-state laminar flow inside circular tubes with solidification. This work was later extended by Des Ruisseaux and Zerkle [2] to study the parameters needed for the establishment of steady state conditions, and by Zerkle [3] to investigate the effects of external insulation on freezing. Özişik and Mulligan [4] considered the transient freezing of a liquid flowing under laminar flow conditions in circular tubes. A variational method of solution used by Bilenas and Jiji [5] for the investigation of the same problem was in good agreement with the results obtained by Özişik and Mulligan [4]. Recently Lock and Nyren [6] applied a perturbation technique to study freezing inside circular tubes.

The problem of internal freezing under turbulent flow conditions is even more involved than that of corresponding laminar because of the complicated transport mechanisms. In the present study we utilize the analysis developed previously by Shibani and Özişik [7] to treat the heat transfer to turbulent flow between parallel plates by the matched asymptotic technique. The results are applicable for liquids with low Prandtl number, that is for liquid metals.

Analysis

Consider the freezing of an incompressible liquid flowing in steady, fully developed, turbulent flow between two smooth, straight parallel plates with the walls kept at a uniform temperature T_1 which is lower than the liquid freezing temperature T_f. The liquid enters the conduit at a uniform and constant temperature T_0 which is greater than T_f. As the liquid flows through, a freeze layer is formed on the inside surface of the wall with thickness increasing along the x-axes as illustrated in Fig. 1. In developing the mathematical model for the analysis it is assumed that the physical properties at each phase remain constant, the problem possesses symmetry about the axial plane, the flow is fully developed, the liquid-solid interface is at the freezing temperature and the axial heat conduction is negligible. The last assumption for the liquid phase is valid for $\mathrm{Pe} > 100$. Then, the energy equation for the liquid phase is taken as

$$u\frac{\partial T_\ell}{\partial x} = \frac{\partial}{\partial y}\left[(\alpha + \epsilon_H)\frac{\partial T_\ell}{\partial y}\right] \quad \text{in} \quad 0 \le y \le \delta, x > 0 \quad (1a)$$

subject to the boundary conditions

$$T_\ell(y, 0) = T_0, \qquad T_\ell(\delta, x) = T_f, \qquad \frac{\partial T_\ell(0, x)}{\partial y} = 0 \quad (1b)$$

The fully developed flow assumption considered in the above formulation is not strictly justified because the flow channel has a vari-

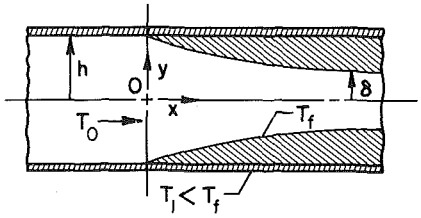

Fig. 1 The coordinate system for freezing of liquid inside parallel plates.

[1] Numbers in brackets designate References at end of paper.

Contributed by the Heat Transfer Division for publication in the JOURNAL OF HEAT TRANSFER. Manuscript received by the Heat Transfer Division June 8, 1976.

able cross-sectional area and consequently $\partial u/\partial x \neq 0$ and $v \neq 0$. Therefore, ignoring the term $v\,\partial T_\ell/\partial y$ in the energy equation (1a) needs some justification. If the velocity component $v(x,y)$ is related to $u(x, y)$ by the integration of the continuity equation and the axial velocity profile is represented by a power-law in the form $u(x, y) = Cu_m(h/\delta)\,[1 - (y/\delta)]^{1/m}$, it can be shown that in equation (1a) the term $v\,\partial T_\ell/\partial y$ can be neglected in comparison to the term $u\,\partial T_\ell/\partial x$ when $(\partial T_\ell/\partial x) \gg (d\delta/dx)\,(\partial T_\ell/\partial y)$. Clearly, this condition is valid so long as the profile of the freeze layer $\delta(x)$ remains a slowly varying function of the position.

The equation for the solid phase is taken as

$$\frac{d^2T_s}{dy^2} = 0, \qquad \text{in } \delta \le y \le h, \qquad x > 0 \tag{2a}$$

with the boundary conditions

$$T_s(h, x) = T_1 \qquad \text{and} \qquad T_s(\delta, x) = T_f \tag{2b}$$

The foregoing two equations are coupled with the energy balance equation at the liquid-solid interface given as

$$k_\ell \frac{\partial T_\ell(\delta, x)}{\partial y} = k_s \frac{\partial T_s(\delta, x)}{\partial y} \tag{3}$$

Here, x and y are the axial and transverse coordinates, u is the axial velocity, T_ℓ and T_s are the temperatures of the liquid and solid phases, α and ϵ_H are the molecular and eddy diffusivities of heat, k_ℓ and k_s are the thermal conductivities of the liquid and the solid, respectively.

The foregoing equations are now expressed in a dimensionless form. Equations (1) for the liquid phase become

$$\Delta(\xi)f(\eta)\frac{\partial\theta_\ell}{\partial\xi} = \frac{\partial}{\partial\eta}\left[\epsilon(\eta)\frac{\partial\theta_\ell}{\partial\eta}\right] \qquad \text{in } 0 \le \eta \le 1, \qquad \xi > 0 \tag{4a}$$

$$\theta_\ell(\xi, 1) = 0, \qquad \theta_\ell(0, \eta) = 1, \qquad \frac{\partial\theta_\ell(\xi, 0)}{\partial\eta} = 0 \tag{4b}$$

Equations (2) for the solid phase become

$$\frac{d^2\theta_s}{d\eta^2} = 0 \qquad \text{in } 1 \le \eta \le 1/\Delta, \qquad \xi > 0 \tag{5a}$$

with the boundary conditions

$$\theta_s(1/\Delta, \xi) = \theta_1 \qquad \text{and } \theta_s(1, \xi) = 0 \tag{5b}$$

And the liquid-solid interface equation (3) becomes

$$\frac{\partial\theta_\ell(1, \xi)}{\partial\eta} = \frac{k_s}{k_\ell}\frac{\partial\theta_s(1, \xi)}{\partial\eta} \tag{6}$$

where various dimensionless variables are defined as

$$\eta = \frac{y}{\delta}, \qquad \Delta = \frac{\delta}{h}, \qquad \epsilon(\eta) = \frac{\alpha + \epsilon_H}{\alpha} = 1 + \frac{\Pr}{\Pr_t}\frac{\epsilon_m}{\nu'}, \tag{7a}$$

$$\theta_\ell = \frac{T_\ell - T_f}{T_0 - T_f}, \qquad \theta_s = \frac{T_s - T_f}{T_0 - T_f}, \qquad \theta_1 = \frac{T_1 - T_f}{T_0 - T_f} \tag{7b}$$

$$\xi = \frac{16x}{cD_e\Pr\cdot\mathrm{Re}}, \qquad D_e = 4h, \qquad c = \frac{1+m}{m} \tag{7c}$$

$$f(\eta) = \frac{u}{cu_m} = (1 - \eta)^{1/m} \tag{7d}$$

where u_m is the bulk mean velocity. The values of the exponent m for the power law velocity depend on the Reynolds number and the total diffusivity of heat $\epsilon(\eta)$ varies with the distance from the wall, Reynolds and Prandtl numbers; both m and $\epsilon(\eta)$ are computed as described in references [7, 8]. A brief explanation of the determination of $\epsilon(\eta)$ is given in the Appendix. In computing $\epsilon(\eta)$ it is assumed that the turbulence itself is unaffected by the curved interface position $\delta(x)$ because of the assumption that $\delta(x)$ is a slowly varying function of position. The quantity $(1/\delta)\,(d\delta/dx)$ characterizes the fractional change of the flow channel width in the direction of flow, consequently, the variation of the flow passage area is considered small so long as this term remains small. In the present analysis a power-law velocity profile is used for the energy equation, it is shown in reference [7] that the heat transfer results obtained from the solution of the energy equation by using a power law velocity profile are in close agreement with those obtained by using the usual logarithmic velocity profile.

Appropriate eigenvalue problem for the solution of equation (4a) is given as

$$\frac{d}{d\eta}\left[\epsilon(\eta)\frac{dH_n(\eta)}{d\eta}\right] + \lambda_n{}^2 f(\eta)\,H_{(\eta)} = 0 \tag{8a}$$

subject to the boundary conditions

$$H'(0) = 0, \qquad H(1) = 0 \tag{8b}$$

with the normalizing condition taken as

$$H(0) = 1 \tag{8c}$$

where H_n and λ_n are the eigenfunctions and eigenvalues, respectively, and the prime denotes differentiation with respect to η.

Nomenclature

A_n = constant defined by equation (12)
c = constant defined by equation (7c)
c' = specific heat
$D_e = 4h$ = equivalent diameter
$f(\eta) = \dfrac{u}{cu_m}$ = dimensionless velocity defined by equation (7d)
F_n = constant defined by equation (10)
G = constant defined by equation (18b)
h = one-half the distance between the plates
H_n = the nth eigenfunction
k = thermal conductivity
m = exponent in the power law velocity
$\Pr = \dfrac{\nu'}{\alpha}$ = Prandtl number
$\Pr_t = \dfrac{\epsilon_m}{\epsilon_H}$ = turbulent Prandtl number
q = heat transfer rate per unit width of the plates
Q = dimensionless heat transfer rate defined by equation (13b)
$\mathrm{Re} = \dfrac{D_e u_m}{\nu'}$ = Reynolds number
T = temperature
T_0 = temperature at the inlet ($x = 0$)
u = mean velocity
u_m = bulk mean velocity
x = axial variable
y = transverse coordinate
α = thermal diffusivity
$\Gamma(P)$ = Gamma function of argument P
$\delta(x)$ = the half width of flow channel
$\Delta(x) = \delta/h$, the dimensionless half width of flow channel
$\epsilon(\eta)$ = dimensionless total diffusivity defined by equation (7a)
ϵ_H = eddy diffusivity of heat
ϵ_m = eddy diffusivity of momentum
η = dimensionless transverse coordinate
θ = dimensionless temperature profile
$\bar{\theta} = (k_s/k_\ell)[T_f - T_1)/T_0 - T_f)]$, dimensionless freezing parameter defined by equation (15b)
λ_n = the nth eigenvalue
ν = constant defined by equation (18a)
ν' = kinematic viscosity
$\xi = \dfrac{16x}{cD_e\Pr\,\mathrm{Re}}$ = dimensionless axial variable
φ_1 = constant defined by equation (18a)

Subscripts

f = freezing conditions
ℓ = liquid phase
s = solid phase
0 = channel center or inlet
1 = channel wall

Then the temperature distribution in the liquid phase is now taken in the form

$$\theta_\ell(\eta, \xi) = \sum_{n=0}^{\infty} F_n H_n(\eta) \cdot \exp\left[-\lambda_n^2 \int_0^\xi \frac{d\xi'}{\Delta(\xi')}\right] \tag{9}$$

and the F_n are evaluated by utilizing the boundary condition at $\xi = 0$, which results in the relation,

$$\sum_{n=0}^{\infty} F_n H_n = 1;$$

the orthogonality property of the eigenfunctions leads to the determination of F_n as

$$F_n = -\frac{2}{\lambda_n \dfrac{\partial H(1)}{\partial \lambda_n}} \tag{10}$$

The temperature gradient at the liquid-solid interface is obtained from equations (9) and (11) as

$$-\frac{\partial \theta_\ell(1, \xi)}{\partial \eta} = 2 \sum_{n=0}^{\infty} A_n \cdot \exp\left[-\lambda_n^2 \int_0^\xi \frac{d\xi'}{\Delta(\xi')}\right] \tag{11}$$

$$A_n = -\frac{F_n H_n'(1)}{2} \tag{12}$$

and the heat transfer rate from the liquid at the liquid-solid interface is determined from the relation

$$q = 2k_\ell \int_0^x \left[-\frac{\partial T_\ell(\delta, x')}{\partial y}\right] dx' \tag{13a}$$

which is written in the dimensionless form as

$$Q = \frac{q}{chu_{0,m}\rho c'(T_0 - T_f)} = \frac{2}{\Delta(\xi)} \int_0^\xi \left[-\frac{\partial \theta_\ell(1, \xi')}{\partial \eta}\right] d\xi' \tag{13b}$$

Here, $u_{0,m}$ is the bulk mean velocity at $\xi = 0$, and ρ and c' are the density and the specific heat of liquid, respectively. By use of the relation (11), equation (13b) becomes

$$Q = \frac{4}{\Delta(\xi)} \sum_{n=0}^{\infty} A_n \int_0^\xi \exp\left[-\lambda_n^2 \int_0^{\xi'} \frac{d\xi''}{\Delta(\xi'')}\right] d\xi' \tag{13c}$$

The temperature distribution in the solid phase is obtained from equations (5) as

$$\theta_s = \frac{\Delta(\xi)}{(1 - \Delta(\xi))} \theta_1(\eta - 1) \tag{14a}$$

and the temperature gradient at the liquid-solid interface becomes

$$\frac{\partial \theta_s(1, \xi)}{\partial \eta} = \frac{\Delta(\xi)\theta_1}{(1 - \Delta(\xi))} \tag{14b}$$

Finally, the expression for the location of the liquid-solid interface, Δ, is obtained by substituting the values of the derivatives $\partial\theta_\ell/\partial\eta$ and $\partial\theta_s/\partial\eta$ from equations (11) and (14b), respectively, in the interface relation (6)

$$\Delta(\xi) = \frac{1}{1 + \bar{\theta} \Big/ \left[2 \sum_{n=0}^{\infty} A_n \cdot \exp\left(-\lambda_n^2 \int_0^\xi \frac{d\xi'}{\Delta(\xi')}\right)\right]} \tag{15a}$$

where the freezing parameter $\bar{\theta}$ is defined as

$$\bar{\theta} = \frac{k_s}{k_\ell} \cdot \left(\frac{T_f - T_1}{T_0 - T_f}\right) \tag{15b}$$

The relations (13c) for the heat flux, Q, and (15a) for the radius of the liquid-solid interface, $\Delta(\xi)$, involve the eigenvalues λ_n^2 and the constants A_n. These quantities are determined from the solution of the eigenvalue problem given by equations (8). Although the first few eigenvalues and eigenfunctions can be obtained by purely numerical means, the numerical solutions become less accurate as the value of n increases. Unfortunately, for the case of low Prandtl number, a large number of eigenvalues and eigenfunctions are needed for the convergence of series forming the solution. Therefore, a combination of a numerical and a matched asymptotic expansion technique is used to determine the eigenvalues λ_n^2 and the constants A_n over a large spectrum of n as now described.

The Computer Calculations of λ_n^2 and A_n. The first four of these eigenvalues and the constants are determined by solving the foregoing eigenvalue problem numerically with a digital computer in double precision arithmetic and the resulting values of λ_n^2 and A_n are presented in Table 1.

The Analytic Solution of λ_n^2 and A_n. The eigenvalues λ_n^2 and the constants A_n are determined analytically by solving the eigenvalue problem given by equations (8) by a matched asymptotic expansion technique as described in reference [7]. The resulting values of the eigenvalues λ_n and the constants A_n which can be used for $n \geq 3$ are given as

$$\lambda_n = \frac{n\pi + \varphi_1}{G} \tag{16}$$

and

$$A_n = \frac{\sin(\pi\nu) \cdot (\nu\lambda_n)^{2\nu}\Gamma(1 - \nu)}{G\lambda_n\Gamma(1 + \nu)} \tag{17}$$

where

$$\varphi_1 = \frac{\pi}{2}\left(\frac{1}{2} + \nu\right), \qquad \nu = \frac{m}{1 + 2m} \tag{18a}$$

and

$$G = \int_0^1 \sqrt{f(\eta)/\epsilon(\eta)}\, d\eta \tag{18b}$$

Here $\Gamma(p)$ is the Gamma function of argument p. The parameter G in equations (16) and (17) is constant for a given Reynolds and Prandtl number. This constant is determined by numerical integration and the resulting values for Re = 10^4 are given in Table 2 for different values of Prandtl number.

Results

The values of λ_n^2 and A_n given in Table 1 combined with those from the asymptotic formulas given by equations (16) and (17) are substituted into equations (15a) and (13c) to determine the location of the liquid-solid interface, $\Delta(\xi)$, and the heat transfer rate, Q, respectively. An iterative procedure is applied to compute $\Delta(\xi)$ from equation (15a) since the quantity $\Delta(\xi)$ appears in both sides of that equation. These quantities are a function of the dimensionless axial

Table 1 Eigenvalues λ_n^2 and constants A_n for Re = 10^4

Prandtl Number	λ_0^2	λ_1^2	λ_2^2	λ_3^2	A_0	A_1	A_2	A_3
0.0	2.6383	25.421	71.500	140.95	.95037	.86528	.83120	.81033
.002	2.6410	25.440	71.550	141.06	.95106	.86569	.83146	.81082
.004	2.6486	25.520	71.789	141.54	.95408	.86754	.83264	.81134
.01	2.718	26.26	74.00	145.98	.9820	.8845	.8434	.8187
.02	2.9786	29.041	82.241	162.68	1.08542	.94565	.88087	.84423
.04	3.737	37.41	107.46	214.10	1.3912	1.1075	.9706	.9044

Table 2 The constant G for $Re = 10^4$

Prandtl Number	0	.002	.004	.01	.02	.04
G	.91907	.91871	.91711	.90268	.85412	.74282

position ξ, the freezing parameter $\bar{\theta}$, Prandtl number, and Reynolds number. Our calculations in the range $10^4 < Re < 10^6$ have shown that the Reynolds number has only negligible effect on both the location of the dimensionless liquid-solid interface and the heat transfer rate. Therefore, the following results presented for the case of $Re = 10^4$ only are also applicable up to $Re = 10^6$. Table 2 lists the values of the constants G appearing in equations (16) and (17) for the determination of eigenvalues λ_n and the constants A_n. The results in Tables 1 and 2 are limited to low Prandtl numbers, which are applicable to liquid metals. Actually for the case of high Prandtl number one need not go through the process of asymptotic expansion technique. Recently Hwang and Sheu [9] studied liquid solidification both analytically and experimentally for laminar flow inside a circular tube. One of the assumptions made in their analysis, as in the present one, included the slow variation of $\delta(x)$ along the channel. Based on the agreement between their analytical and experimental results, it appears that this assumption is a reasonable one. Although the effects of free convection may be important for freezing in laminar flow as pointed out by Zerkle and Sunderland [1], in the experimental investigation of reference [9] this effect was suppressed by using a tube of small diameter. In the case of freezing in turbulent flow considered in the present work, the free convection effects are negligible.

In Fig. 2, the dimensionless position of the liquid-solid interface $\Delta(\xi)$ is plotted versus the dimensionless axial position ξ for Prandtl numbers of 0 and 0.04 and for the values of the freezing parameter $\bar{\theta}$ equal to 0.5, 1, 1.5, and 2.5. It is apparent that for a given $\bar{\theta}$ the variation of Prandtl number from 0 to 0.04 has little effect on the position of the liquid-solid interface. It is also apparent that the thickness of the liquid-solid interface increases with increasing value of the freezing parameter $\bar{\theta}$. That is, a larger value of $\bar{\theta}$ implies a larger cooling rate, for example, as affected by a lower wall temperature; and the result is a thicker freeze layer. The curves are terminated before the closure of the flow passage, because the present analysis is not applicable when the closure takes place.

Fig. 3 shows a plot of the dimensionless total heat transfer rate Q per unit width of the plates as a function of the dimensionless axial position ξ for Prandtl number of 0.01 and $\bar{\theta}$ equal to 0.5, 1, 1.5, 2, and 2.5. The effect of θ on Q is similar to that on Δ; that is increased value

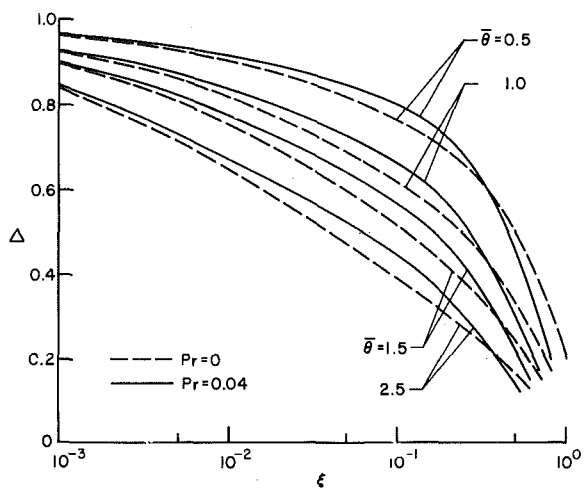

Fig. 2 Effects of Prandtl number and the parameter $\bar{\theta}$ on the location of liquid-solid interface.

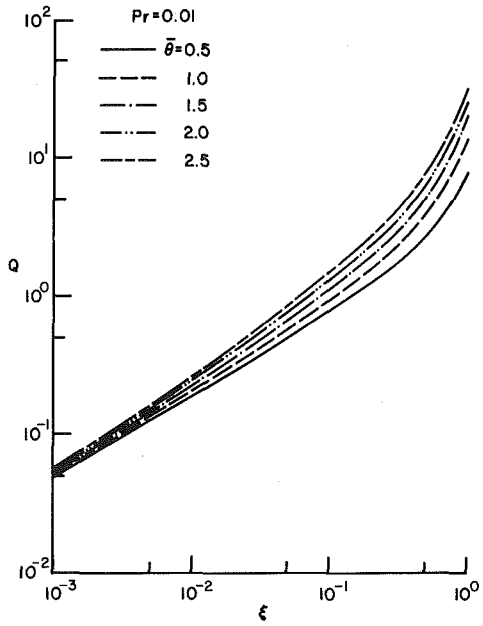

Fig. 3 Effects of the parameter $\bar{\theta}$ on the rate of heat transfer for freezing of liquids in turbulent flow between parallel plates.

of the parameter $\bar{\theta}$ results in an increase in the total heat transfer rate. The results are presented here only for a Prandtl number 0.01, because there is little difference in the results in the range of Prandtl numbers from zero to about 0.04.

Acknowledgment

This investigation was supported in part by the United States National Science Foundation.

References

1 Zerkle, R. D., and Sunderland, J. E., "The Effect of Liquid Solidification in a Tube Upon the Laminar-Flow Heat Transfer and Pressure Drop," ASME Paper No. 67-HT-40, 1967.

2 Des Ruisseaux N., and Zerkle, R. D., "Freezing of Hydraulic Systems," ASME Paper No. 68-HT-40, 1967.

3 Zerkle, R. D., "The Effects of External Thermal Insulation on Liquid Solidification in a Tube," *Proceedings of the Sixth Southeastern Seminar on Thermal Sciences*, 1970, pp. 1–19.

4 Özişik, M. N., and Mulligan, J. C., "Transient Freezing of Liquids in Forced Flow Inside Circular Tubes," JOURNAL OF HEAT TRANSFER, TRANS. ASME Series C, Vol. 91, 1969, p. 385.

5 Bilenas, J. A., and Jiji, L. M., "Axisymmetric Fluid Flow in Tubes With Surface Solidification," *J. Franklin Inst.*, Vol. 289, 1970, p. 265.

6 Lock, G. S. H., and Nyren, R. H., "Analysis of Fully Developed Ice Formation in a Convectively-Cooled Tube," *International Journal of Heat and Mass Transfer*, Vol. 14, 1971, p. 825.

7 Shibani, Ali A., and Özişik, M. N., "A Solution to Heat Transfer in Turbulent Flow between Parallel Plates," *International Journal of Heat and Mass Transfer* (in press).

8 Notter, R. H., and Sleicher, C. A., "A Solution of Turbulent Graetz Problem-III, Fully Developed and Entry Region Heat Transfer Rates," *Chem. Eng. Sci.*, Vol. 27, 1972, p. 2073.

9 Hwang, G. J., and Sheu, J. P., "Liquid Solidification in Combined Hydrodynamic and Thermal Entrance Region of a Circular Tube," *Can. J. Chem. Eng.*, Vol. 54, 1976, p. 66.

APPENDIX

The total eddy diffusivity of heat $\epsilon(\eta)$ is defined as

$$\epsilon(\eta) \equiv \frac{\alpha + \epsilon_H}{\alpha} = 1 + \Pr\frac{\epsilon_H}{\nu'} = 1 + \frac{\Pr}{\Pr_t}\frac{\epsilon_m}{\nu'} \qquad \text{(A-1)}$$

Assuming the shear stress varies linearly with the distance from the wall, we write

Table A-1 Values of $\frac{u_m}{u_{max}}$ and m

Reynolds Number	$\frac{u_m}{u_{max}}$	m
10^4	.788	5.890
5×10^4	.821	7.198
10^5	.832	7.748
5×10^5	.857	9.310
10^6	.865	9.930

$$\frac{\epsilon_m}{\nu'} = \frac{\left.\frac{\partial u}{\partial z}\right|_{z=0} \cdot \eta}{\frac{\partial u}{\partial z}} - 1 \qquad \text{(A-2)}$$

where the velocity distribution is taken as

$$u^+ = \frac{1}{0.091}\tan^{-1}(0.091\ Y^+), \qquad 0 < Y^+ < 45 \qquad \text{(A-3}a\text{)}$$

$$u^+ = 5.1 + 2.5\ \ell n\ Y^+, \qquad 45 < Y^+ < \left[\frac{\mathrm{Re}}{2}\sqrt{f_m/8}\,z\right]_{z=0.15} \qquad \text{(A-3}b\text{)}$$

$$u^+ = \frac{u_{max}}{u_m}\cdot\frac{1}{\sqrt{f_m/8}} - h(z), \qquad Y^+ > \left[\frac{\mathrm{Re}}{2}\sqrt{f_m/8}\,z\right]_{z=0.15} \qquad \text{(A-3}c\text{)}$$

where

$$u^+ = f/\sqrt{f_m/8}, \qquad Y^+ = \frac{\mathrm{Re}}{2}\sqrt{f_m/8}\cdot z \text{ and} \qquad z = 1-\eta$$

and the values of u_{max}/u_m are tabulated in Table A-1. The friction factor f_m and the velocity defect law $h(z)$ are given as

$$f_m = 1/[2\log(\mathrm{Re}\sqrt{f_m}) - 0.8]^2, \qquad h(z) = 5.75\log(1/z) \qquad \text{(A-4)}$$

The turbulent Prandtl number, Pr_t, needed in equation (A-1) is taken for $\mathrm{Pr} \le 1$ as suggested by Notter and Sleicher [8], as

$$\frac{1}{\mathrm{Pr}_t} = \frac{0.025\ \mathrm{Pr}\frac{\epsilon_m}{\nu'} + 90\ \mathrm{Pr}^{3/2}\left(\frac{\epsilon_m}{\nu'}\right)^{1/4}}{1 + 90\ \mathrm{Pr}^{3/2}\left(\frac{\epsilon_m}{\nu'}\right)^{1/4}}\left(1 + \frac{10}{35 + \frac{\epsilon_m}{\nu'}}\right) \qquad \text{(A-5)}$$

In the case of the power law velocity profile the values of the exponent m are computed from the relation

$$m = 2/(\sqrt{1 + 8u_{max}/u_m} - 3) \qquad \text{(A-6)}$$

M. H. Sadd
J. E. Didlake[1]

Department of Mechanical Engineering,
Mississippi State University,
Mississippi State, Miss.

Non-Fourier Melting of a Semi-Infinite Solid

The melting of a semi-infinite solid subjected to a step change in temperature is solved according to a non-Fourier heat conduction law postulated by Cattaneo and Vernotte. Unlike the classical Fourier theory which predicts an infinite speed of heat propagation, the non-Fourier theory implies that the speed of a thermal disturbance is finite. The effect of this finite thermal wave speed on the melting phenomenon is determined. The problem is solved by following a similar method as used by Carslaw and Jaeger for the corresponding Fourier problem. Non-Fourier results differ from Fourier theory only for small values of time. Comparing the temperature profiles and the solid-liquid interface location for aluminum, differences between the two theories were significant only for times on the order of 10^{-9}–10^{-11} s and in a region within approximately 10^{-4}–10^{-5} cm from the boundary surface. However, these results are based on an approximate value of the thermal relaxation time.

Introduction

The heat transfer problem that describes the change of state which occurs with melting or solidification has numerous practical applications, and has been studied in quite some detail (see the review article by Muehlbauer and Sunderland [1][2]). The first discussion of this heat transfer problem was given by Stefan [2] in 1891, from which the title *Stefan's Problem* originated. These melting and solidification problems are rather complicated because of several factors:

1 the interface between the solid and liquid phases moves with an *unknown motion* as latent heat is absorbed or liberated,

2 thermal and mechanical properties of the two phases are in general not the same,

3 the matching conditions at the interface cause the problem to be *nonlinear*.

Carslaw and Jaeger [3] presented an exact solution to the one-dimensional, semi-infinite melting or freezing problem using existing half space solution forms for the temperature profiles in the solid and liquid phases. By satisfying the heat balance and temperature continuity across the phase-change interface, they met all the conditions on the problem. Additional exact and approximate solutions to one- and two-dimensional Stefan-type problems are referenced in [1]. More recent work in this area has been in numerical methods for multidimensional problems.

A review of this literature indicates that all previous studies of the change-of-state heat transfer problem are based on the Fourier heat conduction law

$$q = -k\nabla T \tag{1}$$

Equation (1) along with the conservation of energy gives the *classical parabolic heat equation*

$$\alpha\nabla^2 T = \frac{\partial T}{\partial t} \tag{2}$$

Many investigators [4, 5] have pointed out that Fourier's model possesses several serious shortcomings, the most prominent being the implication of an *infinite speed of heat propagation.* Cattaneo [6, 7] and later Vernotte [8, 9] independently postulated a damped wave model for heat conduction in solids of the form

$$q = -k\nabla T - \tau\frac{\partial q}{\partial t} \tag{3}$$

The quantity τ is called the *material thermal relaxation time* and physically is a result of a finite thermal communication time between material points. Equation (3) combined with the conservation of energy for rigid media gives the *hyperbolic heat conduction equation*

$$\alpha\nabla^2 T = \frac{\partial T}{\partial t} + \tau\frac{\partial^2 T}{\partial t^2} \tag{4}$$

which can also be written as

$$c^2\nabla^2 T = \frac{1}{\tau}\frac{\partial T}{\partial t} + \frac{\partial^2 T}{\partial t^2} \tag{5}$$

where $c^2 = \alpha/\tau$ represents the speed of propagation of thermal signals modeled by equations (3)–(5). Equation (5), sometimes known as the *telegraph equation,* has solutions which take the form of waves propagating through the media at constant speed, c, while decaying

[1] Presently at Sandia Laboratories, Livermore, Calif.

[2] Numbers in brackets designate References at end of paper.

Contributed by the Heat Transfer Division for publication in the JOURNAL OF HEAT TRANSFER. Manuscript received by the Heat Transfer Division April 16, 1976.

in amplitude exponentially with time.

With regard to this theory, the heat flux vector can be expressed explicitly by solving equation (3); the result is

$$\underline{q} = -\frac{k}{\tau}\int_0^t \underline{\nabla} T e^{-(t-\xi)/\tau}\, d\xi \tag{6}$$

Other more general non-Fourier conduction laws of the form of equation (6), i.e., linear integral relations, have also been proposed [5].

Many investigators have pointed out that the effect of a finite speed of propagation is negligible for *most* practical heat transfer applications since the thermal diffusivity is usually several orders of magnitude less than the square of the wave speed. However, several other investigators [10–14] have demonstrated that for many *special* applications such as situations at *cryogenic temperatures, short times,* or *high heat fluxes,* finite wave speed theory can become important. Furthermore, with the advent of laser penetration and welding, explosive bonding, fast flux nuclear reactors, and electrical discharge machining, short time, high heat flux melting situations are becoming more prevalent.

With this in mind, and realizing that no analysis has been done for the melting (or freezing) problem using a non-Fourier theory, the purpose of the present article is to solve the one-dimensional melting problem of a semi-infinite body using the Cattaneo-Vernotte non-Fourier heat conduction theory. The method of attack will parallel the technique used by Carslaw and Jaeger [3] for the Fourier problem, and comparisons with the Fourier theory will be made.

Melting Problem

The problem of the one-dimensional melting of a semi-infinite body is solved here according to the Cattaneo-Vernotte non-Fourier theory given by equations (3)–(6). The body is assumed to occupy the region of space $x \geq 0$, and to be initially at a uniform temperature T_0. The surface temperature at $x = 0$ is suddenly brought to T_w at $t = 0$, and is maintained at T_w for $t > 0$. If T_m is the melting temperature of the medium, then the inequalities, $T_0 < T_m < T_w$ will hold. At any time $t > 0$, the body will be composed of two portions, one solid and one liquid, separated by a moving interface. The location of this phase-change interface will be denoted by $x = s(t)$, and is an unknown in the problem; see the schematic in Fig. 1.

In the liquid portion of the body, $0 < x < s(t)$, the problem is formulated by

$$\alpha_\ell \frac{\partial^2 T_\ell}{\partial x^2} = \frac{\partial T_\ell}{\partial t} + \tau_\ell \frac{\partial^2 T_\ell}{\partial t^2} \tag{7}$$

with

$$T_\ell(0, t) = T_w H(t) \tag{8}$$

where $H(t)$ is the unit Heaviside step function. Likewise, in the solid portion of the body, $s(t) < x < \infty$, the formulation is

$$\alpha_s \frac{\partial^2 T_s}{\partial x^2} = \frac{\partial T_s}{\partial t} + \tau_s \frac{\partial^2 T_s}{\partial t^2} \tag{9}$$

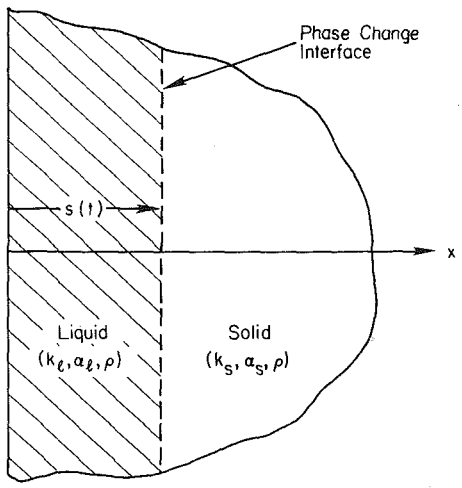

Fig. 1. Schematic of the one-dimensional melting geometry

with

$$T_s(\infty, t) = T_0 \tag{10}$$

At the interface between the solid and liquid phases, the continuity of temperature and energy balance requires that

$$T_s(s(t), t) = T_\ell(s(t), t) = T_m \tag{11}$$

$$q_\ell(s(t), t) - q_s(s(t), t) = L\rho \frac{ds}{dt} \tag{12}$$

where the density is taken to be constant. Using equation (6) in equation (12) and assuming that the relaxation times in the solid and liquid phases are the same[3] gives

$$k_s \frac{\partial T_s(s(t), t)}{\partial x} - k_\ell \frac{\partial T_\ell(s(t), t)}{\partial x} = L\rho \left(\tau \frac{d^2 s}{dt^2} + \frac{ds}{dt}\right) \tag{13}$$

where

$$\tau = \tau_s = \tau_\ell$$

Following the solution method of Carslaw and Jaeger [3], specific half-space solution forms for single phase problems will be used in the solid and liquid regions with conditions (11) and (13) to be satisfied. Baumeister and Hamill's [11, 12] work provides these needed solution forms (also see [15] for more details). First introduce the

[3] This assumption is made for convenience in simplifying equation (12). In general one would expect the relaxation times to be different. However, at present, only estimated values of τ exist.

Nomenclature

$c = \sqrt{\alpha/\tau}$ = thermal wave speed
c_p = specific heat at constant pressure
$H(\cdot)$ = unit Heaviside step function
I_0, I_1, I_2 = modified Bessel functions of order 0, 1, 2
k = thermal conductivity
k_s, k_ℓ = thermal conductivities in the solid and liquid regions
L = latent heat of fusion
m = Fourier constant related to interface location
$\underline{q}$ = heat flux vector
q_s, q_ℓ = heat flux in the solid and liquid regions
$s(t)$ = phase-change interface location
$\tilde{s}(t)$ = dimensionless phase-change interface location
t = time
T = temperature distribution
T_s, T_ℓ = temperature distribution in the solid and liquid regions
T_m = melting temperature
T_0 = initial temperature
T_w = free surface or wall temperature
x = spatial variable
$erfc(\cdot)$ = complimentary error function
$\alpha = k/\rho c_p$ = thermal diffusivity
α_s, α_ℓ = thermal diffusivity in the solid and liquid regions
$\beta = t/2\tau$ = dimensionless time
β^* = dimensionless time when $T_{\text{wave front}} = T_m$
$\delta_s, \delta_\ell = x/2\sqrt{\alpha_{s,\ell}\tau}$ = dimensionless distance in the solid and liquid regions
$\underline{\nabla}$ = vector differential operator
ρ = mass density
τ = material thermal relaxation time
τ_s, τ_ℓ = material thermal relaxation time in the solid and liquid regions

dimensionless variables

$$\delta_{\ell,s} = \frac{x}{2\sqrt{\alpha_{\ell,s}\,\tau}}$$

$$\beta = \frac{t}{2\tau} \tag{14}$$

The solution for the temperature distribution within the liquid region, which satisfies equations (7) and (8), may be written as

$$T_\ell(\delta_\ell, \beta) = T_w + A[1 - F_\ell(\delta_\ell, \beta)] \tag{15}$$

while the solution in the solid region satisfying equations (9) and (10) is

$$T_s(\delta_s, \beta) = T_0 + BF_s(\delta_s, \beta) \tag{16}$$

where A and B are constants to be determined, and

$$F_{\ell,s}(\delta_{\ell,s}, \beta) = H(\beta - \delta_{\ell,s})\left[e^{-\delta_{\ell,s}} + \delta_{\ell,s}\int_{\delta_{\ell,s}}^{\beta} e^{-\xi}\frac{I_1(\sqrt{\xi^2 - \delta_{\ell,s}{}^2})}{\sqrt{\xi^2 - \delta_{\ell,s}{}^2}}\,d\xi\right] \tag{17}$$[4]

with I_1 being the first-order modified Bessel function. Note that on the wave front $x = ct$, and hence $\delta_{\ell,s} = \beta$ and $F_{\ell,s} = e^{-\beta}$.

The location of the phase interface can be redefined in the dimensionless variables δ_ℓ or δ_s by

$$\delta_\ell = \sqrt{\frac{\alpha_s}{\alpha_\ell}}\,\delta_s = \bar{s}(\beta) \tag{18}$$

Therefore, condition (11) at the interface becomes

$$T_w + A[1 - F_\ell(\bar{s}(\beta), \beta)] = T_m$$

$$T_0 + BF_s(\sqrt{\alpha_\ell/\alpha_s}\bar{s}(\beta), \beta) = T_m \tag{19}$$

Similarly condition (13) reads

$$\frac{k_s\sqrt{\alpha_\ell/\alpha_s}(T_m - T_0)\dfrac{\partial F_s}{\partial \delta_s}(\sqrt{\alpha_\ell/\alpha_s}\bar{s}(\beta), \beta)}{F_s(\sqrt{\alpha_\ell/\alpha_s}\bar{s}(\beta), \beta)} + \frac{k_\ell(T_m - T_w)\dfrac{\partial F_\ell}{\partial \delta_\ell}(\bar{s}(\beta), \beta)}{1 - F_\ell(\bar{s}(\beta), \beta)} = L\rho\alpha_\ell\left(\frac{d^2\bar{s}}{d\beta^2} + 2\frac{d\bar{s}}{d\beta}\right) \tag{20}$$

where the constants A and B have been eliminated by using equations (19).

The three conditions (19) and (20) which are to be used to determine the quantities A, B, and $\bar{s}(\beta)$ are nonlinear in $\bar{s}(\beta)$. Consequently to proceed with the solution, some approximations will be made and numerical techniques used. Two basic ideas are to be employed:

1 As indicated in past research, non-Fourier results should approach the corresponding Fourier results as $t \to \infty$.

2 Referring to Fig. 2, which illustrates a typical non-Fourier temperature distribution for increasing values of time, it is evident that there exists a value of time, say β^*, where the temperature at the wave front has decreased from T_w and become equal to T_m. For times $0 < \beta < \beta^*$, the non-Fourier thermal wave is assumed to carry the solid-liquid interface along with it.[5] After the time β^*, the wave discontinuity is less than T_m, and therefore travels in the solid ahead of the phase-change interface; see Fig. 2.

From assumption 2 in the foregoing, the motion of the phase interface for $0 < \beta < \beta^*$ is

$$\bar{s}(\beta) = \beta; \quad 0 < \beta < \beta^* \tag{21}$$

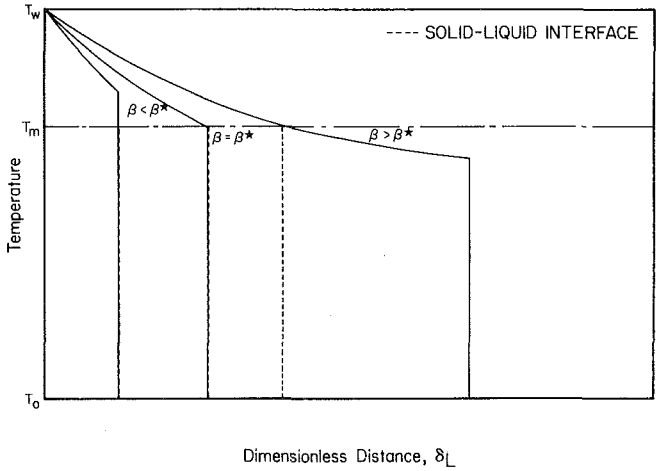

Fig. 2. Typical non-Fourier temperature profile for various values of time

For $\beta > \beta^*$, the interface motion was determined numerically using an empirical equation. The form of this empirical relation was motivated by statement 1, in that $\bar{s}(\beta) \to m\sqrt{\beta}$ (which is the Fourier result, with m a constant) as $\beta \to \infty$. The form of the quantity $F_{\ell,s}(\delta_{\ell,s}, \beta)$ in equation (17), and the asymptotic behavior of the modified Bessel functions, lead to an empirical form

$$\bar{s}(\beta) = e^{\beta}[DI_0(\beta) + EI_1(\beta) + FI_2(\beta)]^{-1}, \quad \beta > \beta^* \tag{22}$$

with D, E, and F being constants.

The constant F can be determined by the long time asymptotic limit giving

$$F = \frac{\sqrt{2\pi}}{m} - D - E \tag{23}$$

Likewise the constant E is found from the initial condition that $\bar{s}(\beta^*) = \beta^*$, yielding the result

$$E = \frac{\dfrac{e^{\beta^*}}{\beta^*} - D[I_0(\beta^*) - I_2(\beta^*)] - \dfrac{\sqrt{2\pi}}{m}I_2(\beta^*)}{I_1(\beta^*) - I_2(\beta^*)}$$

with β^* determined from the corresponding Fourier case to be

$$\beta^* = -\ln[erfc(m/\sqrt{2})] \tag{24}$$

Finally the constant D was determined by a least-squares fit of the curve $\bar{s}(\beta)$ which keeps the quantity $F_\ell(\bar{s}(\beta), \beta)$ a constant (note equation (19)); the result produces

$$D = \frac{1.25315}{m - 0.00309766m^2 - 0.101483m^3 - 0.0142969m^4} \tag{25}$$

The solution to the problem is completed by determining the value of the constant m. The relation for $\bar{s}(\beta)$, equation (22), is substituted into the energy balance (20), and a numerical direct search routine is performed on the resulting expression to give m. This completely determines $\bar{s}(\beta)$, and equations (19) can then be used to find the constants A and B. It should be pointed out that since the form for $\bar{s}(\beta)$ is approximate, equation (20) cannot be exactly satisfied for all values of time β.[6] In other words the quantity m determined from (20) will vary slightly for different values of β; however, the variation was small and was not considered to be a significant error.

Comparison and Discussion

To compare this non-Fourier solution with the corresponding Fourier problem, consider the case of aluminum media with the following properties: ρ = 2.38 g/cm^3 (149 lb/ft^3), L = 400 J/gm (172

[4] The corresponding Fourier problem is formulated in exactly the same way with $F_{\ell,s}(\delta_{\ell,s}, \beta) = \text{erfc}(\delta_{\ell,s}/\sqrt{2\beta})$, see Carslaw and Jaeger [3, 15].

[5] This assumption, based on physical grounds, makes the problem solution approximate because the energy balance and temperature continuity across the interface cannot be satisfied.

[6] This fact is in contrast to the Fourier theory where the energy balance equation and temperature continuity relation can be exactly satisfied by $\bar{s}(\beta) = m\sqrt{\beta}$, see [3, 15].

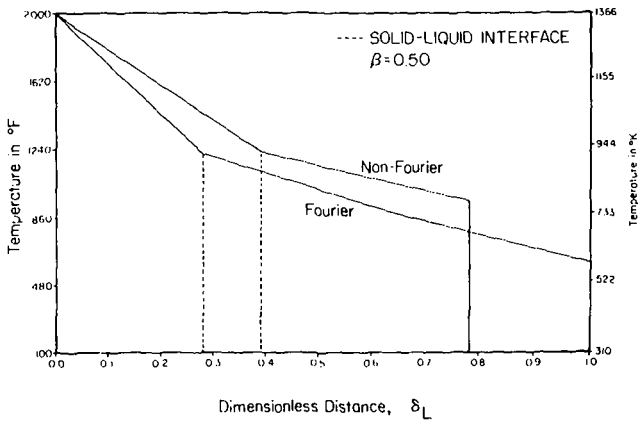

Fig. 3. Temperature profile comparison for aluminum with T_w = 1366 K (2000°F), T_0 = 310 K (100°F), and β = 0.5

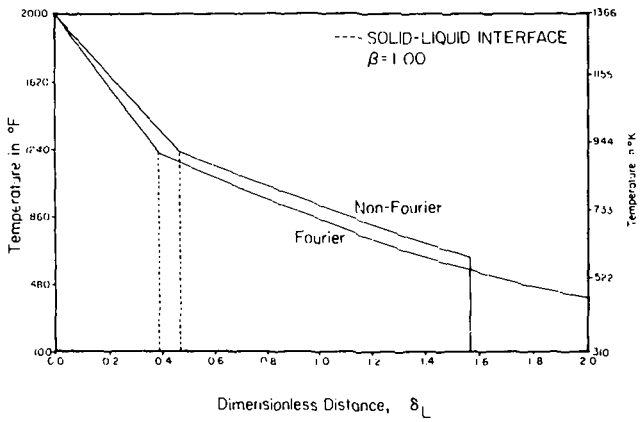

Fig. 4. Temperature profile comparison for aluminum with T_w = 1366 K (2000°F), T_0 = 310 K (100°F), and β = 1.0

Btu/lb), α_ℓ = 0.387 cm²/s (1.5 ft²/hr), α_s = 0.947 cm²/s (3.67 ft²/hr), k_ℓ = 0.968 W/cm-K (56 Btu/hr-ft-°F), k_s = 2.28 W/cm-K (132 Btu/hr-ft-°F), and T_m = 933 K (1220°F). Figs. 3–5 illustrate the comparisons of the temperature profiles predicted by both theories for various times β = 0.5, 1.0, 3.0 with T_w = 1366 K (2000°F) and T_0 = 310 K (100°F).

The figures show the non-Fourier wave front in contrast to the continuous Fourier temperature profile. The predicted location of the solid-liquid interface is also different from each theory. In all cases considered, for small times the non-Fourier temperatures will be higher than the corresponding Fourier values. This fact agrees with previous research in nonmelting situations [14]. Furthermore the non-Fourier interface location will be farther into the media than the Fourier prediction, with the maximum difference occurring at $\beta = \beta^*$. With $\beta > 10$ both theories predict essentially identical behavior.

In order to relate the previous results to actual dimensional quantities, the value of the thermal relaxation time τ must be known. Brazel and Nolan [16] give only estimates of this parameter in the range 10^{-10}- 10^{-12} s. With this estimate of τ, the non-Fourier effects in the melting problem exist for only about 10^{-9}- 10^{-11} s and are confined to about 10^{-4}- 10^{-5} cm from the half-space surface. It should be pointed out that if τ and/or T_w increases, the non-Fourier effects become more prominent. It is felt that these effects begin to border on some special heat transfer situations such as those mentioned in the Introduction.

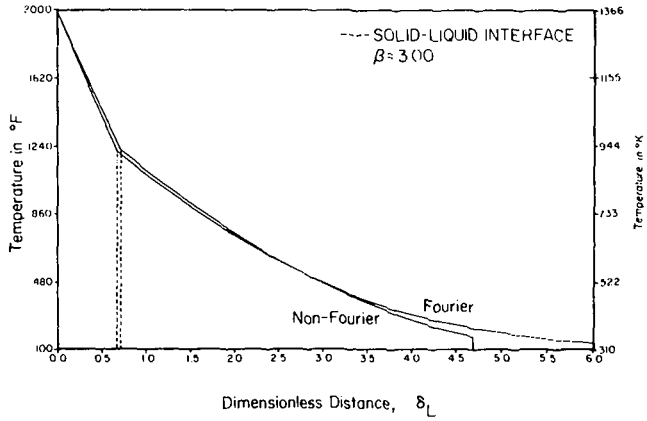

Fig. 5. Temperature profile comparison for aluminum with T_w = 1366 K (2000°F), T_0 = 310 K (100°F), and β = 3.0

Acknowledgment

The research here reported was sponsored by a grant from the National Science Foundation (GK-42138) to the Mississippi State University.

References

1 Muehlbauer, J. C., and Sunderland, J. E., "Heat Conduction With Freezing or Melting," *App. Mech. Rev.*, Vol. 18, 1965, p. 951.

2 Stefan, J., "Über die Theorie der Eisbildung, insbesondere über die Eisbildung in Polarmaere," *Annalen der Physik und Chemie*, Vol. 42, 1891, p. 269.

3 Carslaw, H. S., and Jaeger, J. C., *Conduction of Heat in Solids*, Oxford University Press, London, 1947, p. 71.

4 Coleman, B. D., and Mizel, V. J., "Thermodynamics and Departures From Fourier's Law of Heat Conduction," *Arch. Rat. Mech. Anal.*, Vol. 13, 1963, p. 245.

5 Gurtin, M. E., and Pipkin, A. C., "A General Theory of Heat Conduction With Finite Wave Speeds," *Arch. Rat. Mech. Anal.*, Vol. 31, 1968, p. 113.

6 Cattaneo, C., "On the Conduction of Heat," *Atti del Seminario Mat. Fis. Univ. Modena*, Vol. 3, 1948, p. 3.

7 Cattaneo, C., "A Form of Heat Conduction Equation Which Eliminates the Paradox of Instantaneous Propagation," *Compt. Rend.*, Vol. 247, 1958, p. 431.

8 Vernotte, P., "Paradoxes in the Continuous Theory of the Heat Equation," *Compt. Rend.*, Vol. 246, 1958, p. 3154.

9 Vernotte, P., "The True Heat Equation," *Compt. Rend.*, Vol. 247, 1958, p. 2103.

10 Baumeister, K. J., and Hamill, T. D., "Hyperbolic Heat-Conduction Equation -A Solution for the Semi-Infinite Body Problem," JOURNAL OF HEAT TRANSFER, TRANS. ASME, Series C, Vol. 91, 1969, p. 543.

11 Baumeister, K. J., and Hamill, T. D., "Hyperbolic Heat-Conduction Equation -A Solution for the Semi-Infinite Body Problem," JOURNAL OF HEAT TRANSFER, TRANS. ASME, Series C, Vol. 93, 1971, p. 126.

12 Chan, S. H., Low, J. D., and Mueller, W. K., "Hyperbolic Heat Conduction in Catalytic Supported Crystallites," *AIChE Journal*, Vol. 17, 1971, p. 1499.

13 Chester, M., "Second Sound in Solids," *Phys. Rev.*, Vol. 131, 1963, p. 2013.

14 Maurer, M. J., and Thompson, H. A., "Non-Fourier Effects at High Heat Flux," JOURNAL OF HEAT TRANSFER, TRANS. ASME, Series C, Vol. 95, 1973, p. 284.

15 Didlake, J. E., "Non-Fourier Melting of a Semi-Infinite Solid," MS thesis, Mississippi State University, Dec. 1975.

16 Brazel, J. P., and Nolan, E. J., "Non-Fourier Effects in the Transmission of Heat," *Proceedings 6th Conference Thermal Conductivity*, Dayton, Ohio, Oct., 1966, p. 238.

A. A. Sfeir
Assoc. Professor.

J. A. Clumpner[1]
Assoc. Professor.

American University of Beirut,
Beirut, Lebanon

Continuous Casting of Cylindrical Ingots

The Heat Balance Integral Method is applied to solve for the continuous casting of cylindrical ingots. Unlike previously developed integral solutions the present analysis includes the effect of axial conduction. Comparison with the solution derived by Veynick (which neglects axial conduction) shows that, for small Peclet numbers, the discrepancy between the results can be quite appreciable. In particular the pool depth prediction by the present analysis can be as much as 40 percent shorter. In its present form the method assumes constant temperature in the liquid metal and constant properties in the solidified crust. It is applicable to a variety of surface cooling rates including constant film coefficient, constant heat flux and other more general conditions. It can also take into account superheat of the molten metal.

1 Introduction

The problem of predicting the solidification front and the temperature field for the case of continuous casting process of a cylindrical ingot is of great practical importance. Due to the release of latent heat during the change of phase such a problem is nonlinear and considerably more difficult to solve than the corresponding single phase problem.

Analytical closed form solutions of conduction problems with phase change may be obtained only for a limited number of problems with idealized boundary conditions. For the problem at hand no analytical solutions can be found and most of the attempts at solving it use finite difference or finite element numerical schemes. A large number of these numerical solutions have appeared in the general literature, the most recent of which by Kroeger and Ostrach [1][2] includes the effects of natural convection in the liquid metal. Such numerical methods can be made quite general and include effects of superheat, axial conduction and the like but this is usually accompanied with added complexity.

Other solutions using a heat balance integral method (HBIM) have been developed by Veynik [2], Goodman [3], and Hills [4]. This approach is much simpler to use and is a valuable tool for the analysis of some continuous casting processes. However, the simplifying assumptions used in these solutions introduce inaccuracies for low casting speeds, particularly in the bottom region of deep pools as has been noted by Kroeger [5]. Some of the previously used simplifying assumptions are inherent in the method used; but other assumptions, which we think are more important, are not necessary for the formulation of the problem in terms of the HBIM. This paper develops an HBIM approach which includes conduction in the direction of casting as well as the effect of superheat in the feed metal. The analysis is somewhat more complex than in the previous HBIM solutions but is still far simpler than in any finite difference or finite element formulation.

The HBIM seems to have been developed independantly at about the same time by Goodman [6] and Veynick [2]. Goodman's formulation seems to be more general and is similar to the momentum integral method used in conjunctions with viscous boundary layers. Venick's formulation, on the other hand, seems to have been based on some empirical results which suggest a linear temperature distribution in the solidified crust. The two methods can, in fact, be shown to be identical when the same set of assumptions are applied on both of them. The HBIM consists essentially in defining a region of thickness δ inside which the temperature distribution is represented by some polynomial approximation. The thickness δ is such that the boundary conditions affect the temperature distribution only within that thickness. Beyond this thermal boundary layer, the temperature is usually assumed to be constant. The constants involved in the polynomial approximation for T are found by writing the boundary conditions on one side of the thermal layer and some smoothing conditions on the other side. The problem is then solved by integrating the partial differential equation in one direction thus giving an ordinary differential equation in δ.

The analysis developed in this paper essentially follows the steps outlined previously but differs substantially from the work of Veynick and Goodman in that it includes conduction in both directions radial and axial. The solution will be developed for cylindrical ingots but

[1] Present address: Cabot Corp., Billerica, Mass.

[2] Numbers in brackets designate References at end of paper.

Contributed by the Heat Transfer Division for publication in the JOURNAL OF HEAT TRANSFER. Manuscript received by the Heat Transfer Division September 5, 1975.

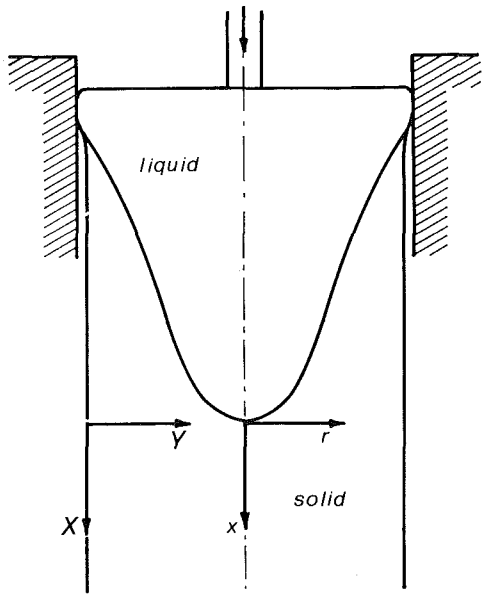

Fig. 1 Schematic diagram of solidification of a continuous casting

may very easily be extended to solve for flat two-dimensional ingots. In developing the method we will show how Veynick's solution can in fact be obtained as a limiting asymptotic form of our analysis for large Peclet numbers.

2 The Heat Balance Integral Equation

A typical continuous casting process is shown in Fig. 1. Liquid metal is supplied continuously at the top of a bottomless mold. The molten metal is then cooled which results in forming a solid metal skin, the strength of this solidified skin must be sufficient to contain the remaining liquid and permit continuous withdrawal of the casting at a constant speed U.

The partial differential equation describing this problem assuming constant material properties is:

$$\frac{k}{\rho C_p}\left[\frac{1}{r}\frac{\partial}{\partial r}\left(r\frac{\partial t}{\partial r}\right)+\frac{\partial^2 t}{\partial x^2}\right]=U\frac{\partial t}{\partial x} \tag{1}$$

with convective cooling on the surface:

$$k\left[\frac{\partial t}{\partial r}\right]_R=-ht_R \tag{2}$$

where t_R is the surface temperature.

Calling the thickness of the solidified crust ℓ, we can write the equation of conservation of energy at the solid liquid interface:

$$\rho U\lambda\frac{d\ell}{dx}=-k\left[\frac{\partial t}{\partial r}\right]_\ell-k\left[\frac{\partial t}{\partial x}\right]_\ell\frac{d\ell}{dx} \tag{3}$$

Assuming the temperature field to be constant in the liquid region, equation (1) may be integrated with respect to r from 0 to R. This integration which is presented in detail in Appendix 1 gives:

$$\frac{d^2\theta}{dX^2}-(1-\delta)\frac{d^2\delta}{dX^2}+\left(\frac{d\delta}{dX}\right)^2-P\frac{d\theta}{dX}$$
$$+\mathrm{P}(1-\delta)(1+\Lambda)\frac{d\delta}{dX}-\mathrm{B}T_R=0 \tag{4}$$

This equation is dimensionless, all distances having been divided by R and all temperatures divided by the solidification temperature t_0. B and P are, respectively, the Biot number and the Peclet number and $\delta=\ell/R$,

$$\theta=\frac{1}{t_0R^2}\int_{R-\ell}^{R}trdr \tag{5}$$

is the nondimensional temperature integral in the solidified crust.

Equation (4) contains three unknowns T_R, δ, and θ. Two of these unknowns namely T_R and θ may be eliminated if one can find a polynomial approximation for $t(r)$ in the solidified crust. When this is done, equation (4) will reduce to an ordinary differential equation in δ. The accuracy of our results will, of course, depend only on the accuracy of the approximating polynomial as equation (4) is an exact equation not involving any approximation.

In Veynick's analysis the conduction term in the X-direction was neglected, using this simplifying assumption equation (4) reduces to

$$\mathrm{P}(1-\delta)(1+\Lambda)\frac{d\delta}{dX}-\mathrm{P}\frac{d\theta}{dX}-\mathrm{B}T_R=0 \tag{6}$$

This is in fact an asymptotic form of equation (4) for large Peclet numbers. This explains the lack of accuracy of Veynick's solution for shallow pools and in the bottom regions of deep pools.

3 Solution for Constant B

3.1 **The Approximating Polynomial.** The temperature distribution inside the solidified crust is assumed to have the form

$$T=a+bY+cY^n \tag{7}$$

where $Y=1-r/R$ is the nondimensional distance measured from the lateral surface of the ingot. The parameters a, b, and c are only function of X and will be determined from the boundary conditions on both sides of the solidified region. The exponent n is constant, it will be determined in terms of B, P, and Λ by writing a boundary condition expressing the heat flow into the section of the ingot at end of solidification.

Writing the boundary conditions for

$$Y=0,\quad [T]_{Y=0}=T_R$$

and

Nomenclature

a, b, c = constants appearing in the polynomial approximation for T
a_1, a_2 = constants appearing in the solution for the surface temperature
h = film coefficient for the cooling at the surface of the ingot
k = thermal conductivity
ℓ = solidified crust thickness
n = exponent appearing in the polynomial approximation for T
r = radial coordinate
t = temperature
t_0 = temperature of solidification
t_R = surface temperature
x = axial coordinate
B = Biot number
C_1, C_2 = constants appearing in the solution for the surface temperature, equation (11)
C_p = specific heat
F_1, F_2 = functions defined in equation (18)
K_1, K_2 = constants appearing in equation (19)
P = Peclet number
R = radius of the ingot
T = dimensionless temperature
U = casting speed
X = dimensionless axial coordinate
X_0 = pool depth
Y = dimensionless radial coordinate measured from the surface inward
δ = dimensionless solidified crust thickness
λ = latent heat
ρ = density
θ = parameter defined by equation (5)
Λ = dimensionless latent heat

$$\left[\frac{\partial T}{\partial Y}\right]_{Y=0} = \mathrm{B}T_R \tag{8}$$

and for

$$Y = \delta, \quad [T]_{Y=\delta} = 1 \tag{9}$$

we find

$$a = T_R$$

$$b = \mathrm{B}T_R$$

and

$$c = \frac{1 - (1 + \mathrm{B}\delta)T_R}{\delta^n}$$

One more boundary condition is necessary in order to determine T_R, this may be provided either by using equation (3) which expresses energy conservation on the solidification front or writing equation (1) at $r = R$. The second alternative is found to be more suitable as will be shown in Appendix 2. The use of equation (1) on the surface yields an ordinary differential equation in T_R:

$$\frac{d^2T_R}{dX^2} - \mathrm{P}\frac{dT_R}{dX} - \mathrm{B}T_R = 0 \tag{10}$$

And, as this equation does not involve δ, it can readily be solved and we get for the case when B is assumed constant:

$$T_R = C_1 \exp(a_1 X) + C_2 \exp(a_2 X) \tag{11}$$

where

$$a_{1,2} = \frac{\mathrm{P}}{2} \pm \sqrt{\frac{\mathrm{P}^2}{4} + \mathrm{B}}$$

and C_1 and C_2 are constants of integration.

3.2 **Solution in the Fully Solidified Ingot.** As the longitudinal conduction terms has not been neglected the solution of the problem requires that we know the amount of heat flux crossing the sections $x = 0$, where as shown in Fig. 1 the origin of the x axis is taken at the section of the ingot where the solidification is fully completed. This requires solving for the temperature field throughout the solidified ingot from $x = 0$ to infinity. The temperature distribution in a moving cylinder subject to a convective cooling on its surface can be derived analytically as in [7] but for simplicity we will use an approximate heat balance integral solution. In the region $x > 0$ equation (4) takes the form

$$\frac{d^2\theta}{dX^2} - \mathrm{P}\frac{d\theta}{dX} - \mathrm{B}T_R = 0 \tag{12}$$

Taking a temperature profile as in (7), we find after substituting for the boundary conditions:

$$T = T_R\left(1 + \mathrm{B}Y - \frac{\mathrm{B}}{n}Y^n\right) \tag{13}$$

Evaluating θ equation (12) becomes an ordinary differential equation in T_R which yields:

$$T_R = \frac{n}{n + (n-1)\mathrm{B}} \exp\left[\frac{p}{2} - \sqrt{\frac{p^2}{4} + \frac{2\mathrm{B}}{2K\mathrm{B} + 1}}\right] x \tag{14}$$

where

$$K = \frac{1}{6} - \frac{1}{n(n+1)(n+2)}$$

The constants of integration having been adjusted so as to have $T(X, Y) \to 0$ as $X \to \infty$, and $T(0, 1) = 1$ when $X = 0$.

We now require that the sum of heat flux by conduction and sensible heat flow on both sides of the section $X = 0$ be the same. At

$$X = 0; \quad T_R = \frac{n}{n + (n-1)\mathrm{B}}$$

comparing equations (7) and (13) we see that the temperature profiles on both sides of $X = 0$ are identical. This proves the continuity of the sensible heat flow across the section $X = 0$. The continuity of the conduction flux requires that:

$$\left(\frac{\partial T}{\partial X}\right)_{X=0^-} = \left(\frac{\partial T}{\partial X}\right)_{X=0^+}$$

but, as we are solving for the temperature distribution on an integral basis we require instead that

$$\int_0^1 \frac{\partial T}{\partial X}(1 - Y)dY$$

be continuous on both sides of the section $X = 0$. This condition will yield:

$$C_1 = \frac{1}{a_1 - a_2}\left\{\left(\frac{dT_R}{dX}\right)_{X=0^+} - a_2 T_R(0)\right\}$$

and (15)

$$C_2 = T_R(0) - C_1$$

Furthermore we also require that the total heat flux that is supplied with the liquid metal be equal to the heat removed along the surface of the ingot. Calling $-X_0$ the distance between the section at which liquid metal is supplied and $X = 0$, this condition reduces to:

$$\int_{X_0}^0 \mathrm{B}T_R dX + \int_0^\infty \mathrm{B}T_R dX = \frac{\mathrm{P}}{2}(1 + \Lambda) \tag{16}$$

And writing that $T_R(-X_0) = 1$ in equation (11), we get two equations for the unknowns n and X_0. These nonlinear algebraic equations are solved using a standard Newton-Raphson iteration method.

It must be noted that equation (10) is valid only if $n > 2$, otherwise δ will appear in this equation. The above analysis will therefore fail whenever we find a root $n \leqslant 2$. In fact, even if this limitation did not exist, it would still be highly undesirable to use temperature profiles with $n < 2$. This is due to the fact that experimental profiles have very low second derivatives near the surface.

In any case, this analysis is found to give $n > 2$ for all useful values of B, P, and Λ. But, in practice, B varies along the ingot length, and it may happen that for a given distribution of surface cooling $\mathrm{B}(X)$, equations (11) and (16) may give $n \leqslant 2$. This would simply indicate that the integral solution in the fully solidified region yields a temperature profile which is a poor representation of the true distribution. Whenever such a thing occurs, a more suitable value of the exponent n could be found by using the exact solution in the fully solidified ingot (reference [7]) instead of the approximate forms given in equations (13) and (14).

3.3 **The Solution for $\delta(X)$.** All the parameters appearing in the expression for T' having been determined the heat balance integral equation (4) reduces to an ordinary differential equation in $\delta(X)$. In fact for the case at hand equation (4) can be integrated once with respect to X from 0 to any section $-X$, this will give:

$$\frac{d\theta}{dX} + (\delta - 1)\frac{d\delta}{dX} - \mathrm{P}\theta + \mathrm{P}(1 + \Lambda)\left(\delta - \frac{\delta^2}{2}\right) - \int_0^{-X} \mathrm{B}T_R dX - \frac{\mathrm{P}}{2}(1 + \Lambda) = Q \tag{17}$$

where Q is the total heat flux crossing the section $X = 0$. Evaluating θ using the polynomial (7) and the definition of θ (5), we get after substituting in (17) and arranging terms the following differential equation:

$$F_1\frac{d\delta}{dX} + F_2 + Q + \int_0^{-X} \mathrm{B}T_R dX = 0 \tag{18}$$

where

$$F_1 = \left(\frac{\delta}{n+2} - \frac{1}{n+1}\right)\{T_R[\mathrm{B}\delta(n-1) + n] - n\}$$

$$F_2 = \left\{\mathrm{P}T_R - \frac{dT_R}{dX}\right\}\left\{\delta + \frac{\mathrm{B}-1}{2}\delta^2 - \mathrm{B}\frac{\delta^3}{3} - (1 + \mathrm{B}\delta)\left(\frac{\delta}{n+1} - \frac{\delta^2}{n+2}\right)\right\} - \mathrm{P}\left\{\delta\left(\frac{n}{n+1} + \Lambda\right) - \frac{\delta^2}{2}\left(\frac{n}{n+2} + \Lambda\right) - \frac{1+\Lambda}{2}\right\}$$

and where T_R, $\int_0^{-x} BT_R dX$ and dT_R/dX are determined from equations (11) and (14), respectively.

Equation (18) is a nonlinear first order ordinary differential equation in δ, its solution can be found numerically using any of the avaiable numerical algorithms. In this study we have solved (18) using a standard fourth order Runge-Kutta method of the Gill's type. While integrating it was found that the equation has a singularity between $-X_0$ and $X = 0$ which necessitated that the solution be carried in two branches one starting from $X = 0$ and going towards $X < 0$, and one starting at $X = -X_0$ and proceeding forward. This process was not found to be inconvenient as the pool depth $-X_0$ is actually known. Starting the integrations at both locations 0 and $-X_0$ was carried out by using an implicit scheme of first order for δ.

4 Solutions for Variable B

The method outlined previously is not limited to the case of constant Biot numbers. Much of the method remains unchanged even when more general assumptions are made regarding B. The only difference will be in the solution of equation (10). For instance, if we assume constant heat flux on the surface of the ingot, i.e., letting $BT_R = b$, the solution (11) will have the form:

$$T_R = K_1 \exp(PX) - \frac{b}{P} X + K_2 \tag{19}$$

where K_1 and K_2 may be determined in the same manner as C_1 and C_2. For a more general variation of B equation (10) will be of the form:

$$\frac{d^2T_R}{dX^2} - P\frac{dT_R}{dX} - f(T_R, X) = 0 \tag{20}$$

and if an analytic solution can be found the remaining part of the analysis will proceed as before. If, on the other hand, equation (20) does not admit an analytic solution, then a family of numerical solutions must be found and one of these solutions must be selected in order to match the condition requiring continuity of heat flux across the surface $X = 0$.

5 Asymptotic Solution for Large P

For the sake of comparison Veynik's solution is rederived using a similar approach to that of the previous section but using the asymptotic form (6) of the heat balance integral equation. Assuming T varies linearly in the solidified crust and has the values:

$$T = T_R \quad \text{at} \quad Y = 0$$

$$T = 1 \quad \text{at} \quad Y = \delta$$

one gets

$$T = T_R + \frac{1 - T_R}{\delta} Y \tag{21}$$

writing the convection boundary condition (2) we get:

$$T_R = \frac{1}{1 + B\delta} \tag{22}$$

Substituting in equation (6) we get an ordinary differential equation in (X) which may be solved analytically to give:

$$PX = \left(\frac{\Lambda}{B} + \frac{1}{2B} + \frac{1}{2B^2}\right)\delta + \left(\Lambda + \frac{1}{2} - \frac{\Lambda}{B} - \frac{1}{6B}\right)\frac{\delta^2}{2} - \left(\Lambda + \frac{1}{3}\right)\frac{\delta^3}{3} - \frac{1}{2B^2}\left(1 + \frac{1}{3B}\right)\ln(1 + B\delta) \tag{23}$$

This expression is identical to the result given by Veynick except for an empirical constant that appears in some of the terms and which according to Veynick, accounts for the actual deviation of the temperature profile from the linear distribution. Equation (23) is also quite similar to the results of Tikhonov and Shvidovski [8] referred to by Veynick.

6 Results and Discussions

The method outlined in the foregoing section was used to solve for the continuous casting problem with $\Lambda = 0.68$ and $B = 1$ and three values of the Peclet number $P = 2.5$, 5, and 10, respectively. The results are shown on Figs. 2–4. For the sake of comparison, the same cases are also solved using Veynick's method, the results are shown on the same figures.

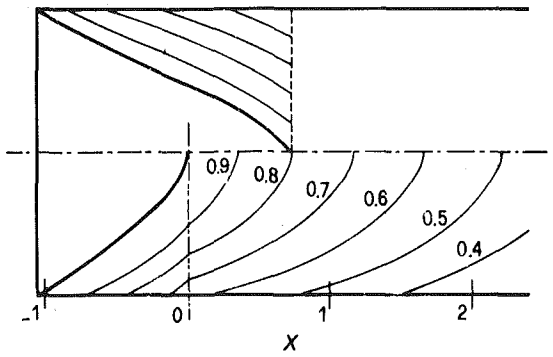

Fig. 2 Solidification profile and isotherms for the case with B = 1, P = 2.5, and Λ = 0.68; the upper half of the figure shows Veynick's solution

Quite a large discrepancy between the two solutions is noted for low P as our analysis predicts an appreciably shorter pool depth. This large discrepancy, which seems surprising at first look, can be justified by the importance of the longitudinal conduction term for low P. In fact, if one tests Veynick's analysis for self-consistancy, i.e., if one is to check the relative magnitudes of conduction heat transfer versus sensible heat flow, we can easily find the ratio to be:

$$\left[P\theta \Big/ \frac{d\theta}{dX}\right]_{X=0} = \frac{(3 + B)P^2}{6B} \tag{24}$$

which shows that for B = 1 and P = 2.5, the conduction heat transfer at the section $X = 0$ is 24 percent of the total flux at that section; this ratio drops to 6 percent for P = 5 and to 1.5 percent for P = 10.

At the largest Peclet number, it is still possible to note a difference in the shape of the bottom of the pool, the present analysis always yields an infinite slope for δ at the center line. On the other hand, the general shape of the pool as well as the pool depth X_0 become quite similar to the results predicted by Veynick.

Figs. 2–4 also show some isotherms in the solidified crust and after completion of the solidification. The shapes of these isotherms are similar to what has been reported in numerical and experimental investigations. It can be noted that a slight discontinuity in the slopes of the isotherms occur at the section $X = 0$; this is due to the fact we only require continuity of the integral of the thermal flux at this section.

Unfortunately, the accuracy of the results cannot be directly evaluated as there are no experimental data that we are aware of that give information on B and on the conditions at large distances after freezing is completed. However, in view of the fact that the method

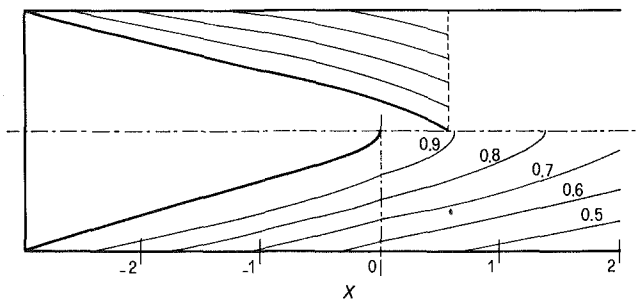

Fig. 3 Solidification profile and isotherms for the case with B = 1, P = 5, and Λ = 0.68; the upper half of the figure shows Veynick's solution

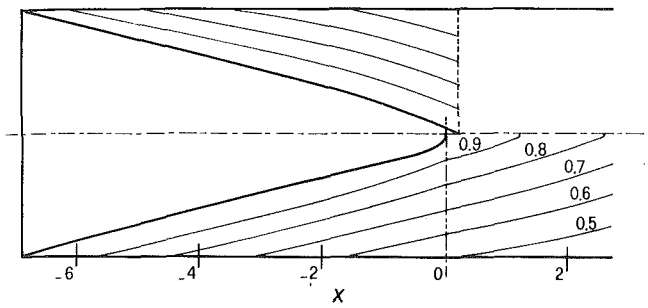

Fig. 4 Solidification profile and isotherms for the case with B = 1, P = 10, and Λ = 0.68; the upper half of the figure shows Veynick's solution (note that the axial scale of the figure is half the radial scale)

is more general than that of Veynick, in that it includes conduction along X, it makes little doubt that the accuracy attained by the present method must be substantially better, particularly for small Peclet numbers.

Although the present analysis is not too cumbersome it would still be advisable to use the asymptotic form (6) and its solution (23) for large Peclet numbers.

Comparing a large number of solutions it appears that, provided one is not too interested in the exact shape of the bottom of the pool, equation (23) can be used whenever

$$\left[\mathrm{P}\theta \Big/ \frac{d\theta}{dX}\right]_{X=0} > 30$$

i.e., when the conduction term is approximately less than 3 percent of the total heat flux crossing the section $X = 0$.

7 Conclusions

The Heat Balance Integral method has been successfully applied to solve for the continuous casting problem of a cylindrical ingot including longitudinal conduction. The analysis is rather simple and can yield the solidification front and the temperature field in the solidified crust within few minutes on a medium size computer. Although the method is appreciably more complicated than the previously developed integral methods, it is far simpler and cheaper to implement than the numerical approach and is suitable for use by the practicing engineers.

In its present form the method assumes constant properties in the solidified region, it neglects superheat and the motion of molten metal in the pool. This last effect does not seem to play an important role according to the recent work of Kroeger and Ostrach [1]. The effect of superheat can be easily taken care of by including it in Λ, i.e., by adding the superheat to the latent heat. This will not affect our analysis as we have not used any boundary condition on the slope of $T(Y)$ at the solidification front. The effect of variable properties is presently under investigation, there are good reasons to believe that the method could be be extended to cover this. It is not certain however if this could be accomplished while keeping the analysis simple enough to make it attractive for practical applications.

References

1 Kroeger, P. G., and Ostrach S., "The Solution of a Two-Dimensional Freezing Problem Including Convection Effects in the Liquid Region," *International Journal of Heat and Mass Transfer*, Vol. 17, 1974, p. 1191.

2 Veynick, A. I., "Theory of Special Casting Methods," TRANS. ASME, 1962.

3 Goodman, T. R., "The Heat Balance Integral and Its Application to Problems Involving a Change of Phase," TRANS. ASME, Vol. 80, 1958, p. 335.

4 Hills, A. W. D., "A Generalized Integral Profile Method for Analysis of Unidirectional Heat flow During Solidification," *Trans. Metall. Soc. A.I.M.E.*, 245, 1969, p. 1471.

5 Kroeger, P. G., "A Heat Transfer Analysis of Solidification of Pure Metals in Continuous Casting Processes," in *Heat Transfer 1970, Proceedings 4th International Heat Transfer Conference*, Vol. 1, Cu. 2.7, Paris, 1970.

6 Goodman, T. R., "The Heat-Balance Integral—Further Considerations and Refinements," JOURNAL OF HEAT TRANSFER, TRANS. ASME, Series C, Vol. 83, 1961, p. 83.

7 Carslaw, H. S., and Jaeger, J. C., *Conduction of Heat in Solids*, Oxford University Press, Second ed., London, 1959.

8 Tikhonov, A. N., and Shvidovsky, E. G., "The Theory of Continuous Castings," *Zhurnal Teoreticheskoy Fiziki*, Vol. XVII, No. 2, 1947.

APPENDIX 1

Derivation of the Integral Equation. In order to derive equation (4), we start by multiplying (1) by r and integrating it along the radial direction from 0 to R. Assuming the temperature field to be constant in the liquid region, this integration will be equivalent to an integration between $R - \ell$ and R.

$$\int_{R-\ell}^{R} \frac{\partial}{\partial r}\left(r\frac{\partial t}{\partial r}\right) dr + \int_{R-\ell}^{R} \frac{\partial^2 t}{\partial x^2} r dr = \frac{C_p U \rho}{k} \int_{R-\ell}^{R} \frac{\partial t}{\partial x} r dr \quad \text{(A1)}$$

The first term may be written as:

$$\int_{R-\ell}^{R} \frac{\partial}{\partial r}\left(r\frac{\partial t}{\partial r}\right) dr = -\frac{Rht_R}{k} - (R-\ell)\frac{\partial t}{\partial r}\Big|_{R-\ell}$$

Applying Leibnitz rule twice, the second term may be written:

$$\int_{R-\ell}^{R} \frac{\partial^2 t}{dx^2} r dr = \frac{d^2}{dx^2}\int_{R-\ell}^{R} rt dr - (R-\ell)t_0 \frac{d^2\ell}{dx^2} + t_0\left(\frac{d\ell}{dx}\right)^2 - (R-\ell)\frac{d\ell}{dx}\left(\frac{\partial t}{\partial x}\right)_{R-\ell}$$

Applying Leibitz rule to the term on the right-hand side we get:

$$\frac{C_p U \rho}{k}\int_{R-\ell}^{R} \frac{\partial t}{\partial x} r dr = \frac{C_p U \rho}{k}\frac{\partial}{\partial x}\int_{R-\ell}^{R} tr dr - \frac{d\ell}{dx} t_0 (R-\ell)$$

Substituting in (A1), grouping terms and using the boundary conditions (2) and (3) we get the final form:

$$\frac{d^2\theta}{dX^2} - (1-\delta)\frac{d^2\delta}{dX^2} + \left(\frac{d\delta}{dX}\right)^2 - \mathrm{P}\frac{d\theta}{dX} + \mathrm{P}(1-\delta)(1+\Lambda)\frac{d\delta}{dX} - \mathrm{B}T_R = 0$$

where:

$$X = \frac{x}{R}; \quad \delta = \frac{\ell}{R}; \quad T_R = \frac{t_R}{t_0} \quad \text{and} \quad \theta = \int_{R-\ell}^{R} \frac{tr}{t_0 R^2} dr$$

And B, P, and Λ are, respectively, the Biot number, Peclet number and the dimensionless latent heat given by:

$$\mathrm{B} = \frac{Rh}{k}, \quad \mathrm{P} = \frac{C_p U R \rho}{k}, \quad \Lambda = \frac{\lambda}{C_p t_0}$$

APPENDIX 2

Choice of Boundary Conditions. A common difficulty with integral methods is to decide a priori which boundary conditions to use in order to get the best accuracy. Sometimes by using higher order polynomials and using more boundary conditions, the solution becomes even less accurate [6].

In our case we choose to write equation (1) on the surface instead of using (3). Besides being more convenient, we feel that this choice is more suitable because θ is mostly sensitive to errors in $t(r)$ for large r. In other words it is preferable to improve our approximating polynomial for t near the surface rather than near the solid-liquid interface. Furthermore, although (3) is not satisfied on a point-by-point basis, it is still satisfied on an integral basis through (16) where we equate the total energy supply to the total energy released on the surface.

Nevertheless, once the solution $\delta(X)$ is found, it becomes possible to find out to what extent equation (3) is not satisfied. To do this we write (3) in the following dimensionless form:

$$\left(\frac{\partial T}{\partial Y}\right)_{\delta} = \mathrm{P}\Lambda\frac{d\delta}{dX}\left[1 + \left(\frac{d\delta}{dX}\right)^2\right]^{-1}$$

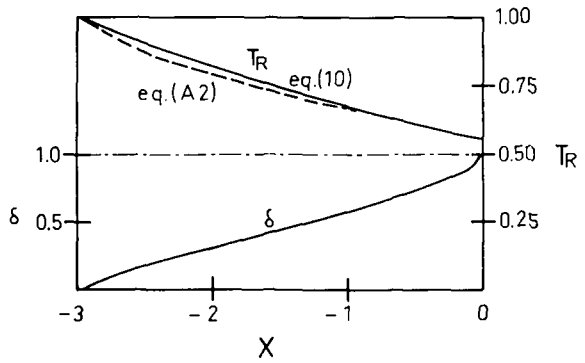

Fig. 5 Comparison between the surface temperatures T_R obtained from equations (10) and (A2) for the case with B = 1, P = 2.5, and Λ = 0.68

from the approximating polynomial for T we get:

$$\left(\frac{\partial T}{\partial Y}\right)_\delta = BT_R + \frac{n}{\delta}[1 - (1 + B\delta)T_R]$$

equating these two expressions we get:

$$T_R = \frac{n - P\Lambda\delta\dfrac{d\delta}{dX}\left[1 + \left(\dfrac{d\delta}{dX}\right)^2\right]^{-1}}{B\delta(n-1) + n} \tag{A2}$$

If equation (3) was satisfied exactly, then the value of T_R obtained from (A2) should be exactly equal to the value obtained from (10). Fig. 5 shows a comparison of these two values for a typical case. The difference is seen to be quite small and it decreases with increasing δ. This is due to the fact that θ becomes less and less sensitive to the value of $t(r)$ for small r.

D. C. Wiggert

Department of Civil Engineering,
Michigan State University,
East Lansing, Mich.

Analysis of Early-Time Transient Heat Conduction by Method of Characteristics

The proposed equations describing early-time one-dimensional heat transfer are hyperbolic with temperature and flux being the dependent variables. The method of characteristics is applied resulting in a solution for the variables as functions of distance and time. A dimensionless parameter δ is introduced which is defined either as the inverse thermal propagation speed or relaxation time. The numerical solution yields explicitness, stability, and accuracy combined with ease of handling time-variable boundary conditions. Examples include predicted response to step inputs of flux or temperature at a surface or interface of materials and illustrate the transition from non-Fourier to Fourier-like diffusion.

Introduction

Recently, investigators have analytically explored the phenomenon of non-Fourier effects occurring at very early times in highly transient heat transfer processes. Examples are high-intensity electromagnetic radiation [3],[1] the sudden contacting of two liquids such as uranium dioxide and sodium [9], and high-rate transfer in rarified media [11]. Traditional heat conduction analysis is based on two basic relations, namely, the first law of thermodynamics and the Fourier law; combined they form a parabolic equation which, depending upon the complexity of the boundary conditions, can be solved either analytically or numerically. Implicit in the Fourier law is the assumption that the thermal propagation speed is infinite, and for most processes this is appropriate. However, for the early-time situations it has been hypothesized that a finite propagation speed must be accounted for, with the result that an additional term containing the time derivative of flux appears in the Fourier equation. One of the first investigators to propose the modification was Vernotte [18], who also pointed out the hyperbolic nature of the modified equations. Subsequently, a number of studies [4, 6, 12, 13, 15, 19] have been directed toward physical and mathematical interpretation of the hypothesis, leading to the presently accepted relaxation model for heat conduction in solids and liquids.

For one-dimensional flow of heat the first law of thermodynamics is given by

$$q_x + \rho c T_t = 0 \tag{1}$$

wherein the subscripts x and t denote partial derivatives with respect to distance and time, respectively. The modified Fourier equation was presented by Vernotte [18] as

$$\tau q_t + q + k T_x = 0 \tag{2}$$

in which τ is defined as a relaxation time, of the order of 10^{-12} to 10^{-14} s [3, 13]. Equations (1) and (2) can be combined to form a dissipative wave equation

$$T_{tt} + \frac{a^2}{\alpha} T_t - a^2 T_{xx} = 0 \tag{3}$$

in which $a = \sqrt{\alpha/\tau}$ is the thermal propagation speed. Equation (3) is a hyperbolic relation and closed form solutions have been found for several initial-value problems [2, 9, 14, 15, 19]; however, if one were to introduce factors such as material property nonlinearity, medium nonhomogeneity, or finite boundaries, analytical formulations would become more complex.

Equations (1) and (2) are analogous to the momentum and continuity relations, respectively, for transient one-dimensional flow in a fluid line with distributed lateral flow [20]; for a system of this kind, a generalized numerical analysis can be formulated by using the method of characteristics technique. The solution of hyperbolic equations by this method has become a widely accepted and versatile procedure for analyzing unsteady flow in hydraulic pipe networks [17] and flood waves in rivers [16], for its application to gas dynamics [7], and for problems dealing with solid mechanics and long-wave incompressible flow [1]. Stability and convergence criteria are satisfied [8], combined with ease of programming and incorporation of time-variable boundary conditions.

[1] Numbers in brackets designate References at end of paper.

Contributed by the Heat Transfer Division for publication in the JOURNAL OF HEAT TRANSFER. Manuscript received by the Heat Transfer Division March 24, 1976.

The intent of this paper is to present a numerical technique for analysis of early-time, one-dimensional heat transfer processes based on the method of characteristics. It will be shown that a variety of initial boundary value problems can readily be formulated and solved within the basic framework, and that the technique provides a viable alternative to Laplace transform methods. In particular, applications will include, but not be limited to, the predicted response to step inputs of flux or temperature at a material surface, or at the interface of two materials, illustrating the transition from non-Fourier to Fourier-like heat diffusion. No attempt has been made to present new data.

It is recognized that some controversy exists regarding the validity of the wave hypothesis, i.e., continuum relationships are questionable in the short time intervals considered. But it will be supposed herein that equation (2) is acceptable.

Analytical Development

In the ensuing development of the method of characteristics the following assumptions are made: (1) the heat conduction process is one-dimensional, (2) the thermal properties are invariant, and (3) the relaxation time τ is known for the given material.

Introducing the dimensionless parameters

$$T^* = T/T_0 \tag{4}$$

$$q^* = qL/kT_0 \tag{5}$$

$$t^* = t\alpha/L^2 \tag{6}$$

$$x^* = x/L \tag{7}$$

and substituting them into equations (1) and (2) yields

$$q_{x^*}{}^* + T_{t^*}{}^* = 0 \tag{8}$$

$$\delta^2 q_{t^*}{}^* + q^* + T_{x^*}{}^* = 0 \tag{9}$$

in which

$$\delta^2 = \tau\alpha/L^2 \tag{10}$$

Note that δ^2 can be interpreted as the dimensionless relaxation time. As $\delta \to 0$, equation (9) becomes the Fourier law. Further significance will be attributed to this parameter in later discussion. Henceforth, the asterisk superscripts will be dropped from the dimensionless variables.

Method of Characteristics. In matrix form equations (8) and (9) can be written

$$\begin{bmatrix} \delta^2 & 0 \\ 0 & 1 \end{bmatrix} \begin{Bmatrix} q \\ T \end{Bmatrix}_t + \begin{bmatrix} 0 & 1 \\ 1 & 0 \end{bmatrix} \begin{Bmatrix} q \\ T \end{Bmatrix}_x + \begin{Bmatrix} q \\ 0 \end{Bmatrix} = 0 \tag{11}$$

Since the equations are hyperbolic, the condition

$$\det \begin{bmatrix} -\lambda\delta^2 & 1 \\ 1 & -\lambda \end{bmatrix} = 0 \tag{12}$$

will yield two real eigenvalues, or characteristic roots [8], namely

$$\lambda = \pm\delta^{-1} \tag{13}$$

The compatibility condition can be computed in a straightforward manner [8] and is given as

$$\delta^2 \frac{dq}{dt} \pm \delta \frac{dT}{dt} + q = 0 \tag{14}$$

which must be integrated along the characteristic lines

$$\frac{dx}{dt} = \pm\delta^{-1} \tag{15}$$

It can be shown that the characteristic lines in dimensional form are simply $\pm a$, the thermal propagation speed; hence δ can be considered additionally as the inverse dimensionless propagation speed.

Numerical Solution. The characteristic directions in the x-t domain are represented in Fig. 1(a). Generally the lines are curved, but since constant material properties are assumed, δ is constant and they become straight. It is necessary to integrate each compatibility relation, equation (14), along its respective characteristic $\overline{AP}$ or $\overline{BP}$ and solve for unknown values of T and q at node P. Values of the dependent variables at nodes A and B are known, either from initial conditions or from an earlier time solution. The domain is divided into a discrete grid Δx by Δt, Fig. 1(b), and the compatibility condition is integrated from time t to $t + \Delta t$:

$$\delta^2 \int_{q_{A,B}}^{q_P} dq \pm \delta \int_{T_{A,B}}^{T_P} dT + \int_t^{t+\Delta t} q\,dt = 0 \tag{16}$$

or, since $dt = \pm\,\delta dx$

$$\delta \int_{q_{A,B}}^{q_P} dq \pm \int_{T_{A,B}}^{T_P} dT \pm \int_{x_{A,B}}^{x_P} q\,dx = 0 \tag{17}$$

The last integral in equation (17) is approximated by the trapezoidal rule formula, thus allowing the equations to be written in finite difference form:

$$\delta(q_P - q_A) + (T_P - T_A) + \frac{1}{2}(q_P + q_A)\Delta x = 0 \tag{18}$$

$$\delta(q_P - q_B) - (T_P - T_B) + \frac{1}{2}(q_P + q_B)\Delta x = 0 \tag{19}$$

A simultaneous solution of equations (18) and (19) will provide values of T_P and q_P at the interior nodes:

$$T_P = \frac{1}{2}[T_A + T_B + (q_A - q_B)(\delta - \Delta x/2)] \tag{20}$$

$$q_P = [(q_A + q_B)(\delta - \Delta x/2) + T_A - T_B][2(\delta + \Delta x/2)]^{-1} \tag{21}$$

Boundary conditions can be treated generally by specifying known time-variable functions of either flux or temperature at the surface of a given material. Then the appropriate compatibility relation, equation (18) or (19), is used to compute the other unknown. For example, consider the case in which the boundary conditions are $T(0, t) = f(t)$ and $q(1, t) = g(t)$, where f and g are known. The solution for $q(0, t)$ is, with equation (19):

$$q_P = [q_B(\delta - \Delta x/2) + f(t_P) - T_B](\delta + \Delta x/2)^{-1} \tag{22}$$

Nomenclature

a = thermal propagation speed, $\sqrt{\alpha/\tau}$
c = specific heat
f = known temperature at left-hand boundary
g = known heat flux at right-hand boundary
k = thermal conductivity
L = reference length
q = heat flux per unit area
Q_0 = reference heat flux per unit area
t = time
T = temperature
T_0 = reference temperature
x = distance
α = thermal diffusivity, $k/\rho c$
$\delta = \sqrt{\tau\alpha/L^2}$
Δx = finite distance interval
Δt = finite time interval
λ = characteristic root
ρ = density
τ = relaxation time

Subscripts

1 = for position where $x < 0$
2 = for position where $x > 0$
A, B = for nodal positions where T and q are known
P = for nodal position where T and q are unknown

Superscript

* = for temporarily denoting dimensionless variables

Correspondingly, the solution for $T(1, t)$ is found with equation (18)

$$T_P = T_A - g(t_P)(\delta + \Delta x/2) + q_A(\delta - \Delta x/2) \tag{23}$$

The boundary characteristic lines are illustrated in Fig. 1(a). Note that initial conditions are to be prescribed at all nodes along the $t = 0$ axis or along an initial characteristic line.

Stability Criterion. For the method of characteristics solution the Courant condition

$$\Delta x/\Delta t \geq \delta^{-1} \tag{24}$$

governs the stability criterion [8]. In the numerical scheme presented herein, the equality of equation (24) is required to be satisfied. Use of the trapezoidal rule to evaluate the last integral in equation (17) is termed a second-order approximation [10]. No additional constraints to insure stability and convergence are necessary since the finite-difference grid of Fig. 1(b) approximates the true grid of characteristics [8]. The characteristics method can also handle situations in which the characteristic root δ becomes variable, e.g., due to nonhomogeneity of the material, or to properties becoming functions of the dependent variables. Techniques for numerically treating these conditions are available [8, 10].

Application

Step Input of Flux Into Semi-Infinite Material. Consider a single material in which initially there is no temperature or flux distribution. At one surface a flux of heat is suddenly imposed, while at the other end a zero heat flux condition is given. In dimensionless terms the boundary conditions and initial values are given by

$$\left.\begin{aligned} q(x, 0) = T(x, 0) = 0, \quad 0 \leq x \leq 1 \\ q(0, t) = 1 \quad \text{and} \quad q(1, t) = 0, \quad t > 0 \end{aligned}\right\} \tag{25}$$

The characteristics grid for numerical analysis of this problem is shown in Fig. 2. As an alternate to the initial condition stated by equation (25), since the disturbance to the system is initiated at $x = 0$, the flux and temperature could be initially specified along the characteristic line $t = \delta x$ emanating from the axis origin. A true semi-infinite analysis would require that no wave propagating from

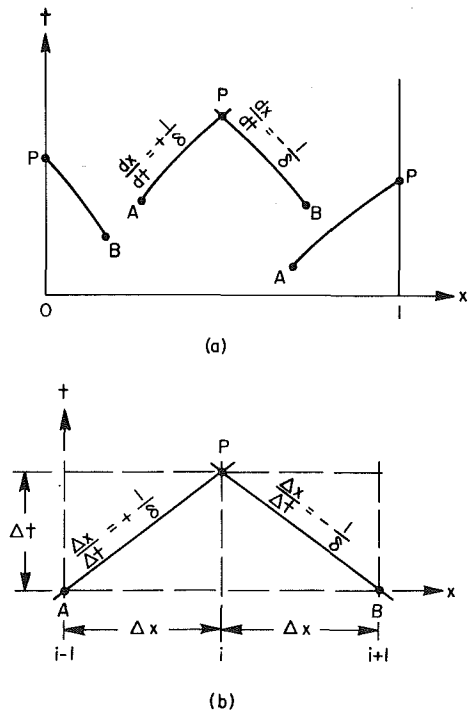

Fig. 1 (a) Characteristic lines in x-t domain; (b) finite difference grid

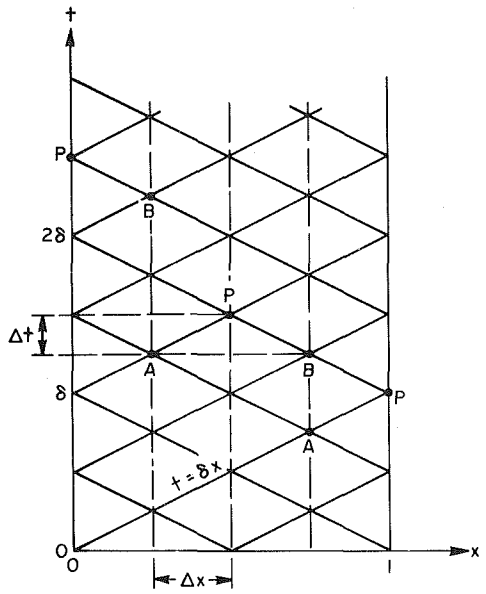

Fig. 2 Characteristics grid for single material

the surface ($x = 0$) be reflected from the finite end ($x = 1$) back again into the medium. Note, however, that the temperature at the surface is not affected by the reflected initial wave until the time 2δ, that is, the time it takes the wave to travel twice the length of the medium.

The initial temperature rise at the surface can be obtained from equation (19) by setting $q_P = 1$, $q_B = T_B = 0$, and by allowing $\Delta x \to 0$. The result is simply

$$T(0, 0+) = \delta \tag{26}$$

and this relation provides a third interpretation of the parameter δ, namely, the initial temperature at the surface when a unit input of heat flux is suddenly imposed.

The numerical solution for the problem stated by equation (25) and with the domain given in Fig. 2 proceeds by solving equations (20) and (21) for T_P and q_P at interior nodes and computing T_P at the boundaries with equations (18) and (19) wherein $q_P = 0$ and $q_P = 1$, respectively. The surface temperature at $x = 0$ as a function of time, for different values of δ, is shown in Fig. 3. The Fourier solution at the surface, given by [5]

$$T = 2\sqrt{t} \sum_{n=0}^{\infty} \{\text{ierfc}\,[n/\sqrt{t}] + \text{ierfc}\,[(n+1)/\sqrt{t}]\} \tag{27}$$

is shown for comparison. It is observed that with increasing δ, the temperatures initially deviate further from the Fourier prediction. However, as time increases, the predicted temperatures will approach the analytic solution of equation (27)

The effect of the right-hand side boundary condition, $q(1, t) = 0$, is related in Fig. 4; for $\delta = 0.8$, and for various times, the computed temperature response is shown distributed along x. Discontinuous wave fronts are evident and they quickly begin to attenuate. Until the first front is reflected from the boundary at $x = 1$ and returns to the opposite end at time $t = 1.60$, the temperature response at $x = 0$ behaves as if the medium were semi-infinite. Thus the computed temperature would be the same as that given by the analytical wave solution, equation (A26) in Appendix B; however, subsequently the temperature responds with a step increase. The discontinuous wave patterns will continue until they have become damped out, resulting in Fourier-like behavior.

It is worthy to note that the step input of flux yields a corresponding initial rise of temperature, as shown by equation (26). Conversely, it is now apparent that if a step input of temperature were imposed at the surface, the corresponding flux would likewise be a step response, given in dimensionless form as $1/\delta$. Even though the limiting argument

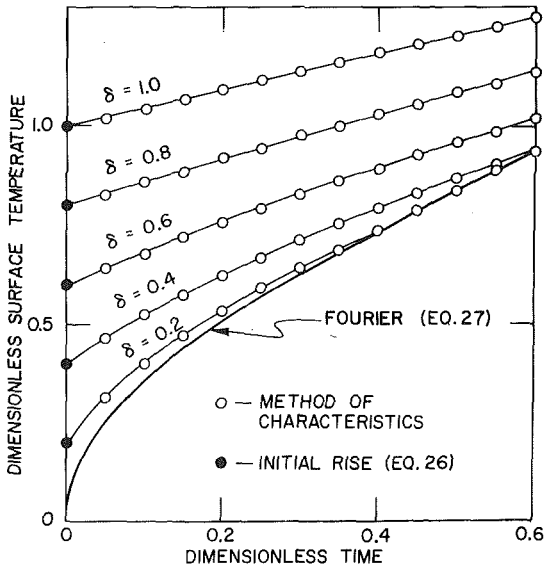

Fig. 3 Dimensionless temperature response at surface for different values of δ

leading to equation (26) is premised upon a numerical relation, the results are corroborated analytically in Appendix B. The hydraulic analog to this situation has been known for many years [17].

Two Suddenly Contacting Materials. In a recent study [9] Kazimi and Erdman analyzed the situation in which uranium dioxide and liquid sodium suddenly come into contact, as part of a hypothetical accident condition in a nuclear reactor. With simplifying assumptions, both the short-time (non-Fourier) and long-time (Fourier) behaviors of the interface temperature were analytically predicted using Laplace transforms; however, the intermediate, or transition values were not treated.

A numerical solution using the characteristics method is formulated beginning with the grid shown in Fig. 5, where the interface exists at location $x = 0$. A special boundary condition can be formulated in which compatibility relations analogous to equation (16) are integrated along the characteristics $\overline{AP}$ and $\overline{BP}$. Each of the two relations, more conveniently written in dimensional form, will contain coefficients dependent upon its location in region one or two:

$$(\rho ca)_1(T_P - T_A) + (q_P - q_A) + \frac{\Delta t}{2\tau_1}(q_P + q_A) = 0 \qquad (28)$$

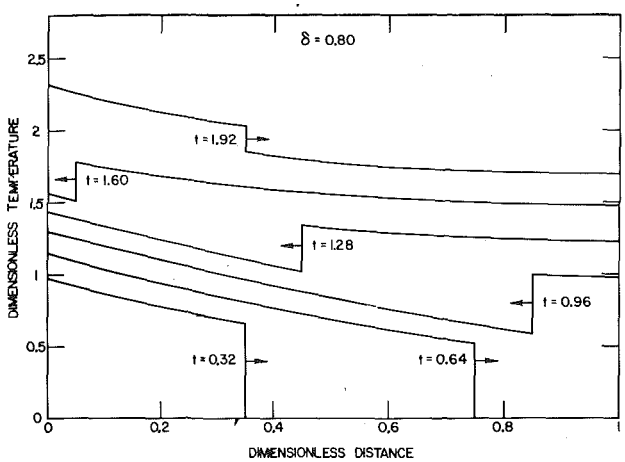

Fig. 4 Dimensionless temperature response within medium for different values of dimensionless time

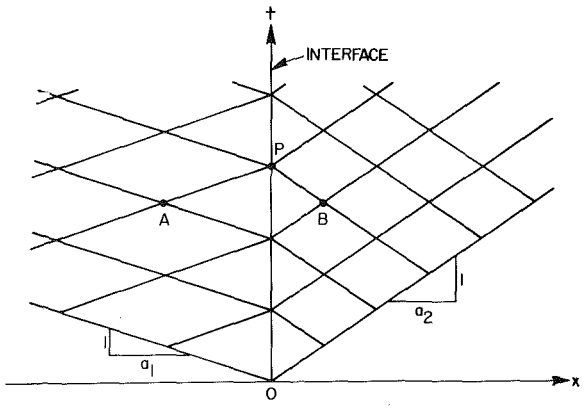

Fig. 5 Characteristics grid for two materials with interface

$$(\rho ca)_2(T_P - T_B) - (q_P - q_B) - \frac{\Delta t}{2\tau_2}(q_P + q_B) = 0 \qquad (29)$$

Simultaneous solution of equations (28) and (29) will yield instantaneous values of temperature and flux at the interface. The solution proceeds at interior regions using equations (20) and (21) with boundary conditions away from the interface treated in the manner described earlier.

The initial temperature and flux at the interface can be obtained by allowing $\Delta t \to 0$ in equations (28) and (29), along with $q_A = q_B = 0$. If $T_A = T_1$ and $T_B = T_2$, where T_1 and T_2 are material temperatures before contact, then

$$T(0, 0+) = \frac{(\rho ca)_1 T_1 + (\rho ca)_2 T_2}{(\rho ca)_1 + (\rho ca)_2} \qquad (30)$$

$$q(0, 0+) = \frac{(\rho ca)_1(\rho ca)_2(T_1 - T_2)}{(\rho ca)_1 + (\rho ca)_2} \qquad (31)$$

Equation 30 is identical to the one developed by Kazimi and Erdman [9].

With the data given in Table 1 the numerical solution of the interface temperature and flux using the method of characteristics is illustrated in Fig. 6. Since the time scale covers four decades, three different time steps are used in the analysis; even so, the values appear to converge after several computations. The interfacial temperature agrees with the early- and late-time approximations [9] and in addition the transition solution is obtained.

Conclusions

The non-Fourier equations describing early-time transient heat conduction have been shown to be hyperbolic [18], with the thermal propagation speed given by $a = \sqrt{\alpha/\tau}$. Dependent variables are temperature and heat flux, and time and distance are independent variables. The method of characteristics is applied to the equations transforming them to two compatibility relations which can be integrated numerically along characteristic lines in the time-distance domain. The numerical solution is formulated with dimensionless

Table 1 Material properties for interface problem [7]

Property	UO_2	Na
ρ (gm/cm)	8.52	0.83
c (cal/gm-°C)	0.12	0.31
k (cal/cm-sec-°C)	0.005	0.0915
τ (sec)	1.69×10^{-13}	6.72×10^{-12}
Initial temp. (°C)	3000	800

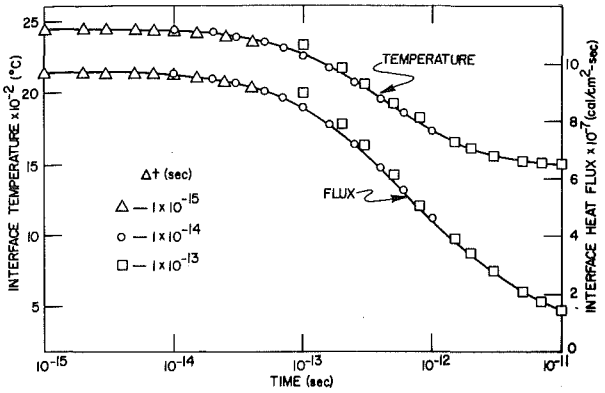

Fig. 6 Temperature and heat flux response at interface

variables, out of which appears a significant parameter δ, which can be interpreted as the dimensionless relaxation time or as the inverse of the dimensionless thermal propagation speed.

Two numerical examples are presented which predict the temperature response to a step input of flux at a material surface, and the response of temperature and flux at an interface of two suddenly contacting materials. These illustrations are given primarily to show the efficacy of the characteristics method. This technique, which has become widely accepted for the analysis of hydraulic transients, offers the advantages of an explicit, stable, and accurate computing scheme combined with ease of programming. For the interface problem shown in Fig. 6, the computer program consists of approximately 80 FORTRAN statements, and with a time step of $\Delta t = 1 \times 10^{-14}$ s, the execution time on a CDC 6500 computer is 1.022 s.

Although not dealt with herein, the method of characteristics solution could readily handle a variety of time-variable boundary conditions or situations in which the material properties become functions of one or more of the dependent variables. In addition, Fourier-like solutions at late times can be obtained by imposing an artificial multiplier upon the first term in equation (2). In this manner, the time step governed by the Courant condition, equation (24), is increased significantly. However, the multiplier must be restricted, so that the magnitude of the modified term remains sufficiently small. This technique, which compares favorably with finite element methods, has been applied successfully to analyze one- and two-dimensional transient porous media flow [21].

Acknowledgments

Appreciation is extended to J. Beck and D. Yen for helpful discussions and review of the text. The figures were prepared by K. Cornelius.

References

1 Abbott, M. B., *An Introduction to the Method of Characteristics*, American Elsevier, New York, 1966.

2 Baumeister, K. J., and Hamill, T. D., "Hyperbolic Heat-Conduction Equation—A Solution for the Semi-Infinite Body Problem," JOURNAL OF HEAT TRANSFER, TRANS. ASME, Series C, Vol. 91, Nov. 1969, pp. 543–548, Feb. 1971, pp. 126–127.

3 Brazel, J. P., and Nolan, E. J., "Non-Fourier Effects in the Transmission of Heat," *Proceedings 6th Conference on Thermal Conductivity*, Dayton, Ohio, 1966, pp. 237–254.

4 Bubnov, V. A., "Wave Concepts in the Theory of Heat," *International Journal of Heat Mass Transfer*, Vol. 19, 1976, pp. 175–184.

5 Carslaw, H. S., and Jaeger, J. C., *Conduction of Heat in Solids*, Oxford University Press, London, 1959.

6 Chester, M., "Second Sound in Solids," *Physical Review*, Vol. 131, No. 5, Sept. 1963, pp. 2013–2015.

7 Courant, R., and Friedrichs, K. O., *Supersonic Flow and Shock Waves*, Interscience, New York, 1948.

8 Forsythe, G. E., and Wasow, W. R., *Finite-Difference Methods for Partial Differential Equations*, Wiley, New York, 1960.

9 Kazimi, M. S., and Erdman, C. A., "On the Interface Temperature of Two Suddenly Contacting Materials," JOURNAL OF HEAT TRANSFER, TRANS. ASME, Series C, Vol. 97, Nov. 1975, pp. 615–617.

10 Lister, M., "The Numerical Solutions of Hyperbolic Partial Differential Equations by the Method of Characteristics," in Ralston, A., and Wilf, H. S., eds., *Mathematical Methods for Digital Computers*, Wiley, New York, 1960.

11 Luikov, A. V., *Analytical Heat Diffusion Theory*, Academic Press, New York, 1968, pp. 9–12, 20–21.

12 Luikov, A. V., Bubnov, V. A., and Soloviev, I. A., "On Wave Solutions of the Heat Conduction Equation," *International Journal Heat Mass Transfer*, Vol. 19, 1976, pp. 245–248.

13 Maurer, M. J., "Relaxation Model for Heat Conduction in Metals," *Journal of Applied Physics*, Vol. 40, No. 13, Dec. 1969, pp. 5123–5130.

14 Maurer, M. J., and Thompson, H. A., "Non-Fourier Effects at High Heat Flux," JOURNAL OF HEAT TRANSFER, TRANS. ASME, Series C, Vol. 95, May 1973, pp. 284–286.

15 Nettleton, R. E., "Relaxation Theory of Thermal Conduction in Liquids," *The Physics of Fluids*, Vol. 3, No. 2, Mar.–Apr. 1960, pp. 216–225.

16 Stoker, J. J., *Water Waves*, Interscience, New York, 1957.

17 Streeter, V. L., and Wylie, E. B., *Hydraulic Transients*, McGraw-Hill, New York, 1967.

18 Vernotte, P., "Les paradoxes de la théorie continue de l'equation de la chaleur," *Compt. Rend.*, Vol. 246, Paris, 1958, pp. 3154–3155.

19 Weyman, H. D., "Finite Speed of Propagation in Heat Conduction Diffusion, and Viscous Shear Motion," *American Journal of Physics*, Vol. 35, No. 6, June 1967, pp. 488–496.

20 Wiggert, D. C., "Unsteady Flows in Lines With Distributed Leakage," *Journal Hydraulics Division, ASCE*, Vol. 94, No. HY1, Jan. 1968, pp. 143–162.

21 Wiggert, D. C., and Wylie, E. B., "Numerical Predictions of Two-Dimensional Transient Groundwater Flow by the Method of Characteristics," *Water Resources Research* Vol. 12, No. 5, Oct. 1976.

APPENDIX A

Numerical Programming Scheme

The nodal subscripts which appear in the integrated finite-difference relations can be replaced by integer notation to facilitate numerical programming. Referring to Fig. 1(*b*), let the index i denote nodal position along x, and N the total number of nodes. At time t, q_i and T_i, $i = 1, \ldots, N$ are known fluxes and temperatures, respectively, and the unknown parameters to be computed at time $t + \Delta t$ are q_{P_i} and T_{P_i}, $i = 1, \ldots, N$. At the interior nodes equations (20) and (21) give

$$T_{P_i} = \frac{1}{2}[T_{i-1} + T_{i+1} + (q_{i-1} - q_{i+1})(\delta - \Delta x/2)] \tag{A1}$$

$$q_{P_i} = [(q_{i-1} + q_{i+1})(\delta - \Delta x/2) + T_{i-1} - T_{i+1}][2(\delta + \Delta x/2)]^{-1} \tag{A2}$$

in which $i = 2, \ldots, N-1$. The left-hand boundary condition is, for example

$$T_{P_1} = f(t + \Delta t) = f_P \tag{A3}$$

$$q_{P_1} = [q_2(\delta - \Delta x/2) + f_P - T_2](\delta + \Delta x/2)^{-1} \tag{A4}$$

and the right-hand boundary condition could be

$$q_{P_N} = g(t + \Delta t) = g_P \tag{A5}$$

$$T_{P_N} = T_{N-1} - g_P(\delta + \Delta x/2) + q_{N-1}(\delta - \Delta x/2) \tag{A6}$$

After all parameters have been evaluated at time $t + \Delta t$, they are substituted into the known arrays, viz.,

$$T_i = T_{P_i} \quad \text{and} \quad q_i = q_{P_i}, \quad i = 1, \ldots, N \tag{A7}$$

and computation proceeds to the next time step. Additional details can be found in reference [13], Chapter 3.

APPENDIX B

Analytical Solution for Semi-Infinite Slab With Step Input of Flux or Temperature

Consider the system of equations given by equations (8) and (9)

$$q_x + T_t = 0 \tag{A8}$$

$$\delta^2 q_t + q + T_x = 0 \tag{A9}$$

The initial conditions are

$$q(x, 0) = T(x, 0) = 0, \quad 0 \le x \le 1 \tag{A10}$$

and the boundary conditions are either

$$(a) \begin{cases} q(0, t) = 1, & t > 0 \quad \text{(A11)} \\ q(x, t) = 0, & t > 0, \quad x \to \infty \quad \text{(A12)} \end{cases}$$

or

$$(b) \begin{cases} T(0, t) = 1, & t > 0 \quad \text{(A13)} \\ T(x, t) = 0, & t > 0, \quad x \to \infty \quad \text{(A14)} \end{cases}$$

It is desired to obtain the solution of the temperature at the surface ($x = 0$) for boundary condition (a) and the flux at the surface for boundary condition (b).

The Laplace transforms for q and T are defined as

$$\hat{q}(x, s) = L[q(x, t)] \quad \text{and} \quad \hat{T}(x, s) = L[T(x, t)] \tag{A15}$$

With the initial conditions included, equations (A8) and (A9) in the transform of q and T become

$$\frac{d\hat{q}}{dx} + s\hat{T} = 0 \tag{A16}$$

$$(\delta^2 s + 1)\hat{q} + \frac{d\hat{T}}{dx} = 0 \tag{A17}$$

and the transformed boundary conditions are

$$(a) \begin{cases} \hat{q}(0, s) = \dfrac{1}{s} & \text{(A18)} \\ \hat{q}(x, s) = 0, \quad x \to \infty & \text{(A19)} \end{cases}$$

or

$$(b) \begin{cases} \hat{T}(0, s) = \dfrac{1}{s} & \text{(A20)} \\ \hat{T}(x, s) = 0, \quad x \to \infty & \text{(A21)} \end{cases}$$

Elimination of $\hat{q}$ in equations (A16) and (A17) yields

$$\frac{d^2\hat{T}}{dx^2} - s(\delta^2 s + 1)\hat{T} = 0 \tag{A22}$$

The general solution is

$$\hat{T}(x, s) = A(s)e^{nx} + B(s)e^{-nx} \tag{A23}$$

in which $A(s)$ and $B(s)$ are dependent upon the boundary conditions, and

$$n = \delta\sqrt{s(s + \delta^{-2})} \tag{A24}$$

Consider boundary condition (a). Combining equations (A17)–(A19) and the derivative of equation (A23) with respect to x gives $A(s) = 0$ and $B(s) = n/s^2$, so that at $x = 0$,

$$\hat{T}(0, s) = \frac{n}{s^2} \tag{A25}$$

The inverse transform becomes [14]

$$T(0, t) = S(t)\delta \exp\left(-\frac{t}{2\delta^2}\right)\left[(1 + t)I_0\left(\frac{t}{2\delta^2}\right) + tI_1\left(\frac{t}{2\delta^2}\right)\right] \tag{A26}$$

where I_0 and I_1 are Bessel functions of the first kind and S is the unit step function. In the limit as $t \to 0+$, the surface temperature is $T(0, 0+) = \delta$, which is identical to the limiting value in the compatibility relation, equation (26).

For boundary condition (b), equations (A20), (A21), and (A23) yield $A(s) = 0$ and $B(s) = 1/s$. A combination of equation (A17) and the derivative of equation (A23) with respect to x at $x = 0$ results in

$$\hat{q}(0, s) = \frac{1}{n} \tag{A27}$$

and the inverse transformation is [2]

$$q(0, t) = S(t)\frac{1}{\delta}\exp\left(-\frac{t}{2\delta^2}\right) I_0\left(\frac{t}{2\delta^2}\right) \tag{A28}$$

As $t \to 0+$, the flux at the surface is $q(0, 0+) = \delta^{-1}$, a result which can also be obtained from the compatibility relation, equation (19).

Y. P. Chang
Department of Mechanical Engineering,
State University of New York at Buffalo,
Buffalo, N. Y.

R. C. H. Tsou[1]
General Electric Co.,
San Jose, Calif.

Heat Conduction in an Anisotropic Medium Homogeneous in Cylindrical Regions—Unsteady State

A number of problems of heat conduction in an anisotropic medium of a monoclinic system which is homogeneous in circular cylinder coordinates are solved through the use of Green's functions. Regions of solid and hollow cylinders, and an infinite region bounded internally by a cylindrical surface with boundary conditions of Dirichlet, Neumann, and mixed types are considered. Calculated results for two examples are shown, and the effects of material anisotropy on the temperature field are discussed. This paper is the first of a series to be reported in the open literature concerning the analytical solution for heat conduction in anisotropic media which are homogeneous in circular cylinder and rectangular coordinate systems.

Introduction

Since Duhamel (1832) and Stokes (1851), the study of anisotropic materials has been of great interest in science and engineering, ranging from solid and fluid mechanics to heat and mass transfer. In recent years, this area of research has become increasingly important due to the rapidly increasing use of man-made materials in laminated and fiber reinforced structures of crystals in electronic equipment and for heat shielding materials in space vehicles. Many natural substances such as woods and sedimentary rocks are anisotropic. Metals which have undergone heavy cold forming also exhibit some kind of anisotropy.

In spite of the importance of anisotropic problems, analytical solutions have been limited to a few special cases: for instance, elastic stressing with the anisotropy homogeneous in rectangular coordinates but in a circular domain [1],[2] and in cases where the displacement components can be expressed in terms of power functions of spatial variables [2]. A shorter account on elastic stresses, thermal stresses, and elastic waves in orthotropic and anisotropic media can be found in [3]. Transport processes in anisotropic, porous media were studied by Neale [4] and Whitaker [5]. Two-dimensional analyses of thermal stresses in a half-space and in a slab were reported by Clements [6] and Tauchert and Akroz [7].

Reported results of analytical solution of anisotropic problems with heat conduction as the principal subject have been very limited. Turhan and Tuna [8] extended an "approximate continuum theory on elasticity" to the solution of heat conduction in infinite composite slabs and cylinders, but no result for the anisotropic case was reported. An exact solution of the same problem was reported by Padovan [9, 10] by employing the method for the solution of finite composite slabs and cylinders of isotropic media, so that eigenvalues in three directions are of discrete spectra and can be easily determined.[3] It is to be pointed out, however, that the exact solution for infinite composite slabs and cylinders of even isotropic media has not been found to date because of the difficulty in the evaluation of eigenvalues with respect to the coordinate normal to the laminates. This difficulty is due to the fact that, if the laminates extend to infinity in one direction, then eigenvalues in that direction are to be of continuous spectrum.

There have been several investigations [11, 12] of the heat conduction in regions of orthotropic media which can be conveniently expressed in terms of rectangular coordinates. The analysis for orthotropic media in cylindrical regions is more complicated even for two-dimensional cases [13, 14].

Numerical solution of anisotropic problems has become possible since the advent of electronic computers and is very useful, especially for arbitrarily shaped domains and variable properties. Finite difference and finite element methods are commonly used. However, the numerical solution of an anisotropic problem is more complicated

[1] Many results of this study were obtained in early 1973 while the second author was with the State University of New York at Buffalo.

[2] Numbers in brackets designate References at end of paper.

Contributed by the Heat Transfer Division for publication in the JOURNAL OF HEAT TRANSFER. Manuscript received by the Heat Transfer Division April 28, 1976.

[3] For isotropic media

than that of the isotropic case. Katayama, et al. [15] devised a scheme using a finite difference method and found his calculated results in good agreement with his experimental data. Chang, et al. [16] employed an integral-equation method to calculate the temperature and heat flux distributions in a square, a circular disk and an annular disk. Cobble [17] investigated the heat conduction with variable properties in a wedge by first transforming the partial differential equation into an ordinary differential equation which was then solved numerically. Most of the foregoing studies were made for boundary conditions of Dirichlet type. For boundary conditions other than the Dirichlet type, the calculation would become more complicated. For problems in an unbounded or partially bounded region, particularly in steady state, the numerical solution will be in general very difficult even on high speed computers.

Experimental information regarding thermal conductivity coefficients of general anisotropic materials is very scarce, except for some orthotropic systems and certain crystals [18, 19]. For the experimental study of thermal conductivity coefficients of an anisotropic solid, it is usual to apply the analytical solution of a one-dimensional case (i.e., to assume the temperature dependence of only one spatial coordinate) which is in the same form as that for an isotropic medium, for instance [18, 20]. However, as was pointed out by Leknitski [2], the simplication of two-dimensional analysis is useful only if a body processes a plane of material symmetry. Therefore, in order to obtain reliable information, analytical solutions of multidimensional anisotropic problems are needed.

The senior author of this paper has worked on this research for a number of years. It was found that the most difficult part in the analytical solution of anisotropic problems is to satisfy the boundary conditions, especially of the mixed (radiative or convective) type. According to the degree of difficulty and the methods of solution, it is convenient to divide anisotropic problems into three classes: the first class considers the region bounded by not more than two surfaces which are normal to any one spatial coordinate; the second class considers the region bounded by surfaces on which boundary conditions of the mixed type is limited to only two surfaces normal to any one spatial coordinate; and the third class considers boundary conditions of the mixed type on more than two surfaces. We shall report our results in the sequence of these classes. Another difficulty results from the usual belief that the classical method of separation of variables is not applicable, for instance [9, 21]. According to our studies in this paper and ensuing ones, it was found that this belief is not true, at least in the broad sense of the technique of separation of variables. It was also found that the analytical solution for temperature is in general difficult to obtain, but the Green's functions can be obtained with less difficulty and for most cases they can be expressed in terms of tabulated functions. Therefore, the use of Green's functions is not only a convenient method but also is probably necessary. Once the Green's function is known, the temperature can be readily obtained by the use of Green's formula.

This paper is concerned only with the analytical solution for heat conduction in an anisotropic medium of a monoclinic system which is homogeneous in circular cylinder coordinates.[4] Boundary conditions of Dirichlet, Neumann, and mixed (or convective) types are considered for four different regions: (1) solid cylinder and (2) hollow cylinder of infinite and finite lengths; and (3) an infinite region bounded internally by a cylindrical surface. Infinite region is also considered. An unsteady problem is defined here as one in which the temperature depends on time, either periodically or transiently, or in any other manner. For brevity we shall refer to Dirichlet, Neumann, and convective boundary conditions as the first, second, and third types, respectively. All the problems in this paper belong to the first class.

According to the foregoing findings, the determination of Green's functions will be the principal subject in this paper and a series of subsequent ones. To systemize the solution for problems in bounded and unbounded regions, we shall construct the Green's functions by the method of integral transforms, though the classical method of separation of variables is sometimes more useful for problems in bounded regions as illustrated in [22].

Fundamental Equations and Formal Solutions

Consider the heat conduction in an anisotropic medium of a monoclinic system which is homogeneous in circular cylinder coordinates and is bounded either externally or internally or both internally and externally. All thermo-physical properties of the medium are assumed constant, and the anisotropy is in the plane normal to the axial direction. Then the differential equation to be solved for unsteady state is in the following form [18, 20]:

$$k_{11}\frac{1}{r}\frac{\partial}{\partial r}\left(r\frac{\partial T}{\partial r}\right)+k_{22}\frac{1}{r^2}\frac{\partial^2 T}{\partial\theta^2}+2k_{12}\frac{\partial^2 T}{r\partial r\partial\theta}+k_{33}\frac{\partial^2 T}{\partial z^2}-\rho c\frac{\partial T}{\partial t}=-Q(r,\theta,z,t) \quad (1)$$

in a given region Ω for $t>0$. According to irreversible thermodynamics [23], the following relations must hold:

$$k_{ii}>0, \qquad k_{ii}k_{jj}-k_{ij}{}^2>0 \text{ for } i\neq j,\ k_{ij}\lesseqgtr 0$$

The boundary conditions may be written in the general form

$$b\frac{\partial T}{\partial n^+}+hT=f_i \text{ on } S \text{ for } t>0 \quad (2)$$

where b and h are constants and either one may be unity or zero so that boundary conditions of the first, second and third types are all included. In equation (2), if S represents the surface, or surfaces, normal to z-axis, then $\partial/\partial n^+$ is the derivative with respect to the outer normal of the surface or surfaces; if S denotes the cylindrical surface, or surfaces, then $\partial/\partial n^+$ is the transverse derivative, or derivative with respect to the outer *conormal*, i.e.,

$$\frac{\partial}{\partial n^+}=\pm\left(\frac{\partial}{\partial r}+\nu_{12}\frac{1}{r}\frac{\partial}{\partial\theta}\right) \quad (3)$$

where the minus and plus signs are for internally and externally cylindrical surfaces, respectively.

The initial condition on T may be written as

$$T=F(r,\theta,z) \text{ in } \Omega \text{ for } t=0 \quad (4)$$

If $G(r,\theta,z,t\,|\,r',\theta',z',t')$ is the Green's function associated with the unsteady problem equations (1), (2), and (4), then the temperature can be obtained by the use of Green's second formula [24]

[4] An anisotropic medium which is homogeneous in one coordinate system becomes heterogeneous in other coordinate systems.

Nomenclature

b = 1 or 0 defined in equation (2)
c = specific heat
f = boundary data defined in equation (2)
F = initial data defined in equation (4)
G = Green's function
h = heat transfer coefficient/k_{11}
J_α = Bessel function of first kind order α
k_{ij} = thermal conductivity coefficients
ℓ = length of cylinder
n = outward normal to surface, or 1, 2, 3 . . . , ∞
n^+ = outward conormal to surface
r = radial coordinate
S = surface
T = temperature
t = time
Y_α = Bessel function of second kind order α
z = axial coordinate
ρ = density
$\lambda_{mn}' = \lambda_{mn}/\sqrt{\nu_{33}}$
$\alpha_1 = k_{11}/\rho c$
$\nu_{ij} = k_{ij}/k_{11}$
δ = Dirac delta function
$\beta = (\nu_{22}-\nu_{12}{}^2)^{1/2}$
ϵ = 1 for $n=0$, 2 for $n\neq 0$
θ = angular coordinate

Subscripts

i,j = 1, 2, 3
s = pertaining to surface

$$T(r, \theta; z, t) = \int_\Omega F(r', \theta', z')G(r, \theta, z, t|r', \theta', z', 0) \times d\Omega(r', \theta' z') + \frac{1}{\rho c}\int_0^t dt' \int_\Omega Q(r', \theta', z', t') \times G(r, \theta, z, t|r', \theta', z', t')d\Omega(r', \theta', z') - \alpha_1 \int_0^t dt' \int_S f(r', \theta', z', t') \times \frac{\partial}{\partial n^+} G(r, \theta, z, t|r', \theta', z', t')dS(r', \theta', z') \quad (5)$$

where Ω and S are the domain and surface, or surfaces, to be concerned; and the presence of α_1 is because we shall divide equation (1) by k_{11} as has been done in equations (2) and (3). If the surface conditions are of the Neumann type, i.e., $b = 1$ and $h = 0$ in equation (2), then the last integral in equation (5) is replaced by

$$-\alpha_1 \int_0^t dt' \int_S f(r', \theta', z', t')G(r, \theta, z, t|r', \theta', z', t')dS(r', \theta', z') \quad (6)$$

Determination of Green's Functions

Since the Green's function satisfies the homogeneous differential equation, except at the source point, and homogeneous initial and boundary conditions, we can write

$$G(r, \theta, z, t|r', \theta', z', t') = G_1(z, t|z', t')G_2(r, \theta, t|r', \theta', t') \quad (7)$$

where $G_1(z, t|z', t')$ satisfies

$$\frac{\partial^2 G_1}{\partial z^2} - \frac{1}{\alpha_1 \nu_{33}}\frac{\partial G_1}{\partial t} = -\frac{1}{\alpha_1 \nu_{33}}\delta(z - z')\delta(t - t') \quad (8)$$

$$G_1 = 0 \text{ for } t = 0$$

and appropriate boundary conditions; and $G_2(r, \theta, t|r', \theta', t')$ satisfies

$$\frac{1}{r}\frac{\partial}{\partial r}\left(r\frac{\partial G_2}{\partial r}\right) + \frac{2\nu_{12}}{r}\frac{\partial^2 G_2}{\partial r \partial \theta} + \frac{\nu_{22}}{r^2}\frac{\partial^2 G_2}{\partial \theta^2} - \frac{1}{\alpha_1}\frac{\partial G_2}{\partial t} = \frac{\delta(r - r')\delta(\theta - \theta')\delta(t - t')}{\alpha_1 w(r)} \quad (9)$$

$$G_2 = 0 \text{ for } t = 0$$

and appropriate boundary conditions, where $w(r)$ denotes a weight function yet to be determined.

For $-\infty < z < \infty$, the solution of equation (8) is well-known

$$G_1(z, t|z', t') = \frac{1}{2\sqrt{\pi \alpha_1 \nu_{33}(t - t')}} \exp\left[-\frac{(z - z')^2}{4\alpha_1 \nu_{33}(t - t')}\right] \quad (10)$$

For a finite cylinder, $0 \le z \le \ell$, with boundary conditions of the third type,

$$b_1\frac{\partial G_1}{\partial z} - h_1 G_1 = 0, \quad z = 0; \quad b_2\frac{\partial G_1}{\partial z} + h_2 G_1 = 0, \quad z = \ell \quad (11)$$

we have

$$G_1(z, t|z', t') = \sum_{n=1}^{\infty} Z_n(z)Z_n(z')e^{-\alpha_1 \nu_{33}\omega_n^2(t - t')} \quad (12)$$

where

$$Z_n(z) = \frac{[2(b_2^2\omega_n^2 + h_2^2)]^{1/2}(b_1\omega_n \cos \omega_n z + h_1 \sin \omega_n z)}{\{(b_1^2\omega_n^2 + h_1^2)[\ell(b_2^2\omega_n^2 + h_2^2) + b_2 h_2) + b_1 h_1(b_2^2\omega_n^2 + h_2^2)\}^{1/2}} \quad (13)$$

and ω_n are the roots of the transcendental equation

$$\tan \omega \ell = \frac{\omega(b_1 h_2 + b_2 h_1)}{b_1 b_2 \omega^2 - h_1 h_2} \quad (14)$$

$G_1(z, t|z', t')$ with boundary conditions of the first and second types can be obtained by specializing equation (13) and (14). For the latter, a term $1/\ell$ is to be added to equation (12).

Thus, our problem now is to find the solution of equation (9) for various regions with various boundary conditions. To this end, we assume that the complex finite Fourier transform can be applied to remove the variable θ, i.e., the Fourier transform of $G(r, \theta, t|r', \theta', t')$ defined by

$$\overline{G}_2(r, t|r', t'; \quad \theta', n) = \int_{-\pi}^{\pi} G_2(r, \theta, t|r', \theta', t')\, e^{-in\theta}d\theta \quad (15)$$

exists and its inverse is

$$G_2(r, \theta, t|r', \theta', t') = \frac{1}{2\pi}\sum_{n=-\infty}^{\infty} \overline{G}(r, t|r', t'; \theta', n)e^{in\theta} \quad (16)$$

where $i = \sqrt{-1}$. Following the usual procedure for the construction of the Green's functions by the Fourier transform [25], we obtain

$$\frac{\partial^2 \overline{G}_2}{\partial r^2} + \frac{(1 + 2\,in\,\nu_{12})}{r}\frac{\partial \overline{G}_2}{\partial r} - \frac{\nu_{22}n^2}{r^2}\overline{G}_2 - \frac{1}{\alpha_1}\frac{\partial \overline{G}_2}{\partial t} = -\frac{e^{-in\theta'}}{\alpha_1 w(r)}\delta(r - r')\delta(t - t') \quad (17)$$

In order to obtain a general formula for all the Green's functions associated with problems to be concerned in this paper, we now follow the classical method to seek the solution of equation (17) in the form

$$\overline{G}_2(r, t|r', t'; \quad \theta', n, \lambda) = \psi(r|r', \theta', n, \lambda)e^{-\alpha_1\lambda^2(t - t')} \quad (18)$$

where λ is an arbitrary constant and $\psi(r|r', \theta', n, \lambda)$ satisfies

$$\psi'' + \frac{1 + i2n\nu_{12}}{r}\psi' + \left(\lambda^2 - \frac{22^{n^2}}{r^2}\right)\psi = -\frac{e^{in\theta'}}{w(r)}\delta(r - r') \quad (19)$$

with superscript primes denoting derivatives with respect to r. This equation can be rewritten in the self-adjoint form with weight function $w(r) = r^{1+2in\nu_{12}}$. The solution of equation (19) has the form

$$\psi(r|r', \theta', n, \lambda) = R(r|r', n, \lambda)\, r^{-in\nu_{12}} r'^{in\nu_{12}} e^{-in\theta'} \quad (20)$$

where $R(r, n, \lambda)$ satisfies

$$R'' + \frac{1}{r}R' + \left(\lambda^2 - \frac{\beta^2 n^2}{r^2}\right)R = -\frac{1}{r}\delta(r - r') \quad (21)$$

and appropriate boundary conditions. The solution of equation (21) will involve Bessel functions of orders $\pm n\beta$. It is important to note that equation (21) involves only n^2, while ψ in equation (20) involves both n^2 and n. Therefore, we do not have to take both $+n$ and $-n$ in the solution of equation (21), but both positive and negative values of n of the exponential and power functions in equation (20) must be taken into account.

We now substitute equation (20) into equation (18) and setting the result into equation (16) to obtain

$$G_2(r, \theta, t|r', \theta', t') = \frac{1}{2\pi}\sum_{\lambda}\sum_{n=-\infty}^{\infty} \mathrm{R}(\mathrm{r}|\mathrm{r}', |\mathrm{n}|\beta, \lambda) - \exp\left[in(\theta - \theta') - in\nu_{12}\ln\frac{r}{r'} - \alpha_1\lambda^2(t - t')\right] \quad (22)$$

or

$$G_2(r, \theta, t|r', \theta', t') = \frac{\epsilon}{2\pi}\sum_{n=0}^{\infty} R(r|r', n\beta, \lambda) \times \cos n\left[(\theta - \theta') - \nu_{12}\ln\frac{r}{r'}\right] e^{-\alpha_1\lambda^2(t - t')} \quad (23)$$

where $\epsilon = 1$ for $n = 0$ and $\epsilon = 2$ for $n \neq 0$.

It can be easily shown by substituting equation (22) into the general boundary condition on $G_2(r, \theta, t|r', \theta', t')$:

$$b\frac{\partial G_2}{\partial n^+} + hG_2 = 0 \text{ for } r = r_s \tag{24}$$

where r_s represents the radius or radii of the cylindrical surface or surfaces that equation (24) is satisfied, if R satisfies the boundary conditions:

$$bR' \pm hR = 0 \text{ for } r = r_s \tag{25}$$

where the plus and minus signs have been defined in equation (3).

Solid Cylinder

Consider a solid cylinder of radius r_0 with boundary condition of the third type on the cylindrical surface. The solution of equation (21) satisfying the boundary condition equation (25) at $r = r_0$ and bounded at $r = 0$ is the Bessel function of the first kind of order $n\beta$,

$$R(r|r', n\beta, \lambda) = J_{n\beta}(\lambda_{mn}r)J_{n\beta}(\lambda_{mn}r')/N_{mn}, \qquad n\beta \geq 0 \tag{26}$$

where λ_{mn} are the roots of the transcendental equation

$$\lambda J_{n\beta}'(\lambda r_0) + hJ_{n\beta}(\lambda r_0) = 0 \tag{27}$$

and the norm, N_{mn}, is

$$N_{mn} = \frac{1}{2\lambda_{mn}^2}(B_0^2 + \lambda_{mn}^2 r_0^2 - n^2\beta^2)J_{n\beta}^2(\lambda_{mn}r_0) \tag{28}$$

with $B_0 = hr_0$ which is usually called Biot number. We substitute equation (26) and (28) into formula (23) and the result to equation (7) to obtain the Green's function with the boundary condition of the third type at the cylindrical surface,

$$G(r, \theta, z, t|r', \theta', z', t') = \frac{\epsilon}{\pi}G_1(z, t|z', t') \times \sum_{m=1}^{\infty}\sum_{n=0}^{\infty}\frac{\lambda_{mn}^2 J_{n\beta}(\lambda_{mn}r)J_{n\beta}(\lambda_{mn}r')}{(B_0^2 + \lambda_{mn}^2 r_0^2 + n^2\beta^2)J_n^2(\lambda_{mn}r_0)} \cdot \cos n\left[(\theta - \theta') - \nu_{12}\ln\frac{r}{r'}\right]e^{-\alpha_1\lambda_{mn}^2(t-t')} \tag{29}$$

where $G_1(z, t|z', t')$ has been given in equation (10) and (12) for infinite and finite cylinders.

The Green's function for the boundary condition of the second type on the cylindrical surface can be found in the same way, or by specializing equation (29) as follows:

$$G(r, \theta, z, t|r', \theta', z', t') = \frac{\epsilon}{\pi}G_1(z, t|z', t')\sum_{m=1}^{\infty}\sum_{n=0}^{\infty} \cdot\left[1 + \frac{\lambda_{mn}^2 J_{n\beta}(\lambda_{mn}r)J_{n\beta}(\lambda_{mn}r')}{(\lambda_{mn}^2 r_0^2 - n^2\beta^2)J^2(\lambda_{mn}r_0)}\right] \cdot \cos n\left[(\theta - \theta') - \nu_{12}\ln\frac{r}{r'}\right]e^{-\alpha_1\lambda_{mn}^2(t-t')} \tag{30}$$

where λ_{mn} are the roots of $J_{n\beta}'(\lambda r_0) = 0$. The Green's function for the boundary condition of the first type on the cylindrical surface is

$$G(r, \theta, z, t|r', \theta', z, t') = \frac{\epsilon}{\pi}G_1(z, t|z', t') \times \sum_{m=1}^{\infty}\sum_{n=0}^{\infty}\frac{J_{n\beta}(\lambda_{mn}r)J_n(\lambda_{mn}r')}{J_{n\beta}'^2(\lambda_{mn}r_0)} \cdot \cos n\left[(\theta - \theta') - \nu_{12}\ln\frac{r}{r'}\right]e^{-\alpha_1\lambda_{mn}^2(t-t')} \tag{31}$$

where λ_{mn} are the roots of $J_n(\lambda\eta_0) = 0$.

Hollow Cylinder

Consider a hollow cylinder of inner and outer radii r_1 and r_2 and suppose that the convective heat transfer coefficients are different at the inner and outer surfaces. The solution of equation (21) satisfying boundary conditions (25), with $b = 1$ and $h = h_1$ at $r = r_1$ and $h = h_2$ at $r = r_2$, is

$$R(r|r', n\beta, \lambda_{mn}) = \frac{1}{N_{mn}}[J_{n\beta}(\lambda_{mn}r) - h_{mn}Y_{n\beta}(\lambda_{mn}r)] \times [J_{n\beta}(\lambda_{mn}r') - h_{mn}Y_{n\beta}(\lambda_{mn}r')] \tag{32}$$

where $Y_{n\beta}$ is the Bessel function of the second kind and order $n\beta$;

$$h_{mn} = \frac{\lambda_{mn}J_{n\beta}'(\lambda_{mn}r_2) + h_2J_{n\beta}(\lambda_{mn}r_2)}{\lambda_{mn}Y_{n\beta}'(\lambda_{mn}r_2) + h_2Y_{n\beta}(\lambda_{mn}r_2)} \tag{33}$$

λ_{mn} are the roots of the transcendental equation.

$$[\beta\lambda Y_{n\beta}'(\lambda r_2) + h_2Y_{n\beta}(\lambda r_2)][\beta\lambda J_{n\beta}'(\lambda r_1) - h_1J_{n\beta}(\lambda r_1)] - [\beta\lambda J_{n\beta}'(\lambda r_2) + h_2Y_{n\beta}(\lambda r_2)][\beta\lambda Y_{n\beta}'(\lambda r_1) - h_1Y_{n\beta}(\lambda r_1)] = 0 \tag{34}$$

and the norm

$$N_{mn} = \frac{1}{2\lambda_{mn}^2}\{[J_{n\beta}(\lambda_{mn}r_2) - h_{mn}Y_{n\beta}(\lambda_{mn}r_2)]^2(B_2^2 + \lambda_{mn}^2 r_2^2 - n^2\beta^2) - [J_{n\beta}(\lambda_{mn}r_1) - h_{mn}Y_{n\beta}(\lambda_{mn}r_1)]^2(B_1^2 + \lambda_{mn}^2 r_1^2 - n^2\beta^2)\} \tag{35}$$

$$B_1 = h_1r_1; \qquad B_2 = h_2r_2$$

Substituting equation (32) into formula (23), we obtain the Green's function associated with the unsteady problem subject to boundary conditions of the third type at the inner and outer surfaces

$$G_2(r, \theta t|r', \theta', t') = \frac{\epsilon}{\pi}\sum_{m=1}^{\infty}\sum_{n=0}^{\infty}\frac{1}{N_{mn}}[J_{n\beta}\lambda_{mn}r) - h_{mn}Y_{n\beta}(\lambda_{mn}r)] \cdot [J_{n\beta}(\lambda_{mn}r') - h_{mn}Y_{n\beta}(\lambda_{mn}r')] \cos n\left(\theta - \theta' - \nu\ln\frac{r}{r'}\right)e^{-\alpha\lambda_{mn}^2(t-t')} \tag{36}$$

Green's functions for boundary conditions of the first and second types, or one type at r_1 and another type at r_2 can be found by the same way, or by specializing equation (36) to each case.

If we substitute equation (36) into equation (7), we obtain the Green's functions $G(r, \theta, z, t|r', \theta', z', t')$ since $G_1(z, t|z', t')$ has been given in equation (12).

Infinite and Internally Bounded Regions

For an infinite region or a region bounded internally by a cylindrical surface of radius r_0, we may seek the solution for $G_2(r, \theta, t|r', \theta', t')$ in the form of

$$u(r, t)\exp\left[\text{in}\left(\theta - \theta' - \nu_{12}\ln\frac{r}{r'}\right)\right] \tag{37}$$

which satisfies the differential equation of $G(r, \theta, t|r', \theta', t')$ if $u(r, t|r', t')$ satisfies the equation

$$\frac{\partial^2 u}{\partial r^2} + \frac{1}{r}\frac{\partial u}{\partial r} - \frac{\beta^2 n^2}{r^2}u - \frac{1}{\alpha_1}\frac{\partial u}{\partial t} = -\frac{\delta(t - t')\delta(r - r')}{\alpha_1 r} \tag{38}$$

For infinite region, we may remove the variable r from equation (38) by the Hankel transform defined by [26]

$$\bar{u}(t, \lambda, n\beta) = \int_0^{\infty} u(r', t)\,J_{n\beta}(\lambda r')r'dr' \tag{39}$$

and its inverse,

$$u(r, t) = \int_0^{\infty}\bar{u}(t, \lambda, n\beta)\,J_{n\beta}(\lambda r)\lambda d\lambda \tag{40}$$

We apply equation (39) to equation (38) to obtain

$$\bar{u}' + \alpha_1\lambda^2\bar{u} = J_{n\beta}(\lambda r')\delta(t - t') \tag{41}$$

The solution of equation (41) satisfying the zero initial condition is

$$\bar{u}(t, \lambda, n\beta) = J_{n\beta}(\lambda r')e^{-\alpha_1\lambda^2(t-t')} \tag{42}$$

Substituting equation (42) into equation (40) and the result into equation (37) and keeping n positive in u, we obtain

$$G_2(r, \theta, t|r', \theta', t') = \frac{\epsilon}{2\pi}\sum_{n=0}^{\infty}\cos n\left(\theta - \theta' - \nu_{12}\ln\frac{r}{r'}\right)$$

$$\cdot \int_0^\infty J_{n\beta}(\lambda r) J_{n\beta}(\lambda r') \lambda d\lambda \quad (43)$$

We multiply $G_1(z, t|z', t')$ of equation (10) to equation (43) to obtain

$$G(r, \theta, z, t|r', \theta', z', t') = \frac{\epsilon}{4\pi\sqrt{\alpha_1 \nu_{33}(t-t')}} \exp\left[-\frac{z-z'^2}{4\alpha_1\nu_{33}(t-t')}\right]$$
$$\cdot \sum_{n=0}^{\infty} \cos n\left[(\theta-\theta') - \nu_{12}\ln\frac{r}{r'}\right] \int_0^\infty J_{n\beta}(\lambda r) J_{n\beta}(\lambda r') \lambda d\lambda \quad (44)$$

This is the fundamental Green's function, or fundamental solution, for an anisotropic medium of a monoclinic system which is homogeneous in circular cylindrical coordinates.

For the internally bounded region, we may remove the variable r from equation (38) by the Weber's transform defined by [27]:

$$\bar{u}(t, \theta, n\beta) = \int_{r_0}^\infty u(r', t) U_{n\beta}(\lambda r') r' dr' \quad (45)$$

and its inverse:

$$u(r, t) = \int_0^\infty \bar{u}(t, \lambda, n\beta) \frac{U_{n\beta}(\lambda r)}{V_{n\beta}(\lambda r_0)} \lambda d\lambda \quad (46)$$

where, for boundary condition of the first type,

$$U_{n\beta}(\lambda r) = J_{n\beta}(\lambda r_0) Y_{n\beta}(\lambda r) - Y_{n\beta}(\lambda r_0) J_{n\beta}(\lambda r) \quad (47)$$

$$V_{n\beta}(\lambda r_0) = J_{n\beta}{}^2(\lambda r_0) + Y_{n\beta}{}^2(\lambda r_0) \quad (48)$$

and, for boundary condition of the third type,

$$U_{n\beta}(\lambda r) = [\lambda Y_{n\beta}'(\lambda r_0) - h Y_{n\beta}(\lambda r_0)] J_{n\beta}(\lambda r) - [\lambda J_{n\beta}'(\lambda r_0) - h J_{n\beta}(\lambda r_0)] Y_{n\beta}(\lambda r) \quad (49)$$

$$V_{n\beta}(\lambda r_0) = [\lambda J_{n\beta}'(\lambda r_0) - h J_{n\beta}(\lambda r_0)]^2 + [\lambda Y_{n\beta}'(\lambda r_0) - h Y_{n\beta}(\lambda r_0)]^2 \quad (50)$$

Applying equation (45) to equation (38) and following the same procedures as those in obtaining equation (44), we obtain

$$G(r, \theta, z, t|r', \theta', z', t') = \frac{\epsilon}{4\pi\sqrt{\pi\alpha_1\nu_{33}(t-t')}} \exp\left[-\frac{(z-z')^2}{4\alpha_1\nu_{33}(t-t')}\right]$$
$$\cdot \sum_{n=0}^{\infty} \cos n\left[(\theta-\theta') - \nu_{12}\ln\frac{r}{r'}\right] \int_0^\infty \frac{U_{n\beta}(\lambda r) U_{n\beta}(\lambda r')}{V_{n\beta}(\lambda r_0)} \cdot e^{-\alpha_1\lambda^2(t-t')} \lambda d\lambda \quad (51)$$

Examples

A solid cylinder without heat generation and initially at zero temperature is subjected to convective heat transfer at the surface from the surrounding fluid whose temperature varies with the angular position only

$$\frac{\partial T}{\partial n^+} + hT = f, \qquad r = r_0 \qquad t > 0 \quad (52)$$

where $f = A \sin\theta$ with A being a constant. We substitute equation (36) for $G(r, \theta, t|r', \theta', t')$ into equation (5) to obtain

$$T(r, \theta, t) = \frac{2Ar_0}{k_{11}} \sum_{m=1}^{\infty} \frac{J_0(\lambda_{m0} r/r_0)}{J_0(\lambda_{m0})} \frac{1}{\lambda_{m0}{}^2 + \beta_0^2} (1 - e^{-\lambda_{m0}{}^2\alpha_1 t/r_0{}^2}) + \frac{J_\beta(\lambda_{m1} r/r_0)}{J_\beta(\lambda_{m1})} \frac{\sin[\theta - \nu_{12}\ln r/r_0)]}{(\lambda_{m1}{}^2 - \beta^2 + \beta_0^2)} (1 - e^{-\lambda_{m1}{}^2\alpha_1 t/r_0{}^2}) \quad (53)$$

where λ_{mn} are the roots of

$$\lambda J_\beta'(\lambda) + \beta_0^2 J_\beta(\lambda) = 0 \quad (54)$$

If the initial temperature of the cylinder is equal to $A \sin\theta$ with homogeneous boundary condition of the third type, we find

$$T(r, \theta, t) = -2T_0 \sum_{m=1}^{\infty} e^{-\lambda_{m1}{}^2\alpha_1 t/r_0} \frac{\lambda_{m1}{}^2 J_\beta(\lambda_{m1} r/r_0)}{(B_0{}^2 + \lambda_{m1}{}^2 - \beta) J_\beta{}^2(\lambda_m)}$$
$$\cdot \left[\cos\left(\theta - \nu_{12}\frac{r}{r_0}\right) \int_0^1 \sin(\nu_{12}\ln\xi) J_\beta(\lambda_{m1}\xi)\xi d\xi + \sin\left(\theta - \nu_{12}\frac{r}{r_0}\right) \int_0^1 \cos(\nu_{12}\ln\xi) J_\beta(\lambda_{m1}\xi)\xi d\xi\right] \quad (55)$$

where λ_{m1} are the roots of equation (54).

Note that equations (53) and (55) reduce to those of corresponding isotropic problems, and that the integrals in equation (55) cannot be expressed in tabulated functions.

Some calculated results of equation (53) and of the isotropic case are shown in Tables 1 and 2. The effects of orthotropy and anisotropy on the temperature field can be easily seen from equation (53) as well as the tables. For the same value of ν_{12}, the parameters β characterizes the orthotropy. The larger the value of β, the lower the temperature in the upper half of the circular area ($0 < \theta < \pi$) and the higher it is in the lower half ($\pi < \theta < 2\pi$) in comparison with the temperature in an isotropic medium. For isotropic and orthotropic media, the temperature fields are symmetric with respect to the axial plane passing through $\theta = \pi/2$, while for an anisotropic medium, the temperature field is asymmetric. For the same value of β, the increase of ν_{12} shifts the maximum and minimum temperatures clockwise. For $\beta = 1$, the surface temperature is the same as that for the isotropic medium. The orthotropy or the anisotropy has no effect to the temperature at $r = 0$.

Discussions and Concluding Remarks

All the Green's functions obtained previously reduce to those for orthotropic media by setting $\nu_{12} = 0$ and to those for isotropic media by putting $\nu_{12} = 0$ and $\beta = \nu_{33} = 1$.

It is seen from the expressions of Green's functions obtained above and the integral equation (5) that an analytical expression for the temperature is difficult to obtain, if the initial condition or the heat production is not zero. It is also seen from these expressions that the homogeneous equation (1) can be separated into ordinary differential equations, though the separation process is slightly more complicated and more restrictive than that for isotropic problems [21]. However, it may be mentioned here that it is more convenient to use the separation of variables for cylindrical regions bounded by two axial planes as will be shown in the ensuing paper.

If the medium is of general anisotropy, or anisotropy only in r–z plane, the method used in this paper is still applicable for the solution of problems of the first class, but the solution is more complicated, involving confluent hypergeometric functions with complex arguments. It also applies to problems of the first class for general anisotropic media homogeneous in rectangular coordinates, although it is more convenient to solve this particular class of problems by the transformation of coordinates [28].

References

1 Kuprudeze, V. D., "Potential Methods in the Theory of Elasticity," Chapter 9, Israel Programs for Scientific Translation 1965.

2 Lekhnitskii, S. G., "Theory of Elasticity of an Anisotropic Elastic Body," Translation by P. Fern., Holden Day, San Francisco, 1963.

3 Hearman, R. F. S., *An Introduction to Applied Anisotropic Elasticity*, University Press, Oxford, 1961.

4 Neale, G., and Neder, W. K., "Diffusion Transport Processes Within Anisotropic and Isotropic Swarms of Spherical Particles," *AIChE Journal*, May, 1976, pp. 420–427.

5 Whitaker, S., "Diffusion and Dispersion in Porous Media," *AIChE Journal*, May, 1967, pp. 420–427.

6 Clements, D. L., "Thermal Stress in an Anisotropic Elastic Half Space," *SIAM Journal Appl. Math.*, Vol. 24, 1973, pp. 332–337.

7 Tauchert, T. R., and Akoz, A. Y., "Stationary Temperature and Stress Fields in an Anisotropic Elastic Slab," *Journal of Applied Mechanics*, Sept. 1975, pp. 647–650.

8 Turhan, D., and Tuna, O. H., "A Heat Conduction Theory for Layered Composites," *METU Journal of Pure and Appl. Sci.*, Vol. 8, 1975, pp. 69–93.

9 Padovan, J., "Solution of Transient Temperature Fields in Laminated Anisotropic Slabs and Cylinders," *Intern. J. Eng. Sci.*, Vol. 13, 1975, pp. 247–260.

10 Padvan, J., "Conduction in Anisotropic Composite Slabs and Cylinders," *Proc. Intern. Conf. of Heat Transfer.*, Tokyo, 1974, Vol. I pp. 147–151.

11 Giedt, W. H., and Hornbaker, D. R., "Transient Temperature Variation in a Thermal Orthotropic Plate," *ARS Journal*, Vol. 32, 1962, pp. 1902–1909.

12 Chao, B. T., "A Note on Conduction of Heat in Anisotropic Media," *Appl. Sci. Res.*, Vol. A12, 1953, pp. 134–138.

Table 1 Dimensionless temperature distribution, $T^* = T/(Ar_0/k_{11})$, for $\beta = 2.0$; $\nu_{12} = 0.5$, Bo = 1.0, Fo = 1.0; $T^* = 0.750$ at $r = 0$ for both media

	0.2		0.4		0.6		0.8		1.0	
r/r_0 / θ	Iso	Aniso	Iso	Aniso	Iso	Aniso	Iso	Aniso	Iso	Aniso
0°	0.754	0.764	0.766	0.790	0.785	0.815	0.809	0.833	0.829	0.829
45°	0.825	0.768	0.907	0.817	0.996	0.888	1.090	0.976	1.180	1.060
90°	0.854	0.764	0.965	0.814	1.080	0.901	1.210	1.020	1.320	1.150
135°	0.825	0.754	0.907	0.783	0.996	0.845	1.090	0.943	1.180	1.060
180°	0.754	0.744	0.766	0.742	0.785	0.754	0.809	0.786	0.829	0.829
225°	0.684	0.740	0.625	0.715	0.573	0.681	0.527	0.642	0.484	0.601
270°	0.654	0.745	0.567	0.718	0.486	0.668	0.411	0.597	0.340	0.506
315°	0.684	0.754	0.625	0.749	0.573	0.724	0.527	0.676	0.484	0.601
360°	0.754	0.764	0.766	0.790	0.785	0.815	0.809	0.833	0.829	0.829

Table 2 Dimensionless temperature distribution, $T^* = T/(Ar_0/k_{11})$, for $\beta = 0.75$; $\nu_{12} = 0.2$, Bo = 1.0, Fo = 1.0; $T^* = 0.750$ at $r = 0$ for both media

	0.2		0.4		0.6		0.8		1.0	
r/r_0 / θ	Iso	Aniso	Iso	Aniso	Iso	Aniso	Iso	Aniso	Iso	Aniso
0°	0.754	0.807	0.766	0.817	0.785	0.824	0.809	0.831	0.829	0.829
45°	0.825	0.905	0.907	0.999	0.966	1.080	1.090	1.160	1.180	1.220
90°	0.854	0.914	0.965	1.040	1.080	1.170	1.210	1.290	1.320	1.390
135°	0.825	0.829	0.907	0.926	0.966	1.030	1.090	1.130	1.180	1.220
180°	0.754	0.701	0.766	0.714	0.785	0.745	0.809	0.788	0.829	0.829
225°	0.684	0.604	0.625	0.532	0.573	0.486	0.527	0.457	0.484	0.436
270°	0.654	0.595	0.567	0.487	0.486	0.402	0.411	0.332	0.340	0.273
315°	0.684	0.679	0.625	0.605	0.573	0.542	0.527	0.487	0.484	0.436
360°	0.754	0.807	0.766	0.817	0.785	0.824	0.809	0.831	0.829	0.829

13 Touryan, K. J., "Transient Temperature Variation in a Thermal Orthotropic Cylindrical Shell," *AIAA Journal,* Vol. 2, 1964, pp. 124–126.

14 Mulholand, G. P., "Diffusion Through Laminated Orthotropic Cylinder," *Proc. Intern. Conf. of Heat Transfer.,* Tokyo, 1974, pp. 250–254.

15 Katayama, K., et al., "Transient Heat Conduction in Anisotropic Solids," *Proc. Intern. Conf. of Heat Trans.,* Tokyo, 1974, pp. 137–141.

16 Chang, Y. P., et al., "The Use of Fundamental Green's Functions for the Solution of Problems of Heat Conduction in Anisotropic Media," *International Journal of Heat and Mass Trans.,* Vol. 16, 1973, pp. 1905–1918.

17 Cobble, M. H., "Nonlinear Anisotropic Temperature Distribution in a Wedge," *International Journal of Heat and Mass Trans.,* Vol. 17, 1974, pp. 379–380.

18 Nye, J. Y., *Physical Properties of Crystals,* Clarendon Press, Oxford, 1960.

19 *Pyrolytic Graphite Handbook,* General Electric Co.

20 Ozisik, M. N., *Boundary Value Problems of Heat Conduction,* International Textbook, 1968.

21 Weiberger, H. F., *Partial Differential Equations,* Blaisdell, Waltham, Mass., 1965, pp. 68–69.

22 Chang, Y. P., and Tsou, C. H., "Heat Conduction in Anisotropic Media Homogeneous in Cylindrical Regions—Steady State," in the same issue of this journal.

23 Prigogine, I., *Thermodynamics of Irreversible Processes,* Charles C. Thomas, Springfield, Ill., 1955.

24 Freidman, A., *Partial Differential Equations of Parabolic Type,* Prentice Hall, Englewood Cliffs, N. J., 1964.

25 Stakgold, I., *Boundary Value Problems of Mathematical Physics,* Vol. II, MacMillan, 1968.

26 Sneedon, I. N., *Fourier Transforms,* McGraw-Hill, 1951.

27 Tichmash, E. C., *Eigenfunction Expansion Associated With Second Order Differential Equations,* University Press, Oxford, 1946.

28 Chang, Y. P., "Analytical Solution of Heat Conduction in Anisotropic Media in Infinite Semi-Infinite and Two-Parallel-Plane Bounded Regions," submitted to *International Journal of Heat and Mass Transfer,* Mar. 1976.

R. D. Small
D. Weihs

Department of Aeronautical Engineering,
Technion—Israel Institute of Technology,
Haifa, Israel

Thermal Traces of a Buried Heat Source

An exact solution in series form is presented for the steady temperature distribution in a semi-infinite solid medium bounded internally by a spherical inclusion of uniform temperature. Heat transfer at the interface is via convection. The solution is obtained by means of a transformation to a bispherical coordinate system. Surface temperatures, which are of engineering interest for monitoring purposes, are also calculated.

1 Introduction

Interest in the monitoring of underground heat sources (sinks) arises in various fields, such as the use of storage tanks for fuels and chemicals, prospecting by satellite thermography, nuclear engineering, etc. One of the simplest ways of detecting the existence of such sources is by measurement of their effects on the surface i.e., the temperature differences produced on the surface.

In the present paper, the surface temperature distribution due to the existence of a buried heat source is studied analytically. A spherical heat source is chosen in order to focus attention on the effects of the thermodynamical parameters and the interaction with the interface, without complications arising from the source shape. Also, this is one of the most efficient shapes for storage tanks.

Solutions of potential problems relating to bodies near plane boundaries are usually obtained approximately by means of reflections. In this method successive approximations resulting from planting a series of image singularities are obtained. It should be noted that application of the method of reflections for the present problem would be extremely difficult due to the convection boundary condition (cf. Section 2) used at the interface. So-called shape factors [1][1] have also been applied to correlate simple source fields with constraints due to the existence of bounded surfaces.

A different approach is taken here. The analysis is performed in an orthogonal coordinate system tailored to the specific problem. As a result of this transformation, the boundary conditions become simpler and an exact solution is achieved. The coordinate system chosen here is the bispherical system. The equation for steady heat conduction (Laplace's equation) remains separable.

An exact solution in series form is obtained for the steady temperature distribution in the semi-infinite solid medium bounded internally by a spherical inclusion of constant and uniform temperature. It is interesting to note that this is the three-dimensional analogue of a plane problem mentioned by Carslaw and Jaeger [2] in a list of yet unsolved tasks in heat conduction for which the possibility of an exact solution exists. Solutions using simpler albeit nonconventional coordinate systems have recently been presented by Yovanovich [3].

2 Analysis

Consider a sphere (Fig. 1) of radius R buried at a depth $D > R$ in

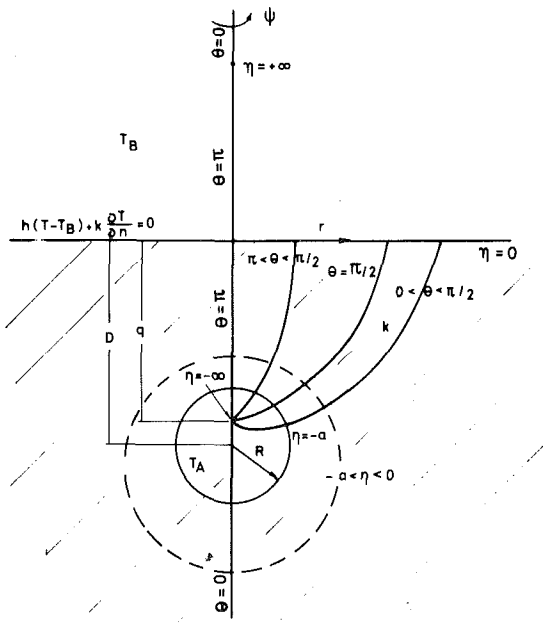

Fig. 1 The bispherical coordinate system

[1] Numbers in brackets designate References at end of paper.

Contributed by the Heat Transfer Division for publication in the JOURNAL OF HEAT TRANSFER. Manuscript received by the Heat Transfer Division May 27, 1976.

a medium of uniform thermal conductivity k. The depth D is measured from a flat free surface at which there exists convection with film heat transfer coefficient h. The internal conductivity of the sphere (which can be solid or fluid-filled) is taken to be much larger than that of the earth around it, so that the sphere temperature T_a is uniform. The temperature of the fluid medium (atmospheric air or water) as well as that of the solid medium far from the interface is taken as $T_b (T_b \neq T_a)$. T_b can be either higher or lower than T_a, corresponding to a cooled or heated source, respectively. The case of steady axisymmetric (in ψ, cf. Fig. 1) heat transfer is studied.

The equation defining heat transfer in the semi-infinite solid medium between the sphere and the interface reduces, under these conditions, to Laplace's equation. In the Cartesian coordinate system the spherical geometry results in a complex formulation of the boundary value problem. On the other hand, a spherical coordinate system leads to similar problems when writing the boundary condition of the flat surface. Accordingly a bispherical coordinate system is used.

In this system (Fig. 1) coaxal spheres are mapped as surfaces of constant η. The surfaces θ = constant are spindles for $\theta > \pi/2$, a sphere at $\theta = \pi/2$ and apple shaped surfaces for $\theta < \pi/2$. The line connecting the sphere centers is defined by $\theta = \pi$ between the limiting points of the system ($\eta = \pm\infty$), and $\theta = 0$ from the limiting points outwards. The metric coefficients of this system are [4]:

$$g_{\eta\eta} = g_{\theta\theta} = \frac{q^2}{(\cosh\eta - \cos\theta)^2}; \qquad g_{\psi\psi} = \frac{q^2 \sin^2\theta}{(\cosh\eta - \cos\theta)^2} \tag{1}$$

where $2q = 2\sqrt{D^2 - R^2}$ is the distance between limiting points.

Laplace's equation in terms of the bispherical coordinates

$$\nabla^2\phi = 0 = \frac{(\cosh\eta - \cos\theta)^3}{q^2 \sin\theta}\left\{\sin\theta \frac{\partial}{\partial\eta}\left(\frac{1}{\cosh\eta - \cos\theta}\frac{\partial\phi}{\partial\eta}\right) + \frac{\partial}{\partial\theta}\left(\frac{\sin\theta}{\cosh\eta - \cos\theta}\frac{\partial\phi}{\partial\theta}\right)\right\} \tag{2}$$

is ρ − separable with $\rho = (\cosh\eta - \cos\theta)^{-1/2}$ and a general solution can be written as

$$\phi = (\cosh\eta - \xi)^{1/2} \sum_{n=0}^{\infty} (\overline{A}_n \cosh m\eta + \overline{B}_n \sinh m\eta) \times [C_n P_n(\xi) + E_n Q_n(\xi)] \tag{3}$$

where $\xi \equiv \cos\theta$, n is the set of non-negative integers, $m = n + \frac{1}{2}$, P_n and Q_n are Legendre polynomials of the first and second kind, respectively, and $\overline{A}_n$, $\overline{B}_n$, C_n, E_n are constant coefficients to be established with the aid of the boundary conditions. The function ϕ is the nondimensional temperature excess in the solid medium defined by $\phi = (T - T_b)/(T_a - T_b)$. The boundary conditions in dimensional quantities are:

On the isothermal sphere

$$T = T_a \qquad \text{at } \eta = -a \tag{4a}$$

where

$$a = \text{argsinh}\sqrt{(D/R)^2 - 1}$$

In the domain of the present solution the temperature is finite and bounded between the sphere and far-field temperatures. For the case of the heated sphere this is written as

$$T_b \leq T \leq T_a \qquad \text{for } \eta \geq -a \tag{4b}$$

On the interface, where n is the normal to the surface

$$k\frac{\partial T}{\partial n} + h(T - T_b) = 0 \qquad \text{at } \eta = 0, \qquad \theta > 0 \tag{4c}$$

In terms of the dependent variable ϕ (excess temperature) the boundary conditions are:

$$\phi = 1 \qquad \text{at } \eta = -a \tag{5a}$$

$$0 \leq \phi \leq 1 \qquad \text{for } -a \leq \eta \tag{5b}$$

and

$$(\cosh\eta - \xi)\frac{\partial\phi}{\partial\eta} + \frac{qh}{k}\phi = 0 \qquad \text{on } \eta = 0 \tag{5c}$$

$Q_n(\xi)$ is unbounded at $\xi = \pm 1$ and, therefore, $E_n = 0$, from equation (5b). Writing $A_n = \overline{A}_n C_n$ and $B_n = \overline{B}_n C_n$ the nondimensional temperature excess, ϕ is

$$\phi = (\cosh\eta - \xi)^{1/2} \sum_{n=0}^{\infty} [A_n \cosh m\eta + B_n \sinh m\eta] P_n(\xi) \tag{6}$$

Substitution of the condition of constant temperature on the sphere (5a) leads to

$$\sum_{n=0}^{\infty} (A_n \cosh ma - B_n \sinh ma) P_n(\xi) = (\cosh a - \xi)^{-1/2} \tag{7}$$

To obtain a condition relating the coefficients A_n and B_n, the right-hand side of equation (7) is now expanded in terms of a series of Legendre polynomials, such that

$$(\cosh a - \xi)^{-1/2} = \sum_{n=0}^{\infty} F_n(n, a) P_n(\xi) \tag{8}$$

where

$$F_n(n, a) = A_n \cosh ma - B_n \sinh ma$$

Multiplying the identity (8) by $P_r(\xi)$, (integer r), and making use of the orthogonality property of Legendre polynomials by integrating from $-1 \leq \xi \leq 1$ the right-hand side of (8) becomes

$$\sum_{n=0}^{\infty} F_n \int_{-1}^{1} P_n(\xi) P_r(\xi) d\xi = F_n \int_{-1}^{1} P_n^2(\xi) d\xi = \frac{2}{2n+1} F_n \tag{9}$$

and

$$F_n = \frac{2n+1}{2} \int_{-1}^{1} \frac{P_n(\xi) d\xi}{(\cosh a - \xi)^{1/2}} = \sqrt{2}\, e^{-ma} \tag{10}$$

Therefore

$$A_n \cosh ma - B_n \sinh ma = \sqrt{2}\, e^{-ma}$$

or

Nomenclature

a = constant value of η (defining sphere surface)
$\overline{A}_n, A_n, \overline{B}_n, B_n, C_n, E_n$ = coefficients in infinite series
D = distance from sphere center to interface
F_n = function of n and a (cf. equation (8))
g = metric coefficient
h = heat transfer coefficient
k = thermal conductivity
K = function of n and N (cf. equations (A.1) and (A.2))
L = function of N and a (cf. equation (A.1))
$m = n + \frac{1}{2}$
n, p = non-negative integers
N = Biot modulus
P_n = Legendre polynomial of order n
q = distance from $\eta = \pm\infty$ to $\eta = 0$ (in bispherical system)
r = coordinate defined by equation (22)
R = sphere radius
T = thermodynamic temperature
α_i = defined by equation (A.2)
η, θ, ψ = bispherical coordinates
$\xi = \cos\theta$
ρ = separation parameter
ϕ = nondimensional temperature excess

Subscripts

a = sphere surface temperature
b = temperature far from interface
i, j, n, p = indices

$$A_n = B_n \tanh ma + \sqrt{2}\frac{e^{-ma}}{\cosh ma}, \qquad (n = 0, 1, 2 \ldots \infty) \quad (11)$$

To find the additional relationship required to obtain the remaining sequence of coefficients B_n, we apply the free surface heat transfer condition (5c) i.e.,

$$\sum_{n=0}^{\infty}\left[NA_n + \left(n+\frac{1}{2}\right)(1-\xi)B_n\right]P_n(\xi) = 0 \quad (12)$$

where $N = q\ h/k$ is a nondimensional number relating the heat transfer coefficients h and k of the two phases and the geometry of the problem, ($q = R \sinh a = \sqrt{D^2 - R^2}$). In this sense N is a Biot modulus characterising the present problem. Using now a recurrence relation for $\xi P_n(\xi)$,

$$\sum_{n=0}^{\infty}\left[NA_n + \left(n+\frac{1}{2}\right)B_n\right]P_n(\xi) = \sum_{n=0}^{\infty} B_n\left[\frac{n+1}{2}P_{n+1}(\xi) + \frac{n}{2}P_{n-1}(\xi)\right] \quad (13)$$

matching coefficients and substituting equation (11) leads to

$$B_1 = \frac{2\sqrt{2}Ne^{-a/2}}{\cosh a/2} + B_0(1 + 2N \tanh a/2) \qquad (n = 0)$$

$$B_{n+1} = \frac{2\sqrt{2}Ne^{-ma}}{(n+1)\cosh ma} + B_n\left[\frac{(2n+1) + 2N \tanh ma}{n+1}\right] - \frac{n}{n+1}B_{n-1} \qquad (n \geq 1) \quad (14)$$

In order to effect a complete solution of the boundary value problem one coefficient of the series B_n (say B_0) is required. Once this is available, the others can be found via equation (14). Integration of condition (12) over the interface surface provides the additional relation needed to close the solution. This essentially uses the source strength to bound the sum of the coefficients.

Hence

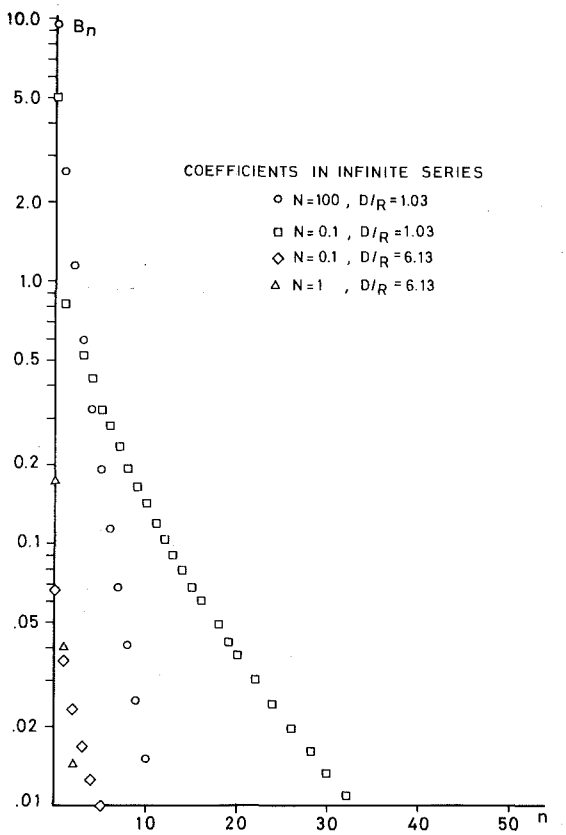

Fig. 2 Values of B_n versus n for different sets of parameters D/R and N

$$\sum_{n=0}^{\infty}\left(n+\frac{1}{2}\right)B_n\int_{-1}^{1}(1-\xi)^{1/2}P_n(\xi)d\xi = -N\sum_{n=0}^{\infty}A_n\int_{-1}^{1}\frac{P_n(\xi)d\xi}{(1-\xi)^{1/2}} \quad (15)$$

after integration yields

$$\sum_{n=0}^{\infty}\frac{B_n}{(m+1)(m-1)} = -2N\sum_{n=0}^{\infty}\frac{A_n}{m} \quad (16)$$

Using equation (11) to eliminate A_n

$$\sum_{n=0}^{\infty}B_n\left(\frac{1}{\left(n+\frac{3}{2}\right)\left(n-\frac{1}{2}\right)} - \frac{2N\tanh ma}{n+\frac{1}{2}}\right) = -2\sqrt{2}N\sum_{n=0}^{\infty}\frac{e^{-(n+1/2)a}}{\left(n+\frac{1}{2}\right)\cosh ma} \quad (17)$$

and when substituting the recurrence relation (14) an equation for B_0 (cf. Appendix) is obtained. Solution of this equation yields the values of all B_n when put back into the recurrence relation (14), completing the solution of the boundary value problem (5).

The solution of Laplace's equation described by equations (6), (11), and (17), while exact and complete, is extremely cumbersome to apply, due to the lengthy algebraic expressions (cf. Appendix). A numerical method, equivalent to the foregoing integral condition (15) is therefore used. This is a form of collocation whereby equation (5c) is applied to a large number of different points on the free surface-designated by different values of ξ. At each of these points, ϕ is approximated by a truncated series of the p leading terms, written as a function of B_n only. Thus, a set of p equations with p unknowns ($B_0, B_1, B_2, \ldots, B_{p-1}$) is obtained. This is now solved by simple matrix inversion. The actual equations are derived by writing (5c) as

$$\sum_{n=0}^{\infty}\left\{\frac{\sqrt{2}Ne^{-ma}}{\cosh ma} + B_n[N\tanh ma + m(1-\xi)]\right\}P_n(\xi) = 0 \quad (18)$$

Taking the first p terms, of each of p values of ξ we obtain the set of equations

$$\sum_{n=0}^{p-1}B_n\left[\tanh ma + \frac{m(1-\xi_i)}{N}\right]P_n(\xi_i) = \sqrt{2}e^{-a/2}\sum_{n=0}^{p-1}\frac{e^{-na}P_n(\xi_i)}{\cosh ma} \quad (19)$$

from which the coefficients B_n ($n = 0, 1, \ldots, p-1$) are obtained by matrix inversion as mentioned before. The accuracy can then be checked by comparing with equation (14). Similar point-matching techniques have been used for potential boundary value problems, including plane heat transfer [5].

3 Results

The nondimensional temperature distribution in the solid medium is, from (6) and (11)

$$\phi(\eta, \xi) = (\cosh\eta - \xi)^{1/2}\sum_{n=0}^{\infty}P_n(\xi)\left[B_n(\sinh m\eta + \tanh ma \cosh m\eta) + \sqrt{2}e^{-ma}\frac{\cosh m\eta}{\cosh ma}\right] \qquad (0 \leq |\eta| \leq a) \quad (20)$$

where B_n is found by either equation (17) and (14), or (19). As mentioned in the previous section, equation (19) was used to obtain numerical values of B_n. Results for some typical cases appear in Fig. 2 and Table 1. The calculations were performed for a wide range of the nondimensional geometrical parameter D/R as well as for various Biot numbers, N. The variation in sphere radius and depth are achieved by transformation to the corresponding values of q and a, via the relations

$$q = \sqrt{D^2 - R^2}; \qquad a = arg\sinh\sqrt{\left(\frac{D}{R}\right)^2 - 1} \quad (21)$$

Table 1 Numerical values of the coefficients B_n

n	D/R = 1.03, N = 0.1	D/R = 6.13, N = 0.1	D/R = 1.54, N = 1	D/R = 1.13, N = 100	D/R = 6.13, N = 10⁴
0	−5.048879	−0.067387	−0.945981	−4.289392	−0.2529187
1	−0.827298	−0.035907	−0.298927	−0.830566	−0.0015776
2	−0.655416	−0.023598	−0.111833	−0.256741	−0.0000107
3	−0.523073	−0.016965	−0.048041	−0.089522	−0.0000001
4	−0.421293	−0.012838	−0.022885	−0.032417	−0.0
5	−0.342725	−0.010051	−0.011773	−0.011897	−0.0
10	−0.140739	−0.003889	−0.000833	−0.000082	−0.0
15	−0.069017	−0.001894	−0.000107	−0.000001	−0.0
20	−0.037688	−0.001034	−0.000019	−0.0	−0.0
25	−0.021943	−0.000602	−0.000004	−0.0	−0.0
30	−0.013232	−0.000363	−0.000001	−0.0	−0.0
40	−0.004819	−0.000132	−0.0	−0.0	−0.0
50	−0.001297	−0.000036	−0.0	−0.0	−0.0
59	−0.000019	−0.000000	−0.0	−0.0	−0.0

Comparison of the cases shown in Fig. 2 for a given geometrical configuration (D/R = const.) shows that B_0 increases, but the rate of decrease of B_n with n grows too so that the contributions from subsequent terms become less important. Increasing D/R for given N causes a general decrease in the values of the coefficients. Thus, for large values of D/R, a very small number of terms is required. This result is to be expected since $D/R \to \infty$ is equivalent to either a sphere in an infinite solid medium ($D \to \infty$), or a point source at a finite distance from a wall ($R \to 0$).

Having obtained the numerical values of B_n as a function of a and N (or D, R, h, and k) one can now calculate the actual temperature distributions from equation (20). Fig. 3 shows the variation of the surface excess temperature $\phi(0, \xi)$ as a function of distance (r/R) from the point directly above the sphere center ($\theta = \pi$) for various values of N. These results are for a sphere situated very close to the surface (the uppermost point of the sphere is only 3 percent of the sphere radius beneath the surface). This configuration is in the range in which the classical method of reflections is inaccurate. The effect of increasing N is to decrease the maximum temperature differences on the surface. This is an expected result, as large N is equivalent to $h > k$ i.e., conduction is the rate-controlling process.

Next, the influence of sphere depth is examined. Fig. 4 describes

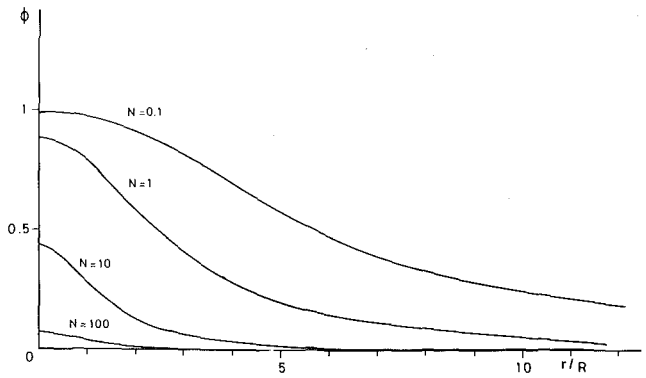

Fig. 3 Nondimensional temperature excess ϕ on the flat surface versus normalized distance from the point directly above the sphere center, for different Biot numbers N, $D/R \simeq 1.03$

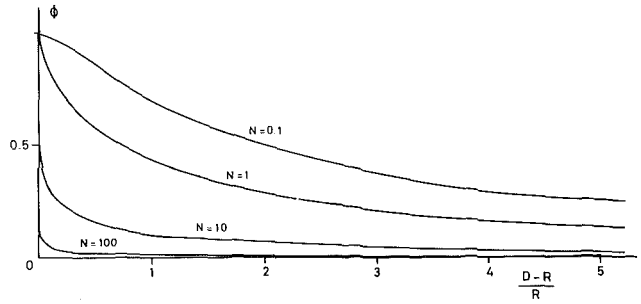

Fig. 4 Maximum nondimensional temperature excess on the flat interface versus nondimensional distance of the highest point on the sphere from the interface

the maximum surface temperature excess, for various N, versus $(D - R)/R$. All the curves tend to the value $\phi = 1$ for $(D - R)/R \to 0$ which describes a sphere touching the surface. This limiting case cannot be calculated by the present method as the coordinate system does not permit finite sized spheres η = const. osculating the flat surface $\eta = 0$. However, the limit is self-evident from the requirement of $T = T_a(\phi = 1)$ on the sphere surface.[2]

The surface temperature distribution for various D/R and $N = 1$ is shown in Fig. 5. The abscissa is the bispherical coordinate θ which allows a more compact display. This can be transformed to the cylindrical coordinate r on the surface, measured from the point directly above the sphere center ($\theta = 180$ deg) by means of

$$r = \frac{q \sin\theta}{\cosh\eta - \cos\theta} \tag{22}$$

The advantage of this description is seen when one recalls that $\eta = \theta = 0$ is equivalent to $r = \infty$.

[2] Such problems can be solved with the aid of the tangent-sphere coordinate system [6].

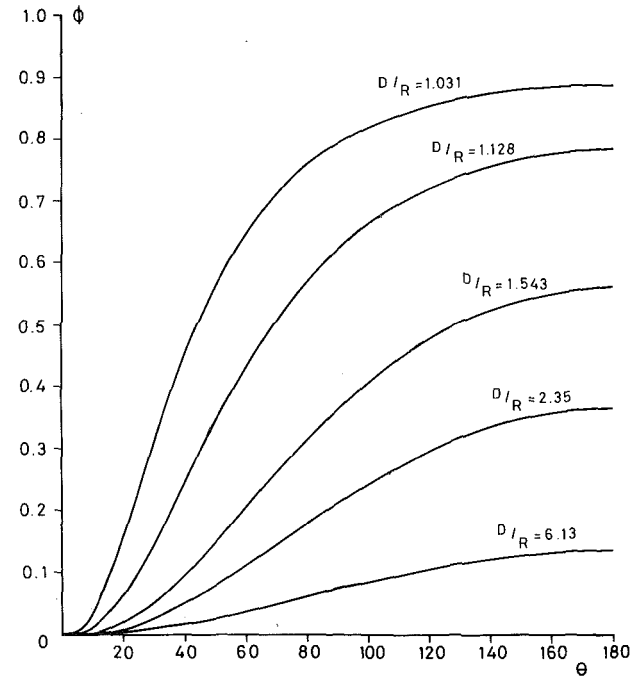

Fig. 5 Nondimensional temperature excess on the flat surface versus θ for various depth ratios D/R, $N = 1$

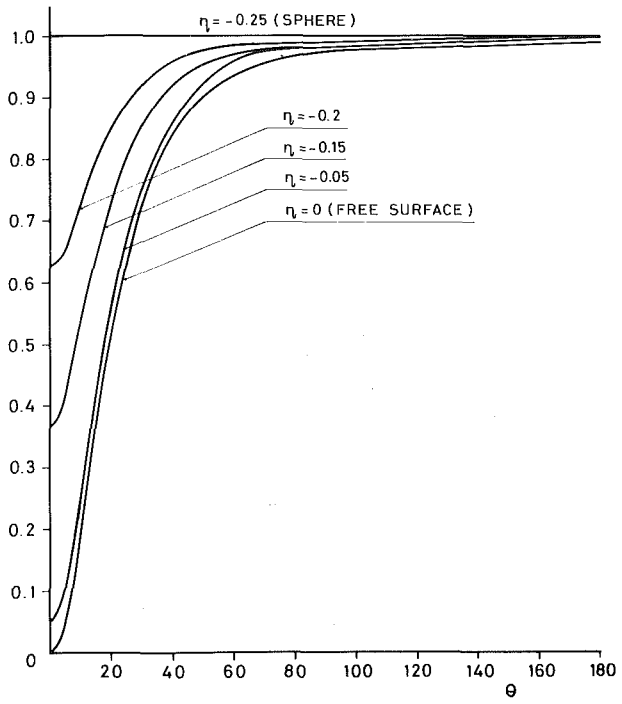

Fig. 6 Nondimensional temperature excess distribution in the solid medium for $D/R = 1.03$, $N = 1$

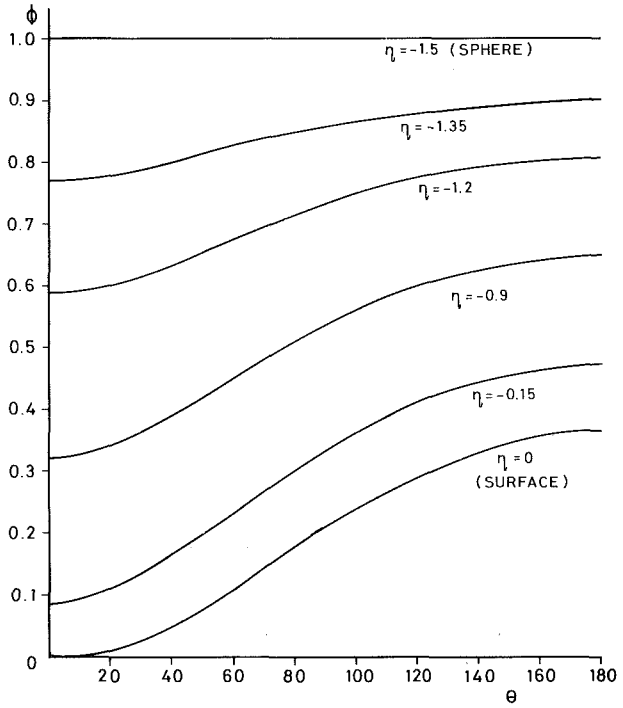

Fig. 7 Nondimensional temperature excess distribution in the solid medium for $D/R = 2.35$, $N = 0.1$

The analysis of the previous section enables us also to calculate the temperature distribution throughout the solid external to the sphere. The results of sample calculations of this sort appear in Figs. 6 and 7. A useful check on the accuracy of the numerical scheme (i.e., the number of terms required for any required accuracy) is obtained here, by recovery of the temperature on the sphere surface. The number of terms taken in the series (20) was deemed sufficient when all points calculated on the sphere surface had $\phi = 1.000000 \pm 0.000001$. Here again the larger D/R, the less terms were required. For the most sensitive case chosen ($D/R \simeq 1.03$, $N = 0.1$) less than 60 terms were required. Larger values of D/R and/or N required less terms to fulfill the foregoing criterion.

Comparison of Figs. 6 and 7 show that for smaller N there is a smaller temperature spread in the solid. This results from the higher thermal conductivity. The temperatures are again given in bispherical coordinates, which can easily be transformed to the Cartesian system, if temperatures at a certain depth are required.

4 Concluding Remarks

The parametric study in Section 3 of the effects of physical dimensions and location as well as heat transfer coefficients shows that even moderate temperature differences at the sphere are noticeable at large relative distance. The sharp changes in surface temperature when moving away from the source position should be of aid in attempts to locate buried heat sources (sinks). In addition to the applications described in the Introduction, interesting biomedical uses suggest themselves including tumor thermography.

The solution given in the present paper is just one of several possible heat transfer problems that can be solved by this method. The requirement of convection causes a mixed boundary value problem. Simpler Dirichlet or Von-Neumann problems are easily derived for isothermal free surface or cases where the heat transfer is prescribed.

References

1 Hahne, E., and Grigull, U., *International Journal of Heat and Mass Transfer*, Vol. 17 1974, p. 267.

2 Carslaw, H. S., and Jaeger, J. C., "Conduction of Heat in Solids," Second ed., Oxford University Press, 1959.

3 Yovanovich, M., *Progress in Astronautics and Aeronautics, Thermophysics and Spacecraft Controls*, Vol. 35, MIT Press, 1973.

4 Moon, P., and Spencer, D. E., *Field Theory Handbook*, Second ed., Springer Verlag, Berlin, 1971.

5 Ojalvo, I. U., and Linzer, F. D., *Quart. J. Mech. Appl. Maths.*, Vol. 18, 1965, p. 41.

6 Small, R. D., and Weihs, D., *J. Appl. Mech.*, Vol. 42, (1975), p. 763.

APPENDIX

Application of the Total Heat Flux Boundary Condition

Equation (17) is of the form

$$\sum_{n=0}^{\infty} B_n K_n = L \tag{A.1}$$

where K_n is a function of n, N, and L is a function of N and a only. Substituting now the recurrence relations (14) into the left-hand side of equation (A.1) one can obtain a single equation in one unknown B_0. Once B_0 is established as a function of N and a, one can find B_1, B_2, etc. As mentioned in the Analysis Section however the recurrence relations give rise to very lengthy and unwieldy expressions. The first five terms of the reduction of B_n to functions of B_0, a and n only are shown here.

Define

$$\alpha_i \equiv \frac{2i + 1 + 2N \tanh\left(i + \frac{1}{2}\right) a}{i + 1};$$

$$K_j = \frac{2\sqrt{2}Ne^{-(j+1/2)a}}{(j+1)\cosh\left(j + \frac{1}{2}\right) a} \tag{A.2}$$

we obtain

$$B_1 = K_0 + \alpha_0 B_0$$

$$B_2 = K_1 + \alpha_1 K_0 + \left(\alpha_1\alpha_0 - \frac{1}{2}\right) B_0$$

$$B_3 = K_2 + \alpha_2 K_1 + \left(\alpha_2\alpha_1 - \frac{2}{3}\right) K_0 + \left[\alpha_2\alpha_1\alpha_0 - \frac{1}{2}\alpha_2 - \frac{2}{3}\alpha_0\right] B_0$$

$$B_4 = K_3 + \alpha_3 K_2 + \left(\alpha_3\alpha_2 - \frac{3}{4}\right) K_1 + \left(\alpha_3\alpha_2\alpha_1 - \frac{3}{4}\alpha_1 - \frac{2}{3}\alpha_3\right) K_0 + \left[\alpha_3\alpha_2\alpha_1\alpha_0 - \frac{3}{4}\alpha_1\alpha_0 - \frac{2}{3}\alpha_3\alpha_1\right] B_0$$

$$B_5 = K_4 + \alpha_4 K_4 + \left(\alpha_4\alpha_3 - \frac{4}{5}\right) K_2 + \left(\alpha_4\alpha_3\alpha_2 - \frac{4}{5}\alpha_2 - \frac{3}{4}\alpha_4\right) K_1 + \left(\alpha_4\alpha_3\alpha_2\alpha_1 - \frac{4}{5}\alpha_2\alpha_1 - \frac{3}{4}\alpha_4\alpha_1\right) K_0 + \left[\alpha_4\alpha_3\alpha_2\alpha_1\alpha_0 - \frac{4}{5}\alpha_2\alpha_1\alpha_0 - \frac{3}{4}\alpha_4\alpha_1\alpha_0 - \frac{1}{2}\alpha_4\alpha_3\alpha_2 + \frac{4}{10}\alpha_2 + \frac{3}{8}\alpha_4 - \alpha_4\alpha_3\alpha_0 - \frac{4}{5}\alpha_0\right] B_0 \quad \text{(A.3)}$$

This sequence of B_n has now to be substituted into equation (17) to obtain the equation for B_0.

K. Saido
Japan NUS Co., Ltd.,
Tokyo, Japan

W. H. Giedt
Department of Mechanical Engineering,
University of California,
Davis, Calif.

Spectral Absorption of Water Vapor and Carbon Dioxide Mixtures in the 2.7 Micron Band[1]

An investigation of the spectral absorption characteristics of water vapor and carbon dioxide mixtures in the 2.7 micron band is described. The absorption of black body radiation by gas mixtures in the central region of a high temperature furnace was measured. The optical path length of 30 cm was bounded by NaCl windows mounted in water-cooled holders. The temperature was essentially uniform in the central one-third of the test cell, and decreased to between 400 800 K at the ends. Representative spectral transmissivity distributions obtained for central temperatures ranging from 1000 to 2200 K and pressures from 0.25 to 3 atm for four different mixture ratios of water vapor and carbon dioxide are presented. Results showed the interaction effect on spectral transmissivity to be greatest at the band center where the maximum change from around 0.40 to 0.48 was observed for approximately equimolar mixtures at a total pressure of 0.5 atm. Since this occurs over a limited wave number range, spectral transmissivities of such mixtures can be acceptably approximated by ignoring the interaction. Spectral distributions predicted from published data for spectral H_2O and CO_2 absorption coefficients and line half-width to spacing ratios are in good agreement with measured distributions.

Introduction

The absorption and emission of infrared radiation by gases is involved in many applications. The familiar products of combustion-water vapor, carbon dioxide, and carbon monoxide are particularly important due to their comparatively high absorptivities and emissivities in the near infrared region. The fractions of water vapor and carbon dioxide in combustion gases are usually large. They are also the most effective in the emission and absorption of infrared radiation. Because of this and of the fact that there are overlapping absorption bands of water vapor and carbon dioxide in the short wavelength region, mixtures of water vapor and carbon dioxide are of special interest and were chosen as the subject of the present investigation.

Charts and methods for calculating the total emission from, or absorption by, gas mixtures of water vapor and carbon dioxide were developed by Hottel and co-workers [1].[2] Use of these results, however, involves the gray body assumption. Although the need for spectral characteristics of these mixtures has been recognized, investigations have been very limited. Ferriso and Ludwig [2] measured spectral emissivities in the 2.7 micron (μm) band for water vapor and carbon dioxide mixtures at atmospheric pressure for temperatures between 1000 and 2200 K. They used a supersonic burner which provided three different mixture ratios of water vapor to carbon dioxide: 1:1, 3:1, and 6:1 on a mole basis. Their measurements were limited to low optical densities, the maximum being 3.12 atm cm. Penner and Varanasi [3] calculated the overlapping effect of the 2.7 and 15 micron absorption bands in water vapor and carbon dioxide mixtures by assuming a "just-overlapping line" wide band model. Their results yielded total emissivities for temperatures up to 1200 K. Subsequent studies of this problem include the work of: (1) Hines and Edwards [4] who developed an empirical wide band method which yielded band absorptances in agreement with homogeneous mixtures measurements in the 500–800 K range; and (2) Lin and Grief [5] who proposed a narrow band summation method.

The objective of the present study was to investigate the spectral absorption of water vapor and carbon dioxide mixtures at temperatures above 1000 K and at high optical densities. Experimental measurements were made with precisely controlled and easily varied mixtures contained in an electrically heated furnace. Although it would be desirable to determine absorption of emission under both isothermal and nonisothermal conditions, suitable window materials for operation much above 1200 K are not available. In many applications, however, the gas mass involved is not isothermal. Measure-

[1] The support of the NASA Marshall Space Flight Center under contract NAS 8-11468 is gratefully acknowledged.

[2] Numbers in brackets designate References at end of paper.

Contributed by the Heat Transfer Division for publication in the JOURNAL OF HEAT TRANSFER. Manuscript received by the Heat Transfer Division April 26, 1976.

ments were therefore made of the spectral absorption by 30-cm long test mixtures, the temperatures of which were essentially uniform in the central one-third and decreased toward each end. Central temperatures were varied from 1000 to 2200 K; corresponding end temperatures varied from 400 to 800 K. Pressures ranged from 0.25 to 3 atm. To provide a background for presenting and discussing the experimental results, a brief review of spectral radiation absorption by gas mixtures is first given in the following section.

H_2O-CO_2 Mixture Infrared Spectral Transmission Characteristics

In the infrared region vibrational-rotational bands are observed at 667, 2349, 3715, and 4978 cm^{-1} for CO_2, and at 1595, 3755, 5331, 7250, and 8807 cm^{-1} for H_2O [6]. In mixtures the vibrational-rotational bands at 3715 cm^{-1} of CO_2 and 3755 cm^{-1} of H_2O water vapor overlap; both are called the 2.7 micron bands.

Negligible Interaction Between Components. The first approximation in the description of absorption in a two-component gas mixture is to assume that the optical path consists of two similar compartments separated by a thin partition which is optically transparent, and that the two different gases fill these compartments. The intensity of the radiation after passing through the first compartment is

$$I_1 = I_0 e^{-k_1(w)p_1L} \tag{1}$$

This is the incident intensity for the second compartment, so that the intensity of the radiation after passing through the second compartment is

$$I_2 = I_1 e^{-k_2(w)p_2L} \tag{2}$$

or

$$I_2 = I_0 e^{-k_1(w)p_1L} e^{-k_2(w)p_2L} \tag{3}$$

where the subscripts 1 and 2 refer to the first and the second compartments, respectively. Therefore, the spectral transmissivity along a path through these two separated gases is given by

$$T_{12}(w) = \frac{I_2}{I_0} = e^{-k_1(w)p_1L} e^{-k_2(w)p_2L} = T_1(w)T_2(w) \tag{4}$$

The spectral absorptivity is given by

$$A_{12}(w) = 1 - T_{12}(w) = 1 - T_1(w)T_2(w)$$
$$= 1 - (1 - A_1(w))(1 - A_2(w))$$
$$= A_1(w) + A_2(w) - A_1(w)A_2(w) \tag{5}$$

Comparison of equations (4) and (5) suggests that the spectral transmissivity will result in a simpler expression for describing the macroscopic radiation characteristics of mixtures. It is for this reason that attention is focused on transmissivity rather than absorptivity.

Next consider the two gases are contained in just one of these two compartments at a total pressure of $p = p_1 + p_2$. Assuming no interaction between the two gases, the ratio of the intensity leaving to the incident intensity is

$$\frac{I}{I_0} = e^{-(k_1(w)p_1L + k_2(w)p_2L)} \tag{6}$$

which is the same as when the gases were in series. Therefore

$$T_m(w) = \frac{I}{I_0} = T_1(w)T_2(w) \tag{7}$$

The validity of this result for low pressures has been demonstrated experimentally [6, p 124].

Instead of partial pressures p_1 and p_2, the total pressure p and mole fractions ξ and η are usually given. Substituting $p_1 = \xi p$ and $p_2 = \eta p$ yields[3]

$$T_m = T_1^{\xi} T_2^{\eta} \tag{8}$$

where T_1 and T_2 are the spectral transmissivities of masses of pure gases 1 and 2 whose pressures, temperatures and optical lengths are the same as those of the gas mixture. Equation (8) is frequently referred to as the multiplication property.

Interaction Between Gases. The actual transmissivity of a mixture of two different gases will differ from that predicted by equation (8) due to the interaction between them. Evaluation of this effect requires determining the influence of each gas on the other in increasing the widths of all the lines in a band. This is a difficult and complex problem (e.g., see references [6, 7], for which no rigorous solution has been obtained. Semiempirical approaches have however been developed. For example, by assuming a statistical band model to be applicable, mean spectral values of the absorption coefficient $k(w)$ and the ratio of the mean line half-width to the line spacing (γ/d) have been determined from spectral data in reference [8]. The actual equation employed is

$$\ln T(w) = \frac{kpL}{\left[1 + \frac{kpL}{4(\gamma/d)}\right]^{1/2}} \tag{9}$$

Simplified theoretical relations were used to evaluate the effective line half-width, including self and foreign gas broadening effects. Values thus determined for k and d versus wave number and temperature are tabulated for H_2O, CO_2 and CO [8]. Predictions of isothermal and segmented optical path spectral characteristics from these values have been found to be within ±20 percent of measured values.

Curtis-Godson Approximation Calculations. To apply the tabulated spectral data of reference [8] to the strongly nonisothermal mixtures investigated, the test path was divided into 9–15 subpaths (smaller subpaths were used for the higher central temperatures).

[3] Hereafter for simplicity, the independent variable w will not always be indicated but should be understood.

Nomenclature

$A(w)$ = average spectral absorptivity at wave number w
d = spectral line spacing
I = intensity of radiation
I_0 = intensity of the incident radiation
$k(w)$ = average spectral absorption coefficient, cm^{-1} atm^{-1}
L = distance or test cell length, cm
p = gas pressure, atm
w = wave number, cm^{-1}
$T(w)$ = average spectral transmissivity at wave number w
$T_i(w)$ = average spectral transmissivity of the ith type gas at wave number w
$T_{12}(w)$ = average spectral transmissivity of two nonmixed gases at wave number w
$T_m(w)$ = average spectral transmissivity of a gas mixture at wave number w
$T_m'(w)$ = average spectral transmissivity of a gas mixture with no interaction between components
$T_t(w)$ = true spectral transmissivity at wave number w
γ = spectral line mean half-width
η = mole fraction of carbon dioxide in a mixture
μ = micro
ξ = mole fraction of water vapor in a mixture
θ = temperature, degrees Kelvin

Subscripts

1 = water vapor
2 = carbon dioxide
m = mixture of water vapor and carbon dioxide

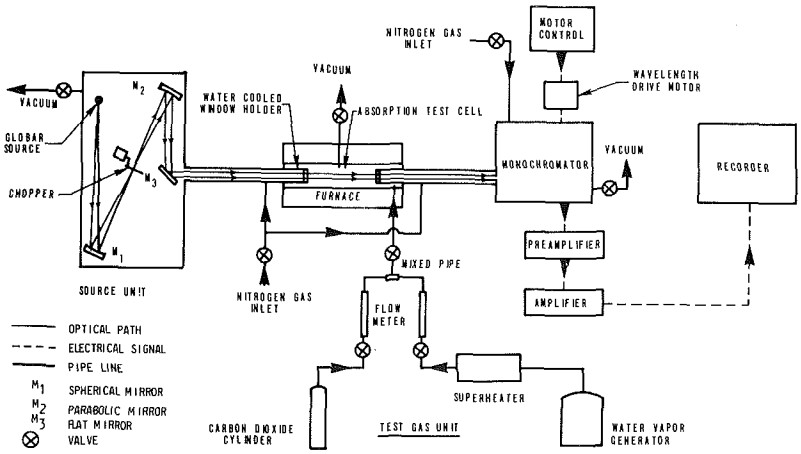

Fig. 1 High temperature infrared absorption system

Each of these was assumed to be at a uniform average temperature which was determined from the distributions in Fig. 2. The determination of the effective absorptivity or transmissivity of such a nonhomogeneous path by allowing two parameters such as the absorption coefficient and line half-width to vary along the path is known as the Curtis-Godson Approximation. The specific procedure was to calculate (1) the product of the mean absorption coefficient and optical density and (2) the quotient of this quantity and (γ/d) according to[4]

$$kpL = \sum_i \left[k_{STP}\left(\frac{p}{p_0}\right)\left(\frac{\theta_0}{\theta}\right)\Delta L \right]_i \tag{11}$$

$$kpL/(\gamma/d) = \sum_i \left[k_{STP}\left(\frac{p}{p_0}\right)\left(\frac{\theta_0}{\theta}\right)\Delta L/(\gamma/d) \right]_i \tag{12}$$

Values of k_{STP} and $1/d$ are taken from the tables in reference [8] and local values of γ are computed from the relations recommended therein.

Spectral transmissivities are then calculated from equation (9) for both H_2O and CO_2. Substitution of these results into equation (8) then yielded spectral transmissivities for a mixture. Since the effect of collision broadening was included in the calculations of the line mean half-width, these results could be expected to account for the interaction between the CO_2 and H_2O.

[4] Spectral absorption coefficients are tabulated for standard temperature and pressure conditions; thus, $k_i = k_{STP}(p/p_0)(\theta_0/\theta)$

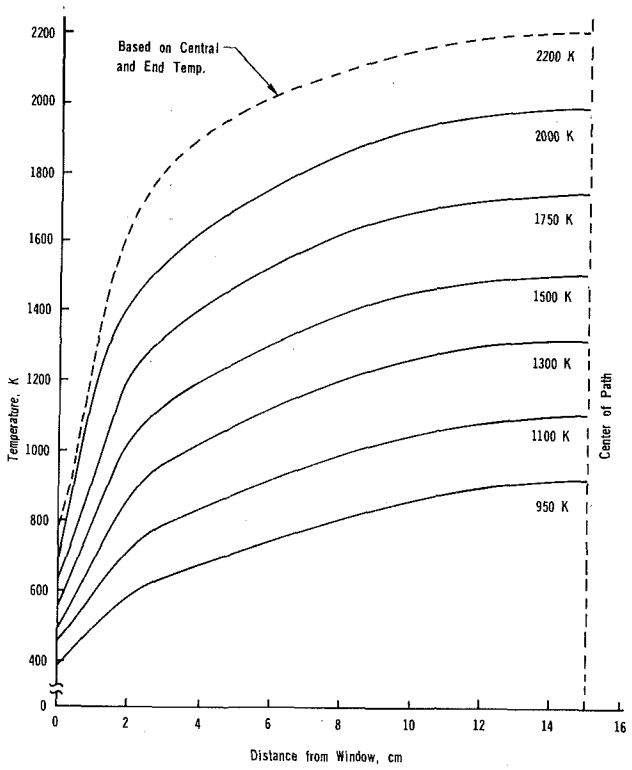

Fig. 2 Measured temperature distributions along absorption path

Experimental Apparatus and Measurements

The experimental program was carried out with an infrared spectral absorption system consting basically of a light source, a graphite resistance high temperature furnace with an inner ceramic tube in which the test gas was contained and a monochromator. The design of the equipment and spectral absorption measurements of CO from 300 to a central temperature of 1800 K are described in reference [9]. By removing the inner ceramic tube, spectral data for CO were obtained up to central temperatures of 2700 K [10]. The system as used for the current study is shown in Fig. 1 and included auxiliary apparatus for supplying filtered carbon dioxide and water vapor. A complete description of the equipment and the experimental procedure followed is given in reference [11].

Spectral absorptivity distributions over the 2.7 micron band were measured under all combinations of the following variables, except as noted:

Central temperature: 950, 1100, 1300, 1500, 1750, 2000, 2100, and 2200 K

Pressure: 0.25, 0.50, 1, 2, and 3 atm

Mole fraction of water vapor to carbon dioxide: 0:1, 0.7:1, 1.9:1, 4.2:1, 11.5:1, and 1:0

Path length: 30 cm

Exceptions: at 950 K, 2 and 3 atm; 1100 K, 3 atm; 2100 K, 0.25, and 0.5 atm; at 2200 K data at only 1 atm

For each central (hot zone) temperature studied, up to 2000 K, the axial temperature distributions were measured with a shielded platinum-platinum/rhodium thermocouple probe. These are shown in Fig. 2. When taking data the test cell temperature was monitored with an optical pyrometer sighted on the center of the alumina tube containing the test mixture. For central temperatures above 2000 K, distributions were approximated from the pyrometer readings and window temperature measurements.

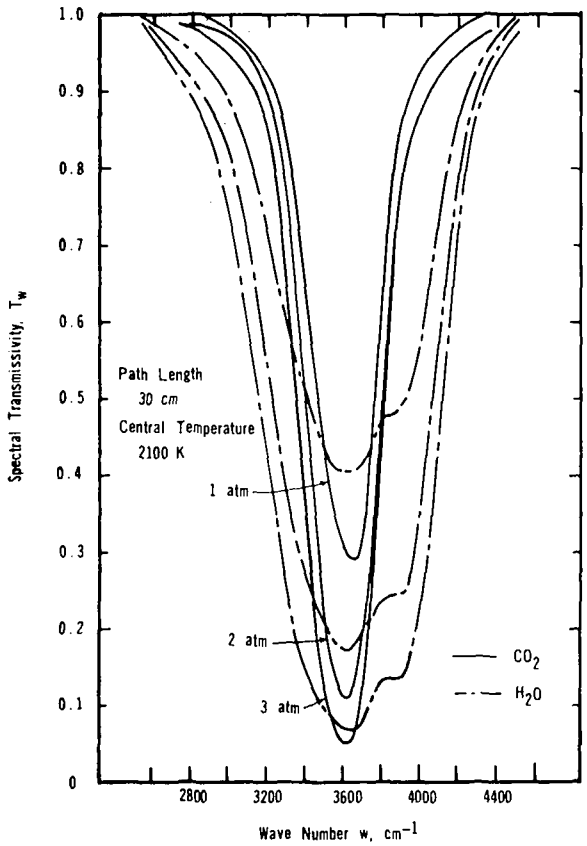

Fig. 3 Spectral transmissivity distributions of CO_2 and H_2O for central temperatures of 2100 K

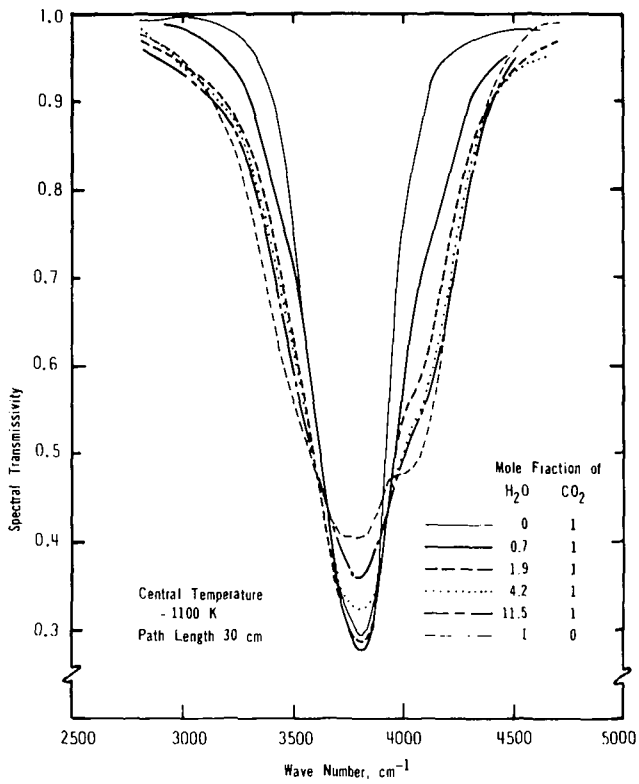

Fig. 5 Mole fraction dependence of spectral transmissivity distributions of CO_2 and H_2O mixtures at 1100 K and 1 atm.

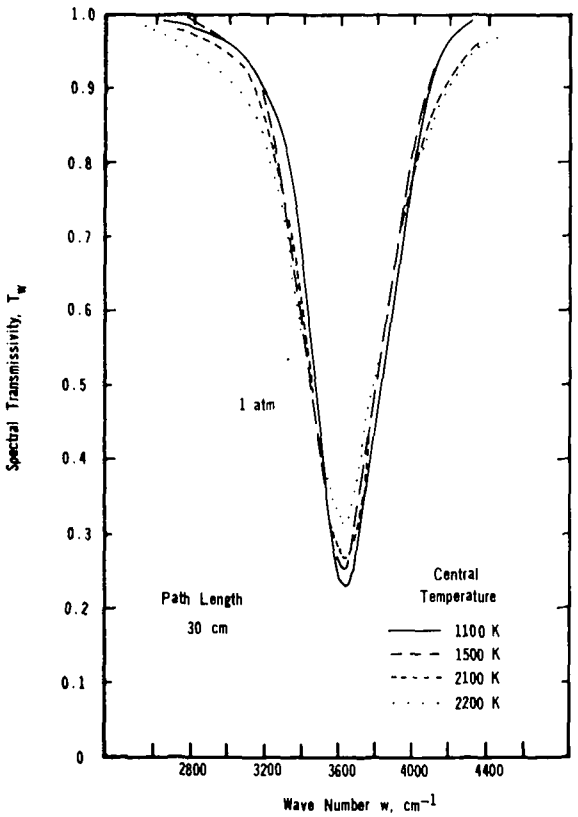

Fig. 4 Effect of temperature on the spectral transmissivity distribution of a 0.7:1 mole fraction mixture of H_2O and CO_2 at 1 atm

Representative results of the transmissivity distributions of pure H_2O and CO_2 are shown in Fig. 3.[5] These curves are for a central temperature of 2100 K and illustrate the significant effect of pressure. That the temperature is relatively unimportant is illustrated in Fig. 4 in which transmissivity distributions of a 0.7:1.0 mole mixture for central temperatures varying from 1100 to 2200 K are plotted. The effect of increasing H_2O content in a mixture at 1100 K and 1 atm is shown in Fig. 5. Here local values of $T(w)$ change by as much as 50 percent in the region between the band center and the wings.

A limited number of measured transmissivity distributions throughout the range of test conditions were selected to illustrate the effect of the interaction between H_2O and CO_2. These are shown in Figs. 6–15. In each, a curve determined from the multiplication property (equation (8)) has been plotted. The values for the individual gas transmissivities used in equation (8) were the appropriate values measured with the same temperature distribution with pure gas present. The differences between these curves and the actual mixture measurements are a measure of the interaction effect. Also included in Figs. 6–15 are curves predicted from the tabulated data in reference [8] as described in the previous section.

Discussion

Figs. 6–9 show transmissivity distributions for mixtures varying from a high mole fraction of H_2O to a high mole fraction of CO_2. The test cell central temperature was 950 K and the pressure was 1 atm. The most significant changes to be noted are directly relatable to the relative proportions of the two gases. That is, spectral transmissivities are lower at the higher wave numbers with increasing H_2O content.

Comparison of the mixture measurements with those calculated

[5] Additional data for H_2O is presented in reference [12] and for H_2O and CO_2 in reference [13].

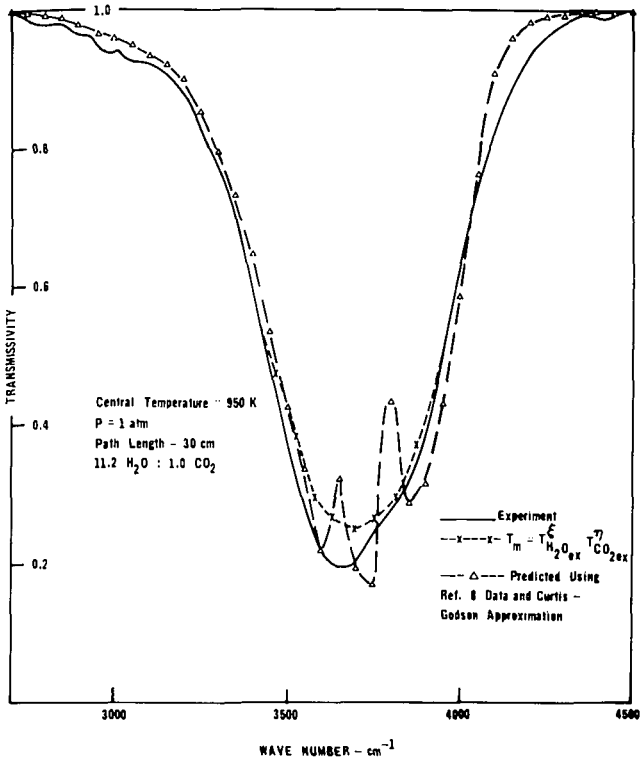

Fig. 6 Spectral transmissivity distributions for a 11.5:1.0 mole fraction mixture of H_2O to CO_2

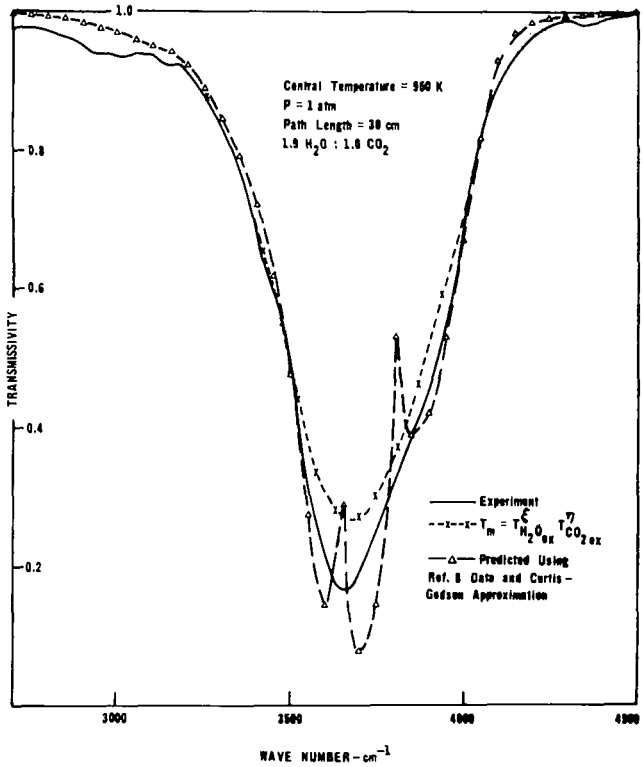

Fig. 8 Spectral transmissivity distribution of a 1.9:1.0 mole fraction mixture of H_2O to CO_2

from equation (8) show a small difference (on the order of 0.05) in the band center. The fact that the measured mixture transmissivities are lower is consistent with the anticipated effect of collision broadening (qualitatively, collisions of the larger CO_2 molecules with the smaller H_2O molecules would increase the line widths of the latter). Agreement between the measured results and those predicted from the tabulated data in reference [8] is good, particularly since the approximate accuracy to be anticipated with these values was indicated

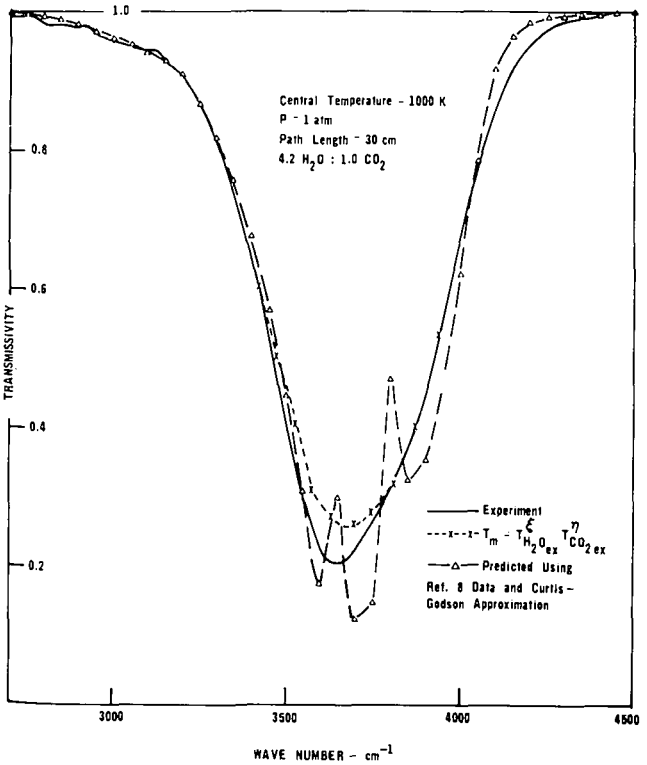

Fig. 7 Spectral transmissivity distributions of a 4.2:1.0 mole fraction mixture of H_2O to CO_2

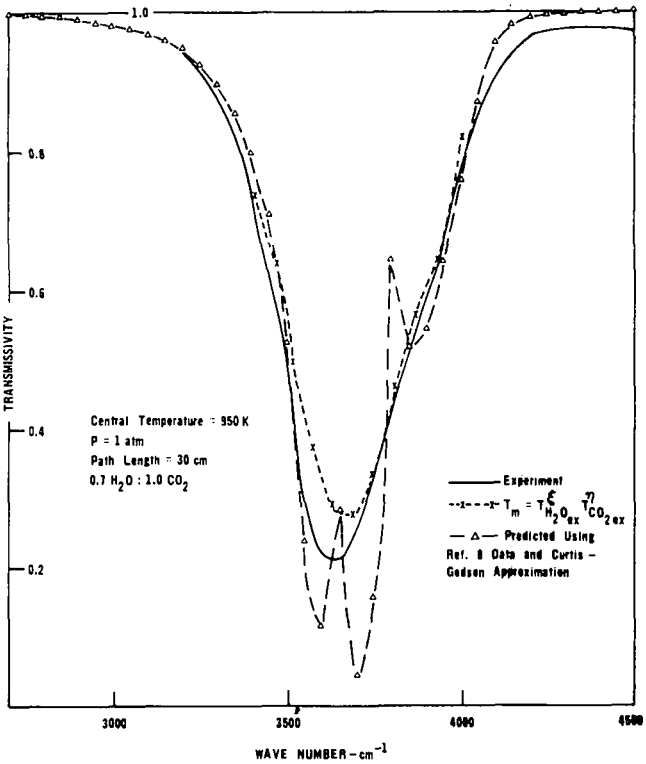

Fig. 9 Spectral transmissivity distributions for a 0.7:1.0 mole fraction mixture of H_2O to CO_2

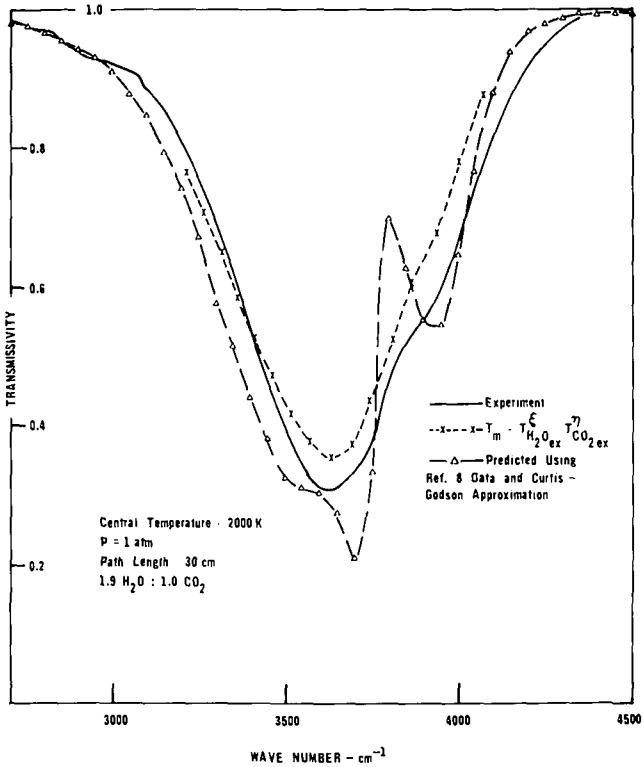

Fig. 10 Spectral transmissivity distribution of a 1.9:1.0 mole fraction mixture of H_2O to CO_2 (T_c = 2000 K, P = 1 atm)

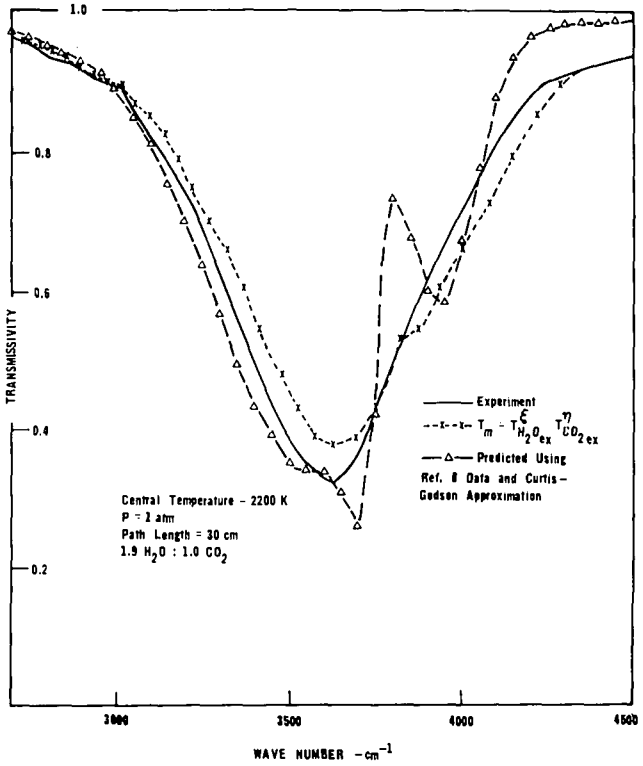

Fig. 11 Spectral transmissivity distribution of a 1.9:1.0 mole fraction mixture of H_2O to CO_2 (T_c = 2200 K, P = 1 atm)

to be ±20 percent. The agreement between the two results in all cases compared is well within this value except around $w = 3800\ cm^{-1}$. This is due to the dip and sharp rise in this region being averaged out in the present measurements.[6] Local variations around $w = 3800\ cm^{-1}$ become more pronounced as the mole fraction of CO_2 is increased. However, comparison of the integrated band absorption for the experimental and predicted curves was within 5 percent.

Referring to Figs. 10 and 11 which are for central temperatures of 2000 and 2200 K at a pressure of 1.0 atm it can be seen by comparison with Fig. 6 (for the same mole fraction ratio but central temperature of 950 K) that temperature does not have a strong effect on the spectral transmission. In general, local values appear to decrease with temperature, the magnitude being on the order of 10 percent as the temperature is doubled.

In contrast, pressure (or optical depth) has a very strong influence. This is illustrated in Figs. 12 15 in which the pressure varies from 0.25 to 3.0 atm for a mole fraction ratio of 4.2 H_2O:1.0 CO_2. Note that in Fig. 14 for which pL = 60 atm cm the center of the band is almost black. In Fig. 15 pL = 90 atm cm. The significant broadening of the band is clearly evident. A second point of interest is that at the higher pressures the distributions calculated from equation (8) are very close to the experimental curves.

For many practical calculations it is advantageous to know the total band absorptance of a gas rather than the detailed spectral variation of its absorptivity or transmissivity. Hence much attention has been devoted to developing techniques for predicting band absorptance of pure gases and mixtures. The situation involving two overlapping bands was the subject of a recent study by Felske and Tien [14]. The applicability of the multiplication property (equation (8)) was assumed and an exponential wide band model is used to establish a simple analytical basis for determining the total band absorptance of two overlapped infrared gas wide bands. The procedure was extended to include nonhomogeneous conditions. Total band absorptances calculated to compare with the present measurements were in excellent agreement with values obtained by integration of the spectral curves.

Summary and Conclusions

The spectral transmission characteristics of mixtures of H_2O and CO_2 were investigated under nonisothermal conditions for optical

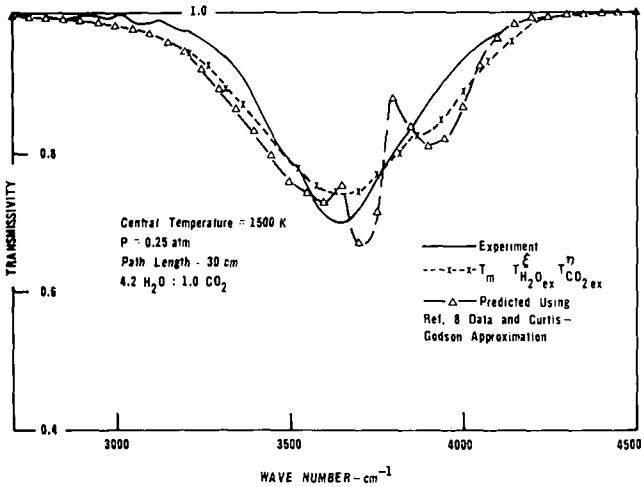

Fig. 12 Spectral transmissivity distribution of a 4.2:1.0 mole fraction mixture of H_2O to CO_2 (T_c = 1500 K, P = 0.25 atm)

[6] The effective width of the slit through which radiation entered the monochrometer was adjusted to include a wave number range between 100 and 150 cm^{-1} to obtain good response in the band wings.

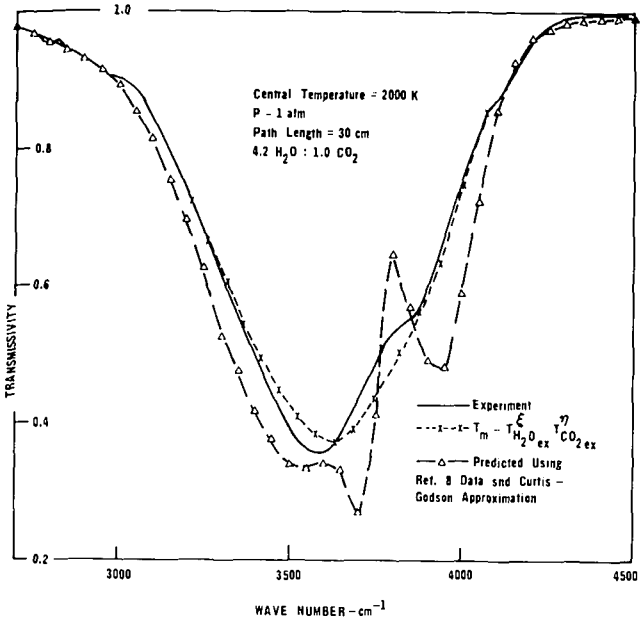

Fig. 13 Spectral transmissivity distribution of a 4.2:1.0 mole fraction mixture of H_2O to CO_2 (T_c = 2000 K, P = 1 atm)

depths varying from 7.5 to 90 atm cm. Test cell central temperatures varied from 950 to 2200 K. Transmissivity distributions predicted from measurements of the individual gases indicated the interaction effect in the mixtures to be greatest at the band center. However, the magnitude of this effect was never greater than 20 percent. Since this occurs only over a short wave number range, it is concluded that the interaction effect may be neglected in practical calculations. Confidence in the measurements was provided by the good agreement found between the experimental spectral distributions and those predicted from available spectral data.

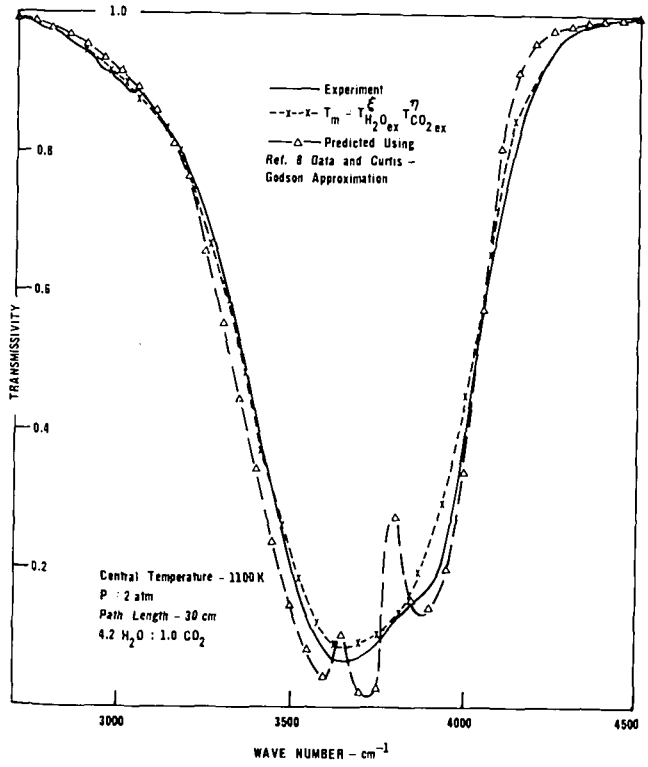

Fig. 14 Spectral transmissivity distribution of a 4.2:1.0 mole fraction mixture of H_2O to CO_2 (T_c = 1100 K, P = 2 atm)

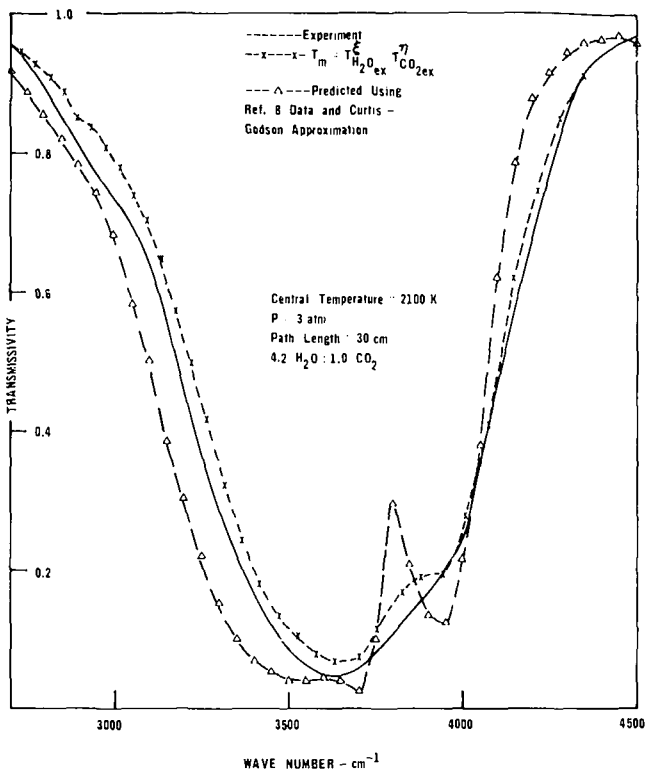

Fig. 15 Spectral transmissivity distributions for a 4.2:1.0 mole fraction mixture of H_2O to CO_2

References

1 Hottel, H. C., *Heat Transmission*, W. H. McAdams, ed., McGraw-Hill, New York, Chapter IV, 1954.

2 Ferriso, C. C., and Ludwig, C. B., "High Temperature Spectral Emissivities of H_2O-CO_2 Mixtures in the 2.7 micron Region," *Appl. Opt.*, Vol. 3, 1964, p. 1435.

3 Penner, S. S., and Varanasi, P., "Effect of (Partial) Overlapping of Spectral Lines on the Total Emissivity of H_2O-CO_2 Mixtures ($T \geq 800$ K)," *JQSRT*, Vol. 6, 1966, p. 181.

4 Hines, W. S., and Edwards, D. K., "Infrared Absorptivities of Mixtures of Carbon Dioxide and Water Vapor," *Chem. Eng. Prog. Symp., Series 64*, 1968, p. 173.

5 Lin, J. D., and Greif, R., "Total Band Absorptance of Carbon Dioxide and Water Vapor including the Effect of Overlapping," *International Journal of Heat and Mass Transfer*, Vol. 17, 1974, p. 793.

6 Goody, R. M., *Atmospheric Radiation*, Oxford University Press, London, 1964.

7 Burch, D. E., Singleton, E. B., and Williams, D., "Absorption Line Broadening in the Infrared," *Appl. Opt.*, Vol. 1, 1962, p. 359.

8 Ferriso, C. C., Boynton, F. P., Ludwig, C. B., Malkmus, W., Streiff, M. L., Suttie, D., and Thomson, J. A. L., "Study on Exhaust Plume Radiation Predictions," *General Dynamics Space Science Laboratory*, GD/C-DBE-66-001 and GD/C-DBE-66-001a, NASA Contract NAS 8-11363, 1966.

9 Tien, C. L., and Giedt, W. H., "Experimental Determination of Infrared Absorption of High-Temperature Gases," *Advances in Thermophysical Properties at Extreme Temperature and Pressures*, ASME, New York, 1965, p. 167.

10 Travis, L. P., and Giedt, W. H., "Infrared Absorption of Carbon Monoxide at High Temperatures," *Heat Transfer 1970*, Elsevier Publishing Company, Amsterdam, Fourth International Heat Transfer Conference, Vol. III, R 1.3, 1970.

11 Giedt, W. H., and Saido, K., "Investigation of Spectral Absorption in the 2.7 μm Bands of Nonisothermal High Temperature H_2O, CO_2 and H_2O-CO_2 Mixtures," University of California, Davis, Department of Mechanical Engineering, Report No. 70-10, 1970.

12 Keil, R. W., and Giedt, W. H., "Spectral Absorptivity Variation of the 2.7 Micron Water Vapor Band at High Temperatures," *Proceedings of the Fifth Symposium on Thermophysical Properties*, ASME, New York, 1970, p. 413.

13 Saido, K., and Giedt, W. H., "Spectral Absorption in the 2.7 Micron Bands of Nonisothermal H_2O and CO_2 at High Temperatures," *Trans. JSME*, Vol. 38, 1972, p. 1790.

14 Felske, J. D., and Tien, C. L., "Wide Band Characterization of the Total Band Absorptance of Overlapping Infrared Gas Bands," *Combustion Science and Technology*, Vol. 11, 1975, p. 111.

N. K. Nakra
Engineer,
The Quaker Oats Co.,
Cedar Rapids, Iowa.
Assoc. Mem. ASME

T. F. Smith
Assoc. Professor,
Division of Energy Engineering,
The University of Iowa,
Iowa City, Iowa.
Mem. ASME

Combined Radiation—Convection for a Real Gas

A study of interaction of radiative transfer with convective transfer is presented for slug flow of an absorbing-emitting gas in a circular tube with an isothermal black wall. The zone method of solution is utilized to evaluate axial gas temperature and wall heat flux distributions using recently developed direct exchange areas for arbitrary zone width to radius ratio. Gas radiative properties are evaluated from the weighted sum of gray gases model with weighting factors and gray gas absorption coefficients applicable for an equimolal mixture of carbon dioxide and water vapor. Results are presented for several values of the governing parameters which are the Boltzmann and Stanton numbers, inlet gas and tube wall temperatures, as well as tube length to diameter ratio. Effects of cooling and heating of the gas are examined.

Introduction

Increasingly higher temperatures, unit capacities, and heat loading requirements of engineering systems have created a need for acceptable methods for prediction of temperature levels and heat transfer rates within these systems. Several of these systems are characterized by flow of a radiatively participating gas through circular channels. Thus, effects of interaction of radiative transfer within a participating medium with conduction and convection must be included in analyses for determination of temperature levels and heat transfer rates for these channels.

Several investigations as reviewed by Wassel, et al. [1][1] were based on solution of the governing integro-differential equations which describe the interaction of radiation with conduction and convection in circular enclosures. Band models were employed in these investigations to describe the frequency dependence of gas radiative properties. Another formulation technique oriented toward engineering analysis is the zone method [2] which is based on the rationale that gas radiative properties may be represented by a weighted sum of a number of gray gases. The zone method has been successfully employed to examine temperature distributions and heat transfer rates in furnaces and circular enclosures [3–7].

The purpose of this paper is to examine interaction of radiative transfer with convective transfer for flow of a radiatively participating gas in circular tube. The zone method is employed to evaluate radiant exchange within the gas as well as between the gas and surrounding surfaces. Gas radiative properties are described by the weighted sum of gray gases model. Results are reported for axial gas temperature distribution as well as local and overall wall heat transfer rates.

Analysis

Description of System. The system selected for this study consists of a radiatively participating gas flowing through a circular tube of length L and diameter D. Slug flow implying uniform velocity and temperature profiles across the tube cross section exists throughout the tube. The gas enters the tube with a mass flow rate $\dot{m}$, inlet temperature T_i, and has attained the steady-state condition. Furthermore, the gas is assumed to be isobaric, uniform in composition and to exhibit a constant specific heat. Gas radiative properties are temperature and pressure-path length dependent and are described for an equimolal mixture of carbon dioxide and water vapor. In the absence of suspended particles, radiation scattering is neglected. Axial heat conduction within the gas is negligible and a constant convective coefficient exists throughout the tube. There are no heat sources within the gas. The tube wall is taken to be black and maintained at a uniform temperature. The conditions at both tube ends are represented by porous black surfaces with inlet surface at the inlet gas temperature and exit surface at either the outlet gas temperature or the tube wall temperature.

Formulation of Equations. The zone method consists of subdividing the enclosure into a number of surface and volume zones small enough for each zone to be assumed to be isothermal and to have uniform properties. A weighted sum of gray gases representation for gas emissivity and absorptivity is utilized where the temperature dependence of gas radiative properties is carried by weighting factors with absorption coefficients being constant. Direct exchange areas [2] which describe the net radiative exchange between respective zones then need to be calculated only once for each gray gas absorption

[1] Numbers in brackets designate References at end of paper.

Contributed by The Heat Transfer Division and presented at the National Heat Transfer Conference, St. Louis, Mo., August 9-11, 1976, of THE AMERICAN SOCIETY OF MECHANICAL ENGINEERS. Revised manuscript received by the Heat Transfer Division October 22, 1976. Paper No. 76-HT-58.

coefficient. Since tube walls are black, total exchange areas, which take into account interreflections, are equal to direct exchange areas. Directed flux areas which account for the nongrayness of the gas are then evaluated utilizing total exchange areas and weighting factors. Evaluation of directed flux areas within the enclosure gives necessary information for a radiant energy balance to be drawn up for each zone.

The energy balance for a volume zone is expressed as

$$\sum_j \overrightarrow{G_jG_i}E_{g,j} + \sum_j \overrightarrow{S_jG_i}E_s + \overrightarrow{S_eG_i}E_e + \overrightarrow{S_oG_i}E_o - 4K_iV_iE_{g,i} + \dot{m}c_p(T_{g,i-1} - T_{g,i}) - hA_s(T_{g,i} - T_s) = 0 \quad (1)$$

The first term in equation (1) represents radiant energy emitted by all volume zones and absorbed by V_i. The next three terms refer to radiant energy leaving all surface zones and absorbed by V_i with tube wall emission included in the second term and emission of the inlet and outlet surfaces accounted for by the third and fourth terms, respectively. Directed flux areas $\overrightarrow{GG}$ and $\overrightarrow{SG}$ are dependent on temperatures of emitting and absorbing zones. Volume zone emission is represented by the fifth term where K_i is evaluated from the gas property model and is dependent on gas temperature. The last two terms of equation (1) respectively represent decrease of sensible enthalpy of the gas flowing through V_i and the convective transfer to the contiguous wall zone. The energy balance of equation (1) may be rewritten as

$$\sum_j \overrightarrow{G_jG_i}\theta_j^4 + \sum_j \overrightarrow{S_jG_i}\theta_s^4 + \overrightarrow{S_eG_i}\theta_e^4 + \overrightarrow{S_oG_i}\theta_o^4 - 4K_iV_i\theta_i^4 + \text{BNO}\,\theta_s^3(\theta_{i-1} - \theta_i) - \text{St BNO}\,\theta_s^3\frac{A_s}{A_t}(\theta_i - \theta_s) = 0 \quad (2)$$

In equation (2), θ_{i-1} is replaced with θ_e when the volume zone is adjacent to the inlet surface.

Similarly, an energy balance on a wall surface zone can be written to yield the following expression for wall heat flux normalized with the emission of a black body at T_r and the wall zone area

$$q_{s,i} = \frac{1}{A_s}\left[\sum_j \overrightarrow{S_jS_i}\theta_S^4 + \overrightarrow{S_eS_i}\theta_e^4 + \overrightarrow{S_oS_i}\theta_o^4 + \sum_j \overrightarrow{G_jS_i}\theta_j^4\right] - \theta_s^4 + \frac{\text{St BNO}}{A_t}\theta_s^3(\theta_i - \theta_s) \quad (3)$$

The first three terms on right-hand side of equation (3) refer to radiant energy leaving all other surface zones and arriving at the considered wall zone. Radiant energy emitted by all volume zones and incident on the wall zone is accounted for by the fourth term. The fifth term denotes emission by the wall zone. The last term in equation (3) represents convective transfer from the contiguous volume zone. Equation (3) can be solved to evaluate wall heat flux after the temperature in each volume zone has been evaluated from equation (2). Total wall heat flux based on total wall surface area is expressed by

$$q_t = \sum_i q_{s,i}/N \quad (4)$$

Total system energy balance is written as

$$q_{\text{in}} = q_t 4Nb/D + q_{\text{out}} \quad (5)$$

where q_{in} includes the enthalpy of inlet gas (BNO $\theta_s^3\theta_e/A_t$) minus the heat flux to the inlet surface. q_{out} refers to the enthalpy of gas leaving the enclosure (BNO $\theta_s^3\theta_o/A_t$) minus the heat flux to the outlet surface. Inlet surface heat flux is evaluated from

$$q_e = \frac{1}{A_t}\left[\sum_j \overrightarrow{S_jS_e}\theta_s^4 + \sum_j \overrightarrow{G_jS_e}\theta_j^4 + \overrightarrow{S_oS_e}\theta_o^4\right] - \theta_e^4 \quad (6)$$

For the outlet surface, the heat flux is obtained by interchanging subscripts "e" and "o" in equation (6).

Method of Solution. Equation (2) represents a set of simultaneous nonlinear algebraic equations where the coefficients of the radiant energy terms are functions of the unknown gas temperature. An iterative technique was employed to solve this system of equations on a digital computer. It was found more convenient to evaluate the coefficients at some gas temperature distribution and hold these quantities constant while new solutions were obtained for the gas temperatures. The coefficients were then evaluated at these temperatures and another set of gas temperature acquired. This iterative procedure was repeated until the difference between successive temperature results was of the order of 10^{-4} or less and the energy balance equation (2) was satisfied within 10^{-4}. Several test cases [8] demonstrated that the numerical results have an accuracy of better than 1 percent.

Gas Radiative Properties

Total gas radiative properties may be represented by the weighted sum of a number of gray gases. The relationship for gas emissivity is

$$\epsilon_g = \sum_n a_{\epsilon,n}(T_g)[1 - \exp(-k_n p_g \ell)] \quad (7)$$

and for gas absorptivity

$$\alpha_g = \sum_n a_{\alpha,n}(T_g, T_s)[1 - \exp(-k_n p_g \ell)] \quad (8)$$

where k_n is pressure absorption coefficient for the nth gray gas component. Weighting factors $a_{\epsilon,n}$ and $a_{\alpha,n}$ may be interpreted to represent the fractional amount of black body energy in the spectral region with gas absorption coefficient k_n. Each set of weighting factors must sum to unity and all weighting factors must be positive. T_s in this discussion refers to the surface temperature where surface radiation originates. Absorption coefficient as introduced in equation (1) is expressed as

$$K = \sum_n a_{\epsilon,n}(T_g)k_n p_g \quad (9)$$

Nomenclature

a_α = weighting coefficient for absorptivity
a_ϵ = weighting coefficient for emissivity
A_s = tube wall zone area, πDb
A_t = tube cross-sectional area, $\pi D^2/4$
A_α = polynomial coefficients for absorptivity
A_ϵ = polynomial coefficients for emissivity
b = zone width
BNO = Boltzmann number, $\dot{m}c_p/\sigma T_r^3$
c_p = specific heat
D = tube diameter
E = black body emissive power
$\overrightarrow{GG}$, $\overrightarrow{GS}$ = directed flux area: volume to volume zones, volume to surface zones
h = convective heat transfer coefficient
k = pressure absorption coefficient
K = absorption coefficient
ℓ = path length
L = tube length
$\dot{m}$ = mass flow rate
N = number of zones
P = combined partial pressure
q = dimensionless heat flux
$\overrightarrow{SS}$, $\overrightarrow{SG}$ = directed flux area: surface to surface zones, surface to volume zones
St = Stanton number, $hA_t/\dot{m}c_p$
T = temperature
V = zone volume, $\pi D^2 b/4$
x = axial distance
α = absorptivity
ϵ = emissivity
σ = Stefan-Boltzmann constant
θ = dimensionless temperature, T/T_r

Subscripts

e = inlet surface
g = gas
o = outlet surface
r = reference
s = tube wall
t = total

Table 1 Absorption and polynomial coefficients

n	k_n, (atm-m)$^{-1}$	$A_{\epsilon,n,1}$	$A_{\epsilon,n,2}\times10^{4}$	$A_{\epsilon,n,3}\times10^{7}$	$A_{\epsilon,n,4}\times10^{11}$
1	0.58862018	-0.053748075	3.0033869	-0.57940111	0.31425209
2	4.2794503	0.30830035	-0.67169883	0.019966627	0.025611416
3	39.602037	0.086454357	0.50666873	-0.17770200	0.13827699
	T_s, K	$A_{\alpha,n,1}$	$A_{\alpha,n,2}\times10^{4}$	$A_{\alpha,n,3}\times10^{7}$	$A_{\alpha,n,4}\times10^{11}$
1	560	0.067939805	2.3562649	-0.63885463	0.45860014
2		0.40307266	-1.5344167	0.24579529	-0.14744737
3		0.093158368	0.44580593	-0.16226524	0.12877854
1	1250	0.30374814	1.6095161	-0.43591611	0.27053110
2		0.39440077	-1.2465587	0.14078103	-0.051469552
3		0.076598017	0.57807828	-0.19437219	0.15104593
1	1960	0.44128900	1.1186038	-0.30625509	0.15674332
2		0.35798003	-0.80310778	0.006458564	0.060928189
3		0.076707698	0.56135450	-0.18729309	0.14358272

A term with one pressure absorption coefficient equal to zero is utilized to represent windows in the spectrum between bands. The temperature dependence of the weighting factors may be described by polynomials of the form

$$a_{\epsilon,n}(T_g) = \sum_i A_{\epsilon,n,i} T_g{}^{i-1} \tag{10}$$

and

$$a_{\alpha,n}(T_g, T_s) = \sum_i A_{\alpha,n,i}(T_s) T_g{}^{i-1} \tag{11}$$

where $A_{\alpha,n,i}$ are a function of T_s. Values for k_n, $A_{\epsilon,n,i}$, and $A_{\alpha,n,i}$ were evaluated for an equimolal mixture of carbon dioxide and water vapor where $p_g = 0.2206$ atm and are given in Table 1 [8]. These coefficients yield total gas emissivity and absorptivity within approximately 1 percent of those given in [2] over a temperature range of 560–1960 K and a pressure-path length range of 0.024–3.0 atm-m. Coefficients recommended by other investigators [3, 9] were found not to yield as accurate results. Interpolation procedures were utilized to obtain values for $A_{\alpha,n,i}$ when irradiation temperatures did not correspond to those given in Table 1.

Direct Exchange Areas

Fundamental to the zone method of solution is evaluation of direct exchange areas which pertain to radiant interchange between two zones. Direct exchange areas were developed by Erkku [10] for a circular tube with the restriction that for zones on the cylinder axis, the zone width is equal to the radius of the tube. With this restriction, the assumption that each zone is isothermal and homogeneous may not be applicable in a wide variety of geometric configurations. Therefore, Nakra, et al. [11] developed direct exchange area expressions for zones on the cylinder axis with arbitrary zone width to radius ratio. In this study, the zone width to radius ratio was taken to be 0.25 so that direct exchange areas evaluated in [11] could be used for each k_n given in Table 1. Directed flux areas [2, 8] were evaluated from weighting factors and direct exchange areas.

Results and Discussion

System Parameters. Axial gas temperature distribution for specified tube geometry and gas radiative properties is expressed in terms of the Boltzmann and Stanton numbers, inlet gas and tube wall temperatures, length to diameter ratio as well as outlet surface temperature. The pressure path length range for which gas properties were developed yields path lengths ranging from 0.11 to 13.8 m. If the tube diameter is selected as the characteristic length, then it must lie within this range and was selected for this study to be 0.6 m. Dimensionless inlet gas and tube wall temperatures for these gas properties are limited to values from 1.0 to 3.5 for a reference temperature of 560 K. The Stanton number range was selected from 0 to 0.01 where the lower limit corresponds to pure radiation and the upper limit is typical for fully developed turbulent flow [12]. Inclusion of radiation with convection alters St evaluated for pure convection. As an approximate means to include effects of radiation in this study, St as based on heat transfer correlations [12] should be increased by about 10 percent [13]. Length to diameter ratios were selected at values of 0.625, 1.25, and 2.5 to enable examination of effects of end surfaces on gas temperature and wall heat flux distributions. For these ratios, entrance effects may exist and the axial variation of St may be important. However, even though these effects may be readily incorporated in the analysis, this was not included in the present study in order to maintain a tractable number of variables. As will be demonstrated, the influence of St is not significant and, thus, radiation and entrance length effects on St will be minimal. Except where noted, the outlet surface temperature is equal to the outlet gas temperature.

Gas Temperature and Wall Heat Flux. Dimensionless gas temperature distributions as a function of dimensionless axial distance are presented in Fig. 1. Results for cooling and heating gas situations where inlet gas temperature is, respectively, greater than or less than tube wall temperature are illustrated. Results are displayed for pure convection (PC), pure radiation (PR) as well as combined radiation and convection (RC). Similar trends are observed along the axial distance for all cases with only outlet gas temperature dependent on tube length as is discussed later.

Consider first cases where the gas is cooled when $\theta_e > \theta_s$. As expected, gas temperatures decrease monotonically with axial distance for all values of the parameters shown in Fig. 1. PC results, which are dependent only on St, yield temperature profiles with a minimum gradient and display the greatest sensitivity to St. Inclusion of radiative transfer, as reflected by BNO, yields lower gas temperatures then for PC. For BNO = 27.9 m^2, gas temperatures differ considerably from those for PC implying that the gas enthalpy rate ($\dot{m}c_pT_g$) must be significantly greater than wall emission ($\sigma T_s{}^4$) in order to neglect radiation effects. As BNO decreases, gas temperatures decrease with minimum temperatures occuring for a stagnant gas where BNO $\approx$ 0. Furthermore, for a specified BNO, gas temperatures decrease as St increases with St influence decreasing as BNO decreases. Stagnant gas results are independent of St as observed from equation (2).

RC results for St $\leq$ 0.001 nearly coincide with PR results for the corresponding BNO and demonstrate that convective transfer is negligible when both transport modes are combined. A similar observation was reported by Perlmutter and Siegel [14]. Furthermore, for values of BNO < 27.9 m^2, PR results predict results for RC over the considered St range within 5 percent with the accuracy improving as BNO decreases.

Consider now the cases where the gas in heated with $\theta_s > \theta_e$. Similar trends are observed for these cases as for cooling gas cases except that gas temperatures increase montonically with axial distance. PC and stagnant gas results yield lower and upper limits, respectively, for gas temperature distributions. Gas temperatures for RC results with BNO = 9.29 m^2 nearly coincide with PC results. Furthermore, results for BNO = 0.929 m^2 differ considerably from those for the stagnant gas. These observations are contrary to those for cooling gas cases and illustrate the nonlinear behavior of results when radiative transfer is considered. RC results nearly coincide with PR results for ST $\leq$ 0.001 and are predicted within 10 percent by the latter results for the considered St range when BNO < 9.29 m^2. For a stagnant gas, gas temperatures are closer to the wall temperature than for cooling gas even though the overall difference between inlet gas and wall temperatures is the same.

Different inlet temperatures yield similar trends as those cited with increasing gas temperature levels for the cooling and heating gas cases as inlet temperature is increased. The change of outlet gas temperature defined as $(\theta_o - \theta_e)/(\theta_s - \theta_e)$ is independent of inlet temperature for PC results but increases as inlet temperature increases for RC results. Effects of BNO and St increase with increasing inlet tem-

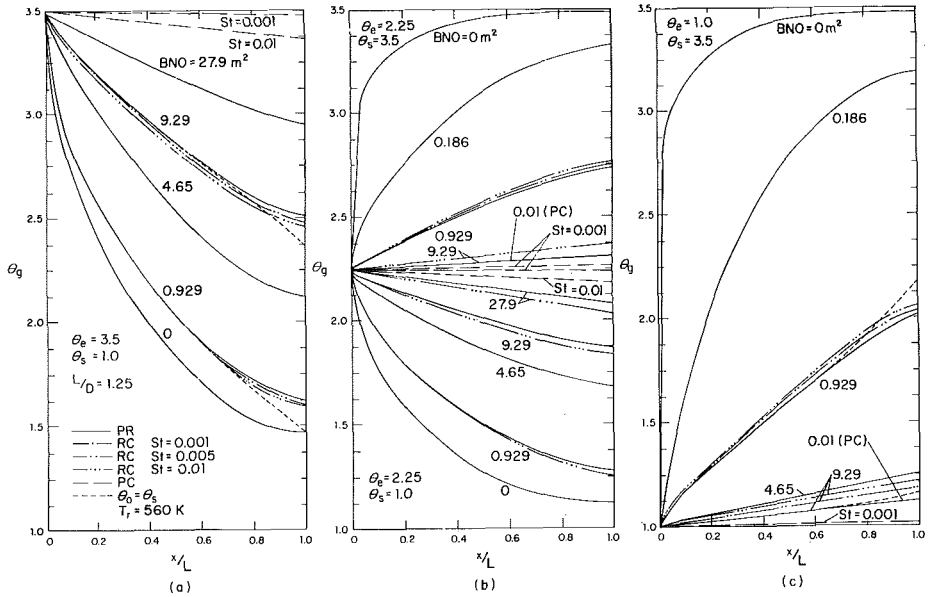

Fig. 1 Gas temperature distribution

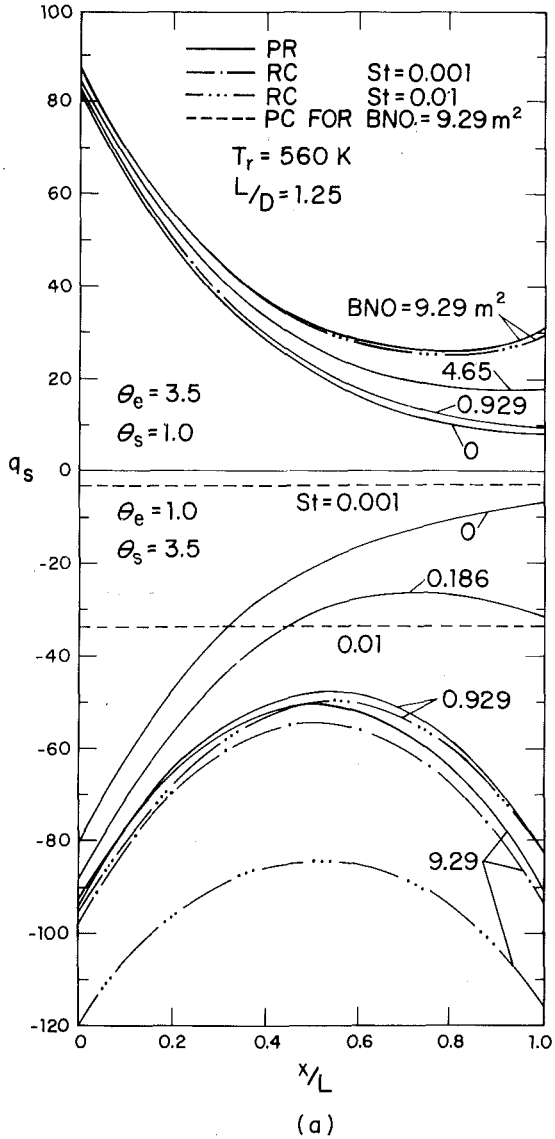

Fig. 2 Wall heat flux distribution

peratures for cooling gas cases whereas opposite trends are observed for heating gas cases.

In the previous discussion, the outlet surface temperature was taken equal to the outlet gas temperature. In Figs. 1(*a*) and 1(*c*), results for BNO = 0.929 and 9.29 m^2 are also presented for gas temperature profiles when the outlet surface temperature is maintained at the tube wall temperature, that is $\theta_o = \theta_s$. This new boundary condition for cooling gas case lowers the gas temperature in the volume zones near the outlet surface and raises the corresponding volume temperatures for the heating gas case.

Dimensionless wall heat flux results required to maintain the wall temperature are illustrated in Fig. 2 as a function of dimensionless axial distance. Gas cooling and heating cases correspond to positive and negative wall heat flux values, respectively.

Cooling gas results are examined first. Wall heat flux distribution exhibits a nonuniform behavior with respect to axial distance. Values of wall heat flux, for the case of PR and RC, are maximum at the wall zone near the inlet surface where the temperature difference for wall and gas is the largest and also the influence of the inlet surface is greatest. The wall heat flux declines along the axial distance as the gas temperature decreases and then may increase for gas zones near the outlet surface. These higher heat flux results near the outlet are attributed to the contribution of the outlet surface which exhibits higher temperatures as BNO increases. Heat flux distribution for stagnant gas yields a lower limit. Wall heat flux results for PC are not displayed since they are of small magnitude for the considered range of parameters. Within the considered St range results for RC are predicted within 2 percent by those for PR for BNO < 9.29 m^2.

For heating gas cases, heat flux results exhibit a decrease (become less negative) with axial distance for wall zones near the inlet and then may increase (become more negative) for zones near the outlet surface. This latter trend is found at higher values of BNO where the outlet surface attains higher temperatures. Results for BNO = 0 exhibit a lower limit when radiation effects are considered. Wall heat flux results for PC are dependent on BNO as shown by equation (3) when the radiation terms are neglected and are presented for BNO = 9.29 m^2 with St = 0.001 and 0.01. Effects of St increase as BNO increases and become significant for BNO = 9.29 m^2.

Representative total wall heat flux values as evaluated from equation (4) are presented in Table 2 for cooling and heating gas cases with $L/D = 1.25$. Results for PR where St = 0 may be interpreted as those for RC with St = 0.001. For the cooling gas, total wall heat flux results are insensitive to St and, thus, convective transfer is negligible.

Table 2 Total wall heat flux

BNO, m^2	q_t	
	St = 0.001	St = 0.01
Cooling Gas, θ_e = 3.5, θ_s = 1.0		
0	28.6	
0.929	29.8	29.7
4.65	34.3	
9.29	39.1	39.0
Heating Gas, θ_e = 1.0, θ_s = 3.5		
0	-27.0	
0.929	-58.9	-60.8
4.65	-63.3	
9.29	-65.3	-95.4

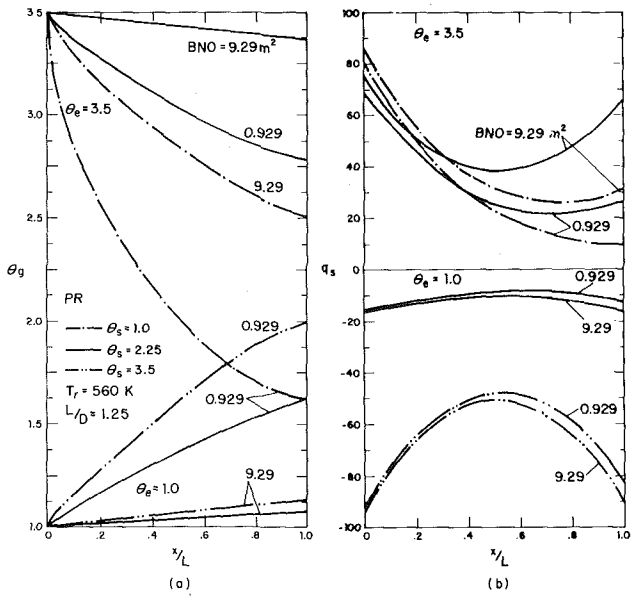

Fig. 3 Effect of wall temperature

The influence of St becomes greater for heating gas at the higher values of the Boltzmann number. For a specified St, total wall heat flux increases for both cooling and heating gas cases as BNO and/or difference between inlet gas and tube wall temperatures increase.

The overall energy balance defined by equation (5) yielded errors based on the inlet gas enthalpy rate or q_e for BNO = 0 of less than 3 and 10 percent for cooling and heating gas cases, respectively, with maximum errors occuring at the small BNO values. These errors are mainly attributed to large changes in gas temperature in the first few volume zones and, thus, finer zone widths are required to attain better accuracy.

The effect of wall temperature level on gas temperature and wall heat flux distributions may be examined by reference to Fig. 3 where PR results are shown for cooling and heating gas cases. Results for PR are only presented since they are representative of those for RC. Gas temperature level increases for both cases as the tube wall temperature increases. Furthermore, as the difference between inlet gas and wall temperatures increases, the effect of BNO on gas temperature also increases. Wall heat flux values for cooling gas are initially higher for θ_s = 1.0 due to the larger temperature difference but as the axial distance increases, a cross over is exhibited and heat flux results are lower for the same wall temperature. This crossover is attributed to the contribution of outlet surface which attains a higher temperature for θ_s = 2.25. For heating gas, wall heat flux values increase as temperature increases. The effect of BNO on wall heat flux increases as inlet gas and wall temperature difference increases for both cases.

The influence of L/D is illustrated in Fig. 4 where results for PR are presented for both cooling and heating gas cases with BNO = 0.929 and 9.29 m^2. Results for wall heat flux are displayed only for BNO = 9.29 m^2. L/D does not have a significant effect on the gas temperature profile and similar trends are observed for all values of this ratio. Only the outlet gas temperature and gas temperature for zones near the outlet surface are affected by L/D. The effect of the outlet surface, however, decreases as the L/D and BNO increases. Wall heat flux decreases as L/D increases and this influence is greater for the heating gas. For cooling gas with L/D = 2.5, wall heat flux values are nearly independent of axial position for values of $x/D > 1.5$, whereas for heating gas, this occurs only for axial positions near the tube center.

Conclusion

Results of this study demonstrate that inclusion of radiative transfer with convective transfer influences gas temperature distribution for the conditions treated. For a cooling gas, the gas temperature decreases monotonically with axial distance and for heating gas, it increases. Pure convection results and those for a stagnant gas yield two outer limits and all other results for pure radiation and those for combined radiation and convection are bracketed by these two limits. The Stanton number does not influence the gas temperature significantly and for the Boltzmann number less than 9.29 m^2, pure radiation results predict results for combined radiation and convection accurate to within 5 percent for cooling gas and 10 percent for heating gas. Gas temperature increases for a cooling gas and decreases for a

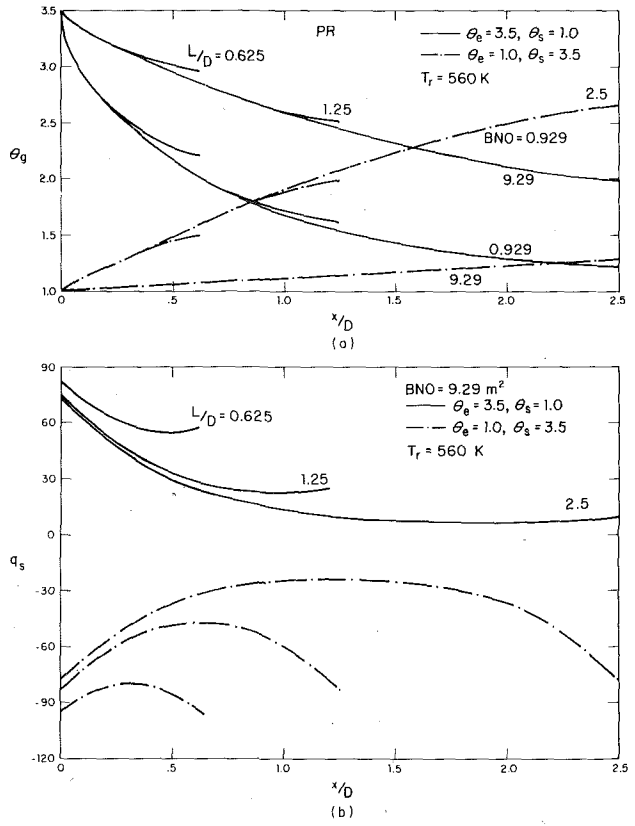

Fig. 4 Effect of length to diameter ratio

heating gas with increase in the Boltzmann number. As the inlet gas or wall temperature increases, gas temperature levels also increase. The length to diameter ratio does not have any qualitative effect on the gas temperature profile but it does determine the outlet gas temperature.

Wall heat flux values decrease monotonically with axial distance and then may increase near the outlet as a result of the radiant energy contribution from the outlet surface which becomes more important as the Boltzmann number increases. The Stanton number does not influence wall heat flux values for cooling gas but for heating gas, significant effects are observed particularly at the higher values of the Boltzmann number. Wall heat flux values also increase with inlet and wall temperature. The length to diameter ratio parameter affects wall heat flux distribution due to contribution from the outlet surface.

Acknowledgments

The authors wish to acknowledge many helpful discussions with R. G. Hering during the initial stages of this study. Computer funds for this study were furnished by the Graduate College.

References

1 Wassel, A. T., Edwards, D. K., and Catton, I., "Molecular Gas Radiation and Laminar or Turbulent Heat Diffusion in a Cylinder With Internal Heat Generation," *International Journal of Heat and Mass Transfer*, Vol. 18, 1975, pp. 1267–1276.

2 Hottel, H. C., and Sarofim, A. F., *Radiative Transfer*, McGraw-Hill, New York, 1967.

3 Hottel, H. C., and Sarofim, A. F., "The Effect of Gas Flow Patterns on Radiative Transfer in Cylindrical Enclosures," *International Journal of Heat and Mass Transfer*, Vol. 8, 1965, pp. 1153–1169.

4 Lowe, A., Wall, T. F., and Stewart, I. McC., "A Zoned Heat Transfer Model of a Large Tangentially Fired Pulverized Coal Boiler," *Fifteenth Symposium on Combustion*, Tokyo, Japan, 1974, pp. 1261–1270.

5 Bueters, K. A., Cogoli, J. G., and Habelt, W. W., "Performance Prediction of Tangentially Fired Utility Furnaces by Computer Model," *Fifteenth Symposium on Combustion*, Tokyo, Japan, 1974, pp. 1245–1260.

6 Johnson, T. R., "Application of Zone Method of Analysis to the Calculations of Heat Transfer from Luminous Flame," PhD thesis, Sheffield University, 1971.

7 Whitacre, G. R., and McCann, R. A., "Comparison of Methods for the Prediction of Radiant Flux Distribution and Temperature," ASME Paper No. 75-HT-9, 1975.

8 Nakra, N. K., "Combined Radiation-Convection for a Real Gas," PhD dissertation, Mechanical Engineering Program, University of Iowa, Iowa City, Iowa, 1975.

9 Taylor, P. B., and Foster, P. J., "The Total Emissivities of Luminous and Nonluminous Flames," *International Journal of Heat and Mass Transfer*, Vol. 17, 1974, pp. 1591–1605.

10 Erkku, H., "Radiant Heat Exchange in Gas Filled Slabs and Cylinders," ScD thesis in Chemical Engineering, M.I.T., 1965.

11 Nakra, N. K., Smith, T. F., and Hering, R. G., "Direct Exchange Areas for Cylindrical Enclosures," Division of Energy Engineering, University of Iowa, TR-E-001-76, 1976.

12 Kreith, F., *Principles of Heat Transfer*, Intext Educational Publishers, 1973.

13 Habib, I. S., and Greif, R. "Heat Transfer to a Flowing Non-Gray Radiating Gas: An Experimental and Theoretical Study," *International Journal of Heat and Mass Transfer*, Vol. 13, 1970, pp. 1571–1582.

14 Perlmutter, M., and Siegel, R., "Heat Transfer by Combined Forced Convection and Thermal Radiation in a Heated Tube," JOURNAL OF HEAT TRANSFER, TRANS. ASME, Series C, Vol. 84, 1962, pp. 301–311.

T. S. Chen
Department of Mechanical and Aerospace Engineering,
University of Missouri—Rolla,
Rolla, Mo.

E. M. Sparrow
Department of Mechanical Engineering,
University of Minnesota, Minneapolis, Minn.

A. Mucoglu
Department of Mechanical and Aerospace Engineering,
University of Missouri—Rolla,
Rolla, Mo.

Mixed Convection in Boundary Layer Flow on a Horizontal Plate

The effects of buoyancy-induced streamwise pressure gradients on laminar forced convective flow and heat transfer over a horizontal flat plate are studied analytically by the local similarity and local nonsimilarity methods of solution. Numerical results for the local surface heat transfer, wall shear stress, and velocity and temperature distributions are presented for gases having a Prandtl number of 0.7. It is found that both the local Nusselt number and the friction factor increase with increasing buoyancy forces for aiding flow and decrease with increasing buoyancy forces for opposing flow. With regard to the heat transfer results, significant buoyancy effects were encountered for $Gr_x/Re_x^{5/2} > 0.05$ *and* < -0.03*, respectively, for aiding and opposing flows. The buoyancy-affected velocity profiles for the aiding-flow case exhibited an overshoot beyond the free stream velocity. Results from previously reported series solutions and from an integral momentum/energy solution were found to be accurate only when the buoyancy effects are small. The present study provides results for intermediate range buoyancy force effects, which have not been reported previously.*

Introduction

In studying forced convective heat transfer over a horizontal surface, it is customary to neglect the effects of buoyancy forces. Such a practice may not be justified when the velocity is small and the temperature difference between the surface and ambient is large. This is because the buoyancy forces arising from the temperature difference induce a longitudinal pressure gradient which in turn modifies the flow field and hence the rate of heat transfer from the surface. Thus, predictions of the heat transfer coefficients in the combined convection regime are of practical interest, as are the conditions under which the buoyancy forces first become significant.

In contrast to the problem of combined convective heat transfer along a vertical flat plate or cylinder, lesser attention has been given to studies of buoyancy force effects on laminar forced convection over a horizontal flat plate. Sparrow and Minkowycz [1][1] and Mori [2] were the first investigators to treat this problem. Their solution was a perturbation series in terms of the buoyancy parameter $\xi = |Gr_x|/Re_x^{5/2}$, and the series was carried through the first two terms. Their results are, therefore, valid only for small buoyancy force effects. Subsequently, Hauptmann [3], Redekopp and Charwat [4], Leal [5], Hieber [6], and Robertson, et al. [7] re-examined the same problem under various restrictions. Hauptmann [3] employed the approximate integral momentum/energy method and obtained solutions via a two-term perturbation series limited to small values of ξ. Leal's analysis [5] pertains particularly to the limiting cases of very large and very small Prandtl numbers (i.e., $Pr \to \infty$ and $Pr \to 0$, respectively) and was carried out using the method of matched asymptotic expansions.

In his analysis, Hieber [6] obtained solutions for a forced-flow dominated near region ($\xi \ll 1$) and for a buoyancy dominated far region ($\xi \gg 1$), the solutions for both regions being expressed by suitable three-term perturbation series in ξ. Surprisingly, for the small ξ region, the use of an additional term beyond those of [1] did not result in an improvement of the predictions of the heat transfer coefficient. In the range between the small ξ and large ξ solutions, a graphical interpolation was suggested as a means for estimating the heat transfer results. The analysis of Robertson, et al. [7] is for a plate of finite length situated in a low Reynolds number flow and is, therefore, different from that for boundary layer flow at relatively large Reynolds numbers. These workers solved the full momentum and energy equations by a finite difference method. In their study, Redekopp and Charwat [4] dealt with the situation in which the free stream velocity varies as a power of streamwise coordinate. Their solutions were expressed in perturbation series as in [1].

For boundary layer flow of gases ($Pr \sim 0.7$), firmly established combined convection results are available for $\xi \ll 1$ and $\xi \gg 1$, but not for the practically interesting intermediate range, say up to $\xi = 1$. This has motivated the present investigation. As will be shown shortly, the present formulation of the problem and its solution method differ

[1] Numbers in brackets designate References at end of paper.

Contributed by the Heat Transfer Division for publication in the JOURNAL OF HEAT TRANSFER. Manuscript received by the Heat Transfer Division September 3, 1976.

from those of the previous studies and, in particular, the ξ limitations related to perturbation series are lifted. The conservation equations are transformed such that they can lend themselves to local nonsimilarity solutions. As is well established, in the local nonsimilarity method all the terms in the transformed conservation equations are retained, and terms are selectively neglected only in the derived subsidiary equations. This accounts for the high accuracy of the numerical results provided by the local nonsimilarity solution method.

Numerical solutions and results were obtained for Pr = 0.7, including both the cases in which the buoyancy, respectively, aids and opposes the forced convection flow. For the aiding case, the solutions encompassed the range of ξ between zero and one. The opposing flow solutions were for ξ between zero and 0.03.

Analysis

Consider a horizontal flat plate aligned parallel to a uniform free stream with velocity u_∞ and temperature T_∞. The plate is maintained at a constant temperature T_w. As demonstrated in [1], the buoyancy force associated with the temperature difference $(T_w - T_\infty)$ induces a streamwise pressure gradient which interacts with the laminar forced convection boundary layer adjacent to the plate. The coordinates are chosen such that x represents the distance along the plate from its leading edge and y represents the distance normal to the surface. It is convenient to take y as positive in the vertical upward direction for flow above the plate and as positive in the vertical downward direction for flow below the plate. The sign of the gravity force responds appropriately to the assigned direction for y.

In the analysis, the fluid properties are assumed to be constant except that the density variations within the fluid are considered only to the extent that they contribute to the buoyancy forces. The governing equations for the problem under consideration are the following boundary layer equations [1]

$$\partial u/\partial x + \partial v/\partial y = 0 \tag{1}$$

$$u(\partial u/\partial x) + v(\partial u/\partial y) = \nu(\partial^2 u/\partial y^2) \pm g\beta\partial/\partial x\left[\int_y^\infty (T - T_\infty)dy\right] \tag{2}$$

$$u(\partial T/\partial x) + v(\partial T/\partial y) = \alpha(\partial^2 T/\partial y^2) \tag{3}$$

in which u and v are, respectively, the velocity components in the x and y directions, T is the fluid temperature, β is the expansion coefficient, ν is the kinematic viscosity, and α is the thermal diffusivity. The second term on the right-hand side of equation (2) is the pressure gradient due to buoyancy. The plus and minus signs preceding that term pertain, respectively, to flow above and below the plate. The boundary conditions for equations (1)–(3) are

$$u = v = 0, \quad T = T_w \text{ at } y = 0$$
$$u \to u_\infty, \quad T \to T_\infty \text{ as } y \to \infty \tag{4}$$

As the first step in solving the system of equations (1)–(4) by the local nonsimilarity method, it is necessary to make a transformation from the (x, y) coordinates to the $(\xi(x), \eta(x, y))$ coordinates by introducing

$$\xi = \xi(x), \quad \eta = y\sqrt{u_\infty/\nu x} \tag{5}$$

The coordinate $\eta(x, y)$ is a pseudo-similarity variable which reduces to a true similarity variable for boundary layers that are similar. The coordinate $\xi(x)$ depends only on x and is so chosen that x does not appear explicitly in the transformed conservation equations and their boundary conditions. In addition, one introduces a reduced stream function $F(\xi, \eta)$ and a dimensionless temperature $\theta(\xi, \eta)$ defined, respectively, as

$$F(\xi, \eta) = \psi(x, y)/\sqrt{\nu u_\infty x}, \quad \theta(\xi, \eta) = (T - T_\infty)/(T_w - T_\infty) \tag{6}$$

wherein $\psi(x, y)$ is the stream function that satisfies the continuity equation (1) with

$$u = \partial\psi/\partial y, \quad v = -(\partial\psi/\partial x) \tag{7}$$

Substitution of equations (5) and (6) into equations (2)–(4) results in the following system of equations

$$F''' + \tfrac{1}{2}FF'' \pm \tfrac{1}{2}\xi\left[\eta\theta + \int_\eta^\infty \theta d\eta + \xi\int_\eta^\infty (\partial\theta/\partial\xi)d\eta\right] = \tfrac{1}{2}\xi[F'(\partial F'/\partial\xi) - F''(\partial F/\partial\xi)] \tag{8}$$

$$(1/\mathrm{Pr})\theta'' + \tfrac{1}{2}F\theta' = \tfrac{1}{2}\xi[F'(\partial\theta/\partial\xi) - \theta'(\partial F/\partial\xi)] \tag{9}$$

$$F'(\xi, 0) = 0, \quad F(\xi, 0) = 0, \quad \theta(\xi, 0) = 1 \tag{10a}$$

$$F'(\xi, \infty) = 1, \quad \theta(\xi, \infty) = 0 \tag{10b}$$

In the foregoing equations, the primes denote partial differentiation with respect to η, Pr is the Prandtl number, and $\xi(x)$ is found to have the expression

$$\xi = |\mathrm{Gr}_x|/\mathrm{Re}_x^{5/2} \tag{11}$$

in which

$$\mathrm{Gr}_x = g\beta(T_w - T_\infty)x^3/\nu^2, \quad \mathrm{Re}_x = u_\infty x/\nu \tag{12}$$

are, respectively, the local Grashof and Reynolds numbers.

The use of the absolute magnitude in the definition of ξ requires that additional interpretation be given for the $\pm$ sign that appears on the left-hand side of equation (8). For flow above the plate, the plus and minus signs, respectively, pertain to the cases $T_w > T_\infty$ and $T_w < T_\infty$. For flow below the plate, the plus sign is associated with $T_w < T_\infty$ and the minus sign with $T_w > T_\infty$.

To facilitate the solution, the integral terms in equation (8) are removed by differentiating the equation once with respect to η to yield a fourth order differential equation. This, in turn, requires an additional boundary condition for $F(\xi, \eta)$, which is obtained by evaluating equation (8) at $\eta = 0$. If, in addition to F and θ, the dependent variables

$$G = \partial F/\partial\xi, \quad \phi = \partial\theta/\partial\xi \tag{13}$$

Nomenclature

C_f = local friction factor
F = reduced stream function, equation (6)
G = ξ-derivative of F
g = gravitational acceleration
Gr_x = local Grashof number, $g\beta(T_w - T_\infty)x^3/\nu^2$
k = thermal conductivity
Nu_x = local Nusselt number, $q_w x/(T_w - T_\infty)k$
Pr = Prandtl number
q_w = local surface heat transfer rate per unit area
Re_x = Reynolds number, $u_\infty x/\nu$
T = fluid temperature
T_w = wall temperature
T_∞ = free stream temperature
u = axial velocity component
u_∞ = free stream velocity
v = normal velocity component
x = axial coordinate
y = transverse coordinate
α = thermal diffusivity
β = coefficient of thermal expansion
η = pseudo-similarity variable, equation (5)
θ = dimensionless temperature, equation (6)
μ = dynamic viscosity
ν = kinematic viscosity
ξ = buoyancy parameter, $|\mathrm{Gr}_x|/\mathrm{Re}_x^{5/2}$
τ_w = wall shear stress
ϕ = ξ-derivative of θ
ψ = stream function

Subscript

0 = pure forced convection

are introduced, the system of equations describing the problem at hand can be written as

$$F'''' + \tfrac{1}{2}(FF''' + F'F'') \pm \tfrac{1}{2}\xi\eta\theta' \mp \tfrac{1}{2}\xi^2\phi = \tfrac{1}{2}\xi(F'G'' - F'''G) \quad (14)$$

$$(1/\mathrm{Pr})\theta'' + \tfrac{1}{2}F\theta' = \tfrac{1}{2}\xi(F'\phi - \theta'G) \quad (15)$$

$$F'(\xi, 0) = F(\xi, 0) = 0, \quad \theta(\xi, 0) = 1 \quad (16a)$$

$$F'''(\xi, 0) = \mp\tfrac{1}{2}\xi \int_0^\infty \theta d\eta \mp \tfrac{1}{2}\xi^2 \int_0^\infty \phi d\eta \quad (16b)$$

$$F'(\xi, \infty) = 1, \quad \theta(\xi, \infty) = 0 \quad (16c)$$

Equations (14) and (15) are two coupled equations with four unknown functions F, G, θ, and ϕ. It is to be noted that the present problem is unusual among those encountered in boundary layer studies in that integrals appear in one of the boundary conditions (equation 16b). In the present study, the system of equations (14)–(16) will be solved by the local nonsimilarity method. Furthermore, since the local similarity solution for the problem has not been previously published, it will be presented first.

The local similarity model corresponds to the first level of truncation in which the terms involving G, G'', and ϕ appearing in equations (14)–(16) are neglected. Thus, the governing equations for the local similarity model are

$$F'''' + \tfrac{1}{2}(FF''' + F'F'') \pm \tfrac{1}{2}\xi\eta\theta' = 0 \quad (17)$$

$$(1/\mathrm{Pr})\theta'' + \tfrac{1}{2}F\theta' = 0 \quad (18)$$

$$F'(\xi, 0) = F(\xi, 0) = 0, \quad \theta(\xi, 0) = 1 \quad (19a)$$

$$F'''(\xi, 0) = \mp\tfrac{1}{2}\xi \int_0^\infty \theta d\eta \quad (19b)$$

$$F'(\xi, \infty) = 1, \quad \theta(\xi, \infty) = 0 \quad (19c)$$

In the foregoing equations, F and θ are coupled and equations (17) and (18) must be solved simultaneously. With the values of ξ prescribed, these equations can be treated as coupled ordinary differential equations and solved by conventional techniques for similarity boundary layers.

The formulation of the systems of equations for the local nonsimilarity models will now be briefly discussed. To begin with, one derives successive sets of subsidiary equations by differentiating equations (14)–(16) with respect to ξ once to obtain the first set and twice to obtain the second set of subsidiary equations, and so on. Certain terms in these sets of subsidiary equations are then neglected according to the level of truncation at which the solution is being sought (see, for example, [8–10]). In the present study, the truncation is at the second level (the next level beyond local similarity), and terms containing $\partial G/\partial\xi$ and $\partial\phi/\partial\xi$ and their η-derivatives in the first set of subsidiary equations are neglected. However, the transformed conservation equations (14) and (15) are left intact. The system of equations for the second level of truncation can then be summarized as:

(a) Equations (14) and (15)

(b) The truncated equations for G and ϕ

$$G'''' + \tfrac{1}{2}(FG''' + F''G') + F'''G \pm \tfrac{1}{2}\eta(\theta' + \xi\phi') \mp \xi\phi + \tfrac{1}{2}\xi(GG''' - G'G'') = 0 \quad (20)$$

$$(1/\mathrm{Pr})\phi'' + \tfrac{1}{2}F\phi' - \tfrac{1}{2}F'\phi + G\theta' + \tfrac{1}{2}\xi(G\phi' - G'\phi) = 0 \quad (21)$$

(c) The boundary conditions

$$F'(\xi, 0) = F(\xi, 0) = G'(\xi, 0) = G(\xi, 0) = \phi(\xi, 0) = 0$$

$$\theta(\xi, 0) = 1 \quad (22a)$$

$$F'''(\xi, 0) = \mp\tfrac{1}{2}\xi \int_0^\infty \theta d\eta \mp \tfrac{1}{2}\xi^2 \int_0^\infty \phi d\eta \quad (22b)$$

$$G'''(\xi, 0) = \mp\tfrac{1}{2} \int_0^\infty \theta d\eta \mp \frac{3}{2}\xi \int_0^\infty \phi d\eta \quad (22c)$$

$$F'(\xi, \infty) = 1, \quad G'(\xi, \infty) = \theta(\xi, \infty) = \phi(\xi, \infty) = 0 \quad (22d)$$

It can be seen that equations (14), (15), (20), and (21) are coupled and they must be solved simultaneously for the four unknown functions F, G, θ, and ϕ. With ξ regarded as a constant prescribable parameter, these equations may be treated as a system of coupled ordinary differential equations of the similarity type.

The primary physical quantities of interest are the local Nusselt number Nu_x, the local friction factor C_f, the velocity distribution $u/u_\infty = F'(\xi, \eta)$, and the temperature distribution $(T - T_\infty)/(T_w - T_\infty) = \theta(\xi, \eta)$. The first two quantities are defined, respectively, by

$$\mathrm{Nu}_x = \frac{q_w}{T_w - T_\infty}\frac{x}{k}, \quad C_f = \frac{\tau_w}{\rho u_\infty^2/2} \quad (23)$$

With the aid of equations (5) and (6), along with the definition of the wall shear stress $\tau_w = \mu(\partial u/\partial y)_{y=0}$ and the use of Fourier's law $q_w = -k(\partial T/\partial y)_{y=0}$, it follows that

$$\mathrm{Nu}_x/\sqrt{\mathrm{Re}_x} = -\theta'(\xi, 0), \quad C_f\sqrt{\mathrm{Re}_x} = 2F''(\xi, 0) \quad (24)$$

Numerical Solutions

Each of the systems of equations for the local similarity model and for the second-level local nonsimilarity model was solved by employing the Runge-Kutta integration scheme in conjunction with Newton-Raphson shooting method to fulfill the conditions at the edge of the boundary layers (i.e., at large η values). In the solution for the second level of truncation, a predictor-corrector integration scheme was employed to improve the accuracy of the Runge-Kutta scheme.

The major difference in the numerical solutions of the present problem and those encountered in conventional boundary layer problems lies in the handling of the θ and ϕ integrals which appear in the boundary conditions $F'''(\xi, 0)$ and $G'''(\xi, 0)$, equations (19b), (22b), and (22c). Indeed, the presence of these integrals introduces an additional iteration loop into the shooting method. To elucidate this matter, we consider the governing equations for the second level of truncation.

To solve these equations for a prescribed value of ξ, one needs to start by guessing the values of the θ and ϕ integrals, in addition to guessing the unavailable starting values of $F''(\xi, 0)$, $G''(\xi, 0)$, $\theta'(\xi, 0)$, and $\phi'(\xi, 0)$. These inputs enable the governing equations to be integrated across the boundary layer and, simultaneous with this integration, the θ and ϕ integrals are evaluated. These values are employed to replace the initial guesses for the θ and ϕ integrals, but the initial guesses for $F''(\xi, 0), \ldots, \phi'(\xi, 0)$ are retained. With these inputs for the integrals, the boundary layer integration is repeated and new values of the θ and ϕ integrals are obtained, which are used as input to still another cycle of boundary layer integration, and so on. This procedure is repeated, keeping $F''(\xi, 0), \ldots, \phi'(\xi, 0)$ fixed until the input and output values of the θ and ϕ integrals are in agreement within a prescribed tolerance. Then, $F''(\xi, 0), \ldots, \phi'(\xi, 0)$ are altered in accordance with the shooting method.

In the numerical computations, the effects of step size $\Delta\eta$ and boundary layer thickness η_∞ on the numerical results as well as on the convergence of the solutions were examined in detail. It was found that for the second level of truncation, sufficiently accurate numerical results were obtained with a step size of $\Delta\eta = 0.02$ when the values of η_∞ were varied from 8 to 6 as the buoyancy parameter $\mathrm{Gr}_x/\mathrm{Re}_x^{5/2}$ increased from -0.03 to 1.0. A solution was considered to be converged when the difference between the input and output values of the θ and ϕ integrals came within 10^{-4} and 10^{-3}, respectively, and the magnitudes of the conditions at the edge of the boundary layer $F'(\xi, \eta_\infty) - 1$, $F''(\xi, \eta_\infty)$, $\theta(\xi, \eta_\infty)$, $\theta'(\xi, \eta_\infty)$ and $G'(\xi, \eta_\infty)$, $G''(\xi, \eta_\infty)$, $\phi(\xi, \eta_\infty)$, $\phi'(\xi, \eta_\infty)$ became respectively less than 5×10^{-4} and 5×10^{-3} simultaneously. Convergence of the numerical solutions was found to be rather difficult to attain when smaller values of the aforementioned criteria were imposed.

Results and Discussion

The numerical solutions were carried out for a Prandtl number of 0.7, which is typical for gases in general and specifically for air. For buoyancy aided flow ($\mathrm{Gr}_x/\mathrm{Re}_x^{5/2} > 0$), the buoyancy parameter

Table 1 Results for $F''(\xi, 0)$ and $-\theta'(\xi, 0)$, Pr = 0.7

	Local Similarity		Local Nonsimilarity	
$Gr_x/Re_x^{5/2}$	F''(ξ,0)	-θ'(ξ,0)	F''(ξ,0)	-θ'(ξ,0)
-0.03	0.26576	0.28075	0.27851	0.28194
-0.02	0.28918	0.28510	0.29611	0.28515
-0.01	0.31119	0.28905	0.31553	0.28972
0	0.33206	0.29268	0.33206	0.29268
0.1	0.50358	0.31928	0.47673	0.31934
0.2	0.63974	0.33733	0.58915	0.33751
0.3	0.75769	0.35141	0.68915	0.35073
0.4	0.86387	0.36311	0.77849	0.36178
0.5	0.96162	0.37320	0.85920	0.37138
0.6	1.05290	0.38212	0.93694	0.37949
0.7	1.13900	0.39014	1.00878	0.38719
0.8	1.22084	0.39746	1.07592	0.39423
0.9	1.29909	0.40419	1.14158	0.40063
1.0	1.37421	0.41044	1.20469	0.40658

$Gr_x/Re_x^{5/2}$ was varied parametrically over the range from zero to one. For the case where the buoyancy opposes the forced convection flow ($Gr_x/Re_x^{5/2} < 0$), solutions were obtained for $Gr_x/Re_x^{5/2} = -0.01$, -0.02, and -0.03, but convergence could not be attained for smaller $Gr_x/Re_x^{5/2}$ values at the second level of truncation. The numerical values of $\theta'(\xi, 0)$ and $F''(\xi, 0)$, which are directly related to the Nusselt number and friction factor results, are listed in Table 1 for the $Gr_x/Re_x^{5/2}$ values for which solutions have been obtained. The tabulated information has been employed for the preparation of Nusselt number and friction factor graphs, and trends will be identified when the figures are discussed.

Local Nusselt numbers are presented in Fig. 1 as a function of the buoyancy parameter $Gr_x/Re_x^{5/2}$, with the results of the present investigation depicted by dotted and solid lines, respectively, for the local similarity and second level local nonsimilarity solutions. The very close agreement between these two sets of results is a strong indicator of their high accuracy. Also shown in the figure are the results from the two-term and three-term series solutions of [1] and of [6], the integral momentum/energy solution of [3], and the graphically based interpolation curve of [6].

The Nusselt number trends are consistent with the expected effects

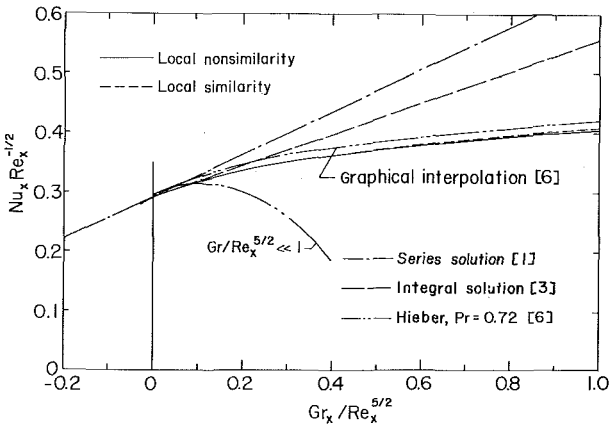

Fig. 1 Local Nusselt number results, Pr = 0.7

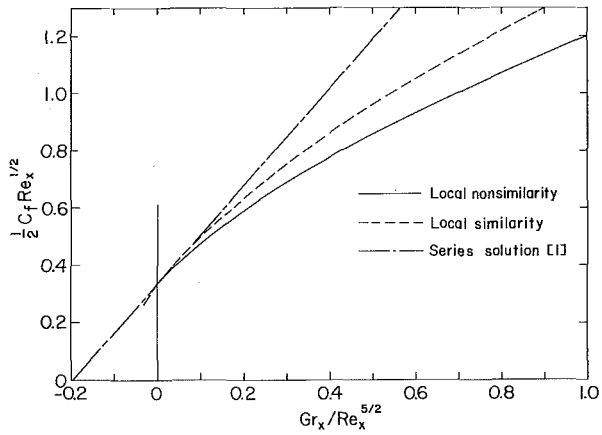

Fig. 2 Local friction factor results, Pr = 0.7

of favorable and adverse pressure gradients. When $Gr_x/Re_x^{5/2}$ is positive, the buoyancy induces a favorable pressure gradient which accelerates the flow and increases the Nusselt number. On the other hand, the adverse pressure gradient that is induced at negative $Gr_x/Re_x^{5/2}$ values retards the flow and decreases the Nusselt number.

The present Nusselt number results will now be compared with those of other investigators. The close agreement of Hieber's interpolation curve with the present results is quite remarkable and somewhat surprising. The curve was drawn as a reasonable bridge between his small $Gr_x/Re_x^{5/2}$ and large $Gr_x/Re_x^{5/2}$ series solutions, and its accuracy, as witnessed by Fig. 1, could not have been forecast in advance.

The other solutions depicted in Fig. 1 yield results of lower accuracy. The two-term series overestimates the buoyancy effect and is substantially in error at the larger abscissa values. The results of the three-term series do not show an improvement compared with those of the two-term series, only a change in the sign of the error. The range of validity of both series appears to be confined to $Gr_x/Re_x^{5/2}$ values less than 0.1. The integral momentum/energy solution yields a linear variation which also substantially overestimates the buoyancy effect for $Gr_x/Re_x^{5/2} > 0.2$.

Another perspective on the Nusselt number results will be presented shortly, following the skin friction results. The latter are plotted in Fig. 2. The skin friction is seen to increase markedly in response to a favorable buoyancy-induced pressure gradient. For negative $Gr_x/Re_x^{5/2}$, the skin friction drops off sharply as the adverse pressure gradient retards the flow. It is reasonable to expect that as $Gr_x/Re_x^{5/2}$ becomes more negative, the strengthening of the adverse pressure gradient will ultimately cause flow separation. Although the range of computed negative $Gr_x/Re_x^{5/2}$ values is too small to permit a definite determination, it appears that separation could occur for $Gr_x/Re_x^{5/2} \sim -0.1$. Fig. 2 also contains a straight line depicting the two-term series solution. As for the Nusselt number, the series solution also overestimates the effect of buoyancy on the skin friction.

The skin friction values from the local similarity and second level local nonsimilarity solutions do not agree quite as well as the Nusselt number results. This outcome is consistent with the greater sensitivity of the skin friction to the buoyancy-induced pressure gradient, thereby making it more sensitive to any approximations in the analysis. Previous experience based on solutions carried to the third level of truncation suggests that the second level results of Fig. 2 are of sufficient accuracy for any practical purpose, especially since the skin friction is not of major importance for very low speed flows.

The extent to which the forced convection Nusselt numbers and friction factors are affected by the buoyancy-induced pressure gradient is most effectively visualized in terms of the ratios $Nu_x/Nu_{x,0}$ and $C_f/C_{f,0}$. The reference quantities $Nu_{x,0}$ and $C_{f,0}$ respectively denote the local Nusselt number and friction factor for pure forced

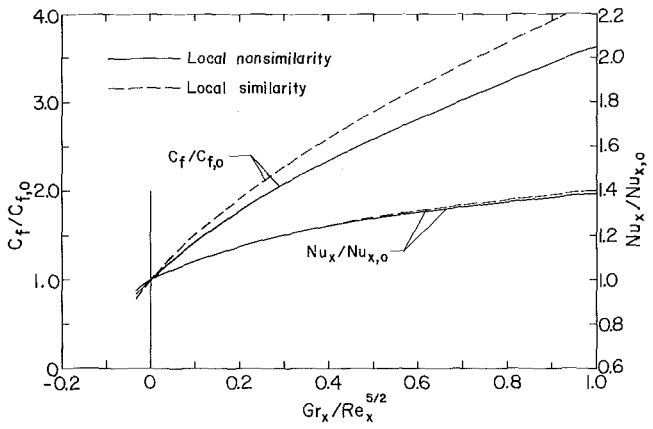

Fig. 3 Buoyancy-induced departures of the local Nusselt number and friction factor from pure forced convection, Pr = 0.7

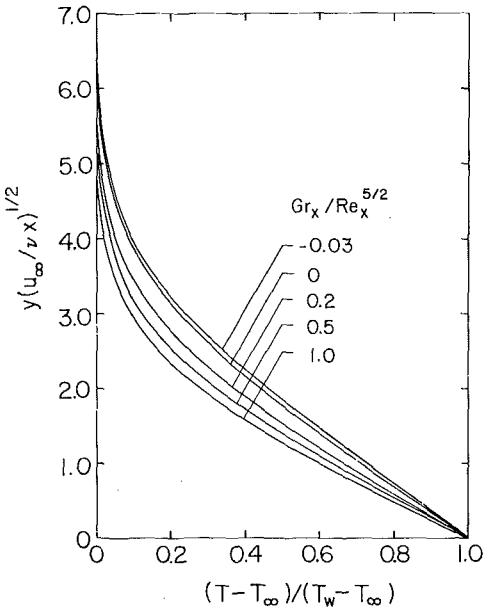

Fig. 5 Representative temperature profiles, Pr = 0.7

convection. The departure of these ratios from unity provides a direct measure of the influence of buoyancy.

In Fig. 3, $Nu_x/Nu_{x,0}$ and $C_f/C_{f,0}$ are plotted as a function of the buoyancy parameter $Gr_x/Re_x^{5/2}$ with different ordinate scales being employed to accommodate the difference in the magnitudes of the Nusselt number and friction factor ratios. Inspection of the figure indicates that whereas both Nu_x and C_f increase as the buoyancy parameter increases, the Nusselt number is much less responsive to the buoyancy. For instance, for $Gr_x/Re_x^{5/2} = 0.5$, $Nu_x/Nu_{x,0}$ is about 1.27 while $C_f/C_{f,0}$ is about 2.6. The lesser responsiveness of the Nusselt number is in evidence for opposing flow conditions as well as for aiding flow conditions.

The results of Fig. 3 also enable the thresholds of significant buoyancy effects to be identified. If the thresholds are defined by five percent departures from pure forced convection, then for the case of aiding flows, buoyancy effects become significant at $Gr_x/Re_x^{5/2}$ values of 0.05 and 0.01, respectively, for heat transfer and friction. For opposing flows, the $Gr_x/Re_x^{5/2}$ threshold for friction is -0.01 while the heat transfer threshold is about -0.03.

It is interesting to see how the buoyancy induced pressure gradient affects the velocity and temperature fields in the boundary layer. To this end, representative velocity profiles for several values of the buoyancy parameter $Gr_x/Re_x^{5/2}$ are shown in Fig. 4. It is seen from the figure that for assisting flow, the velocity gradient at the wall increases as the buoyancy increases, with an accompanying increase in the velocity near the wall and an overshooting of the velocity beyond its free stream value. At $Gr_x/Re_x^{5/2} = 1$, for example, the overshoot is about 11.5 percent. For the opposing flow, on the other hand, the effect of buoyancy is to reduce the velocities compared to those for pure forced convection. For even smaller $Gr_x/Re_x^{5/2}$ values, S-shaped profiles typical of retarded boundary layers are expected.

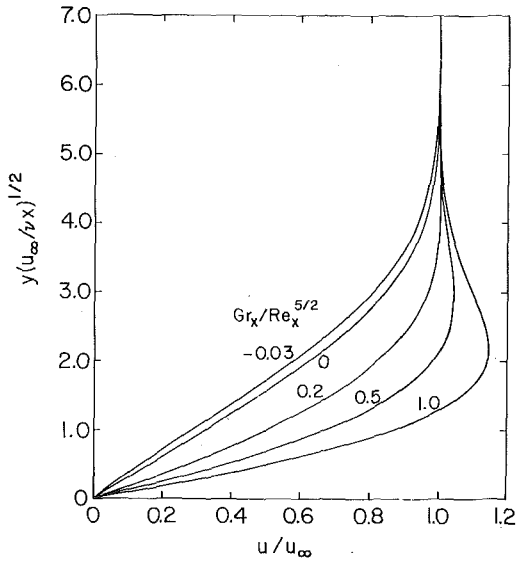

Fig. 4 Representative velocity profiles, Pr = 0.7

In Fig. 5 are shown representative temperature profiles. The most noteworthy trends with increasing buoyancy for the case of assisting flow are the increase in temperature gradient at the wall and the decrease in the thermal boundary layer thickness. The opposite trends are in evidence for the case of opposing flow.

Conclusions

The effect of buoyancy-induced streamwise pressure gradients on forced convection boundary layer flow over a horizontal flat plate has been analyzed by the local nonsimilarity method of solution. Numerical results have been obtained for values of the buoyancy parameter $Gr_x/Re_x^{5/2}$ between -0.03 and 1.0 and for a Prandtl number of 0.7. With respect to the heat transfer results, significant buoyancy effects are encountered for $Gr_x/Re_x^{5/2} \geq 0.05$ and for $Gr_x/Re_x^{5/2} \leq -0.03$, respectively, for aiding and opposing flows. For $Gr_x/Re_x^{5/2} = 0.5$, the increase in the Nusselt number due to buoyancy is about 27 percent. The skin friction is much more affected than is the heat transfer. For instance, at $Gr_x/Re_x^{5/2} = 0.5$, the friction factor in the presence of buoyancy is about 2.6 times that of a corresponding forced convection flow. The buoyancy-affected velocity profiles for the aiding-flow case exhibit an overshoot beyond the free stream velocity.

Acknowledgment

This work was supported by a grant from the National Science Foundation (NSF ENG 75-15033).

References

1 Sparrow, E. M., and Minkowycz, W. J., "Buoyancy Effects on Horizontal Boundary-Layer Flow and Heat Transfer," *International Journal of Heat and Mass Transfer*, Vol. 5, 1962, pp. 505–511.

2 Mori, Y., "Buoyancy Effects in Forced Laminar Convection Flow over a Horizontal Flat Plate," JOURNAL OF HEAT TRANSFER, TRANS. ASME, Series C, Vol. 83, 1961, pp. 479–482.

3 Hauptmann, E. G., "Laminar Boundary-Layer Flows With Small

Buoyancy Effects," *International Journal of Heat and Mass Transfer*, Vol. 8, 1965, pp. 289–295.

4 Redekopp, L. G., and Charwat, A. F., "Role of Buoyancy and the Boussinesq Approximation in Horizontal Boundary Layers," *Journal of Hydronautics*, Vol. 6, 1972, pp. 34–39.

5 Leal, L. G., "Combined Forced and Free Convection Heat Transfer from a Horizontal Flat Plate," *Journal of Applied Mathematics and Physics (ZAMP)*, Vol. 24, 1973, pp. 20–42.

6 Hieber, C. A., "Mixed Convection Above a Heated Horizontal Surface," *International Journal of Heat and Mass Transfer*, Vol. 16, 1973, pp. 769–785.

7 Robertson, G. E., Seinfeld, J. H., and Leal, G. E., "Combined Forced and Free Convection Flow Past a Horizontal Flat Plate," *AIChE Journal*, Vol. 19, 1973, pp. 998–1008.

8 Sparrow, E. M., Quack, H., and Boerner, C. J., "Local Non-similarity Boundary-Layer Solutions," *AIAA Journal*, Vol. 8, 1970, pp. 1936–1942.

9 Minkowycz, W. J., and Sparrow, E. M., "Local Nonsimilar Solutions for Natural Convection on a Vertical Cylinder," JOURNAL OF HEAT TRANSFER, TRANS. ASME, Series C, Vol. 96, 1974, pp. 178–183.

10 Chen, T. S., and Mucoglu, A., "Buoyancy Effects on Forced Convection Along a Vertical Cylinder," JOURNAL OF HEAT TRANSFER, TRANS. ASME, Series C, Vol. 97, 1975, pp. 198–203.

Tsai-Tse Kao
Sr. Thermal Hydraulic Engineer,
Nuclear Department,
Foster Wheeler Energy Corp.,
Livingston, N. J.
Assoc. Mem. ASME

G. A. Domoto
Assoc. Professor,
Department of Mechanical Engineering,
Columbia University,
New York, N. Y.
Mem. ASME

H. G. Elrod, Jr.
Professor,
Department of Mechanical Engineering,
Columbia University,
New York, N. Y.
Mem. ASME

Free Convection Along A Nonisothermal Vertical Flat Plate

A technique has been developed for the solution of free convection problems on a vertical flat plate with arbitrary (though smooth) temperature or heat-flux distributions. The general theory is developed with local similarity as a first approximation, and universal functions for improvement. Comparisons with highly accurate numerical solutions validate the use of one simple correction term for most applications. Computations are readily performed with the use of a hand-held mini-computer. Four illustrative computational examples are carried out with the aid of the two working charts provided for air.

Introduction

The purpose of this paper is to present a rapid and accurate method for the computation of heat-transfer parameters for free convection along a vertical flat plate subjected to arbitrarily prescribed wall temperature or wall heat flux. Very few publications on this subject is presently available in the existing literature. Finite-difference type of numerical computational programs have been reported for the cases of constant wall temperature and a step-jump discontinuity in wall temperature [1,2].[1] There are Karman-Pohlhausen type of approximate solutions in references [3, 4, 5, 6], and similarity solutions for free convection over a nonisothermal vertical plate have been provided by Sparrow and Gregg [7] and by Finston [8]. Yang [9] has verified that the similarity possibilities have essentially been covered by these authors; namely, the cases of power-law and exponential dependence of wall temperature upon elevation. Gebhart and Mollendorf [10] have included viscous dissipation in their analysis, and have provided more extensive solutions for the foregoing cases.

Foote [11] had discussed the possibility of solving the general problem in power series, and solutions for a number of particular cases have been obtained by Niuman and Pohlhausen [12]. A Görtler-type of series expansion has been tried by Kelleher and Yang [13], to accommodate more general wall temperature variations. Kuiken [14] also obtained an expansion for the case where wall temperature variation is expressed in a power series in the stream-wise coordinate.

In what follows, a coordinate transformation is introduced to treat the problem of nonisothermal free convection with rather general wall temperature or heat flux distribution. A new parameter, characterizing the nonisothermal conditions of the wall is introduced. The resulting transformed equations are solved by an asymptotic method which has been used successfully by Kao and Elrod [15], and Kao [16] recently in their treatment of nonsimilar boundary layer equations.

The present method yields exceptionally accurate results, and desk computations can readily be carried out. Graphs and tables are provided for the cases of Prandtl number equal to 0.7 to facilitate such computation. Four examples are given to illustrate the present technique. Since no numerical solutions seem to be available for comparison, a difference-differential numerical computation program (see Appendix) was developed to permit comparisons, and thereby demonstrate the effectiveness of the present method.

Transformation of Boundary Layer Equations

A detailed analysis of free convection under general conditions has been given recently by Kuiken [17]. Here we shall limit ourselves to the usual boundary-layer equations. Those governing free convection over a vertical flat plate with either prescribed wall temperature or heat flux are given by:

Continuity

$$\partial u/\partial x + \partial v/\partial y = 0 \tag{1}$$

Momentum

$$u\partial u/\partial x + v\partial u/\partial y = g\bar{\beta}(T - T_\infty) + \nu\partial^2 u/\partial y^2 \tag{2}$$

[1] Numbers in brackets designate References at end of paper.

Contributed by The Heat Transfer Division and presented at the Winter Annual Meeting, Houston, Texas, November 30–December 5, 1975, of THE AMERICAN SOCIETY OF MECHANICAL ENGINEERS. Revised manuscript received by the Heat Transfer Division October 22, 1976. Paper No. 75-WA/HT-15.

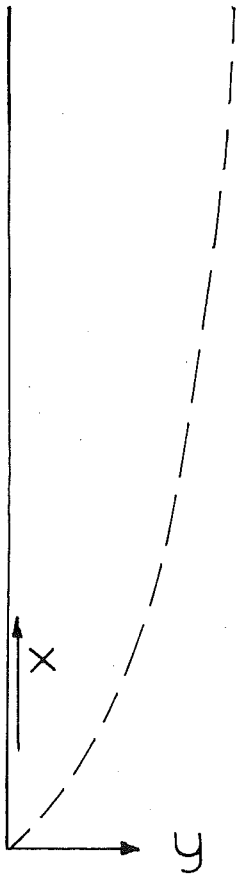

Fig. 1 Coordinate system

Energy

$$\partial T/\partial x + v\partial T/\partial y = \alpha\partial^2 T/\partial y^2 \tag{3}$$

with boundary conditions

$$u(x, 0) = v(x, 0) = 0, \quad u(x, \infty) = 0, \quad T(x, \infty) = T_\infty \tag{4}$$

$$T(x, 0) = T_w(x) \quad \text{or} \quad \partial T(x, 0)/\partial y = -q_w(x)/k \tag{5}$$

The coordinate system is shown in Fig. 1.

Mass continuity is satisfied automatically by the introduction of a stream function ψ, defined as

$$u = \partial\psi/\partial y \tag{6}$$

$$v = -\partial\psi/\partial x \tag{7}$$

In order to lessen the dependency of the solution on the stream-wise coordinate, we introduce the following coordinate transformation:

$$\xi = \int_0^x F(x)dx \tag{8}$$

$$\varkappa = C_1 F(x)^{1/2} y/\xi^{1/4} \tag{9}$$

where $F(x) = T_W - T_\infty$ for the case of prescribed variable wall temperature, and,

$$F(x) = Q^{2/3}\{5/6 \int_0^x Q^{2/3}dx\}^{1/5} \tag{10}$$

$$Q(x) = q_w(x)/C_1 k \tag{11}$$

$$C_1 = (g\bar{\beta}/4\nu^2)^{1/4} \tag{12}$$

for the case of prescribed variable wall heat flux.

One can easily verify that, for the case of power-law distributions of wall temperature or heat flux, the foregoing coordinate transformations reduce essentially to those of the similarity cases given by Sparrow and Gregg [7]. The following nondimensional stream function and nondimensional temperature are introduced.

$$f(\xi, \varkappa) = F(x)^{1/2}\psi/4C_1\nu\xi^{3/4} \tag{13}$$

$$\theta(\xi, \varkappa) = (T - T_\infty)/F(x) \tag{14}$$

The resulting transformed equations are:

$$f''' + (3 - 2\tilde{\beta})ff'' - 2f'^2 + \theta = 4\xi(f'\partial f'/\partial\xi - f''\partial f/\partial\xi) \tag{15}$$

$$\theta''/\mathrm{Pr} + (3 - 2\tilde{\beta})f\theta' - 4\tilde{\beta}f\theta = 4\xi(f'\partial\theta/\partial\xi - \theta'\partial f/\partial\xi) \tag{16}$$

where

$$\tilde{\beta} = \xi/F(x)^2 dF/dx \tag{17}$$

Here primes denote derivatives with respect to κ. The boundary conditions are given in the following:

$$f(\xi, 0) = f'(\xi, 0) = 0, \quad f'(\xi, \infty) = 0, \quad \theta(\xi, \infty) = 0 \tag{18}$$

$$\theta(\xi, 0) = 1 \quad \text{or} \quad \theta'(\xi, 0) = -1 \tag{19}$$

For the case of prescribed wall temperature, the nondimensional heat transfer parameter at the wall is:

$$\mathrm{Nu}_x/\mathrm{Gr}_x^{1/4} = -\frac{\theta'(\xi, 0)}{\sqrt{2}}\left[(T_w - T_\infty)x \Big/ \int_0^x (T_w - T_\infty)dx\right]^{1/4} \tag{20}$$

where

$$\mathrm{Nu}_x = \bar{h}x/k$$

and

$$\mathrm{Gr}_x = g\bar{\beta}(T_w - T_\infty)x^3/\nu^2$$

Nomenclature

f = nondimensional stream function
F = defined in equation (10)
g = gravitational acceleration
$\mathrm{Gr}_x = g\bar{\beta}(T_w - T_\infty)x^3/\nu$
$\bar{h}$ = heat transfer coefficient
k = thermal conductivity
$\mathrm{Nu}_x = \bar{h}x/k$
Pr = Prandtl number
T = temperature variable
u = velocity in the x-direction
v = velocity in the y-direction
x = coordinate along the plate
y = coordinate normal to the plate
α = thermal diffusivity
$\tilde{\beta}$ = wall temperature or heat flux variation parameter as defined in Eq. (17)
$\bar{\beta}$ = coefficient of volumetric expansion
$\epsilon(\tilde{\beta}) = 4\xi d\tilde{\beta}/d\xi$
ψ = stream function
ξ = transformed stream-wise coordinate
$\varkappa$ = transformed normal coordinate
$\theta = (T - T_\infty)/F$
ν = kinematic viscosity

Subscripts

W = surface condition
∞ = conditions in the ambient
0 = zero order solution
1 = first order solution

Superscript

$'$ = derivative with respect to the independent variable

Table 1

	Prescribed Wall Temperature		Prescribed Wall Heat Flux	
β	$\theta_s'(\beta, 0)$	$f_0''(\beta, 0)$	$\theta_s(\beta, 0)$	$f_0''(\beta, 0)$
1.0	-0.7344	0.6369	1.2802	0.7665
0.8	-0.6946	0.6453	1.3385	0.0830
0.6	-0.6511	0.6537	1.4096	0.8457
0.4	-0.6040	0.6621	1.4968	0.8961
0.2	-0.5534	0.6705	1.6053	0.9563
0	-0.4995	0.6789	1.7425	1.0296
-0.2	-0.4423	0.6872	1.9204	1.1211
-0.4	-0.3821	0.6954	2.1591	1.2387
-0.6	-0.3188	0.7036	2.6956	1.2970
-0.8	-0.2527	0.7117	3.0058	1.6246
-1.0	-0.1838	0.7197	3.8780	1.9889
-1.2	-0.1122	0.7276	5.7556	2.7038
-1.4	-0.0380	0.7354	13.6787	5.2311
-1.5	0	0.7393	∞	

Local Similarity Solution

Before proceeding to the present method of solution, it is useful to examine equations (15) and (16) from the standpoint of local similarity. No application of the local similarity concept appears to have been published for the present problem. This is probably due to the fact that the transformation for the stream-wise coordinate equations (8), (10), and (11) has never previously been applied. By this concept, the right-hand sides of equations (15) and (16) are presumably rendered small, and, as a first approximation, may be discarded. The resulting equations become a set of ordinary differential equations with $\tilde{\beta}$ appearing only as a parameter. The solution at each stream-wise station becomes locally autonomous, and is completely independent of the solutions at other stream-wise locations. Thus,

$$f''' + (3 - 2\tilde{\beta})ff'' - 2f'^2 + \theta = 0 \tag{21}$$

$$\theta''/\mathrm{Pr} + (3 - 2\tilde{\beta})f\theta' - 4\tilde{\beta}f'\theta = 0 \tag{22}$$

$$f(\xi, 0) = f'(\xi, 0) = 0, \quad f'(\xi, \infty) = 0, \quad \theta(\xi, \infty) = 0 \tag{23}$$

$$\theta(\xi, 0) = 1 \quad \text{or} \quad \theta'(\xi, 0) = -1 \tag{24}$$

Uncertainty concerning the neglect of the right-hand side of equations (15) and (16) is the weakness of this local similarity concept.

Equations (21)–(24) have been solved by us on an IBM 360/91 computer. A standard shooting technique as described by Nachtsheim and Swigert [18] is used. The results are tabulated in Table 1 and Fig. 2, for a Prandtl number of 0.7.

Present Method

In the present analysis, we first change from the (ξ, x) coordinates to the $(\tilde{\beta}, x)$ coordinates.
Thus,

$$f''' + (3 - 2\tilde{\beta})ff'' - 2f'^2 + \theta = \epsilon(\tilde{\beta})(f'\partial f'/\partial\tilde{\beta} - f''\partial f/\partial\tilde{\beta}) \tag{25}$$

$$\theta''/\mathrm{Pr} + (3 - 2\tilde{\beta})f\theta' - 4\tilde{\beta}f'\theta = \epsilon(\tilde{\beta})(f'\partial\theta/\partial\tilde{\beta} - \theta'\partial f/\partial\tilde{\beta}) \tag{26}$$

where

$$\epsilon(\tilde{\beta}) = 4\xi d\tilde{\beta}/d\xi \tag{27}$$

Note that if $\epsilon(\tilde{\beta})$ is zero, the foregoing equations admit similarity solutions automatically. Thus it would appear to be possible to generate expansions for f and θ with $\epsilon(\tilde{\beta})$ treated as a small parameter.

Next, we seek to expand $\tilde{\beta}$, f, and θ into power series of $\epsilon(\tilde{\beta})$.
Thus,

$$\tilde{\beta} = \beta + \epsilon(\tilde{\beta})\Delta_0(\beta) + \epsilon^2\Delta_1 + \ldots \tag{28}$$

$$f = f_0(\beta, x) + \epsilon(\tilde{\beta})f_1(\beta, x) + \epsilon^2 f_2 + \ldots \tag{29}$$

$$\theta = \theta_0(\beta, x) + \epsilon(\tilde{\beta})\theta_1(\beta, x) + \epsilon^2\theta_2 + \ldots \tag{30}$$

where β is a shifted value of $\tilde{\beta}$. Upon substituting the foregoing expressions into equations (25) and (26), and equating like terms of power of $\epsilon(\tilde{\beta})$, the first two sets of equations are:
Order unity

$$f_0''' + (3 - 2\beta)f_0f_0'' - 2f_0'^2 + \theta_0 = 0 \tag{31}$$

$$\theta_0''/\mathrm{Pr} + (3 - 2\beta)f_0\theta_0' - 4\beta f_0'\theta_0 = 0 \tag{32}$$

$$f_0(\beta, 0) = f_0'(\beta, 0) = 0, \quad f_0'(\beta, \infty) = 0, \quad \theta_0(\beta, \infty) = 0 \tag{33}$$

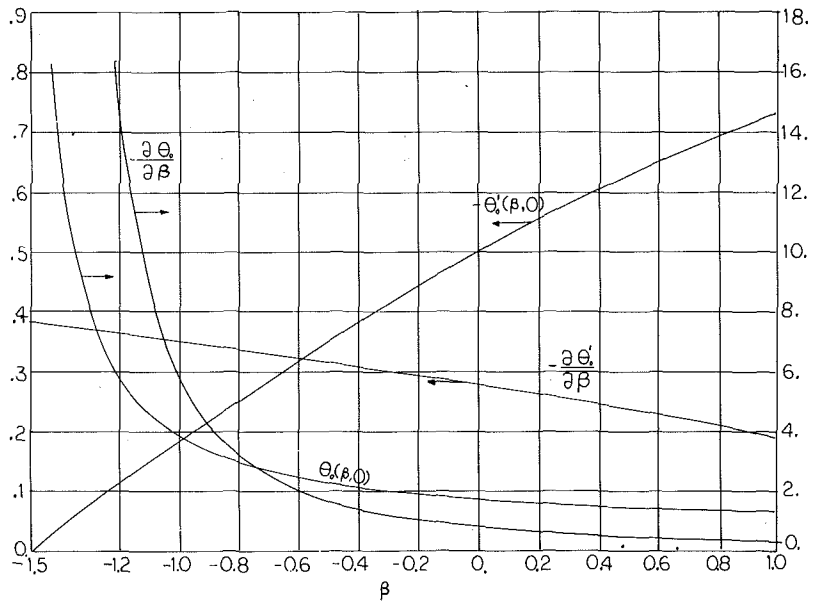

Fig. 2 Zero order solutions

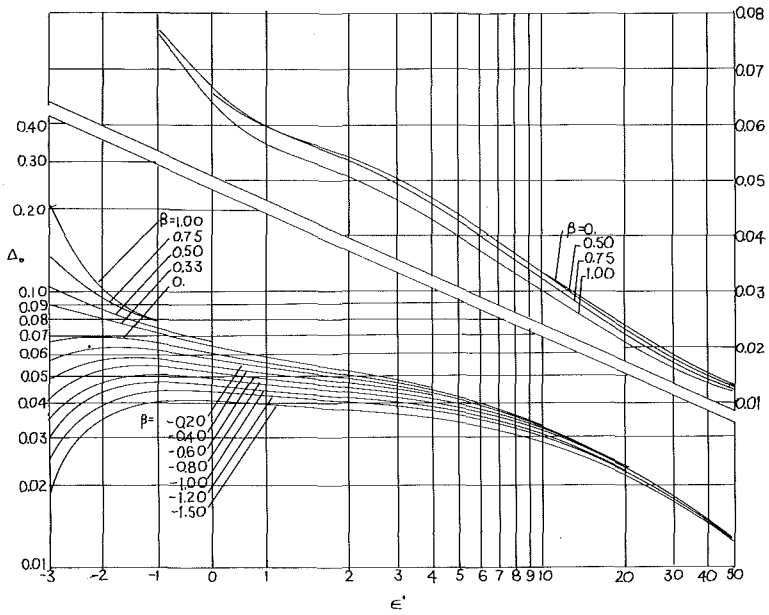

Fig. 3 Δ_0 for prescribed wall temperature case

In addition, if the wall temperature is specified

$$\theta_0(\beta', 0) = 1 \tag{34a}$$

and if the heat flux is specified

$$\theta_0'(\beta, 0) = -1 \tag{34b}$$

Order ϵ:

$$f_1''' + (3 - 2\beta)f_0 f_1'' - (4 + \epsilon')f_0' f_1' + (3 - 2\beta + \epsilon')f_0'' f_1 + \theta_1 = (1 - \epsilon'\Delta_0)(f_0'\partial f_0'/\partial\beta - f_0''\partial f_0/\partial\beta) + 2\Delta_0 f_0 f_0'' \tag{35}$$

$$\theta_1''/\mathrm{Pr} + (3 - 2\beta)f_0\theta_1' - (4\beta + \epsilon')f_0'\theta_1 = (1 - \epsilon'\Delta_0)(f_0'\partial\theta_0/\partial\beta - \theta_0'\partial f_0/\partial\beta) - (3 - 2\beta + \epsilon')\theta_0' f_1 + 4\beta f_0'\theta_0 + 2\Delta_0(2f_0'\theta_0 + f_0\theta_0') \tag{36}$$

The function Δ_0 (and thus β) is found by requiring that the zeroth order solution θ_0 approximate as closely as possible either the wall heat flux (when wall temperature is specified) or the wall temperature (when wall heat flux is specified). In the case of specified wall temperature, $\theta_1(\beta, \epsilon', 0) = 0$ is needed to satisfy the boundary condition, and $\theta_1'(\beta, \epsilon', 0)$ is set to zero in order that the zeroth order solution should by itself yield wall heat flux with accuracy to the order ϵ. In the case of specified wall heat flux, $\theta_1'(\beta, \epsilon', 0) = 0$ satisfies the boundary condition, and $\theta_1(\beta, \epsilon, 0)$ is set to zero in order that θ_0 at the wall will provide a good approximation to the wall temperature with accuracy of order ϵ. In each case, the overconstrain in boundary conditions leads to determination of Δ_0, the shifting function in the assigned value of β renders a most accurate local similarity solution. Thus, the following boundary conditions are specified for equations (35) and (36):

$$f_1(\beta, 0) = f_1'(\beta, 0) = \theta_1(\beta, 0) = \theta_1'(\beta, 0) = 0 \tag{37}$$

$$f_1'(\beta, \infty) = \theta_1(\beta, \infty) = 0 \tag{38}$$

Note that Δ_0 depends on two parameters (i.e., β, ϵ') where ϵ' is given at the stream-wise station of interest. Once Δ_0 is found, the value of β can be found from equation (28), which is an implicit algebraic equation and can readily be solved either by iteration or by a graphical method. As with the local similarity model, the present method can be carried out without having to determine solutions for upstream stations. All necessary upstream wall information is built into the parameters $\tilde{\beta}$ and ϵ'.

Equations (35) and (36) involve derivatives of f_0 and θ_0 with respect to β. The primary difficulty lies in computing these nonhomogeneous terms. If a finite-difference method is used, a number of similarity solutions in the neighborhood of β must be known to a high precision. This difficulty can be resolved by introducing two auxiliary equations for $\bar{g} = \partial f_0/\partial\beta$ and $\bar{h} = \partial\theta_0/\partial\beta$. By differentiating equations (31)–(34), we get:

$$\bar{g}''' + (3 - 2\beta)f_0\bar{g}'' - 4f_0'\bar{g}' + (3 - 2\beta)f_0''\bar{g} + \bar{h} = 2f_0 f_0'' \tag{39}$$

$$\bar{h}''/\mathrm{Pr} + (3 - 2\beta)f_0\bar{h}' - 4\beta f_0'\bar{h} = 4f_0'\theta_0 + 4\beta\theta\bar{g}' + 2f_0\theta_0' - (3 - 2\beta)\theta_0'\bar{g} \tag{40}$$

with boundary conditions given by

$$\bar{g}(\beta, 0) = \bar{g}'(\beta, 0) = \bar{g}'(\beta, \infty) = \bar{h}(\beta, \infty) = 0 \tag{41}$$

$$\bar{h}(\beta, 0) = 0 \qquad \text{for prescribed wall temperature}$$

or

$$\bar{h}'(\beta, 0) = 0 \qquad \text{for prescribed wall flux} \tag{42}$$

Thus equations (31)–(42) were solved as a system of ordinary differential equations. A standard shooting technique was used. Results for Δ_0 when Pr = 0.7 are presented in Figs. 3 and 4. Results for $\bar{h}'(\beta, 0)$ in the prescribed wall temperature case, and for $\bar{h}(\beta, 0)$ in the prescribed wall flux case are given in Fig. 2.

In the next section, four examples will be considered.

Sinusoidal Wall Temperature Variations

In this example, we shall illustrate the typical procedure for determining the wall heat flux by the present method. With the wall temperature given at selected locations along the wall, ξ can be evaluated by the trapezoidal rule starting from the leading edge, using equation (8). Next, a central differencing scheme can be used to evaluate all the derivatives. $\tilde{\beta}$ and ϵ are next determined from equations (17) and (27) respectively, and then ϵ'. Once this information at a particular location is known, we can proceed to calculate the heat flux using the technique presented in the previous section. In the present example, we select the location $x = 1.8$, thus

(*a*) $x = 1.8$, $\tilde{\beta} = -0.2912$, $\epsilon = -7.7723$, $\epsilon' = 19.1415$;
(*b*) now guess $\beta = -0.2$;
(*c*) from Fig. 3 $\Delta_0 = 0.0242$;
(*d*) equation (28) gives an improved $\beta = -0.103$;

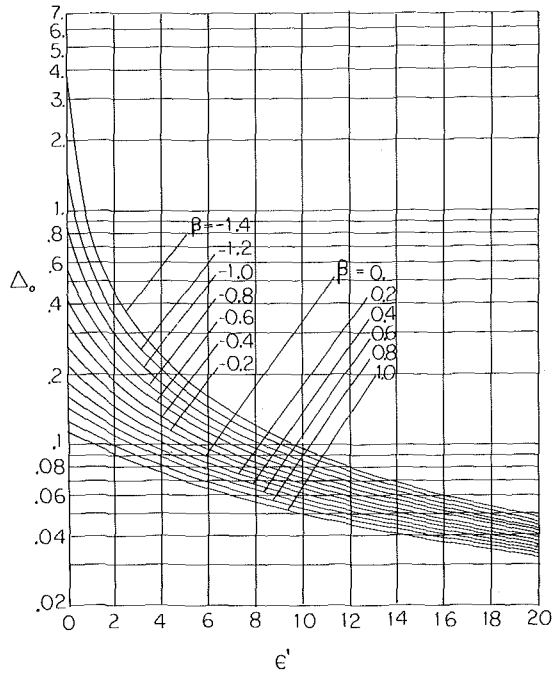

Fig. 4 Δ_0 for prescribed wall heat flux case

(*e*) from Fig. 3, we find that Δ_0 is essentially the same as before. Then from Fig. 2, $\theta_0'(\beta, 0) = -0.475$.

The foregoing result, as well as others, is set forth in Table 2 and in Fig. 5.

Comparison in Fig. 5 of our nondimensional heat-flux with that from the difference-differential solution development in the Appendix, shows excellent agreement. Also shown are results from the local-similarity model. As can been seen, the local-similarity method gives considerable error at points far away from the leading edge.

Exponential Wall Temperature Variation

For this case, the wall temperature variation is given by:

$$T_w - T_\infty = Ae^{mx}$$

where x is the position along the vertical plate. As pointed out by Gebhart and Mollendorf [10], the similarity solution obtained for this case by Sparrow and Gregg [7], is, in fact, an asymptotic solution for $x \to \infty$, or for a vertical plate starting from $x = -\infty$. The present

Table 2 Free connection with sinusoidal wall temperature variations

x	$T_w - T_\infty$	ξ	$\tilde{\beta}$	ε	ε'	β	θ'(x,0)
0	0	0	0.5	0		0.5	-0.63
0.2	0.1987	0.01987	0.4899	-0.02556	3.3692	0.4911	-0.627
0.4	0.3894	0.07868	0.4747	-0.08524	4.4651	0.4782	-0.625
0.6	0.5646	0.1742	0.4481	-0.2122	5.0567	0.4543	-0.62
0.8	0.7174	0.3023	0.4066	-0.4296	5.7136	0.4242	-0.612
1.0	0.8415	0.4582	0.3472	-0.7887	6.7636	0.3779	-0.60
1.2	0.9320	0.6355	0.2632	-1.3995	8.3440	0.3129	-0.585
1.4	0.9854	0.8273	0.1440	-2.4842	10.6229	0.2259	-0.564
1.6	0.9996	1.0258	-0.02977	-4.5117	12.1510	0.1078	-0.53
1.8	0.9738	1.2231	-0.2912	-7.7723	19.1415	-0.103	-0.475
2.0	0.9093	1.4115	-0.7055	-17.6310	29.5809	-0.379	-0.39
2.2	0.8085	1.5832	-1.4157	-41.036	47.836	-0.874	-0.23
2.3	0.7457	1.6609	-1.9863	-61.0638	55.5842	-1.0703	-0.16
2.4	0.6755	1.7316	-2.7798	-116.8529			
2.6	0.5155	1.8507	-5.9286				
2.8	0.3380	1.9307					

analysis shows that for a semi-infinite vertical plate, the solution is nonsimilar. Also, notice that the present analysis is valid if $m = 0$, and reduces to the case of constant wall temperature automatically, whereas the transformation given by Sparrow and Gregg gives no results for the constant wall temperature case.

According to the transformation of equations (8), (17), and (27),

$$\xi = A(e^{mx} - 1)/m$$

$$\tilde{\beta} = 1 - e^{-mx}$$

$$\epsilon(\tilde{\beta}) = 4e^{-mx}(1 - e^{-mx})$$

and

$$d\epsilon(\tilde{\beta})/d\tilde{\beta} = 4(2e^{-mx} - 1)$$

The nondimensional heat transfer parameter is given by:

$$\mathrm{Nu}_x/\mathrm{Gr}_x{}^{1/4} = -\theta'(\beta, 0)\{mxe^{mx}/(e^{mx} - 1)\}^{1/4}/\sqrt{2}$$

Comparisons in Fig. 6, for the case $m = 1$ and Prandtl number = 0.7, show excellent agreement between the present results and those of the accurate difference-differential method. Also shown are results from the local similarity model and from Sparrow and Gregg's [7] similarity solution.

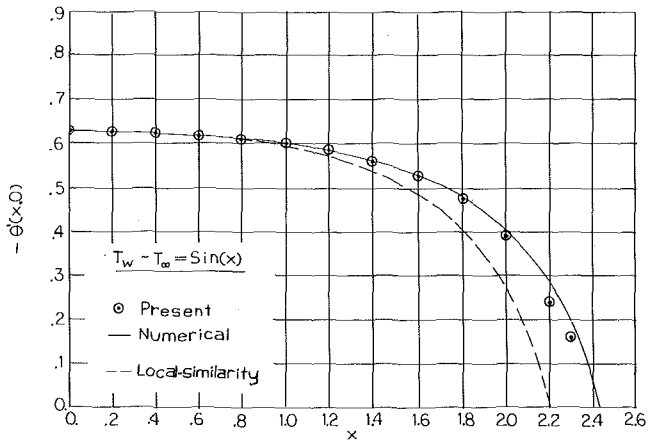

Fig. 5 Comparison of non-dimensional temperature gradient for sinusoidal wall temperature variation

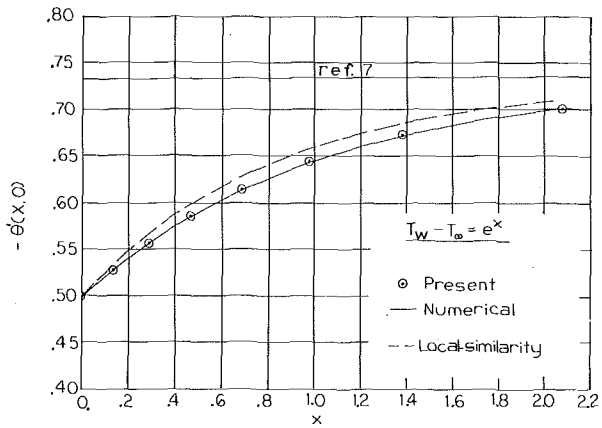

Fig. 6 Comparison of nondimensional temperature gradient for exponential variation in wall temperature

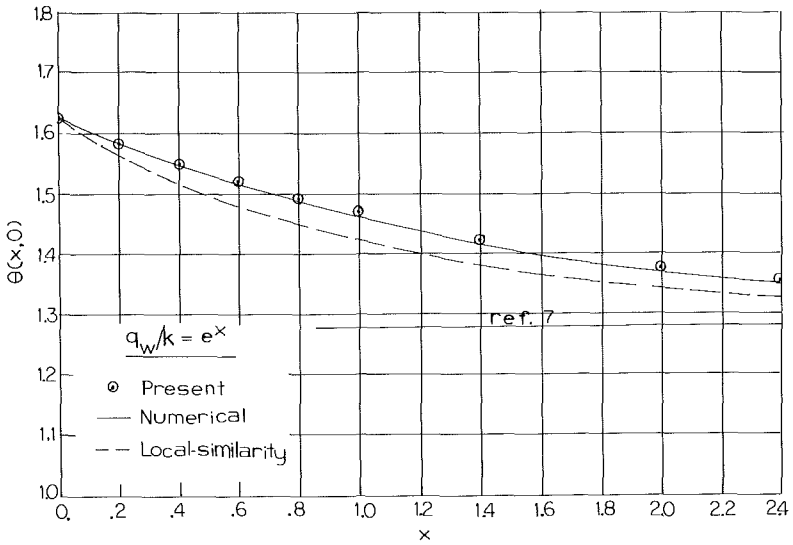

Fig. 7 Comparison of nondimensional wall temperatures with exponential variation in wall heat flux

Exponentially Increasing Wall Heat Flux

As a first example for prescribed wall heat flux case, let us consider the case of exponentially increasing wall heat flux, i.e.,

$$q_w(x)/k = e^x$$

where x is the distance from the leading edge. Without loss of generality, we take $C_1 = (g\bar{\beta}/4\nu^2)^{1/4} = 1$.

Fig. 7 gives the results for the nondimensional wall temperature for Pr = 0.7 at several stations, as obtained by the present method, and by the difference differential method, and by local-similarity. Agreement between the present solution and the numerical solution is excellent. Also shown is the asymptotic similarity solution of Sparrow and Gregg [7].

Linearly Increasing or Decreasing Wall Heat Flux

The wall heat flux is given by:

$$q_w(x)/k = (1 \pm x)$$

where x is the distance measured from the leading edge. Here again, we have taken $C_1 = 1$. Comparisons for the linearly increasing flux case in Fig. 8 show that the local similarity does quite well. But the present solution is even better. For the linear decreasing flux case, comparisons in Fig. 9 show that the present solution does well up to about $x = 0.5$, whereas local similarity deviates considerably for $x > 0.3$. Both lose accuracy as $x \to 1$. But it should be noted that normalization factor used for θ (see equation (10)) exaggerates discrepancies when the heat flux is small.

Conclusion

A method of determining the temperature, heat flux relations in laminar free convection along a nonisothermal vertical plate has been described. The basic feature of this new technique involves finding

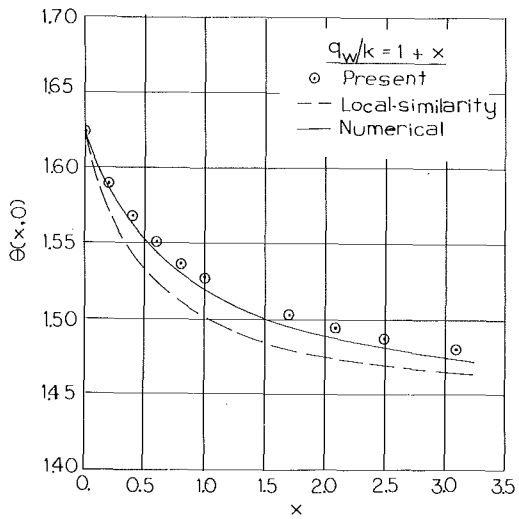

Fig. 8 Comparison of nondimensional wall temperature with linearly increasing wall heat flux

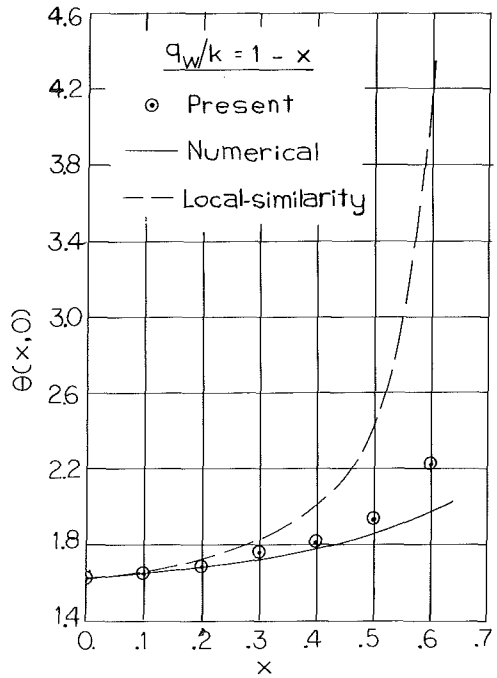

Fig. 9 Comparison of nondimensional wall temperature with linearly decreasing wall heat flux

a shifted value of $\tilde{\beta}$, the temperature similarity parameter, such that the corresponding similarity solution provides accurate predictions of heat flux or surface temperature. Four examples have been given to demonstrate the effectiveness of the present technique.

Owing to the expository nature of this paper, the applications presented herein have dealt only with the free convection in the fluid adjacent to a heat transfer surface. But the results obtained here can also be used to study more complex situations, such as coupled free convection conduction problems. In such cases the universal functions obtained for the prescribed wall temperature case can be used in conjunction with a numerical iterative process to match both the temperature and heat flux at the wall interface. Computational experiments dealing with such problems remain to be carried out.

References

1 Hellums, J. D., and Churchill, S. W., "Computation of Natural Convection by Finite Difference Method," *International Development in Heat Transfer, Proceedings 1961–1962 International Heat Transfer Conference*, ASME, 1963, pp. 985–993.

2 Hayday, A. A., Bowlus, D. A., and McGraw, R. A., "Free Convection From a Vertical Flat Plate With Step Discontinuities in Surface Temperature," JOURNAL OF HEAT TRANSFER, TRANS. ASME, Series C, Vol. 89, No. 2 Apr. 1967, pp. 244–250.

3 Sparrow, E. M., "Laminar Free Convection on a Vertical Plate With Prescribed Non-Uniform Heat Flux or Prescribed Non-Uniform Wall Temperature," NACA TN-3508, 1955.

4 Smith, J. R., "A Computer Program for Laminar Free Convection on a Vertical Plate With Prescribed Non-Uniform Wall Heat Flux or Prescribed Non-Uniform Wall Temperature," Unpublished MS thesis, Ohio State University, Columbus, Ohio, 1968.

5 Sutton, S. B., "A Study of Free Convection From a Vertical Plate With Sinusoidal Temperature Distribution," AIAA Paper No. 71–988.

6 Seigel, R., "An Analysis of Laminar and Turbulent Free Convection From a Smooth Vertical Plate With Uniform Heat Dissipation per Unit Surface Area," G. E. Report R54GL89, 1954.

7 Sparrow, E. M., and Gregg, J. L., "Similar Solutions for Free Convection From a Non-Isothermal Vertical Plate," Trans. ASME, Vol. 80, 1958, pp. 379–387.

8 Finston, M., "Free Convection Past a Vertical Plate," *Z. Angew. Math. Phys.*, Vol. 7, 1956, pp. 527–529.

9 Yang, K. T., "Possible Similarity Solutions for Laminar Free Convection on Vertical Plates and Cylinders," *Journal of Applied Mechanics*, TRANS. ASME, Series E, Vol. 82, No. 2, 1960, pp. 230–236.

10 Gebhart, B., and Mollendorf, J., "Viscous Dissipation in External Natural Convection Flows," *Journal of Fluid Mechanics*, Vol. 38, 1969, pp. 97–107.

11 Foote, J. R., "An Asymptotic Method for Free Convection Past a Vertical Plate," *Z. Angew. Math. Phys.* Vol. 9, 1958, pp. 64–67.

12 Niuman, F., and Pohlhausen, K., "Remarks on the Paper by M. Finston: Free Convection Past a Vertical Plate," *Z. Angew. Math. Phys.*, Vol. 9, 1958, pp. 67–69.

13 Kelleher, M., and Yang, K. T., "A Gortler-Type Series for Laminar Free Convection Along a Non-Isothermal Vertical Plate," *Quart. J. of Mech. and Appl. Math.*, Vol. 25, Part 4, 1972, pp. 445–457.

14 Kuiken, H. K., "Free Convection Past a Vertical Plate," *Applied Sci. Research*, Vol. 20, 1969, pp. 205–215.

15 Kao, T., and Elrod, H. G., "Laminar Shear Stress Pattern in Non-Similar Boundary Layers," *AIAA Journal*, Vol. 12, No. 10, Oct. 1974.

16 Kao, T., "An Asymptotic Method for the Computation of Laminar Shear Stress and Heat Flux in Forced and Free Convection," Ph.D. dissertation, Department of Mechanical Engineering, Columbia University, N. Y., N. Y., Apr. 1974.

17 Kuiken, H. K., "Boundary Layer Conditions in Free Convection," *Journal of Engineering Math.*, Vol. 2, No. 1, 1968, pp 95–105.

18 Nachtscheim, P. R., and Swigert, P., "Satisfaction of Asymptotic Boundary Conditions in Numerical Solution of Systems of Non-Linear Equations of Boundary Layer Type," NASA TN-D3004, 1965.

19 Smith, A. M. O., and Clutter, D. W., "Solution of Incompressible Laminar Boundary Layer Equations," *AIAA Journal*, Vol. 1, No. 9, Sept. 1963, pp. 2062–2071.

20 Smith, A. M. O., and Clutter, D. W., "Machine Calculation of Compressible Laminar Boundary Layers," *AIAA Journal*, Vol. 3, No. 4, Apr. 1965, pp. 639–647.

Appendix

Since accurate numerical solutions for laminar free convection along a nonisothermal flat plate do not seem to be available in the literature for comparison, a difference-differential solution suggested by Smith and Clutter [19, 20] in their treatment of forced convection problems is developed in this Appendix.

Both equations (15) and (16) contain first derivatives with respect to ξ. These can be approximated by the classical Lagrangian method in terms of values of the functions at two or more points, which need not be equally spaced. A three-point approximation formula for derivative with respect to ξ is used in this report, except for the second point along the stream-wise direction where a two-point formula is used. Thus, at station n, equations (15) and (16) become:

$$f_n''' + (3 - 2\tilde{\beta})f_n f_n'' - 2f_n'^2 + \theta_n = 4\xi_n\{f_n'(\alpha_n f_n' - \beta_n f_{n-1}' + \gamma_n f_{n-2}') - f_n''(\alpha_n f_n - \beta_n f_{n-1} + \gamma_n f_{n-2})\} \quad \text{(A1)}$$

$$1/\mathrm{Pr}\,\theta_n'' + (3 - 2\tilde{\beta}_n)f_n\theta_n' - 4\tilde{\beta}_n f_n'\theta_n = 4\xi_n\{f_n'(\alpha_n\theta_n - \beta_n\theta_{n-1} + \gamma_n\theta_{n-2}) - \theta_n'(\alpha_n f_n - \beta_n f_{n-1} + \gamma_n f_{n-2})\} \quad \text{(A2)}$$

where

$$\alpha_n = (2\xi_n - \xi_{n-1} - \xi_{n-2})/[(\xi_n - \xi_{n-1})(\xi_n - \xi_{n-2})]$$

$$\beta_n = (\xi_n - \xi_{n-2})/[(\xi_n - \xi_{n-1})(\xi_{n-1} - \xi_{n-2})]$$

$$\gamma_n = (\xi_n - \xi_{n-1})/[(\xi_n - \xi_{n-2})(\xi_{n-1} - \xi_{n-2})]$$

with boundary conditions at each station given by:

$$f_n(\xi_n, 0) = f_n'(\xi_n, 0) = 0, \quad \theta_n(\xi_n, 0) = 1 \quad \text{or} \quad \theta_n'(\xi_n, 0) = -1$$

$$f_n'(\xi_n, \infty) = 0, \quad \theta_n(\xi_n, \infty) = 0$$

With solutions at stations $n - 1$ and $n - 2$ considered known, the problem is to find the solution at station n. At each station n, a standard shooting technique as described by Nachtsheim and Swigert [18] can be used to find $f_n''(\xi_n, 0)$ and $\theta_n'(\xi_n, 0)$. The solution proceeds downstream, station by station. Since the method is of implicit type, the solution is always stable.

O. A. Plumb[1]
L. A. Kennedy
Mem. ASME

Mechanical Engineering Department,
State University of New York at Buffalo,
Buffalo, N. Y.

Application of a K-ϵ Turbulence Model to Natural Convection From a Vertical Isothermal Surface

A K-ϵ turbulence model similar to that proposed by Jones and Launder is applied to the calculation of the turbulent natural convective boundary layer on a vertical, isothermal surface. Conservation equations for the turbulent kinetic energy, dissipation rate of turbulent kinetic energy, and mean square temperature fluctuations are solved numerically along with the turbulent momentum and energy equations using the Spalding-Patankar boundary layer method. Various model constants and wall functions, and wall terms were tested. The results are compared with available experimental data and found to be in reasonable agreement.

Introduction

Turbulent natural convection from vertical heated surfaces is important in many technological applications, including among others, heat dissipation from large radiators, heat losses to cryogenic tankage, and fire propagation. Despite the large number of applications, until recently this type of flow has received relatively little attention either experimentally or theoretically. Although analytical tools for predicting transition and the subsequent flow have improved significantly in recent years, transition and turbulent modeling, particularly for buoyancy driven flows remains a poorly understood area of fluid mechanics.

Several investigators have calculated such flows using integral methods including Eckert and Jackson [1],[2] Bayley [2], and more recently, Kato, et al. [3]. Although the results of these calculations agree well with available experimental data with respect to the heat transfer, the assumed velocity and temperature profiles have been shown to be in error particularly the 1/7 power law profiles of Eckert and Jackson. (The solution of Kato does not assume profiles of velocity and temperature but assumes an eddy diffusivity distribution from which mean profiles of velocity and temperature are deducted.) More recently several investigators: Cebeci and Khattab [4], Mason and Seban [5], and Noto and Matsumoto [6] have obtained numerical results by assuming an eddy diffusivity distribution analogous to that used in forced convection. Again the results of these studies agree quite well with available experimental data. Mason and Seban carry the calculation one step further by solving the equation for the kinetic energy of the turbulence and calculating the turbulent viscosity from the dimensionally correct combination of the kinetic energy and an algebraically determined mixing length. However, they did not include the effects of buoyancy on the turbulent kinetic energy. This flow has also been calculated by Nee and Yang [7] using the phenomenological turbulent theory of Nee and Kovasznay [8].[3]

Experimental work in this area has been presented by Cheesewright [9], Warner and Arpaci [10], Lock and Trotter [11], Fujii [12], Vliet and Liu [13], Smith [14], as well as several others. The foregoing investigators have presented a great deal of data on the heat transfer and mean velocity and temperature profiles, however relatively little data are available with regard to the turbulence structure of the flow or the mean velocity in the near wall viscous sublayer region which controls the heat transfer. The most extensive experimental study of the turbulent structure of such a flow is that presented by Smith [14]. Some comments on the turbulent intensity are made by Vliet and Liu, Cheesewright, and Lock and Trotter whereas Papailiou and Lykoudis [15] present experimental data on the intensity of temperature fluctuations in liquid mercury. Kutateladze, et al. [16] presents some turbulent data for a similar flow in ethyl alcohol.

The present study was undertaken to develop a turbulence model which can be used to calculate buoyancy driven wall boundary layers without an a priori assumption with regard to profiles of velocity, temperature and the eddy diffusivity. This resulted in a calculation

[1] Present address: Department of Mechanical Engineering, Washington State University, Pullman, Wash.

[2] Numbers in brackets designate References at end of paper.

Contributed by The Heat Transfer Division of THE AMERICAN SOCIETY OF MECHANICAL ENGINEERS, and presented at the National Heat Transfer Conference, St. Louis, Mo., August 9–11, 1976. Revised manuscript received by the Heat Transfer Division September 22, 1976. Paper No. 76-HT-17.

[3] We are indebted to a reviewer for pointing out this reference.

technique which removes some of the integral method assumptions and is more generally applicable to flows of this nature involving more complex geometries as well as reacting flows and recirculating flows where the methods discussed previously may not be suitable.

The method employed in this study uses the Reynolds averaged equations of motion subject to a set of closure hypotheses suitable for accurate computation. Recent progress by Donaldson and Jones and Launder [17] with phenomenological turbulence models in forced flows indicates that this is a sensible approach.

Due to its demonstrated success in calculating a wide variety of forced flows, the K-ϵ model of Jones and Launder was selected as a starting point for application to buoyancy driven flows. Since the initiation of this study, work has been published by Taminini [18] and Rodi and Chen [19] demonstrating the ability of modified K-ϵ models in calculating buoyant plumes.

The Turbulence Model

Numerous authors have proposed closure models for turbulent flows in an attempt to accurately predict the turbulent shear stresses. Prandtl [20] and Kolmogorov [21] proposed that the turbulent viscosity should be proportional to the square root of the turbulent kinetic energy and a length scale representative of the energy containing eddies. A transport equation for the turbulent kinetic energy can be derived from the Navier-Stokes equations through Reynolds decomposition. Various authors have developed transport equations for different variables in order to determine the length scale. In the K-ϵ models characterized by that of Jones and Launder [17] the length scale is taken to be the dissipation length scale ($\epsilon = K^{3/2}/L$). Thus, the turbulent viscosity can be written

$$\mu_T = C_\mu \rho K^2/\epsilon \tag{1}$$

where C_μ is a constant of proportionality.[4] The assumptions of high Reynolds number where the flow tends toward isotropy is essential to the development of equation (1).

In order to account for the contribution of buoyancy to the turbulent kinetic energy and dissipation rate, a third transport equation for the mean square temperature fluctuations must be included in the model. Thus, at high Reynolds numbers where the dissipation process is essentially isotropic and the effects of molecular viscosity are negligible, the transport equations for the three turbulence parameters of interest can be written in the boundary layer approximation as follows:

$$\rho \frac{U\partial K}{\partial x} + \rho \frac{V\partial K}{\partial y} = \frac{\partial}{\partial y}\left[\frac{\mu_T}{\sigma_K}\frac{\partial K}{\partial y}\right] + \mu_T\left(\frac{\partial U}{\partial y}\right)^2 - \rho\epsilon + \rho g\beta\overline{ut} \tag{2}$$

$$\rho \frac{U\partial \epsilon}{\partial x} + \rho \frac{V\partial \epsilon}{\partial y} = \frac{\partial}{\partial y}\left[\frac{\mu_T}{\sigma_\epsilon}\frac{\partial \epsilon}{\partial y}\right] + C_1\frac{\epsilon}{K}\mu_T\left(\frac{\partial U}{\partial y}\right)^2 - C_2\frac{\rho\epsilon^2}{K} + C_3\rho g\beta\frac{\epsilon}{K}(\overline{ut}) \tag{3}$$

$$\rho \frac{U\partial q}{\partial x} + \rho \frac{V\partial q}{\partial y} = \frac{\partial}{\partial y}\left[\frac{\mu_T}{\sigma_q}\frac{\partial q}{\partial y}\right] + C_{q1}\mu_T\left(\frac{\partial T}{\partial y}\right)^2 - C_{q2}\rho\frac{\epsilon}{K}q \tag{4}$$

An appropriate model for the correlation between temperature fluctuations and vertical velocity fluctuations must be determined in order to close the system of equations. Following the arguments presented by Launder and Spalding [23] it is proposed that

$$\overline{ut} = C_4(qK)^{1/2} \tag{5}$$

Equations (2)–(5) along with the equations of continuity, momentum in the Boussinesq approximation, and energy form a closed system of equations, describing a turbulent buoyancy driven flow at high turbulent Reynolds number. The σ's represent turbulent Prandtl numbers for the parameters in question and the C's are model "constants" preceding terms which are inexact in that their derivation relies heavily on dimensional arguments. This model for the contribution of buoyancy to the turbulent kinetic energy has also been proposed by Taminini in calculating a turbulent diffusion flame.

The model constants used in the calculations are given in Table 1. Numerical values for C_μ, C_1, C_2, σ_K, and σ_ϵ are those recommended by Jones and Launder [17]. By assuming similar contributions from buoyancy and gradient production terms, C_3 can be shown to equal C_1. The value for C_4 was chosen based upon the experimental data of Smith. The constants C_{q1}, C_{q2}, and σ_q are those used by Taminini in turbulent diffusion studies.

In order to predict accurately the behavior of the flow near the wall, particularly in the viscous sublayer where the turbulent Reynolds number is small, the effects of molecular viscosity and nonisotropic dissipation must be taken into account. The former can be easily added by its inclusion in the diffusive terms in all of the transport equations. The wall functions and wall terms which are added to account for the nonisotropic behavior near the walls are those of Jones and Launder [17] with one exception. They suggest adding an additional wall term to the equation for the dissipation rate (circled term in equation (7)) to give better agreement with the experimental results for the turbulent kinetic energy. However, in the present calculations, this term was dropped because it cannot be justified from a physical standpoint in buoyant flows. The resulting equations depict the complete turbulence model.

[4] Rodi [22] discusses conditions under which C_μ can be considered constant.

Nomenclature

C_p = specific heat
$C_1, C_2, C_3, C_4, C_{q1}, C_{q2}, C_\mu$ = empirical model constants
F_1, F_2, F_3, F_μ = empirical wall functions
Gr = local Grashof number
g = acceleration of gravity
K = kinetic energy of turbulence (T.K.E.)
k = thermal conductivity
Nu_x = local Nusselt number
Re_T = turbulent Reynolds number
q = mean squared temperature fluctuations
T = mean temperature
t = fluctuating temperature
U = mean velocity in vertical direction
u = fluctuating velocity in vertical direction
u_b = buoyant velocity $[(g\beta x\Delta t)^{1/2}]$
u^* = friction velocity $(\sqrt{\tau_w/\rho})$
$u^+ = U/u^*$
V = mean horizontal velocity
V_E = entrainment velocity
v = fluctuating horizontal velocity
x = vertical coordinate
y = horizontal coordinate
y^+ = dimensionless horizontal coordinate $\left(\frac{yu^*}{\nu}\right)$
α = thermal diffusivity
β = coefficient of thermal expansion
δ = boundary layer thickness
ϵ = dissipation rate of T.K.E.
η = laminar similarity variable $\left(\frac{y}{x}\sqrt[4]{Gr}\right)$
μ = molecular viscosity
μ_T = turbulent viscosity
ν = kinematic viscosity
ρ = density
σ = Prandtl number
$\sigma_K, \sigma_\epsilon, \sigma_T, \sigma_q$ = turbulent Prandtl number
ψ = stream function
ψ_E = stream function at the outer edge of boundary layer
ω = dimensionless stream function (ψ/ψ_E)

Table 1 Model constants for high Reynolds number turbulence model

C_μ	C_1	C_2	C_3	C_4	C_{q1}	C_{q2}	σ_k	σ_ϵ	σ_q
0.09	1.44	1.92	1.44	0.5	2.8	1.7	1.0	1.3	.9

$$\rho\frac{U\partial K}{\partial x}+\rho\frac{V\partial K}{\partial y}=\frac{\partial}{\partial y}\left[\left(\mu+\frac{\mu_T}{\sigma_K}\right)\frac{\partial K}{\partial y}\right]+\mu_T\left(\frac{\partial U}{\partial y}\right)^2-\rho\epsilon+\rho g\beta C_4(qK)^{1/2}-2\mu\left(\frac{\partial K^{1/2}}{\partial y}\right)^2 \quad (6)$$

$$\rho\frac{U\partial\epsilon}{\partial x}+\rho\frac{V\partial\epsilon}{\partial y}=\frac{\partial}{\partial y}\left[\left(\mu+\frac{\mu_T}{\sigma_\epsilon}\right)\frac{\partial\epsilon}{\partial y}\right]+C_1F_1\frac{\epsilon}{K}\mu_T\left(\frac{\partial U}{\partial y}\right)^2-C_2F_2\rho\frac{\epsilon^2}{K}+C_3F_3C_4\rho g\beta\epsilon\left(\frac{q}{K}\right)^{1/2}+2\nu\mu_T\left(\frac{\partial^2U}{\partial y^2}\right)^2 \quad (7)$$

$$\rho\frac{U\partial q}{\partial x}+\rho\frac{V\partial q}{\partial y}=\frac{\partial}{\partial y}\left[\left(\frac{\mu}{\sigma}+\frac{\mu_T}{\sigma_q}\right)\frac{\partial q}{\partial y}\right]+C_{q1}\mu_T\left(\frac{\partial T}{\partial y}\right)^2-C_{q2}\rho\frac{\epsilon}{K}q-2k\left(\frac{\partial q^{1/2}}{\partial y}\right)^2 \quad (8)$$

$$\mu_T=C_\mu F_\mu\frac{\rho K^2}{\epsilon} \quad (9)$$

The wall functions F_1, F_2, and F_μ which are functions of the turbulent Reynolds number were chosen by Jones and Launder by applying the model to well-documented turbulent forced flow. The assigned forms of Jones and Launder are used in the present calculation for these three functions, i.e.,

$$F_1=1.0$$
$$F_2=1.0-0.3\exp(-\mathrm{Re}_T^2)$$
$$F_\mu=\exp[-2.5/(1+\mathrm{Re}_T/50)]$$
$$F_3=1.0 \quad (10)$$

where the turbulence Reynolds number is defined as, $\mathrm{Re}_T=\rho K^2/\mu\epsilon$. The function F_3 was not evaluated by Jones and Launder since they did not deal with buoyant flows and in this study was given a value of unity; however, further work may reveal that its optimum value is otherwise.

The wall term appearing in equation (6) is again that proposed by Jones and Launder. Its necessity arises from the need to assign a boundary condition to ϵ at the wall. This boundary condition was set equal to zero for lack of an exact prediction. Thus, ϵ, in equation (7) can be considered the isotropic part of the dissipation rather than the total dissipation. With this assumption it can be shown that the wall term appearing in equation (6) will give the correct behavior of the turbulent kinetic energy in the near wall region. A similar argument can be used to derive the wall term shown in equation (8) for the mean squared temperature fluctuations. Hoffman [24] has shown that the wall term in equation (6) can be written alternately as

$$\frac{2\mu}{y}\frac{\partial K}{\partial y} \quad (11)$$

to again get the correct behavior of K near the wall. Whether equation (11) or the term shown in equation (6) is used makes little difference in the final results.

Equations (6)–(8) along with

Continuity:

$$\frac{\partial U}{\partial x}+\frac{\partial V}{\partial y}=0 \quad (12)$$

Momentum:

$$\rho\frac{U\partial U}{\partial x}+\rho\frac{V\partial U}{\partial y}=\frac{\partial}{\partial y}\left[(\mu+\mu_T)\frac{\partial U}{\partial y}\right]+\rho g\beta(T-T_\infty) \quad (13)$$

Energy:

$$\frac{U\partial T}{\partial x}+\frac{V\partial T}{\partial y}=\frac{1}{\rho}\frac{\partial}{\partial y}\left[\left(\frac{\mu}{\sigma}+\frac{\mu_T}{\sigma_T}\right)\frac{\partial T}{\partial y}\right] \quad (14)$$

were numerically evaluated with several different values of σ_T. For plane jets and plumes $\sigma_T=0.5$ has been shown to give results which agree well with experiment, thus, one might assume that this is an appropriate value, particularly outside of the velocity maximum. The experimental data of Smith [14] and the works of Blom and Pai and Whitelaw discussed in [23] indicate that σ_T should be somewhat higher inside the velocity maximum. Various constant values for σ_T were examined but the choice which gave best agreement with experiment in the present case was

$$\sigma_T=2.5\text{–}2.0(y/\delta) \quad (15)$$

The value of 2.5 at the wall represents a linear extrapolation of Smith's data and equation (15) results in the desired value of 0.5 near the outer edge of the boundary layer.

Numerical Method

The Patankar-Spalding [25] finite difference procedure was chosen for the numerical solution of the system of equations presented in the previous section because of the numerous advantages it offers in the calculation of boundary layer flows. The Von Mises transformation is applied to the five partial differential equations replacing the y-coordinate with a normalized stream function, $\omega=\psi/\psi_E$, where ψ_E is the value of the stream function at the outer edge of the boundary layer. The equations then take the form

$$\frac{\partial\Phi}{\partial x}+\frac{\rho\omega V_E}{\psi_E}\frac{\partial\Phi}{\partial\omega}=\frac{\partial}{\partial\omega}\left[\left(\mu+\frac{\mu_T}{\sigma_\Phi}\right)\frac{\rho U}{{\psi_E}^2}\frac{\partial\Phi}{\partial\omega}\right]+S \quad (16)$$

where S represents the source or sink terms for the variable in question Φ. The implicit difference equations are formed using an integral approach with the exception of the x derivatives which were formed using a differential approach. This modification to the technique was made in order to eliminate forward step size dependence of the results when a variable grid spacing is used in the cross-stream direction. The primary advantage of this solution technique is that it allows the grid system to expand with the boundary layer and the resulting tridiagonal system can be inverted quite rapidly.

The basic program was tested by calculating laminar natural convection from a vertical isothermal surface. This calculation was performed utilizing 41 cross-stream grid points and a forward step of 0.05 times the boundary layer thickness. Under these conditions the boundary layer was calculated over the range of Grashof numbers from 6.5×10^3 to 1.0×10^9 with less than 20 s of CPU time on the CDC 6400. The heat transfer results compared with the similarity solution to less than 1 percent. However near the outer edge of the boundary layer, profiles of velocity and temperature tend to zero slighter faster than they do in the similarity solution. Satisfactory results for laminar, boundary layers could probably be attained even faster by increasing the forward step size and decreasing the number of cross-stream grids. Although this was not pursued the speed and accuracy of the numerical calculation is indeed impressive.

Previous users of the K-ϵ turbulence model, as well as other two equation turbulence models, have initialized the calculation in the fully turbulent region and proceeded upstream to the region of interest. This approach naturally requires the availability of experimental data for both mean and turbulent quantities of interest. In the case of natural convection from a vertical surface experimental data on turbulence quantities is almost completely lacking in the literature. In addition, experimental results for the mean velocity and temperature profiles in the viscous sublayer are extremely sparse.

It was found that the calculation can be initiated in the laminar region by introducing a small amount of turbulent kinetic energy at a point which creates a numerical transition at the Grashof number corresponding to the transition which is observed experimentally. At a Grashof number of 4.0×10^8 the turbulent calculation was initiated by the introduction of a small amount of turbulent kinetic energy and

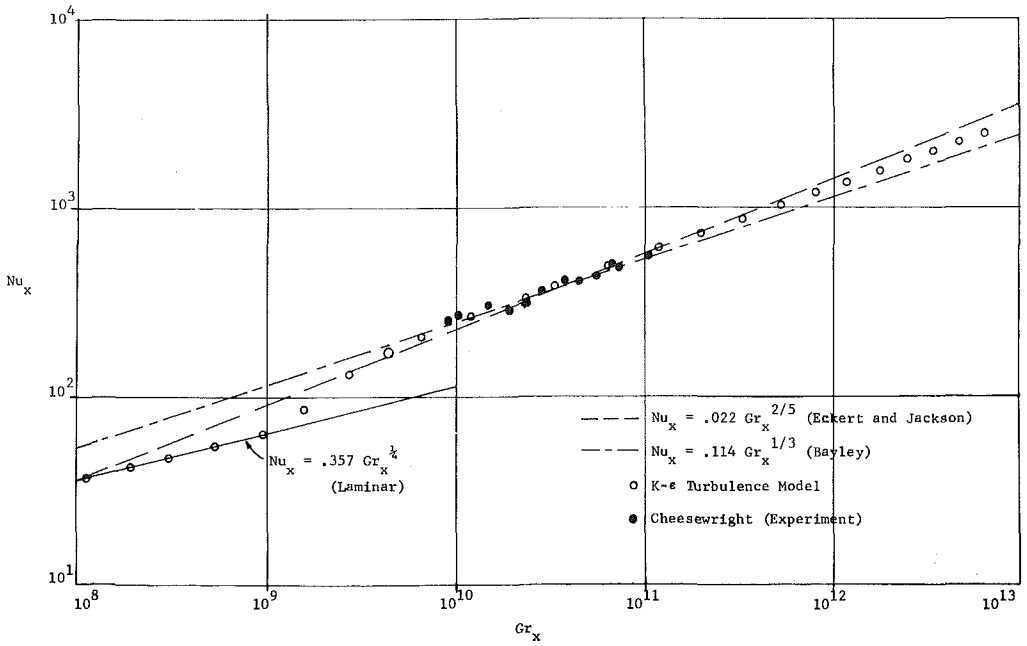

Fig. 1 Local Nusselt number versus Grashof number

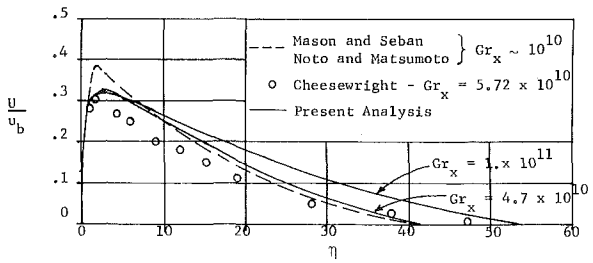

Fig. 2 Velocity profiles

a dissipation rate which approximately balanced the production and dissipation of turbulent kinetic energy at both the outer and inner edge of the boundary layer. This resulted in a numerical transition near Gr = 1.0–2.0 × 10^9 which is where the transition is observed to take place in heat transfer experiments.

The wall terms and wall functions act to damp the turbulent kinetic energy in the viscous sublayer where the molecular viscosity dominates the turbulent transport. In forced flows, the importance of these wall terms decrease as one moves toward the free stream values. However, in buoyant flows, the maximum velocity occurs within the boundary layer and these wall terms will also influence the damping at the outer edge of the boundary layer. Thus in order to overcome this difficulty the wall functions and wall terms were only applied out to the velocity maximum.

The calculations presented in this report utilized 40 cross-stream grids in the laminar and transition regions and 80 in the fully turbulent region. In order to check the adequacy of this number, runs were made with 40 grids in the turbulent region with no appreciable change in the results. The grid network was not evenly distributed across the boundary layer. Roughly half of the grid points were inside of the velocity maximum where steep gradients of all of the flow variables occur. In addition, it was essential to maintain several grids within the viscous sublayer in order to obtain satisfactory results. Forward step sizes of 4 or 5 percent of the total boundary layer thickness proved to be effective; larger forward steps led to decreased accuracy.

The entrainment rate at the outer edge of the boundary layer is calculated from the momentum equation in the form of equation (16) which can be rewritten

$$\rho V_E = \frac{\psi_E}{\omega}\left\{\frac{\partial}{\partial\omega}\left[(\mu+\mu_T)\frac{\rho U}{{\psi_E}^2}\frac{\partial U}{\partial\omega}\right] + \frac{g\beta(T-T_\infty)}{U} - \frac{\partial U}{\partial x}\right\}\frac{\partial U}{\partial\omega} \quad (17)$$

Equation (17) is solved at the second grid point from the outer edge. At this point the $\partial U/\partial x$ term and the buoyancy term are negligible which simplifies the computation.

Results and Discussion

The heat transfer results are presented in Fig. 1 and compared with available experimental results and empirical correlations. (All calculations were performed for Pr = 0.72.) The results tend to fall between the 2/5 power law of Eckert and Jackson's integral analysis and the 1/3 power law of Bayley at higher Grashof numbers. The experimental data of Cheesewright, and Fujii fits the Eckert and Jackson correlation fairly closely whereas the experimental results of Warner and Arpaci (not shown on the figure) are best fit with Bayley's correlation. The model tends to slightly over predict the heat transfer if a constant value of $\sigma_T = 0.9$ is used but agrees well when σ_T is given by equation (15). The model cannot be expected to predict transition, thus the results between Grashof numbers of 10^9 and 10^{10} should not be taken as accurate. They merely provide a means of leading the model to the fully turbulent results which are of interest.

Turbulent velocity and temperature profiles are shown in Figs. 2 and 3. These are plotted versus η, the laminar similarity parameter, not to infer that this is the correct similarity parameter for turbulent natural convection, but merely as a matter of convenience since previous results have been presented in this manner. The velocity is normalized with the buoyant velocity, $u_b = \sqrt{g\beta x\Delta T}$. The velocity profiles calculated using the K-ϵ model agree more closely with the experimental data than do previous numerical results in that the velocity maximum is less pronounced and the profile beyond the maximum is more linear. However, the predicted velocity is still slightly higher than that determined experimentally. This could be a result of equation (17) overpredicting the entrainment rate. If the

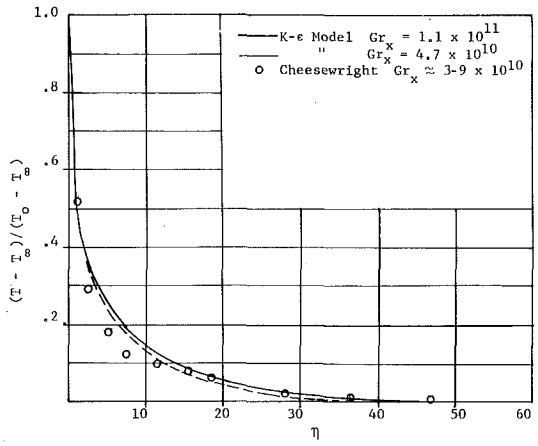

Fig. 3 Temperature profiles

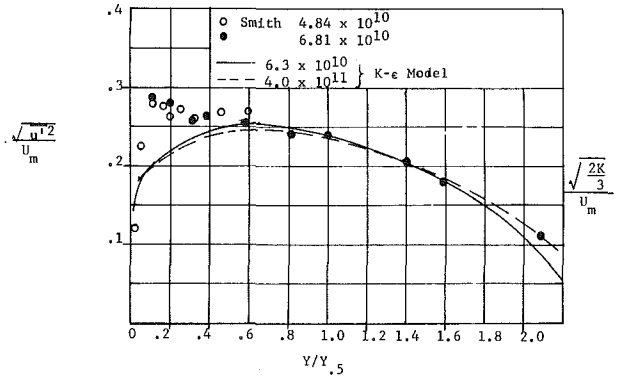

Fig. 5 Comparison of K and experimental $\overline{u^2}$ ($Y_{0.5}$ is Y at which $U/U_{max} = 0.5$)

velocity profiles are plotted as U/U_{max} they agree very closely with experimental data of Cheesewright and Vliet and Liu. The calculated temperature profiles shown in Fig. 3 agree quite closely with available experimental results.

The three turbulent quantities predicted by the K-ϵ model are shown in Fig. 4 for two Grashof numbers. The calculated kinetic energy and mean squared temperature fluctuations are compared with the experimental data of Smith in Figs. 5 and 6. The experimental data indicate a maximum turbulent intensity slightly less than 0.3. The experiments of Vliet and Liu in water indicates similar results whereas Kutateladze's data for ethyl alcohol at a Rayleigh number of 10^8 gives a maximum intensity of 0.36.

For both the turbulent kinetic energy and the temperature fluctuations, the model results agree closely with experiments in the outer region. However, in both cases the model fails to predict the sharp measured peak occurring inside the velocity maximum. This can be attributed to a combination of the inadequacy of the wall functions and wall terms and the assumption that the dissipation rate is zero at the wall. However, the experimental data in this range is questionable due to the experimental difficulties in measuring intensities near the wall. The results of Bill [26] in water demonstrate a smooth curve without the near wall peak in agreement with the K-ϵ model.

The near wall results deserve some attention since this is where the heat flux is controlled and also probably the most questionable part of the model since it is here that the calculated turbulent quantities deviate from experiments. An asymptotic solution to the boundary layer equations for natural convection near the wall [27], results in the following velocity and temperature distributions:

$$U = \left(\frac{\partial U}{\partial y}\right)_{y=0} y + \frac{g\beta\Delta T}{2\nu} y^2 - \frac{g\beta\left(\frac{\partial T}{\partial y}\right)_{y=0}}{6\nu} y^3 + U_4 y^4 + \ldots \quad (18)$$

$$T - T_w = \left(\frac{\partial T}{\partial y}\right)_{y=0} y + T_4 y^4 + \ldots \quad (19)$$

The first appearance of turbulence quantities being in the coefficients of y^4 (U_4 and T_4). Equation (19) is the same as that for forced convection. However, the asymptotic velocity profile does not contain the quadratic and cubic terms in y in the case of forced convection indicating a linear velocity profile in the viscous sublayer. However, it can be shown that in air at moderate ΔT's, the quadratic and cubic terms are small in comparison to the first term, thus reducing equation (18) to basically the forced convection form. From the asymptotic solution it can also be shown that the turbulent viscosity should go as y^3 near the wall.

Experimental and calculated near wall velocity profiles are shown in dimensionless form in Fig. 7 along with equation (18). The near wall results ($y^+ < 5$), both experimental and calculated, appear to agree closely with the forced convection form ($u^+ = y^+$) which falls slightly below the curve of equation (18). Since the wall terms used were developed for forced flows and not optimized for buoyant flows, this

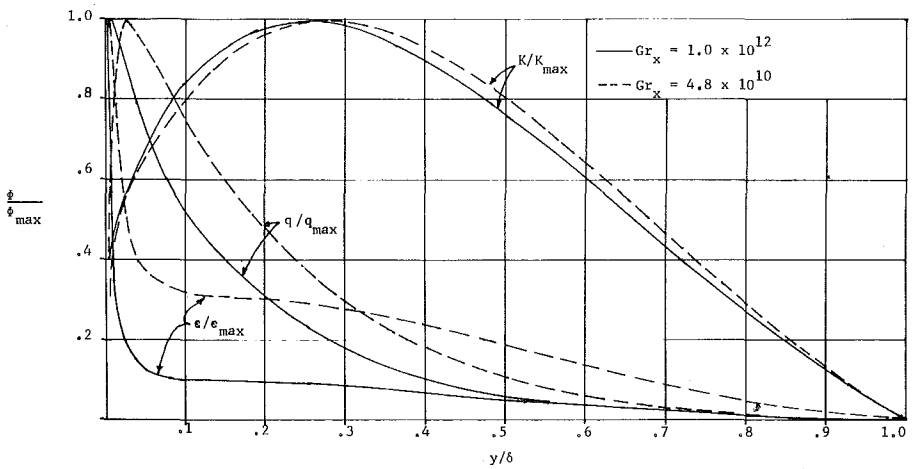

Fig. 4 Normalized turbulence quantities

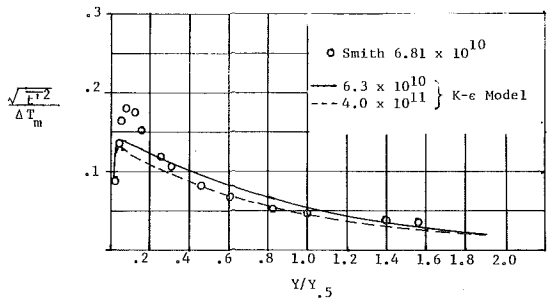

Fig. 6 Comparison of predicted and experimental t^2

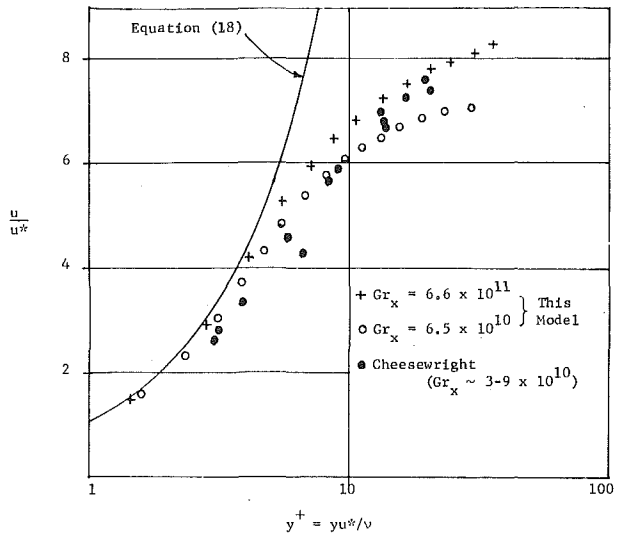

Fig. 7 Near wall velocity profiles

small discrepancy in the near wall region is reassuring that the modeling approach is sound. There does seem to be a logarithmic region between the viscous sublayer and the velocity maximum, however, the model results indicate that the slope of the logarithmic region is a function of Grashof number. In the narrow range of Grashof numbers observed by Cheesewright, the velocity profile varies little with Grashof number although there is a large amount of scatter in the data close to the wall. A prediction of u^* from Cheesewright's data is also difficult, thus, the experimental points plotted in Fig. 7 are questionable. The model does result in the linear temperature distribution predicted by equation (19) and also calculates a turbulent viscosity which goes as y^3 in the viscous sublayer.

The development of the boundary layer thickness and maxima in the profiles of velocity, turbulent kinetic energy, and mean squared temperature fluctuations as the flow progresses downstream can be simply related to the Grashof number, Gr_x. Once the numerical calculation has surpassed the transition region ($Gr_x \approx 10^{10}$) all four flow variables are found to follow simple power laws. The velocity maximum increases by a 1/7 power law indicating that the boundary layer grows linearly with x. The maxima in the turbulent kinetic energy and mean squared temperature fluctuations follow $Gr_x^{1/4}$ and $Gr_x^{-1/10}$, respectively. The experimental work of Papailiou and Lykoudis in liquid mercury indicated a decrease in intensity of temperature fluctuation closely approximated by $Gr_x^{-1/4}$.

A sensitivity study was carried out in order to determine the effect of the various model constants on the calculated results. The coefficients C_1, C_2, C_μ, σ_K, σ_ϵ were not included since they have been optimized against experiment for forced flows and used with a reasonable degree of success by several previous investigators. The result of varying the constants C_3, C_4, C_{q1}, C_{q2}, and σ_q by ±20 percent are shown in Table 2. It can be seen that the effect of C_3 on the model results is quite strong leading in some cases to amplified effects (>20 percent). It has an appreciable effect on all of the parameters examined in the study. The constant C_4 can be varied by ±20 percent with a less than 5 percent effect on all of the parameters except the maximum turbulent kinetic energy and the maximum dissipation rate. It

Table 2 Results of Sensitivity Study—numbers represent percent change of parameter in question. Upper left: $Gr_x = 1.0 \times 10^{11}$; lower right: $Gr_x = 1.0 \times 10^{12}$.

CONSTANT TESTED	U_{max}	K_{max}	ϵ_{max}	q_{max}	N_{ux}	δ_x
C_3 = 1.15 (-20%)	-6.3 / -5.3	+17.0 / +28.3	+18.2 / +24.3	+17.9 / +18.1	+20.2 / +23.6	+26.6 / +39.5
C_3 = 1.73 (+20%)	+5.7 / +4.1	-14.8 / -17.3	-17.5 / -17.1	-14.4 / -12.7	-14.5 / -14.7	-16.1 / -20.5
C_4 = .4 (-20%)	+1.1 / + .4	-7.0 / -7.6	-10.7 / -9.6	-1.8 / -1.3	-4.1 / -4.7	-2.8 / -3.1
C_4 = .6 (+20%)	- .6 / - .4	+7.0 / +8.0	+9.8 / +11.2	+1.0 / +.15	+3.9 / +4.9	+2.8 / +2.7
C_{q2} = 1.36 (-20%)	- .6 / - .4	+4.6 / +6.1	+4.6 / +6.8	+15.2 / +18.1	+2.4 / +3.5	+2.8 / +3.5
C_{q2} = 2.04 (+20%)	+ .6 / + .4	-3.5 / -4.4	-4.0 / -4.4	-11.8 / -13.0	-1.7 / -2.4	-1.8 / -2.3
C_{q1} = 2.24 (-20%)	+ .6 / + .4	-3.9 / -4.2	-5.5 / -5.2	-20.6 / -20.5	-2.1 / -2.4	- .9 / +1.6
C_{q1} = 3.36 (+20%)	- .6 / 0.0	+3.2 / +3.8	+4.3 / +4.6	+20.5 / +21.3	+1.6 / +2.3	+ .9 / +1.6
σ_q = .68 (-20%)	0.0 / - .4	+1.8 / +2.9	+ .8 / +1.6	-4.5 / -3.5	+1.1 / +1.4	+2.8 / +3.5
σ_q = 1.02 (+20%)	+ .6 / + .4	-1.4 / -2.1	- .7 / -1.2	+3.6 / +2.8	- .8 / -1.0	- .9 / -2.3
σ_T = .9	+5.7 / +9.0	-2.8 / +4.4	-9.6 / +1.6	-52.1 / -51.1	-43.8 / +54.3	-7.3 / -5.8
σ_T = .5	+8.6 / +11.8	-10.2 / -2.3	-22.2 / -9.2	-70.9 / -69.4	+67.0 / +86.4	-12.7 / -11.2
σ_T = 1.75 - 1.25 (y/δ)	-1.1 / -1.2	-1.8 / -1.9	-2.6 / -3.2	+ .9 / +1.4	+..9 / + .5	+ .9 / + .4
σ_T = 2.5 - 2.5 (y/δ)	+2.3 / +2.9	-3.2 / - .8	-5.5 / -1.6	-21.4 / -20.5	+13.9 / +16.6	-3.7 / -3.1

should be noted that C_4 cannot be considered a universal constant for all free convection-type flows, since in the general case where stable stratification may exist $\overline{ut}$ or C_4 must be permitted to change sign. The constants C_{q1} and C_{q2} have a significant effect only on q since the contribution of buoyancy to the turbulent kinetic energy is small in comparison to the mean shear (gradient production). The effects of the turbulent Prandtl number, σ_q, are quite small.

It can be seen from test numbers 11–14 (Table 2) that the effect of the turbulent Prandtl number, σ_T, is quite strong with respect to the resulting Nusselt number and the mean squared temperature fluctuations. The cases tested utilizing a constant value of σ_T, both result in extremely high Nusselt numbers as well as low levels of temperature fluctuations. Test number 14 yielded results quite similar to those calculated using the Prandtl number variation obtained through the use of equations (18) and (19).

In one additional test the wall function f_3 was changed from unity to a form equal to that used for f_2. The results indicated no significant effect.

While time has not allowed us to examine the pros and cons of the present approach with that of Nee and Yank [7], it is interesting to note despite the differences in the modeling of the various turbulence processes, both closure model lead to identical behaviors of the velocity, temperature and turbulent viscosity variations in the sublayer. It would prove interesting to examine and compare the prediction of the turbulent structure quantities of both approaches but this has not been done at this time.

Conclusions

The K-ϵ turbulence model for wall boundary layers proposed by Jones and Launder and modified to incorporate the effects of buoyancy can be used with a reasonable degree of accuracy to calculate turbulent buoyancy driven wall boundary layers. This adds to the confidence in the universality of the empirical constants and lends some support to the selection of wall functions and wall terms of Jones and Launder with the exception of the wall term discarded in the present study. The model slightly overpredicts the velocity in the outer portion of the boundary layer and does not precisely predict the peaks in the turbulent kinetic energy and turbulent fluctuations in the near wall region. However the results compare to a reasonable degree of accuracy with the experimental results available in the literature. Further refinements in the model await the availability of more experimental data for this type of flow, particularly with regard to turbulence quantities and mean velocity and temperature distributions in the viscous sublayer.

References

1 Eckert, E. R. G., and Jackson, T. W., "Analysis of Turbulent Free Convection Boundary Layer on a Flat Plate," NACA Technical Note 2207, 1950.

2 Bayley, F. J., "An Analysis of Turbulent Free-Convection Heat Transfer," *Proc. Inst. Mech. Engineers,* Vol. 169, No. 20, 1955, p. 361.

3 Kato, H., Nishiwaki, M., and Hirata, M., "On the Turbulent Heat Transfer by Free Convection From a Vertical Plate," *International Journal of Heat and Mass Transfer,* Vol. 11, 1968, pp. 1117–1125.

4 Cebeci, T., and Khattab, A., "Prediction of Turbulent Free-Convective Heat Transfer From a Vertical Flat Plate," JOURNAL OF HEAT TRANSFER, TRANS. ASME, Series C, Vol. 97, 1975, pp. 469–471.

5 Mason, H. B., and Seban, R. A., "Numerical Predictions for Turbulent Free Convection From Vertical Surfaces," *International Journal of Heat and Mass Transfer,* Vol. 17, 1974, pp. 1329–1336.

6 Noto, K., and Matsumoto, R., "Turbulent Heat Transfer by Natural Convection Along an Isothermal Vertical Flat Surface," JOURNAL OF HEAT TRANSFER, TRANS. ASME, Series C, Vol. 97, 1975, pp. 621–624.

7 Nee, V. W., and Yank, K. T., "Structure of Turbulent Free Convection Boundary Layer Along a Vertical Plate," Heat Transfer 1970, Vol. IV, *Proceedings 4th International Heat Transfer Conference,* Versailles, Elsevier Publishing Co., Amsterdam, pp. Ncl. 12.

8 Nee, V. W., and Kovasznay, L. S. G., "A Simple Phenomenological Theory of Turbulent Shear Flows," *The Physics of Fluids,* Vol. 12, No. 3, 1969, pp. 473–484.

9 Cheesewright, R., "Turbulent Natural Convection From a Vertical Plane Surface," JOURNAL OF HEAT TRANSFER, TRANS. ASME, Series C, Vol. 90, 1968, pp. 1–8.

10 Warner, C. Y., and Arpaci, V. S., "An Experimental Investigation of Turbulent Natural Convection in Air Along a Vertical Heated Flat Plate," *International Journal of Heat and Mass Transfer,* Vol. 11, 1968, pp. 397–406.

11 Lock, G. S. H., and Trotter, F. J. deB., "Observations on the Structure of a Turbulent Free Convection Boundary Layer," *International Journal of Heat and Mass Transfer,* Vol. 11, 1968, pp. 1225–1232.

12 Fujii, T., "Experimental Studies of Free Convection Heat Transfer," *Bull. Japan Soc. of Mech. Eng.,* Vol. 2, 1959, pp. 555–558.

13 Vliet, G. C., and Liu, C. K., "An Experimental Study of Turbulent Natural Convection Boundary Layers," JOURNAL OF HEAT TRANSFER, TRANS. ASME, Series C, Vol. 91, 1969, pp. 517–531.

14 Smith, R. R., "Characteristics of Turbulence in Free Convection Flow Past a Vertical Plate," PhD thesis, Queen Mary College, University of London, 1972.

15 Papailiou, D. D., and Lykoudis, P. S., "Turbulent Free Convection Flow," *International Journal of Heat and Mass Transfer,* Vol. 17, 1974, pp. 161–172.

16 Kutateladze, S. S, Kirdyashkin, A. G., and Ivakin, V. P., "Turbulent Natural Convection on a Vertical Plate and in a Vertical Layer," *International Journal of Heat and Mass Transfer,* Vol. 15, 1972, pp. 193–202.

17 Jones, W. P., and Launder, B. E., "The Prediction of Laminarization With a 2-Equation Model of Turbulence," *International Journal of Heat and Mass Transfer,* Vol. 15, 1972, pp. 301.

18 Taminini, F., "On the Numerical Prediction of Turbulent Diffusion Flames," Presented at the joint meeting of the Central and Western States Section of the Combustion Institute, Southwest Research Institute, San Antonio, Tex., Apr. 21–22, 1975.

19 Chen, C., and Rodi, W., "A Mathematical Model for Stratified Turbulent Flows and Its Application to Buoyant Jets," XVIth Congress, International Association for Hydraulic Research, Sao Paulo, 1975.

20 Prandtl, L., "Uber ein neues Fommelsystem Fur de Ausgebildete Turbulenz," *Nachr. Akad. Wiss.,* Gottingen, Math.-Phys., K1, 1945.

21 Kolmogorov, A. N., "Equations of Turbulent Motion in an Incompressible Fluid," *Izv. Akad. Nauk,* USSR, Vol. VI, No. 1.2, 1942, pp. 56–58.

22 Rodi, W., "A Note on the Empirical Constant in the Kolmogorov-Prandtl Eddy-Viscosity Expression," *Journal of Fluids Engineering,* TRANS. ASME, Series I, Vol. 97, 1975, pp. 386–389.

23 Launder, B. E., and Spalding, D. B., *Mathematical Models of Turbulence,* Academic Press, London, 1972, pp. 134–315.

24 Hoffman, G. H., "Improved Form of the Low Reynolds Number K-ϵ Turbulence Model," *The Physics of Fluids,* Vol. 18, No. 3, 1975, pp. 309–312.

25 Patankar, S. V., and Spalding, D. B., *Heat and Mass Transfer in Boundary Layers,* Second Ed., Intertext Books, London.

26 Bill, R. G., "The Development of Turbulent Transport in a Vertical Natural Convection Boundary Layer," PhD thesis, Cornell University, Ithaca, New York, 1976.

27 Plumb, O. A., "An Experimental and Numerical Examination of Buoyancy Driven Wall Boundary Layers," PhD thesis, State University of New York at Buffalo, 1976.

R. L. D. Cane
Research Officer,
Division of Building Research,
National Research Council,
Ottawa, Canada

K. G. T. Hollands
Assoc. Professor.

G. D. Raithby
Assoc. Professor,
Department of Mechanical Engineering.

T. E. Unny
Professor,
Department of Civil Engineering.

University of Waterloo,
Waterloo, Canada

Free Convection Heat Transfer Across Inclined Honeycomb Panels

Experimentally obtained Nusselt number-Rayleigh number plots are presented for free convective heat transfer across honeycomb panels, heated from below, and inclined with respect to the horizontal at angles of 0, 30, 45, 60, and 90 deg. Aspect ratios of honeycomb cells of 2, 3, 4, and 5 are included; the fluid contained in the cells is air. Substantial suppression of free convection is observed when compared with an air layer of the same depth but not containing a honeycomb. Heat transfer associated with the base flow is found to be of only moderate importance at angles near horizontal, but of considerable consequence for angles near the vertical. The honeycomb walls used were partly transparent to thermal radiation, and a strong radiative coupling is indicated. A correlation equation for the Nusselt number, valid over part of the experimental range, is presented.

Introduction

Although considerable attention has been given to free convective heat transfer across honeycomb panels in the horizontal position, [1–7],[1] very little information exists for predicting free convective heat transfer across inclined panels. Notwithstanding the studies which have touched on the inclined case, [8–11], there is insufficient published information at the present time to permit the rational design of honeycombs for particular applications. The situation has been recently reviewed in [7].

An important proposed use of honeycombs is for the purpose of suppressing the free convective heat transfer which would otherwise occur in an inclined layer of fluid, heated from below. The insertion of a honeycomb into this fluid layer is known, in the case of a horizontal layer, to completely suppress convection currents for all Rayleigh numbers, Ra, less than a critical value, denoted by Ra_c. In the case of an inclined layer, it is known that a finite convective motion, called the base flow, exists for any Ra greater than zero. This base flow, which is driven by the component of gravity *along* the heated bounding surface of the honeycomb panel, is expected to make only a modest contribution to the heat transfer, at least until very high Rayleigh numbers are reached. However, the actual magnitude of the heat transfer associated with the base flow, and the Rayleigh number at which it becomes significant, are at the present time largely unknown. Also largely unknown is the critical Rayleigh number at which this base flow becomes unstable. This latter instability is expected to be due to the "top-heavy" nature of the fluid layer and hence is expected to be driven by the component of gravity normal to the heated bounding surface.

The present paper presents an extensive set of measurements on this problem, for a square-celled, diathermous honeycomb. Experimental plots of Nusselt versus Rayleigh number are presented for angles of inclination, θ, measured from horizontal ranging from 0 to 90 deg, and for aspect ratios ranging from 2 to 5. The fluid used is air and in all cases (except at $\theta = 90$ deg), heating is from the lower face of the honeycomb.

The major engineering application of this study is to the design of a class of flat plate solar collectors in which a honeycomb is placed between the absorber plate and the glass cover in order to suppress free convective and radiative heat losses, as described for example in [20]. In this application there exists a short-wave (solar) radiant input to the honeycomb, which is not simulated in the present experiments. However, since the honeycomb must be made highly nonabsorbing to solar radiation (in order that the collector function efficiently), the effect of the short-wave input on the free convective phenomena are expected to be slight.

Description of Experiment

All experiments were performed on the University of Waterloo Natural Convection Apparatus which is fully described elsewhere [3,

[1] Numbers in brackets designate References at end of paper.

Contributed by the Heat Transfer Division for publication in the JOURNAL OF HEAT TRANSFER. Manuscript received by the Heat Transfer Division May 20, 1976.

12, 13]. The procedure and data reduction was also the same as described in these papers. Full details of the complete experiment are given in [14]. The measured heat transfer across the honeycomb includes contributions from conduction along the honeycomb walls and radiation, as well as the free convection heat transfer. In order to separate out the free convective component, it was necessary to subtract away the sum of the wall conduction and radiative components. This sum was determined for a particular honeycomb from measurements at subcritical pressures with $\theta = 0$, as discussed in [3]. As also discussed in [3], an error analysis indicated that the maximum expected error in the apparatus for the Nusselt number is about 3 percent, and in the Rayleigh number, 2 percent. All properties (both honeycomb and air) were evaluated at the arithmetic mean of the plate temperatures. Since ΔT was kept small ($\Delta T \approx 5$ K), temperature variation of properties is not considered an important factor in the experiments. The mean temperature, T_m, was kept at 305 ± 10 K.

Sketched in Fig. 1, the honeycombs were constructed from 0.038-mm (0.0015-in.) thick polyethylene film, by heat-sealing preslit strips at periodic join-lines. The width of the join-lines was kept small (approximately 0.25 mm), thereby ensuring nearly square cell corners. Table 1 gives the actual dimensions of the honeycombs used. As in [3], polyethylene was chosen for the honeycomb material because, in thin films, it has a very high transmittance to long-wave (3–30 μm) thermal radiation. This high transmittance, along with the low emissivity, of the polished copper plates which form the bounding surfaces of the honeycomb in the test apparatus, was originally expected to insure a decoupling of the thermal radiation mode of heat transfer across the honeycomb, from the free convective mode. However, as will be discussed later in the paper, a strong radiative coupling was still observed. Hence a full specification of the radiant parameters is necessary.

The spectral binormal radiative transmittance of the polyethylene film was measured on a spectro-photometer and, assuming no scattering and an index of refraction for polyethylene of 1.52, the total normal transmittance τ, reflectance ρ, and absorptance, α, for a black-body source at $T_m = 305$ K were calculated. The result was: $\tau = 0.819$, $\rho = 0.067$, and $\alpha = 0.114$. The total normal emissivity at 305 K is consequently $\epsilon = 0.114$ and the corresponding hemispheric value was calculated to be 0.130. Most of the absorption occurred in two bands, one at 6.9 μm, the other at 14.2 μm. The copper plate emissivity was $\epsilon_p = 0.065$. The thermal conductivity of polyethylene walls was taken at 0.54 W/m K, with an uncertainty of about ± 10 percent [21].

Since the temperature difference across the honeycomb was kept small (≈ 5 K), it is permissible to assume that the radiative interaction can be linearized. Assuming this, and assuming also that a grey radiant

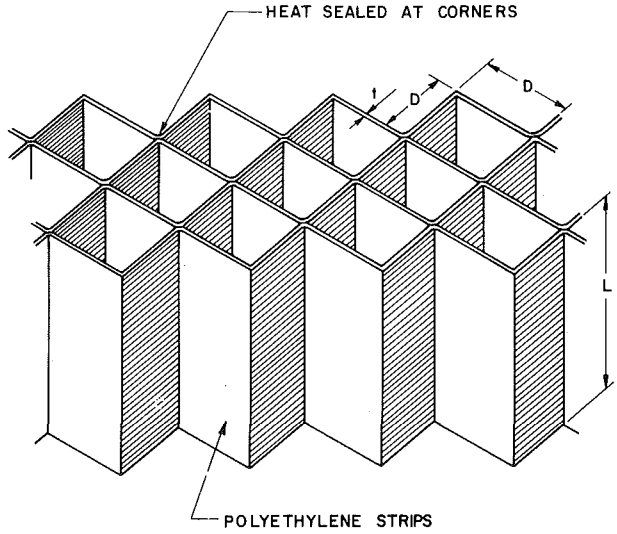

Fig. 1 Figure showing dimensions and method of fabricating square-celled honeycomb

analysis applies, the Nusselt number can be shown to be a function of the following dimensionless groups:

$$\mathrm{Nu} = \mathrm{Nu}(\mathrm{Ra}, \mathrm{Pr}, \theta, A, C, H, N, \rho, \epsilon, \epsilon_p) \quad (1)$$

(In fact, ρ need not be listed, as will be demonstrated later.) Certain of the variables were kept constant for all experimental runs. These included the Prandtl number (Pr = 0.71), as well as ρ, ϵ, and ϵ_p, whose values are given in the foregoing. Other variables were kept "quasi-constant:" thus except for one honeycomb, C was kept at 166 ± 25 percent; H was kept at 6×10^{-5} ± 25 percent; and N was kept at 15.6 ± 25 percent. Since it was anticipated that rather large variations in these quantities would be required in order to have a significant effect on Nu, these variables were considered constant. Consequently, for the present experiment:

$$\mathrm{Nu} = \mathrm{Nu}(\mathrm{Ra}, \theta, A) \quad (2)$$

The primary purpose of the experiment was to examine the effect of Ra, θ, and A on Nu, and the range of values of these variables was consequently made large. The ranges were: for A, $A = 2, 3, 4$, and 5; for θ, $\theta = 0, 30, 45, 60$, and 90 deg; and for Ra, $\sim 10^3 < \mathrm{Ra} < \sim 10^6$. In all, six square-celled, polyethylene honeycombs were tested; their

Nomenclature

A = apsect ratio of honeycomb cell; $A = L/D$
C = wall admittance group: $C = k_f L/(k_w \delta)$
C^* = revised wall admittance group, which includes radiative effect, defined by equation (4)
D = honeycomb cell width, see Fig. 1, for square cell; distance across hexagonal flats for hexagonal honeycomb
g = acceleration of gravity
H = cell coupling group; $H = k_f \delta/k_w L$
k_f = thermal conductivity of fluid
k_w = thermal conductivity of honeycomb wall
L = height of honeycomb panel, see Fig. 1
N = radiation group; $N = 4\sigma T_m{}^3 L/k_f$
Nu = Nusselt number; $\mathrm{Nu} = qL/(k_f \Delta T)$
Pr = Prandtl number of fluid; $\mathrm{Pr} = \nu/\lambda$
q = free convective component of heat transfer across honeycomb panel
Ra = Rayleigh number; $\mathrm{Ra} = g\beta\Delta T L^3/(\nu\lambda)$
Ra_D = modified Rayleigh number; $\mathrm{Ra}_D = g\beta\Delta T D^4/L\nu\lambda = \mathrm{Ra}/A^4$
ΔT = temperature difference across honeycomb; $\Delta T = T_1 - T_2$
T_1, T_2 = temperature of lower and upper bounding faces of honeycomb, respectively
T_m = mean absolute temperature of honeycomb walls; $T_m = (T_1 + T_2)/2$
t = thickness of honeycomb wall (see Fig. 1)
α = total absorptivity of single film of honeycomb wall to radiation from a black body at T_m
β = coefficient of volumetric expansion of air
δ = half-thickness of honeycomb wall, $\delta = t/2$
ϵ = total emissivity of single film of honeycomb wall, at T_m
ϵ_p = total emissivity of plates bounding honeycomb on top and bottom
λ = thermal diffusivity of fluid
ν = kinematic viscosity of fluid
θ = angle of inclination of honeycomb face from horizontal
ρ = total reflectivity of single film of honeycomb wall to radiation from a black body at T_m
σ = Stefan-Boltzmann constant
τ = total transmittance of single film of honeycomb wall to radiation from a black body at T_m.

Table 1 Properties of six polyethylene honeycombs tested

Honeycomb #	L inch (cm)	D inch (cm)	A	C	Hx10^5	N	C*
1	3.000 (7.62)	1.000 (2.54)	3	200	1.25	18.99	13.1
2	1.875 (4.76)	0.625 (1.59)	3	125	2.00	11.87	19.0
3	2.500 (6.35)	0.625 (1.59)	4	167	1.50	15.82	25.3
4	3.125 (7.94)	0.625 (1.59)	5	208	1.200	19.78	31.7
5	2.000 (5.08)	1.000 (2.54)	2	133	1.900	12.66	8.7
6	1.250 (3.18)	0.625 (1.59)	2	83	3.000	7.91	12.7
		Average		153			18.4

various dimensions and pertinent dimensionless groups are given in Table 1. An additional honeycomb made from polycarbonate and having hexagonal cells was also tested. It will be described more completely later in the paper, as will the results applying to it.

Results

The measured Nusselt number-Rayleigh number plots are shown in Fig. 2. Also shown on these graphs, for comparison, are the Nusselt number curves which would apply for free convective heat transfer

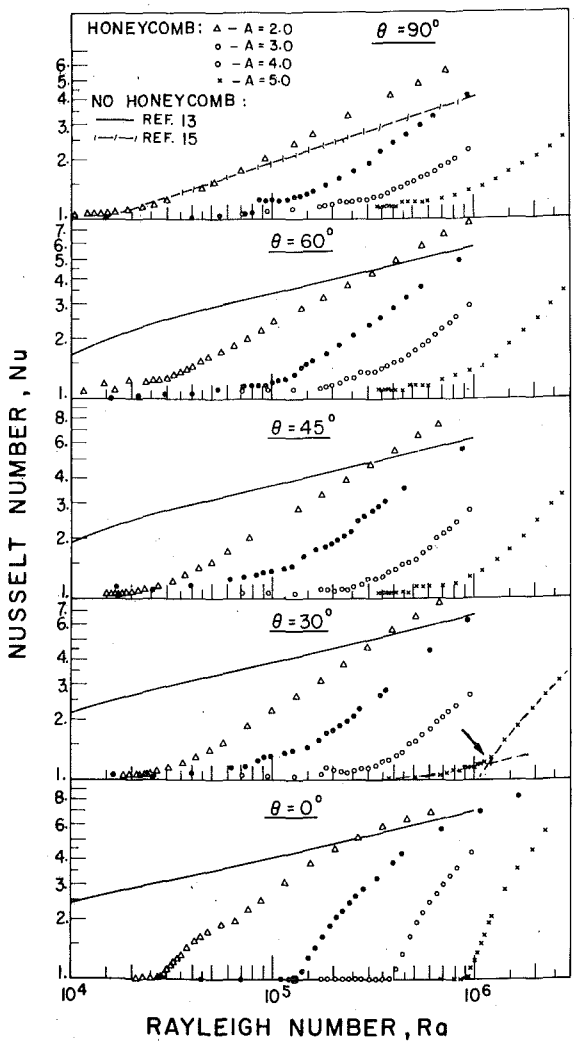

Fig. 2 Experimental results for various aspect ratios and angles of inclination in the form of Nusselt number-Rayleigh number plots

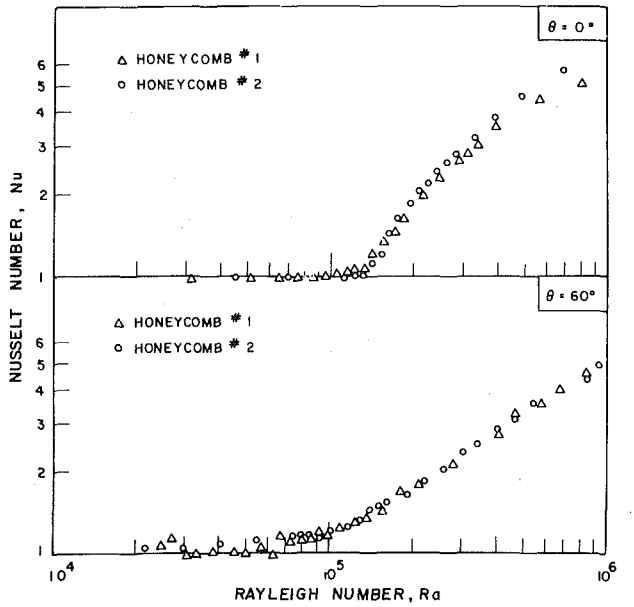

Fig. 3. A check on dimensional similarity and the importance of variations in the groups *C, H,* and *N*—these two honeycombs have the same aspect ratio *A*, but are of different actual dimensions (see Table 1)

across slots of very small aspect ratio, but containing *no* honeycomb [13, 15]. Thus the difference between the data and the curves is an indication of the effectiveness of the honeycomb in suppressing free convection.

The data for $\theta = 0$ deg are exactly as have been observed earlier [1, 3]—i.e., a Nusselt number of unity, indicating complete convective suppression, until a critical Rayleigh number is reached, after which there is a dramatic rise in Nu with Ra. The inclined data show the same general trend, but with an initial gradual rise in Nusselt number, making it difficult to define a critical Rayleigh number for the inclined case. A similar trend was observed by Sun [8] for rectangular-celled honeycombs. As discussed in [8] and updated in [7], this region of initial gradual rise is almost certainly associated with the base flow which, as discussed earlier, occurs for any $Ra > 0$ (provided $\theta \neq 0$) and is driven by the component of gravity along the bounding surface (i.e., $g \sin \theta$). The more dramatic rise[2] in Nusselt number in the inclined case, noted at values of Ra slightly greater than the corresponding Ra_c for $\theta = 0$, is most probably due to the top-heavy instability, driven by the component of gravity normal to the bounding surfaces, $g \cos \theta$. At $\theta = 90$ deg there appears to be no instability of this kind and it is therefore felt that the observed heat transfer is due entirely to base flow. This is supported by the close agreement noted in [16] between the present data and the predictions of a numerical solution for the base flow.

It is interesting to note that the results in Fig. 2 show that at some Rayleigh number, and at low aspect ratios, the effect of the honeycomb can be to *increase* the heat transfer over that which would occur with no honeycomb present. This result is felt to be due to the honeycomb breaking up the thick, insulative boundary layers which would otherwise form along the heated and cooled faces. Such an effect was also found in [16], for $\theta = 90$ deg, based on a numerical solution of the governing equations.

As a check on dynamic similarity, and to test the hypothesis that, over the ranges of *C, H,* and *N* covered in the experiments, the effect of these variables is negligible, Fig. 3 was plotted. This figures shows a comparison of the measured Nusselt numbers for two different

[2] This rise is perhaps most easily observed in the case $\theta = 30$ deg, $A = 5$ (see arrow).

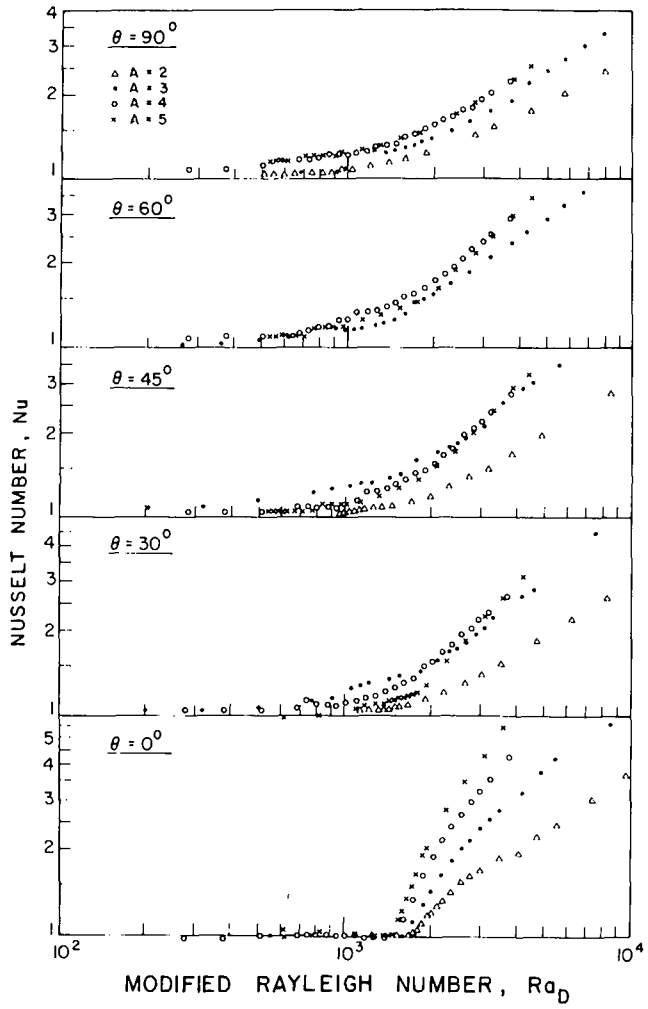

Fig. 4 Experimental results plotted in terms of Ra_D rather than Ra

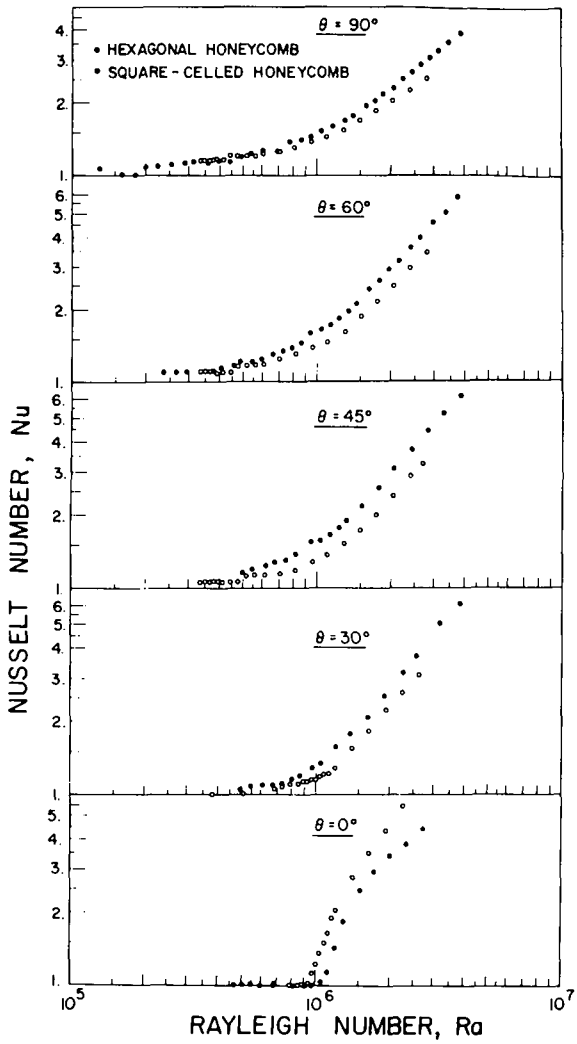

Fig. 5 Comparison of two honeycombs, one square-celled, the other hexagonal, compared at the same hydraulic diameter ($A = 5$)—the hexagonal-celled honeycomb also has a higher wall emissivity

honeycombs (Honeycombs 1 and 2, Table 1), both having the same values of A (namely 3), but of different dimensions and consequently, slightly different values of C, H, and N. The close agreement should indicate the insensitivity to these variables. Close agreement was also found when Honeycombs Nos. 3 and 4, which are both of aspect ratio 2, were compared.

The data of Fig. 2 are plotted in slightly different form in Fig. 4, where a modified Rayleigh number, Ra_D, defined by

$$Ra_D = \frac{g\beta\Delta T D^4}{\nu\alpha L} = Ra/A^4$$

has been used. This group has been put forward previously by Edwards [17, 19], for large aspect ratio stability studies at $\theta = 0$, and by Hart [18] for large aspect ratio base flow studies at $\theta = 90$ deg. Consequently, for large aspect ratios this group alone was anticipated to characterize the heat transfer, for a fixed angle θ, at least for small and moderate Rayleigh number, and Fig. 3 shows that within the bounds of experimental error, this is in fact the case provided $A \geq 4$ and $\theta \neq 0$.

Correlation Equation for Heat Transfer

Simple correlation equations for the function $Nu = Nu(Ra, \theta, A)$ covering the full set of experimental data, have been sought by the authors but without success. However, a single correlation equation covering the important subrange:

$$\frac{Ra}{A^4} \leqq 6000; \quad 30 \text{ deg} \leqq \theta \leqq 90 \text{ deg}; \quad A \geqq 4$$

has been found. The equation is:

$$Nu = 1 + 0.89 \cos\left(\theta - \frac{\pi}{3}\right)\left(\frac{Ra}{2420A^4}\right)^{2.88-1.64\sin\theta} \tag{3}$$

This equation fits all the data in its range to within ± 7½ percent. (Provided differences of the order of 20 percent are acceptable, it also holds holds for $A = 3$.) For the range $0 < \theta < 30$, deg linear interpolation between equation (3) and the correlation equation for $\theta = 0$ deg given in (3) is recommended. Although strictly tested only for $A = 4$ and 5, the equation is expected to be valid for all $A \geq 4$, since, as discussed previously, (Ra/A^4) is expected to characterize the heat transfer for large A. For $A \leq 3$, direct use of Fig. 2 is recommended for determining heat transfer.

Hexagonal Honeycomb

Honeycombs considered for flat plate solar collectors are likely to be different from those of the present study in that: (i) they may not be square-celled, and (ii) the wall material will likely be thicker and have higher emissivity. To examine the effect of these two changes, another honeycomb was studied on the apparatus. Details of this honeycomb are as follows: cell shape–hexagonal; wall material—polycarbonate (Lexan, General Electric Reg. T.M.); average wall thickness = 0.01 cm; distance across flats-D = 0.95 cm; aspect ratio = L/D = 5; wall emissivity = 0.39; $C = 94$, $H = 10.7 \times 10^{-5}$, $N = 11.9$, $C^* = 16.1$. Fig. 5 shows the measured Nusselt numbers for this hon-

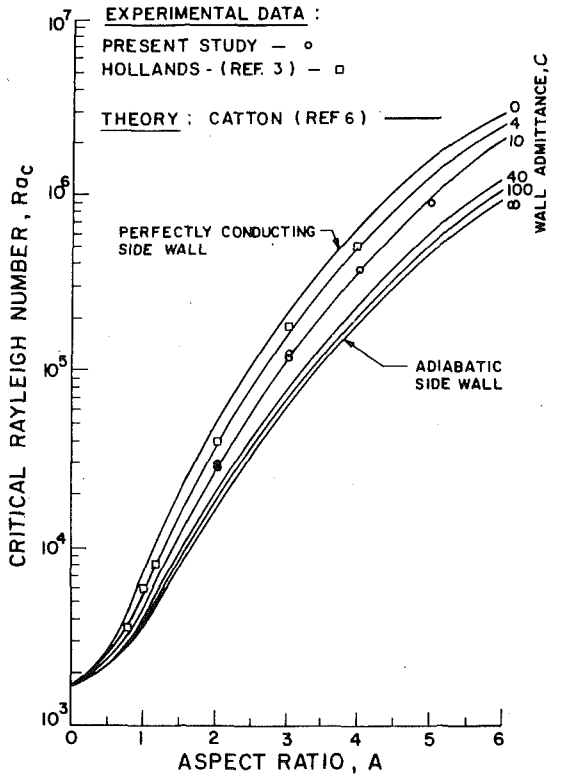

Fig. 6 Comparison of the critical Rayleigh numbers at $\theta = 0$, predicted by Catton [6], and those measured in the present study and in [3]

eycomb. Also plotted for comparison are the results for a square-celled polyethylene honeycomb of the same aspect ratio (Honeycomb No. 5). The broad behavior of the Nusselt number is the same for both honeycombs; interestingly, the hexagonal honeycomb permits less heat transfer at $\theta = 0$ and more for $\theta > 0$. Disagreement is largest at Rayleigh numbers well past critical; it does not usually exceed 20 percent but is well outside the bounds of experimental error. It should be noted that the two honeycombs are compared for the same hydraulic diameter.

Critical Rayleigh Number at $\theta = 0$

The critical Rayleigh numbers exhibited in Fig. 2 for $\theta = 0$ can be compared with the various theories which apply to this stability problem, and the present section is devoted to this comparison. It should be noted that this comparison is of importance not only for the scholarly concern of testing the validity of the theories, but also in underlining how sensitive the free convective heat transfer data in Fig. 2 are to the radiative effects, a point of some engineering significance.

The individual honeycomb cells are assumed to be thermally isolated from each other so that an adiabatic plane can be assumed to be drawn at the half thickness line of each of the partitions of the honeycomb. The stability of the fluid contained in such a square cell has been analyzed by Catton [6], and his theoretical predictions for $Ra_c(A, C)$ are shown as the solid lines in Fig. 6. This theory does not account for radiation but according to Sun and Edwards [5], the effect of thermal radiation can be accounted for by using in these plots an effective value of C, namely C^*, given by

$$\frac{1}{C^*} = \frac{1}{C} + \frac{\epsilon}{4 - \epsilon} \frac{N}{A^2} \tag{4}$$

(The use of this formula is subject to a number of assumptions which will be discussed later.)

Values of C and C^* for the various honeycombs are given in Table 1 and the measured values Ra_c for these honeycombs are plotted in Fig. 6. The average value of C for all honeycombs is about 150; that for C^* is about 18. It is seen that if radiation effects were ignored the present data points would be expected to fall approximately along the theoretical line for $C = 150$; however, they fall about 50 percent above this line. If, on the other hand, the value of C is modified to include radiation effects, then the data points should fall along a line of about $C = 18$, and they fall only about 15 percent above that line. In view of the various assumptions involved in the use of equation (4) (which are discussed shortly), the latter agreement must be considered to be quite good. As previously pointed out by Sun and Edwards [19], the engineering significance of the higher critical Rayleigh numbers experienced due to the radiative coupling is to enhance the suppression. Although this radiant effect has only been analyzed for $\theta = 0$ deg, it is likely to have an equally strong influence on the free convective heat transfer observed at the other angles in Fig. 2.

Although not part of the present study, the critical Rayleigh numbers of [3] are also plotted in Fig. 6 for further comparison with the theory. These honeycombs were fabricated from 0.004-in. thick polyethylene film, using opaque pressure sensitive tape. Allowing for the presence of the tape, the value of C for these honeycombs is calculated to be approximately 100, while that for C^*, approximately 3. They are, therefore, in excellent agreement with the theory if the effect of radiation is included. In [3] it was argued that the difference between the experimental points and the theory for $C = 100$ was not due to radiation but due to conductive interaction between cells, as represented by the group H. In view of the agreement just alluded to, it now seems that the radiative effect is the more likely explanation. However, in our opinion it is likely that the group H has an important effect on free convection in the *inclined* position due to the effects of the base flow.

As mentioned previously, the use of equation (4) in the present experiments involves a number of assumptions and these should be discussed. Strictly, the equation applies to an infinite ($A = \infty$) circular cylinder with opaque grey diffuse side walls. The honeycombs used in the present experiments are square-celled, of finite height, and have nonopaque, nongrey sidewalls. To account for the effect of finite A, an alternate theory contained in [8] must be used. This theory, which is less exact than that of Catton, gives about the same agreement with the present experiments as that shown in Fig. 6. Although the experimental honeycombs are not opaque, they can, for all practical purposes, be treated as opaque, as can be seen from the following argument. Consider a hypothetical isolated cell having sidewalls of one half thickness of those of the experiment; let the sidewalls be immediately bounded on the outside of the cell with a perfect reflector of thermal radiation which reflects in a perfectly *specular* manner. Due to the symmetry of the honeycomb about any sidewall, this hypothetical cell behaves radiantly and thermally in a manner identical to the actual honeycomb cell. Therefore the honeycomb cell can be considered to be opaque, with the same emissivity as that of the actual film, but with specular rather than diffusely reflecting sidewalls. (Note that this also implies that ρ can be dropped from the list of variables in equation (1), since the reflectance and transmittance are lumped together and the effective reflectance is $1 - \epsilon$.) Since equation (4) applies to diffuse rather than specular sidewalls, in applying it to the present problem one would expect differences of the order of those applying to diffuse vis-a-vis specular radiant analysis. In a long passage, such as a honeycomb cell, quite substantial differences of this type are found, with a specular passage generally transferring more heat than an opaque passage of the same emissivity. Consequently, a stronger radiant effect on free convection would be expected in the present instance, and this is exactly what is required to make theory and experiment agree in Fig. 6.

Conclusions

1 Free convection heat transfer across an air layer can be effectively suppressed by a thin-walled square or hexagonal-celled honeycomb, even in the inclined position. (Effective suppression for an inclined liquid layer with rectangular-celled honeycombs has been previously reported by Sun [8].)

2 Fig. 2, along with correlation equation (3), can be used for designing thin-walled, partly-transparent square-celled or hexagonal-celled honeycombs suitable for use in inclined solar collectors. Discrepancies in Nusselt number of the order of 20 per cent may be expected, since it is not likely that all dimensionless groups will be exactly matched, nor will the cell shape be completely matched. Further research is required to establish completely the effect of these parameters.

3 Even though a honeycomb material may be largely transparent ($\tau > 0.8$) to thermal radiation, a coupling of the radiative and free convective modes may still be evident. Stability theories accounting for radiant coupling, but based upon opaque sidewalls can be used with reasonable accuracy to predict critical Rayleigh numbers for partly transparent sidewalls; however, for better results, the theories should be based upon specularly reflecting sidewalls, rather than diffuse.

Acknowledgments

This work was supported by the Energy Research and Development Administration (ERDA) (Solar Heating and Cooling Branch) of the U.S. Government, under contract number E(11-1)-2597.

The National Research Council of Canada provided the original funds for building up the apparatus, for which thanks are also given.

The authors are also indebted to Prof. D. K. Edwards for a useful discussion involving the radiation effects, and to Professors Edwards and Catton of UCLA for providing the theoretical part of Figure 5 for tracing.

We wish to thank Mr. K. N. Marshall of Lockheed Palo Alto Research Laboratories, for providing the hexagonal honeycomb for testing, and Mr. Dean Smart and Mr. Samy El-Cherbiny for carrying out the tests on this honeycomb.

References

1 Catton, I., and Edwards, D. K., "Effect of Side-walls on Natural Convection Between Horizontal Plates Heated From Below," JOURNAL OF HEAT TRANSFER, TRANS. ASME, Series C, Vol. 89, No. 4, Nov. 1967, pp. 295–299.

2 Sun, W. M., and Edwards, D. K., "Natural Convection in Cells of Finite Conducting Walls Heated From Below," *Heat Transfer 1970, Proceedings of the 4th International Heat Transfer Conference,* Versailles, France, 1970, Paper NC 2.3, Elsevier Publishing Co., Amsterdam.

3 Hollands, K. G. T., "Natural Convection in Horizontal Thin-Walled Honeycomb Panels," JOURNAL OF HEAT TRANSFER, TRANS. ASME, Series C, Vol. 95, 1973, pp. 439–444.

4 Kent, A. C., and Bowyer, J. M., "Thermal Convection in Air of Small Cells Heated From Below," *Ind. Eng. Chem. Fundam.,* Vol. 11, No. 3, 1972, pp. 319–323.

5 Edwards, D. K., and Sun, W. M., "Effect of Wall Radiation on Thermal Instability in a Vertical Cylinder," *International Journal of Heat and Mass Transfer,* Vol. 14, 1971, pp. 15–18.

6 Catton, Ivan, "Effect of Wall Conduction on the Stability of a Fluid in a Rectangular Region Heated From Below," JOURNAL OF HEAT TRANSFER, TRANS. ASME, Series C, Vol. 94, 1972, pp. 446–452.

7 Buchberg, H., Catton, Ivan, and Edwards, D. K., "Natural Convection in Enclosed Air Spaces A Review of Application to Solar Energy, Collection," JOURNAL OF HEAT TRANSFER, TRANS. ASME, SERIES C, Vol. 98, 2, 1976, pp. 182–188.

8 Sun, W. M., "Effect of Arbitrary Wall Conduction and Radiation on Free Convection in a Cylinder," PhD thesis, University of California, Los Angeles, 1970.

9 Charters, W. W. S., and Peterson, L. F., "Free Convection Suppression Using Honeycomb Cellular Materials," *Solar Energy,* Vol. 13, 1972, pp. 353–361.

10 Chun, K. R., and Crandall, W. E., "Effect of Mylar Honeycomb Layer on Solar Collector Performance," ASME Paper No. 74-WA/HT-11, presented at Winter Annual Meeting, N.Y., 1974.

11 Edwards, D. K., Arnold, J. N., Catton, I., "End Clearance Effects on Rectangular-Honeycomb Solar Collectors," paper presented at the meeting, ISES 75, Los Angeles, Calif., July 28–Aug. 1, 1975.

12 Hollands, K. G. T., and Konicek, L., "Experimental Study of the Stability of Differentially Heated Inclined Air Layers," *International Journal of Heat and Mass Transfer,* Vol. 16, 1973, pp. 1467–1476.

13 Hollands, K. G. T., Unny, T. E., Raithby, G. D., and Konicek, L., "Free Convective Heat Transfer Across Inclined Air Layers," JOURNAL OF HEAT TRANSFER, TRANS. ASME, Series C, Vol. 98, No. 2, 1976, pp. 189–193.

14 Cane, R. L. D., "Free Convection in Inclined Air Layers Constrained by a Square-Celled Honeycomb," MASc thesis, Department of Mechanical Engineer, University of Waterloo, Waterloo, Ontario, Canada, 1976.

15 Raithby, G. D., Hollands, K. G. T., and Unny, T. E., "Free Convection Heat Transfer Across Fluid Layers of Large Aspect Ratios," ASME Paper No. 76-HT-37, presented at the National Heat Transfer Conference, ASME AIChE, St. Louis, Aug. 8–11, 1976.

16 Rajaram, S., "Numerical Study of Free Convective Heat Transfer Across Rectangular Cells," MASc thesis, Department of Mechanical Engineering, University of Waterloo, Waterloo, Ontario, Canada, 1976.

17 Heitz, W. L., and Westwater, J. W., "Critical Rayleigh Numbers for Natural Convection of Water Confined in Square Cells With L/D From .5 to 8," JOURNAL OF HEAT TRANSFER, TRANS. ASME, Series C, Vol. 93, 1971, pp. 188–195;, (Discussion by D. K. Edwards.)

18 Hart, J. E., "Stability of Thin Non-Rotating Hadley Circulations," *J. Atmos. Sci.,* Vol. 29, No. 4, 1972, pp. 687–697.

19 Edwards, D. K., and Sun, W. M., "Prediction of the Onset of Natural Convection in Rectangular Honeycomb Structures," Paper 7/62, 1970 International Solar Energy Society Conference, published by the Australian and New Zealand Section of the Society, 191 Royal Parade, Parkville, Victoria 3052.

20 Hollands, K. G. T., "The Use of Honeycomb Devices in Flat-Plate Solar Collectors," *Solar Energy,* Vol. 9, No. 3, 1965, pp. 159–164.

21 Hanson, D., and Bernier, G. A., "Thermal Conductivity of Polyethylene-The Effect of Crystal Size, Density and Orientation," *Polymer Engineering and Science,* Vol. 12, No. 3, 1972, pp. 204–208.

N. Seki
Professor.

S. Fukusako
Asst. Professor.

M. Sugawara
Assistant.

Department of Mechanical Engineering,
Hokkaido University,
Sapporo, Japan

A Criterion of Onset of Free Convection in a Horizontal Melted Water Layer With Free Surface

The problem considered in this paper is the determination of the Rayleigh number marking the onset of free convection in a horizontal melted layer of ice heated from above under uniform radiant heat flux. In this analysis, linear perturbation techniques are used to derive a sixth-order differential equation subject to hydrodynamic and thermal boundary conditions. The series-solution method is utilized to obtain an eigenvalue equation for the case where the lower surface (ice surface) is kept at 0°C and the upper free surface is subjected to the general thermal conditions. An experimental determination of the onset of free convection, when the heat transfer mode changes from conduction to convection, is obtained from the fact that the temperature distribution in a melted water layer starts to deviate from its linear profile. At the same time, a peculiar variational inflection of the water-surface temperature occurs. From the present investigation, it can be demonstrated both analytically and experimentally that the critical Rayleigh number $\overline{Ra}_c$ in a horizontal melted water layer with a density inversion is dependent on the free water-surface temperature T_2 for $T_2 < 8°C$, while $\overline{Ra}_c$ for $T_2 \cong 8°C$ is independent of T_2.

Introduction

In a horizontal melted layer of ice heated from above under constant wall temperature, the free convection can take place if the Rayleigh number exceeds its critical value resulting from a peculiar characteristic of water having its density inversion at 4°C. It is well recognized that the convection has a considerable effect on the melting rate of ice.

Boger and Westwater [1][1] investigated the effect of free convection on melting and indicated that the critical Rayleigh number, corresponding to the onset of free convection in the aforementioned layer, was about 1700. Yen and Galea [2] treated the same problem and showed that the critical Rayleigh number for water was not a single value as for common fluids having monotonic relationship of density, but varied with the temperature of the upper rigid surface. Sun, et al. [3] presented analytical results for the effect of density inversion of water on hydrodynamic instability in a melted layer with a rigid or free upper surface (without surface tension). He pointed out that their experimental values of the critical Rayleigh number for the former were in good agreement with the results predicted analytically. Recently, Tankin and Farhadieh [4] studied the role of free convection on the formation of ice by using a Mach-Zehnder interferometer and found that the critical Rayleigh number for the case of freezing from below was about 480. Seki, et al. [5] presented their experimental investigation pertaining to the aforementioned system such as melting ice heated from above and reported that the critical Rayleigh number was about 500 for higher temperature of rigid surface than about 9°C. Katto and Iwanaga [6] demonstrated that the critical Rayleigh number predicted experimentally by them and Seki, et al. [5] agreed well with that given by a modification of the analytical results obtained by Sun, et al. [3].

On the other hand, a somewhat more complicated situation arises if a horizontal melted layer of ice is heated from above under constant radiant heat flux. Such a case is schematically illustrated in Fig. 1. Fig. 1(a) shows a typical phenomenon in a horizontal melted layer whose upper free-surface temperature is higher than 4°C. In such a case, the fluid density in the layer increases at first downward from the free surface and then decreases. The fluid layer, therefore, consists of a potentially stable and a potentially unstable layers. As will be seen in Fig. 1(b), if the free-surface temperature is in the range of 0–4°C, the entire liquid layer is potentially unstable due to the buoyancy force existing in the layer. In the case of Fig. 1(a), the upper boundary effects, that is, the hydrodynamic boundary conditions including surface tension and the thermal boundary condition are only felt indirectly

[1] Numbers in brackets designate References at end of paper.

Contributed by the Heat Transfer Division for publication in the JOURNAL OF HEAT TRANSFER. Manuscript received by The Heat Transfer Division March 3, 1976.

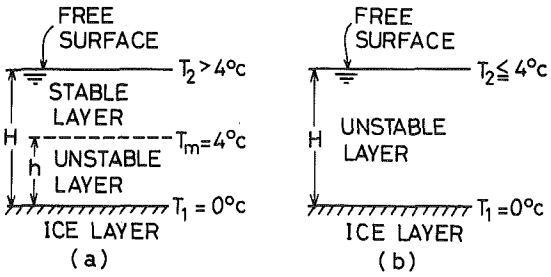

Fig. 1 Illustration of the effect of maximum density in a melted water layer

by the potentially unstable layer. And if the thickness of the stable layer decreases relative to that of the unstable one, it is obvious that these effects would become more significant. This then corresponds to an increased effect of surface boundary conditions on the onset of free convection in the unstable layer. But, in the case of Fig. 1(*b*), these effects are felt directly by the potentially unstable liquid layer. Thus, the problem of the onset of free convection in such a system may be somewhat complicated.

Sugawara, et al. [7] presented an experimental investigation pertaining to the aforementioned system and reported that the critical Rayleigh number $\overline{\mathrm{Ra}}_c$ for the case of Fig. 1(*a*) was about 500 for T_2 ranging from 9 to 65°C; that is, the thickness of the potentially stable liquid layer is relatively large. Recently, Sparrow, et al. [15] predicted analytically the onset of convective motion in a horizontal melted liquid layer formed from below by using a nonlinear rest-state temperature distribution in the layer. They pointed out that the variation of the critical Rayleigh number was distinctly affected by the convective boundary condition (i.e., the value of Biot number) rather than the rest-state temperature distribution, while the effect of Stefan number on the critical Rayleigh number was small. Also they recasted their stability results in terms of parameters which was a priori prescribable for the physical system.

The purpose of this study is to determine the critical Rayleigh number marking the onset of free convection in a horizontal melted layer of ice heated from above. This problem, which incorporates both a maximum density at 4°C and upper free surface, differs distinctly from the other instability problems. Therefore, the discussions in the present investigation are mainly focused on correlating the critical Rayleigh number with the effects of the density inversion and the surface tension of the free surface (i.e., Marangoni number). In the present analysis, linear perturbation techniques are utilized to derive a sixth-order differential equation subject to the hydrodynamic and the thermal boundary conditions. Experimental determinations of the critical Rayleigh number $\overline{\mathrm{Ra}}_c$ are also made and compared with the analytical results predicted for the free-surface temperature ranged from 1.5 to 12°C.

Fundamental Equations and Boundary Conditions

Perturbation Equations. The system of coordinates is shown in Fig. 2. Distance from the lower rigid surface is denoted by z'; $z' = 0$ corresponds to the lower rigid surface and $z' = H$ corresponds to the upper free surface. The coordinate axes x' and y' lie in a horizontal plane and the horizontal extent of the water layer is assumed to be sufficiently great so that the edge effects may be neglected. Under steady-state quiescent conditions, the temperature distribution in the water layer may be considered to be linear as shown in Fig. 2.

Perturbation equations can be obtained in the similar manner to that by Sparrow, et al. [15] as following. Introducing the dimensionless quantities $(x, y, z) = (x', y', z')/H$, $(u, v, w) = (u', v', w')H/\nu$, $\theta = \theta'/(T_2 - T_1)$, $t = t'\kappa/H^2$ and Prandtl number $\mathrm{Pr} = \nu/\kappa$, the linearized equations for perturbation components are obtained in the following dimensionless forms after eliminating pressure terms.

$$\frac{1}{\mathrm{Pr}}\frac{\partial}{\partial t}\nabla^2 w = -\mathrm{Gr}(1 + \delta_1 z + \delta_2 z^2)\nabla_1^2\theta + \nabla^4 w \tag{1}$$

$$\frac{\partial\theta}{\partial t} + \mathrm{Pr}\, w\frac{\partial T_0}{\partial z} = \nabla^2\theta \tag{2}$$

where $\nabla_1^2 = (\partial^2/\partial x^2 + \partial^2/\partial y^2)$ and a density-temperature relationship within the temperature ranges concerned is assumed to be

$$\rho = \rho_m\{1 - \gamma_1(T - T_m)^2 - \gamma_2(T - T_m)^3\} \tag{3}$$

The Grashof number Gr, coefficients δ_1 and δ_2 are defined as

$$\mathrm{Gr} = \frac{gH^3(T_2 - T_1)}{\nu^2}2\gamma_1(T_m - T_1)\left\{1 - \frac{3\gamma_2}{2\gamma_1}(T_m - T_1)\right\} \tag{4}$$

$$\left.\begin{aligned}\delta_1 &= -\frac{T_2 - T_1}{T_m - T_1}\left\{1 - \frac{3\gamma_2}{\gamma_1}(T_m - T_1)\right\}\Big/\left\{1 - \frac{3\gamma_2}{2\gamma_1}(T_m - T_1)\right\}\\ \delta_2 &= -\left(\frac{T_2 - T_1}{T_m - T_1}\right)^2\frac{3\gamma_2}{2\gamma_1}(T_m - T_1)\Big/\left\{1 - \frac{3\gamma_2}{2\gamma_1}(T_m - T_1)\right\}\end{aligned}\right\} \tag{5}$$

It should be noted that equations (1) and (2) are obtained under an assumption that all of physical properties except ρ related to body force are independent of temperature. Furthermore, equation (4) is derived from the fact that ρ_m/ρ_0 can be stated as unity in the range of temperature concerned, where ρ_0 is density at a reference temperature and ρ_m density at 4°C.

One considers an arbitrary disturbance in terms of normal modes, supposing the perturbations w and θ have the following forms

$$w = W(z)\exp\{i(a_x x + a_y y) + \phi t\} \tag{6}$$

$$\theta = \Theta(z)\exp\{i(a_x x + a_y y) + \phi t\} \tag{7}$$

Nomenclature

a = wave number
Bi = Biot number, $\alpha H/\lambda$
C = constant
D = operator
g = acceleration of gravity
Gr = Grashof number, defined in equation (4)
h = depth of potentially unstable layer
H = depth of melted water layer
Ma = Marangoni number, $\sigma_0\Phi(T_2 - T_1)H/(\rho\nu\kappa)$
p' = perturbation pressure
p_0 = static pressure
P = pressure
Pr = Prandtl number, ν/κ
Ra = Rayleigh number, Pr·Gr
Ra_c = critical Rayleigh number
$\overline{\mathrm{Ra}}_c$ = modified critical Rayleigh number, defined in equations (16) and (17)
t = nondimensional time
t' = time
T = temperature
T_0 = steady-state temperature
T_1 = temperature of lower surface
T_2 = temperature of upper free surface
T_{2c} = temperature of upper free surface at critical time
T_m = temperature at maximum density, 4°C
u', v', w' = velocity components
u, v, w = nondimensional velocity components
x', y', z' = coordinates
x, y, z = nondimensional coordinates
α = heat transfer coefficient, defined in equation (14)
β = coefficient of thermal expansion (absolute value)
θ' = perturbation temperature
κ = thermal diffusivity
λ = thermal conductivity
ν = kinematic viscosity
ρ = density
σ_0 = surface tension of water at 0°C

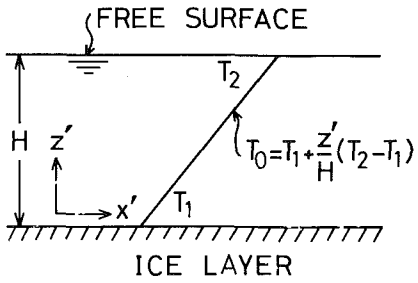

Fig. 2 The system of coordinates

where $a = (a_x^2 + a_y^2)^{1/2}$ is the wave number of the disturbance and ϕ is a constant. Equations (1) and (2) now become

$$\{(D^2 - a^2)^2 - \phi(D^2 - a^2)/\mathrm{Pr}\}W = -\mathrm{Gr}(1 + \delta_1 z + \delta_2 z^2)a^2\Theta \quad (8)$$

$$\{(D^2 - a^2) - \phi\}\Theta = \mathrm{Pr}(\partial T_0/\partial z)W \quad (9)$$

where the operator D denotes d/dz. Considering the temperature profile in steady state to be linear, equations (8) and (9) can be combined together to yield,

$$\{(D^2 - a^2)^2 - (\phi/\mathrm{Pr})(D^2 - a^2)\}\{(D^2 - a^2) - \phi\}\Theta = -\mathrm{Ra}(1 + \delta_1 z + \delta_2 z^2)a^2\Theta \quad (10)$$

where Ra = Pr·Gr. It has been shown by Pellew and Southwell [8] that the threshold of instability is marked by $\phi = 0$. The thus-reduced form of equation (10) is an ordinary differential equation for the perturbation temperature Θ.

Boundary Conditions. The lower bounding surface of the water layer is assumed to be a rigid perfect conductor because the ice layer is kept at 0°C. On the surface, all the velocity components vanish identically. Moreover, the surface temperature would be unperturbed by any flow or temperature disturbance in the liquid layer. Therefore, one can easily obtain the following conditions for Θ after Sparrow, et al. [15].

$$\Theta = 0, \quad D^2\Theta = 0 \quad \text{and} \quad D(D^2 - a^2)\Theta = 0 \quad (11)$$

On the other hand, the conditions of the upper free surface become somewhat complicated. It can be pointed out after Kobayashi [10] that the appropriate conditions at the upper free surface taking into account the effect of the surface tension on normal stress condition are

$$\left.\begin{aligned} w' = 0, \quad & \mu(\partial w'/\partial x' + \partial u'/\partial z') = -\sigma_0\Phi\partial T/\partial x' \\ \text{and} \quad & \mu(\partial v'/\partial z' + \partial w'/\partial y') = -\sigma_0\Phi\partial T/\partial y' \end{aligned}\right\} \quad (12)$$

where σ_0 is the surface tension of water at 0°C and Φ is the coefficient in the $\sigma - T$ relation expanded to the first order in powers of T. Since there have been many discussions so far by Sparrow, et al. [9], Kobayashi [10], and Nield [11] about the general thermal boundary conditions, the detailed procedure will not be repeated here. For the present system, the conditions on Θ may be finally taken as

$$(D^2 - a^2)\Theta = 0, \quad D^2(D^2 - a^2)\Theta = -\mathrm{Ma}a^2\Theta \quad \text{and} \quad D\Theta + \mathrm{Bi}\Theta = 0 \quad (13)$$

where $\mathrm{Ma} = \sigma_0\Phi(T_2 - T_1)H/(\rho\nu\kappa)$ is the Marangoni number and $\mathrm{Bi} = \alpha H/\lambda$ the Biot number, where α is the heat transfer coefficient. For the present system the heat balance at the free surface yields

$$\lambda\left.\frac{\partial T}{\partial z'}\right|_H = q + \alpha|T_\infty - T|_H \quad (14)$$

where T_∞ is environmental temperature, q is heat flux aside from convection, e.g., radiative heat flux reaching the surface, and λ denotes the thermal conductivity of water. Therefore, it might be expected that the value of Biot number ($= \alpha H/\lambda$) ranges from 0 to ∞ in the present study.

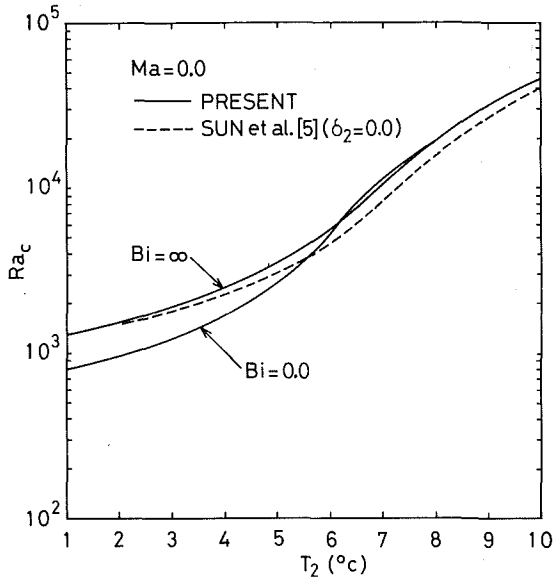

Fig. 3 Critical Rayleigh number

Solution of the Perturbation Equation

Method of Solution. Solution of equation (10) must be subjected to the boundary conditions (11) and (13). In view of the complexity of the equations (11) and (13) involving higher derivatives of Θ, a numerical technique originally developed by Sparrow, et al. [9] is employed. A general solution of equation (10) with $\phi = 0$ may be constructed in power series of z, whose constants are to be determined from the boundary conditions. Numerical computations to find the critical Rayleigh number Ra_c are carried out with the aid of the FACOM 230-75 Digital Computer at the Computer Center of Hokkaido University.

Numerical Results and Discussions. For the present model as $T_1 = 0$°C, the coefficients δ_1 and δ_2 in equation (5) can be rewritten as

$$\delta_1 = -T_2(1 - C)/4 \quad \text{and} \quad \delta_2 = -(T_2/4)^2 C \quad (15)$$

where $C = 3\gamma_2/2\gamma_1(T_m - T_1)/\{1 - 3\gamma_2/2\gamma_1\cdot(T_m - T_1)\}$. Therefore, δ_1 and δ_2 can be determined as each function of T_2, utilizing a set of γ_1 and γ_2 after Yen [13]; $\gamma_1 = 0.793953 \times 10^{-5}$°C^{-2}, $\gamma_2 = -0.655908 \times 10^{-7}$°C^{-3}. Thus, the numerical calculation could be carried out using the aforementioned method of solution.

In Fig. 3, the predicted Rayleigh numbers marking the onset of free convection are presented graphically in a form of Ra_c versus T_2 for Ma = 0. The previous result (dotted line) by Sun, et al. [5] is shown along with the present results. In this figure, there are two solid lines; the one for Bi = 0 corresponds to a fixed heat flux and the other for Bi = ∞ to a fixed temperature at the free surface. Detailed calculated values for these results are listed in Table 1. On the first inspection of this figure, it will be seen that for a given Bi, Ra_c increases monotonically with increasing T_2, but its sensitivity to Bi varies for a given T_2. Furthermore, as can be seen in Fig. 3, the predicted curves of Ra_c for Bi = 0 and Bi = ∞ intersect each other at about $T_2 = 6.2$°C. One can find a similar result to the aforementioned one in the prediction of Ra_c by Sun, et al. [3], which has not physically been understood in the present time.

Sparrow, et al. [9] investigated the effects of the thermal boundary conditions at the surface on the onset of free convection for common fluids and found that the critical Rayleigh number was greatest under the condition of fixed free-surface temperature and decreases monotonically as the condition of fixed heat flux is approached. In the present system of fluid with density inversion, the effect of Bi on Ra_c is indicated through the plotted results of $\mathrm{Ra}_c/(\mathrm{Ra}_c)_{\mathrm{Bi}=0}$ versus

Table 1 Numerical values of the critical Rayleigh numbers

Bi = 0			Bi = ∞		
T_2 °C	a	Ra_c	T_2 °C	a	Ra_c
1	2.091	791.970	1	2.684	1280.742
2	2.100	966.713	2	2.687	1526.506
3	2.115	1234.006	3	2.692	1881.140
4	2.114	1691.229	4	2.703	2434.750
5	2.222	2632.157	5	2.732	3406.985
6	2.582	5221.343	6	2.830	5450.224
7	3.571	11365.792	7	3.282	10473.549
8	4.171	19664.021	8	4.065	19303.566
9	4.592	30897.616	9	4.595	30930.386
10	5.087	46772.996	10	5.091	46770.041

Bi for various value of T_2 for the case of Ma = 0. As will be seen in Fig. 4, it is clear that the effect of thermal boundary condition is greatest under the condition of fixed free-surface temperature and smallest under the condition of fixed heat flux. But the sensitivity to Bi is considerably varied depending on T_2, that is, it decreases with increasing T_2. This may be due to the fact that the upper boundary effect becomes less significant as the thickness of stable layer increases.

Pearson [11], Nield [12], Kobayashi [10], and Smith [14] studied the effect of the surface tension on the onset of free convection and reported that the surface tension motivated the onset of instability, so that the critical Rayleigh number decreased with increasing effect of surface tension. Moreover, Nield [12] and Kobayashi [10] concluded that this effect depended considerably on the thermal boundary conditions and was greatest for Bi = 0, while vanishing for Bi = ∞. Fig. 5 indicates the aforementioned effect on the present system under consideration through the plotting of predicted results of $Ra_c/(Ra_c)_{Ma=0}$ versus Ma for various values of Bi for the case of T_2 = 4°C. As can be seen in this figure, it should be noted that the effect of Ma on Ra_c is opposite to that predicted by previous investigators [12],[2] [10]. This discrepancy may be understood by the following fact. Under the present physical system with free convection, which is caused by the density inversion in the melted water layer where the temperature of the free surface (T_2) is higher than that of the bottom surface (T_1 = 0), the direction of the surface tension is opposite to that of convective motion at the upper free surface. On the other hand, in the previous investigations with free convection, which is caused by a monotonic density-temperature relationship in a liquid layer where $T_2 < T_1$, the direction of surface tension is the same as that of convective motion at the upper free surface. Furthermore, the effect of thermal boundary condition at the free surface on the onset of free convection for a given Ma is greatest for Bi = 0 and smallest for Bi = ∞, which is very close to the results for common fluids. $Ra_c/(Ra_c)_{Ma=0}$ reaches about 3.67 for Ma = 10000 in the case of Bi = 0.

The dependence of $Ra_c/(Ra_c)_{Ma=0}$ on Ma is demonstrated in Fig. 6 for particular values of T_2 for the case of Bi = 0. It will be seen that $Ra_c/(Ra_c)_{Ma=0}$ increases monotonically with increasing Ma and is most sensitive to Ma in the range of 100–1000. However, there is a marked difference in the effect of Ma on the onset of free convection for varying T_2. For $T_2 > 4$°C, the thickness of the potentially stable layer in the melted water layer increases as T_2 increases. Therefore,

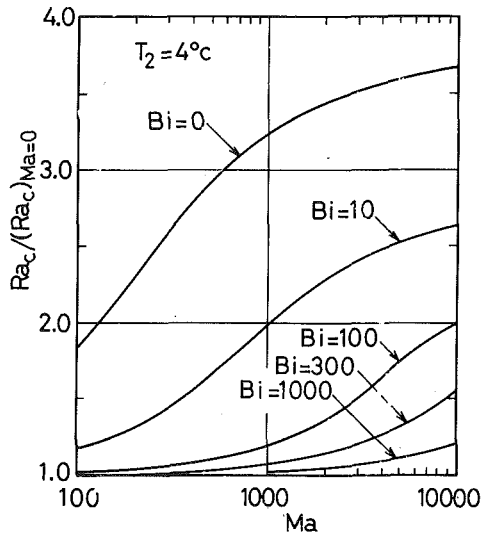

Fig. 5 $Ra_c/(Ra_c)_{Ma=0}$ versus Ma in the case of T_2 = 4°C.

[2] Nield [12] indicated a possibility that the critical Rayleigh number increased due to the negative Marangoni number, which was applicable to a layer of liquid adhering to a ceiling which was cooler than the air below, or to a liquid with negative coefficient of volume expansion cooled from below.

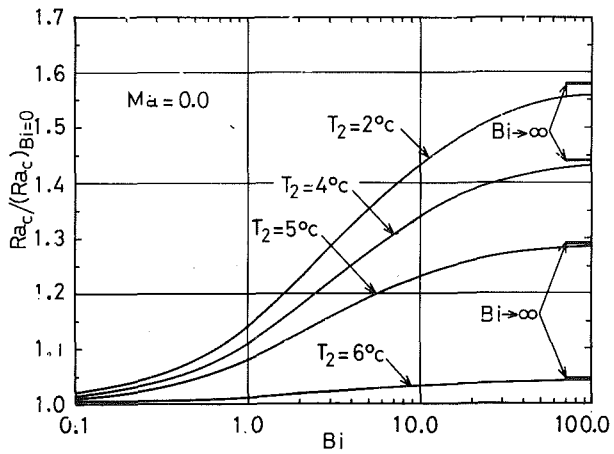

Fig. 4 $Ra_c/(Ra_c)_{Bi=0}$ versus Bi in the case of Ma = 0

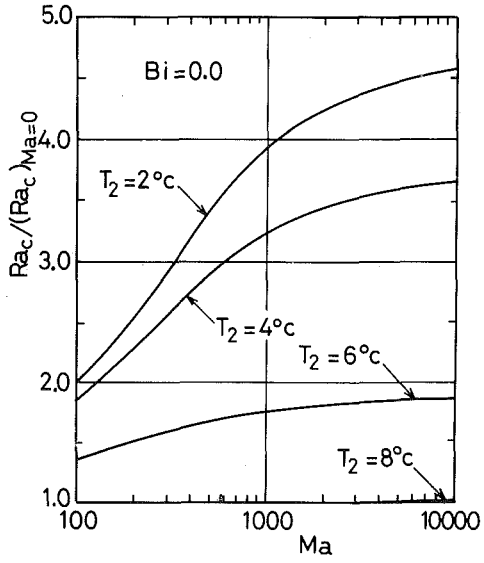

Fig. 6 $Ra_c/(Ra_c)_{Ma=0}$ versus Ma in the case of Bi = 0

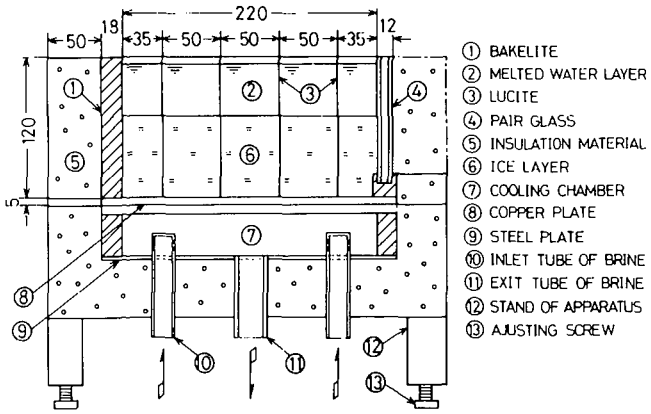

Fig. 7 A vertical cross-sectional schematic view of the experimental apparatus

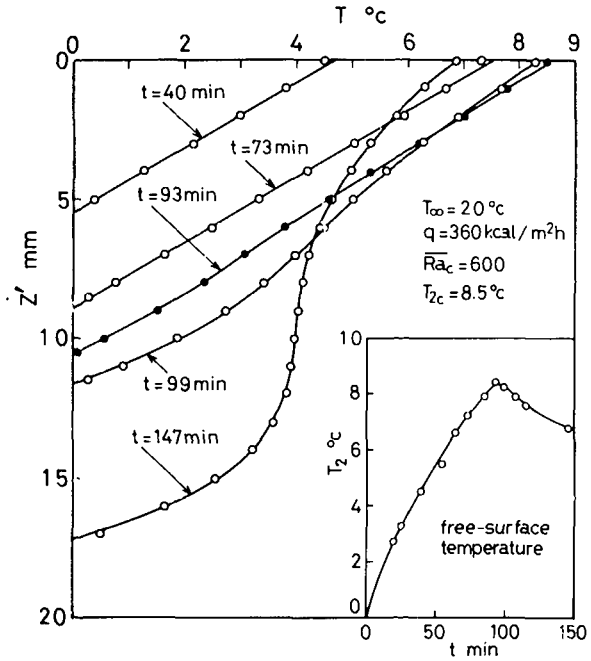

Fig. 8 Temperature-distribution change in a melted layer and temperature change at the free surface with time proceeding

it may be understood that the thermal boundary condition of the free surface becomes less significant as T_2 increases, which results in the decreased effect of Ma on the onset of free convection. Thus, of interest is the fact that the effect of Marangoni number Ma on the onset of free convection can be considerably evaluated even in the range of $T_2 > 4°C$, as will be seen in Fig. 6. This behavior may be due to the fact that the upward motion of free convection in the unstable layer exceeds the 4°C isotherm, that is, the upward current penetrates the 4°C isotherm and stretches for a considerable distance into the upper stable layer as pointed out by [4].

Experiments and Procedures

The experimental procedures are described in detail elsewhere [7]. A vertical cross-sectional schematic view of the experimental apparatus is shown in Fig. 7. The testing ice is surrounded by two concentric, square partition walls, 150 × 150 mm and 220 × 220 mm. The walls of the concentric partition wall are made of lucite plate. The 50 mm annulus of ice between the testing ice and the inner partition wall and the 35-mm annulus of ice between the inner and the outer partition wall are each utilized as guard region for minimizing heat exchange with surroundings. Insulating material, styrofoam of 50 mm in thickness surrounding the outside of the test section, insure that the heat flow in the melted layer is kept in one-dimensional and downward throughout the run. The 19 infrared lamps of 100V-375W as heat sources are so arranged to radiate uniformly onto the surface of the testing ice, to maintain the condition of uniform heat flux at the free surface of melted water layer. The radiation heat fluxes are calibrated by using a radiation thermometer prior to the run. A thermocouple probe, the frame of which consisted of two separated bamboo arms of about 0.3 mm in diameter, is used as a measuring instrument of the temperature distribution in the melted water layer. A C-C thermocouple, 0.05 mm in diameter with 20-mm length, is stretched horizontally by the help of both edges of the bamboo arms. Thus, it may be expected that this minimizes heat loss from the thermocouples. Moreover, this probe is connected to a traversing instrument with a precision dial indicator.

During each run, the thermocouple-probe is inserted into the melted water layer near the upper free surface. To obtain the temperature distribution the probe is moved slowly down to measure the temperature of every desired water depth after marking the temperature of the water surface. A relation between temperature and depth in the melted water layer could be thus obtained at the same time. Bubble-free, homogeneous ice from the distilled water is prepared for the melting experiment and kept uniformly at 0°C in a controlled cold room before running.

The criterion of the onset of free convection in the melted layer, which corresponds to the critical Rayleigh number, is experimentally determined during melting of ice. Fig. 8 shows a typical experimental result of temperature-distribution change in the layer and that of the temperature change at the free surface with time proceeding. The thickness of the melted water layer thus increases with time proceeding, therefore, it is not constant in all of the runs. Furthermore, strictly speaking, the state of heat transfer in the layer may not be in steady state. However, it is clear from the figure that the temperature distribution in the melted layer remains almost linear during a short period just after the start of melting, which means that the system concerned remains in quasi-steady state when the critical Rayleigh number is determined, but it suddenly starts to deviate from such a linear profile at a critical time when the temperature variation of the free surface has its refracting point, as can be seen in Fig. 8. It might be expected that these phenomena mean the fact that the onset of free convection in the layer has just occurred at that time. The critical time of the onset of free convection is thus decided and the critical Rayleigh number is evaluated after measuring both the thickness of unstable layer and the temperature difference between upper and bottom surfaces.

On the other hand, Sparrow, et al. [15] indicated that the rest-state temperature profile departed more and more from a straight one as Stefan number increased and that the critical Rayleigh number was not so much affected by the values of Stefan number but significantly affected by those of Biot number. Therefore, the present analytical assumption that the rest-state temperature profile is linear and all of velocity components vanish identically at the interface may be quite adequate because of Stefan number subjected to ice-to-water phase change being the degree of 10^{-2}, the order of which suggests the melting velocity is very slow.

The flatness of ice surface is also frequently evaluated using a small wooden probe connected to the traversing instrument with a precision dial indicator during each of the runs. It is ascertained that the flatness of the ice surface is within ±0.1 mm in deviation before the onset of free convection in the melted layer.

Experimental Results and Discussions

Modified Critical Rayleigh Number $\overline{Ra}_c$. The classical stability criterion of the onset of free convection in a horizontal layer of common fluid heated from below is experimentally expressed in terms of $Ra = g\beta(T_2 - T_1)H^3/(\nu\kappa)$ in which the values of all properties are

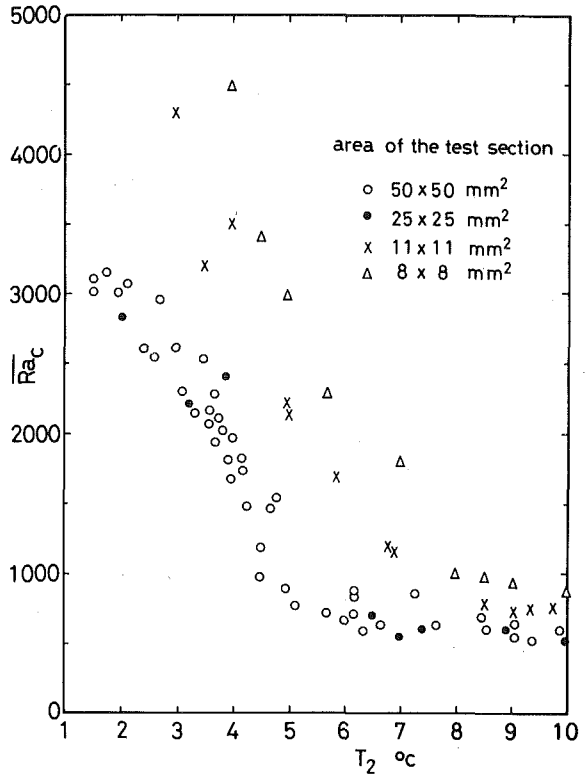

Fig. 9 Effect of container side walls on $\overline{Ra_c}$

evaluated at the arithmetic mean value of T_1 and T_2. But under the present study for $T_1 = 0°C$ and $T_2 = 8°C$, if the value of β is evaluated at the arithmetic mean temperature, it is obvious that $Ra_c = 0$. This violates the classical stability criterion. So that, in the present study, the modified critical Rayleigh number is defined as

$$\overline{Ra_c} = g\beta(T_m - T_1)h^3/(\nu\kappa) \quad \text{for } T_2 > 4°C \tag{16}$$

$$\overline{Ra_c} = g\beta(T_2 - T_1)H^3/(\nu\kappa) \quad \text{for } T_2 \leqq 4°C \tag{17}$$

where β, ν, and κ are each evaluated at 2°C in equation (16) and at the arithmetic mean temperature in equation (17). Such a definition as equation (16) is also made by Sugawara, et al. [7] and Katto and Iwanaga [6]. Therefore, the critical Rayleigh number thus defined and that adopted in the present analysis could be connected with each other to yield the following relations,

$$\overline{Ra_c} = \frac{Ra_c}{2}\left\{\frac{T_m - T_1}{T_2 - T_1}\right\}^4 \Big/ \left\{1 - \frac{3\gamma_2}{2\gamma_1}(T_m - T_1)\right\} \quad \text{for } T_2 > 4°C \tag{18}$$

$$\overline{Ra_c} = \frac{Ra_c}{2}\left\{1 + \frac{T_m - T_2}{T_m - T_1}\right\} \Big/ \left\{1 - \frac{3\gamma_2}{2\gamma_1}(T_m - T_1)\right\} \quad \text{for } T_2 \leqq 4°C \tag{19}$$

Examination of Possible Effect of Container Side Walls. Fig. 9 shows the experimental results indicating the relation between $\overline{Ra_c}$ and T_2 for various test containers having 50×50 mm^2, 25×25 mm^2, 11×11 mm^2, and 8×8 mm^2 in surface area, respectively. It can be seen from this figure that there is little effect of the side walls on the evaluation of $\overline{Ra_c}$ in case of the surface area being larger than 25×25 mm^2. All of experimental results in this paper, therefore, are obtained by using a container having 50×50 mm^2 in surface area through all of the runs.

Comparison Between Experimental and Analytical Results. The experimental values of the Marangoni number at the onset of free convection are utilized to evaluate the critical Rayleigh number analytically. Detailed numerical results are summarized in Table 2. Fig. 10 indicates a graphical comparison between the experimental and

Table 2 Numerical values of the critical Rayleigh numbers

T_2 °C	Ma	a	Ra_c	$\overline{Ra_c}$
1	7219.2	4.062	3828.942	3192.099
2	11731.6	4.070	4429.718	3165.387
3	15633.2	4.069	5184.884	3087.512
4	19232.6	4.065	6202.521	2954.798
4.5	22254.6	4.064	6861.245	2040.575
5	23010.5	4.063	7654.225	1493.553
6	30085.3	4.069	9868.940	928.678
7	38946.1	4.105	13513.125	686.378
8	47806.5	4.239	19936.553	593.594
10	78991.5	5.097	47107.095	574.494
12	110450.5	6.915	89782.844	528.041

the analytical $\overline{Ra_c}$ in the case of uniform heat flux (Bi = 0). Previous results by Sun, et al. [5] and Katto and Iwanaga [6] are shown together with the present predicted results. As will be seen from Figs. 3 and 10, it seems that Ra_c increases while $\overline{Ra_c}$ decreases and the values of Ra_c differ from those of $\overline{Ra_c}$. Such a discrepancy may be due to the different physical definition between Ra_c and $\overline{Ra_c}$.

The appearance of refraction of predicted $\overline{Ra_c}$ at 4°C in Fig. 10 is considered to be resulted from the different mathematical definition of $\overline{Ra_c}$ between $T_2 \leqq 4°C$ and $T_2 > 4°C$, while an abrupt dropping in predicted $\overline{Ra_c}$ for $T_2 > 4°C$ may physically indicate the fact that the boundary conditions concerning the surface tension and the heat transfer at the free surface become less significant as T_2 increases, as pointed out in the following illustration. The surface-tension effect at the free surface is scarcely felt by the potentially unstable layer for $T_2 \geqq 8°C$ because of the considerable thickness of the stable layer. Therefore, it can be understood in Fig. 10 that $\overline{Ra_c}$ is nearly uniform in this range. However, as can be seen in this figure, the critical Ray-

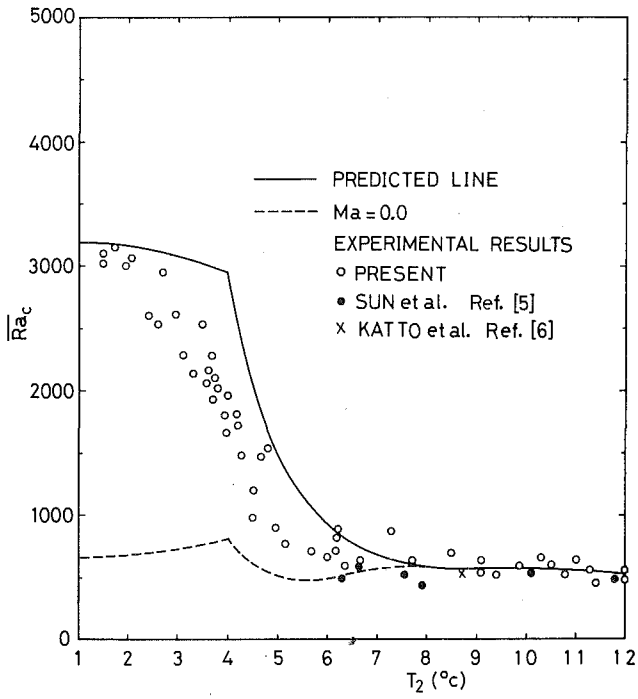

Fig. 10 Comparison of experimental and analytical results

leigh number for $T_2 < 8°C$ increases surprisingly as T_2 decreases. It is obvious that the role of the surface tension at the free surface would become more significant on the onset of free convection as the thickness of the stable layer decreases. So that, it can be pointed out that if the surface temperature of a melted water layer decreases, the thickness of the stable layer decreases, which corresponds to the increased effect of surface tension on the onset of free convection.

The discrepancy between the predicted results and the experimental data may be due to the following several assumptions adopted in the present analysis: (*a*) the free-surface deformation accompanying free convection, as indicated by Kayser and Berg [16], is assumed to be negligible ($w = 0$); (*b*) the predicted results are obtained under the condition of a fixed heat flux ($Bi = 0$); (*c*) the possible condensation or evaporation at the free surface is assumed to be negligible.

In Fig. 10, however, it is indicated that the experimental results of $\overline{Ra}_c$ are in good agreement with the predicted ones for $T_2 \geqq 8°C$. This may be due to the fact that in this temperature region the upper conditions are little sensitive to the potentially unstable layer, namely, the effects of the thermal and the hydrodynamic conditions at the free surface on the onset of free convection in a horizontal melted water layer almost disappears for $T_2 \geqq 8°C$.

Conclusions

1 For $T_2 < 8°C$, the criterion of hydrodynamic stability in a melted water layer is found to be dependent on T_2 and increases due to the surface tension at the free surface as T_2 decreases, which means the thickness of the stable layer above the unstable one decreases. On the other hand, for $T_2 \geqq 8°C$, the criterion is found to be independent of T_2 and the present analytical results approaches asymptotically a limiting value of $\overline{Ra}_c \simeq 500$ predicted by Sun, et al. [5] and Katto and Iwanaga [6] experimentally.

2 The present analytical results of $\overline{Ra}_c$ predicted by taking into account both the hydrodynamic condition including the effect of surface tension and the thermal boundary one at the free surface of a melted water layer are in good agreement with the experimental ones.

References

1 Boger, D. V., and Westwater, J. W., "Effect of Buoyancy on the Melting and Freezing Process," JOURNAL OF HEAT TRANSFER, TRANS. ASME, Series C, Vol. 89, 1967, pp. 81–89.

2 Yen, Y. C., and Galea, F., "Onset of Convection in a Water Layer Formed Continuously by Melting Ice," *The Physics of Fluids*, Vol. 12, 1969, pp. 509–516.

3 Sun, Z. S., Tien, C., Yen, Y. C., "Thermal Instability of a Horizontal Layer of Liquid with Maximum Density," *AIChE Journal*, Vol. 15, 1969, pp. 910–915.

4 Tankin, R. S., and Farhadieh, R., "Effect of Thermal Convection Currents on Formation of Ice," *International Journal of Heat and Mass Transfer*, Vol. 14, 1971, pp. 953–961.

5 Seki, N., Fukusako, S., and Sugawara, M., "Onset of Convection in a Layer of Water Formed by Melting Ice From Above Rigid Hot Surface," Preprints of JSME–Meeting of Heat Engineering, Paper No. 740–17, 1974, pp. 91–94.

6 Katto, Y., and Iwanaga, Y., "Onset of Natural Convection in a Water Layer With a Upper Stable Layer," Preprints of 12th Japan heat Transfer Symposium, a 311, 1975, pp. 178–180.

7 Sugawara, M., Fukusako, S., and Seki, N., "Experimental Studies of the Melting of a Horizontal Ice Layer," *Bulletin of the JSME*, Vol. 18, 1975, pp. 714–721.

8 Pellew, A., and Southwell, R. V., "On Maintained Convection Motion in a Fluid Heated From Below," *Proc. R. Soc.* [A] 176, 1940, pp. 312–343.

9 Sparrow, E. M., Goldstein, R. J., and Jonsson, V. K., "Thermal Instability in a Horizontal Fluid Layer: Effect of Boundary Conditions and Non-Linear Temperature Profile," *Journal of Fluid Mechanics*, Vol. 18, 1964, pp. 513–528.

10 Kobayashi, R., "Instabilität einer von Unter Erwärten Flüssigkeitsschicht bei Gleichzeitiger Berücksichtigung von Oberflächenspannung und Auftriebskraft," *ZAMP*, Vol. 18, 1967, pp. 845–851.

11 Pearson, J. R. A., "On Convection Cells Induced by Surface Tension," *Journal of Fluid Mechanics*, Vol. 4, 1958, pp. 489–500.

12 Nield, D. A., "Surface Tension and Buoyancy Effects in Cellular Convection," *Journal of Fluid Mechanics*, Vol. 19, 1964, pp. 341–352.

13 Yen, Y. C., "Effects of Density Inversion on Free Convective Heat Transfer in Porous Layer Heated From Below," *Int. J. Heat Mass Transfer*, Vol. 17, 1974, pp. 1349–1356.

14 Smith, K. A., "On Convective Instability Induced by Surface-Tension Gradients," *Journal of Fluid Mechanics*, Vol. 24, 1966, pp. 401–414.

15 Sparrow, E. M., Lee, L., and Shamsundar, N., "Convective Instability in a Melt Layer Heated from Below," JOURNAL OF HEAT TRANSFER, TRANS. ASME, Series C, Vol. 98, 1976, pp. 88–94.

16 Kayser, W. V., and Berg, J. C., "Surface Relief Accompanying Natural Convection in Liquid Pools Heated From Below," *Journal of Fluid Mechanics*, Vol. 57, 1973, pp. 739–752.

I. K. Madni
Asst. Mechanical Engineer,
Department of Applied Science,
Brookhaven National Laboratory,
Upton, N.Y.
Assoc. Mem. ASME

R. H. Pletcher
Assoc. Professor,
Department of Mechanical Engineering and
Engineering Research Institute,
Iowa State University,
Ames, Iowa.
Mem. ASME

Prediction of Turbulent Forced Plumes Issuing Vertically Into Stratified or Uniform Ambients

A finite difference calculation method is used to solve the conservation equations of mass, momentum, and energy in differential form for a buoyant turbulent forced plume discharging vertically into both a uniform and a stratified quiescent ambient. This flow configuration is of interest relative to the discharge of thermal or sewage effluents into the ocean and the discharge of effluents from chimneys and cooling towers into a still atmosphere. The effects buoyancy on the turbulent transport model are discussed. The predictions, including the predicted maximum height of rise for the stratified ambient case, are compared with available experimental data and the results of other prediction methods.

Introduction

Vertical buoyant jets or forced plumes occur in engineering applications related to the discharge of thermal or sewage effluent into oceans or lakes and the discharge of effluents from chimneys and cooling towers into a still atmosphere. In many applications the plume rise is not vertical due to the effects of currents or crosswinds. However, predictions of vertical plumes are useful, since, for atmospheric discharges, the most adverse conditions for plume rise and dispersion are a ground based atmospheric inversion (stable stratification of the atmosphere) accompanied by no crosswind, and ground based inversions usually occur with still air [1].[1] Thus, if the height of rise and other plume properties can be predicted under these limiting conditions, a conservative estimate of the performance of the plume under more general field conditions can be made.

Theoretical analyses in terms of approximate methods for prediction of vertical buoyant jets and plumes in uniform ambients have been mostly integral in nature and date back to Schmidt's work in 1941 [2], which considered the mechanics of convective plumes (pure buoyancy cases, no initial momentum). Rouse, et al. [3] carried out similar work in 1952. They arrived at a theoretical solution for a source of pure buoyancy using an integral method. Morton's [4] analysis included the effect of initial momentum and served as the forerunner for later, more general formulations such as those of Fan [5], Fan and Brooks [6], and Hirst [7]. Numerical treatment of the partial-differential equations governing the vertical plume flow in a uniform ambient by finite-difference methods has been restricted to the work of Trent [8], Trent and Welty [9], and Oosthuizen [10]. No finite-difference analyses to predict the height of rise of plumes in stratified ambients have been observed. Several integral techniques have, however, been proposed [4–6, 11–13].

In the present paper, a finite-difference prediction method for vertical buoyant turbulent jets in both uniform and stratified ambients is described. The effects of buoyancy on the turbulent transport model are discussed. The predictions, including the predicted maximum height of rise for the stratified ambient case, are compared with available experimental data and the results of other prediction methods.

Flow Configuration

Fig. 1(*a*) shows the configuration of a heated jet issuing into a uniform ambient. The jet is accelerated by buoyancy, causing the center-line velocity at discharge to start increasing. In a uniform ambient, the jet will rise indefinitely, unless interrupted by a free surface (in case of submerged ocean outfalls) because, regardless of the reduction in buoyancy by mixing, the jet is always somewhat buoyant with respect to the environment.

In Fig. 1(*b*) the jet can be seen discharging into a stably stratified ambient. This plume will not rise indefinitely. The net buoyancy force on the jet is decreased as the plume moves upward due to the entrainment of the denser ambient fluid. In addition, for the stably stratified configuration, the ambient density is decreasing with elevation. Thus, as the plume ascends, due to both of these effects, the density difference relative to the local ambient steadily decreases, eventually reducing to zero. At this stage, there is no accelerating force, and the flow continues upward by virtue of the vertical momentum

[1] Numbers in brackets designate References at end of paper.

Contributed by the Heat Transfer Division for publication in the JOURNAL OF HEAT TRANSFER. Manuscript received by the Heat Transfer Division July 14, 1976.

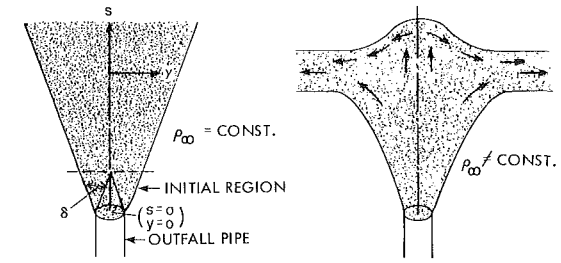

Fig. 1 Flow configurations

it possesses, only to encounter negative buoyancy forces (due to local ambient fluid being lighter than jet fluid) that eventually cause total loss of upward momentum. At this level of maximum rise, the plume fluid is denser than the local surroundings and consequently will cascade downward around the upward flow, to ultimately spread laterally at a level of neutral buoyancy.

Both the height at which buoyancy first goes to zero, called the zero buoyancy height, z_B, and the height at which momentum reduces to zero, called the zero momentum height, z_M, are important unknowns to be determined by the prediction method.

Analysis

Governing Equations. We will assume that the fluid is incompressible and neglect density variations everywhere except in the buoyancy force term. This is commonly called the "Boussinesq approximation." The flow configuration and coordinate system are shown in Fig. 1. In accordance with boundary layer assumptions and neglecting viscous dissipation, the conservation equations of mass, momentum and energy for an axisymmetric buoyant jet can be written:

Continuity.

$$\frac{\partial}{\partial s}(uy) + \frac{\partial}{\partial y}(vy) = 0 \tag{1}$$

s-Momentum.

$$u\frac{\partial u}{\partial s} + v\frac{\partial u}{\partial y} = \frac{1}{\rho y}\frac{\partial}{\partial y}(y\tau) + \frac{(\rho_\infty - \rho)}{\rho_0}g \tag{2}$$

Energy.

$$u\frac{\partial t}{\partial s} + v\frac{\partial t}{\partial y} = \frac{1}{\rho c_p y}\frac{\partial}{\partial y}(-yq) \tag{3}$$

Appropriate boundary conditions are:

$$\frac{\partial u}{\partial y}(s, 0) = \frac{\partial t}{\partial y}(s, 0) = 0; \quad v(s, 0) = 0$$

$$\lim_{y\to\infty} u(s, y) = u_\infty(s); \quad \lim_{y\to\infty} t(s, y) = t_\infty(s) \tag{4}$$

Initial distributions of u and t must be provided at a starting value of s.

The shear stress, τ, includes both the viscous and apparent turbulent contributions

$$\tau = \mu\frac{\partial u}{\partial y} - \rho\overline{v'u'} \tag{5}$$

and, likewise, the heat flux, q, includes both molecular and turbulent transport

$$q = -k\frac{\partial t}{\partial y} + \rho c_p\overline{v't'} \tag{6}$$

The density difference term in equation (2) is related to the temperature of the fluid through

$$\frac{\rho_\infty - \rho}{\rho_0} = \beta(t - t_\infty) \tag{7}$$

Equation (7) is a linear equation of state and is valid for both gases and liquids for temperature differences of practical interest to thermal discharges. Here β, the volume expansivity of the fluid, is a function of temperature.

Model for the Turbulent Transport. Using the Boussinesq concept of eddy viscosity, τ can be evaluated as

$$\tau = \rho(\nu + \nu_T)\frac{\partial u}{\partial y} = \rho n\frac{\partial u}{\partial y} \tag{8}$$

Nomenclature

c_p = specific heat at constant pressure
d_0 = diameter of jet or plume at discharge
Fr_0 = discharge Froude number, $u_0^2/gd_0(\rho_{\infty_0} - \rho_0)/\rho_0$, dimensionless
g = acceleration of gravity
G = stability parameter, $g(\Gamma - \lambda)/T_{0,a}$
H = discharge depth
k = thermal conductivity
ℓ = mixing length
n = total or effective kinematic viscosity
n_H = total or effective diffusivity for heat
Pr = Prandtl number, ν/α
q = heat flux due to molecular and turbulent transport
r_0 = radius of jet or plume at discharge
s = distance along jet or plume axis
Sc = Schmidt number
s_ℓ = starting length
t = temperature
T = nondimensional temperature, $(t - t_\infty)/(t_0 - t_\infty)$
$T_{0,a}$ = discharge temperature, in degrees absolute
$\overline{T}$ = stratification parameter, $(\rho_\infty - \rho_0)/[-r_0(d\rho_\infty/dz)]$
u = s-component of time mean velocity
v = y-component of time mean velocity
y = radial distance from jet center line
$y_{1/2}$ = radial distance from jet center line to point at which $(u - u_\infty)/(u_c - u_\infty) = 0.5$
$yt_{1/2}$ = radial distance from jet center line to point at which $(t - t_\infty)/(t_c - t_\infty) = 0.5$
z = vertical distance
z_M = zero momentum height
z_B = zero buoyancy height
α = thermal diffusivity, $k/\rho c_p$
β = isobaric volume expansivity, $-(\partial\rho/\partial t)_p/\rho_{\mathrm{ref}}$
δ = mixing layer thickness
μ = viscosity
ν = kinematic viscosity, μ/ρ
ρ = density
τ = total or effective shear stress in s-momentum equation
λ = degree of ambient stratification, $-dt_\infty/dz$
Γ = adiabatic lapse rate of the atmosphere

Subscripts

c = evaluated at edge of core or at jet center line if no core exists
e = evaluated at outer edge of jet
$\frac{1}{2}$ = evaluated at velocity half-radius
0 = value at jet discharge
p = evaluated at constant pressure
T = turbulent flow quantity
∞ = free stream or ambient value
max = maximum
min = minimum
ref = reference value

Superscripts

$(\ )'$ = primes on dependent variables denote fluctuating quantities
$\overline{(\ )}$ = bars on dependent variables denote time mean quantities

where ν_T is the turbulent viscosity and n the total effective viscosity. It was assumed that the turbulent diffusivities for heat and momentum are related through

$$\alpha_T = \nu_T/\mathrm{Pr}_T \tag{9}$$

where Pr_T is the turbulent Prandtl number which was set equal to a constant value of 0.7 for the calculations described in the present paper. The heat flux, q, can be written as

$$q = -\rho c_P(\alpha + \nu_T/\mathrm{Pr}_T)\frac{\partial t}{\partial y} = -\rho c_p n_H \frac{\partial t}{\partial y} \tag{10}$$

where n_H is the effective thermal diffusivity.

In the present work, a simple mixing length model

$$\nu_T = \ell^2\left|\frac{\partial u}{\partial y}\right|, \quad \ell = 0.0762\delta \tag{11}$$

where δ is the width of the mixing layer (see Fig. 1) was found to work well in the initial region, which is defined as the region between the point of discharge and the streamwise station where mixing first penetrates to the jet center line as signalled by a decrease in the center-line temperature from the discharge value. The streamwise distance required for this to occur is the starting length, s_ℓ.

The choice of constant in equation (11) and the definition of δ are related. For example, if δ were based on defining the jet boundary as the point where $(u - u_c)/(u_\infty - u_c) = 0.9995$ instead of 0.99 as used in the present analysis, a smaller constant would be required. This remark also applies to the constant in equation (12).

In the main region of flow downstream of the starting length, Prandtl's constant viscosity model,

$$\nu_T = 0.0246 y_{1/2}(u_{\max} - u_{\min}) \tag{12}$$

was found to provide good agreement with the available experimental data.

It is worth mentioning that the model of equation (12) is different from the model endorsed in [14] for horizontal nonbuoyant jet flows.

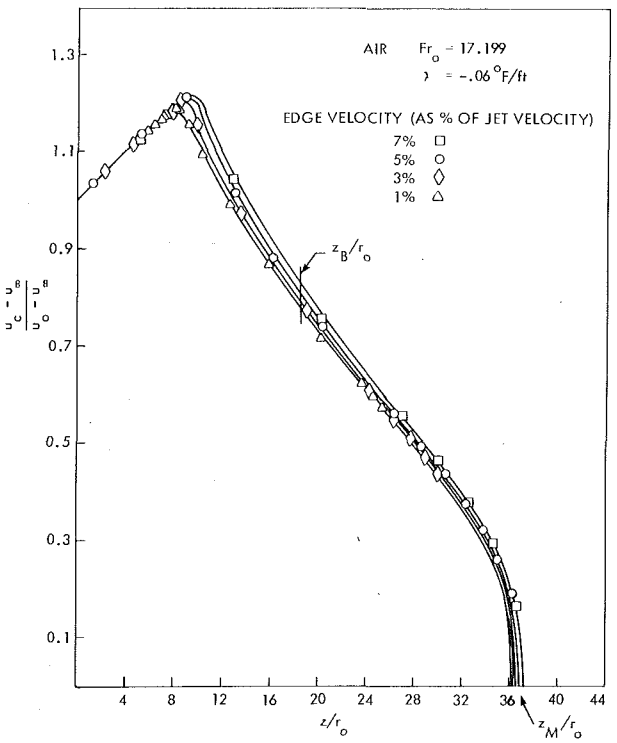

Fig. 2 Predicted center-line velocity decay, zero buoyancy height and zero momentum height for several values of prescribed edge velocity; buoyant jets in stratified ambient

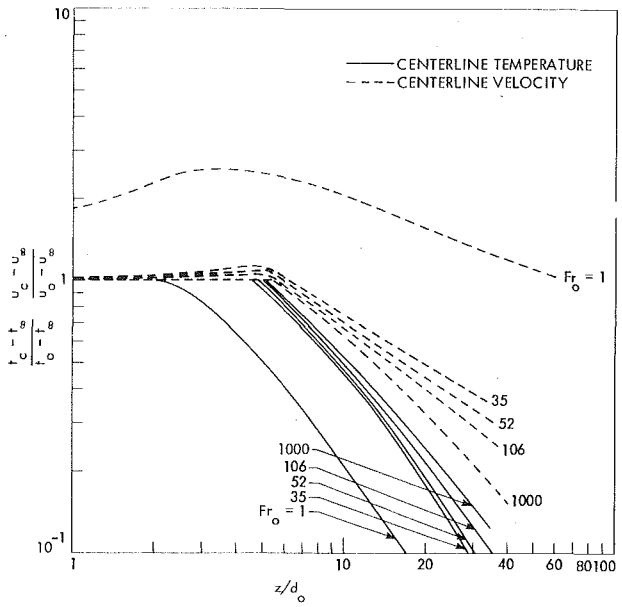

Fig. 3 Predicted effect of Fr_0 on decay of center-line velocity and temperature; vertical buoyant jet or plume in uniform ambient

This is not surprising, however, since the main thrust of [14] was the introduction of the velocity ratio function F as a novel feature which could be applied to simple models to improve their predictions over a wide range of velocity ratios. In fact, it was shown in [15] that good predictions of center-line decay values were also obtained for a wide range of velocity ratios using the function F along with the model of equation (12). The failure of any simple model suggested to date with a single set of constants to predict accurately the flow in both the initial and main regions was noted in [14]. Recourse was not taken to the more complex multiequation models, since the combination of equations (11) and (12) very economically provided reasonably good agreement with the available experimental data.

Calculation Method. An explicit finite difference formulation of the Dufort-Frankel type was used to solve the conservation equations (equations (1)–(3)) which are parabolic in character permitting the solution to be marched in the streamwise direction starting with initial distributions of velocity and temperature at discharge. Details of the difference formulation can be found in [14, 15] and need not be reported here. Streamwise steps of 8–10 percent of the width of the mixing zone were possible with the method. Most calculations were made by dividing the discharge radius into 20 equal Δy increments.

It is fairly common practice when computing jet flows into a quiescent ambient ($u_\infty = 0$) by a finite difference method to use a small nonzero velocity as the edge boundary condition ($u_e \neq 0$) to prevent the equations from becoming singular at the outer boundary and to avoid excessive restriction on the streamwise step size due to any stability constraints. The majority of the calculations described in the present paper were made using $u_e = 0.05\, u_0$. Fig. 2 shows the results of several calculations for a stratified ambient where u_e was set equal to 7, 5, 3, and 1 percent of the jet discharge velocity to determine the sensitivity of the solution to the assumed value of u_e. The effect of replacing $u_e = 0$ with $0.05\, u_0$ seems small, and extrapolating to give values of z_m/r_0 and z_B/r_0 corresponding to $u_e = 0$ showed a deviation of less than 2 percent.

Most of the calculations reported in this paper have required less than one minute and none more than two minutes of computation time on the IBM 360/65 computer.

Results

Uniform Ambient. Fig. 3 shows the general pattern of predicted

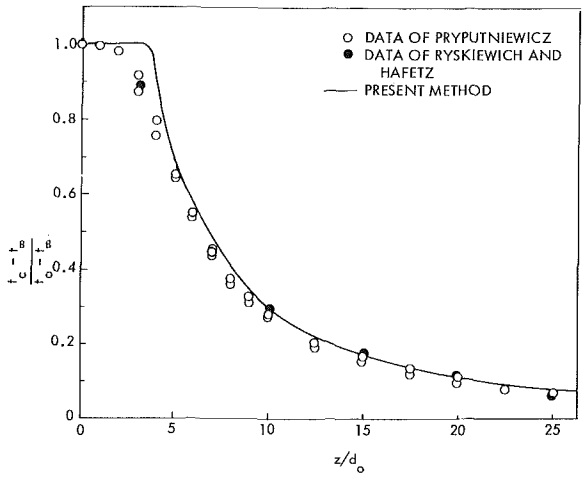

Fig. 4 Predicted and experimental decay of center-line temperature for Fr_0 = 4.0; buoyant vertical jet in uniform ambient

growth and decay of center-line values of velocity and temperature over a Froude number range from 1 to 1000. We note in particular that at low Froude numbers the jet is accelerated significantly due to buoyancy and this results in a dissimilarity in the decay patterns for velocity and temperature. Due to the similarity in the transport equations governing the nondimensional species concentration and temperature in fully turbulent flow ($Sc_T \approx 0.7$ for species also), Fig. 3 can be used to estimate the decay of the nondimensional center-line species concentration also.

Figs. 4–6 compare the predicted center-line temperature decay with the experimental results of Pryputniewicz [16, 17] and Ryskiewich and Hafetz [18] for Froude numbers of 4, 16, and 64. Comparisons for Froude numbers as high as 2500 can be found in [15]. Except for a ten ency to overpredict the starting length, the agreement between the predictions and the measurements is quite good and somewhat better than the Fan and Brooks [6] prediction shown in Figs. 5 and 6.

The experimental data of Pryputniewicz was taken with $(t_0 - t_{\infty_0})$ equal to 100°F, which translates to a density difference of only about 3 percent, not significant enough to affect the validity of the Boussi-

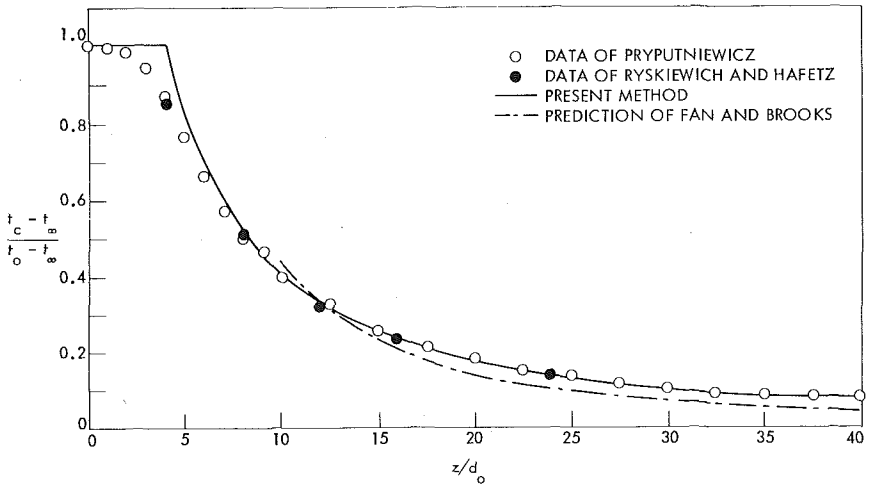

Fig. 5 Center-line temperature comparisons for Fr_0 = 16; buoyant vertical jet in uniform ambient

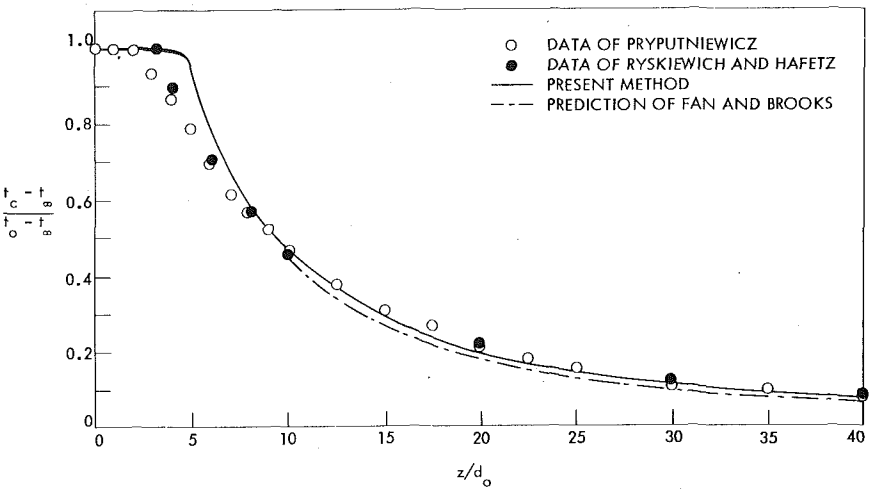

Fig. 6 Center-line temperature comparisons for Fr_0 = 64; buoyant vertical jet in uniform ambient

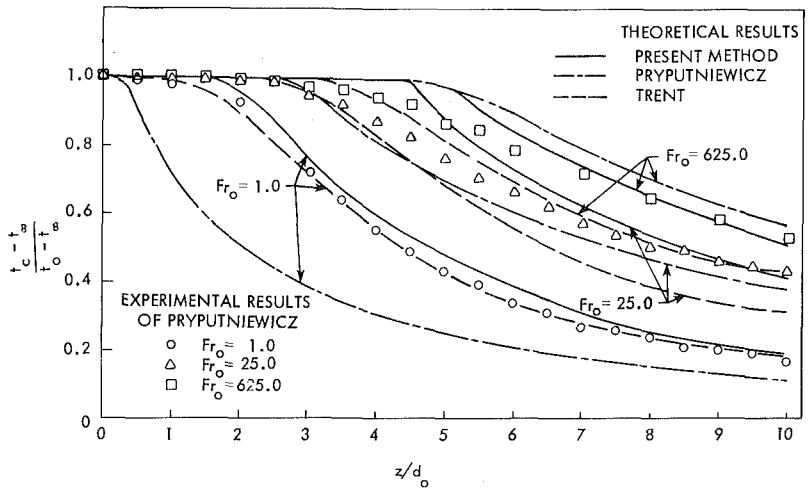

Fig. 7 Comparisons with experimental and theoretical results; buoyant vertical jet in uniform ambient

nesq assumption or the assumption of linear equation of state for density (equation (12)) used in the present analysis.

Further comparisons with the measurements of Pryputniewicz [16, 17] for the uniform ambient case are shown in Fig. 7 for Froude numbers of 1, 25, and 625. The finite-difference predictions of Trent and the predictions of Pryputniewicz [16] using the integral method of Hirst [7] are also shown in Fig. 7. Overall, the present method appears to provide the best agreement with the experimental data which, of course, is subject to uncertainties in measurement, even though the level of uncertainty has not been stated in [16 or 18].

For the vertical jet, the buoyancy forces act in the streamwise direction and the effects of buoyancy on the effective viscosity in the boundary layer form of the equations are not expected to be as great as for configurations in which the buoyancy forces act in the transverse direction. However, from Figs. 4–7 we can detect a slight tendency for the present turbulence model to underpredict the center-line decay for low Froude numbers (large relative buoyancy effect) and overpredict for the largest values of Fr suggesting that buoyancy may serve to increase the effective viscosity slightly. In [15] where more comparisons are indicated, the model is also seen to slightly underpredict for Fr = 1 and overpredict for Fr = 625 and 2500. Overall, however, the predictions of the model are seen to be quite good despite its simplicity. Except for the prediction of the initial region where further work is called for, the disagreement between predictions and the experimental data was so small that there appeared to be no clear basis upon which to attribute this discrepancy solely to the effects of buoyancy on the turbulent viscosity. Buoyancy likely influences the transverse turbulent mixing slightly, but we feel that the present study suggests that it is of secondary importance for the vertical configuration for the entire range of Froude numbers considered.

The question naturally arises as to the usefulness of the predictions of the present method for the case of vertical discharges into relatively shallow water where surface effects are expected to come into play. The effect of the water surface is to retard reduction of the plume temperature in the vicinity of the surface [17].

An effective depth can be defined as that height above the jet discharge beyond which the plume experiences no further entrainment and continues to the surface with this temperature unaffected [19]. The jet behaves as a free jet within its depth. Pryputniewicz and Bowley [16, 17] and Ryskiewich and Hafetz [18] experimentally examined the effect of discharge depth on center-line temperature decay. The conclusion from the former was that the rate of center-line decay was relatively independent of the discharge depth for Fr_0 below 256. According to the latter, the same conclusion holds for Fr_0 as high as 900. In their experiments, which were carried out for flows with discharge depths ranging from $H/d_0 = 10$ to 80, and for a wide range of Fr_0, the effective depth was found to be 92–93.5 percent of total depth for Fr_0 as high as 900, i.e., the results are relatively independent of discharge depth up to that value of the discharge Froude number. This provides an idea of the range of Fr_0 values over which the present method can be used to predict shallow water discharges.

In a typical ocean outfall configuration for a 1000 MW unit (nuclear or fossil), the discharge Froude number would range between 50 and 100 [20], well within the range of applicability of the present analysis. In general, the present analysis can also be used to give an estimate of the maximum temperature at the surface by calculating as usual up to the effective depth, and allowing the plume temperature to remain constant above that height.

Stratified Ambient. Predictions of the zero buoyancy height by the present method are seen to agree well with the theory of Fox [12] in Fig. 8 where coordinates derived by Sneck and Brown [1] for air are used. Sneck and Brown found that the Fox theory agreed well with their experiments in air for modest z_B/r_0.

Table 1 compares the predicted results for maximum height of rise with the measurements of Abraham and Eysink [21], Fan [5], and Fox [12] and the predictions of the integral theory of Fox. The present method is seen to give quite good agreement with the measurements. The Fox theory is observed to significantly underpredict the measured maximum height of rise in most of these comparisons with measurements obtained with liquids, although better agreement has been noted for liquids at higher discharge Froude numbers [12] and in air for conditions resulting in modest values of z_m/r_0 [1]. The reason for this discrepancy is not clear to the authors.

It is interesting to observe that the present method based on boundary layer assumptions does give reasonably good predictions

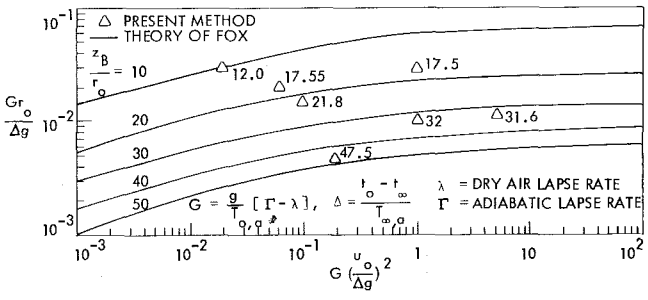

Fig. 8 Zero buoyancy plume height; vertical plume in stratified ambient

Table 1 Maximum height of rise for vertical plumes into stratified ambients

Number	Discharge Froude Number, Fr_0	Stratification Parameter, $\bar{T}$		z_M/r_0 Measured	z_M/r_0 Predicted Present Method	z_M/r_0 Predicted Fox Theory
1	54.5	83		61	61.2	35
2	50.5	141	Abraham & Eysink	74	72.7	50
3	69	94		64	65	44
4	605	134		68	72.5	49
5	324	205	Fan	86	105	72
6	63	1586	Fox	104	115	--

for the maximum height of rise. The maximum height of rise comparisons are summarized in Fig. 9 where z_m/r_0 predicted by the present method are plotted against the experimental values. The predictions of Hirst [13] over the same range of z_m/r_0 are also included in the figure.

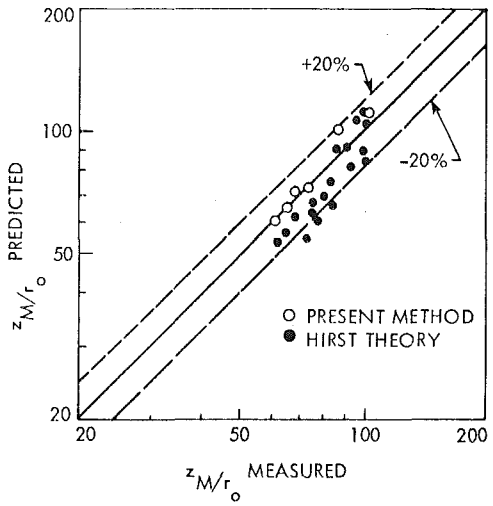

Fig. 9 Maximum height of rise for vertical plumes discharged to stratified ambients

Concluding Remarks

A finite difference prediction method with a simple turbulence model is seen to provide good agreement with experimental data for buoyant jets discharging vertically into both a uniform and a stratified quiescent ambient. The method permits the prediction of the maximum height of rise, which should be of considerable interest in discharge design. In the uniform ambient case, the predictions for temperature can be interpreted in terms of species concentration without requiring the additional solution of the equation for species concentration. The reason for this generality is that for fully turbulent flows, the partial differential equation governing the concentration of effluent, in nondimensional form, is the same as the nondimensional energy equation. In the stratified ambient case, the boundary conditions usually are different for the two equations, but the method can be readily extended to provide simultaneous solutions for species concentration, also.

It should be noted that a fairly good level of agreement between predictions and measurements has been obtained with a turbulence model which does not account for the effects of buoyancy on the turbulent mixing. This suggests that the influence of buoyancy on the turbulent transport is of secondary importance for vertically discharging buoyant jets, although a trend which suggests that buoyancy may tend to enhance the apparent turbulent viscosity slightly can be discerned in Figs. 4–6.

Acknowledgment

This work has been supported by the Engineering Research Institute, Iowa State University, through funds provided by the National Science Foundation under Grants GK 18810 and ENG 74-22193.

References

1 Sneck, H. J., and Brown, D. H., "Plume Rise from Large Thermal Sources Such as Dry Cooling Towers," JOURNAL OF HEAT TRANSFER, TRANS. ASME, Series C, Vol. 96, 1974, pp. 232–238.

2 Schmidt, W., "Turbulente Ausbreiting Eines Stromes Erhitzter Luft," *Zietschrift Für Angewandte Mathematik Und Mechanik* Vol. 21, 1941, pp. 265–278, 351–363.

3 Rouse, H., Yih, C. S. and Humphreys, H. W., "Gravitational Convection From a Boundary Source," *Tellus*, Vol. 4, 1952, pp. 201–210.

4 Morton, B. R., "Forced Plumes," *Journal of Fluid Mechanics* Vol. 5, 1959, pp. 151–163.

5 Fan, L. N., "Turbulent Buoyant Jets Into Stratified or Flowing Ambient Fluids," Keck Lab. of Hydraulics and Water Resources, California Institute of Technology, Report No. KH-R-15, 1967.

6 Fan, L. N., and Brooks, N. H., "Numerical Solutions of Turbulent Buoyant Jet Problems," Keck Lab. of Hydraulics and Water Resources, California Institute of Technology, Report No. KH-R-18, 1969.

7 Hirst, E. A., "Analysis of Round Turbulent, Buoyant Jets Discharged to Flowing Stratified Ambients," Report No. ORNL-4585, Oak Ridge National Laboratory, 1971.

8 Trent, D. S., "A Numerical Model for Predicting Energy Dispersion in Thermal Plumes Issuing From Large, Vertical Outfalls in Shallow Coastal Water," PhD dissertation, Oregon State University, Corvallis, 1972.

9 Trent, D. S., and Welty, J. R., "Numerical Thermal Plume Model for Vertical Outfalls in Shallow Water," Report No. EPA-R2-73-162, Environmental Protection Agency, 1973.

10 Oosthuizen, P. H., "Low Velocity Heated Air Jets," Presented at the Fourth Western Canadian Heat Transfer Conference, Winnipeg, Manitoba, 1972.

11 Hart, W. E., "Jet Discharge into a Fluid With a Density Gradient," *ASCE Journal of Hydraulics Division* Vol. 87, HY6 1961, pp. 171–200.

12 Fox, D. G., "Forced Plume in a Stratified Fluid," *Journal of Geophysical Research*, Vol. 75, No. 33, 1970, 6818–6835.

13 Hirst, E. A., "Buoyant Jets Discharged to Quiescent Stratified Ambients," *Journal of Geophysical Research* Vol. 76, No. 30 1971, pp. 7375–7384.

14 Madni, I. K., and Pletcher, R. H., "Prediction of Jets in Coflowing and Quiescent Ambients," *Journal of Fluids Engineering*, TRANS. ASME, Series C, Vol. 97, 1975, pp. 558–567.

15 Madni, I. K., "A Finite-Difference Analysis of Turbulent, Axisymmetric, Buoyant Jets and Plumes," PhD thesis, Department of Mechanical Engineering, Iowa State University, 1975.

16 Pryputniewicz, R. J., and Bowley, W. W., "An Experimental Study of Vertical Buoyant Jets Discharged Into Water of Finite Depth," JOURNAL OF HEAT TRANSFER, TRANS. ASME, Series C, Vol. 97, 1975, pp. 274–281.

17 Pryputniewicz, R. J., "An Experimental Study of the Free Surface Effects on a Submerged Vertical Buoyant Jet," MS thesis, University of Connecticut, 1974.

18 Ryskiewich, B. S., and Hafetz, L., "An Experimental Study of the Free Surface Effect on a Buoyant Jet," General Dynamics Report No. U440-74-103, 1975.

19 Robidue, R. F., "The Discharge of Submerged Buoyant Jets Into Water of Finite Depth," General Dynamics Report No. U440-72-121, Nov., 1972.

20 Harleman, D. R. F., and Stolzenbach, K. D., "Fluid Mechanics of Heat Disposal From Power Generation," *Annual Review of Fluid Mechanics*, 1972, pp. 7–31.

21 Abraham, G., and Eysink, W. D., "Jets Issuing Into Fluid With a Density Gradient," *Journal of Hydraulic Research* Vol. 7, No. 2 1969, pp. 145–175.

H. Saito
Asst. Professor,
Industrial Mechanical Engineering Department,
Muroran Institute of Technology,
27-1 Mizumoto-cho,
Muroran, Japan

N. Seki
Professor,
Mechanical Engineering Department,
Faculty of Engineering,
Hokkaido University,
Kita 12, Nishi 8,
Sapporo, Japan

Mass Transfer and Pressure Rise in Moist Porous Material Subjected to Sudden Heating

In this paper the authors treat heat and mass transfer which may occur in a moist porous material when it is subjected to a sudden heating of a prescribed temperature at the surface. The basic equations describing the heat and mass transfer and their dimensionless forms are presented. Thereafter, a procedure to solve the basic equations is mentioned by using their finite difference equations. Referring to the results of the numerical computations, the influences of various parameters including thermal conductivity, heat capacity, void fraction, mobility, and initial water content of the material upon temperature, pressure, and moisture distributions in the material are discussed in detail. As a conclusion of these discussions, the authors present an empirical formula to predict the maximum pressure. The proposed formula is compared with experimental results and it is found that the formula is useful for the prediction of the maximum pressure occurring in the material during heating.

Introduction

When a moist porous material is suddenly heated at its surface, a steep pressure rise due to evaporation of water contained in the material occurs in the vicinity of the heating surface and causes the water vapor transfer to a region of lower temperature in the material. The characteristic feature of this process is that the transfers of heat and mass occur simultaneously in the material and a moving boundary exists in it, which separates it into two regions with different thermodynamic properties. In addition, an absorption of latent heat and evaporation of water occur at this boundary. The problem concerning the pressure rise and the vapor transfer is not only interesting from the scientific point of view but also significantly important for the industrial practice. Casting in sand mold is one of the examples related. When a molten metal is poured into a green sand mold, a sudden pressure rise which often causes serious defects of casting products such as pinhole, blowhole, or penetration occurs at the interface between the metal and the mold [1].[1] Therefore, to find out any effective measure in order to avoid the rise, it could be said that the investigation of heat and mass transfer in the green sand mold should be performed in more detail.

Only a few studies of the transfer phenomena in casting mold have been reported up to now. For example, H. G. Levelink and H. van den Berg dealt with a pressure vibration which occurred when a molten metal was cast in a green sand mold and pointed out through their discussions that various defects such as penetration, scabbing, or the other rough surface finish should be considered to be originated from the explosive evaporation of water contained in the mold [2].

In this paper the authors will present the computed results of unsteady temperature, pressure, and water content distributions in a moist porous material, the surface of which is suddenly changed to and maintained at a constant temperature, after stating their governing equations describing heat and mass transfer in the material. Especially from the standpoint of practical usefulness, the progressive variation of the maximum pressure in the material is mainly discussed and a consolidated formula to predict it will be proposed in a form of power function and compared with the experimental data.

Basic Differential Equations

Now consider heat and mass transfer in a moist porous layer of thickness L and initial temperature T_i, the one surface of which is suddenly changed to and maintained at a constant temperature T_0, as shown in Fig. 1. If the heating temperature T_0 is higher than the saturation temperature of water contained in the layer, the moving boundary B demarcates the layer into two regions, that is, dry and wet regions. Therefore, the basic equations governing heat and mass transfer in the layer should be derived individually for each region.

The present theoretical model is based on the following assumptions:

(1) No liquid water movement is present in the material. This

[1] Numbers in brackets designate References at end of paper.

Contributed by the Heat Transfer Division for publication in the JOURNAL OF HEAT TRANSFER. Manuscript received by the Heat Transfer Division July 26, 1976.

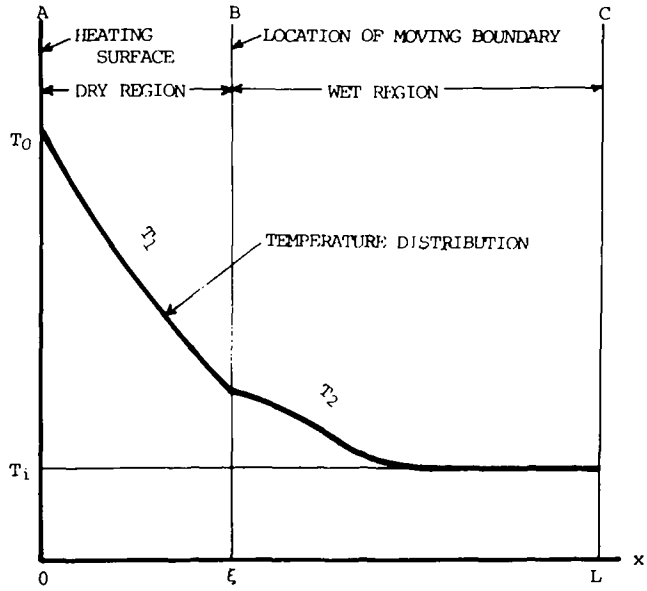

Fig. 1 Schematic view of temperature distribution in a heated moist porous material

assumption is based on the fact that if the volume of the liquid water is negligibly small in comparison with void fraction of the material, its transfer rate can be considered to be negligible.

(2) Air and the other inert gas in the material have no significant influence on heat transfer. This assumption is based on the fact that their enthalpies are effectively smaller than that of water vapor.

(3) Vapor and liquid water in the wet region are in thermodynamic equilibrium at every position. This assumption seems to be reasonable considering that the temperature change in the wet region takes place comparatively slowly and in addition the effective area participating in condensation and evaporation of water are considered to be extremely large in porous material.

(4) Darcy's law is valid for vapor flow through the material.

(5) Thermal conductivity, heat capacity, and mobility are constant in each region.

(6) The volume occupied by liquid water in the material is negligibly small in comparison with void fraction of the material.

From these assumptions the mass transfer equations for each region are introduced as follows:

$$\frac{\partial \epsilon_1}{\partial \tau} = K_1 \frac{\partial}{\partial x_1}\left(\frac{1}{\upsilon_1}\frac{\partial P_1}{\partial x_1}\right) \quad 0 \leqq x_1 \leqq \xi \tag{1}$$

$$\frac{\partial \epsilon_2}{\partial \tau} = K_2 \frac{\partial}{\partial x_2}\left(\frac{1}{\upsilon_{s2}}\frac{\partial P_2}{\partial x_2}\right) \quad \xi \leqq x_2 \leqq L \tag{2}$$

Since the vapor in the dry region is considered to be superheated, the relations of $\epsilon_{s1} = \epsilon_1$, $\epsilon_\ell = 0$, $\epsilon_1 = \psi/\upsilon_1$ should hold. Therefore, equation (1) can be rewritten in the following form:

$$\frac{\partial \epsilon_1}{\partial \tau} = \frac{K_1}{\psi}\frac{\partial}{\partial x_1}\left(\epsilon_1 \frac{\partial P_1}{\partial x_1}\right) \quad 0 \leqq x_1 \leqq \xi \tag{3}$$

From the assumption (3), υ_{s2} in equation (2) is equal to specific volume of dry saturated vapor, υ_2'', at its corresponding pressure, P_2. This means the following relations should hold:

$$\upsilon_{s2} = \upsilon_2'' = (\psi - \epsilon_{\ell 2}\upsilon_2')/\epsilon_{s2}$$

Furthermore, assumption (6) yields the relation $\upsilon_{s2} = \psi/\epsilon_{s2}$. Substituting this into equation (2), the following mass transfer equation for the wet region can be obtained:

$$\frac{\partial \epsilon_2}{\partial \tau} = \frac{K_2}{\psi}\frac{\partial}{\partial x_2}\left(\epsilon_{s2}\frac{\partial P_2}{\partial x_2}\right) \quad \xi \leqq x_2 \leqq L \tag{4}$$

A product of difference of water content between up- and downstream of the moving boundary and its moving velocity should be equal to the difference in the amount of vapor flowing into and out of the boundary. Accordingly, mass balancing equation at the moving boundary is expressed as follows:

$$(\epsilon_{x_2=\xi} - \epsilon_{x_1=\xi})\frac{d\xi}{d\tau} = \frac{K_1}{\psi}\left(\epsilon_1\frac{\partial P_1}{\partial x_1}\right)_{x_1=\xi} - \frac{K_2}{\psi}\left(\epsilon_{s2}\frac{\partial P_2}{\partial x_2}\right)_{x_2=\xi} \tag{5}$$

Since the heat transfer in a moist porous material is considered to be the sum of the enthalpy transferred by vapor movement and the heat by conduction by the assumptions (1) and (3), the heat transfer equations for each region can be described as follows:

$$c\rho\frac{\partial T_1}{\partial \tau} + \frac{(\epsilon_1 i_1)}{\partial \tau} = \lambda_1\frac{\partial^2 T_1}{\partial x_1^2} + \frac{K_1}{\psi}\frac{\partial}{\partial x_1}\left(\epsilon_1\frac{\partial P_1}{\partial x_1}\right) \quad 0 \leqq x_1 \leqq \xi \tag{6}$$

$$c\rho\frac{\partial T_2}{\partial \tau} + \frac{\partial(\epsilon_2 i_2)}{\partial \tau} = \lambda_2\frac{\partial^2 T_2}{\partial x_1^2} + \frac{K_2}{\psi}\frac{\partial}{\partial x_2}\left(\epsilon_{s2} i_{s2}\frac{\partial P_2}{\partial x_2}\right) \quad \xi \leqq x_2 \leqq L \tag{7}$$

Heat balancing equation at the moving boundary is

$$\{(\epsilon_1 i_1)_{x_1=\xi} - (\epsilon_2 i_2)_{x_2=\xi}\}\frac{d\xi}{d\tau} = -\lambda_1\left(\frac{\partial T_1}{\partial x_1}\right)_{x_1=\xi} + \lambda_2\left(\frac{\partial T_2}{\partial x_2}\right)_{x_2=\xi} - \frac{K_1}{\psi}\left(\epsilon_1 i_1\frac{\partial P_1}{\partial x_1}\right)_{x_1=\xi} + \frac{K_2}{\psi}\left(\epsilon_{s2} i_{s2}\frac{\partial P_2}{\partial x_2}\right)_{x_2=\xi} \tag{8}$$

Nomenclature

a = thermal diffusivity of sand (m^2/h)
c_ℓ = specific heat of water (KJ/kg K)
$c\rho$ = heat capacity of dry sand (KJ/m^3K)
i = enthalpy of vapor (KJ/kg)
K = mobility of sand (m^4/h N)
L = thickness of sand layer (m)
P = pressure (N/m^2)
T = temperature (K)
T_0 = heating temperature (K)
υ = specific volume of water vapor (m^3/kg)
x = distance from heating surface (m)
ϵ = mass of water contained in unit volume of moist sand (kg/m^3)
λ = thermal conductivity (KJ/mh K)
ξ = position of moving boundary measured from heating surface (m)
τ = time (h)
ψ = porosity of dry sand (m^3/m^3)

Dimensionless Parameters and Variables

$\tilde{H}$ = heat capacity ratio (= $c_\ell\epsilon_i/c\rho$)
$\tilde{i}$ = dimensionless enthalpy (= $\epsilon_i i/c\rho T_i$)
$\tilde{K}$ = dimensionless mobility (= $KP_i c\rho/\lambda\psi$)
$\tilde{P}$ = dimensionless pressure (= P/P_i)
$\tilde{T}$ = dimensionless temperature (= T/T_i)
$\tilde{W}$ = dimensionless initial water content (= $\psi/\epsilon_i\upsilon_\ell$)
$\tilde{x}$ = dimensionless distance (= x/L)
$\tilde{\epsilon}$ = dimensionless water content (= ϵ/ϵ_i)
$\tilde{\sigma}$ = ratio of thermal conductivities (= λ_1/λ_2)
$\tilde{\tau}$ = dimensionless time (= $a\tau/L^2$)
$\tilde{\omega}$ = ratio of mobilities (= K_2/K_1)
$\tilde{\xi}$ = dimensionless position of moving boundary (= ξ/L)
η = dimensionless variable (defined by equation (12))
ζ = dimensionless variable (defined by equation (13))

Suffixes

0 = heating surface
1 = dry region
2 = wet region
s = water vapor
ℓ = liquid water
i = initial state
j = truncation with respect to time
m = truncated point corresponding to moving boundary
n = truncation with respect to space

The boundary and initial conditions relevant to the present problem are

$$x = 0: T_1 = T_0, \quad \frac{\partial P_1}{\partial x_1} = 0 \tag{9}$$

$$x = L: T_2 = T_i, \quad P_2 = P_i \tag{10}$$

$$\tau = 0: T_1 = T_2 = T_i, \quad P_1 = P_2 = P_i \tag{11}$$

The boundary condition concerning the pressure gradient in equation (9) takes into consideration the realistic phenomena that immediately after pouring a molten metal into a casting mold, there should be no clearance at the interface between the metal and the mold and also no vapor flow at this position.

Introduction of Dimensionless Variables and Transformation of Basic Equations

Since it is generally very difficult to obtain the exact solution of the basic equations mentioned previously with respect to T, P, and ϵ analytically, a numerical computation is employed to obtain their solutions in the present study. The numerical method to analyze the problem with moving boundary has been reported extensively by previous investigators, for examples, by Murray and Landis [3], by Landau [4], and so on. Especially the characteristics of the method proposed by Landau consists of the transformation of independent variables with which a moving boundary is reduced to a fixed boundary and seems to be advantageous to the present problem in which the equations describing the conditions at the moving boundary involve unknown variables such as T and P.

According to the Landau transformation, the independent variables concerning the position of dry and wet regions are transformed into the following forms:

$$\eta = \frac{\tilde{\xi} - \tilde{x}_1}{\tilde{\xi}} \quad 0 \leqq \tilde{x}_1 \leqq \tilde{\xi} \tag{12}$$

$$\zeta = \frac{\tilde{x}_2 - \tilde{\xi}}{1 - \tilde{\xi}} \quad \tilde{\xi} \leqq x_2 \leqq 1 \tag{13}$$

Substituting the dimensionless parameters and variables tabulated in the nomenclature and the variables defined by equations (12) and (13) into the basic equations, equations (3)–(11), the following transformed expression can be obtained, respectively:

$$\tilde{\xi}^2 \frac{\partial \tilde{\epsilon}_1}{\partial \tilde{\tau}} = \tilde{K}_1 \frac{\partial}{\partial \eta}\left(\tilde{\epsilon}_1 \frac{\partial \tilde{P}_1}{\partial \eta}\right) - \tilde{\xi}\dot{\tilde{\xi}}(1-\eta)\frac{\partial \tilde{\epsilon}_1}{\partial \eta} \quad 0 \leqq \eta \leqq 1 \tag{3a}$$

$$(1-\tilde{\xi})^2 \frac{\partial \tilde{\epsilon}_2}{\partial \tilde{\tau}} = \tilde{K}_1\tilde{\omega}\frac{\partial}{\partial \zeta}\left(\tilde{\epsilon}_{s2}\frac{\partial \tilde{P}_2}{\partial \zeta}\right) + (1-\tilde{\xi})\dot{\tilde{\xi}}(1-\zeta)\frac{\partial \tilde{\epsilon}_2}{\partial \zeta} \quad 0 \leqq \zeta \leqq 1 \tag{4a}$$

$$(\tilde{\epsilon}_{2\xi=0} - \tilde{\epsilon}_{1\eta=0})\tilde{\xi}\dot{\tilde{\xi}}(1-\tilde{\xi}) = -(1-\tilde{\xi})K_1\left(\tilde{\epsilon}_1\frac{\partial \tilde{P}_1}{\partial \eta}\right)_{\eta=0} - \tilde{\xi}\tilde{K}_1\tilde{\omega}\left(\tilde{\epsilon}_{s2}\frac{\partial \tilde{P}_2}{\partial \zeta}\right)_{\zeta=0} \tag{5a}$$

$$\tilde{\xi}^2\left\{\frac{\partial \tilde{T}_1}{\partial \tilde{\tau}} + \frac{\partial(\tilde{\epsilon}_1\tilde{\imath}_1)}{\partial \tilde{\tau}}\right\} = \frac{\partial^2 \tilde{T}_1}{\partial \eta^2} + \tilde{K}_1\frac{\partial}{\partial \eta}\left(\tilde{\epsilon}_1\tilde{\imath}_1\frac{\partial \tilde{P}_1}{\partial \eta}\right) - \tilde{\xi}\dot{\tilde{\xi}}(1-\eta)\left\{\frac{\partial \tilde{T}_1}{\partial \eta} + \frac{\partial(\tilde{\epsilon}_1\tilde{\imath}_1)}{\partial \eta}\right\} \quad 0 \leqq \eta \leqq 1 \tag{6a}$$

$$(1-\tilde{\xi})^2\left\{\frac{\partial \tilde{T}_2}{\partial \tilde{\tau}} + \frac{\partial(\tilde{\epsilon}_2\tilde{\imath}_2)}{\partial \tau}\right\} = \tilde{\sigma}\frac{\partial^2 \tilde{T}_2}{\partial \zeta^2} + \tilde{K}_1\tilde{\omega}\frac{\partial}{\partial \zeta}\left(\tilde{\epsilon}_{s2}\tilde{\imath}_{s2}\frac{\partial \tilde{P}_2}{\partial \zeta}\right) + (1-\tilde{\xi})\dot{\tilde{\xi}}(1-\zeta)\left\{\frac{\partial \tilde{T}_2}{\partial \zeta} + \frac{\partial(\tilde{\epsilon}_2\tilde{\imath}_2)}{\partial \zeta}\right\} \quad 0 \leqq \zeta \leqq 1 \tag{7a}$$

$$\{(\tilde{\epsilon}_2\tilde{\imath}_2)_{\zeta=0} - (\tilde{\epsilon}_1\tilde{\imath}_1)_{\eta=0}\}\tilde{\xi}\dot{\tilde{\xi}}(1-\tilde{\xi}) = -(1-\tilde{\xi})\left\{\left(\frac{\partial \tilde{T}_1}{\partial \eta}\right)_{\eta=0} + \tilde{K}_1\left(\tilde{\epsilon}_1\tilde{\imath}_1\frac{\partial \tilde{P}_1}{\partial \eta}\right)_{\eta=0}\right\} - \tilde{\xi}\left\{\tilde{\sigma}\left(\frac{\partial \tilde{T}_2}{\partial \zeta}\right)_{\zeta=0} + \tilde{K}_1\tilde{\omega}\left(\tilde{\epsilon}_{s2}\tilde{\imath}_{s2}\frac{\partial \tilde{P}_2}{\partial \zeta}\right)_{\zeta=0}\right\} \tag{8a}$$

$$\eta = 1: \tilde{T}_1 = \tilde{T}_0, \frac{\partial \tilde{P}_1}{\partial \eta} = 0 \tag{9a}$$

$$\zeta = 1: \tilde{T}_2 = \tilde{T}_i\ (=1), \quad \tilde{P}_2 = P_i\ (=1) \tag{10a}$$

$$\tilde{\tau} = 0: \tilde{T}_1 = \tilde{T}_2 = \tilde{T}_i\ (=1), \quad \tilde{P}_2 = \tilde{P}_1 = \tilde{P}_i\ (=1) \tag{11a}$$

where $\dot{\tilde{\xi}} = \frac{d\tilde{\xi}}{d\tilde{\tau}}$. The transformed coordinate system is shown in Fig. 2.

Numerical Analysis

1 **Finite Difference Equations.** Using backward finite difference with respect to time, the basic equations, equation (3*a*)–(8*a*), are expanded into the following finite difference equations, respectively:

$$(\tilde{K}_1 Y_1\tilde{\epsilon}_{1,n,j} + \frac{1}{4}\tilde{K}_1 Y_1 E_1)\tilde{P}_{1,n-1,j} - 2\tilde{K}_1 Y_1\tilde{\epsilon}_{1,n,j}\tilde{P}_{1,n,j} + (\tilde{K}_1 Y_1\tilde{\epsilon}_{1,n,j} - \frac{1}{4}\tilde{K}_1 Y_1 E_1)\tilde{P}_{1,n+1,j} - \frac{1}{2}\tilde{\xi}_j\dot{\tilde{\xi}}_j(1-\eta)Y_2 E_1 - \tilde{\xi}_j{}^2(\tilde{\epsilon}_{1,n,j} - \tilde{\epsilon}_{1,n,j-1}) = 0 \tag{3b}$$

$$(\tilde{K}_1\tilde{\omega}Z_1\tilde{\epsilon}_{s2,n,j} + \frac{1}{4}\tilde{K}_1\tilde{\omega}Z_1 E_2)\tilde{P}_{2,n-1,j} - 2\tilde{K}_1\tilde{\omega}Z_1\tilde{\epsilon}_{s2,n,j}\tilde{P}_{2,n,j} + (\tilde{K}_1\tilde{\omega}Z_1\tilde{\epsilon}_{s2,n,j} - \frac{1}{4}\tilde{K}_1\tilde{\omega}Z_1 E_2)\tilde{P}_{2,n+1,j} + \frac{1}{2}(1-\tilde{\xi}_j)(1-\zeta)\tilde{\xi}_j Y_2 E_2 - (1-\tilde{\xi}_j)^2(\tilde{\epsilon}_{2,n,j} - \tilde{\epsilon}_{2,n,j-1}) = 0 \tag{4b}$$

$$(\tilde{\epsilon}_{2,m,j} - \tilde{\epsilon}_{1,n,j})\tilde{\xi}_j\dot{\tilde{\xi}}_j(1-\tilde{\xi}_j) = -(1-\tilde{\xi}_j)\frac{\tilde{K}_1}{\Delta\eta}\tilde{\epsilon}_{1,m,j}(\tilde{P}_{1,m-1,j} - \tilde{P}_{m,j}) - \tilde{\xi}_j\frac{\tilde{K}_1\tilde{\omega}}{\Delta\zeta}\tilde{\epsilon}_{2,m,j}(\tilde{P}_{s2,m+1,j} - \tilde{P}_{m,j}) \tag{5b}$$

$$\left\{Y_1 - \frac{1}{2}\tilde{\xi}_j\dot{\tilde{\xi}}_j(1-\eta)Y_2\right\}\tilde{T}_{1,n-1,j} - (2Y_1 + \tilde{\xi}_j{}^2)\tilde{T}_{1,n,j} + \left\{Y_1 + \frac{1}{2}\tilde{\xi}_j\dot{\tilde{\xi}}_j(1-\eta)Y_2\right\}\tilde{T}_{1,n+1,j} + \tilde{\xi}_j{}^2\{T_{1,n,j-1} - (\tilde{\epsilon}_1\tilde{\imath}_i)_{n,j} + (\tilde{\epsilon}_1\tilde{\imath}_1)_{n,j-1}\} - \frac{1}{2}\tilde{\xi}_j\tilde{\xi}_j(1-\eta)Y_2 I_1$$

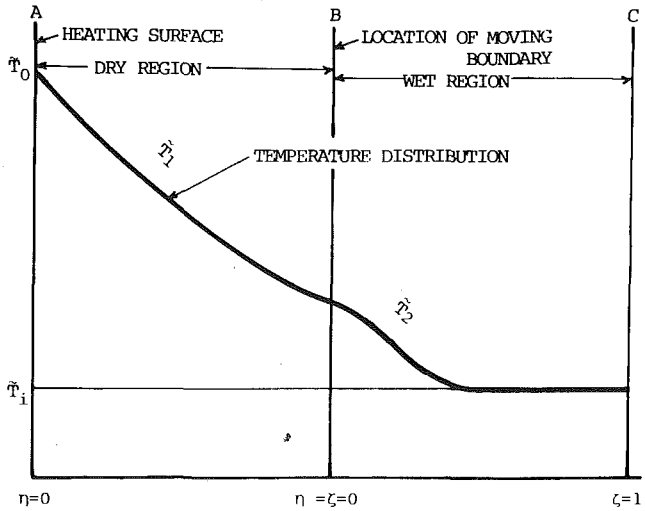

Fig. 2 Transformed coordinate system

$$+\frac{1}{4}\tilde{K}_1 Y_1 I_1(\tilde{P}_{1,n-1,j}-\tilde{P}_{1,n+1,j})+\tilde{K}_1 Y_1(\tilde{\epsilon}_1\tilde{i}_1)_{n,j}D_1=0 \quad (6b)$$

$$\left\{\tilde{\sigma}Z_1+\frac{1}{2}(1-\tilde{\xi}_j)\dot{\tilde{\xi}}_j(1-\zeta)Z_2\right\}\tilde{T}_{2,n-1,j}$$
$$-\{2\tilde{\sigma}Z_1+(1-\tilde{\xi}_j{}^2)\}\tilde{T}_{2,n,j}+\left\{\tilde{\sigma}Z_1-\frac{1}{2}(1-\tilde{\xi}_j)\dot{\tilde{\xi}}\right.$$
$$\left.\times(1-\zeta)Z_2\right\}\tilde{T}_{2,n+1,j}+(1-\tilde{\xi}_j)\{\tilde{T}_{2,n,j-1}-(\tilde{\epsilon}_2\tilde{i}_2)_{n,j}$$
$$+(\tilde{\epsilon}_2\tilde{i}_2)_{n,j-1}\}+\frac{1}{2}(1-\tilde{\xi}_j)\dot{\tilde{\xi}}_j(1-\zeta)Z_2I_2$$
$$+\frac{1}{4}\tilde{K}_1\tilde{\omega}Z_1I_2(\tilde{P}_{2,n-1,j}-\tilde{P}_{2,n+1,j})+\tilde{K}_1\tilde{\omega}Z_1(\tilde{\epsilon}_{s2}\tilde{i}_{s2})_{n,j}D_2=0 \quad (7b)$$

$$\{(\tilde{\epsilon}_2\tilde{i}_2)_{mj}-(\tilde{\epsilon}_1\tilde{i}_1)_{m,j}\}\dot{\tilde{\xi}}_j\dot{\tilde{\xi}}_j(1-\tilde{\xi}_j)$$
$$=-(1-\tilde{\xi}_j)\left\{\frac{1}{\Delta\eta}(\tilde{T}_{1,m-1,j}-\tilde{T}_{m,j})+\frac{\tilde{K}_1}{\Delta\eta}(\tilde{\epsilon}_1\tilde{i}_1)_{m,j}(\tilde{P}_{1,m-1,j}\right.$$
$$\left.-\tilde{P}_{m,j})\right\}-\tilde{\xi}_j\left\{\frac{\tilde{\sigma}}{\Delta\zeta}(\tilde{T}_{2,m+1,j}-\tilde{T}_{m,j})+\frac{\tilde{K}_1\tilde{\omega}}{\Delta\zeta}(\tilde{\epsilon}_1\tilde{i}_2)_{m,j}\right. \quad (8b)$$
$$\left.\times(\tilde{P}_{2,m+1,j}-\tilde{P}_{m,j})\right\}$$

where

$$Y_1=\frac{\Delta\tilde{\tau}}{\Delta\eta^2},\quad Y_2=\frac{\Delta\tilde{\tau}}{\Delta\eta},\quad Z_1=\frac{\Delta\tilde{\tau}}{\Delta\zeta^2},\quad Z_2=\frac{\Delta\tilde{\tau}}{\Delta\zeta}$$

$$E_1=\tilde{\epsilon}_{1,n-1,j}-\tilde{\epsilon}_{1,n+1,j},\quad E_2=\tilde{\epsilon}_{2,n-1,j}-\tilde{\epsilon}_{2,n+1,j}$$

$$I_1=(\tilde{\epsilon}_1\tilde{i}_1)_{n-1,j}-(\tilde{\epsilon}_1\tilde{i}_1)_{n+1,j},\quad I_2=(\tilde{\epsilon}_{s2}\tilde{i}_{s2})_{n-1,j}-(\tilde{\epsilon}_{s2}\tilde{i}_{s2})_{m+1,j}$$

$$D_1=\tilde{P}_{1,n+1,j}-2\tilde{P}_{1,n,j}+\tilde{P}_{1,n-1,j},\quad D_2=\tilde{P}_{2,n+1,j}-2\tilde{P}_{2,n,j}+\tilde{P}_{2,n+j}$$

2 Outline of Numerical Computation. Since the calculation for $\tilde{\xi}=0$ cannot be performed in the present method, the computation must be started from a point advancing by small initial increment, $\tilde{\xi}=\Delta\tilde{\xi}$, which is assumed appropriately. In order to calculate $\tilde{T}$ and $\tilde{P}$ for any $\tilde{\tau}$, their approximate values are first estimated by putting the values of $\tilde{\epsilon}$ and $\tilde{i}$ assumed previously, which are the functions of both $\tilde{T}$ and $\tilde{P}$, into the finite difference equations and then $\tilde{\epsilon}$ and $\tilde{i}$ are evaluated by substituting those obtained into the equations of state of water and water vapor. This procedure should be repeated until the discrepancies between the assumed and the calculated values of $\tilde{\epsilon}$ and $\tilde{i}$ become insignificant. The routine of such numerically calculating procedure is outlined as follows:

1 Space increments of $\Delta\eta$ and $\Delta\zeta$ are decided appropriately. Initial $\tilde{T}_i$ and the corresponding $\tilde{P}_i$, $\tilde{\epsilon}_i$, and $\tilde{i}_i$ evaluated from the equation of state are assigned to each truncated point.

2 Initial increment $\Delta\tilde{\xi}$ is assumed. Time increment $\Delta\tilde{\tau}$ is decided as a time interval required to evaporate water contained in the increment $\Delta\tilde{\xi}$.

3 $\dot{\tilde{\xi}}$ is calculated from the relation $\dot{\tilde{\xi}}=\Delta\tilde{\xi}/\Delta\tilde{\tau}$. Putting this into equation (5b), $\tilde{P}_m$ is obtained. $\tilde{T}_m$ is evaluated by using the equation of state for saturated water vapor as a saturation temperature corresponding to this pressure.

4 $\tilde{P}_1$ can be calculated by solving the so-called tridiagonal equations, equation (3b), under the condition of (9a). $\tilde{T}_1$ can be also obtained in the same way.

5 $\tilde{\epsilon}_1$ and $\tilde{i}_1$ are evaluated by substituting $\tilde{P}_1$ and $\tilde{T}_1$ into the equation of state.

(6) $\tilde{T}_2$ is calculated from equation (7b) and condition (9a) in the same way as step 4. $\tilde{P}_2$, $\tilde{\epsilon}_{s2}$, and $\tilde{\epsilon}_{\ell 2}$ are obtained from the equation of state.

7 By substituting the results of step 6 into equation (7b), $\tilde{\epsilon}_2$ can be calculated and then $\tilde{i}_2$ can be computed.

8 Procedures 3–7 should be repeated until the discrepancies become insignificant between the values of $\tilde{\epsilon}$ and $\tilde{i}$ assumed in step 3 and those calculated in steps 5 and 7.

9 Calculation for the next time step is performed by using new $\Delta\tilde{\xi}$ estimated from equation (8b) and also repeating the procedures 3–8.

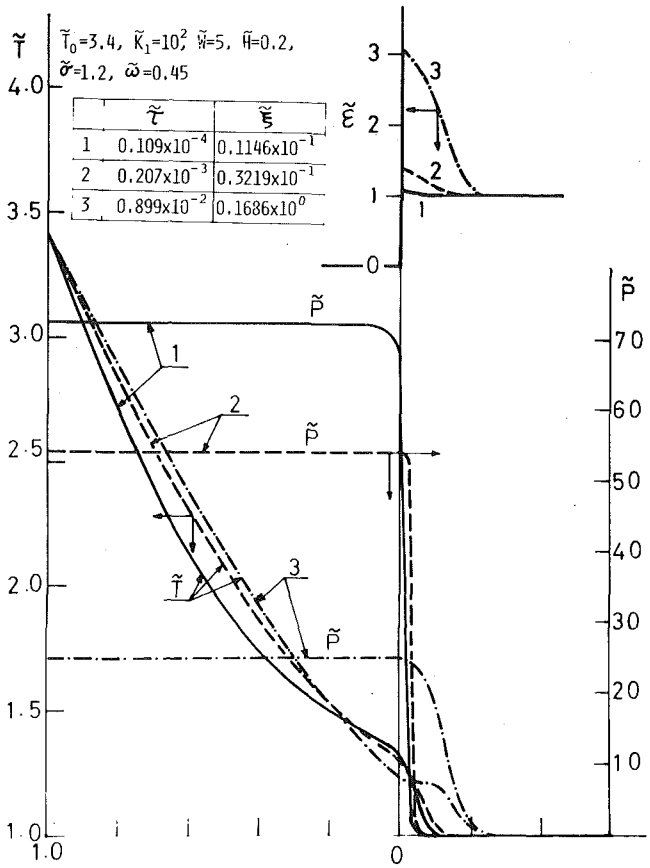

Fig. 3 An example of the calculated results of the distributions of temperature, pressure, and moisture content

The formulas proposed by Tanishita [5] were used in the present calculations as an equation of state of water and water vapor.

Results and Discussion

The calculations were carried out for various combinations of the following parameters: $\tilde{K}_1=10^2$, 10^3, and 1.5×10^3, $\tilde{W}=11.7$, 10, 5.8, 5.0, 3.9, and 10/3, $\tilde{H}=0.05$, 0.1, 0.2, and 0.3, $\tilde{T}_0=3.4$, 4.5, and 5.5, $\tilde{\omega}=0.45$, $\tilde{\sigma}=1.2$, $L=0.1$. Some calculated results are shown in the following figures, Figs. 3–5, to understand how much these parameters influence the transfer phenomena in a moist porous material.

1 Distributions of Temperature, Pressure, and Moisture Content. Fig. 3 shows the dimensionless temperature, pressure, and moisture content distributions in a moist material with dimensionless time $\tilde{\tau}$ as a parameter. The abscissa of this figure is η for dry region and ζ for wet region; therefore the position of $\eta=\zeta=0$ corresponds to that of the moving boundary. It will be seen in this figure that the dimensionless temperature distribution curve in the dry region has a tendency to be a slightly slack shape within a small $\tilde{\tau}$, but to become a tight shape with increasing $\tilde{\tau}$. The dimensionless temperature distribution curve in the wet region forms "wen" in the vicinity of the moving boundary at first and grows up to "plateau" as the dimensionless time $\tilde{\tau}$ advances. Such "wen" or "plateau" shaped temperature distributions can be almost always observed in heat transfer phenomena accompanied with mass transfer and its phase change. This may be due to the latent heat delivered by water vapor evaporated at the moving boundary and transferred to a region of lower temperature and then condensed. As also seen in Fig. 3, the dimensionless temperature at the moving boundary increases at first and reaches its maximum value and, thereafter, decreases with increasing dimensionless time $\tilde{\tau}$. Such a tendency should correspond to the pressure variation at the moving boundary, since the temperature at this point must coincide with the saturation temperature associated

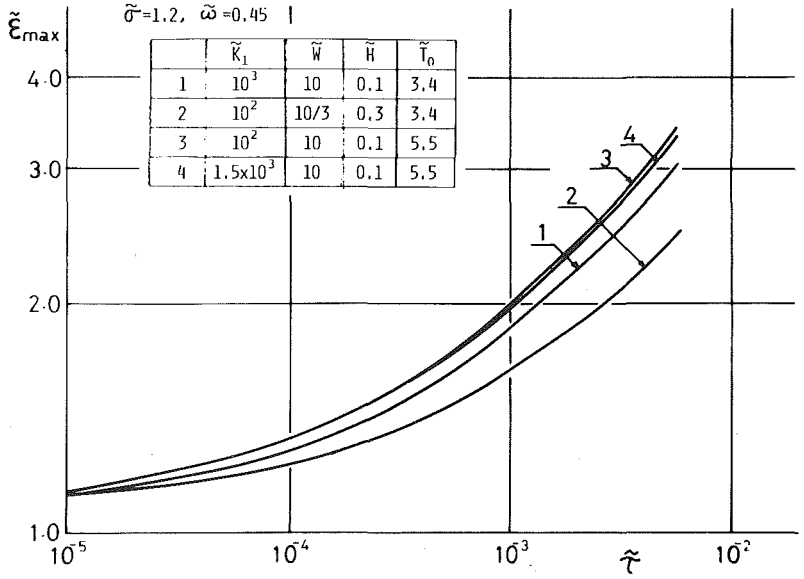

	$\tilde{K}_1$	$\tilde{W}$	$\tilde{H}$	$\tilde{T}_0$
1	10^3	10	0.1	3.4
2	10^2	10/3	0.3	3.4
3	10^2	10	0.1	5.5
4	1.5×10^3	10	0.1	5.5

Fig. 4 Change of $\tilde{\varepsilon}_{max}$ with $\tilde{\tau}$

with the pressure.

The dimensionless moisture content distribution curves are also indicated on the right side of upper portion of Fig. 3. It is clearly seen that the dimensionless moisture distribution is not so varied within a small $\tilde{\tau}$ but the accumulation of the moisture is concentrated in the vicinity of the moving boundary with increasing $\tilde{\tau}$. This accumulation may be a result of the recondensation of the vapor which has traveled from the moving boundary to the wet region. In this figure it is interesting to recognize that the accumulation is limited to a comparatively narrow portion in the wet region.

Fig. 4 presents the variations of the dimensionless moisture content at the moving boundary, $\tilde{\varepsilon}_{max}$, against dimensionless time $\tilde{\tau}$. Comparing the curves 3 and 4 in this figure, it can be seen that the dimensionless mobility $\tilde{K}_1$ has little influence on the accumulation. Furthermore, the curves 1 and 3 show that the dimensionless heating temperature $\tilde{T}_0$ has a great influence upon the accumulation compared with that of dimensionless mobility $\tilde{K}_1$. But the most effective parameter among those is the dimensionless water content $\tilde{W}$, which consists in a ratio of void fraction and initial water content in the material.

The dimensionless pressure distribution shown in Fig. 3 is almost flat in the dry region; however, it asymptotes to $\tilde{P}_i$ (=1) in the wet region after abruptly falling down near the moving boundary. In addition, a tendency can be seen in this figure for the dimensionless pressure in the dry region to decrease with increasing dimensionless time $\tilde{\tau}$ as it propagates over the wet region. This may be understood by considering as follows: The vapor generated at the moving boundary should have a pressure required to flow through the material. However, since no vapor generation occurs in the dry region and no vapor flows through the heating surface, the vapor generated at the moving boundary should be forced to flow toward the wet region. For this reason the dimensionless pressure distribution in the dry region becomes almost flat.

Fig. 5 shows the pressure variation at the moving boundary for the various combinations of the dimensionless parameters against $\tilde{\tau}$. In this figure, the dimensionless pressure at the moving boundary, which may be considered to be equal to the pressure at the heating surface of the material and to have an important role in practice, rises rapidly and reaches its peak within $\tilde{\tau} \simeq 2 \times 10^{-5}$ to 5×10^{-5} and then decreases with increasing $\tilde{\tau}$. It is also observed in this figure that an increased pressure rise is generated by increased value of the dimensionless heating temperature $\tilde{T}_0$ and decreased) values of the dimensionless mobility $\tilde{K}_1$ and the dimensionless water content $\tilde{W}$. In practical casting it is widely known that a vapor pressure in a mold increases with increasing moisture content and temperature of a molten metal and with decreasing porosity and permeability (i.e., mobility) of the mold. The calculated results presented previously reasonably agree with the experience concerning the qualitative behavior of the vapor pressure.

2 Dependency of the Maximum Pressure on the Dimensionless Parameters. In this section, the influences of the various dimensionless parameters on the maximum pressure, $\tilde{P}_{max}$, which may

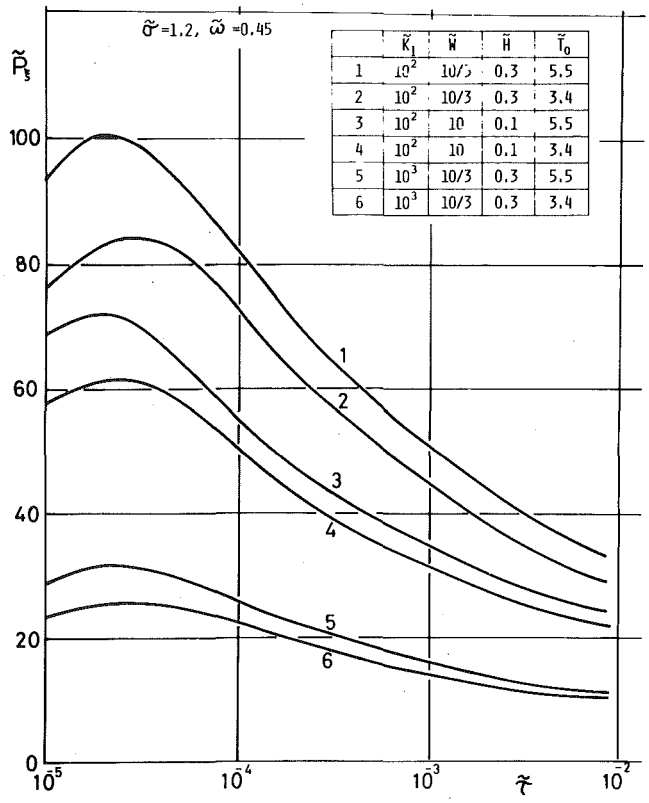

	$\tilde{K}_1$	$\tilde{W}$	$\tilde{H}$	$\tilde{T}_0$
1	10^2	10/3	0.3	5.5
2	10^2	10/3	0.3	3.4
3	10^2	10	0.1	5.5
4	10^2	10	0.1	3.4
5	10^3	10/3	0.3	5.5
6	10^3	10/3	0.3	3.4

Fig. 5 Maximum pressure change with $\tilde{\tau}$

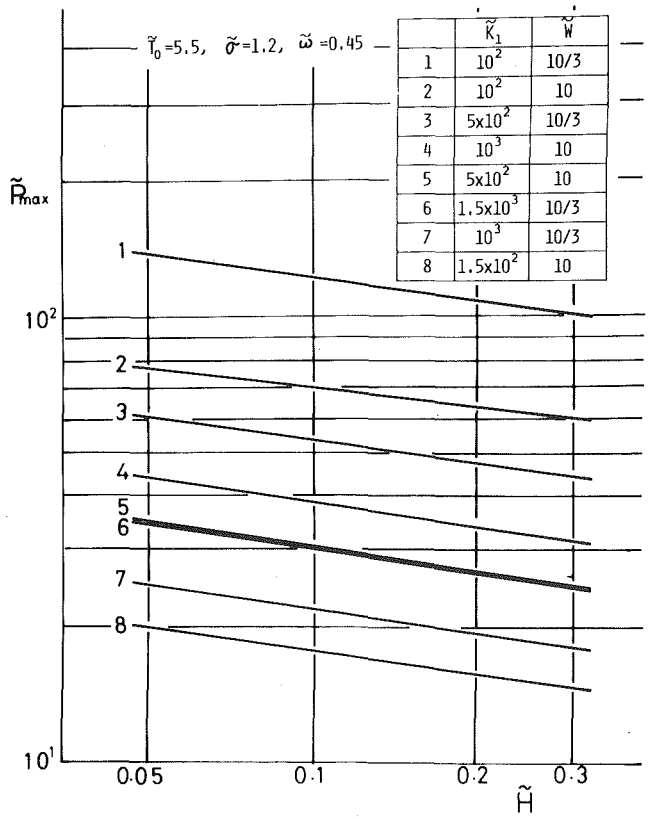

	$\tilde{K}_1$	$\tilde{W}$
1	10^2	10/3
2	10^2	10
3	5×10^2	10/3
4	10^3	10
5	5×10^2	10
6	1.5×10^3	10/3
7	10^3	10/3
8	1.5×10^2	10

Fig. 6 $\tilde{H}$-dependence of $\tilde{P}_{max}$

play an important role in practical use, are to be discussed.

Figs. 6–9 present the dependency of the maximum pressure, $\tilde{P}_{max}$, upon heat capacity ratio $\tilde{H}$, dimensionless water content $\tilde{W}$, dimensionless heating temperature $\tilde{T}_0$, and dimensionless mobility $\tilde{K}_1$, respectively.

Fig. 6 shows the change of the maximum pressure $\tilde{P}_{max}$ against heat capacity ratio $\tilde{H}$ for several combinations of the dimensionless mobility $\tilde{K}_1$ and water content $\tilde{W}$ in case of the prescribed dimensionless heating temperature $\tilde{T}_0$ (=5.5). This figure tells us that the maximum pressure $\tilde{P}_{max}$ decreases with increasing heat capacity ratio $\tilde{H}$. This fact may be explained as follows: A larger value of $\tilde{H}$ results either from larger initial water content ϵ_i or from smaller heat capacity $c\rho$ of the material. However, only the latter case is realistic because each line in Fig. 6 should have a fixed value of $\tilde{W}$ and $\tilde{K}_1$; therefore $c\rho$ should decrease with increasing $\tilde{H}$ so as to keep $\tilde{W}$ constant; finally, thermal conductivity λ must decrease so that $\tilde{K}_1$ may be maintained at a fixed value. Consequently, a larger $\tilde{H}$ means that the heat supplied to the moving boundary decreases.

And it can be also observed in Fig. 6 that a higher value of the maximum pressure $\tilde{P}_{max}$ can be produced by a smaller values of the dimensionless mobility $\tilde{K}_1$ and dimensionless water content $\tilde{W}$. Fig. 7 shows the results rearranged in order to clarify the dependability of $\tilde{P}_{max}$ on $\tilde{W}$. This figure suggests that the maximum pressure $\tilde{P}_{max}$ which decreases with increasing dimensionless water content $\tilde{W}$ can be expressed as a linear function on a double logarithmic sheet.

In general, the dimensionless heating temperature $\tilde{T}_0$ is considered to have an effect on the maximum pressure $\tilde{P}_{max}$. Fig. 8 presents the variation $\tilde{P}_{max}$ against $\tilde{T}_0$. In this figure it will be found that the maximum pressure $\tilde{P}_{max}$ increases with progression of the dimensionless heating temperature $\tilde{T}_0$, although the effectiveness of $\tilde{T}_0$ to $\tilde{P}_{max}$ is little different according to the values of $\tilde{K}_1$, $\tilde{W}$, and $\tilde{H}$.

However, the most sensitive factor to the maximum pressure $\tilde{P}_{max}$ is dimensionless mobility $\tilde{K}_1$. As will be seen in Fig. 9, $\tilde{P}_{max}$ increases with decreasing $\tilde{K}_1$. The physical reasoning behind this fact is as follows: A small value of the dimensionless mobility $\tilde{K}_1$ could result either from a small value of mobility K_1, which indicates a resistability of vapor transfer causing pressure rise, or from a larger value of thermal diffusivity $\lambda/c\rho$. The latter case means that the more heat supplied to the moving boundary, the higher the pressure rise produced.

As a consequence of the foregoing qualitative discussions, it may be concluded that a high pressure in the material will be caused by a large value of dimensionless heating temperature $\tilde{T}_0$ as well as small values of dimensionless water content $\tilde{W}$, dimensionless mobility $\tilde{K}_1$, and heat capacity ratio $\tilde{H}$.

3 Empirical Formula to Predict $\tilde{P}_{max}$ and Its Comparison With Experimental Results. A special characteristics observed in each of Figs. 6–9 indicates the fact that the lines correlating the maximum pressure $\tilde{P}_{max}$ with each dimensionless parameter are almost straight and parallel on a double logarithmic sheet. This fact means that $\tilde{P}_{max}$ is predictable by means of a product of power functions of these dimensionless parameters.

Thus, the calculated values of the maximum pressure $\tilde{P}_{max}$ might be represented by the following empirical formula with a good accuracy:

$$\tilde{P}_{max} = 595.4\ \tilde{W}^{-0.4516} \times \tilde{T}_0^{0.5357} \times \tilde{K}_1^{-0.5008} \times \tilde{H}^{-0.1752} \quad (14)$$

Fig. 10 is a result comparing the empirical formula (14) with the experimental values. The abscissa of this figure is the value obtained by substituting the dimensionless parameters, values of which are

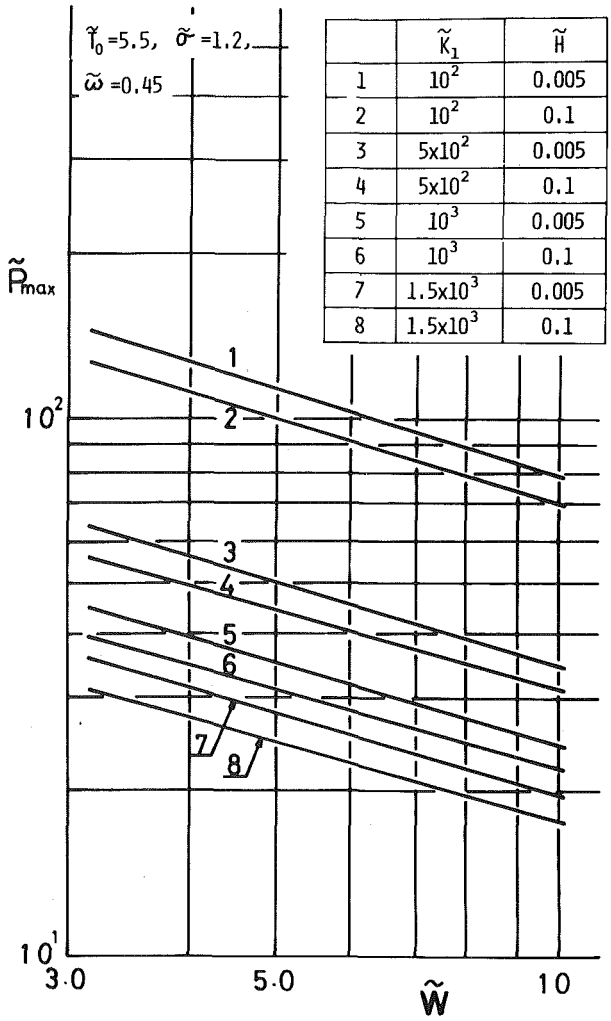

	$\tilde{K}_1$	$\tilde{H}$
1	10^2	0.005
2	10^2	0.1
3	5×10^2	0.005
4	5×10^2	0.1
5	10^3	0.005
6	10^3	0.1
7	1.5×10^3	0.005
8	1.5×10^3	0.1

Fig. 7 $\tilde{W}$-dependence of $\tilde{P}_{max}$

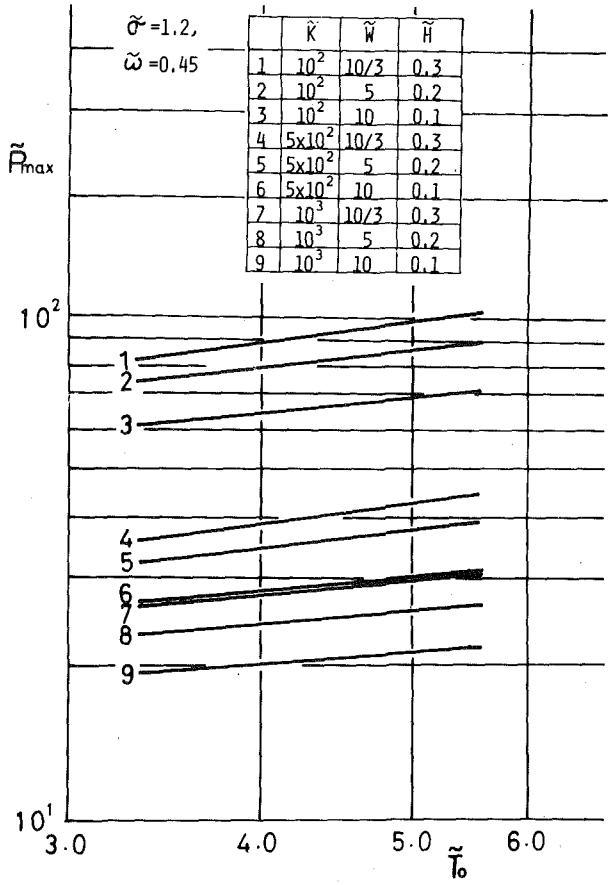

	$\tilde{K}$	$\tilde{W}$	$\tilde{H}$
1	10^2	10/3	0.3
2	10^2	5	0.2
3	10^2	10	0.1
4	5×10^2	10/3	0.3
5	5×10^2	5	0.2
6	5×10^2	10	0.1
7	10^3	10/3	0.3
8	10^3	5	0.2
9	10^3	10	0.1

Fig. 8 $\tilde{T}_0$-dependence of $\tilde{P}_{max}$

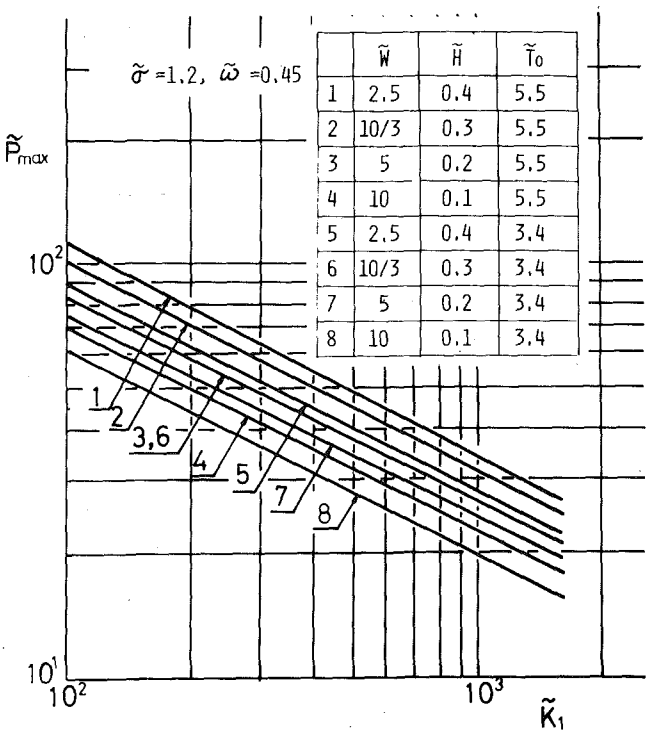

	$\tilde{W}$	$\tilde{H}$	$\tilde{T}_0$
1	2.5	0.4	5.5
2	10/3	0.3	5.5
3	5	0.2	5.5
4	10	0.1	5.5
5	2.5	0.4	3.4
6	10/3	0.3	3.4
7	5	0.2	3.4
8	10	0.1	3.4

Fig. 9 $\tilde{K}_1$-dependence of $\tilde{P}_{max}$

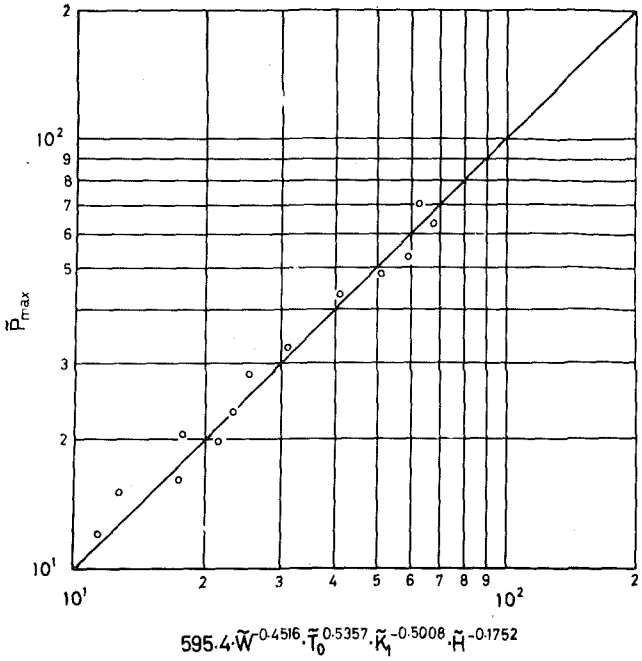

Fig. 10 Comparison of the values predicted by equation (14) with those obtained by the experiments

measured in each experiment, into the right side of equation (14), and the ordinate is the maximum pressure $\tilde{P}_{max}$ obtained in each run of the present experiment.

The experimental results marked with open circles in Fig. 10 were obtained as follows: The experiments were carried out by using a steel pipe of 90 mm ID and 230 mm length, which was filled with rammed moisture sand and heated at one end. Both ends of the pipe were covered up and shielded with aluminum sheet 1-mm thick to prevent leakage of the vapor generated in the pipe and crumbling of the sand. The sand fill was heated by pressing one end of the pipe on a heating metal maintained at a prescribed temperature. The distributions of the temperature and the pressure were obtained by measuring their values at every position of distance 2.5 mm, 5 mm, 10 mm, 15 mm . . . from the heated end. The temperatures were measured by inserting thermocouples into these positions and the pressure by guiding water vapor to semiconductor pressure transducers through copper tubes of 1.5 mm ID. The employed testing sands were olivine and silicate sand in which 1 perccent (by weight) of caoline clay was added as a caking substance.

As will be seen in Fig. 10, the experimental results are a little scattered. This may come from the following reasons: (1) a step temperature rise could not be perfectly realized in the present experiments, (2) moreover, the undesirable heat transfer from the wall of the pipe to the sand was inevitable, and (3) there were considerable difficulties in ramming the sand uniformly and in guiding the vapor pressure without condensation in the guiding pipes.

However, from the tendency of the experimental results in Fig. 10, it might be justified to say that the maximum pressure occurring in a moist porous material subjected to step heating can be predicted by the empirical formula of equation (14).

Acknowledgment

The authors wish to express their heartfelt gratitude to Prof. Dr. T. Saito, Hokkaido University, for his valuable guidance to this research.

References

1 Heine, R. W., and Rosenthal, P. C., *Principles of Metal Casting*, McGraw-Hill New York, 1955, p. 117.

2 Levelink, C. A., and van den Berg, H., "Water Explosion as a Cause of Casting Defects," *Modern Casting*, Vol. 54, No. 2, 1968, p. 69.
3 Murray, W. D., and Landis, F., "Numerical and Machine Solutions of Transient Heat-Conduction Problem Involving Melting or Freezing. Part 1 Method of Analysis and Sample Solutions" JOURNAL OF HEAT TRANSFER, TRANS. ASME, Series C, Vol. 82, 1959, p. 106.
4 Landau, H. G., "Heat Conduction in a Melting Solid," *Quart. of Applied Math.* Vol. 8, 1950, p. 81.
5 Tanishita, I., "A New Characteristic Equation for Steam," *Trans. of JSME*, Vol. 10, No. 38, 1944, p. II 24

T. T. Lie
Research Officer,
Fire Research Section,
Division of Building Research,
National Research Council of Canada,
Ottawa, Canada.

Temperature Distributions in Fire-Exposed Building Columns

A procedure based on a finite difference method is described for calculating the temperature history of fire-exposed protected steel columns with rectangular cross section and heat generation or absorption in the insulation. Comparison with results of tests and those obtained from an analytical solution of the heat transfer equations indicates that the accuracy of the method is adequate for fire engineering purposes. The method is also suitable for the calculation of temperatures in monolithic building components such as solid concrete columns, beams, and walls. It can also be used for the calculation of temperatures of any system in which a perfect conductor or well stirred fluid is enclosed in an encasement, for example, water-filled hollow steel columns or beams, and exposed to a radiative heat source of varying temperature.

Introduction

It is known that exposure to fire reduces the strength of load-bearing building components such as columns, beams, and walls. One method of preventing excessive loss of strength and consequent collapse of a building is to restrict the temperature rise in these components by providing protection. One of the problems in selecting an appropriate protection is the evaluation of its effect on the fire performance of a component. In the past this could be determined only by experiment. Recent developments, however, have made it possible to solve many fire performance problems by calculation, which is far less expensive and time consuming.

In order to calculate the fire performance of a building component it is necessary to know the temperature history of the component during exposure to fire. In this paper a numerical method is described for the calculation of the temperature field in fire-exposed columns. The calculation procedure is based on an improved version of a finite difference method, which offers the advantage of a network of points with which the corners of rectangular configurations can be reached without difficulty [1].[1] It was applied in a study [2] describing the heat flow in fire-exposed square steel columns protected by an insulating material. In the present paper, this study is extended to the calculation of the temperature history of columns with rectangular cross sections (Fig. 1). In addition, the possibility of taking into account heat generation or heat absorption by the protecting material has been included. Furthermore, comparisons made in a previous paper [2] between calculated and experimental results are supplemented in this paper by comparisons between results obtained from the numerical method and those from an analytical solution of the heat transfer equations.

Calculation Method

With the technique described earlier [1, 2], the cross section of the insulating protection is divided into several elementary regions as

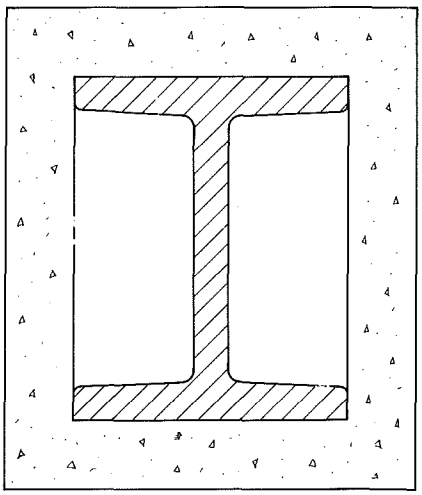

Fig. 1 Cross section of a typical protected steel column

[1] Numbers in brackets designate References at end of paper.

Contributed by the Heat Transfer Division for publication in the JOURNAL OF HEAT TRANSFER. Manuscript received by the Heat Transfer Division March 29, 1976.

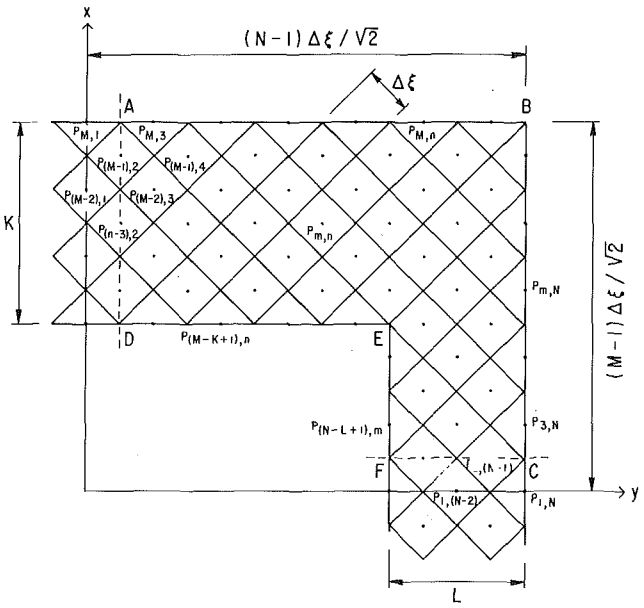

Fig. 2 The arrangement of the elementary regions of a one-quarter section of column protection

shown in Fig. 2. They are square inside the insulation and triangular at its boundaries. The temperature at the center of each element is taken as representative of that of the entire element. The representative point for each triangular boundary element is located on the hypotenuse.

Because the thermal conductivity of steel is normally at least 20 times higher than that of the protection, steel will be considered as a perfect conductor. This implies that the temperature of the steel core will be assumed to be uniform over its entire volume. Consequently, the two-dimensional network need not be extended over the cross-sectional area of the steel core. Instead the subdivision of the steel core can be done in a more convenient way as will be described later. Furthermore, it will be assumed that the capacity of the air enclosed by the protection is negligible in comparison with that of the steel.

For reasons of symmetry, only one-quarter of the section need be considered when calculating the temperature distribution in a cross section. As shown in Fig. 2 in an x-y coordinate system the representative point of the protection $P_{m,n}$ for the region $R_{m,n}$ has the coordinates $x = (m-1)\,\Delta\xi/\sqrt{2}$ and $y = (n-1)\,\Delta\xi/\sqrt{2}$. The points $m = 1$ and $n = 1$ coincide with the origin $x = 0$ and $y = 0$. m increases in the x direction and attains a value $m = M$ at the boundary $A - B$, where as n increases in the y direction and has a value $n = N$ at the boundary $B - C$. As can be seen in the figure, only those points of the x-y plane are defined for which $(m + n)$ is an odd number.

To calculate the temperature history of the insulation and steel, a heat equation is written for each elementary region for the times $j\Delta t$ where $j = 0, 1, 2 \ldots$ and Δt is an appropriate time increment. With the aid of these equations, the temperature of each region can be successively evaluated for any time $t = (j + 1)\,\Delta t$ if the temperature at the time $t = j\Delta t$ is known.

It should be mentioned that the applicability of the method to be described is not limited to protected steel columns. It can be applied to any assembly consisting of a central core of a well stirred material or a material with relatively high thermal conductivity, surrounded by a rectangular envelope of much lower conductivity, which is exposed to heating on all four sides. By removing the core and extending the insulation to the center of the section, it can also be used for the calculation of the temperature history of monolithic columns or beams.

Moisture movement is not taken into account in the model. The effect of moisture on the temperature rise of steel is in general small, and in most cases negligible. Under normal conditions, usually assumed to be an environment of about 50 percent relative humidity and 20°C temperature, most inorganic building materials do not hold more than 1 percent moisture by volume. For such materials the effect of moisture on the time to reach the critical steel temperature is a few percent and not significant. Concretes, however, may hold 3–6 percent of moisture. Experiments and calculations, using a model in which it is assumed that the moisture moves to the inner surface of the insulation and evaporates at this surface, indicate that the predicted failure times will be on the safe side by about 10 to 15 percent [2]. It is possible to make a correction for the effect of moisture using a semi-empirical method. For application in practice, however, a safety margin of 10 to 15 percent is acceptable. It is likely that for concretes the main deviations from calculated results will in practice be caused by the variability of the thermal properties of the concrete, since this is normally a mixture of cement, sand, and gravel of various shape, size, and composition. Spalling of the concrete may also significantly affect the fire performance of a column.

Equations for the Outer Boundary of Insulation

In a fire, heat is transferred from the fire to an exposed object by convection and radiation. According to existing information the heat

Nomenclature

a = coefficient
A = area of the inner surface of the insulation
b = coefficient
c = specific heat; without subscript: specific heat of insulation
d = coefficient
D = thickness of insulation
$h = \dfrac{\rho c A}{c_s W}$
$j = 0, 1, 2, \ldots$
k = thermal conductivity of insulation
K = number of mesh points in and on the insulation along the x-axis
ℓ = distance in insulation
L = number of mesh points in and on the insulation along the y-axis
$m = 1, 2, 3, \ldots$
M = number of mesh points along the x-axis
$n = 1, 2, 3, \ldots$
N = number of mesh points along the y-axis
P = point
Q = rate of heat generation or absorption
R = elementary region
t = time
T = temperature
W = mass of steel core
x = coordinate
y = coordinate
α = fraction
β = roots of $\beta tg\beta D = h$
Δ = increment
$\Delta\xi$ = mesh width
ϵ = emissivity
$\bar{\epsilon}$ = emissivity factor
$\kappa = \dfrac{k}{\rho c}$
ρ = density of insulation
σ = Stefan-Boltzmann constant

Subscripts

a = average
f = of the fire
i = of the insulation
$k = 1, 2, 3, \ldots$
m, M = at a mesh point in the mth or Mth column, respectively
n, N = at a mesh point in the nth or Nth row, respectively
0 = initial
r = pertaining to radiation
s = of the steel core

Superscript

j = at $t = j\Delta t$

transferred in a typical case by convection to an object is less than 10 percent of the radiative heat [3]. It is known that above a certain level of the coefficient of heat transfer, which is easily obtained in fires and furnaces, the temperature of the surface of the exposed object will be very close to the temperature of the environment [5, 12]. In this region changes of the order of 10 percent will have little effect on the surface temperature and thus on the temperature in the exposed object. Therefore, to simplify the heat transfer model, the convective heat transfer will be neglected in this study.

Furthermore, it will be assumed that the radiative heat transfer to the exposed object is approximately that of a black body. As explained subsequently, this assumption will cause only a small error.

In an actual fire, heat is received from luminous flames, which have a high emissivity. If the thickness of the flames is sufficient, the emissivity may reach values of about 0.9 or higher, and thus approaches that of a black body. For the same reason as in the case of convection, an error of the order of 10 percent in the radiative heat transfer will have little effect on the surface temperatures of the exposed object if the heat transfer is high. The high heat transfer from fires is simulated in furnaces by making them large, so that the flames have sufficient thickness, and by selecting furnace wall materials that produce wall temperatures close to the flame temperature. In the present study a column is considered that is exposed to fire on four sides. It will be assumed that the fire temperature follows a standard temperature-time relation according to that specified in ASTM E119-73 [4], although the calculation procedure is valid for any other temperature-time relation. Several analytical expressions that approximately describe this curve exist [5, 6]. Here the following expression will be used:

$$T_f = T_0 + 1200 - 550 \exp(-0.6t) + 200 \exp(-3.0t) - 850 \exp(-12.0t) \quad (1)$$

where T_f and T_0 are, respectively, the fire and ambient temperature in degrees centigrade and t is the time after the start of the fire in hours. This form, consisting of exponential functions, has been chosen because of the advantage that when used as a boundary condition the heat transfer equations are analytically solvable.

The heat transmitted from the fire to an elementary surface region $R_{M,n}$ along the boundary A-B (see Fig. 2) during the period $j\Delta t < t \leqslant (j+1)\Delta t$ for a unit height of the column can be written as

$$\sqrt{2}\,\Delta\xi\sigma\epsilon_i\,[(T_f{}^j + 273)^4 - (T_{M,n}{}^j + 273)^4]\,\Delta t \quad (2)$$

From the region $R_{M,n}$ heat is transferred by conduction to the two neighboring regions, $R_{(M-1),(n-1)}$ and $R_{(M-1),(n+1)}$. This heat can be given as

$$\left(\frac{k_{(M-1),(n-1)}{}^j + k_{M,n}{}^j}{2}\right)(T_{M,n}{}^j - T_{(M-1),(n-1)}{}^j)\,\Delta t + \left(\frac{k_{(M-1),(n+1)}{}^j + k_{M,n}{}^j}{2}\right)(T_{M,n}{}^j - T_{(M-1),(n+1)}{}^j)\,\Delta t \quad (3)$$

During exposure heat may be generated in the protecting material, because of decomposition of the material. It is also possible that heat is absorbed because of dehydration or transformation processes in the material. If Q is the rate of heat generation (+) or absorption (−) per unit volume, then the heat gain or loss in an elementary region $R_{M,n}$ because of this heat generation or absorption is for a time period Δt

$$1/2(\Delta\xi)^2\,Q\Delta t \quad (4)$$

The sensible heat absorbed by the element in this period is

$$1/2(\Delta\xi)^2\,(\rho c)_{M,n}{}^j\,(T_{M,n}{}^{j+1} - T_{M,n}{}^j) \quad (5)$$

By adding all heat gains and losses given by equations (2)–(5), the following heat balance for an elementary region $R_{M,n}$ is obtained:

$$1/2(\Delta\xi)^2\,(\rho c)_{M,n}{}^j\,(T_{M,n}{}^{j+1} - T_{M,n}{}^j) = \sqrt{2}\,\Delta\xi\sigma\epsilon_i\,[(T_f{}^j + 273)^4 - (T_{M,n}{}^j + 273)^4]\,\Delta t - \left(\frac{k_{(M-1),(n-1)}{}^j + k_{M,n}{}^j}{2}\right)(T_{M,n}{}^j - T_{(M-1),(n-1)}{}^j)\,\Delta t - \left(\frac{k_{(M-1),(n+1)}{}^j + k_{M,n}{}^j}{2}\right)(T_{M,n}{}^j - T_{(M-1),(n+1)}{}^j)\,\Delta t + 1/2(\Delta\xi)^2\,Q\Delta t \quad (6)$$

The temperature $T_{M,n}{}^{j+1}$ at the time $(j+1)\Delta t$ for an elementary region $R_{M,n}$ can be solved for from the equation (6). For an elementary region $R_{m,N}$ along the boundary $B-C$ (Fig. 2) the temperature $T_{m,N}{}^{j+1}$ can be derived in a similar manner.

In equation (6) the quantities ρ, c, k, ϵ_i, and Q are assumed to be known. If the temperatures in all elementary regions at the time $t = j\Delta t$ are known, the temperatures in these regions at the time $t = (j+1)\,\Delta t$ can be calculated from these equations. By using the newly calculated temperatures of the various regions as initial temperature and repeating the calculation process, the temperatures at the times $(j+2)\,\Delta t$, $(j+3)\,\Delta t$, etc., can be derived for each elementary region.

Equations for the Inside of Insulation

In the same way as for elementary regions at the outer boundary, the temperatures in the insulation can be calculated by writing heat balance equations for the inside elementary regions. For a region $R_{m,n}$ represented by point $P_{m,n}$, the heat balance equation for a unit height of the column and a time period Δt is

$$(\Delta\xi)^2\,(\rho c)_{m,n}{}^j\,(T_{m,n}{}^{j+1} - T_{m,n}{}^j) = \left[\left(\frac{k_{(m-1),(n-1)}{}^j + k_{m,n}{}^j}{2}\right)(T_{(m-1),(n-1)}{}^j - T_{m,n}{}^j) + \left(\frac{k_{(m+1),(n-1)}{}^j + k_{m,n}{}^j}{2}\right)(T_{(m+1),(n-1)}{}^j - T_{m,n}{}^j) + \left(\frac{k_{(m-1),(n+1)}{}^j + k_{m,n}{}^j}{2}\right)(T_{(m-1),(n+1)}{}^j - T_{m,n}{}^j) + \left(\frac{k_{(m+1),(n+1)}{}^j + k_{m,n}{}^j}{2}\right)(T_{(m+1),(n+1)}{}^j - T_{m,n}{}^j)\right]\Delta t + Q(\Delta\xi)^2\Delta t \quad (7)$$

The temperature $T_{m,n}{}^{j+1}$ of an inside elementary region $R_{m,n}$ at the time $(j+1)\,\Delta t$ can be solved for from equation (7).

Equations for the Inner Boundary of Insulation and for the Steel Core

To describe the heat transfer along the inner boundary of the insulation a model presented in a previous paper [2] will be used. As shown in Fig. 1, a certain fraction α of the inner surface of the insulation of a protected steel column is usually in direct contact with the steel core, and a fraction $(1-\alpha)$ is separated from the steel core by an air gap. The mechanism of heat transfer along the areas of contact is conduction. Heat is transferred through the air gap by radiation and convection. Because the radiative heat transfer is predominant at temperatures normally found in protected steel columns during fire exposure, the convective heat transfer is not taken into account. It can be shown by estimating the maximum steel temperature rise that can be caused by free convection that, for columns normally met with in practice, the heat transferred to the steel by convection is small in comparison with that by conduction and radiation. For example, for a steel column that has been tested (Fig. 6), it can be derived that the temperature rise of the steel in one hour because of convective heating is less than 2°C. This is a small fraction of the temperature rise of about 350°C in one hour measured during the test. In the derivation it has been assumed that the heat transfer by convection resembles that of a vertical plate in air. Because in reality the top and bottom of the column are closed, this model overestimates the convective heat transfer. The air temperature has been assumed to be 10°C higher than the steel temperature at any time, which is approximately the maximum temperature difference observed during tests in the space enclosed by the insulation. The area of the steel exposed to heating by convection is 0.5 m^2 and the mass of the steel 73 kg/m length.

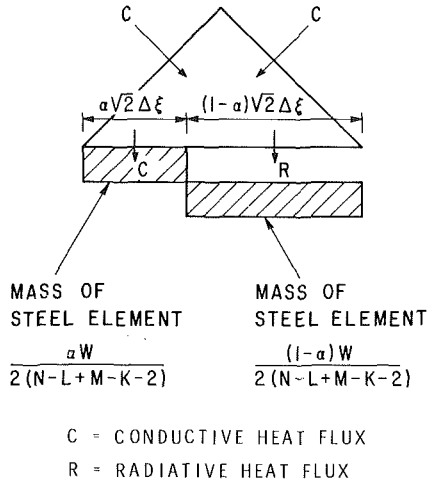

Fig. 3 Model of mechanism of heat transfer for a triangular elementary region of the inner surface of insulation

The model to describe the mechanism of heat transfer at triangular elementary regions of the inner surface of the insulation is shown in Fig. 3. In this model the total mass of the steel core is divided into a number of elementary pieces equal to the number of elementary regions along the inner surface of the insulation, i.e., into $2(N - L + M - K - 2)$ pieces. It is assumed that a fraction α of each elementary mass is in direct contact with the adjacent elementary insulation surface, and thus receives heat from the insulation by conduction, while a fraction $(1 - \alpha)$ of its mass is at some distance from the elementary surface and receives heat by radiation. By varying α from 0 to 1 all possible practical conditions, including pure radiative and pure conductive heat transfer to the steel core, can be simulated. If the steel is everywhere in contact with the insulation, for example, in the case of tubular steel columns, $\alpha = 1$. If there is no contact, as in the case of a wall built around the steel without touching it, $\alpha = 0$. In the case of the column shown in Fig. 1, α is approximately 0.5. In practice the shape and size of the columns are known and α can be estimated, but considering the worst case of $\alpha = 1$ is probably sufficient.

Along the boundary $D - E$ (see Fig. 2), the radiative heat transferred to the steel core from the elementary region $R_{(M-K+1),n}$ through a fraction $(1 - \alpha)$ of the inner surface of the insulation bounding this region is during the period $j\Delta t < t \leq (j + 1)\,\Delta t$

$$(1-\alpha)\sqrt{2}\,\Delta\xi\sigma\bar{\epsilon} \times [(T_{(M-K+1),n}{}^{j} + 273)^4 - (T_{sr}{}^{j} + 273)^4]\,\Delta t \quad (8)$$

In the same period heat is transferred by conduction from the neighboring regions to each triangular elementary region $R_{(M-K+1),n}$ at the inner surface of the insulation, and to each fraction of the elementary steel masses that are in contact with the inner insulation surface. Since, by assumption, steel is regarded as a perfect conductor, the temperatures of those fractions of elementary steel masses that are in direct contact with the insulation surface are identical to those of the adjacent elementary regions of insulation. Consequently, their presence can be taken into account by adding their heat capacities to those of the adjacent elementary insulation regions.

By adding all heat gains and losses, the following heat balance equation can be written for a period $j\Delta t < t \leq (j + 1)\,\Delta t$ for each triangular elementary region $R_{(M-K+1),n}$ and each fraction of steel attached to it:

$$\left[1/2(\Delta\xi)^2\,(\rho c)_{(M-K+1),n}{}^{j} + \frac{\frac{\alpha}{4}\,W(c_s)_{(M-K+1),n}{}^{j}}{\frac{N-L+M-K-2}{2}}\right] \times (T_{(M-K+1),n}{}^{j+1} - T_{(M-K+1),n}{}^{j})$$

$$= \left\{\left(\frac{k_{(M-K+2),(n-1)}{}^{j} + k_{(M-K+1),n}{}^{j}}{2}\right) \times (T_{(M-K+2),(n-1)}{}^{j} - T_{(M-K+1),n}{}^{j}) + \left(\frac{k_{(M-K+2),(n+1)}{}^{j} + k_{(M-K+1),n}{}^{j}}{2}\right) \times ((T_{M-K+2),(n+1)}{}^{j} - T_{(M-K+1),n}{}^{j}) + (1-\alpha)\sqrt{2}\,\Delta\xi\sigma\bar{\epsilon} \times [(T_{M-K+1),n}{}^{j} + 273)^4 - (T_{sr}{}^{j} + 273)^4] + 1/2(\Delta\xi)^2\,Q\right\}\Delta t \quad (9)$$

where $(c_s)_{(M-K+1),n}{}^{j}$ is the specific heat of steel at a temperature of $T_{(M-K+1),n}{}^{j}$.

The temperature $T_{(M-K+1),n}{}^{j+1}$ of an elementary region $R_{(M-K+1),n}$ with attached steel fraction, along the boundary $D - E$ at the time $(j + 1)\Delta t$, can be found by solving equation (9) for this temperature. For the boundary $E - F$ (Fig. 2) the temperature $T_{m,(N-L+1)}{}^{j+1}$ of an elementary region $R_{M,(N-L+1)}$ with attached steel fraction can be derived in a similar manner.

One of the parameters still unknown in equation 9 is the steel temperature $T_{sr}{}^{j}$ of that part of the steel that receives heat by radiation. Although the model assumes that the steel temperature is uniform, evaluation of $T_{sr}{}^{j}$ is necessary, as an intermediate step in the procedure of calculation of the uniform steel temperature. This steel temperature is obtained later by adding all enthalpies of the steel elements, part of which are heated by radiation and part by conduction, and dividing the sum by the heat capacity of the steel.

$T_{sr}{}^{j}$ can be derived in a similar way to the temperatures of the elementary regions in the insulation by writing a heat balance for the steel. From such a heat balance it follows that the temperature $T_{sr}{}^{j+1}$ at the time $(j + 1)\,\Delta t$ is given by

$$T_{sr}{}^{j+1} = T_{sr}{}^{j} + \frac{4\sqrt{2}\,\Delta\xi\sigma\Delta t\bar{\epsilon}}{c_{sr}{}^{j}\,W}\left[\sum_{n=3,5,\ldots}^{N-L}(T_{(M-K+1),n}{}^{j} + 273)^4 + \sum_{m=3,5,\ldots}^{M-K}(T_{m,(N-L+1)}{}^{j} + 273)^4 - \frac{N-L+M-K-2}{2}(T_{sr}{}^{j} + 273)^4\right] \quad (10)$$

Although the temperature field in the protection may be of interest in other cases, e.g., if the protection is made of concrete and contributes to carrying the loading, normally the temperature of the steel core is of primary importance. Because this temperature often determines the strength of the steel, knowledge of it is essential for predicting the time of collapse of building components.

The steel core temperature can be derived by equating the enthalpy of the steel core to that of the sum of the enthalpies of all steel pieces constituting the steel core. This results in the following equation:

$$\int_{T_{sr}{}^{j+1}}^{T_{s}{}^{j+1}} c_s dT = \frac{2\alpha}{N-L+M-K-2}\left[\sum_{n=3,5,\ldots}^{N-L}\int_{T_{sr}{}^{j+1}}^{T_{(M-K+1),n}{}^{j+1}} c_s dT + \sum_{m=3,5,\ldots}^{M-K}\int_{T_{sr}{}^{j+1}}^{T_{m,(N-L+1)}{}^{j+1}} c_s dT\right] \quad (11)$$

where

$T_s{}^{j+1}$ = the steel core temperature at the time $(j + 1)\,\Delta t$

c_s = the specific heat of steel

According to available data [7, 8], the specific heat of steel may be given as a function of its temperature T by the expression

$$c_s = 440 + 0.478T \quad (12)$$

where c_s is in $J/kg°C$ and T in °C.

Substitution of c_s in equation (11) and integrating gives for the steel core temperature

$$T_s^{j+1} = \frac{-b + \sqrt{b^2 - 4ad}}{2a} \tag{13}$$

where

$$a = 0.239$$

$$b = 220$$

$$d = -2\frac{\alpha}{N - L + M - K - 2}\left\{\sum_{n=3,5,\ldots}^{N-L} \times [220\, T_{(M-K+1),n}^{j+1} + 0.239\,(T_{(M-K+1),n}^{j+1})^2] + \sum_{m=3,5,\ldots}^{M-K} [220\, T_{m,(N-L+1)}^{j+1} + 0.239\,(T_{m,(N-L+1)}^{j+1})^2]\right\} + \alpha\,[220\, T_{sr}^{j+1} + 0.239\,(T_{sr}^{j+1})^2]$$

Auxiliary Equations

To calculate the temperatures of the elementary regions along the lines of symmetry $A - D$ and $F - C$, it is necessary to know the temperatures of the regions $P_{m,1}$ and $P_{1,n}$. These temperatures are obtained by equating the temperatures of symmetrical points. Thus along line $A-D$:

$$T_{m,1}^{j+1} = T_{m,3}^{j+1} \tag{14}$$

and along line $F - C$:

$$T_{1,n}^{j+1} = T_{3,n}^{j+1} \tag{15}$$

With the aid of equations (6), (7), (9), (10), and (13)–(15), it is now possible to calculate the temperature distribution in the insulation, on its boundaries, and the temperature of the steel core for any $(j + 1)\,\Delta t$ time level, if the temperatures at the $j\Delta t$ level are known. Initially, only the temperatures at the $t = 0$ level, which are usually equal to room temperature, are known. Starting from these temperatures, the temperature history of the protection and the steel core can be determined up to any specified time or temperature level with the aid of the aforementioned equations.

It is known that the solutions are not stable for all values of the mesh width $\Delta\xi$ and time increment Δt. In order to insure that any error existing in the solution at some time level will not be amplified in the subsequent calculations, a stability criterion has to be satisfied which for a selected value of $\Delta\xi$ limits the maximum value of Δt [9]. For fire-exposed columns and beams the criterion of stability is usually most restrictive along the boundary $A - B$ between fire and insulation.

Analytical Solution

In previous studies [2, 10], calculated results were compared with experimental results for a number of steel sizes and protecting materials. The comparisons showed that for these cases the maximum deviation between calculated and experimental temperatures was about 15 percent, which may be regarded as reasonably accurate in the field of fire engineering. A few of the comparisons are shown in Figs. 4–6. In Figs. 4 and 5 measured and calculated steel temperatures are compared for protected steel columns that were exposed to heating at temperatures according to the standard temperature-time relation given by equation (1). In Fig. 6 the comparison is for a column that was exposed to heating according to a temperature-time curve that closely resembles an actual fire temperature curve. To obtain more information on the accuracy of the numerical method, the results obtained by the method described in this paper will also be compared with those obtained from analytical solutions of the equations that determine the steel temperature. For this purpose a protected steel column will be considered of which the steel is everywhere in contact with the insulation ($\alpha = 1$). If certain assumptions are satisfied, it is possible to give an analytical solution of these equations. The assumptions are

(*a*) The heat that passes the insulating casing is immediately and uniformly distributed over the steel;

(*b*) The thermal capacity of the air cavity (if any) enclosed by the casing is negligible in relation to that of the steel;

(*c*) The insulation is so thin that the difference in insulation thickness at the corners can be neglected and it is permissible to

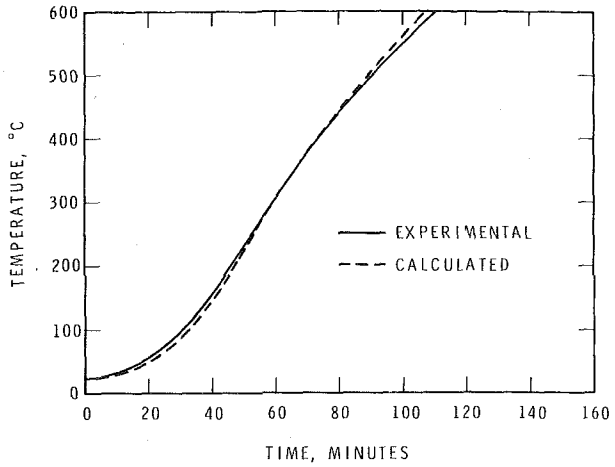

Fig. 5 Steel temperature as a function of time (size steel core: 20 × 20 cm; insulation of heavy clay brick)

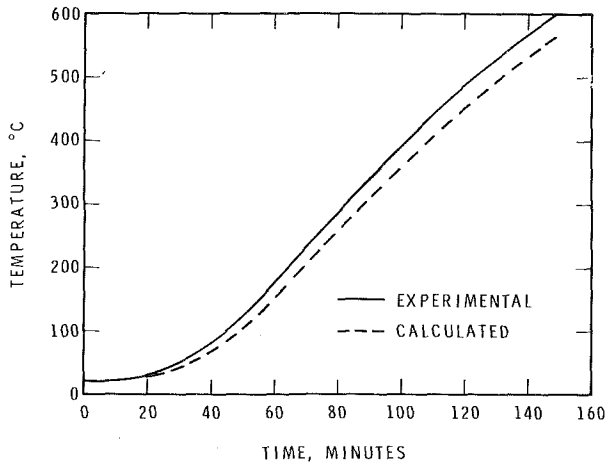

Fig. 4 Steel temperature as a function of time (size steel core: 15 × 15 cm; insulation of insulating fire brick)

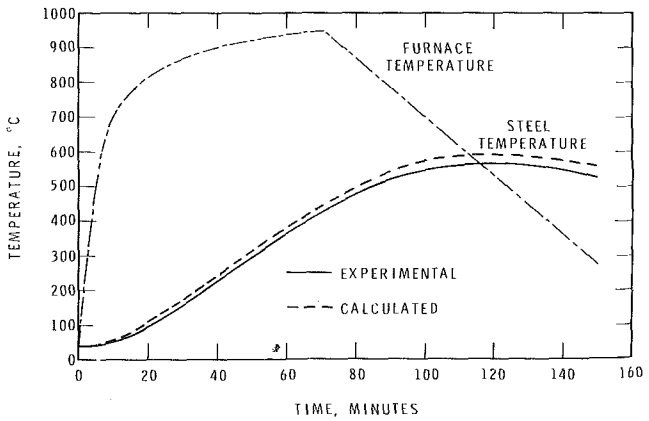

Fig. 6 Steel and furnace temperature as a function of time (size steel core: 25 × 25 cm; insulation of vermiculite board)

consider a heat flow through the insulation over an area equal to the area of the interface between the insulating material and the contents; and

(*d*) The material constants are invariable or can be replaced by a constant average value.

The heat transfer equation and boundary and initial conditions that determine the temperature in the insulation and steel are as follows:

The temperature of the insulation T satisfies the differential equation for thermal conduction:

$$\rho c \frac{\partial T}{\partial t} = k \frac{\partial^2 T}{\partial \ell^2} \tag{16}$$

At the exposed surface of the insulation, the temperature is assumed to follow the fire temperature course given by equation (1).

At the interface between insulation and steel, the heat flow per unit time to the steel is equal to the increase in enthalpy of the steel. Hence, for $\ell = D$

$$-kA \frac{\partial T}{\partial \ell} = c_s W \frac{\partial T}{\partial t} \tag{17}$$

Initially, the temperature of the column is equal to the room temperature, so that $T = T_0$ for $t = 0$.

The method of solving the foregoing equations is given in reference [11]. In principle, this method uses the solution of equations (16) and (17) for a constant fire temperature [12] as starting point. With the aid of Duhamel's theorem, the solution for varying fire temperature is derived. For a temperature rise at the exposed surface that follows the temperature-time relation given by equation (1), the solution for the steel temperature T_s is as follows:

$$\begin{aligned} T_s - T_0 = {} & 1200 - 1200 \sum_{k=1}^{\infty} f(\beta_k) \exp(-\kappa \beta^2{}_k t) \\ & -550 \sum_{k=1}^{\infty} f(\beta_k) \frac{\kappa \beta_k{}^2}{\kappa \beta_k{}^2 - 0.6} (\exp(-0.6t) - \exp(-\kappa \beta^2{}_k t)) \\ & +200 \sum_{k=1}^{\infty} f(\beta_k) \frac{\kappa \beta_k{}^2}{\kappa \beta_k{}^2 - 3.0} (\exp(-3.0t) - \exp(-\kappa \beta^2{}_k t)) \\ & -850 \sum_{k=1}^{\infty} f(\beta_k) \frac{\kappa \beta_k{}^2}{\kappa \beta_k{}^2 - 12.0} (\exp(-12.0t) - \exp(-\kappa \beta^2{}_k t)) \end{aligned} \tag{18}$$

where

$$\kappa = \frac{k}{\rho c}$$

$$\beta_k = \text{roots of } \beta tg \beta D = h$$

$$h = \frac{\rho c A}{c_s W}$$

$$f(\beta_k) = \frac{2(\beta_k{}^2 + h^2) \sin \beta_k D}{\beta_k [D(\beta_k{}^2 + h^2) + h]}$$

For equation (18) T_s and T_0 are in degrees centigrade, t in hours, and κ in square meters per hour.

Comparison of Results of Numerical and Analytical Method

For comparison a column model and exposure conditions were chosen that resembled as closely as possible those assumed in the analytical method. To approach one-dimensional heat transfer through the insulation it should be thin in comparison with the inner perimeter of the cross section of the insulation. In this case an insulation thickness of 1 cm and two steel core sizes of 10 × 10 cm and 15 × 15 cm cross section were selected. To obtain temperatures on the fire-exposed surface that closely follow the fire temperature course, it is essential that the thermal properties of the insulation be such that the product $k_i \rho_i c_i$ be low [12]. A combination that was found to produce surface temperatures that were reasonably close to the fire temperature (see Fig. 7) and did not give rise to extremely long calculation times was $k_i = 50$ J/mh °C; $\rho_i c_i = 3 \times 10^6$ J/m^3 °C.

To make conditions in the numerical method as close as possible to those in the analytical method, it was assumed that the emissivity of both the fire and insulation was one, and that the mechanism of heat transfer from the insulation to the steel core was conduction. For the mass of the steel a value of 20 kg/m column length was chosen and for the specific heat a value equal to that given by equation (17) for a temperature of 20°C.

Calculated results are given in the Tables 1 and 2. In Table 1 the steel temperatures at various times are shown for a 10 × 10-cm steel column insulated by a 1-cm thick protection. Column No. 1 of the Table gives the temperatures calculated by the analytical method, and columns 2, 3, and 4 give the average steel temperatures calculated by the numerical method for various mesh widths. The temperatures in column No. 2 are for a 1-cm thick insulation subdivided into five layers, those in column No. 2 are for subdivision into seven layers, and those in column No. 3 into nine layers.

It is seen that the differences in temperature between the analytical and numerical method reduce with an increase in the number of layers, but for more than seven layers the reduction is small. Irrespective of the number of layers, there is still a difference between the analytical and numerical results, which for higher steel temperatures amounts to several degrees. It is likely that these differences are caused by the higher temperatures at the corners of the insulation, as can be seen in Fig. 4. Whereas the heat transfer in the numerical model is two dimensional, the analytical model assumes one dimensional heat transfer through the insulation. By decreasing the ratio of the thickness of insulation to the column cross-section size, the influence of the corners on the steel temperature can be reduced. In Table 2 the calculated temperatures are shown for a 15 × 15-cm column.

As can be seen in columns No. 1 and 3 of Table 2, the differences between the results of the analytical and numerical methods for this larger column reduce to less than 2°C over the temperature range of

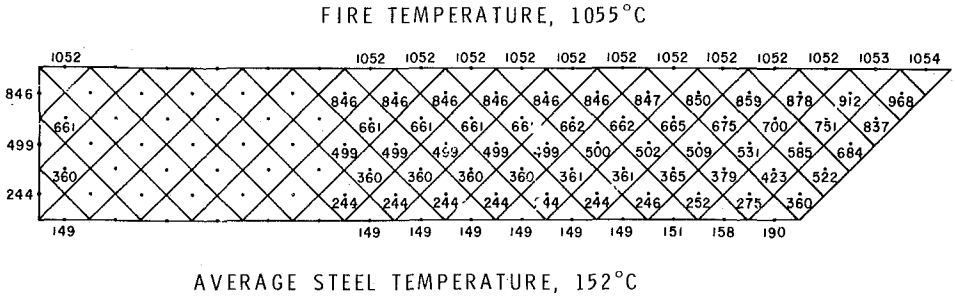

Fig. 7 Typical temperature distribution in an one-eighth section of the insulation of a steel column (size steel core: 10 × 10 cm; insulation thickness: 1 cm; exposure time: 2 hours)

Table 1 Steel temperature (C°) of 10- × 10-cm column

TIME (Min)	ANALYTICAL METHOD (No.1)	NUMERICAL METHOD 5 LAYERS (No.2)	7 LAYERS (No.3)	9 LAYERS (No.4)
0	20.0	20.0	20.0	20.0
30	21.9	24.1	22.7	22.3
60	47.2	51.9	48.8	47.8
90	93.5	98.9	95.9	94.8
120	148.8	155.0	152.4	151.6
150	207.8	214.9	212.8	212.1
180	267.4	275.7	274.1	273.3
210	326.4	335.8	334.6	334.2
240	383.7	394.2	393.4	393.1
270	438.9	450.2	449.7	449.6
300	491.4	503.6	503.4	---

Table 2 Steel temperature (C°) of 15- × 15-cm column

TIME (Min)	ANALYTICAL METHOD (No.1)	NUMERICAL METHOD 5 LAYERS (No.2)	7 LAYERS (No.3)
0	20.0	20.0	20.0
30	22.8	25.5	23.7
60	56.7	62.2	57.9
90	116.7	122.2	117.3
120	186.3	191.8	186.7
150	258.6	264.2	259.1
180	330.2	336.3	331.2
210	399.8	406.2	401.0
240	466.2	472.8	467.7
255	497.9	504.8	499.7

20 to approximately 500°C. In terms of the time to reach a specific steel temperature the differences are less than 1 min. In the field of fire resistance of building components such an error is negligible. Even if the faster method is used by dividing the insulation into five layers instead of seven, the errors are still small, as shown in column No. 2 of Table 2.

Conclusion

In the past the fire performance of building components could be determined only by experiment. Recent developments, in particular development of numerical techniques and better knowledge of material properties at elevated temperatures, have made it possible to solve many fire performance problems by calculation. Calculation has the advantage that it is far less expensive and time consuming than performance tests.

In this study a procedure based on a finite difference method is described for calculating the temperature history of fire-exposed protected steel columns with rectangular cross section and heat generation or absorption in the insulation. Comparison with results of tests and those obtained from an analytical solution of the heat transfer equations indicates that the accuracy is adequate for fire engineering purposes.

The method is also suitable for the calculation of temperatures in monolithic building components such as solid concrete columns, beams, and walls. It can also be used for the calculation of temperatures of any system in which a perfect conductor or well stirred fluid is enclosed in an encasement, for example, water-filled hollow steel columns or beams, and exposed to a radiative heat source of varying temperature.

This paper is a contribution from the Division of Building Research, National Research Council of Canada, and is published with the approval of the Director of the Division.

References

1 Harmathy, T. Z., "Thermal Performance of Concrete Masonry Walls in Fire," American Society for Testing and Materials, Special Technical Publication No. 464, 1970, pp. 209–243.

2 Lie, T. T., and Harmathy, T. Z., "A Numerical Procedure to Calculate the Temperature of Protected Steel Columns Exposed to Fire," Fire Study No. 28, Division of Building Research, National Research Council of Canada, 1972, NRCC 12535.

3 Trinks, W., and Mawhinney, M. W., *Industrial Furnaces,* Carnegie Inst. Technology, Wiley, New York, 1961.

4 "Standard Methods of Fire Tests of Building Constructions and Materials," American Society for Testing and Materials, Designation E119-73, Part 18, 1974, pp. 610–628.

5 Lie, T. T., *Fire and Buildings,* Applied Science Publishers Ltd., London, 1972.

6 Williams-Leir, G., "Analytic Equivalents of Standard Fire Temperature Curves," *Fire Technology,* Vol. 9, No. 2, 1973, pp. 132–136.

7 Liley, P. E., Touloukian, Y. S., and Gambill, W. R., *Physical and Chemical Data, Chemical Engineers Handbook,* J. H. Perry, Sec. 3., McGraw-Hill, New York, 1963.

8 British Iron Steel Res. Assoc., *Physical Constants of Some Commercial Steels at Elevated Temperatures,* Butterworths Sci. Publ., London, 1953.

9 Dusinberre, G. M., *Heat Transfer Calculations by Finite Differences,* International Textbook Company, Scranton, Pa., 1961.

10 Konicek, L., and Lie, T. T., "Fire Tests on Protected Steel Columns under Different Fire Severities," Fire Study No. 34, Division of Building Research, National Research Council of Canada, 1974, NRCC 14170.

11 Lie, T. T., "Temperature of Protected Steel in Fire. Behaviour of Structural Steel in Fire," Symposium No. 2, Ministry of Technology and Fire Offices' Committee Joint Fire Research Organization, H.M.S.O., London, 1968, pp. 100–110.

12 Carslaw, H. S., and Jaeger, J. C., *Conduction of Heat in Solids,* Oxford University Press, London, 1959.

journal of heat transfer

technical notes

Effect of Tilt and Horizontal Aspect Ratio on Natural Convection in a Rectangular Honeycomb

J. N. Arnold[1], D. K. Edwards,[1] and I. Catton[1]

Introduction

For a horizontal solar heat collector it has been shown [1, 2][2] that natural convection can be effectively suppressed by placing a properly-sized low-aspect-ratio honeycomb of thin, poorly conducting material between the absorber plate and coverglass. Lalude and Buchberg [3] performed an optimization study and concluded that best cost-effectiveness for a 80°C collection temperature was to be obtained with a cell having an aspect ratio d/L between 0.2 and 0.25 and a W/d of 6. At the time of their study little was known about the effect of tilt θ and horizontal aspect ratio W/L on natural convection. As shown in Fig. 1, L is the length between the heated collector surface and the cooled glass cover, i.e., the thickness or depth of the honeycomb core; d is the up-slope distance between tilted sides of the honeycomb; and W is the horizontal or East-West distance between vertical ends of the rectangular honeycomb. The present work was carried out to obtain the effect of tilt θ and horizontal aspect ratio W/L on natural convection in a rectangular honeycomb with two of the three sizes (d and L) fixed but with various W dimensions.

Apparatus and Procedure

The experimental apparatus and procedure employed is essentially that of Sun and Edwards [4, 5]. Gasketed seals were added to the ends of the apparatus to permit tilt to any desired angle [6, 7]. In this work three sets of multicelled rectangular honeycombs were used; dimensions are shown in Table 1. The cell walls were made with varnished paperboard 0.35-mm thick. The three honeycombs had nearly the same height and aspect ratio, but different values of horizontal aspect ratio.

The ratio of the heat flow in the heated-from-below position to that in the heated-from-above position is the Nusselt number

$$\mathrm{Nu} = \frac{k_{\mathrm{eff}}}{k} = \frac{qL}{k\Delta T} \tag{1}$$

where q is the conductive-convective heat flux, k is the thermal conductivity of the fluid, and ΔT is the temperature difference between the two copper plates enclosing the fluid. Minor corrections were made in the computerized data reduction program for wall conduction and departures from strict steady-state operation. Details of the data reduction procedure and an error analysis are contained in references [5, 7].

Nusselt number was determined from the data as a function of Rayleigh number based on total length between heated and cooled plates

$$\mathrm{Ra}_L = \frac{g\beta\Delta TL^3}{\kappa\nu} = \mathrm{Ra}_d(L/d)^4 \tag{2}$$

where g is the gravitational acceleration, β volume expansion coefficient, κ is thermal diffusivity, and ν is kinematic viscosity. Under the assumption of constant transport properties, small variation in density, and low inertia effects (or high Prandtl number), the equations of motion indicate that Nusselt number depends upon Rayleigh number. Within these constraints any high Prandtl number fluid can be used for experimental purposes. Silicone oils were chosen as the conductive-convective medium. Measurements made with an in-

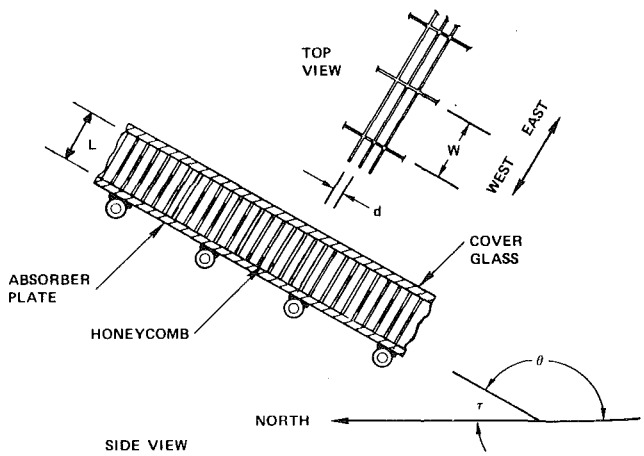

Fig. 1 Rectangular honeycomb dimensions

[1] Energy and Kinetics Department, School of Engineering, UCLA. Mems. ASME.

[2] Numbers in brackets designate References at end of technical note.

Contributed by the Heat Transfer Division of THE AMERICAN SOCIETY OF MECHANICAL ENGINEERS. Manuscript received by the Heat Transfer Division September 14, 1976.

Table 1 Dimensions of the rectangular honeycombs

Honeycomb[a]	Aspect ratio (d/L)	Horizontal aspect ratio (W/L)	Height (L)
$R1$	0.253	0.51	18.95 mm
$R2$	0.270	1.13	18.42 mm
$R3$	0.255	2.15	18.82 mm

[a] Rectangular honeycombs $R1$ and $R3$ are identical with those of reference [4].

Table 2 Effect of angle of inclination on Rayleigh number for Nu = 1.1

Angle θ	Rayleigh number at Nu = 1.1 $R1$	$R2$	$R3$
180 deg (Nu = 1)	29,000	12,000	12,500
150 deg	20,000	11,500	11,500
135 deg	12,000	9800	9800
120 deg	9500	9500	9500
90 deg	8500	8500	8500

Table 3 Effect of angle of inclination on Rayleigh Number for Nu = 1.25

Angle θ	Rayleigh number at Nu = 1.25 $R1$	$R2$	$R3$
180 deg	38,000	18,500	18,000
150 deg	37,500	20,000	19,500
135 deg	35,000	22,000	21,500
120 deg	27,500	24,000	25,000
90 deg	26,000	26,000	26,000

frared-opaque fluid will give an upper limit on convective transfer, since an added stabilizing effect of wall thermal radiation exchange occurs in an infrared-transparent fluid [8].

Results and Discussion

Figs. 2(*a*)–2(*e*) are plots of the dimensionless variables, Nusselt versus Rayleigh number, for the three rectangular honeycombs studied, $R1$, $R2$, and $R3$, respectively. Sun's unpublished data [5] cover the conditions for curves *a*, *b*, and *c*. The data are not plotted here, because they are not felt to be as self-consistent and reliable as the new data shown. Perhaps the most serious discrepancy between the present data and older unpublished data is an indicated critical Rayleigh number of 36,400 for honeycomb $R1$ at θ = 180 deg versus 29,000 found in the present study. In regard to tilt, the figures show that at low angles of inclination from the vertical (θ = 90 deg), there is feeble motion that increases slowly with Rayleigh number up to Rayleigh numbers of at least 20,000. At angles θ = 150 and 135 deg the convection grows even more slowly with increasing Rayleigh number up to a point at which there is a transition, presumably from a two-dimensional creeping motion to a cellular convection. The θ = 120 deg curves also display such a transition, but at larger values of Rayleigh number. For θ = 180 deg (horizontal, heated from below) there is only conduction until the critical value of Rayleigh number is reached, at which point a cellular convection initiates and makes Nusselt number rise very rapidly with further increase in Rayleigh number.

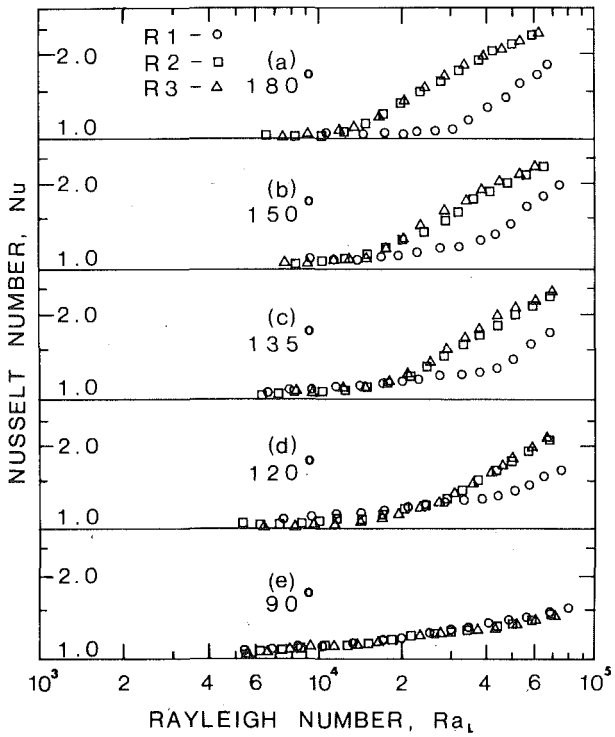

Fig. 2 Nusselt number versus Rayleigh number at indicated values of θ

With regard to horizontal aspect ratio, it is seen that there are only small differences between honeycombs $R2$ and $R3$. This fact indicates that there is little vertical end wall effect for horizontal aspect ratios greater than unity. Comparing core $R1$ with $R2$ and $R3$ one sees that at θ = 90 deg all three honeycombs plot on top of each other. As the angle of inclination is increased from θ = 90 deg, the $R2$ and $R3$ data depart from the $R1$ curves at successively lower Rayleigh numbers. This behavior shows the expected result that honeycombs with small horizontal aspect ratios are more effective in suppressing cellular convection at the higher Rayleigh numbers.

Each set of data shows that as the honeycomb is inclined, a Nusselt number of 1.1 occurs at successively lower values of Rayleigh number. Table 2 displays these values of Rayleigh number. Looking at the table one can see that, as the rectangular honeycombs are rotated from the horizontal (θ = 180 deg), the Rayleigh numbers at Nu = 1.1 approach the same value for all three horizontal aspect ratios. This behavior indicates that the vertical end walls have little if any effect for values of Nusselt number close to initiation and angles of θ = 120 deg and below. The two cells, $R2$ and $R3$, show little effect from the end walls on initiation even at angles of 120–180 deg. The difference seen is likely due to a minor L/d effect, rather than a W/L effect. Table 2 shows that for angles of inclination of θ = 135 deg and above there is a pronounced increase in critical Rayleigh number in honeycomb core $R1$ due to the small value of W/L.

Table 3 shows the values of Rayleigh number at a Nusselt number equal to 1.25, a value probably quite acceptable to a solar collector designer. In this case the effect of tilt is much different than that for Nu = 1.1. Again the $R2$ and $R3$ honeycombs are very close to each other for each of the five angles. Any difference is likely due to a minor L/d effect. The marked difference is that Rayleigh number increases consistently as the angle of inclination is decreased from θ = 180 to 90 deg. In addition there is a pronounced horizontal aspect ratio effect seen with honeycomb $R1$. The behavior indicates that, as the cell is rotated from the horizontal to the vertical position, the end wall effect is decreased until the honeycomb acts as if the end walls were not there.

Buchberg, et al. [9] give a review of natural convection heat transfer related to solar collector design. At the time of that review there were only limited experimental data indicating that honeycombs could act to reduce greatly natural convection heat transfer even when tilted. Charters and Peterson [10] questioned whether honeycombs could do so when tilted. Cane, et al. [11] measured combined convection and radiation through air for a square cell of aspect ratio 0.33, and Edwards, et al. [12] had data measured with silicone oil for a rectangular cell ($R3$ as described here) at θ = 150 deg only. The present more

complete data, particularly those in Table 3, add support to the belief that a honeycomb designed to suppress convection at $\theta = 180$ deg will serve well to reduce it to an acceptably low level even when tilted.

The designer may wonder how honeycombs of other aspect ratios will perform. The theoretical results of Catton [13, 14] predict the onset of convection for cells of arbitrary aspect ratio d/L and horizontal aspect ratio W/L for values between 0.125 and 12 and infinite Prandtl number, and for $\theta = 180$ deg. The theoretically-predicted result for a square cell with $L/d = 3$ is $Ra_{cr} = 0.7 \times 10^5$ for infinite Pr [13]. It seems to be in rough agreement with the experimental results of Heitz and Westwater [15], $Ra_{cr} = 10^5$ for water (Pr = 6 to 11), and Cane, et al. [11], $Ra_{cr} = 1.3 \times 10^5$ for air (Pr = 0.7) with a radiation effect. For low aspect ratios theory indicates an $(L/d)^4$ dependence, and the experimental results agree approximately [15]. Catton predicts $Ra_{cr} = 2.85 \times 10^4$, 1.20×10^5, and 1.10×10^4 for $d/L = 0.25$, and $W/L = 0.5$, 1, and 2, respectively versus the present results of $Ra_{cr} = 2.9 \times 10^4$, 1.2×10^4, and 1.25×10^4 for $\theta = 180$ deg and values of d/L and W/L that correspond approximately. It thus appears that aspect ratio will have a strong influence upon critical Rayleigh number, approaching $(L/d)^4$ for small d/L, but as confirmed here horizontal aspect ratio W/L has a weak effect when it is larger than unity.

In the case of large d/L the effect of Prandtl number being 0.7 instead of infinity is apparently to lower Nusselt number by approximately 13 percent [9]. Of considerable more importance than a minor Prandtl number dependency is the strong effect of radiation heat transfer through air in raising critical Rayleigh number [8]. For cells $R2$ and $R3$ containing air at $\theta = 180$ deg, Edwards and Sun [16] reported $Ra_{cr} = 2.78 \times 10^4$ and 2.60×10^4 respectively, twice as great as measured here with silicone oil. The radiation increases the heat loss by conduction from a thermal perturbation described in the discussion of reference [15] by radiatively cooling the wall adjacent to hot fluid and vice versa.

Summary and Conclusions

Heat transfer in rectangular honeycombs with an aspect ratio of approximately 0.25 but with three different horizontal aspect ratios was reported. Little effect of horizontal aspect ratio was found for values greater than unity. It was also found that at $\theta = 90$ deg there was no apparent effect of horizontal aspect ratio down to values 0.5 and that heat transfer depended only upon the aspect ratio. Conversely at near-horizontal orientations, there is a marked effect of horizontal aspect ratio for values below unity. With a Nusselt number of 1.25 as a design limit, the ability of a rectangular honeycomb with $d/L = 0.25$ and $W/L \geq 1$ to inhibit natural convection improves with tilt from the horizontal.

References

1 Buchberg, H., Lalude, O. A., and Edwards, D. K., "Performance Characteristics of Rectangular Honeycomb Solar-Thermal Converters," *Solar Energy*, Vol. 13, 1971, pp. 193–221

2 Hollands, K. G. T., "Natural Convection in Horizontal Thin-Walled Honeycomb Panels," JOURNAL OF HEAT TRANSFER, TRANS. ASME, Series C, Vol. 95, 1973, pp. 439–44.

3 Lalude, O. A., and Buchberg, H., "Design of Honeycomb Porous Bed Solar Air Heaters," *Solar Energy*, Vol. 13, 1971, pp. 223–242.

4 Sun, W. M., and Edwards, D. K., "Natural Convection in Cells With Finite Conducting Walls Heated From Below," *Heat Transfer 1970, Proceedings of the Fourth International Heat Transfer Conference*, Versailles, France, Paper NC 2.3, Elsevier Publishing Co., Amsterdam, Sept. 1970.

5 Sun, W. M., "Effect of Arbitrary Wall Conduction and Radiation on Free Convection in a Cylinder," PhD dissertation, University of California, Los Angeles, 1970.

6 Arnold, J. N., "Experimental Investigation of Natural Convection in Finite Rectangular Regions Inclined at Various Angles from 0° to 180°," MS thesis, University of California, Los Angeles, 1974.

7 Arnold, J. N., Bonaparte, P. N., Catton, I., and Edwards, D. K., "Experimental Investigation of Natural Convection in a Finite Rectangular Region Inclined at Various Angles from 0° to 180°," *Proceedings of the 1974 Heat Transfer and Fluid Mechanics Institute*, L. R. Davis and R. E. Wilson, eds., Stanford University Press, 1974, pp. 321–329.

8 Edwards, D. K., and Sun, W. M., "Effect of Wall Radiation on Thermal Instability in a Vertical Cylinder," *International Journal of Heat and Mass Transfer*, Vol. 14, 1971, pp. 15–18.

9 Buchberg, H., Catton, I., and Edwards, D. K., "Natural Convection in Enclosed Spaces—A Review of Application to Solar Energy Collection," JOURNAL OF HEAT TRANSFER TRANS. ASME, Series C, Vol. 98, 1976, pp. 182–188.

10 Charters, W. W. S., and Peterson, L. F., "Free Convection Suppression Using Honeycomb Cellular Materials," *Solar Energy*, Vol. 13, 1972, pp. 353–361.

11 Cane, R. L. D., Hollands, K. G. T., Raithby, G. D., and Unny, T. E., "Convection Suppression in Inclined Honeycombs," presented at ISES 1975 Congress, UCLA, July 28–August 1, 1975.

12 Edwards, D. K., Arnold, J. N., and Catton, I., "End-Clearance Effects on Rectangular-Honeycomb Solar Collectors," *Solar Energy*, Vol. 18, 1976, pp. 253–257.

13 Catton, Ivan, "The Effect of Insulating Vertical Walls on the Onset of Motion in a Fluid Heated From Below," *International Journal of Heat Mass Transfer*, Vol. 15, 1972, pp 665–672.

14 Catton, Ivan, "Effect of Wall Conduction on the Stability of a Fluid in a Rectangular Region Heated From Below," JOURNAL OF HEAT TRANSFER, TRANS. ASME Series C, Vol. 94, 1972, pp. 446–452.

15 Heitz, W. L., and Westwater, J. W., "Critical Rayleigh Numbers for Natural Convection of Water Confined in Square Cells With L/D From 0.5 to 8," JOURNAL OF HEAT TRANSFER, TRANS. ASME, Series C, Vol. 93, 1971 pp. 188–195.

16 Edwards, D. K., and Sun, W. M., "Predictions of the Onset of Natural Convection in Rectangular Honeycomb Structures," 1970 ISES Conference, Melbourne, Australia, Mar. 1970.

Buoyancy Cross-Flow Effects on Longitudinal Boundary Layer Flow Along a Heated Horizontal Hollow Cylinder

L. S. Yao[1] and I. Catton[2]

1 Introduction

The three-dimensional laminar boundary layer over a heated surface when gravity-driven buoyancy effects introduce significant cross-flow into an otherwise axially axisymmetric flow geometry is considered in this paper. The effect of surface heating on laminar boundary-layer stability and transition has been analyzed by Wazzan, Okamura, and Smith [1],[3] and the effects on separation by Aroesty and Berger [2]. The buoyancy cross-flow effects have not, however, been included in such studies.

The physical model chosen for study is a hollow, semi-infinite cylinder of radius a, which is aligned with its axis parallel to a uniform flow and normal to the direction of gravity. The uniform flow is assumed to have a velocity u_∞ and temperature T_∞. The surface of the cylinder is heated to a constant temperature $T_w (T_w > T_\infty)$. For most external flows, the buoyancy force can be neglected in a small pure forced convection region of size $0\ (u_\infty \nu^{1/3}/[\beta g(T_w - T_\infty)]^{2/3})$ downstream of the leading edge. Beyond that region the effect of buoyancy cross-flow increases as the fluid flows downstream. There is, however, a region where it is still small and can be treated as second order. Further downstream, a distance of $a \cdot \mathrm{Re}/\mathrm{Gr}^{1/2}$, the initially small buoyancy effect becomes as a second-order effect. The solution of the intermediate region, where the buoyancy effect is second order, is presented in this paper. In this region, the fluid which is entrained by the basic forced laminar boundary-layer flow is given a cross-flow component by the buoyancy effect of the heated walls. Because of this entrainment, the secondary flow velocity grows linearly in the downstream direction. This is a different situation from the usual pure

[1] The Rand Corporation, 1700 Main Street, Santa Monica, Calif. Assoc. Mem. ASME.

[2] Assoc. Professor, University of California, Los Angeles, Calif. Mem. ASME

[3] Numbers in brackets designate References at end of technical note.

Contributed by the Heat Transfer Division of THE AMERICAN SOCIETY OF MECHANICAL ENGINEERS. Manuscript received by the Heat Transfer Division June 17, 1976.

complete data, particularly those in Table 3, add support to the belief that a honeycomb designed to suppress convection at $\theta = 180$ deg will serve well to reduce it to an acceptably low level even when tilted.

The designer may wonder how honeycombs of other aspect ratios will perform. The theoretical results of Catton [13, 14] predict the onset of convection for cells of arbitrary aspect ratio d/L and horizontal aspect ratio W/L for values between 0.125 and 12 and infinite Prandtl number, and for $\theta = 180$ deg. The theoretically-predicted result for a square cell with $L/d = 3$ is $Ra_{cr} = 0.7 \times 10^5$ for infinite Pr [13]. It seems to be in rough agreement with the experimental results of Heitz and Westwater [15], $Ra_{cr} = 10^5$ for water (Pr = 6 to 11), and Cane, et al. [11], $Ra_{cr} = 1.3 \times 10^5$ for air (Pr = 0.7) with a radiation effect. For low aspect ratios theory indicates an $(L/d)^4$ dependence, and the experimental results agree approximately [15]. Catton predicts $Ra_{cr} = 2.85 \times 10^4$, 1.20×10^5, and 1.10×10^4 for $d/L = 0.25$, and $W/L = 0.5$, 1, and 2, respectively versus the present results of $Ra_{cr} = 2.9 \times 10^4$, 1.2×10^4, and 1.25×10^4 for $\theta = 180$ deg and values of d/L and W/L that correspond approximately. It thus appears that aspect ratio will have a strong influence upon critical Rayleigh number, approaching $(L/d)^4$ for small d/L, but as confirmed here horizontal aspect ratio W/L has a weak effect when it is larger than unity.

In the case of large d/L the effect of Prandtl number being 0.7 instead of infinity is apparently to lower Nusselt number by approximately 13 percent [9]. Of considerable more importance than a minor Prandtl number dependency is the strong effect of radiation heat transfer through air in raising critical Rayleigh number [8]. For cells $R2$ and $R3$ containing air at $\theta = 180$ deg, Edwards and Sun [16] reported $Ra_{cr} = 2.78 \times 10^4$ and 2.60×10^4 respectively, twice as great as measured here with silicone oil. The radiation increases the heat loss by conduction from a thermal perturbation described in the discussion of reference [15] by radiatively cooling the wall adjacent to hot fluid and vice versa.

Summary and Conclusions

Heat transfer in rectangular honeycombs with an aspect ratio of approximately 0.25 but with three different horizontal aspect ratios was reported. Little effect of horizontal aspect ratio was found for values greater than unity. It was also found that at $\theta = 90$ deg there was no apparent effect of horizontal aspect ratio down to values 0.5 and that heat transfer depended only upon the aspect ratio. Conversely at near-horizontal orientations, there is a marked effect of horizontal aspect ratio for values below unity. With a Nusselt number of 1.25 as a design limit, the ability of a rectangular honeycomb with $d/L = 0.25$ and $W/L \geq 1$ to inhibit natural convection improves with tilt from the horizontal.

References

1 Buchberg, H., Lalude, O. A., and Edwards, D. K., "Performance Characteristics of Rectangular Honeycomb Solar-Thermal Converters," *Solar Energy*, Vol. 13, 1971, pp. 193–221

2 Hollands, K. G. T., "Natural Convection in Horizontal Thin-Walled Honeycomb Panels," JOURNAL OF HEAT TRANSFER, TRANS. ASME, Series C, Vol. 95, 1973, pp. 439–44.

3 Lalude, O. A., and Buchberg, H., "Design of Honeycomb Porous Bed Solar Air Heaters," *Solar Energy*, Vol. 13, 1971, pp. 223–242.

4 Sun, W. M., and Edwards, D. K., "Natural Convection in Cells With Finite Conducting Walls Heated From Below," *Heat Transfer 1970, Proceedings of the Fourth International Heat Transfer Conference*, Versailles, France, Paper NC 2.3, Elsevier Publishing Co., Amsterdam, Sept. 1970.

5 Sun, W. M., "Effect of Arbitrary Wall Conduction and Radiation on Free Convection in a Cylinder," PhD dissertation, University of California, Los Angeles, 1970.

6 Arnold, J. N., "Experimental Investigation of Natural Convection in Finite Rectangular Regions Inclined at Various Angles from 0° to 180°," MS thesis, University of California, Los Angeles, 1974.

7 Arnold, J. N., Bonaparte, P. N., Catton, I., and Edwards, D. K., "Experimental Investigation of Natural Convection in a Finite Rectangular Region Inclined at Various Angles from 0° to 180°," *Proceedings of the 1974 Heat Transfer and Fluid Mechanics Institute*, L. R. Davis and R. E. Wilson, eds., Stanford University Press, 1974, pp. 321–329.

8 Edwards, D. K., and Sun, W. M., "Effect of Wall Radiation on Thermal Instability in a Vertical Cylinder," *International Journal of Heat and Mass Transfer*, Vol. 14, 1971, pp. 15–18.

9 Buchberg, H., Catton, I., and Edwards, D. K., "Natural Convection in Enclosed Spaces—A Review of Application to Solar Energy Collection," JOURNAL OF HEAT TRANSFER TRANS. ASME, Series C, Vol. 98, 1976, pp. 182–188.

10 Charters, W. W. S., and Peterson, L. F., "Free Convection Suppression Using Honeycomb Cellular Materials," *Solar Energy*, Vol. 13, 1972, pp. 353–361.

11 Cane, R. L. D., Hollands, K. G. T., Raithby, G. D., and Unny, T. E., "Convection Suppression in Inclined Honeycombs," presented at ISES 1975 Congress, UCLA, July 28–August 1, 1975.

12 Edwards, D. K., Arnold, J. N., and Catton, I., "End-Clearance Effects on Rectangular-Honeycomb Solar Collectors," *Solar Energy*, Vol. 18, 1976, pp. 253–257.

13 Catton, Ivan, "The Effect of Insulating Vertical Walls on the Onset of Motion in a Fluid Heated From Below," *International Journal of Heat Mass Transfer*, Vol. 15, 1972, pp 665–672.

14 Catton, Ivan, "Effect of Wall Conduction on the Stability of a Fluid in a Rectangular Region Heated From Below," JOURNAL OF HEAT TRANSFER, TRANS. ASME Series C, Vol. 94, 1972, pp. 446–452.

15 Heitz, W. L., and Westwater, J. W., "Critical Rayleigh Numbers for Natural Convection of Water Confined in Square Cells With L/D From 0.5 to 8," JOURNAL OF HEAT TRANSFER, TRANS. ASME, Series C, Vol. 93, 1971 pp. 188–195.

16 Edwards, D. K., and Sun, W. M., "Predictions of the Onset of Natural Convection in Rectangular Honeycomb Structures," 1970 ISES Conference, Melbourne, Australia, Mar. 1970.

Buoyancy Cross-Flow Effects on Longitudinal Boundary Layer Flow Along a Heated Horizontal Hollow Cylinder

L. S. Yao[1] and I. Catton[2]

1 Introduction

The three-dimensional laminar boundary layer over a heated surface when gravity-driven buoyancy effects introduce significant cross-flow into an otherwise axially axisymmetric flow geometry is considered in this paper. The effect of surface heating on laminar boundary-layer stability and transition has been analyzed by Wazzan, Okamura, and Smith [1],[3] and the effects on separation by Aroesty and Berger [2]. The buoyancy cross-flow effects have not, however, been included in such studies.

The physical model chosen for study is a hollow, semi-infinite cylinder of radius a, which is aligned with its axis parallel to a uniform flow and normal to the direction of gravity. The uniform flow is assumed to have a velocity u_∞ and temperature T_∞. The surface of the cylinder is heated to a constant temperature $T_w (T_w > T_\infty)$. For most external flows, the buoyancy force can be neglected in a small pure forced convection region of size $0\ (u_\infty \nu^{1/3}/[\beta g(T_w - T_\infty)]^{2/3})$ downstream of the leading edge. Beyond that region the effect of buoyancy cross-flow increases as the fluid flows downstream. There is, however, a region where it is still small and can be treated as second order. Further downstream, a distance of $a \cdot \mathrm{Re}/\mathrm{Gr}^{1/2}$, the initially small buoyancy effect becomes as a second-order effect. The solution of the intermediate region, where the buoyancy effect is second order, is presented in this paper. In this region, the fluid which is entrained by the basic forced laminar boundary-layer flow is given a cross-flow component by the buoyancy effect of the heated walls. Because of this entrainment, the secondary flow velocity grows linearly in the downstream direction. This is a different situation from the usual pure

[1] The Rand Corporation, 1700 Main Street, Santa Monica, Calif. Assoc. Mem. ASME.

[2] Assoc. Professor, University of California, Los Angeles, Calif. Mem. ASME

[3] Numbers in brackets designate References at end of technical note.

Contributed by the Heat Transfer Division of THE AMERICAN SOCIETY OF MECHANICAL ENGINEERS. Manuscript received by the Heat Transfer Division June 17, 1976.

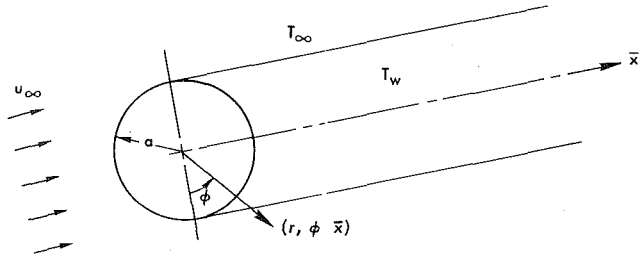

Fig. 1 Physical model and coordinates

free convection flow, where all boundary-layer entrainment is through buoyancy, and where the axial entrainment is zero.

2 Analysis

The nondimensional Boussinesq boundary-layer equations in cylindrical coordinates, as shown in Fig. 1, are

$$\frac{\partial u}{\partial x} + \frac{\partial w}{\partial r} + \frac{\partial v}{\partial \phi} = 0 \tag{1a}$$

$$u\frac{\partial u}{\partial x} + w\frac{\partial u}{\partial r} + v\frac{\partial u}{\partial \phi} = \frac{\partial^2 u}{\partial r^2} \tag{1b}$$

$$u\frac{\partial v}{\partial x} + w\frac{\partial v}{\partial r} + v\frac{\partial v}{\partial \phi} = \frac{\partial^2 v}{\partial r^2} + \epsilon \cdot \sin\phi \cdot \theta \tag{1c}$$

$$u\frac{\partial \theta}{\partial x} + w\frac{\partial \theta}{\partial r} + w\frac{\partial \theta}{\partial \phi} = \frac{1}{\mathrm{Pr}}\frac{\partial^2 \theta}{\partial r^2} \tag{1d}$$

after neglecting smaller order terms under the condition that

$$\mathrm{Gr}/\mathrm{Re}^{3/2} > 1 \tag{2}$$

The nondimensional variables used in scaling equations (1) are

$$u = \frac{\bar{u}}{u_\infty}, \quad v = \frac{\bar{v}}{u_\infty}, \quad w = \frac{\bar{w}\sqrt{\mathrm{Re}}}{u_\infty} \quad \text{(velocities)}$$

$$\theta = \frac{T - T_\infty}{T_w - T_\infty} \quad \text{(temperature)}$$

$$x = \frac{\bar{x}}{a}, \quad r = \frac{(\bar{r} - a)\sqrt{\mathrm{Re}}}{a} \quad \text{(coordinates)}$$

$$\mathrm{Re} = \frac{u_\infty a}{\nu} \quad \text{(Reynolds number)}$$

$$\mathrm{Gr} = \frac{\beta \bar{g} a^3 (T_w - T_\infty)}{\nu^2} \quad \text{(Grashof number)}$$

$$\mathrm{Pr} = \nu/\alpha \quad \text{(Prandtl number)}$$

$$\epsilon = \mathrm{Gr}/\mathrm{Re}^2 \tag{3}$$

where a is the radius of the cylinder, ν is the kinematic viscosity, u_∞ and T_∞ are the free stream velocity and temperature, respectively, T_w is the wall temperature, α is the thermal diffusivity, $\bar{g}$ is the gravitational acceleration, and β is the thermal expansional coefficient, which is related to density by $\rho = \rho_\infty[1 - \beta(T - T_\infty)]$. The terms of the transverse curvature effects, which have been neglected in equations (1), reflect the fact that the thickness of the boundary layer $0(a/\sqrt{\mathrm{Re}})$ is much thinner than the radius, a, of the cylinder.

As mentioned previously, for the region very close to the leading edge of the cylinder, the buoyancy effect is negligible. The magnitude of this region, defined by equation (2), is of the order

$$\bar{x} \sim \frac{u_\infty \nu^{1/3}}{[\beta \bar{g}(T_w - T_\infty)]^{2/3}}$$

Downstream of the leading-edge region, the solution of the equations in (1) can be expanded into a series of ϵ, if ϵ is small.

$$u = f_0' + \epsilon(2x)^2 F_1' \cos\phi + \ldots$$

$$v = \epsilon(2x) F_2' \sin\phi + \ldots \tag{4}$$

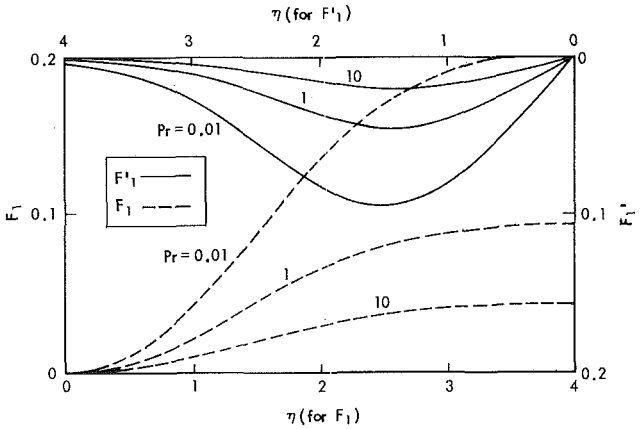

Fig. 2 F_1 and F_1' functions

$$w = \frac{1}{\sqrt{2x}}(\eta f_0' - f_0) + \epsilon(2x)^{3/2}(\eta F_1' - 5F_1 - F_2)\cos\phi + \ldots$$

$$\theta = \theta_0 + \epsilon(2x)^2 G \cos\phi + \ldots \tag{4}$$

Substitution of the expansion given by equations (4) into equations (1), and the collection of terms of equal order will result in the perturbation equations. The perturbation equations of lowest order are

$$f_0''' + f_0 f_0'' = 0 \tag{5a}$$

$$\theta_0'' + \mathrm{Pr} f_0 \theta_0' = 0 \tag{5b}$$

where the prime denotes a derivative with respect to η, with $\eta = r/\sqrt{2x}$ being the Blasius similarity variable. The solution of equation (5a) is the Blasius solution. Equation (5b) is the forced-convection energy equation, whose solution was first given by Pohlhausen in 1921.

The first-order perturbation equations are:

$$F_1''' + f_0 F_1'' - 4f_0' F_1' + 5f_0'' F_1 = -f_0'' F_2 \tag{6a}$$

$$F_2''' + f_0 F_2'' - 2f_0' F_2' = -\theta_0 \tag{6b}$$

$$\frac{1}{\mathrm{Pr}} G'' + (f_0 G' - 4f_0' G) = -\theta_0'(5F_1 + F_2) \tag{6c}$$

The associated boundary conditions for equations (10) are

$$F_1(0) = F_1'(0) = F_1'(\infty) = 0$$

$$F_2(0) = F_2'(0) = F_2'(\infty) = 0$$

$$G(0) = G(\infty) = 0 \tag{7}$$

The expansion (4) breaks down at a distance of $0(a \cdot \mathrm{Re}/\mathrm{Gr}^{1/2})$, corresponding physically to the point beyond which the buoyancy cross-flow effect, initially small, could become as important as the forced-convention effects.

3 Results and Discussion

Numerical values of the functions F_1, F_1', F_2, F_2', and G are integrated numerically and presented in Figs. 2–4 for Pr = 0.01, 1, 10. Equations (4) show that the buoyancy force stabilizes the flow and accelerates its speed over the lower half of the cylinder ($-\pi/2 < \phi < \pi/2$). Over the upper half of the cylinder ($\pi/2 < \phi < 3\pi/2$), the axial flow is decelerated and may be destabilized. The cross-flow is accelerated by the buoyancy force from the lower stagnation point ($\phi = 0$) to attain its maximum value at $\phi = \pi/2$, and then decelerated to its upper stagnation point ($\phi = \pi$). It is interesting to note that the solution (4) represents the case of a vertical flat plate when $\phi = \pi/2$ for the region near the leading edge where the cross-flow is small. For a vertical flat plate, the cross-flow is decoupled from the axial flow; in

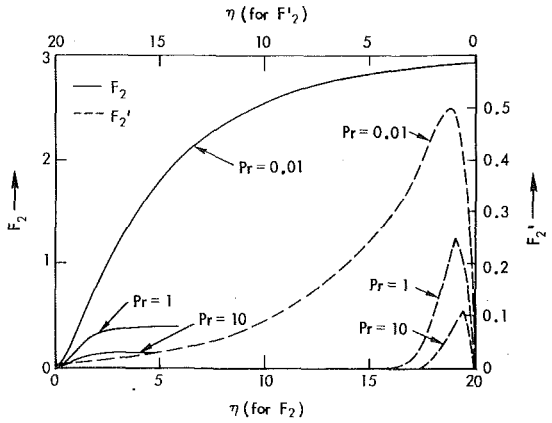

Fig. 3 F_2 and F_2' functions

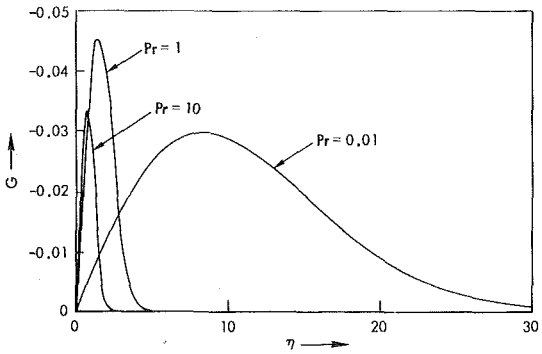

Fig. 4 G function

other words, the cross-flow does not affect the axial flow and the temperature distribution. The magnitude of the circumferential velocity, v, is being increased as a linear function of the axial coordinate, and eventually becomes one of the dominant velocity components when the fluid flows far enough downstream.

The local Nusselt number with respect to a and $(T_w - T_\infty)$ can be derived from equation (12), which is

$$\mathrm{Nu}_x = -\sqrt{\frac{\mathrm{Re}}{2x}}\left[\theta_0'(0) + \epsilon(2x)^2 G'(0) \cdot \cos\phi + \ldots\right] \tag{8}$$

The first term of equation (8) represents the Nusselt number for a pure forced convection. The relative importance of heat transfer due to cross-flow can be indicated by

$$\mathrm{Nu}_x/(\mathrm{Nu}_x)_{fc} = 1 + \epsilon(2x)^2 G_1'(0)/\theta_0'(0) \cdot \cos\phi + \ldots \tag{9}$$

where fc denotes the forced convection. Equation (9) shows that the cross-flow enhances the heat transfer on the lower half of the cylinder and degrades it on the upper half of the cylinder. Values of $G'(0)/\theta_0'(0)$ are given in Table 1 for Pr = 0.01, 1, 10.

The local shear stress at the cylinder surface can be computed from the equation

Table 1 Enhancement parameters for heat transfer and wall shear stress

Pr	$G'(0)/\theta_0'(0)$	$F_1''(0)/f_0''(0)$	$F_2''(0)$
0.01	0.08638	0.19509	0.92627
1	0.09959	0.09959	0.61904
10	0.06576	0.04458	0.39761

$$\tau_{rx} = \mu\left(\frac{\partial u}{\partial r}\right)_{r=0} \quad \text{and} \quad \tau_{r\phi} = \left(\frac{\partial v}{\partial r}\right)_{r=0}$$

Introducing the series expansions (4), the relative importance of the cross-flow effect on the axial shear stress can be found by

$$\frac{\tau_{rx}}{(\tau_{rx})_{fc}} = 1 + \epsilon(2x)^2 \frac{F_1''(0)}{f_0''(0)} \cdot \cos\phi + \ldots \tag{10}$$

The circumferential shear stress can be shown to be proportional to

$$\tau_{r\phi} \sim \epsilon\sqrt{2x}\, F_2''(0) \cdot \sin\phi \tag{11}$$

Values of $F_1''(0)/f_0''(0)$ and F_2'' are also given in Table 1. As can be seen, for $\phi \simeq \pi$, the ratio decreases as ϵx^2 increases, which indicates the possibility of enhanced separation. For moderate free-stream velocities, separation could occur within several radii of the leading edge. Further, the unevenly distributed axial shear stress, equation (10), can induce a pitch moment and could cause an oscillation of the moving cylinder.

Equations (9) and (10) indicate that the cross-flow effect on heat transfer and shear stress for a heated horizontal cylinder grows rapidly when the fluid flows downstream, proportionally to x^2. This means that an initially small cross-flow effect, which may be neglected in the region close to the leading edge of the cylinder, cannot be ignored for a heated, long slender body.

The analysis is applicable to flow over the outer or the inner surface of a heated hollow cylinder. It is also applicable to flow over a slender body of revolution if the pressure gradient associated with the nose shape is negligible. The series solution presented in this work demonstrates that buoyancy effects can have a strong effect on developing flow along a heated horizontal cylinder even in the region of $0(a)$ and supplies the upstream boundary conditions for calculations downstream of this region. In the downstream region, which is of 0(a Re/$\mathrm{Gr}^{1/2}$), the magnitude of the buoyancy-induced cross-flow is of the same order as the axial flow and no similarity solution is possible.

Acknowledgment

The authors wish to express their sincere appreciation to Drs. Carl Gazley, Jr., S. A. Berger, J. Aroesty, and W. S. King for the stimulating discussions and to G. M. Harpole for the numerical analysis necessary to complete this work.

References

1 Wazzan, A. R., Okamura, T. T., and Smith, A. M. O., "The Stability and Transition of Heated and Cooled Incompressible Laminar Boundary Layers," *Proceedings Fourth International Heat Transfer Conference*, Vol. 2, Paris-Versailles, 1970.

2 Aroesty, J., and Berger, S. A., *Controlling the Separation of Laminar Boundary Layers in Water: Heating and Suction*, The Rand Corporation, R-1789-ARPA, Sept. 1975.

Radiation-Convection Interaction in an Absorbing-Emitting Liquid in Natural Convection Boundary Layer Flow[1]

J. D. Bankston,[2] J. R. Lloyd,[3] and J. L. Novotny[4]

Nomenclature

$\overline{A}_i$ = dimensionless total band absorption of ith region A_i/ω_i
d_i = intensity of the ith band compared to all bands
$e_{b\omega j}'$ = derivative of Planck function at ω_j with respect to temperature
f = dimensionless stream function defined by $\Psi = (5^4 g\beta q_w \nu^3/k)^{1/5} x^{4/5} f(\eta, \xi)$
Gr* = modified Grashof number, $g\beta q_w x^4/k\nu^2$
Pr = Prandtl number
Q_i = radiation integral, $\rho_w \int_0^\infty \theta' \overline{A}_i'(u_{1i})dz - \int_0^\eta \theta' \overline{A}_i'(u_{2i})dz + \int_\eta^\infty \theta' \overline{A}_i'(-u_{2i})dz$
S_i = integrated band intensity
u_{1i}, u_{2i} = optical depth
γ = a measure of the radiative flux at the wall, $= 4\epsilon_w n^2 \sigma T_\infty^3 x/k(\mathrm{Gr}^*/5)^{1/5}$
ϵ_w = wall emissivity
η = similarity variable, $\eta = y/x\ (\mathrm{Gr}^*/5)^{1/5}$
θ = dimensionless temperature, $\theta = k/xq_w(\mathrm{Gr}^*/5)^{1/5}\ (T_\infty - T)$
ν = kinematic viscosity
ξ = radiation interaction parameter, $\xi = x^2 \Sigma_i S_j e_{b\omega j}'/k(\mathrm{Gr}^*/5)^{2/5}$
σ = Stephan Boltzman constant
Ψ = stream function
ω = wave number

Introduction

Considerable interest has been shown in radiation interaction with conduction or convection for heat transfer in fluids. Initially emphasis was placed on studying the interaction in gases. This work proceeded from gray-gas studies, such as that of Cess [1],[5] to non-gray analyses employing limiting forms to approximate the band profile, e.g., Bratis and Novotny [2], and more recently to an analysis by Novotny, et al. [3] employing the method of local nonsimilarity and the continuous correlation of Tien and Lowder [4] to account for the band absorption.

Radiation interaction in heat-transfer processes in liquids has recently received considerable attention due to the fact that the band absorptance is considerably greater for absorbing emitting liquids than gases. Thus, the approximate methods for analyzing radiation effects, such as by Bratis and Novotny [2], cannot be applied to liquids such as CCl_4. Additionally, liquids are interesting because their radiation interaction effects are independent over a wide range of pressures. Poltz [5, 6] and Poltz and Jugel [7], in analytical and experimental studies of radiation-conduction interaction in horizontal liquid layers heated from above, found that there were indeed significant radiation effects for a number of fluids. Schödel and Grigull [8] in a similar analysis considered radiation-conduction interaction and the dependency of the absorption coefficient on wavelength. They demonstrated that the heat flux by radiation was much greater than previously thought by Poltz and Jugel [7], and that it constituted an appreciable portion of the total heat transfer. The analysis was confirmed through the interferometric evaluation of temperature profiles in layers of different fluids.

An analysis comparing the effects of different band profiles of the Lorentz, Gaussian, and exponential types was performed by Novotny and Bratis [9] for radiation-conduction interaction in liquid carbon tetrachloride. They concluded that use of the exponential band profile over all wavelengths more closely represented the actual interaction process. In another study Novotny, et al. [10] presented two models for the total band absorption of absorbing-emitting liquids. The models, functions of two adjustable parameters, were based upon the exponential profile. The results were compared to total band absorption data and to a prediction based on spectral integration. Although both models appeared to be sufficiently accurate for heat-transfer work, the authors preferred their random model.

The present note concerns radiation-convection interaction in a liquid in natural convection flow adjacent to a vertical surface will constant wall heat flux. Local nonsimilarity techniques are employed. The method has certain advantages over other techniques in that it provides an internal check on the accuracy of the solution and permits the use of continuous correlations rather than limiting approximations to the total band absorptance.

Analysis

The geometry of the problem is shown in the insert of Fig. 1. The analysis is essentially the same as found in reference [3] for gases and is given in complete detail in reference [11]. Since no limiting approximations were made in the radiation analysis, all that is necessary to convert this analysis to a liquid is to modify the band absorption formulation to fit the liquid behavior. This illustrates the versatility of this method. Only the final equations will be included herein. Carbon tetrachloride is the working fluid in the present work and the random model recommended by Novotny, et al. [10] is used to account for the total band absorption.

The continuity equation, the momentum equation, and the energy equation are transformed into dimensionless form through the use of η, the usual natural convection similarity variables, ξ, the local nonsimilarity variable which depends on x, the distance along the surface, Gr*, the modified Grashof number, θ, the dimensionless temperature, and f, the dimensionless stream function. The resulting governing equations in dimensionless form are given by

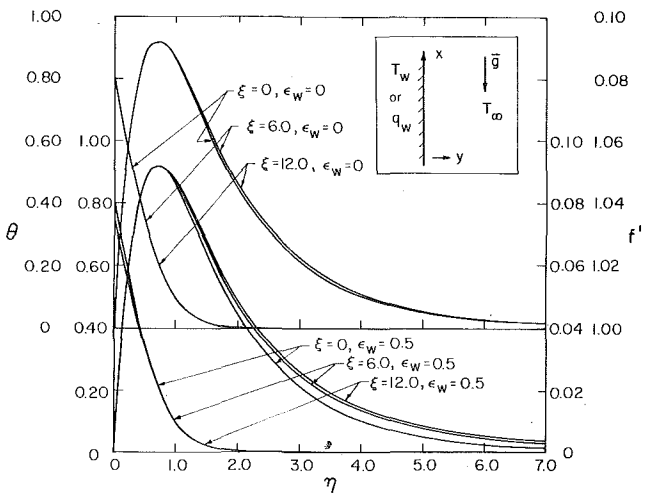

Fig. 1 Velocity and temperature distribution, q_w = constant

[1] This work was sponsored under National Science Foundation Grant GK-20382.

[2] Aerospace and Mechanical Engineering, University of Notre Dame, Notre Dame, Ind. Presently: School of Engineering, University of New Orleans, New Orleans, La.

[3] Aerospace and Mechanical Engineering, University of Notre Dame, Notre Dame, Ind.

[4] Aerospace and Mechanical Engineering, University of Notre Dame, Notre Dame, Ind. Deceased.

[5] Numbers in brackets designate References at end of technical note.

Contributed by the Heat Transfer Division of THE AMERICAN SOCIETY OF MECHANICAL ENGINEERS. Manuscript received by the Heat Transfer Division January 28, 1976.

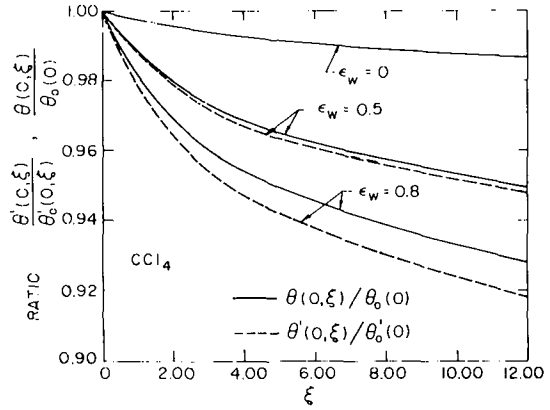

Fig. 2 Effect of radiation on wall temperature and wall temperature gradient, q_w = constant

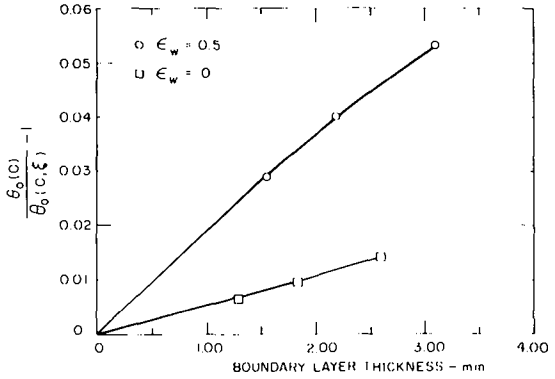

Fig. 3 Radiation effect as a function of thermal boundary layer thickness, q_w = constant

$$\frac{\theta''}{\mathrm{Pr}} - f'\theta + 4f\theta' + \frac{3}{2\mathrm{Pr}}\xi\sum_i d_i Q_i = 2\xi\left(f'\frac{d\theta}{d\xi} - \theta'\frac{df}{d\xi}\right) \tag{1}$$

and

$$f''' - 3(f')^2 + 4ff'' - \theta = 2\xi\left(f'\frac{df'}{d\xi} - f''\frac{df}{d\xi}\right) \tag{2}$$

Here the primes denote differentiation with respect to η. The boundary conditions are similarly transformed. The boundary conditions are

$$\theta'(0,\xi) = 1.0 + \gamma\theta(0,\xi) - 3/2\epsilon_w\xi\sum_i d_i\int_0^\infty \theta\bar{A}_i'(u_i)dz \tag{3}$$

$$\theta(\infty,\xi) = f(0,\xi) = f'(0,\xi) = f'(\infty,\xi) = 0 \tag{4}$$

Under the local similarity concept θ and f are considered to be slowly varying functions of ξ. Thus, to a first approximation, the right-hand side of equations (1) and (2) are considered to be negligible and are dropped. This results in a set of equations and boundary conditions referred to as the local similarity model.

Differentiating the governing equations (1) and (2) and their boundary conditions with respect to ξ, a set of equations and boundary conditions are obtained which together with equations (1) and (2) are termed the two equation local nonsimilarity model. If second-order partials of ξ are then neglected, these equations may be solved simultaneously along with equations (1) and (2). The additional equations which complete the two equation model are

$$\frac{\phi''}{\mathrm{Pr}} - g'\theta + 6\theta'g - 3f'\phi + 4f\phi' + \frac{3}{2\mathrm{Pr}}\sum_j d_j Q_j = 0 \tag{5}$$

$$g''' - 8f'g' + 4fg'' + 6f''g - \phi = 0 \tag{6}$$

Boundary conditions:

$$\theta'(0,\xi) = 1 + \gamma\theta(0,\xi) - \frac{3}{2}\epsilon_w\xi\sum_i d_i\int_0^\infty \theta\bar{A}_i'(u_i)dz \tag{7}$$

$$\phi'(0,\xi) = \gamma\phi(0,\xi) + \frac{2\epsilon_w\sigma n^2 T_\infty^3(\mathrm{Gr}^*/5)^{1/5}\theta(0,\xi)}{x\sum_i S_j e_{b\omega j}'} - \frac{3}{2}\epsilon_w\sum_i d_i\int_0^\infty \theta\bar{A}_i'(u_i)dz - \frac{3}{2}\epsilon_w\xi\sum_i d_i\int_0^\infty \phi\bar{A}_i'(u_i dz - \frac{3\epsilon_w x\xi}{4(\mathrm{Gr}^*/5)^{1/5}}\sum_i\frac{d_i S_i}{b_i}\int_0^\infty \theta\bar{A}_i'(u_i)dz \tag{8}$$

$$\phi(\infty,\xi) = g(0,\xi) = g'(0,\xi) = g'(\infty,\xi) = 0$$

Here

$$\phi = \partial\theta/\partial\xi \quad \text{and} \quad -g = \partial f/\partial\xi \tag{9}$$

This two-equation model is expected to yield a better solution than the local simularity model since a first-level approximation to the right-hand side of equations (1) and (2) is obtained. This procedure of obtaining approximations to the next higher order differential with respect to ξ is continued until good agreement is obtained between successive levels. Good agreement is an indication of a valid solution, according to Sparrow and Yu [12]. Since the equations thus derived are in the form of total differential equations with only one independent variable, η, straightforward Runge-Kutta integration can be employed.

Results

Solutions were obtained using both the local similarity and the two-equation nonsimilarity approximations for wall emittances of 0, 0.5, and 0.8. Essentially no difference was found between the two models for values of ξ out to 12, the maximum value calculated, and thus only the local similarity results are presented. Fig. 1 presents the velocity and temperature profiles for wall emissivities of 0 and 0.5, respectively, with ξ being the parameter. The case of $\epsilon = 0$, $\xi = 0$ corresponds to no radiation at all. For wall emittance of 0 there is very little effect due to radiation for either the velocity or temperature profiles. As the wall emittance is increased the effect of radiation is increased, as is evidenced by the thicker boundary layers for both velocity and temperature and the lower temperature gradient at the wall. The nonsimilar behavior is ordered in both wall emittance and interaction parameter ξ. From Fig. 1 it may be deduced that for the range of parameters studied here, the wall emittance has a greater effect on the velocity and temperature profiles than ξ. This effect can be clearly seen from Fig. 2. Fig. 2 plots the ratio of the wall temperature and the wall temperature gradients with radiation included to the convective heat flux without radiation as a function of ξ. It might be mentioned that this figure enables the calculation of radiation heat fluxes since the total wall heat is the sum of the convective plus radiative components and is a constant. Thus, for a wall emissivity of zero and one can find the constant value and then proceed from there.

No experimental data corresponding to the conditions of the present study are available; however, a measure of the accuracy of the solutions may be obtained from the results listed by Novotny and Bratis [9]. In their work involving perfectly reflecting walls, it was shown that the effect of radiation interaction with conduction in CCl_4 is nearly linear with depth of the liquid layer for depths less than 5 mm. One would expect, then, that for small thermal boundary layer thicknesses (say, less than 5 mm) the radiation effect would increase nearly linearly with boundary layer thickness. The radiation effect predicted in the present study for $\epsilon = 0$ or a perfectly reflecting wall is plotted against the boundary layer thickness, defined as the location where $\theta = 0.01\ \theta$ wall, in Fig. 3. The effect is, indeed, nearly linear with boundary layer thickness further indicating validity of the present results. Shown also in the figure are the predictions for $\epsilon_w = 0.5$ which

also are almost linear, but with a slight downward curve.

It has been shown that the present method yields solutions which are reasonable in comparison with available data. This successful extension of the analysis method for gases of Novotny, et al. [3] to liquid carbon tetrachloride points out the versatility of the method of analysis. That this technique has been demonstrated to work indicates that the technique of Sparrow and Yu [12] can indeed be applied quite successfully to radiation analyses. Also, it is expected that this technique can be used for other liquids as long as the band absorption formulation is known. It is emphasized that this extension to a liquid required essentially no change in the analysis and only slight modification of the computer program for the gas analysis [3].

References

1 Cess, R. D., "The Interaction of Thermal Radiation with Free Convection Heat Transfer," *International Journal of Heat Mass Transfer,* Vol. 9, 1966, pp. 1269–1277.

2 Bratis, J. C., and Novotny, J. L., "Radiation-Convection Interaction in Real Gases," *AIAA Progress in Astronautics and Aeronautics,* Vol. 31, 1973, pp. 329–348.

3 Novotny, J. L., Lloyd, J. R., and Bankston, J. D., Jr., "Local Non-Similarity Applied to Free Convection Boundary Layers with Radiation Interaction," AIAA Paper No. 74-653, Thermophysics and Heat Transfer Conference, Boston, Mass., July 1974, Also see AIAA 1974 Thermophysics Volume to be published 1976.

4 Tien, C. L., and Lowder, J. E., "A Correlation of Total Band Absorptance of Radiative Gases," *International Journal of Heat Mass Transfer,* Vol. 9, 1974, pp. 698–701.

5 Poltz, H., "Die Warmeleitfahigkeit von Flussigkeiten II. Der Strahlungsanteil der Effektiven Warmeleitfahigkeit," *International Journal of Heat Mass Transfer,* Vol. 8, 1965, pp. 515–527.

6 Poltz, H., "Die Warmeleitfahigkeit von Fluzzigkeiten III. Abhangigkeit der Warmeleitfahigkeit von der Schichtdicke bei roganischen Flussigkeiten," *International Journal of Heat Mass Transfer,* Vol. 8, 1965, pp. 609–620.

7 Poltz, H., and Jugel, R., "The Thermal Conductivity of Liquids—IV. Temperature Dependence of Thermal Conductivity," *International Journal of Heat Mass Transfer,* Vol. 10, 1967, pp. 1075–1088.

8 Schödel, G., and Grigull, U., "Kombinierte Warmeleitung and Warmestrahlung in Flussigkeiten," *Heat Transfer,* 1970, Vol. 3, Elsevier, Amsferdam, Article R.2.2.

9 Novotny, J. L., and Bratis, J. C., "Radiative Transfer in Liquid CCl_4," *Journal Quant. Spectrosc. Radiat. Transfer,* Vol. 12, 1972, pp. 901–911.

10 Novotny, J. L., Negrelli, D. E., and Van den Driessche, T., "Total Band Absorption Models for Absorbing-Emitting Liquids CCl_4," JOURNAL OF HEAT TRANSFER TRANS. ASME, Series C, Vol. 96, 1974, pp. 27–31.

11 Bankston, J. D., "Analytical Study of Radiation-Convection Interaction of Absorbing-Emitting Fluids in Non-Similar Natural Convection Boundary Layer Flow," PhD dissertation, Aerospace and Mechanical Engineering, University of Notre Dame, Notre Dame, Ind., 1975.

12 Sparrow, E. M., and Yu, H. S., "Local Non-Similarity Thermal Boundary Layer Solutions," JOURNAL OF HEAT TRANSFER, Vol. 93, 1972, pp. 328–334.

Heat Conduction in a Stack of Parallelograms Separated by Thin Partition Walls

K. C. Chung[1] and K. N. Astill[1]

Nomenclature

b = thickness of partition wall
D = height of parallelogram
K_b = thermal conductivity of partition wall
K_s = thermal conductivity of solid
ℓ = dimensionless length of parallelogram; L/D
L = length of parallelogram
q = local heat flux density
Q = total heat flux across $x = \ell/2$
Qr = total heat flux in a rectangle
Rk = ratio of conductances; $(Kb/b)/(Ks/D)$
T = temperature
x, y = rectangular coordinates
$x, \tilde{y}$ = parallelogrammic coordinates
α = angle between y and $\tilde{y}$ coordinates
$\delta x, \delta y, \delta\tilde{y}$ = grid space in x-, y-, and $\tilde{y}$-direction, respectively
η = ratio of heat flux; Q/Qr
ω = relaxation factor

Subscripts

h, c, m = high, low and medium value, respectively
i, j = grid number in $\tilde{y}$- and x-direction, respectively
M, N = number of grids in x- and $\tilde{y}$-direction, respectively

Superscript

k = order of iteration

Introduction

For two-dimensional conduction of rectangular solids with simple boundary conditions, many analytical solutions, either steady or transient, are known. The solutions are in forms of double Fourier series which are obtainable by separation of variables or conformal mapping. The latter case is applicable only for either the Dirichlet problem or the Newmann problem.

During the investigation of convective heat transfer in a composite wall structure, as conceived by Trefethen,[2] the need for establishing a reference heat flux of conduction arose. It was decided to use two-dimensional conduction in a stack of parallelograms separated by thin partition walls. No analytical solutions were found to exist.

Suppose there is an infinitely long, one-dimensional slab with different constant temperatures along both boundaries. When this slab contains equally spaced, inclined parallel partition walls between the two isothermal walls (Fig. 1(a)), the steady temperature distribution and overall heat flux will depend on the angle of inclination and conductance of the partition walls. The effect of these variables on heat transfer and conduction is investigated numerically in this study.

Formulation of the Problem

Two-dimensional equation of heat conduction in a rectangular coordinate system for steady state is

$$\frac{\partial^2 T}{\partial x^2} + \frac{\partial^2 T}{\partial y^2} = 0 \tag{1}$$

Since each of the component parallelograms in the slab is identical thermally, as well as in the shape, attention can be given to a single isolated element. This is shown in Fig. 1(b) along with definitions of the coordinate axes. Variables are made nondimensional by the following definitions: $x' = x/D$, $y' = y/D$, $\tilde{y}' = \tilde{y}/D$, and $T' = (T - T_m)/(T_h - T_m)$, where $T_m = (T_h + T_c)/2$. Dropping primes yields a dimensionless governing equation in the same form of equation (1). For convenience of treating boundary conditions the x–y coordinates are

[1] Department of Mechanical Engineering, Tufts University, Medford, Mass.

Contributed by the Heat Transfer Division of THE AMERICAN SOCIETY OF MECHANICAL ENGINEERS. Manuscript received by the Heat Transfer Division March 22, 1976.

[2] Trefethen, L. M. and Chung, K. C., "Natural Convection in a Vertical Stack of Inclined Parallelogrammic Cavities," (paper in preparation).

also are almost linear, but with a slight downward curve.

It has been shown that the present method yields solutions which are reasonable in comparison with available data. This successful extension of the analysis method for gases of Novotny, et al. [3] to liquid carbon tetrachloride points out the versatility of the method of analysis. That this technique has been demonstrated to work indicates that the technique of Sparrow and Yu [12] can indeed be applied quite successfully to radiation analyses. Also, it is expected that this technique can be used for other liquids as long as the band absorption formulation is known. It is emphasized that this extension to a liquid required essentially no change in the analysis and only slight modification of the computer program for the gas analysis [3].

References

1 Cess, R. D., "The Interaction of Thermal Radiation with Free Convection Heat Transfer," *International Journal of Heat Mass Transfer,* Vol. 9, 1966, pp. 1269–1277.

2 Bratis, J. C., and Novotny, J. L., "Radiation-Convection Interaction in Real Gases," *AIAA Progress in Astronautics and Aeronautics,* Vol. 31, 1973, pp. 329–348.

3 Novotny, J. L., Lloyd, J. R., and Bankston, J. D., Jr., "Local Non-Similarity Applied to Free Convection Boundary Layers with Radiation Interaction," AIAA Paper No. 74-653, Thermophysics and Heat Transfer Conference, Boston, Mass., July 1974, Also see AIAA 1974 Thermophysics Volume to be published 1976.

4 Tien, C. L., and Lowder, J. E., "A Correlation of Total Band Absorptance of Radiative Gases," *International Journal of Heat Mass Transfer,* Vol. 9, 1974, pp. 698–701.

5 Poltz, H., "Die Warmeleitfahigkeit von Flussigkeiten II. Der Strahlungsanteil der Effektiven Warmeleitfahigkeit," *International Journal of Heat Mass Transfer,* Vol. 8, 1965, pp. 515–527.

6 Poltz, H., "Die Warmeleitfahigkeit von Fluzzigkeiten III. Abhangigkeit der Warmeleitfahigkeit von der Schichtdicke bei roganischen Flussigkeiten," *International Journal of Heat Mass Transfer,* Vol. 8, 1965, pp. 609–620.

7 Poltz, H., and Jugel, R., "The Thermal Conductivity of Liquids—IV. Temperature Dependence of Thermal Conductivity," *International Journal of Heat Mass Transfer,* Vol. 10, 1967, pp. 1075–1088.

8 Schödel, G., and Grigull, U., "Kombinierte Warmeleitung and Warmestrahlung in Flussigkeiten," *Heat Transfer,* 1970, Vol. 3, Elsevier, Amsferdam, Article R.2.2.

9 Novotny, J. L., and Bratis, J. C., "Radiative Transfer in Liquid CCl_4," *Journal Quant. Spectrosc. Radiat. Transfer,* Vol. 12, 1972, pp. 901–911.

10 Novotny, J. L., Negrelli, D. E., and Van den Driessche, T., "Total Band Absorption Models for Absorbing-Emitting Liquids CCl_4," JOURNAL OF HEAT TRANSFER TRANS. ASME, Series C, Vol. 96, 1974, pp. 27–31.

11 Bankston, J. D., "Analytical Study of Radiation-Convection Interaction of Absorbing-Emitting Fluids in Non-Similar Natural Convection Boundary Layer Flow," PhD dissertation, Aerospace and Mechanical Engineering, University of Notre Dame, Notre Dame, Ind., 1975.

12 Sparrow, E. M., and Yu, H. S., "Local Non-Similarity Thermal Boundary Layer Solutions," JOURNAL OF HEAT TRANSFER, Vol. 93, 1972, pp. 328–334.

Heat Conduction in a Stack of Parallelograms Separated by Thin Partition Walls

K. C. Chung[1] and K. N. Astill[1]

Nomenclature

b = thickness of partition wall
D = height of parallelogram
K_b = thermal conductivity of partition wall
K_s = thermal conductivity of solid
ℓ = dimensionless length of parallelogram; L/D
L = length of parallelogram
q = local heat flux density
Q = total heat flux across $x = \ell/2$
Qr = total heat flux in a rectangle
Rk = ratio of conductances; $(Kb/b)/(Ks/D)$
T = temperature
x, y = rectangular coordinates
$x, \tilde{y}$ = parallelogrammic coordinates
α = angle between y and $\tilde{y}$ coordinates
$\delta x, \delta y, \delta\tilde{y}$ = grid space in x-, y-, and $\tilde{y}$-direction, respectively
η = ratio of heat flux; Q/Qr
ω = relaxation factor

Subscripts

h, c, m = high, low and medium value, respectively
i, j = grid number in $\tilde{y}$- and x-direction, respectively
M, N = number of grids in x- and $\tilde{y}$-direction, respectively

Superscript

k = order of iteration

Introduction

For two-dimensional conduction of rectangular solids with simple boundary conditions, many analytical solutions, either steady or transient, are known. The solutions are in forms of double Fourier series which are obtainable by separation of variables or conformal mapping. The latter case is applicable only for either the Dirichlet problem or the Newmann problem.

During the investigation of convective heat transfer in a composite wall structure, as conceived by Trefethen,[2] the need for establishing a reference heat flux of conduction arose. It was decided to use two-dimensional conduction in a stack of parallelograms separated by thin partition walls. No analytical solutions were found to exist.

Suppose there is an infinitely long, one-dimensional slab with different constant temperatures along both boundaries. When this slab contains equally spaced, inclined parallel partition walls between the two isothermal walls (Fig. 1(a)), the steady temperature distribution and overall heat flux will depend on the angle of inclination and conductance of the partition walls. The effect of these variables on heat transfer and conduction is investigated numerically in this study.

Formulation of the Problem

Two-dimensional equation of heat conduction in a rectangular coordinate system for steady state is

$$\frac{\partial^2 T}{\partial x^2} + \frac{\partial^2 T}{\partial y^2} = 0 \tag{1}$$

Since each of the component parallelograms in the slab is identical thermally, as well as in the shape, attention can be given to a single isolated element. This is shown in Fig. 1(b) along with definitions of the coordinate axes. Variables are made nondimensional by the following definitions: $x' = x/D$, $y' = y/D$, $\tilde{y}' = \tilde{y}/D$, and $T' = (T - T_m)/(T_h - T_m)$, where $T_m = (T_h + T_c)/2$. Dropping primes yields a dimensionless governing equation in the same form of equation (1). For convenience of treating boundary conditions the x–y coordinates are

[1] Department of Mechanical Engineering, Tufts University, Medford, Mass.

Contributed by the Heat Transfer Division of THE AMERICAN SOCIETY OF MECHANICAL ENGINEERS. Manuscript received by the Heat Transfer Division March 22, 1976.

[2] Trefethen, L. M. and Chung, K. C., "Natural Convection in a Vertical Stack of Inclined Parallelogrammic Cavities," (paper in preparation).

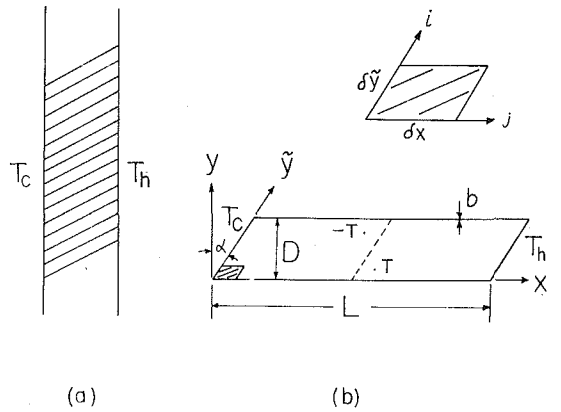

Fig. 1 Stack of parallelograms in a two-dimensional slab with constant temperature walls and its finite grid coordinates

converted to an x–$\tilde{y}$ coordinate system, which results in the following relationship:

$$\frac{\partial}{\partial y} = \frac{1}{\cos\alpha}\left(\frac{\partial}{\partial \tilde{y}} - \sin\alpha\frac{\partial}{\partial x}\right) \tag{2}$$

Therefore, the governing equation (1) in dimensionless form will be, in x–$\tilde{y}$ plane:

$$\frac{\partial^2 T}{\partial x^2} - 2\sin\alpha\frac{\partial^2 T}{\partial x\,\partial \tilde{y}} + \frac{\partial^2 T}{\partial \tilde{y}^2} = 0 \tag{3}$$

Boundary conditions in this coordinate system are:

$$\left.\begin{aligned} T &= -1 \text{ at } x = 0 \\ T &= 1 \text{ at } x = \ell \end{aligned}\right\} \tag{4a}$$

$$\frac{\partial T}{\partial \tilde{y}} = \text{prescribed implicitly at } \tilde{y} = 0 \text{ and } \tilde{y} = 1/\cos\alpha \tag{4b}$$

The problem domain is divided into $M \times N$ small parallelogram meshes with dimensions δx by $\delta\tilde{y}$ in x–$\tilde{y}$ plane as shown in Fig. 1(b). The finite difference formulation of equation (3) is based on central differences. At node i, j, the explicit form of the equation for new temperature is

$$\begin{aligned} T_{i,j}{}^{k+1} = T_{i,j}{}^{k} + \omega\{&A_1(T_{i,j+1} + T_{i,j-1}) + A_2(T_{i+1,j} + T_{i-1,j}) \\ &+ A_3(T_{i+1,j+1} + T_{i-1,j-1} - T_{i+1,j-1} - T_{i-1,j+1}) - T_{i,j}{}^{k}\} \end{aligned} \tag{5}$$

where

$$A_1 = \delta\tilde{y}^2/2(\delta x^2 + \delta\tilde{y}^2), \quad A_2 = \delta x^2/2(\delta x^2 + \delta\tilde{y}^2),$$
$$A_3 = -\delta x\delta\tilde{y}\sin\alpha/4(\delta x^2 + \delta\tilde{y}^2)$$

and ω is a relaxation factor chosen to accelerate convergence.

Thickness, b, of the partition wall is assumed small enough such that heat conduction in x-direction along the wall is negligible. Heat flux density across the partition wall is

$$q_j = -K_s\left(\frac{\partial T}{\partial y}\right)_{1,j} = -K_s\left(\frac{\partial T}{\partial y}\right)_{N+1,j} = -K_b(T_{1,j} - T_{N+1,j})/b \tag{6}$$

From equation (2) and (6) we have

$$\left(\frac{1}{\cos\alpha}\frac{\partial T}{\partial \tilde{y}} - \tan\alpha\frac{\partial T}{\partial x}\right)_{1,j} = (K_b/K_s)(T_{1,j} - T_{N+1,j})/b \tag{7}$$

Using the Taylor series expansion the temperature gradient at the partition wall is approximated by

$$\left(\frac{\partial T}{\partial \tilde{y}}\right)_{1,j} \simeq \left(\frac{\partial T}{\partial \tilde{y}}\right)_{2,j} - \delta\tilde{y}\left(\frac{\partial^2 T}{\partial \tilde{y}^2}\right)_{2,j} \simeq (-T_{3,j} + 4T_{2,j} - 3T_{1,j})/2\delta\tilde{y} \tag{8}$$

Similarly,

$$\left(\frac{\partial T}{\partial \tilde{y}}\right)_{N+1,j} \simeq (T_{N-1,j} - 4T_{N,j} + 3T_{N+1,j})/2\delta\tilde{y} \tag{9}$$

These approximations are identical to fitting a second degree polynomial and taking the first derivative. Using the expressions (6)–(9), the following formulas of iteration for wall temperatures are obtained.

$$T_{1,j}{}^{k+1} = \{B_1 T_{N+1,j} + 4T_{2,j} - T_{3,j} - B_2(T_{1,j+1} - T_{1,j-1})\}^k/B_3 \tag{10}$$

and

$$\begin{aligned} T_{N+1,j}{}^{k+1} = \{&B_1 T_{1,j} + 4T_{N,j} - T_{N-1,j} \\ &- B_2(T_{N+1,j+1} - T_{N+1,j-1})\}^k/B_3 \end{aligned} \tag{11}$$

where

$$B_1 = 2Rk/M, \quad B_2 = \delta\tilde{y}\sin\alpha/\delta x \quad \text{and } B_3 = B_1 + 3.$$

Numerical Procedure

Numerical iteration leading to a steady-state solution is carried out using the relaxation formula (5) with the static boundary conditions (4a) and the dynamic boundary conditions (10) and (11). To reduce computing time without sacrificing quality of solutions the following three considerations were made.

1 **Temperature Field as an Odd Function.** (i) With the center point as an origin of x–$\tilde{y}$ coordinate, the geometry of the problem is symmetric with respect to the origin; (ii) since differential operator of the governing equation (iii) is symmetric either an even or odd function can satisfy the equation; (iii) boundary conditions at the partition walls satisfy a relationship

$$\begin{aligned} &\left\{\left(\frac{\partial T}{\partial \tilde{y}}\right)\frac{1}{\cos\alpha} - \left(\frac{\partial T}{\partial x}\right)\tan\alpha\right\}_{\tilde{y}=0} \\ &\qquad = \left\{\left(\frac{\partial T}{\partial \tilde{y}}\right)\frac{1}{\cos\alpha} - \left(\frac{\partial T}{\partial x}\right)\tan\alpha\right\}_{\tilde{y}=1/\cos\alpha} \end{aligned} \tag{12}$$

and this equation admits either even and odd functions; and (iv) constant temperatures at both isothermal walls require the temperature function to be odd. By (i), (ii), (iii), and (iv) it is concluded that the temperature field is symmetric with opposite sign with respect to the center point. This is illustrated in Fig. 1(b). Therefore, it is possible to reduce the number of grids to about a half with a new boundary at $j = M/2 + 2$ instead of the old one at $j = M + 1$. The new boundary condition can be established dynamically as:

$$T_{i,M/2+2}{}^{k+1} = -T_{N+2-i,M/2}{}^{k}, \; i = 1, 2, \ldots, N+1 \tag{13}$$

2 **Computation of Heat Flux Across $x = \ell/2$.** It was noticed that overall heat flux as well as local flux might be estimated inconsistently from one case to another when normal temperature gradients are computed along the constant temperature walls. For instance, the temperature gradient by first order approximation of Taylor series would heavily depend on grid size. This requires a large number of grids in x-direction. With second order approximation (equivalent to second degree polynomial approximation) it was even worse since a negative gradient could appear locally in the sharp corner. Therefore, heat flux was computed across $x = \ell/2$ with central differences for temperature gradients. Local heat flux density normal to $x = \ell/2$ is

$$\begin{aligned} q_i = -K_s\left(\frac{T_h - T_m}{D}\right)&\left\{\frac{\partial T}{\partial \tilde{y}}\tan\alpha - \frac{\partial T}{\partial x}\frac{1}{\cos\alpha}\right\}_{i,M/2+1}, \\ &i = 1, 2, \ldots, N+1 \end{aligned} \tag{14}$$

At the partition wall ($i = 1$ or $N + 1$) $\partial T/\partial\tilde{y}$ is approximated according to the equations (8) and (9). Thus, the total heat flux across $x = \ell/2$ is:

$$Q = \sum_{i=1}^{N}(q_i + q_{i+1})D\delta\tilde{y}/2 \tag{15}$$

It was found that the heat flux estimation at $x = \ell/2$ reduced the

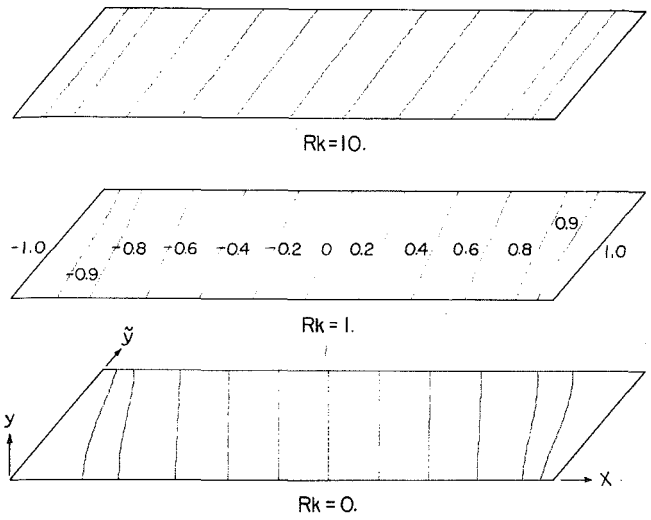

Fig. 2 Steady-state isotherms in a two-dimensional parallelogrammic solid with $L/D = 5$ and $\alpha = 40°$

Table 1 Variation of the ratio of heat flux, η, with aspect ratio, L/D, angle of inclination, α, and ratio of conductances, Rk

L/D	Rk / α	0	1	10	100	1000	∞
2	0	1.000	1.000	1.000	1.000	1.000	1.000
	20	1.037	1.080	1.122	1.131	1.132	1.133
	40	1.199	1.430	1.650	1.698	1.703	1.704
	60	2.121	2.924	3.775	3.975	3.998	4.000
5	0	1.000	1.000	1.000	1.000	1.000	1.000
	20	1.016	1.073	1.121	1.131	1.132	1.133
	40	1.081	1.386	1.645	1.698	1.703	1.704
	60	1.318	2.668	3.748	3.972	3.997	4.000
10	0	1.000	1.000	1.000	1.000	1.000	1.000
	20	1.009	1.072	1.121	1.131	1.132	1.133
	40	1.042	1.371	1.642	1.698	1.703	1.704
	60	1.154	2.589	3.740	3.972	3.997	4.000
20	0	1.000	1.000	1.000	1.000	1.000	1.000
	20	1.003	1.068	1.121	1.131	1.131	1.133
	40	1.023	1.367	1.642	1.697	1.702	1.704
	60	1.076	2.550	3.733	3.972	3.995	4.000

strong dependence of solutions on number of grids and eliminates inconsistencies.

3 **Adoption of a Variable Relaxation Factor.** The relaxation factor, ω, could be increased dynamically from 1 to 2 or over to speed up convergence during the iteration.

Results

Number of grids, $M \times N$, employed ranges from 11×10 to 21×10 for a half of the domain depending on aspect ratio, L/D. Numerically the procedure was always stable and converged fast to a steady state. In Fig. 2 steady-state isotherms are shown for the case $L/D = 5$ with $\alpha = 40$ deg. With increasing Rk the isotherms approach those without partition walls. When $\alpha = 0$, temperature distribution was independent of Rk as expected having the isotherms parallel with y-axis, since the conduction was one-dimensional. A ratio of heat flux, η, was defined such that $\eta = Q/Qr$ as a shape parameter of conduction, where Qr represents total flux of one dimensional conduction. Dependence of η on α and Rk is shown in Fig. 3 for $L/D = 5$ and overall results of η with variations of L/D, Rk and α are listed in Table 1. The ratio of heat flux, η, increases monotonically with the angle α, since the increase of α reduces real thickness of the slab shortening the effective path length of conduction. If a different aspect ratio, thickness of the slab versus length of the constant temperature wall of the parallelogrammic solid, is used, the effect of inclined, poorly conducting partition walls would increase the effective path length actually decreasing conduction. Higher ratio of conductances, Rk, however, always causes more heat transfer with the total flux approaching the value for one-dimensional slab.

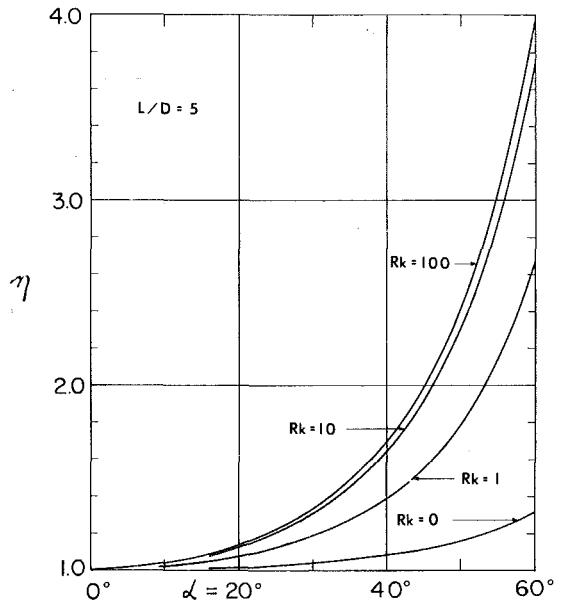

Fig. 3 Variation of the ratio of heat flux, η, with angle of inclination, α, and ratio of conductances, Rk, when $L/D = 5$

Two-Dimensional Effects on Heat Transfer Rates From an Array of Straight Fins

N. V. Suryanarayana,[1]

Arrays of fins are frequently used to increase heat transfer rates from one fluid to another separated by a solid wall. Because of the differences in heat transfer rates from the unfinned and finned parts,—two dimensional effects exist. However, heat transfer rates from the fins are often computed on the basis of uniform fin base temperature. The purpose of this note is to examine the errors involved in computing the heat transfer rates from fins on the basis of uniform base temperature.

The model of the fin examined is shown in Fig. 1. If the uniform base temperature is denoted by T_0, the heat transfer rate from a single fin is given by

[1] Assoc. Professor, Department of Mechanical Engineering and Engineering Mechanics, Michigan Technological University, Houghton, Mich. Mem. ASME.

Contributed by the Heat Transfer Division of THE AMERICAN SOCIETY OF MECHANICAL ENGINEERS. Manuscript received by the Heat Transfer Division July 12, 1976.

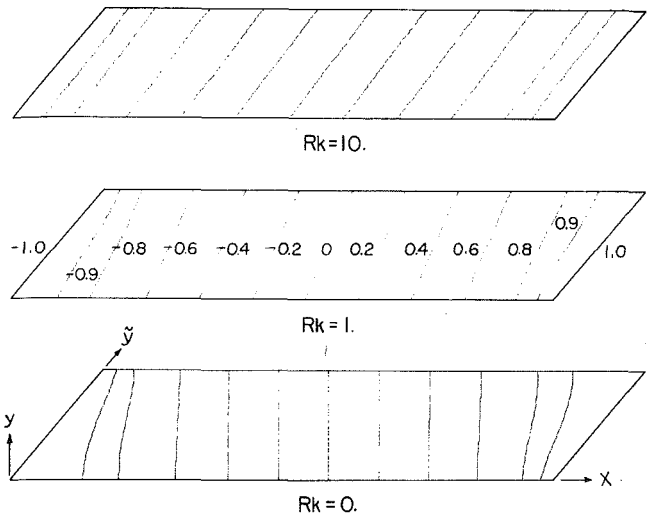

Fig. 2 Steady-state isotherms in a two-dimensional parallelogrammic solid with $L/D = 5$ and $\alpha = 40°$

Table 1 Variation of the ratio of heat flux, η, with aspect ratio, L/D, angle of inclination, α, and ratio of conductances, Rk

L/D	Rk / α	0	1	10	100	1000	∞
2	0	1.000	1.000	1.000	1.000	1.000	1.000
	20	1.037	1.080	1.122	1.131	1.132	1.133
	40	1.199	1.430	1.650	1.698	1.703	1.704
	60	2.121	2.924	3.775	3.975	3.998	4.000
5	0	1.000	1.000	1.000	1.000	1.000	1.000
	20	1.016	1.073	1.121	1.131	1.132	1.133
	40	1.081	1.386	1.645	1.698	1.703	1.704
	60	1.318	2.668	3.748	3.972	3.997	4.000
10	0	1.000	1.000	1.000	1.000	1.000	1.000
	20	1.009	1.072	1.121	1.131	1.132	1.133
	40	1.042	1.371	1.642	1.698	1.703	1.704
	60	1.154	2.589	3.740	3.972	3.997	4.000
20	0	1.000	1.000	1.000	1.000	1.000	1.000
	20	1.003	1.068	1.121	1.131	1.131	1.133
	40	1.023	1.367	1.642	1.697	1.702	1.704
	60	1.076	2.550	3.733	3.972	3.995	4.000

strong dependence of solutions on number of grids and eliminates inconsistencies.

3 **Adoption of a Variable Relaxation Factor.** The relaxation factor, ω, could be increased dynamically from 1 to 2 or over to speed up convergence during the iteration.

Results

Number of grids, $M \times N$, employed ranges from 11×10 to 21×10 for a half of the domain depending on aspect ratio, L/D. Numerically the procedure was always stable and converged fast to a steady state. In Fig. 2 steady-state isotherms are shown for the case $L/D = 5$ with $\alpha = 40$ deg. With increasing Rk the isotherms approach those without partition walls. When $\alpha = 0$, temperature distribution was independent of Rk as expected having the isotherms parallel with y-axis, since the conduction was one-dimensional. A ratio of heat flux, η, was defined such that $\eta = Q/Qr$ as a shape parameter of conduction, where Qr represents total flux of one dimensional conduction. Dependence of η on α and Rk is shown in Fig. 3 for $L/D = 5$ and overall results of η with variations of L/D, Rk and α are listed in Table 1. The ratio of heat flux, η, increases monotonically with the angle α, since the increase of α reduces real thickness of the slab shortening the effective path length of conduction. If a different aspect ratio, thickness of the slab versus length of the constant temperature wall of the parallelogrammic solid, is used, the effect of inclined, poorly conducting partition walls would increase the effective path length actually decreasing conduction. Higher ratio of conductances, Rk, however, always causes more heat transfer with the total flux approaching the value for one-dimensional slab.

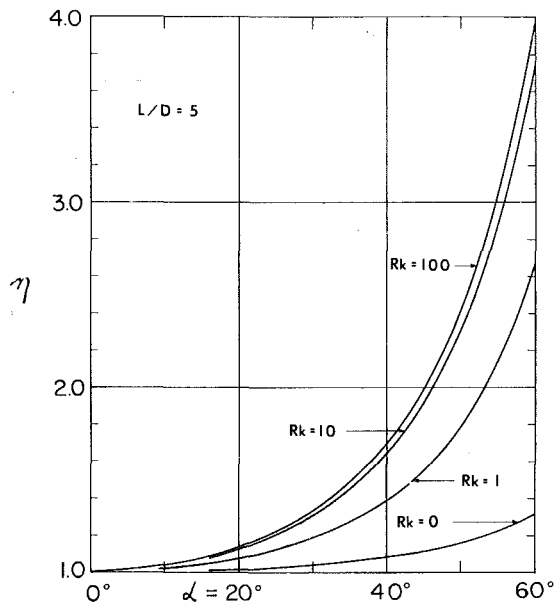

Fig. 3 Variation of the ratio of heat flux, η, with angle of inclination, α, and ratio of conductances, Rk, when $L/D = 5$

Two-Dimensional Effects on Heat Transfer Rates From an Array of Straight Fins

N. V. Suryanarayana,[1]

Arrays of fins are frequently used to increase heat transfer rates from one fluid to another separated by a solid wall. Because of the differences in heat transfer rates from the unfinned and finned parts,—two dimensional effects exist. However, heat transfer rates from the fins are often computed on the basis of uniform fin base temperature. The purpose of this note is to examine the errors involved in computing the heat transfer rates from fins on the basis of uniform base temperature.

The model of the fin examined is shown in Fig. 1. If the uniform base temperature is denoted by T_0, the heat transfer rate from a single fin is given by

[1] Assoc. Professor, Department of Mechanical Engineering and Engineering Mechanics, Michigan Technological University, Houghton, Mich. Mem. ASME.

Contributed by the Heat Transfer Division of THE AMERICAN SOCIETY OF MECHANICAL ENGINEERS. Manuscript received by the Heat Transfer Division July 12, 1976.

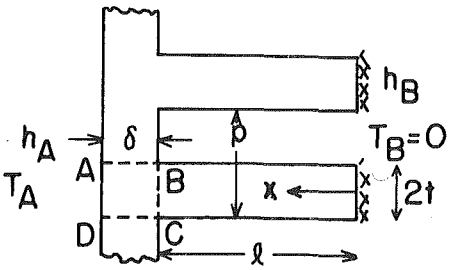

Fig. 1 Model of fins

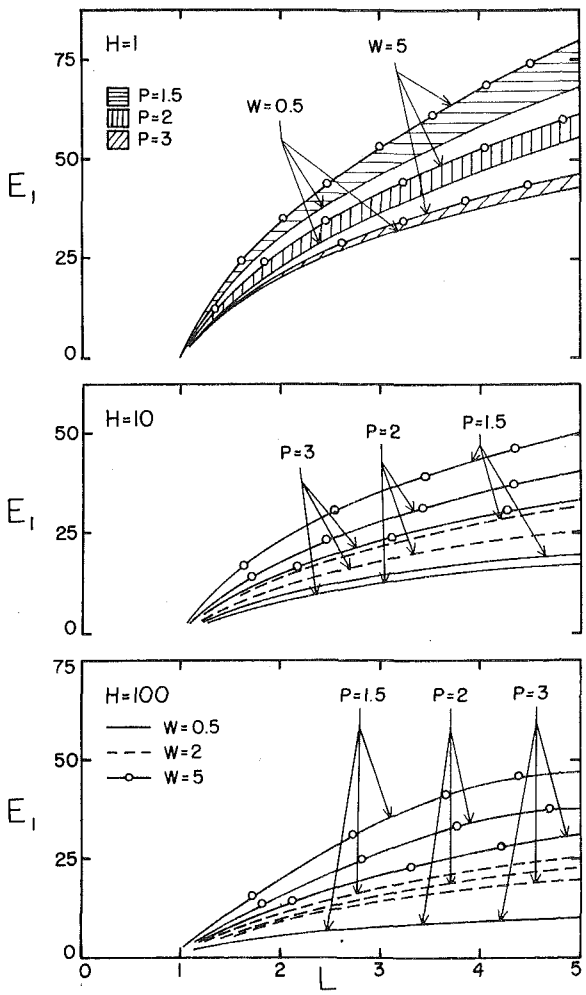

Fig. 2 Error in fin heat transfer for computational model 1

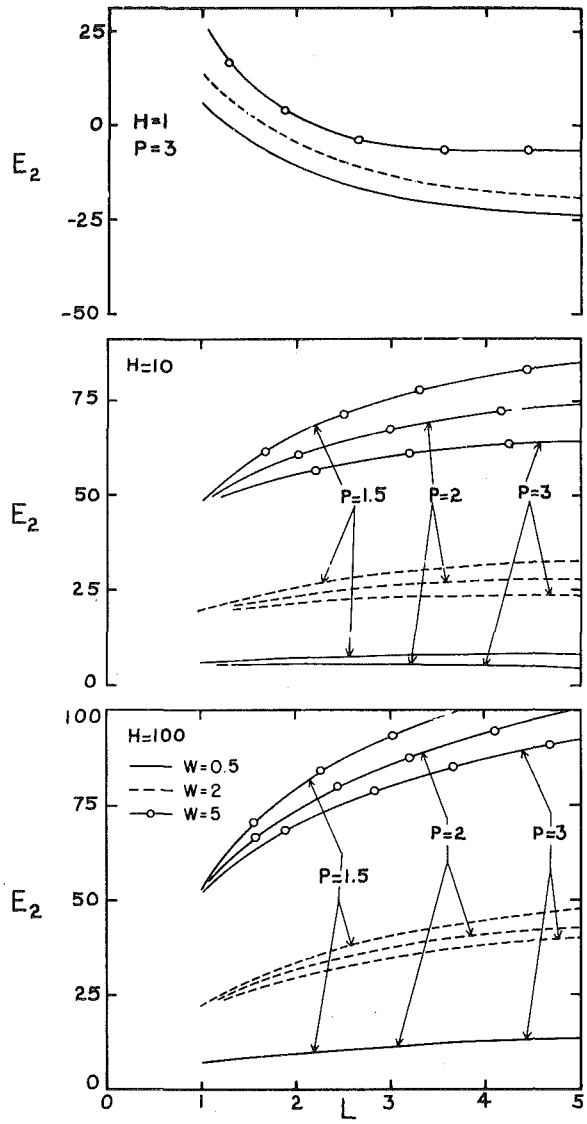

Fig. 3 Error in fin heat transfer for computational model 2

$$\frac{Q}{kbT_A} = \frac{T_0}{T_A}\sqrt{\mathrm{Bi}}\tanh\left(\sqrt{\mathrm{Bi}}\frac{\ell}{t}\right) \tag{1}$$

Q is half the heat transfer rate from a single fin, k is the thermal conductivity of the material of the fin, b is the width of the fin, $\mathrm{Bi} = h_B t/k$. A conventional approach to the determination of the base temperature of the fin is to assume it to be the same as would exist at BC in the unfinned situation [1].[2] Sparrow and Hennecke [2] examined the temperature depression as a result of the higher heat transfer rate (compared with the unfinned part) from a single fin. In a recent paper [3], Sparrow and Lee analyzed the effect of such temperature depression on heat transfer rates from an array of fins, employing uniform, but different, temperatures at the base of the fin and the unfinned parts.

While it is usual to assume the base temperature of the fin to be the same as that for the unfinned case, other possibilities exist. These are: (*a*) to ignore the thermal resistance of the wall (part ABCD in Fig. 1) and employ convective boundary condition at the base BC; and (*b*) matching the temperature and heat transfer rates at surface BC, assuming surfaces AB and CD to be perfectly insulated—ignoring the heat transfer rate from the unfinned part. The results obtained by employing each of the foregoing possibilities for determining the fin base temperature are summarized below:

(1) Base temperature equal to that in the unfinned case

$$\frac{T_{0s}}{T_A} = \frac{1}{\frac{1}{H} + \mathrm{Bi}\cdot W + 1} \tag{2}$$

(2) Convective boundary condition

[1] Numbers in brackets designate References at end of technical note.

$$x = \ell, k\frac{dT}{dx} + h_A(T_{x=L} - T_A) = 0$$

$$\frac{T_{0c}}{T_A} = \frac{1}{1 + \dfrac{1}{H\sqrt{\text{Bi}}}\tanh(\sqrt{\text{Bi}}\,L)} \tag{3}$$

(3) Matching temperature and heat transfer rate (treating the wall ABCD and the fin as two one-dimensional domains)

$$\frac{T_{0m}}{T_A} = \frac{1}{1 + \left(\dfrac{1}{H} + \text{Bi}\cdot W\right)\dfrac{1}{\sqrt{\text{Bi}}}\tanh(\sqrt{\text{Bi}}\,L)} \tag{4}$$

In the foregoing equations T_{0s}, T_{0c}, and T_{0m} represent the base temperature employing the appropriate boundary condition; $H = h_A/h_B$; W is the dimensionless wall thickness δ/t and L is the dimensionless length of the fin ℓ/t. When these expressions are substituted for T_0/T_A in equation 1, the corresponding fin heat transfer rates Q^*_{0s}, Q^*_{0c} and Q^*_{0m} are obtained, where the asterisk is used to signify heat transfer rates computed on the basis of one-dimensional analysis.

To examine the validity of the foregoing approximations, the actual heat transfer rates from the fin, Q, were computed by using finite differences. One-dimensional analysis of fins require that Bi $\ll$ 1 and hence solutions were carried out for Bi = 0.1. Heat transfer rates were computed for all possible combinations of the values of the variables affecting the accuracy of one-dimensional analysis, as given in the following:

H = 1, 10, 100; P = 1.5, 2.0, 3.0; W = 0.5, 1, 2, 5;
L = 1, 2.5, 5.0 where $P = p/2t$

Defining the errors involved in the assumption of uniform base temperatures as $E_1 = 100\,(Q^*_{0s} - Q)/Q$, $E_2 = 100\,(Q^*_{0c} - Q)/Q$, and $E_3 = 100\,(Q^*_{0m} - Q)/Q$ they are presented in Figs. 2–4 for the range of variables indicated previously. From an examination of these figures, the following conclusions can be drawn.

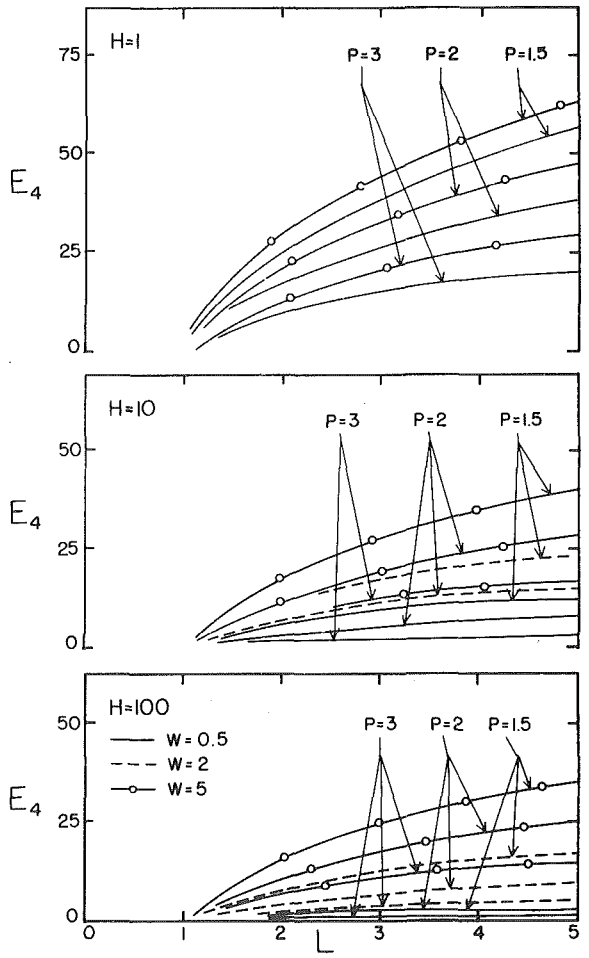

Fig. 5 Error in heat transfer from unfinned portion of the wall for a computational model which neglects the presence of the fins

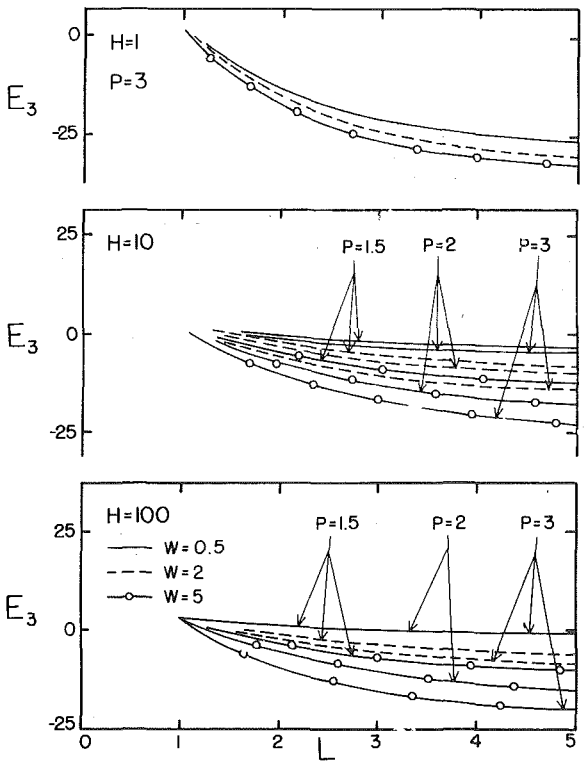

Fig. 4 Error in fin heat transfer for computational model 3

1 The assumption of equality of fin base temperature and the corresponding unfinned surface temperature leads to an overestimation of the heat transfer rates. The magnitude of the error can be considerable—as high as 80 percent (H = 1, W = 5, P = 1.5). For a given value of H, the error increases with an increase in the wall thickness, an increase in the length, and a decrease in the pitch. Also, the error increases with a decrease in the value of H. For very short fins (ℓ/t = 1), it gives satisfactory values.

2 The use of convective boundary condition (equation (3)) gives reasonably satisfactory values of heat transfer rates for thin walls (W = 0.5). But as the wall thickness increases, the wall resistance to heat transfer becomes significant and ignoring this resistance leads to considerable overestimation of the heat transfer rates for values of H greater than 10. The use of convective boundary condition is generally unsatisfactory for wall thickness of $W > 0.5$.

3 Matched boundary conditions (equation (4)) are generally satisfactory, particularly for high values of H. In general, it tends to an underestimation of the heat transfer rates but the error is usually within −25 percent.

From this study covering a limited range of the variables involved, it can be seen that the assumption of a uniform base fin temperature based on the unfinned situation can lead to significant errors in the computed heat transfer rates from the fins. It may be more appropriate to compute the heat transfer rates from the fins with the assumption of uniform base temperature based on matched boundary conditions, equation (4).

Another consequence of the increased heat transfer through the

fins is the temperature depression of the surface to which the fins are attached as compared with the temperature computed for the no fin situation. The heat transfer rates from the unfinned part based on the temperature for the no fin situation tends to be higher than the actual heat transfer rates and the magnitude of the error $E_4 = 100\ (Q^*_{UF} - Q_{UF})/Q_{UF}$ where Q^*_{UF} = heat transfer from the unfinned part based on the temperature for the no fin situation and Q_{UF} = actual heat transfer rate from the unfinned part is shown in Fig. 5. As can be expected, the errors are higher for lower values of the pitch P, and the ratio of the heat transfer coefficients H. An increase in the wall thickness increases the error.

Acknowledgment

The author wishes to thank the Michigan Technological University for providing the computer facilities and Mr. Larry Slominski for his assistance in the computer programing.

References

1 Kern, D. Q., and Kraus, A. D., *Extended Surface Heat Transfer*, McGraw Hill, New York, 1972.

2 Sparrow, E. N., and Hennecke, D. K., "Temperature Depression at the Base of a Fin," JOURNAL OF HEAT TRANSFER, TRANS. ASME, Series C, Vol. 92, 1970, pp. 204–206.

3 Sparrow, E. M., and Lee, L., "Effects of Fin Base Temperature Depression in a Multi-Fin Array," JOURNAL OF HEAT TRANSFER, TRANS. ASME, Series C, Vol. 97, 1975, pp. 463–465.

Heat Conduction in an Anisotropic Medium Homogeneous in Cylindrical Regions—Steady State[1]

Y. P. Chang[2] and R. C. H. Tsou[3]

Introduction

This is one of a series of papers concerning the analytical solution of heat conduction in anisotropic media, and the second for homogeneous anisotropic medium in circular cylinder coordinates. All notations used in this paper are the same as those defined in [1],[4] which appears in the same issue of this journal, and considers the steady-state solutions of the same problems.

According to the conclusion drawn in [1], it is, in general, difficult to obtain the analytical solution for the temperature, but the Green's function can be obtained with less difficulty. Since Green's functions satisfy homogeneous equations, those in steady state can be readily obtained from those in unsteady state by the integration of the latter with respect to time from zero to infinity. The result thus obtained, however, will be in the form of a double (or triple) series, if the latter is a double (or triple) series. It is sometimes difficult to reduce the double (or triple) series into a single (or double) series. Therefore, it is more convenient to determine the Green's functions for steady problems directly from the solution of their governing equations.

Basic Equations and Formal Solutions

For a monoclinic system, the governing equations are:

$$k_{11}\frac{1}{r}\frac{\partial}{\partial r}\left(r\frac{\partial T}{\partial r}\right) + k_{22}\frac{1}{r^2}\frac{\partial^2 T}{\partial \theta^2} + 2k_{12}\frac{\partial^2 T}{r\partial r\partial\theta} + k_{33}\frac{\partial^2 T}{\partial z^2} = -Q(r,\theta,z) \text{ in } \Omega \quad (1)$$

$$b\frac{\partial T}{\partial n^+} + hT = f_i \quad \text{on surface } S \quad (2)$$

If $G(r, \theta, z|r', \theta', z')$ is the Green's function associated with equations (1) and (2), then the temperature can be obtained by the use of Green's second formula [2]

$$T(r,\theta,z) = \frac{1}{k_{11}}\int_\Omega Q(r',\theta',z')G(r,\theta,z|r',\theta',z')d\Omega(r',\theta',z') - \int_S f(r',\theta',z')\frac{\partial}{\partial n^+}G(r,\theta,z|r',\theta',z')dS(r',\theta',z') \quad (3)$$

for boundary conditions of the first and third types, k_{11} appears because we have divided the governing equation by k_{11}. If the surface conditions are of the second type, then the last integral in equation (3) is replaced by

$$\int_S f(r',\theta',z')G(r,\theta,z|r',\theta',z')dS(r',\theta',z') \quad (4)$$

If all boundary conditions are of Neumann type for either a solid or hollow cylinder of finite or infinite length, the Green's function does not exist, but we can still construct the generalized Green's function. Of course, the consistency condition relating Q and f are to be satisfied a priori, i.e.,

$$\int_\Omega Q d\Omega + \int_S f_i dS = 0$$

Green's Functions for Solid and Hollow Cylinders

If either Q or f depends on r, θ, and z, then the Green's function $G(r, \theta, z|r', \theta', z')$ is governed by

$$\frac{1}{r}\frac{\partial}{\partial r}\left(r\frac{\partial G}{\partial r}\right) + 2\nu_{12}\frac{\partial^2 G}{r\partial r\partial\theta} + \nu_{22}\frac{1}{r^2}\frac{\partial^2 G}{\partial\theta^2} + \nu_{33}\frac{\partial^2 G}{\partial z^2} = -\frac{1}{w(r)}\delta(r-r')\delta(\theta-\theta')\delta(z-z') \quad (5)$$

and the appropriate boundary conditions. By following the same procedure as we used in the determination of Green's functions associated with unsteady problems [1], we obtain

$$G(r,\theta,z|r',\theta',z') = \frac{\epsilon}{2\pi}\sum_{m=1}^{\infty}\sum_{n=0}^{\infty}R(r|r',n\beta,\lambda)\cos\left(n[(\theta-\theta') - \nu_{12}\ln\frac{r}{r'}\right)Z_{mn}(z|z') \quad (6)$$

where $R(r|r', n\beta, \lambda_{mn})$ satisfies

$$R'' + \frac{1}{r}R' + \left(\lambda_{mn}{}^2 - \frac{\beta^2 n^2}{r^2}\right)R = -\frac{1}{r}\delta(r-r') \quad (7)$$

$$bR' \pm hR = 0 \quad \text{for } r = r_3 \quad (8)$$

and Z_{mn} satisfies

$$Z'' + \frac{\lambda_{mn}{}^2}{\nu_{33}}Z = -\frac{1}{\nu_{33}}\delta(z-z')e^{-in\theta'} \quad (9)$$

$$bZ' \pm hZ = 0 \quad \text{for } z = 0, z = \ell \quad (10)$$

The solution of equation (9) satisfying equation (10) is

[1] Many results of this study were obtained in early 1973 while the second author was with the State University of New York at Buffalo.

[2] Department of Mechanical Engineering, State University of New York at Buffalo, Buffalo, N. Y.

[3] General Electric Co., San Jose, Calif.

[4] Numbers in brackets designate References at end of technical note.

Contributed by the Heat Transfer Division of THE AMERICAN SOCIETY OF MECHANICAL ENGINEERS. Manuscript received by the Heat Transfer Division April 28, 1976.

fins is the temperature depression of the surface to which the fins are attached as compared with the temperature computed for the no fin situation. The heat transfer rates from the unfinned part based on the temperature for the no fin situation tends to be higher than the actual heat transfer rates and the magnitude of the error $E_4 = 100\ (Q^*_{UF} - Q_{UF})/Q_{UF}$ where Q^*_{UF} = heat transfer from the unfinned part based on the temperature for the no fin situation and Q_{UF} = actual heat transfer rate from the unfinned part is shown in Fig. 5. As can be expected, the errors are higher for lower values of the pitch P, and the ratio of the heat transfer coefficients H. An increase in the wall thickness increases the error.

Acknowledgment

The author wishes to thank the Michigan Technological University for providing the computer facilities and Mr. Larry Slominski for his assistance in the computer programing.

References

1 Kern, D. Q., and Kraus, A. D., *Extended Surface Heat Transfer*, McGraw Hill, New York, 1972.

2 Sparrow, E. N., and Hennecke, D. K., "Temperature Depression at the Base of a Fin," JOURNAL OF HEAT TRANSFER, TRANS. ASME, Series C, Vol. 92, 1970, pp. 204–206.

3 Sparrow, E. M., and Lee, L., "Effects of Fin Base Temperature Depression in a Multi-Fin Array," JOURNAL OF HEAT TRANSFER, TRANS. ASME, Series C, Vol. 97, 1975, pp. 463–465.

Heat Conduction in an Anisotropic Medium Homogeneous in Cylindrical Regions—Steady State[1]

Y. P. Chang[2] and R. C. H. Tsou[3]

Introduction

This is one of a series of papers concerning the analytical solution of heat conduction in anisotropic media, and the second for homogeneous anisotropic medium in circular cylinder coordinates. All notations used in this paper are the same as those defined in [1],[4] which appears in the same issue of this journal, and considers the steady-state solutions of the same problems.

According to the conclusion drawn in [1], it is, in general, difficult to obtain the analytical solution for the temperature, but the Green's function can be obtained with less difficulty. Since Green's functions satisfy homogeneous equations, those in steady state can be readily obtained from those in unsteady state by the integration of the latter with respect to time from zero to infinity. The result thus obtained, however, will be in the form of a double (or triple) series, if the latter is a double (or triple) series. It is sometimes difficult to reduce the double (or triple) series into a single (or double) series. Therefore, it is more convenient to determine the Green's functions for steady problems directly from the solution of their governing equations.

Basic Equations and Formal Solutions

For a monoclinic system, the governing equations are:

$$k_{11}\frac{1}{r}\frac{\partial}{\partial r}\left(r\frac{\partial T}{\partial r}\right) + k_{22}\frac{1}{r^2}\frac{\partial^2 T}{\partial \theta^2} + 2k_{12}\frac{\partial^2 T}{r\partial r\partial\theta} + k_{33}\frac{\partial^2 T}{\partial z^2} = -Q(r,\theta,z) \text{ in } \Omega \quad (1)$$

$$b\frac{\partial T}{\partial n^+} + hT = f_i \quad \text{on surface } S \quad (2)$$

If $G(r, \theta, z|r', \theta', z')$ is the Green's function associated with equations (1) and (2), then the temperature can be obtained by the use of Green's second formula [2]

$$T(r,\theta,z) = \frac{1}{k_{11}}\int_\Omega Q(r',\theta',z')G(r,\theta,z|r',\theta',z')d\Omega(r',\theta',z') - \int_S f(r',\theta',z')\frac{\partial}{\partial n^+}G(r,\theta,z|r',\theta',z')dS(r',\theta',z') \quad (3)$$

for boundary conditions of the first and third types, k_{11} appears because we have divided the governing equation by k_{11}. If the surface conditions are of the second type, then the last integral in equation (3) is replaced by

$$\int_S f(r',\theta',z')G(r,\theta,z|r',\theta',z')dS(r',\theta',z') \quad (4)$$

If all boundary conditions are of Neumann type for either a solid or hollow cylinder of finite or infinite length, the Green's function does not exist, but we can still construct the generalized Green's function. Of course, the consistency condition relating Q and f are to be satisfied a priori, i.e.,

$$\int_\Omega Qd\Omega + \int_S f_i dS = 0$$

Green's Functions for Solid and Hollow Cylinders

If either Q or f depends on r, θ, and z, then the Green's function $G(r, \theta, z|r', \theta', z')$ is governed by

$$\frac{1}{r}\frac{\partial}{\partial r}\left(r\frac{\partial G}{\partial r}\right) + 2\nu_{12}\frac{\partial^2 G}{r\partial r\partial\theta} + \nu_{22}\frac{1}{r^2}\frac{\partial^2 G}{\partial\theta^2} + \nu_{33}\frac{\partial^2 G}{\partial z^2} = -\frac{1}{w(r)}\delta(r-r')\delta(\theta-\theta')\delta(z-z') \quad (5)$$

and the appropriate boundary conditions. By following the same procedure as we used in the determination of Green's functions associated with unsteady problems [1], we obtain

$$G(r,\theta,z|r',\theta',z') = \frac{\epsilon}{2\pi}\sum_{m=1}^{\infty}\sum_{n=0}^{\infty}R(r|r',n\beta,\lambda)\cos\left(n[(\theta-\theta') - \nu_{12}\ln\frac{r}{r'}\right)Z_{mn}(z|z') \quad (6)$$

where $R(r|r', n\beta, \lambda_{mn})$ satisfies

$$R'' + \frac{1}{r}R' + \left(\lambda_{mn}{}^2 - \frac{\beta^2 n^2}{r^2}\right)R = -\frac{1}{r}\delta(r-r') \quad (7)$$

$$bR' \pm hR = 0 \quad \text{for } r = r_3 \quad (8)$$

and Z_{mn} satisfies

$$Z'' + \frac{\lambda_{mn}{}^2}{\nu_{33}}Z = -\frac{1}{\nu_{33}}\delta(z-z')e^{-in\theta'} \quad (9)$$

$$bZ' \pm hZ = 0 \quad \text{for } z = 0, z = \ell \quad (10)$$

The solution of equation (9) satisfying equation (10) is

[1] Many results of this study were obtained in early 1973 while the second author was with the State University of New York at Buffalo.

[2] Department of Mechanical Engineering, State University of New York at Buffalo, Buffalo, N. Y.

[3] General Electric Co., San Jose, Calif.

[4] Numbers in brackets designate References at end of technical note.

Contributed by the Heat Transfer Division of THE AMERICAN SOCIETY OF MECHANICAL ENGINEERS. Manuscript received by the Heat Transfer Division April 28, 1976.

$Z_{mn}(zz')$

$$= \frac{(e^{\lambda_{mn}'z} + h_{mn}'e^{-\lambda_{mn}'z})[e^{\lambda_{mn}'z'} + (1/h_{mn}')e^{-\lambda_{mn}'z'}]}{2\lambda_{mn}'[h_{mn}' - (1/h_{mn}')e^{2\lambda_{mn}'\ell}]} \quad (11)$$

For a solid cylinder of radius r_0 with boundary conditions of the third type on the cylindrical surface, the solution of equation (7) satisfying the boundary condition (8) at $r = r_0$ is in the same form as equation (26) in [1]. Thus, we obtain the Green's function with the boundary conditions of the third type at the cylindrical surface and at the ends, $z = 0, \ell$.

$G(r, \theta, z|r', \theta', z')$

$$= \frac{\epsilon}{2\pi}\sum_{n=1}^{\infty}\sum_{n=0}^{\infty}\frac{J_{n\beta}(\lambda_{mn}r)J_{n\beta}(\lambda_{mn}r')}{(B_0^2 + \lambda_{mn}^2 r_0^2 + n^2\beta^2)J_{n\beta}^2(\lambda_{mn}r)} \cdot \cos n\left(\theta - \theta - \nu_{12}\ln\frac{r}{r'}\right) \cdot \frac{(e^{\lambda_{mn}'z} + h_{mn}'e^{-\lambda_{mn}'z})[e^{\lambda_{mn}'z'} + (1/h_{mn}')e^{-\lambda_{mn}'z'}]}{\lambda_{mn}'[h_{mn}' - (1/h_{mn}'e^{2\lambda_{mn}'\ell})]} \quad (12)$$

Green's functions with boundary conditions of other types can be obtained by specializing equation (12) to each case.

For a hollow cylinder of inner and outer radii r_1 and r_2 with the convective heat transfer coefficients different at the inner and outer surfaces, the solution of equation (7) satisfying boundary conditions (8), is given by equation (32) in [1]. Substituting equation (11) and equation (32) of [1] into equation (6) gives the Green's function with boundary conditions of the third type on the cylindrical surfaces. Green's functions with boundary conditions of the first type, or one type at r_1 and another type at r_2 can be found in the same way, or by specializing the general result to each case.

If the cylinder is infinitely long and the heat generation and boundary conditions are invariant in axial direction, i.e., $Q = Q(r, \theta)$ and $f = f(r_s, \theta)$, the Green's functions can be obtained by following the same procedure.

$$G(r\theta|r', \theta') = \frac{\epsilon}{2\pi}\sum_{n=0}^{\infty}R(r|r', n\beta)\cos n\left[(\theta - \theta') - \nu_{12}\ln\frac{r}{r'}\right] \quad (13)$$

where $R(r|r', n\beta)$ satisfies the equation

$$R'' + \frac{1}{r}R' - \frac{n^2\beta^2}{r^2}R = -\frac{1}{r}\delta(r - r') \quad (14)$$

and the appropriate boundary condition. The solution of equation (14) depends upon whether $n = 0$, $n \neq 0$, $r < r'$, and $r > r'$. For boundary conditions of the third type, we can obtain the Green's function for $r < r'$,

$$G(r, \theta|r', \theta') = \frac{1}{2\pi}\left(\frac{1}{B_0} + \ln\frac{r_0}{r'}\right) + \frac{1}{2\pi\beta}\sum_{n=1}^{\infty}\frac{1}{n}\left[h_{on}\left(\frac{rr'}{r_0^2}\right)n\beta + \left(\frac{r}{r'}\right)^{n\beta}\right]\cdot\cos n\left[(\theta - \theta') - \nu_{12}\ln\frac{r}{r'}\right] \quad (15)$$

For $r > r'$, we just interchange r and r' in equation (15) except in the cosine function. If the boundary condition at $r = r_0$ is of the first type, $G(r, \theta|r', \theta')$ can be obtained by setting $B_0 = \infty$, and hence $h_{on} = 1$. For boundary conditions of the second type, the Green's function does not exist, but we can construct the generalized Green's function. By the same procedure as used for isotropic media [3], we obtain for $r < r'$

$$G_2(r, \theta|r', \theta') = \frac{r^2}{4\pi r_0^2} + \frac{1}{2\pi}\ln\frac{r_0}{r'} + \frac{1}{2\pi\beta}\sum_{n=1}^{\infty}\frac{1}{n}\left[\left(\frac{rr'}{r_0^2}\right)^{n\beta} + \left(\frac{r}{r'}\right)^{n\beta}\right]\cdot\cos n\left[(\theta - \theta') - \nu_{12}\ln\frac{r}{r'}\right] + \text{const} \quad (16)$$

and for $r' < r$, we simply interchange r and r' in equation (16) except in the cosine function.

For a hollow cylinder with boundary conditions of the third type with h_1 and h_2 at r_1 and r_2, we obtain for $r < r'$

$$G(r, \theta|r', \theta') = \frac{\left(\frac{1}{B_1} + \ln\frac{r}{r'}\right)\left(\frac{1}{B_2} + \ln\frac{r_2}{r'}\right)}{2\pi\left(\frac{1}{B_1} + \frac{1}{B_2} + \ln\frac{r_2}{r_1}\right)} + \frac{1}{2\pi\beta}\sum_{n=1}^{\infty}\cos n\left(\theta - \theta' - \nu_{12}\ln\frac{r}{r'}\right) \cdot \frac{h_{1n}h_{2n}[rr'/(r_1r_2)^2]^{n\beta} + h_{1n}[r/(r_1^2r')]^{n\beta} + h_{2n}[r/(r_2^2r')^{n\beta} + (rr')]^{n\beta}}{n(h_{1n}r_1^{-2n\beta} - h_{2n}r_2^{-2n\beta})} \quad (17)$$

where $h_{1n} = (n\beta - B_1)/(n\beta + B_1)$ and $h_{2n} = (n\beta - B_2)/(n\beta + B_2)$. For $r > r'$, we just interchange r and r' in equation (17) except those in the cosine function. Green's functions for boundary conditions of the first type or any combination of the first, second and third type, can be found by the same way, or by specializing equation (17) to each case. However, if boundary conditions at r_1 and r_2 are all of the second type, Green's function does not exist but we can still construct the generalized Green's function for $r < r'$

$$G(r, \theta|r', \theta') = \frac{1}{4\pi(r_2^2 - r_1^2)}\left(r^2 + 2r_1^2\ln\frac{r_1}{r} + 2r_2^2\ln\frac{r_2}{r'}\right) + \frac{1}{2\pi\beta} \times \sum_{n=1}^{\infty}\frac{[rr'/(r_1r_2)^2]^{n\beta} + [r/(r_1^2r')]^{n\beta} + [r'/(r_2^2r)]^{n\beta} + (rr')^{-n\beta}}{n(r_1^{-2n} - r_2^{-2n})} \cdot \cos n[(\theta - \theta') - \nu_{12}\ln(r/r')] + \text{const} \quad (18)$$

and for $r' < r$ we just interchange r and r' in equation (18) except in the cosine function.

Infinite and Internally Bounded Regions

For an infinite region or a region bounded internally by a cylindrical surface of radius r_0, we may seek the solution for $G_1(r, \theta, z|r', \theta', z')$ in the form of

$$v(r, z)\exp\left[in\left(\theta - \theta' - \nu_{12}\ln\frac{r}{r'}\right)\right] \quad (19)$$

which satisfies equation (5) if $v(r, z)$ satisfies

$$\frac{\partial^2 v}{\partial r^2} + \frac{1}{r}\frac{\partial v}{\partial r} - \frac{\beta^2 n^2}{r^2}v + \nu_{33}\frac{\partial^2 v}{\partial z^2} = -\frac{1}{r}\delta(r - r')\delta(z - z') \quad (20)$$

For infinite region, we may apply the Hankel transform as was done in [1] to obtain

$$G(r, \theta, z\, r', \theta', z') = \frac{\epsilon}{2\pi}\int_0^{\infty}e^{-(\lambda/\sqrt{\nu_{33}})(z-z')}\sum_{n=0}^{\infty}J_n(\lambda r)J_{n\beta}(\lambda r') \cdot \cos n\left[(\theta - \theta') - \nu_{12}\ln\frac{r}{r'}\right]d\lambda \quad (21)$$

This is the fundamental solution of heat conduction in an anisotropic medium of the monoclinic system which is homogeneous in circular cylinder coordinates.

For the internally bounded region, we apply Weber's transform [1] to obtain

$$G(r, \theta, z|r', \theta', z') = \frac{\epsilon}{2\pi}\int_0^{\infty}e^{-(\lambda/\sqrt{\nu_{33}})(z-z')}\sum_{n=0}^{\infty}\frac{U_{n\beta}(\lambda r)U_{n\beta}(\lambda r')}{V_{n\beta}(\lambda r_0)}\cos n\left[(\theta - \theta') - \nu_{12}\ln\frac{r}{r'}\right]d\lambda \quad (22)$$

where the functions $U_{n\beta}$ and $V_{n\beta}$ are identical to those given by

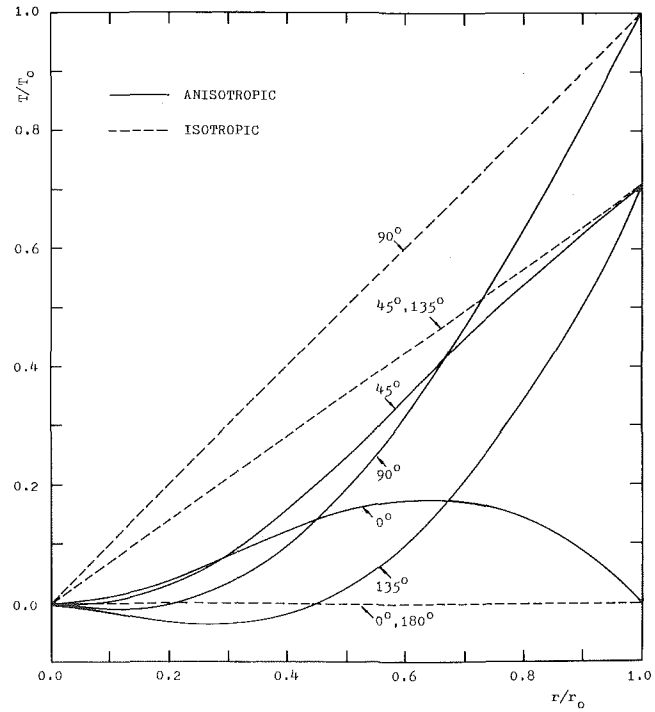

Fig. 1 Temperature distribution, $\beta = 2$, $\nu_{12} = 1$, $\nu_{12} = 5$

equations (47)–(50) in [1] for boundary conditions of the first and third types.

Note from equation (21) that the fundamental solution, or Green's function in free space of anisotropic media which are homogeneous in cylindrical coordinates, can no longer be expressed in a closed form as is possible for isotropic media or anisotropic media which are homogeneous in rectangular coordinates [4].

Orthotropic and Anisotropic Effects

To investigate the orthotropic and anisotropic effects on the temperature field, we consider two examples.

1 An infinite solid cylinder whose surface is kept at $T_0 \sin\theta$ where T_0 is a constant. We specialize equation (12) to the case for first-type boundary condition and the result is substituted into equation (3) to obtain

$$T(r, \theta) = T_0 \left(\frac{r}{r_0}\right)^{\beta} \sin\left(\theta - \nu_{12} \ln \frac{r}{r_0}\right) \tag{23}$$

2 A hollow cylinder with temperatures at the inner and outer surfaces kept at $T(r_1\theta) = T_1$ and $T(\theta) = T_0 \sin\theta$ where T_1 and T_0 are constant. For this case, we specialize equation (17) by setting $B_1 = B_2 = \infty$ to obtain:

$$G(r, \theta|r', \theta') = \frac{\ln(r'/r_1)\ln(r_2/r)}{2\pi \ln(r_2/r_1)} + \frac{1}{2\pi\beta} \sum_{n=1}^{\infty} \frac{(rr'/r_2)^{n\beta} - (r'/r)^{n\beta} - (r_1/r_2)^{2n\beta} + (r_1^2/rr')^{n\beta}}{n[(r_2/r_1)]^{-2n\beta} - 1} \cdot \cos n\left(\theta - \theta' - \nu_{12} \ln \frac{r}{r'}\right) \tag{24}$$

For $r' > r$ we just interchange r' and r in equation (24) except in the cosine function. Applying equation (24) to equation (3) and using the given boundary conditions, we obtain

$$T = T_1 \frac{\ln(r_2/r)}{\ln(r_2/r_1)} + T_0 \frac{r_1^{-2\beta} r^{\beta} - r^{-\beta}}{r_1^{-2\beta} r_2^{\beta} - r_2^{-\beta}} \sin\left(\theta - \nu_{12} \ln \frac{r}{r_2}\right) \tag{25}$$

Note that equations (23) and (25) reduce to those of the corresponding orthotropic problems by setting $\nu_{12} = 0$ and $\beta = \nu_{22}$, and to those of isotropic cases by setting $\beta = 1$ and $\nu_{12} = 0$.

The orthotropy of the material is characterized by ν_{22} and the anisotropy by ν_{12}. For a given value of ν_{12}, the stronger the orthotropy, the larger the value of β. On the other hand, for a given value of ν_{22}, the stronger the anisotropy, the smaller the value of β. We now consider the solution (23). In an orthotropic medium ($\beta = \nu_{22}$), the temperature in the interior of the circular cross-sectional area is lower for $\beta > 1$ and higher for $\beta < 1$ than the temperature in an isotropic medium ($\beta = 1$) at the same position in the upper half of the circular area ($0 < \theta < \pi$) but opposite effects occur in the lower half of the circular area ($\pi < \theta < 2\pi$). The increase of ν_{12} decreases β and hence increases the amplitude of temperature for a given value of r and shifts the highest and lowest temperature clockwise by an angle of $\nu_{12} \ln(r/r_0)$. These discussions can be clearly seen from the calculated results of equation (23) as shown in Fig. 1. The same discussions can be made regarding equation (24).

Separation of Variables

We next show how the results of equations (23) and (25) can be obtained directly by the classical method. If we assume that $T(r, \theta) = \psi(r)\phi(\theta)$, then the homogeneous partial differential equation for $T(r, \theta)$ can be separated into two ordinary differential equations

$$\phi' - \lambda\phi = 0 \tag{26}$$

$$r^2\psi'' + (2in\nu_{12} + 1)r\psi' + in\nu_{12}\psi = 0 \tag{27}$$

The solution of equation (26) satisfying the periodic condition is

$$\phi = e^{i\lambda'\theta} \quad \lambda = n = 0, \pm 1, \pm 2, \pm 3, \ldots \tag{28}$$

Equation (27) has the solution in the form

$$\psi = R(r) r^{-in\nu_{12}}$$

where $R(r)$ satisfies

$$R'' + \frac{1}{r}R' - \frac{n^2\beta^2}{r^2} = 0$$

Thus, we can assume the solution for $T(r, \theta)$ in the series form

$$T(r, \theta) = \sum_{n=-\infty}^{\infty} R_{n\beta}(r) r^{-in\nu_{12}} e^{in\theta} \tag{29}$$

From the given boundary conditions, and the solution for $R(r)$, which is well known, we obtain the results of equation (23) and (25).

Discussions and Concluding Remarks

All of the Green's functions obtained above reduce to those for orthotropic media by setting $\nu_{12} = 0$ and to those for isotropic media by putting $\nu_{12} = 0$ and $\beta = \nu_{33} = 1$.

It is seen from the expressions for Green's functions obtained above, and the integral equation (3) that an analytical expression for the temperature is difficult to obtain, if there is heat production in the medium.

All the problems in this paper can also be solved by Fourier's method, although the separation process is slightly more complicated and restrictive for general anisotropic problems. Thus, the usual conclusion that the technique of separation of variables does not apply to anisotropic problems (for instance, references [5, 6]), is not always true at least in the broad sense of this technique.

References

1 Chang, Y. P., and Tsou, R. C. H., "Heat Conduction in an Anisotropic Medium in Cylindrical Regions—Unsteady State," to appear.

2 Miranda, C., "Partial Differential Equation of Elliptic Type," Springer, Berlin, 1955.

3 Stakgold, I., *Boundary Value Problems of Mathematical Physics*, Vol. II, MacMillan, N. Y., 1968.

4 Chang, Y. P., "Analytical Solution for Heat Conduction in Anisotropic Media in Infinite, Semi-Infinite and Two-Plane Bounded Regions," submitted to *International Journal of Heat and Mass Transfer*, Mar. 1976.

5 Weinberger, H. F., *Partial Differential Equations*, Blaisdell, Waltham, Mass, 1965, pp. 68–69.

6 Padovan, J., "Solution of Transient Temperature Fields in Laminated Anisotropic Slabs and Cylinders," *Intern. J. Eng. Sci.*, Vol. 13, 1975, pp. 247–260.

Heat Transfer in a Three-Dimensional Anisotropic Solid of Arbitrary Shape

G. P. Mulholland[1] and B. P. Gupta[2]

Introduction

The mathematical difficulties associated with most technical problems prohibit an exact, closed-form analytical solution. These difficulties can be caused by the form of the governing partial differential equation or by the boundary conditions associated with the problem. It is the latter situation which is considered in this work; that is the situation wherein the bounding surface of the solid may or may not conform to a standard orthogonal curvilinear reference frame.

The particular problem dealt with in this paper is the heat transfer in a three-dimensional anisotropic body of arbitrary shape having as thermal boundary conditions the most general linear type. The solution method uses a computer routine which constructs orthonormal functions and provides series coefficients which correspond to the given boundary conditions. A very detailed discussion of this orthonormalization procedure has been given by Davis [1][3] and Sparrow [2], so only the important features will be discussed here.

The basic problem is to solve the differential equation of heat conduction for a three-dimensional anisotropic solid, equation (1). The bounding surface of the region need only be a continuous closed curve. After the governing equation is transformed to Laplace's equation, equation (11), by means of equations (4) and (8), the solution method involves two distinct steps [2]. In the first step, a system of linear algebraic equations is generated by evaluating the boundary condition at a discrete set of points. The second step utilizes the orthonormalization subroutine to satisfy the linear equations in the least-squares sense. The orthonormal functions utilized in the computer subroutine are formed by means of the Gram-Schmidt method [1, 2].

With the original equation transformed to a Laplace-type equation, the solution can be written as

$$\Theta = \sum_{i=1}^{N} b_i f_i(x_1, y_1, z_1)$$

The b_i are arbitrary constants to be determined from the boundary conditions by means of the orthonormalization procedure, while the f_i are obtained from the three-dimensional harmonic functions. Thus, the temperature distribution at any point within the solid can be found since the b_i and f_i are known.

Problem

The governing partial differential equation for the heat transfer in a three-dimensional anisotropic solid whose thermal properties are constant is given by [3]

$$K_{11}{}^1\frac{\partial^2 T}{\partial \xi^2} + K_{22}{}^1\frac{\partial^2 T}{\partial \eta^2} + K_{33}{}^1\frac{\partial^2 T}{\partial \delta^2} + (K_{23}{}^1 + K_{32}{}^1)\frac{\partial^2 T}{\partial \eta \partial \delta} + (K_{31}{}^1 + K_{13}{}^1)\frac{\partial^2 T}{\partial \delta \partial \xi} + (K_{12}{}^1 + K_{21}{}^1)\frac{\partial^2 T}{\partial \xi \partial \eta} + q = 0 \quad (1)$$

Associated with equation (1) are known conditions at the surface which can be boundary conditions of the first, second, or third kind [4] and will be discussed later.

Equation (1) can be transformed to a canonical form in the following manner: Let the conductivity matrix be denoted by A

$$A = \begin{bmatrix} K_{11}{}^1 & K_{12}{}^1 & K_{13}{}^1 \\ K_{21}{}^1 & K_{22}{}^1 & K_{23}{}^1 \\ K_{31}{}^1 & K_{32}{}^1 & K_{33}{}^1 \end{bmatrix}, \quad K_{ij} = K_{ji}, \quad i = 1, 2, 3, \quad j = 1, 2, 3 \quad (2)$$

This matrix can be reduced to a diagonal matrix since it is symmetric. The elements of the diagonal matrix are the eigenvalues of the matrix A and are obtained from the eigenvalue equation:

$$(K_{11}{}^1 - \lambda)[(K_{22}{}^1 - \lambda)(K_{33}{}^1 - \lambda) - K_{23}{}^{12}] - K_{12}{}^1[K_{12}{}^1(K_{33}{}^1 - \lambda) - K_{23}{}^1K_{13}{}^1] + K_{13}{}^1[K_{12}{}^1K_{23}{}^1 - (K_{22}{}^1 - \lambda)K_{13}{}^1] = 0 \quad (3)$$

The roots of equation (3) are the principal conductivities of the system and can be represented as K_1, K_2, and K_3 along the principal axes x, y, and z. The principal axes are related to the ξ, η, δ, coordinate system by

$$\begin{bmatrix} x \\ y \\ z \end{bmatrix} = \begin{bmatrix} B \end{bmatrix}^T \begin{bmatrix} \xi \\ \eta \\ \delta \end{bmatrix} \quad (4)$$

where

B = normalized eigenvector matrix corresponding to matrix A
B^T = transpose of matrix B

The elements of the matrix B are the directional cosines between the principal axes and the reference axes. Transforming equation (1) into the principal coordinate system, we obtain

$$K_1\frac{\partial^2 T}{\partial x^2} + K_2\frac{\partial^2 T}{\partial y^2} + K_3\frac{\partial^2 T}{\partial z^2} + q = 0 \quad (5)$$

In addition, let

$$x_1 = \frac{x}{\sqrt{K_1}}, \qquad y_1 = \frac{y}{\sqrt{K_2}}, \qquad z_1 = \frac{z}{\sqrt{K_3}} \quad (6)$$

so that equation (5) becomes

$$\frac{\partial^2 T}{\partial x_1{}^2} + \frac{\partial^2 T}{\partial y_1{}^2} + \frac{\partial^2 T}{\partial z_1{}^2} + q = 0 \quad (7)$$

If the heat generation term q is a constant, the transformation [2]

$$\Theta = \frac{T}{q} + \frac{1}{6}(x_1{}^2 + y_1{}^2 + z_1{}^2) \quad (8a)$$

will reduce equation (5) to Laplace's equation. For q not constant, the transformation [2]

$$\Theta = T + \sum_{i=1}^{N} C_i G_i(x_1, y_1, z_1) \quad (8b)$$

where

$$\frac{\partial^2 G_i}{\partial x_1{}^2} + \frac{\partial^2 G_i}{\partial y_1{}^2} + \frac{\partial^2 G_i}{\partial z_1{}^2} = f_i(x_1, y_1, z_1) \quad (9)$$

$$q = \sum_{i=1}^{N} C_i f_i(x_1, y_1, z_1) \quad (10)$$

will reduce equation (5) to Laplace's equation. The C_i in equations (8b) and (10) will be obtained from the orthonormalization procedure since the $f_i(x_1, y_1, z_1)$ and $q(x_1, y_1, z_1)$ will be known.

Under the transformation given by either equation (8a) or (8b), equation (7) becomes

$$\frac{\partial^2 \Theta}{\partial x_1{}^2} + \frac{\partial^2 \Theta}{\partial y_1{}^2} + \frac{\partial^2 \Theta}{\partial z_1{}^2} = 0 \quad (11)$$

which is the three-dimensional Laplace equation. The most convenient method for generating solutions of equation (11) is by means of the three-dimensional harmonic functions [2]

[1] Department of Mechanical Engineering, New Mexico State University, Las Cruces, N. M. Mem. ASME.
[2] Department of Mechanical Engineering, New Mexico State University, Las Cruces, N. M.
[3] Numbers in brackets designate References at end of technical note.
Contributed by the Heat Transfer Division of THE AMERICAN SOCIETY OF MECHANICAL ENGINEERS. Manuscript received by the Heat Transfer Division May 27, 1976.

$$R_{mn} = r^n P_n{}^m(\cos\Theta)\sin n\phi, \qquad m \le n \tag{12a}$$

and

$$R_{mn} = r^n P_n{}^m(\cos\Theta)\cos n\phi, \qquad m \le n \tag{12b}$$

The $P_n{}^m$ are the associated Legendre polynomials and r, Θ and ϕ are the coordinates in a spherical reference frame. The first five of these harmonic functions are tabulated in Appendix A and are denoted by $f_i(x_1, y_1, z_1)$. Additional terms can easily be generated by using equation (12). With the f_i known, the solution for Θ is given by

$$\Theta(x_1, y_1, z_1) = \sum_{i=1}^{N} b_i f_i(x_1, y_1, z_1) \tag{13}$$

where the b_i are arbitrary constants to be determined from the boundary conditions. The solution given by equation (13) is unique since it is a solution of Laplace's equation. A convenient method for checking round-off error has been given by Davis [1]. His method consists of checking the norm of the least-square approximation of a function F by n functions f_i. The norm is supposed to be monotonically decreasing, but it may increase after decreasing for a while. This increase indicates a serious round-off error and the computation should be stopped. Davis [1] also presents a method for "straightening out" the orthonormal vectors.

Boundary Conditions

The most general thermal boundary condition can be represented by

$$A_1\left(\frac{\partial T}{\partial n}\right)_{\xi_B,\eta_B,\delta_B} = A_2 T(\xi_B, \eta_B, \delta_B) + A_3 \tag{14}$$

where n is the outer normal at the bounding surface and the A_1, A_2, and A_3 are arbitrary known functions. The normal derivative is given by

$$\frac{\partial T}{\partial n} = \mu_1\frac{\partial T}{\partial x_1} + \mu_2\frac{\partial T}{\partial x_2} + \mu_3\frac{\partial T}{\partial x_3} \tag{15}$$

where

$$\mu_i = \frac{1}{\sqrt{K_i}}(\ell B_{1i} + mB_{2i} + pB_{3i}) \qquad i = 1, 2, 3$$

and where ℓ, m, and p are direction cosines and the B_{ij}, ($i = 1, 2, 3$, $j = 1, 2, 3$) are the elements of the normalized eigenvector matrix B. Substitution of equations (8), (13), and (15) into equation (14) gives

$$A_1 P\left(\mu_1\sum_{i=1}^{N} b_i\frac{\partial f_i}{\partial x_1}\bigg|_B + \mu_2\sum_{i=1}^{N} b_i\frac{\partial f_i}{\partial y_1}\bigg|_B + \mu_3\sum_{i=1}^{N} b_i\frac{\partial f_i}{\partial z_1}\bigg|_B\right) = A_2 P\sum_{i=1}^{N} b_i f_i\bigg|_B + \psi \tag{16}$$

where

$$\psi = \frac{q}{6}[(2\mu_1 x_1 + 2\mu_2 y_1 + 2\mu_3 z_1)A_1 - (x_1{}^2 + y_1{}^2 + z_1{}^2)A_2]_B + A_3; \qquad P = q$$

for q constant and

$$\psi = A_1\sum_{i=1}^{N} C_i\left(\mu_1\frac{\partial G_i}{\partial x_1} + \mu_2\frac{\partial G_i}{\partial y_1} + \mu_3\frac{\partial G_i}{\partial z_1}\right)_B - A_2\sum_{i=1}^{N} C_i G_i|_B + A_3; \qquad P = 1$$

for q not constant. Equation (16) can be written in a more compact form as

$$\sum_{i=1}^{N} b_i h_i(x_{1B}, y_{1B}, z_{1B}) = \psi/P = A_4 \tag{17}$$

where

$$h_i = \left(A_1\mu_1\frac{\partial f_i}{\partial x_1} + A_1\mu_2\frac{\partial f_i}{\partial y_1} + A_1\mu_3\frac{\partial f_i}{\partial z_1} - A_2 f_i\right)_B \tag{18}$$

Since the quantities h_i and A_4 are known at the boundaries, the b_i can be determined from the orthonormalization process. With the b_i known, the temperature distribution is found either by means of equation (8a) or q constant or by means of equation (8b) for q not constant.

The temperature distribution in the original reference frame can be obtained from equation (6) and the transformation

$$\begin{bmatrix}\xi\\ \eta\\ \delta\end{bmatrix} = [B^{\mathrm{T}}]^{-1}\begin{bmatrix}\mathrm{x}\\ \mathrm{y}\\ \mathrm{z}\end{bmatrix} \tag{19}$$

where $[B^{\mathrm{T}}]^{-1}$ = inverse of the transposed eigenvector matrix B.

The boundary points can be read into the computer either by algebraic equations or by a three-dimensional matrix. For example, in the illustrative problems which follow, 72 points on the boundary were used for the calculations. These points were read into the computer by means of algebraic equations but a three-dimensional matrix could have been used just as easily. In fact, for completely general boundary contours, a matrix input would have to be utilized.

Examples

For the first illustration, the steady-state temperature distribution in an isotropic sphere will be considered. This particular problem was chosen because the exact solution can be easily obtained and comparisons can be made between the exact and the orthonormalization solution.

The pertinent properties are

$$K_{11}{}^1 = K_{22}{}^1 = K_{33}{}^1 = 0.214 \text{ cal/cm K hr}; \quad T(\xi_B, \eta_B, \delta_B) = 0°\text{C}$$

$$K_{ij}{}^1 = 0, \quad i = 1, 2, 3, \quad j = 1, 2, 3, \quad i \ne j; \quad q = 0.5 \text{ cal/cm}^3\text{-hr}$$

Since the sphere is isotropic, the matrix B becomes an identity matrix and by using the transformation given by equation (8a), we obtain the three-dimensional Laplace equation, equation (11). The solution for $\Theta(x_1, y_1, z_1)$ is given by equation (13) where the b_i were obtained by imposing the boundary conditions at the surface. Temperature calculations were made for seven values of the radius and the agreement between the exact solution and the appropriate solution was within 0.6 percent at all points.

For the next example, a prolate spheriod will be considered. The relationship between the ξ, η, δ coordinate system and the prolate spheriodal system (α, β, γ) is given by

$$\xi = e\sinh\alpha\sin\beta\sin\gamma; \qquad \eta = e\cosh\alpha\cos\beta; \qquad \delta = -e\sinh\alpha\sin\beta\cos\gamma$$

Let

$$\cos\alpha = 5; \qquad e = 0.75; \qquad K_{11}{}' = 0.264 \text{ cal/cm K-hr}; \qquad K_{22}{}' = 0.231 \text{ cal/cm K-hr}'$$

$$K_{33}{}' = 0.214 \text{ cal/cm K-hr}; \qquad K_{21}{}' = K_{12}{}' = 0.029 \text{ cal/cm K-hr}$$

$$K_{31} = K_{13} = K_{23} = K_{32} = 0$$

$$q = 0.5 \text{ cal/cm}^3 \text{ hr}$$

$$T(\xi_B, \eta_B, \delta_B) = 0$$

The foregoing property values are characteristic of some of the common forms of graphite (e.g., ATJ). For this case, the eigenvector matrix B becomes

$$B = \begin{bmatrix}0.866 & -0.5 & 0\\ 0.5 & 0.866 & 0\\ 0 & 0 & 1\end{bmatrix}$$

and the principal conductivities are

Table 1 Temperature at selected points within spheroid

ξ(cm)	η(cm)	δ(cm)	TEMPERATURE (°C) ANISOTROPIC	ISOTROPIC
0.319	-1.125	1.8092	2.971	3.059
1.1809	-1.125	1.4073	3.002	3.174
1.8092	-1.125	-0.319	3.074	3.230
2.0891	0.0	0.3684	3.184	3.288
0.319	1.125	1.8092	3.0635	3.0593
0.6283	1.125	1.7263	3.096	3.110
1.7263	1.125	0.6283	3.174	3.223

Table 2

ξ(cm)	η(cm)	δ(cm)	Temperature (°C) n = 2	n = 5	n = 9	n = 14
0.319	-1.125	1.8092	2.812	2.895	2.971	2.971
1.1809	-1.125	1.4073	2.854	2.876	3.002	3.002
2.0891	0	-0.319	3.000	2.935	3.074	3.074
0.6283	1.125	1.7263	3.042	3.116	3.096	3.096
1.7263	1.125	0.6283	3.399	3.360	3.174	3.174

$$K_1 = 0.281 \text{ cal/cm K hr}$$

$$K_2 = 0.214 \text{ cal/cm K hr}$$

$$K_3 = 0.214 \text{ cal/cm K hr}$$

Proceeding in the same manner as before, we obtain the b_i coefficients

$b_1 = 9.64567$ $b_6 = 0.108 \times 10^{-6}$ $b_{11} = -0.5708 \times 10^{-8}$
$b_2 = 0.48322 \times 10^{-5}$ $b_7 = -0.765 \times 10^{-6}$ $b_{12} = 0.577 \times 10^{-8}$
$b_3 = -0.111 \times 10^{-5}$ $b_8 = 0.101 \times 10^{-2}$ $b_{13} = -0.169 \times 10^{-8}$
$b_4 = 0.135 \times 10^{-4}$ $b_9 = -0.841 \times 10^{-2}$ $b_{14} = 0.565 \times 10^{-8}$
$b_5 = 0.1376 \times 10^{-1}$ $b_{10} = -0.327 \times 10^{-7}$

and the temperature distribution is then given by

$$T(x_1, y_1, z_1) = q \sum_{i=1}^{\infty} b_i f_i(x_1, y_1, z_1) - \frac{q}{6}(x_1^2 + y_1^2 + z_1^2)$$

Some values for the temperature at various positions within the body are given in Table 1 for the anisotropic and isotropic ($K = 0.231$ cal/cm°K-hr) cases. The difference between the two solutions ranges from 0 to 7 percent dependeng on the location within the solid. The total time required to calculate the temperature at 30 points within the solid was 5.04 s on an IBM360/65 computer using 14 terms in the series, equation (13).

The rapid convergence of the series, equation (13), is shown in Table 2 for this particular problem. After five terms, all the values are within 5 percent of the actual temperatures and there is no change in the temperature, within three significant figures after the decimal point, for more than nine terms in the series.

Acknowledgments

The authors would like to thank Mr. Michael Frisch of the University of Minnesota Computer Center and Dr. A. Haji-Sheikh of the University of Texas at Arlington for providing them with the ORTHON subroutine.

References

1 Davis, P. J., "Orthonormalizing Codes in Numerical Analysis," in *Survey of Numerical Analysis*, J. Todd, ed., McGraw-Hill, New York, 1962.

2 Sparrow, E. M., "Solution of Heat Transfer Problems by Orthonormalization Methods," in *Computational Approaches in Applied Mechanics*, E. Sevin, ed., ASME, 1969, pp. 85–106.

3 Carslaw, H. S., and Jaeger, J. C., *Conduction of Heat in Solids*, Clarendon Press, Oxford, 1959.

4 Ozisik, M. N., *Boundary Value Problems of Heat Conduction*, International Textbook Co., Seranton, Pa., 1968.

5 Sparrow, E. M., and Haji-Sheikh, A., "Flow and Heat Transfer in Ducts of Arbitrary Shape with Arbitrary Thermal Boundary Conditions," JOURNAL OF HEAT TRANSFER, TRANS. ASME, Series C, Vol. 88, 1966, pp. 351–358.

6 Sparrow, E. M., and Haji-Sheikh, A., "Transient and Steady Heat Conduction in Arbitrary Bodies with Arbitrary Boundary and Initial Conditions," JOURNAL OF HEAT TRANSFER, Vol. 90, 1968, pp. 103–108.

Appendix A

The *f* Functions

For a spherical frame, the first five f functions are:

$$f_1 = 1, \qquad f_2 = r\cos\Theta, \qquad f_3 = r\sin\Theta\cos\phi$$

$$f_4 = r\sin\Theta\cos\phi, \qquad f_5 = \frac{r^2}{2}(3\cos^2\Theta - 1)$$

For the foregoing functions, ϕ is the angle between the positive x axis and the projection of r on the x-y plane while Θ is the angle between the positive z-axis and r.

On the Solution of Transient Conduction With Temperature-Dependent Thermal Conductivity

R. C. Mehta[1]

Nomenclature

a = thickness of finite slab, or length of rectangular plate
b = width of rectangular plate
B = Biot number, $ha/k(\theta)$
C_p = specific heat
h = heat transfer coefficient
$k(\theta) = k_0(1 + \beta\theta)$
k_0 = reference thermal conductivity at $T = T_0$
$K(\theta) = k(\theta)/k_0$
t = time
T = temperature
X = dimensionless coordinate, x/a
x, y = coordinates
α_0 = reference thermal diffusivity, $k_0/(\rho C_p)$
β = constant (thermal conductivity coefficient)
ρ = density
τ = dimensionless time, $\alpha_0 t/a^2$
ξ, ϕ = dimensionless coordinates, $\pi x/a$ and $\pi y/b$, respectively
θ = dimensionless temperature

Introduction

The high temperature range involved and considerable variation of thermal conductivity with temperature for many present-day

[1] Propulsion Engineering Division, Vikram Sarabhai Space Centre, Trivandrum, India

Contributed by the Heat Transfer Division of THE AMERICAN SOCIETY OF MECHANICAL ENGINEERS. Manuscript received by the Heat Transfer Division August 31, 1976.

Table 1 Temperature at selected points within spheroid

ξ(cm)	η(cm)	δ(cm)	TEMPERATURE (°C) ANISOTROPIC	ISOTROPIC
0.319	-1.125	1.8092	2.971	3.059
1.1809	-1.125	1.4073	3.002	3.174
1.8092	-1.125	-0.319	3.074	3.230
2.0891	0.0	0.3684	3.184	3.288
0.319	1.125	1.8092	3.0635	3.0593
0.6283	1.125	1.7263	3.096	3.110
1.7263	1.125	0.6283	3.174	3.223

Table 2

ξ(cm)	η(cm)	δ(cm)	Temperature (°C) n = 2	n = 5	n = 9	n = 14
0.319	-1.125	1.8092	2.812	2.895	2.971	2.971
1.1809	-1.125	1.4073	2.854	2.876	3.002	3.002
2.0891	0	-0.319	3.000	2.935	3.074	3.074
0.6283	1.125	1.7263	3.042	3.116	3.096	3.096
1.7263	1.125	0.6283	3.399	3.360	3.174	3.174

$$K_1 = 0.281 \text{ cal/cm K hr}$$

$$K_2 = 0.214 \text{ cal/cm K hr}$$

$$K_3 = 0.214 \text{ cal/cm K hr}$$

Proceeding in the same manner as before, we obtain the b_i coefficients

$b_1 = 9.64567$ $b_6 = 0.108 \times 10^{-6}$ $b_{11} = -0.5708 \times 10^{-8}$
$b_2 = 0.48322 \times 10^{-5}$ $b_7 = -0.765 \times 10^{-6}$ $b_{12} = 0.577 \times 10^{-8}$
$b_3 = -0.111 \times 10^{-5}$ $b_8 = 0.101 \times 10^{-2}$ $b_{13} = -0.169 \times 10^{-8}$
$b_4 = 0.135 \times 10^{-4}$ $b_9 = -0.841 \times 10^{-2}$ $b_{14} = 0.565 \times 10^{-8}$
$b_5 = 0.1376 \times 10^{-1}$ $b_{10} = -0.327 \times 10^{-7}$

and the temperature distribution is then given by

$$T(x_1, y_1, z_1) = q \sum_{i=1}^{\infty} b_i f_i(x_1, y_1, z_1) - \frac{q}{6}(x_1^2 + y_1^2 + z_1^2)$$

Some values for the temperature at various positions within the body are given in Table 1 for the anisotropic and isotropic ($K = 0.231$ cal/cm°K-hr) cases. The difference between the two solutions ranges from 0 to 7 percent dependeng on the location within the solid. The total time required to calculate the temperature at 30 points within the solid was 5.04 s on an IBM360/65 computer using 14 terms in the series, equation (13).

The rapid convergence of the series, equation (13), is shown in Table 2 for this particular problem. After five terms, all the values are within 5 percent of the actual temperatures and there is no change in the temperature, within three significant figures after the decimal point, for more than nine terms in the series.

Acknowledgments

The authors would like to thank Mr. Michael Frisch of the University of Minnesota Computer Center and Dr. A. Haji-Sheikh of the University of Texas at Arlington for providing them with the ORTHON subroutine.

References

1 Davis, P. J., "Orthonormalizing Codes in Numerical Analysis," in *Survey of Numerical Analysis*, J. Todd, ed., McGraw-Hill, New York, 1962.

2 Sparrow, E. M., "Solution of Heat Transfer Problems by Orthonormalization Methods," in *Computational Approaches in Applied Mechanics*, E. Sevin, ed., ASME, 1969, pp. 85–106.

3 Carslaw, H. S., and Jaeger, J. C., *Conduction of Heat in Solids*, Clarendon Press, Oxford, 1959.

4 Ozisik, M. N., *Boundary Value Problems of Heat Conduction*, International Textbook Co., Seranton, Pa., 1968.

5 Sparrow, E. M., and Haji-Sheikh, A., "Flow and Heat Transfer in Ducts of Arbitrary Shape with Arbitrary Thermal Boundary Conditions," JOURNAL OF HEAT TRANSFER, TRANS. ASME, Series C, Vol. 88, 1966, pp. 351–358.

6 Sparrow, E. M., and Haji-Sheikh, A., "Transient and Steady Heat Conduction in Arbitrary Bodies with Arbitrary Boundary and Initial Conditions," JOURNAL OF HEAT TRANSFER, Vol. 90, 1968, pp. 103–108.

Appendix A

The *f* Functions

For a spherical frame, the first five f functions are:

$$f_1 = 1, \qquad f_2 = r\cos\Theta, \qquad f_3 = r\sin\Theta\cos\phi$$

$$f_4 = r\sin\Theta\cos\phi, \qquad f_5 = \frac{r^2}{2}(3\cos^2\Theta - 1)$$

For the foregoing functions, ϕ is the angle between the positive x axis and the projection of r on the x-y plane while Θ is the angle between the positive z-axis and r.

On the Solution of Transient Conduction With Temperature-Dependent Thermal Conductivity

R. C. Mehta[1]

Nomenclature

a = thickness of finite slab, or length of rectangular plate
b = width of rectangular plate
B = Biot number, $ha/k(\theta)$
C_p = specific heat
h = heat transfer coefficient
$k(\theta) = k_0(1 + \beta\theta)$
k_0 = reference thermal conductivity at $T = T_0$
$K(\theta) = k(\theta)/k_0$
t = time
T = temperature
X = dimensionless coordinate, x/a
x, y = coordinates
α_0 = reference thermal diffusivity, $k_0/(\rho C_p)$
β = constant (thermal conductivity coefficient)
ρ = density
τ = dimensionless time, $\alpha_0 t/a^2$
ξ, ϕ = dimensionless coordinates, $\pi x/a$ and $\pi y/b$, respectively
θ = dimensionless temperature

Introduction

The high temperature range involved and considerable variation of thermal conductivity with temperature for many present-day

[1] Propulsion Engineering Division, Vikram Sarabhai Space Centre, Trivandrum, India

Contributed by the Heat Transfer Division of THE AMERICAN SOCIETY OF MECHANICAL ENGINEERS. Manuscript received by the Heat Transfer Division August 31, 1976.

materials require that the variation of conductivity with temperature be considered in the analysis of transient heat conduction. Owing to the attendant nonlinearity of the governing equation, an exact solution to this problem is not feasible except for the limiting case of a one-dimensional semi-infinite slab [1].[2] Many approximate solutions are therefore reported both for one-dimensional [2–5] and two-dimensional [5, 6] heat flow in finite regions.

For modest nonlinearities, Mingle [7] has employed a "numerical perturbation technique" for one-dimensional case utilizing the exact solution in conjunction with an iterative scheme. The present note reports an iterative solution for the transient temperature distribution in a two-dimensional finite solid with variable thermal conductivity.

The Iterative Procedure

For the purpose of illustration, we describe the procedure for one-dimensional problem. Extension of the method for two-dimensional heat flow is straightforward as shown in an example presented later in the text.

The description of transient conduction in a one-dimensional slab having two parallel surfaces S_n ($n = 1, 2$) is given in dimensionless form as follows:

$$\frac{\partial\theta}{\partial\tau}(X,\tau) = \frac{\partial}{\partial X}\left[K(\theta)\frac{\partial\theta}{\partial X}(X,\tau)\right] \quad \text{in region } R,\ \tau > 0 \tag{1}$$

$$\frac{\partial\theta}{\theta X}(S_n,\tau) = \mathrm{B}_n[\theta(S_n,\tau)] \quad \text{on boundary } S_n,\ \tau > 0 \tag{2}$$

$$\theta(X,0) = F(X) \quad \text{in region } R \tag{3}$$

We now consider the constant property solution as an initial guess to the foregoing nonlinear problem. The solution for the constant property case is well known [8] and can be written in terms of eigenfunction $\psi(\lambda_m, X)$ as:

$$\theta(X,\tau) = \sum_{m=1}^{\infty} \exp[-\lambda_m^2\tau]\psi(\lambda_m, X)\int_R \psi(\lambda_m, \overline{X})F(\overline{X})d\overline{X} \tag{4}$$

To take into account the effect of the variable thermal conductivity on the temperature distribution, we make an assumption that at any section X in the region R, thermal conductivity remains constant over a small interval ΔX. The solution of the governing equation (1) is expected to be locally represented in a form similar to that given by equation (4), with a perturbation on τ and λ_m that are related to the thermal conductivity. An iteration scheme is then set up for the temperature field for the "$i + 1$"th iteration to be given by

$$\theta^{i+1}(X,\tau) = \sum_{m=1}^{\infty} \exp[-K(\theta^i)(\lambda_m{}^i)^2\tau]\psi(\lambda_m{}^i, X) \times \int_R \psi(\lambda_m{}^i, \overline{X})F(\overline{X})d\overline{X}, \quad 0 \leq X \leq R;\ \tau > 0 \tag{5}$$

In the iteration scheme, terms on the right-hand side of equation (5) are evaluated from the ith iteration to obtain the $i + 1$ iterate directly from the left-hand side of the equation. The calculation then continues until convergence within the tolerance ϵ is achieved. It is to be noted that the eigenvalues $\lambda_m{}^i$ depend on $\mathrm{B}_n{}^i(S_n, \tau)$ which is a function of the current value of the thermal conductivity at the surface and are the same for all X in the region R. It is appropriate to mention here that a somewhat similar procedure in conjunction with a finite element approach has been used by Myers [9] for solving two-dimensional steady-state conduction.

Convergence

The convergence of the iteration equation (5) is now examined. It is mentioned by Scarborough [10] that the criterion for convergence for the iteration is given by $|\partial\varphi/\partial\theta| < 1$ in the neighborhood of the desired value θ, where φ represents the right-hand side of equation (5). Therefore, it requires that

$$\left|\sum_{m=1}^{\infty}\left[-\frac{dK(\theta)}{d\theta}\right]\lambda_m{}^2\tau\exp[-K(\theta)\lambda_m{}^2\tau]\psi(\lambda_m, X) \times \int_R \psi(\lambda_m, \overline{X})F(\overline{X})d\overline{X}\right| < 1 \tag{6}$$

The expression $\psi\int_R \psi F d\overline{X}$ is always less than or equal to 1. It can be shown that the expression $\lambda_m{}^2\tau\exp[-K(\theta)\lambda_m{}^2\tau]$ has a maximum of $1/2.718K(\theta)$ at $\lambda_m{}^2\tau = 1/K(\theta)$. To satisfy equation (6), we now obtain the approximate convergence criteria as:

$$\left|\frac{1}{2.718K(\theta)}\cdot\frac{dK(\theta)}{d\theta}\right| < 1 \tag{7}$$

For example, in the case of $K(\theta) = 1 + \beta\theta$, it can be shown that $|\beta| < 2.718$ for achieving convergence of the iteration process. This limit of β is satisfied in many practical cases. Thus, equation (7) establishes the approximate limits on the permissible variation of the thermal conductivity with temperature. Similar criterion is applicable for the two-dimensional problem also.

Examples

1 **The Finite Slab.** Here the equations to be solved are the governing equation (1) with the following boundary and initial conditions:

$$\left.\begin{aligned} &\frac{\partial\theta}{\theta X}(0,\tau) = 0;\ \tau > 0 \\ &\theta(1,\tau) = 1;\ \tau > 0 \\ &\text{and } \theta(X,\tau) = 0;\ \text{for all } X \end{aligned}\right\} \tag{8}$$

Linear variation of thermal conductivity with temperature is considered:

$$K(\theta) = 1 + \beta\theta \tag{9}$$

Using the present iteration scheme, the temperature distribution is obtained for values of β equal to 0.5 and -0.5. This is compared with the finite difference solution of [11] where a two-time-level, Crank-Nicholson implicit method is used while a Taylor's forward projection method is employed to take into account the nonlinearities. The local order of accuracy of the numerical solution is given by $[(\Delta X)^2 + (\Delta\tau)^2]$; and its stability and convergence are reported in references [11, 12]. 20 space intervals and a time increment of 0.005 are taken to insure convergence of solution.

Fig. 1 shows that the present results are in good agreement with the finite difference solution:

2 **The Rectangular Plate.** Consider the case of a finite rectangular plate ($0 \leq \xi \leq \pi, 0 \leq \phi \leq \pi$) of uniform temperature $\theta = 1$ at $\tau < 0$, and the temperature of the edges is maintained at zero for $\tau > 0$. The thermal conductivity $K(\theta)$ is assumed to be a linear function of temperature and is represented by

$$K(\theta) = [1 + \beta\theta(\xi, \phi; \tau)] \tag{10}$$

The governing differential equation of heat conduction is given by

$$\frac{\partial\theta}{\partial\tau} = \pi^2\left\{\left(\frac{\partial}{\partial\xi}[K(\theta)]\frac{\partial\theta}{\partial\xi}\right) + R^2\left(\frac{\partial}{\partial\phi}[K(\theta)]\frac{\partial\theta}{\partial\phi}\right)\right\} \tag{11}$$

and the initial and boundary conditions are as follows:

$$\left.\begin{aligned} &0 \leq \xi \leq \pi;\ 0 \leq \phi \leq \pi,\ \tau < 0;\ \theta = 1 \\ &\xi = 0, \pi;\ \phi = 0, \pi;\ \tau > 0;\ \theta = 0 \end{aligned}\right\} \tag{12}$$

where $R = a/b$

[2] Numbers in brackets designate References at end of technical note.

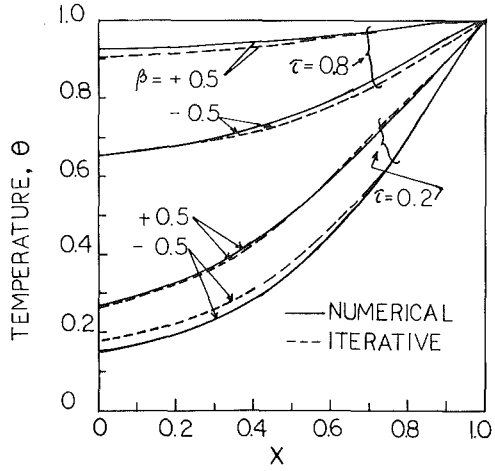

Fig. 1 Comparison of temperature distribution from iterative and numerical solutions for a slab of thickness *a*

The constant property solution [6] is given by

$$\theta(\xi, \phi; \tau) = \frac{16}{\pi^2} \sum_k \sum_\ell \frac{1}{k\ell} \sin(k\xi) \sin(\ell\phi) \times \exp\{[-\pi^2(k^2 + R^2\ell^2)]\tau\}; \quad k, \ell = 1, 3, 5, \ldots, N \quad (13)$$

The iterative equation becomes

$$\theta^{i+1}(\xi, \phi; \tau) = \frac{16}{\pi^2} \sum_k \sum_\ell \frac{1}{k\ell} \sin(k\xi) \sin(\ell\phi) \times \exp\{[-\pi^2(k^2 + R^2\ell^2)][1 + \beta\theta^i]\tau\}; \quad (14)$$

The temperature distribution across the semiwidth of a finite rectangular plate with $R = 1/2$ and $\phi = \pi/2$ using iterative procedure. It is interesting to note that only three iterations are required to obtain the desired accuracy of 10^{-4}. Fig. 2 reveals that the present results are in good agreement with finite difference solution of reference [6], thus demonstrating the convergence and accuracy of the present scheme.

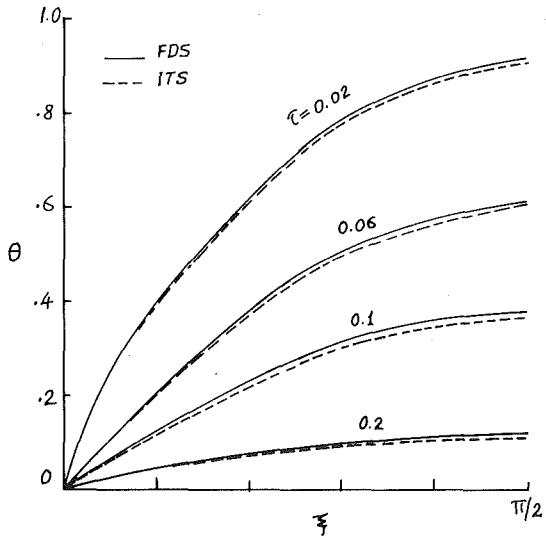

Fig. 2 Temperature distributions across the semiwidth of a finite rectangular plate at midsection $\phi = \pi/2$ for a variable thermal conductivity $\beta = 0.5$ obtained using the iterative method (ITS), compared to temperature distribution obtained through finite difference method (FDS) [3], $R = 1/2$

Concluding Remarks

An iterative procedure is presented to determine the transient temperature distribution in one- and two-dimensional finite regions with variation of thermal conductivity with temperature. Closed-form constant property solution is taken as the initial guess. The results obtained by this method are in good agreement with the numerical solution. The convergence criteria for the iteration process is also indicated. The scheme is convenient and efficient, and appears to be particularly attractive for use with programable calculators which can quickly obtain analytical solutions for a number of problems. It has the advantage that the temperatures can be directly found at any specified time whereas the numerical approach requires the development of the temperature profile right from the initial state.

Acknowledgments

The author is indebted to the referees and to Professor E. M. Sparrow for their valuable help and suggestions during the preparation of the present note.

References

1 Yang, K. T., "Transient Conduction in a Semi-Infinite Solid With Variable Thermal Conductivity," *Journal of Applied Mechanics*, TRANS. ASME, Vol. 89, 1958, pp. 146–147.

2 Goodman, T. R., "Application of Integral Methods to Transient Nonlinear Heat Transfer," *in Advances in Heat Transfer*, Hartnett, J. P. and Irvine, T. F. eds., Vol. 1, Academic Press, New York, 1964.

3 Krajewski, B., "On a Direct Variational Method for Nonlinear Heat Transfer," *International Journal of Heat and Mass Transfer*, Vol. 18, 1975, pp. 495–502.

4 Mastanaiah, K., and Muthunayagam, A. E., "Transient Conduction in a Finite Slab With Variable Thermal Conductivity," *AIAA Journal*, Vol. 13, 1975, pp. 954–956.

5 Aziz, A., and Benziz, J. Y., "Application of Perturbation Techniques to Heat Transfer Problem With Variable Thermal Properties," *International Journal of Heat and Mass Transfer*, Vol. 19, 1976, pp. 271–276.

6 Hays, D. F., and Curd, H. N., "Heat Conduction in Solids Temperature-Dependent Thermal Conductivity," *International Journal of Heat and Mass Transfer*, Vol. 11, 1968, pp. 285–295.

7 Mingle, J. O., "Computational consideration in Nonlinear Diffusion," *International Journal for Numerical Methods in Engineering*, Vol. 7, 1973, pp. 103–116.

8 Özisik, M. N., *Boundary Value Problem of Heat Conduction*, International Text Book Co., 1968.

9 Myers, G. E., *Analytical Methods in Conduction Heat Transfer*, McGraw Hill, New York, 1971.

10 Scarborough, J. B., *Numerical Mathematical Analysis*, Oxford and IBH Publishing Co., Calcutta, Indian Edition 1968, pp. 208–211.

11 Mastanaiah, K., "On the Numerical Solution of Phase Change Problems in Transient Non-Linear Heat Conduction," *International Journal for Numerical Methods in Engineering*, Vol. 10, 1976, pp. 833–844.

12 Von Rosenberg, D. U., *Methods for the Numerical Solution of Partial Differential Equations*, Elsevier Publishing Co., 1969.

Thermal Contact Conductance Correlation for Stacks of Thin Layers in High Vacuums

F. R. Al-Astrabadi,[1] P. W. O'Callaghan,[2] S. D. Probert,[3] and A. M. Jones[4]

[1] Research Officer, School of Mechanical Engineering, Cranfield Institute of Technology, Cranfield, Bedford, United Kingdom.

[2] Lecturer, School of Mechanical Engineering, Cranfield Institute of Technology, Cranfield, Bedford, United Kingdom.

[3] Professor, School of Mechanical Engineering, Cranfield Institute of Technology, Cranfield, Bedford, United Kingdom.

[4] Lecturer, School of Mechanical Engineering, Cranfield Institute of Technology, Cranfield, Bedford, United Kingdom.

Contributed by the Heat Transfer Division of THE AMERICAN SOCIETY OF MECHANICAL ENGINEERS. Manuscript received by the Heat Transfer Division August 4, 1976.

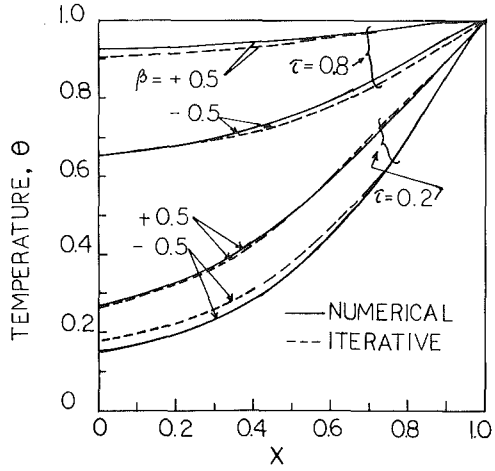

Fig. 1 Comparison of temperature distribution from iterative and numerical solutions for a slab of thickness *a*

The constant property solution [6] is given by

$$\theta(\xi, \phi; \tau) = \frac{16}{\pi^2} \sum_k \sum_\ell \frac{1}{k\ell} \sin(k\xi) \sin(\ell\phi) \times \exp\{[-\pi^2(k^2 + R^2\ell^2)]\tau\}; \quad k, \ell = 1, 3, 5, \ldots, N \quad (13)$$

The iterative equation becomes

$$\theta^{i+1}(\xi, \phi; \tau) = \frac{16}{\pi^2} \sum_k \sum_\ell \frac{1}{k\ell} \sin(k\xi) \sin(\ell\phi) \times \exp\{[-\pi^2(k^2 + R^2\ell^2)][1 + \beta\theta^i]\tau\}; \quad (14)$$

The temperature distribution across the semiwidth of a finite rectangular plate with $R = 1/2$ and $\phi = \pi/2$ using iterative procedure. It is interesting to note that only three iterations are required to obtain the desired accuracy of 10^{-4}. Fig. 2 reveals that the present results are in good agreement with finite difference solution of reference [6], thus demonstrating the convergence and accuracy of the present scheme.

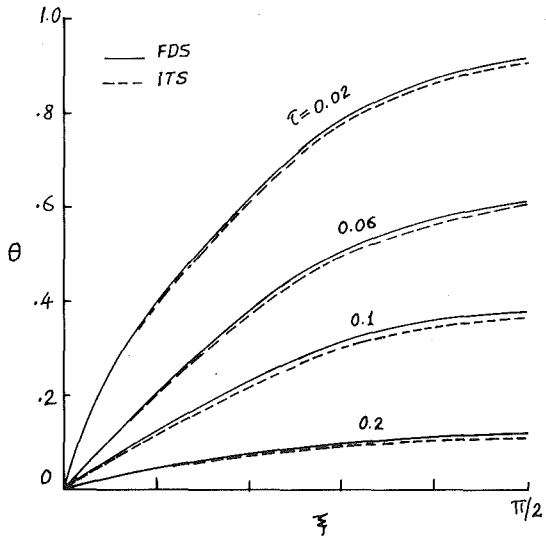

Fig. 2 Temperature distributions across the semiwidth of a finite rectangular plate at midsection $\phi = \pi/2$ for a variable thermal conductivity $\beta = 0.5$ obtained using the iterative method (ITS), compared to temperature distribution obtained through finite difference method (FDS) [3], $R = 1/2$

Concluding Remarks

An iterative procedure is presented to determine the transient temperature distribution in one- and two-dimensional finite regions with variation of thermal conductivity with temperature. Closed-form constant property solution is taken as the initial guess. The results obtained by this method are in good agreement with the numerical solution. The convergence criteria for the iteration process is also indicated. The scheme is convenient and efficient, and appears to be particularly attractive for use with programable calculators which can quickly obtain analytical solutions for a number of problems. It has the advantage that the temperatures can be directly found at any specified time whereas the numerical approach requires the development of the temperature profile right from the initial state.

Acknowledgments

The author is indebted to the referees and to Professor E. M. Sparrow for their valuable help and suggestions during the preparation of the present note.

References

1 Yang, K. T., "Transient Conduction in a Semi-Infinite Solid With Variable Thermal Conductivity," *Journal of Applied Mechanics*, TRANS. ASME, Vol. 89, 1958, pp. 146–147.

2 Goodman, T. R., "Application of Integral Methods to Transient Nonlinear Heat Transfer," *in Advances in Heat Transfer*, Hartnett, J. P. and Irvine, T. F. eds., Vol. 1, Academic Press, New York, 1964.

3 Krajewski, B., "On a Direct Variational Method for Nonlinear Heat Transfer," *International Journal of Heat and Mass Transfer*, Vol. 18, 1975, pp. 495–502.

4 Mastanaiah, K., and Muthunayagam, A. E., "Transient Conduction in a Finite Slab With Variable Thermal Conductivity," *AIAA Journal*, Vol. 13, 1975, pp. 954–956.

5 Aziz, A., and Benziz, J. Y., "Application of Perturbation Techniques to Heat Transfer Problem With Variable Thermal Properties," *International Journal of Heat and Mass Transfer*, Vol. 19, 1976, pp. 271–276.

6 Hays, D. F., and Curd, H. N., "Heat Conduction in Solids Temperature-Dependent Thermal Conductivity," *International Journal of Heat and Mass Transfer*, Vol. 11, 1968, pp. 285–295.

7 Mingle, J. O., "Computational consideration in Nonlinear Diffusion," *International Journal for Numerical Methods in Engineering*, Vol. 7, 1973, pp. 103–116.

8 Özisik, M. N., *Boundary Value Problem of Heat Conduction*, International Text Book Co., 1968.

9 Myers, G. E., *Analytical Methods in Conduction Heat Transfer*, McGraw Hill, New York, 1971.

10 Scarborough, J. B., *Numerical Mathematical Analysis*, Oxford and IBH Publishing Co., Calcutta, Indian Edition 1968, pp. 208–211.

11 Mastanaiah, K., "On the Numerical Solution of Phase Change Problems in Transient Non-Linear Heat Conduction," *International Journal for Numerical Methods in Engineering*, Vol. 10, 1976, pp. 833–844.

12 Von Rosenberg, D. U., *Methods for the Numerical Solution of Partial Differential Equations*, Elsevier Publishing Co., 1969.

Thermal Contact Conductance Correlation for Stacks of Thin Layers in High Vacuums

F. R. Al-Astrabadi,[1] P. W. O'Callaghan,[2] S. D. Probert,[3] and A. M. Jones[4]

[1] Research Officer, School of Mechanical Engineering, Cranfield Institute of Technology, Cranfield, Bedford, United Kingdom.

[2] Lecturer, School of Mechanical Engineering, Cranfield Institute of Technology, Cranfield, Bedford, United Kingdom.

[3] Professor, School of Mechanical Engineering, Cranfield Institute of Technology, Cranfield, Bedford, United Kingdom.

[4] Lecturer, School of Mechanical Engineering, Cranfield Institute of Technology, Cranfield, Bedford, United Kingdom.

Contributed by the Heat Transfer Division of THE AMERICAN SOCIETY OF MECHANICAL ENGINEERS. Manuscript received by the Heat Transfer Division August 4, 1976.

Nomenclature

A = nominal contact area between successive layers in a stack, m^2
C = thermal conductance of interface per unit nominal area of contact, $W\ m^{-2}\ K^{-1}$
C^* = dimensionless conductance of interface per unit area
$f(\ )$ = function of parameters stated within the bracket
I = number of layer-to-layer interfaces in a stack
k = bulk material thermal conductivity, $W\ m^{-1}\ K^{-1}$
M = hardness of the surface of a layer, $N\ m^{-2}$
n = exponent of the load
N = total number of contact planes in a stack including those between the flux meters ($= I + 2$)
P = applied loading, $N\ m^{-2}$
P^* = dimensionless loading pressure applied to stacks
$\dot{Q}$ = thermal current flowing through a stack, W
R = thermal resistance per contact of unit nominal area ($\equiv 1/C$), $m^2\ K\ W^{-1}$
t = individual layer thickness, m
T = temperature, K
Δ = difference between
ϵ = porosity of either a metal powder or metal fibre assembly ($0 \leq \epsilon \leq 1$)

Subscripts

B = for the bulk material
LL = for the layer-to-layer assembly
ML = for the flux meter-to-layer assembly
s = of the solid
TOT = total for the stack
TOT, N = for a stack of $(N - 1)$ layers

Introduction

Stacks of thin metallic layers are sometimes used as thermal insulators because each interface has a very low ratio of real-to-apparent area of contact [1, 2].[5] Such stacks may also possess relatively high compressive strengths [3]. The overall insulation achieved depends on the deformation behavior of the bulk material, the hardnesses and surface topographies of the contacting surfaces, the oxide layers present, and upon the number of interfaces employed in series [4]. The solid-solid contact conductance (i.e., in the absence of an interfacial fluid) per contact also depends upon the individual layer thicknesses chosen [2, 4, 5]. The thermal resistance of a stack of thin layers may be as much as two orders of magnitude greater than that of a solid specimen of the parent material having similar overall dimensions [6]. However, because the resistance across each contact is often high, large tranverse heat losses can occur from stacks and so appreciably reduce the accuracy of the presented conclusions.

Theoretical predictions for stacks of thin layers are much more complex than those associated with single contacts between semi-infinite bodies due to our ignorance concerning the heat flow paths across individual layers. Stack deformation behavior depends upon the initial buckle and the individual layer thickness [3, 7]. Thus macroscopic measurements for stacks of thin layers can give only qualitative indications of individual surface-to-surface contact resistance behavior.

This investigation was initiated to provide designers with a dimensionless correlation for use in predicting overall thermal contact conductances of stacks of thin solid layers in high vacuums.

Experimental Procedure

A longitudinal heat flow system is normally used to measure the thermal conductance of contacts [4, 8–13]: the design criteria for this system are described in detail elsewhere [13]. The experimental module consists of a heater, two identical stainless-steel flux meters with the stack under test mounted between them, and a water-cooled heat sink in vertical sequence. The determination of the total conductance between the heat-flux meters involves estimating the mean steady-state temperature drop between the neighboring end faces of the two flux meters ΔT_{TOT} as well as the corresponding heat flux, $\dot{Q}/A$. For this system

$$C_{TOT} = \frac{\dot{Q}}{A\ \Delta T_{TOT}} \tag{1}$$

A stack containing $(N - 1)$ layers held between the faces of the flux meters has a total of N contact planes, including the two extreme contacts with the flux meters and I ($= N - 2$) layer-to-layer interfaces. Thus, the total resistance is given by:

$$R_{TOT,N} = 2R_{ML} + (N - 1)R_B + (N - 2)(R_{LL})_{N-2} \tag{2}$$

For a single layer, $N = 2$ and so

$$R_{TOT,2} = 2R_{ML} + R_B \tag{3}$$

Thus,

$$(R_{LL})_{N-2} = \frac{(R_{TOT,N} - R_{TOT,2})}{N - 2} - R_B \tag{4}$$

So the conductance of an interface per unit area for a stack can be deduced from measured overall resistances and the bulk resistances of thin layers. The latter are very unlikely ever to exceed 10 percent of the appropriate total stack resistance, and will in most cases be of the order of 1 percent or less [2, 4, 5]. The specimen assemblies considered were of such large lateral dimensions and the mechanical loadings high enough that even fifteen layer systems experienced lateral heat losses of less than 5 percent of the axial heat current (as estimated from the difference between the two flux-meter indications).

Total thermal conductances were obtained for several stacks [8–10], under various loadings (ranging from 10^4 to $6.5 \times 10^6\ Nm^{-2}$), and in high vacuums ($\sim 10^{-5}$ torr) in order to inhibit lateral heat losses.

Dimensional Analysis

From an analysis of the available experimental data (see Table 1), it was decided that the thermal contact conductance of stacks of thin layers depends principally upon P, M, t, and k_s, i.e.,

$$C_{LL} = f(P, M, t, k_s) \tag{5}$$

Using Buckingham's Pi-theorem, equation (5) yielded two-dimensionless numbers, namely

$$C^* = C_{LL}t/k_s \quad \text{and} \quad P^* = \frac{P}{M}$$

Thus, $(C_{LL}t)$ can be considered as the effective thermal conductivity of a stack which is a significant parameter to facilitate comparisons between the behaviors of different multilayer stacks as mechanically strong insulators [4, 14].

Ideally, at relatively low loads, the hardness M in the analysis should be replaced by the effective elastic modulus of the stack (i.e., the load divided by the product of the nominal area A and the compressive stress). Unfortunately this parameter was not specified in the literature for many of the stacks considered.

Conductance Correlation

A least-squares straight-line fit was made for the entire population of published data including that recently obtained by the authors (see Fig. 1): the following relationship emerged

$$C^* = 3.025\ (P^*)^{0.58} \tag{6}$$

with a correlation coefficient of 0.96. The success of the correlation can be judged by the relatively narrow scatter band, so demonstrating the validity of the dimensionless groups chosen for the analysis. Fried [21] reviewed critically the correlation and prediction techniques for thermal contact conductance of single contacts and observed that $0.66 \leq n \leq 1$ for different data sets—depending upon the choice of influential parameters. Some of these correlations showed significant scatter [18, 19] which was attributed to ignoring a vital variable.

[5] Numbers in brackets designate References at end of technical note.

Table I Details of stacks for which experimental data are included in Fig. 1

Material	Layer Thickness t (mm)	Roughness (μm)	Hardness M (GNm^{-2})	Conductivity of material of a layer k_s ($Wm^{-1}K^{-1}$)	Number of Layers in the Stack Considered	Symbol in fig. 1.	Source of information (Reference Number)
Tool steel	0.672	0.65	4.96	10.00	52	●	4
Stainless steel	0.056	0.37	3.20	15.00	601	+	
Carp	0.178	0.43	0.42	0.35	104	○	
Razorblade steel	0.108	0.062	8.20	23.0	304	△	
Brass	0.280	1.18	2.03	96.0	110	×	
Stainless steel (304)	0.02	-	1.60	15.95	107	△	2
Stainless steel (302)	0.10	-	1.70	13.0	209	▽	
Tufnol-plated steel	0.10	-	0.43	0.35	110	▽	
Sindany.	3.50	9.107	0.21	0.70	2	□	8
Melinex	0.175	0.427	0.20	0.18	2	◆	
P.T.F.E.	2.40	2.046	0.02	0.25	2	▲	
Perspex	1.50	0.2	0.22	0.30	2	▼	
Mica	0.025	<0.001	0.30	0.52	2	◇	
Grain-orientated electrical steel lamination	0.28	0.56	1.34	25.0	6	■	10
Non-orientated electrical lamination	0.35	0.331	1.84	30.0	6	◇	
Tin-c. ted steel	0.292	1.19	0.85	45.0	6	⊙	9
Mica (bonded)	0.076	-	0.30	0.365	2	⬢	14
Laminated board (T - 30LR)	1.522	-	0.5	0.640	3	⬡	

Equation (6) for stacks is similar in general terms to previous correlations for single contacts [15–20], i.e., conductance is proportional to (load)^n but differs in the particular values obtained for the constant of proportionality and for the exponent, n. However a strict comparison between data for single contacts and data for multilayer stacks cannot be made because of the differing deformation behaviors for stacks: predominantly layer flattening occurs at low loads [3] whereas at high loads the mechanism is almost entirely asperity deformation [7]. The extents of these regions, depend upon the load applied, material properties, and upon the loading history of the contact.

Miller and Fletcher [20] developed a dimensionless equation, which correlated data for a variety of metal powders or assemblies of metal fibres within a standard deviation of 16 percent. The dimensionless expression used, formulated in terms of the physical properties of the porous assemblies, is of the form

$$\frac{Ct}{k} = 2.335\left[\frac{P}{M}(1-\epsilon)\right]^{0.72} \tag{7}$$

This correlation was extended to permit the prediction of the conductance of single layer, metallic shims and foils by setting the po-

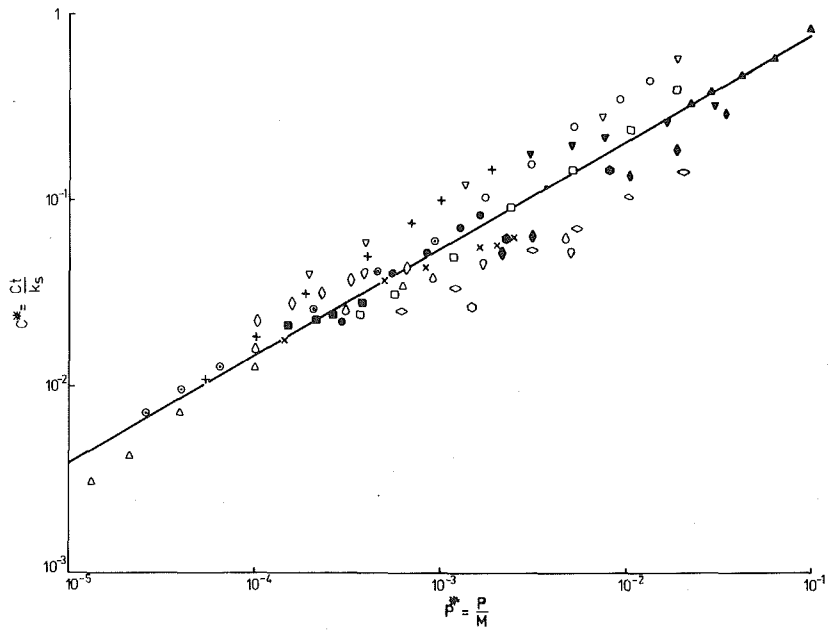

Fig. 1 Variation of the dimensionless conductance of an interface with applied loading for various stacks of thin layers in high vacuum.

rosity term equal to zero. The expression was somewhat analogous to the expression developed in the present investigation, but the correlation resulted in the prediction being up to 40 percent different from the experimental data.

The present dimensionless correlation permits the prediction of thermal contact conductance for stacks of thin layers in high vacuums for a range of dimensionless loading of $10^{-5} \leqslant P/M \leqslant 10^{-1}$.

References

1 Probert, S. D., Thomas, T. R., and Warman, D., "A Mechanically Strong Thermal Insulator for Cryo-Systems," *Thermal Insulation*, Probert, S. D. and Hub, D. R., eds. Elsevier, Amsterdam, 1968, pp. 29–37.

2 Mikesell, R. P., and Scott, R. B., "Heat Conduction Through Insulating Supports in Very Low Temperature Equipment," *J. Res. Natn. Bur. Stand.*, No. 6, 1956–1957, pp. 371–378.

3 Probert, S. D., and Jones, M. C., "Compressive Behaviour of Thin Layered Thermally Insulating Structural Supports," *J. Strain Analysis*, Vol. 1, 1966, pp. 283–289.

4 Thomas, T. R., and Probert, S. D., "Thermal Resistance of Some Multilayer Contacts," *International Journal of Heat and Mass Transfer*, Vol. 9, 1966, pp. 739–754.

5 Berman, R., "Some Experiments on Thermal Contact at Low Temperatures," *Journal Appl. Phys.*, Vol. 27, 1956, pp. 318–323.

6 Minges, M. L., "Thermal Contact Resistance, I,—A Review of the Literature," Paper presented at 1964 Thermal Conductivity Conference, London, 1964.

7 Howells, R. I. L., Probert, S. D., and Jenkins, J. H., "Deformation of Stacks of Thin Layers Under Normal Compressive Loads," *Journal of Strain Analysis*, Vol. 4, No. 2, 1969, pp. 115–120.

8 Al-Astrabadi, F. R., O'Callaghan, P. W., Jones, A. M., and Probert, S. D., "Thermal Resistance Resulting From Commonly-Used Inserts Between Stainless-Steel, Static, Bearing Surfaces," *WEAR*, Vol. 40, No. 3, 1976, pp. 339–350.

9 Al-Astrabadi, F. R., "Thermal Resistance of Pressed Contacts," PhD thesis, Cranfield Institute of Technology, U.K., 1977.

10 O'Callaghan, P. W., Jones, A. M., and Probert, S. D., "Thermal Resistance of Stacks of Transformer Laminations," To be published in *Applied Energy*.

11 Jones, A. M., O'Callaghan, P. W., and Probert, S. D., "Effects of Interfacial Distortions on Thermal Resistance of the Contact Between Cylinders," *Heat Transfer With Thermal Control Applications, Proceedings Astronautics & Aeronautics*, Vol. 39, Yovanovich, M. M., ed. MIT Press, Cambridge, Mass., 1975, pp. 21–44.

12 O'Callaghan, P. W., and Probert, S. D., "Thermal Resistance and Directional Index of Pressed Contacts Between Smooth Non-Wavy Surfaces," *J. Mech. Eng. Science*, Vol. 16, 1974, pp. 41–55.

13 Jones, A. M., "Thermal Contact Resistance," PhD thesis, University of Wales, 1975.

14 Gyorog, D. A., "Investigation of Thermal Insulation Materials for Contacting Surfaces," *Heat Transfer and Spacecraft Thermal Control, Proceedings Astronautics & Aeronautics*, Vol. 24, Lucas, J. W., ed., MIT Press, Cambridge, Mass., 1970, pp. 310–336.

15 Tien, C. L., "A Correlation for Thermal Contact Conductance of Nominally-Flat Surfaces in a Vacuum," *Proceedings 7th Thermal Conductivity Conference*, U.S. Bureau of Standards, 1968, pp. 755–759.

16 Cooper, M. G., Mikic, B. B., and Yovanovich, M. M., "Thermal Contact Conductance," *International Journal of Heat Mass Transfer*, Vol. 12, 1969, pp. 279–300.

17 Thomas, T. R., and Probert, S. D., "Thermal Contact Resistance: The Directional Effect and Other Problems," *International Journal of Heat Mass Transfer*, Vol. 13, 1970, pp. 789–807.

18 Hsieh, C. K., and Touloukian, Y. S., "Correlation and Prediction of Thermal Contact Conductance for Nominally-Flat Surfaces," *Thermal Conductivity*, Plenum Press, New York, 1969.

19 Thomas, T. R., and Probert, S. D., "Correlations for Thermal Contact Conductance in Vacuo," JOURNAL OF HEAT TRANSFER, TRANS. ASME, Series C, Vol. 94, 1972, pp. 276–280.

20 Miller, R. G., and Fletcher, L. S., "Thermal Contact Conductance Correlation for Porous Metals," *Heat Transfer With Thermal Control Applications, Progress, Astronautics & Aeronautics*, Vol. 39, Yovanovich, M. M., ed., MIT Press, Cambridge, Mass., 1975, pp. 81–92.

21 Fried, E., Discussion on "Correlations for Thermal Contact Conductance in Vacuo," JOURNAL OF HEAT TRANSFER, Vol. 94, No. 3, 1972, p. 281.

Heat Transfer in the Entrance Region of a Straight Channel: Laminar Flow With Uniform Wall Heat Flux

M. S. Bhatti[1] and C. W. Savery[2]

Nomenclature

a = half channel width
c_p = specific heat
h = local heat transfer coefficient
k = thermal conductivity
Nu = ha/k, Nusselt number
p = local pressure within the channel
p_0 = pressure at channel inlet
$P = (p_0 - p)/(\frac{1}{2}\rho u^2{}_0)$, local axial pressure drop
Pr = $\mu c_p/k$, Prandtl number
$\dot{q}''_w$ = wall heat flux
T = local fluid temperature
T_0 = fluid temperature at channel inlet
T_b = bulk fluid temperature
T_w = channel wall temperature
$\tilde{u}$ = axial velocity in the core or in the boundary layer
u = axial boundary layer velocity
u_0 = uniform axial velocity at the channel inlet
u_∞ = axial core velocity
$U = u_\infty/u_0$, axial core velocity
x = axial coordinate
$X = \nu x/u_0 a^2$, axial coordinate
y = transverse coordinate
δ = hydrodynamic boundary layer thickness
δ_t = thermal boundary layer thickness
$\zeta = \delta_t/\delta$, boundary layer shape factor
μ = dynamic viscosity
$\nu = \mu/\rho$, kinematic viscosity
ρ = fluid density

Introduction

The problem of simultaneous development of velocity and temperature fields in a straight channel with uniform wall heat flux has been attacked by various investigators. Hwang and Fan [1][3] numerically integrated the energy equation using point velocities presented by Bodoia and Osterle. Han [2] used a velocity profile which he developed using Langhaar's linearizing approximations. Siegel and Sparrow [3] employed the Karman-Pohlhausen method to solve for the temperature field. They used an approximate momentum transfer analysis based on the application of Bernoulli's equation to the fluid core. Naito [4] employed the Karman-Pohlhausen method to solve for the velocity as well as the temperature field using fourth order polynomials. In the present work, a new analytical solution to the flow development problem is used. It is based on the application of mac-

[1] Senior Engineer, Owens-Corning Fiberglas Corp., Granville, Ohio. Mem. ASME.

[2] Assoc. Professor, Drexel University, Philadelphia, Pa. Mem. ASME.

Contributed by the Heat Transfer Division of THE AMERICAN SOCIETY OF MECHANICAL ENGINEERS. Manuscript received by the Heat Transfer Division August 19, 1976.

[3] Numbers in brackets designate References at end of technical note.

rosity term equal to zero. The expression was somewhat analogous to the expression developed in the present investigation, but the correlation resulted in the prediction being up to 40 percent different from the experimental data.

The present dimensionless correlation permits the prediction of thermal contact conductance for stacks of thin layers in high vacuums for a range of dimensionless loading of $10^{-5} \leqslant P/M \leqslant 10^{-1}$.

References

1 Probert, S. D., Thomas, T. R., and Warman, D., "A Mechanically Strong Thermal Insulator for Cryo-Systems," *Thermal Insulation*, Probert, S. D. and Hub, D. R., eds. Elsevier, Amsterdam, 1968, pp. 29–37.

2 Mikesell, R. P., and Scott, R. B., "Heat Conduction Through Insulating Supports in Very Low Temperature Equipment," *J. Res. Natn. Bur. Stand.*, No. 6, 1956–1957, pp. 371–378.

3 Probert, S. D., and Jones, M. C., "Compressive Behaviour of Thin Layered Thermally Insulating Structural Supports," *J. Strain Analysis*, Vol. 1, 1966, pp. 283–289.

4 Thomas, T. R., and Probert, S. D., "Thermal Resistance of Some Multilayer Contacts," *International Journal of Heat and Mass Transfer*, Vol. 9, 1966, pp. 739–754.

5 Berman, R., "Some Experiments on Thermal Contact at Low Temperatures," *Journal Appl. Phys.*, Vol. 27, 1956, pp. 318–323.

6 Minges, M. L., "Thermal Contact Resistance, I,—A Review of the Literature," Paper presented at 1964 Thermal Conductivity Conference, London, 1964.

7 Howells, R. I. L., Probert, S. D., and Jenkins, J. H., "Deformation of Stacks of Thin Layers Under Normal Compressive Loads," *Journal of Strain Analysis*, Vol. 4, No. 2, 1969, pp. 115–120.

8 Al-Astrabadi, F. R., O'Callaghan, P. W., Jones, A. M., and Probert, S. D., "Thermal Resistance Resulting From Commonly-Used Inserts Between Stainless-Steel, Static, Bearing Surfaces," *WEAR*, Vol. 40, No. 3, 1976, pp. 339–350.

9 Al-Astrabadi, F. R., "Thermal Resistance of Pressed Contacts," PhD thesis, Cranfield Institute of Technology, U.K., 1977.

10 O'Callaghan, P. W., Jones, A. M., and Probert, S. D., "Thermal Resistance of Stacks of Transformer Laminations," To be published in *Applied Energy*.

11 Jones, A. M., O'Callaghan, P. W., and Probert, S. D., "Effects of Interfacial Distortions on Thermal Resistance of the Contact Between Cylinders," *Heat Transfer With Thermal Control Applications, Proceedings Astronautics & Aeronautics*, Vol. 39, Yovanovich, M. M., ed. MIT Press, Cambridge, Mass., 1975, pp. 21–44.

12 O'Callaghan, P. W., and Probert, S. D., "Thermal Resistance and Directional Index of Pressed Contacts Between Smooth Non-Wavy Surfaces," *J. Mech. Eng. Science*, Vol. 16, 1974, pp. 41–55.

13 Jones, A. M., "Thermal Contact Resistance," PhD thesis, University of Wales, 1975.

14 Gyorog, D. A., "Investigation of Thermal Insulation Materials for Contacting Surfaces," *Heat Transfer and Spacecraft Thermal Control, Proceedings Astronautics & Aeronautics*, Vol. 24, Lucas, J. W., ed., MIT Press, Cambridge, Mass., 1970, pp. 310–336.

15 Tien, C. L., "A Correlation for Thermal Contact Conductance of Nominally-Flat Surfaces in a Vacuum," *Proceedings 7th Thermal Conductivity Conference*, U.S. Bureau of Standards, 1968, pp. 755–759.

16 Cooper, M. G., Mikic, B. B., and Yovanovich, M. M., "Thermal Contact Conductance," *International Journal of Heat Mass Transfer*, Vol. 12, 1969, pp. 279–300.

17 Thomas, T. R., and Probert, S. D., "Thermal Contact Resistance: The Directional Effect and Other Problems," *International Journal of Heat Mass Transfer*, Vol. 13, 1970, pp. 789–807.

18 Hsieh, C. K., and Touloukian, Y. S., "Correlation and Prediction of Thermal Contact Conductance for Nominally-Flat Surfaces," *Thermal Conductivity*, Plenum Press, New York, 1969.

19 Thomas, T. R., and Probert, S. D., "Correlations for Thermal Contact Conductance in Vacuo," JOURNAL OF HEAT TRANSFER, TRANS. ASME, Series C, Vol. 94, 1972, pp. 276–280.

20 Miller, R. G., and Fletcher, L. S., "Thermal Contact Conductance Correlation for Porous Metals," *Heat Transfer With Thermal Control Applications, Progress, Astronautics & Aeronautics*, Vol. 39, Yovanovich, M. M., ed., MIT Press, Cambridge, Mass., 1975, pp. 81–92.

21 Fried, E., Discussion on "Correlations for Thermal Contact Conductance in Vacuo," JOURNAL OF HEAT TRANSFER, Vol. 94, No. 3, 1972, p. 281.

Heat Transfer in the Entrance Region of a Straight Channel: Laminar Flow With Uniform Wall Heat Flux

M. S. Bhatti[1] and C. W. Savery[2]

Nomenclature

a = half channel width
c_p = specific heat
h = local heat transfer coefficient
k = thermal conductivity
Nu = ha/k, Nusselt number
p = local pressure within the channel
p_0 = pressure at channel inlet
$P = (p_0 - p)/(\frac{1}{2}\rho u^2{}_0)$, local axial pressure drop
Pr = $\mu c_p/k$, Prandtl number
$\dot{q}''_w$ = wall heat flux
T = local fluid temperature
T_0 = fluid temperature at channel inlet
T_b = bulk fluid temperature
T_w = channel wall temperature
$\tilde{u}$ = axial velocity in the core or in the boundary layer
u = axial boundary layer velocity
u_0 = uniform axial velocity at the channel inlet
u_∞ = axial core velocity
$U = u_\infty/u_0$, axial core velocity
x = axial coordinate
$X = \nu x/u_0 a^2$, axial coordinate
y = transverse coordinate
δ = hydrodynamic boundary layer thickness
δ_t = thermal boundary layer thickness
$\zeta = \delta_t/\delta$, boundary layer shape factor
μ = dynamic viscosity
$\nu = \mu/\rho$, kinematic viscosity
ρ = fluid density

Introduction

The problem of simultaneous development of velocity and temperature fields in a straight channel with uniform wall heat flux has been attacked by various investigators. Hwang and Fan [1][3] numerically integrated the energy equation using point velocities presented by Bodoia and Osterle. Han [2] used a velocity profile which he developed using Langhaar's linearizing approximations. Siegel and Sparrow [3] employed the Karman-Pohlhausen method to solve for the temperature field. They used an approximate momentum transfer analysis based on the application of Bernoulli's equation to the fluid core. Naito [4] employed the Karman-Pohlhausen method to solve for the velocity as well as the temperature field using fourth order polynomials. In the present work, a new analytical solution to the flow development problem is used. It is based on the application of mac-

[1] Senior Engineer, Owens-Corning Fiberglas Corp., Granville, Ohio. Mem. ASME.

[2] Assoc. Professor, Drexel University, Philadelphia, Pa. Mem. ASME.

Contributed by the Heat Transfer Division of THE AMERICAN SOCIETY OF MECHANICAL ENGINEERS. Manuscript received by the Heat Transfer Division August 19, 1976.

[3] Numbers in brackets designate References at end of technical note.

roscopic mechanical energy equation in the entrance region. The temperature field is determined utilizing the Karman-Pohlhausen method.

Analysis

The flow is idealized as having two regions: a viscous boundary layer and an essentially inviscid core. The usual boundary layer theory simplifications are applied. The origin of the coordinate system is at the leading edge of one of the plates forming the channel with y measured toward the axis of symmetry.

From a generalization of the fully developed velocity profile, the following velocity distribution, in terms of variable pressure gradient and local boundary layer thickness, is assumed for the hydrodynamic entrance region.

$$u = -\frac{1}{2\mu}\frac{dp}{dx}(2y\delta - y^2) \tag{1}$$

Introducing equation (1) into the macroscopic mass balance equation, there results a cubic equation in (δ/a) whose physically admissible root is

$$\left(\frac{\delta}{a}\right) = \frac{3(U-1)}{U} \tag{2}$$

Substituting equation (2) back into the cubic equation, the pressure gradient is found to be

$$\frac{dp}{dx} = -\frac{2}{9}\left(\frac{\mu u_0}{a^2}\right)\frac{U^3}{(U-1)^2} \tag{3}$$

Alternatively equation (3) can be obtained from equation (1) by noting that at $y = \delta$, $u = u_\infty$. The rest of the momentum transfer quantities are also expressible in terms of U. Finally the variation of U with X is determined from the macroscopic mechanical energy equation which yields

$$\frac{dU}{dX} = \frac{70U^2(3-2U)}{(U-1)^2(513-297U)} \tag{4}$$

whence

$$X = \frac{594U^2 + 90U - 684 - 15U\ln(3-2U) - 1308U\ln U}{280U} \tag{5}$$

Equations (4) and (5) show that the flow becomes fully developed, i.e., U attains its ultimate constant value of 3/2, asymptotically at $X = \infty$. Introducing equation (4) into equation (3) and integrating, we obtain

$$P = \frac{3}{140}[22U^2 - 10U - 12 - 15\ln(3-2U)] \tag{6}$$

The point pressures computed from equation (6) are in excellent accord with the extensive pressure drop measurements by Beavers, et al. [5].

Campbell and Slattery [6] employed a similar approach to solve the problem of flow development in a circular tube. They assumed a velocity profile in terms of δ and then utilizing the macroscopic mass balance, momentum balance and mechanical energy equations determined δ, p and u_∞ in terms of x. The simultaneous application of the mechanical energy equation and the momentum equation involves a redundancy since the former is derivable from the latter. For this reason the present approach entailing the use of the mechanical energy equation alone is more appealing.

Now that the momentum transfer analysis is complete, we direct our attention to the heat transfer analysis. For this purpose, we shall utilize the integrated form of the energy equation

$$\rho c_p \frac{d}{dx}\int_0^{\delta_t}(T - T_0)\,\tilde{u}dy = \dot{q}_w'' \tag{7}$$

where the wall heat flux $\dot{q}_w''$ is uniform.

The temperature distribution required in the solution of equation (7) is taken to be

$$(T - T_0) = \frac{5}{8}\left(\frac{\dot{q}_w''\delta_t}{k}\right)\left[1 - \frac{8}{5}\left(\frac{y}{\delta_t}\right) + \frac{4}{5}\left(\frac{y}{\delta_t}\right)^3 - \frac{1}{5}\left(\frac{y}{\delta_t}\right)^4\right] \tag{8}$$

which is a generalization of the fully developed temperature profile. The velocity distribution required in the solution of equation (7) is already determined. In the interval $0 \le y \le \delta$, $\tilde{u} = u(x, y)$ and the interval $\delta \le y \le a, \tilde{u} = u_\infty(x)$.

Bearing in mind that for fluids with $\mathrm{Pr} \ge 1$, $\delta_t \le \delta$ and for fluids with $\mathrm{Pr} < 1$, $\delta_t > \delta$, we introduce equation (8) together with equations (1) and (4) into equation (7), carry out the indicated operations and eventually obtain

$$10\zeta^4 - 49\zeta^3 + \frac{140UX}{3\mathrm{Pr}(U-1)^2} = 0 \quad (\mathrm{Pr} \ge 1) \tag{9}$$

$$189\zeta^5 - 175\zeta^4 + \left[70 - \frac{280UX}{3\mathrm{Pr}(U-1)^2}\right]\zeta^3 - 7\zeta + 1 = 0 \quad (\mathrm{Pr} < 1) \tag{10}$$

This pair of algebraic equations in conjunction with equations (2) and (5) allows the determination of the local thermal boundary layer thickness and thence the local temperature via equation (8).

The heat transfer results will be presented in terms of the local Nusselt number defined as $\mathrm{Nu} = ha/k$, where the heat transfer coefficient is defined by $\dot{q}_w'' = h(T_w - T_b)$. The local wall temperature can be obtained from equation (8) by setting $y = 0$. The local bulk temperature can be evaluated by equating the enthalpy increase of the fluid to the total heat transfer rate at the wall. Thus

$$\frac{1}{\mathrm{Nu}} = \left[\frac{5}{8}\left(\frac{\delta_t}{a}\right) - \frac{X}{\mathrm{Pr}}\right] \tag{11}$$

Results and Discussion

The local Nusselt numbers were calculated for nine Prandtl number fluids employing equations (9) and (10) together with equation (11). They are shown in Fig. 1. An asymptotic value of 35/17 is reached when the flow becomes thermally and hydrodynamically developed. The previous investigators reported the local Nusselt numbers for the Prandtl number range 0.01–1000. In this analysis the Prandtl number range 0.01–10,000 is treated.

Fig. 2 gives a comparison of the analytical predictions for the local Nusselt number by various investigators. To avoid crowding of the figure, the continuous curves of the present analysis only are shown. The point Nusselt numbers of Hwang and Fan [1] are the ones quoted by them in their paper. Being impossible to read the numbers accurately from the published figures, the point Nusselt numbers attributed to Siegel and Sparrow [3] and to Naito [4] were calculated using the algebraic equations furnished in their papers.

In the neighborhood of the origin, Naito's predictions [4] show a maximum deviation of 15 percent from the present analysis. The predictions of references [1, 3], on the other hand, show a maximum deviation of 10 percent. For the most part, the results of the four analyses agree within 5 percent. As X tends to ∞, the predictions of the present analysis and those of Hwang and Fan [1] continue to display close agreement. However, the predictions of Naito [4] and to a lesser extent those of Siegel and Sparrow [3] deviate from the present analysis. The reason for this can be traced to the fact that in the present analysis as well as in the numerical analysis of Hwang and Fan [1], the flow becomes developed asymptotically at $X = \infty$. In the analyses of Siegel and Sparrow [3] and Naito [4], on the contrary, the flow becomes developed abruptly at a finite distance from the channel inlet.

Conclusion

Notwithstanding quite different momentum transfer analyses, with varying degrees of approximations, employed by them, the local Nusselt number predictions of the various investigators are in unexpectedly close agreement with one another. Therefore, it appears that in the entrance region of a straight channel, heat transfer rates are rather insensitive to momentum diffusion rates.

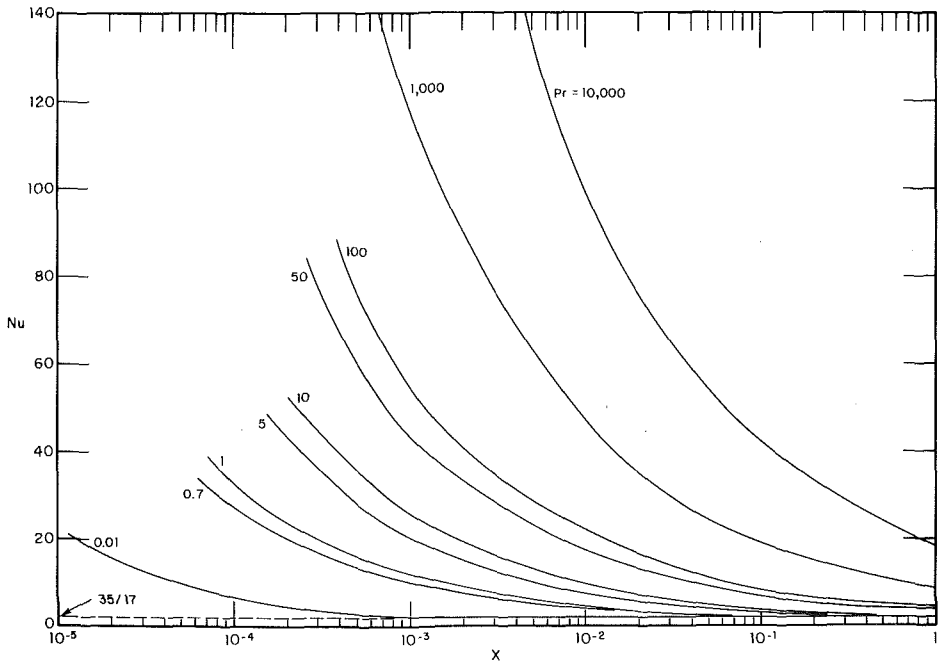

Fig. 1 Local Nusselt numbers in the entrance region of a straight channel

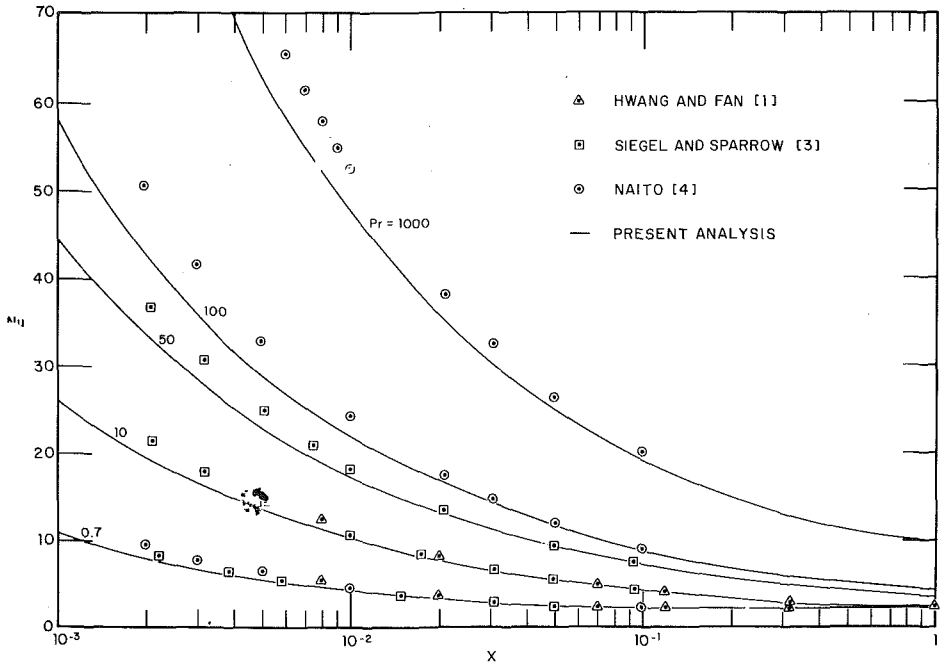

Fig. 2 Comparison of the local Nusselt number predictions by the various investigators

Acknowledgment

This work was sponsored by the National Science Foundation, Division of Engineering, under Grant No. ENG 73-08 125 A01.

References

1 Hwang, C. L., and Fan, L. T., "Finite Difference Analysis of Forced-Convection Heat Transfer in Entrance Region of a Flat Rectangular Duct," *Appl. Sci. Res.*, A13, 1964, pp. 401–422.

2 Han, L. S., "Simultaneous Development of Temperature and Velocity Profiles in Flat Ducts," *Proceedings 1961 International Heat Transfer Conference*, Boulder, Col., 1961, pp. 591–597.

3 Siegel, R., and Sparrow, E. M., "Simultaneous Development of Velocity and Temperature Distributions in a Flat Duct With Uniform Wall Heating," *AIChE Journal*, Vol. 5, No. 1, 1959, pp. 73–75.

4 Naito, E., "Laminar Heat Transfer in the Entrance Region Between Parallel Plates—The Case of Uniform Heat Flux, Heat Transfer," *Japanese Research*, Vol. 4, No. 2, 1975, pp. 63–74.

5 Beavers, G. S., Sparrow, E. M., and Magnuson, R. A., "Experiments on Hydrodynamically Developing Flow in Rectangular Ducts of Arbitrary Aspect Ratio," *International Journal of Heat and Mass Transfer*, Vol. 13, 1970, pp. 689–702.

6 Campbell, W. D., and Slattery, J. C., "Flow in the Entrance of a Tube," *Journal of Basic Engineering*, TRANS. ASME, Series D, Vol. 85, Mar. 1963, pp. 41–46.

Heat Transfer to Flowing Gas-Solid Mixtures

M. K. Wahi[1]

Nomenclature

C_a = heat capacity of air
C_s = heat capacity of solids
D = test section inside diameter
h = local heat transfer coefficient
Nu = Nusselt number (hD/k)
$Nu_{101.4}$ = Asymptotic Nusselt number (at x/D = 101.4)
q = local heat Flux
Re = air Reynolds number
T_{mm} = mixed mean temperature
T_0 = temperature at inlet of test section
T_w = tube-wall temperature
W_a = air flow rate
W_s = solids flow rate
x = axial distance

Introduction

The behavior of flowing fluids with suspended solid particles has been studied for many years. Depew [1][2] studied the flow up the vertical, configuration (A), in quite detail. His experimental results were confirmed by Rajpaul [2], using an almost identical apparatus. The cited publications and the previous related work were summarized excellently by Soo [3]. Using the same apparatus as Rajpaul [2] this author investigated the effect of test section orientation, namely flow down the vertical (B) and horizontal (C), and compared the results of the three configurations [4]. More recently, a detailed technical review of the subject was published [5] without discussing reference [4] work. This note very briefly reviews that work.

Experimental Apparatus and Techniques

Flow System. The experimental apparatus used in this investigation is shown schematically in Fig. 1.

The 80-in. long test section consisted of type 304 stainless-steel seamless tubing, 18 mm ID by 0.508 ± 0.075-mm wall thickness. The electrically heated test section was instrumented with 18 pairs of spot-welded Iron-Constantan 30 gauge thermocouples. The range of variables involved was two constant air-Reynolds numbers, 15,000 and 30,000; three sizes of spherical glass particles, 30, 62, and 200 micron (μ) and solid loading ratios of 0–10 kg/kg. The glass microspheres were added to the air-stream from a weighing hopper at a controlled rate, and they were returned to a storage hopper by a double effect cyclone separator. Operation of the system was quasi-steady, with the steady period of operation dependent on the solids rate.

Three different test section arrangements were tested with flow direction being vertically up, vertically down or horizontally. These arrangements would be referred to as configurations A, B, or C, respectively. The air alone runs were made for all three configurations. However, since sufficient data had already been taken by Depew [1] and verified by Rajpaul [2] in details for the configuration A, it was unnecessary to make air-solid runs for this arrangement. Comparable data were taken for the arrangements B and C and then the results of all three orientations were compared.

Analysis of Results. The local Nusselt number, hD/k, is based on the local heat transfer coefficient, which is defined by:

$$h = \frac{q}{T_w - T_{mm}}$$

T_{mm} is the mixed-mean temperature that would exist if the phases were in thermal equilibrium and is based upon an energy balance:

$$T_{mm} = T_0 + \frac{\pi_q D x}{W_a C_a + W_s C_s}$$

The heat flux is assumed to be uniform since the tube electrical resistivity is nearly constant, the heat loss is a small part of the total heat transferred, and the tube wall conduction is estimated to be negligible. The Reynolds number is always based on the mean flow rate and physical properties of the air. The air properties were evaluated at arithmetic average of the inlet and outlet mixed-mean temperatures in the test section.

Results and Discussion

Heat Transfer with 30 μ Particles. Nusselt number ratios (ratio of local value of Nu to Nu at x/D = 101.4) are presented in Fig. 2 as a function of axial distance for high and low loading ratios with the air Reynolds number held constant at 15,000. Comparable results from [2] for the configuration "A" are also plotted in Fig. 2. These results are typical of the various runs made at this air rate and they show the essential characteristics of the system performance. Fig. 3 is similar to Fig. 2 and shows comparable data for A and B at the higher Reynolds number. Unfortunately for case C, data at higher Reynolds number could not be taken due to difficulties with the solids feed valve. Fig. 4 is a plot of the asymptotic Nusselt number as a function of solids loading ratio with the comparable results from [2] also shown. Fig. 4 also shows similar curves for Re = 30,000 for A and B. The curves drawn through data for configuration A are also reproduced from [2].

It is observed from Figs. 2 and 3 that the thermal-entry length is more sensitive to variation in the loading ratio than it is to a variation in Reynolds number. Also note that the prolonged thermal-entry length effects are not so pronounced for configurations B and C as for A, but the trend is qualitatively the same.

Similarly Fig. 4 shows that the decrease in Nusselt number is not as profound for B and C as for A, the qualitative trends being same in all three configurations. A minimum value of 25 is reached at a loading ratio of 0.9 to 1.0 in case A while it decreased only to 30–32 in cases B and C. Calculations showed that, on the average, the Nusselt number levels for case B were higher than for case A by 15 and 25 percent, respectively, for Reynolds numbers of 15,000 and 30,000. For case C the results were 13 percent higher at 15,000 Reynolds number than for case A.

Heat Transfer with 62 and 200 μ Particles. For reasons of brevity the plotted results are not shown here and may be found in reference [4]. For 62μ the Nusselt number levels differed by only 2 percent from A to B or A to C, well within the experimental error ±4.5 percent. At higher Reynolds number the level of Nusselt numbers is about 7 percent higher for B and C than for A, but the change in Nusselt number is minimal. Thus, qualitatively, the trend is the same for all three configurations. For 200μ the comparison of results indicated that within experimental error (±4.5 percent) there is no significant difference in the results for three arrangements. The average difference in Nusselt number levels was 2.5 percent at lower Reynolds number and 9 percent at higher Reynolds number.

Particle-Size Effects on Heat Transfer. Fig. 5 shows the heat transfer results in terms of particle size effects for configurations B and C at both Reynolds numbers. The trends do show that effect on Nusselt number with varying loading ratio is most significant for 30μ and least significant for the 200μ particles. This is in agreement with the known results for the case A.

Discussion. For vertical flow directions, A and B, the direction of flow should have little effect, if any, on the turbulent transport of heat to the mixture, and the only expected effect is that due to residence time for the particles to absorb heat from the air. When the mixture is flowing upward, (A), the solids travel approximately 10 percent slower than air while in downward flow (B) the solids velocity

[1] Senior Engineer, Landing Gear Research, Boeing Commercial Airplane Company, Renton, Wash.

[2] Numbers in brackets designate References at end of technical note.

Contributed by the Heat Transfer Division of THE AMERICAN SOCIETY OF MECHANICAL ENGINEERS. Manuscript received by the Heat Transfer Division May 19, 1976.

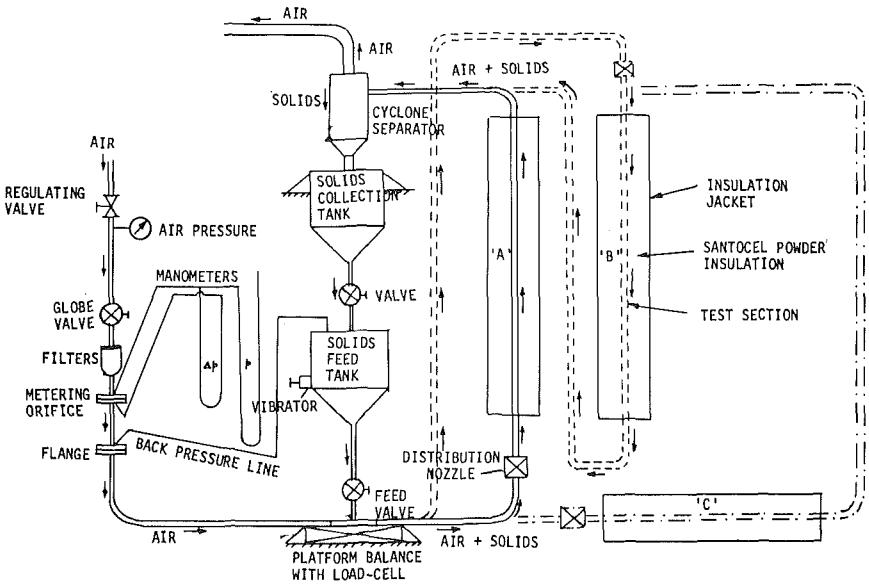

Fig. 1 Test section schematic diagram

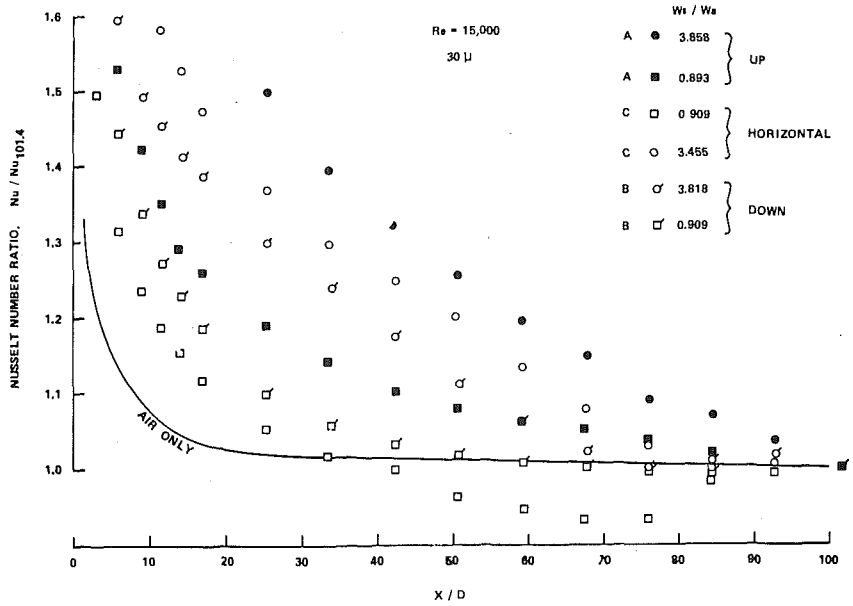

Fig. 2 Effect of solids loading ratio on thermal-entry length

is about 10 percent greater than the air velocity. Thus, the solids have somewhat greater time for heat transfer in case A, and this additional residence time should allow them to approach better thermal equilibrium with the air than in case B.

Based on the foregoing discussion, less variation in the Nusselt numbers should be expected for A than for B. This is contrary to the observed effects, Fig. 4, where local Nusselt numbers were always higher in case B than in case A, i.e., better thermal equilibrium was achieved in case B. Several possibilities exist for this discrepancy. The stratification effects observed by Van Zoonan [5] for the vertical flow might be different for configurations A and B. Bouncing flow observation made by Bagnold, Adam, and Wen, as reported in [5] were different for different particle size and may very well be different for different flow orientations.

Stratification effects were expected in case C where the solid particles should flow touching the lower surface of the tube due to their own weight. This should have resulted in one side of the tube being much cooler than the other. This effect was observed, however, for both side to side and top to bottom with the temperature difference variation from 6 to 36°F. An investigation revealed improper alignment of the test section with a sag being present in the tube. The test section was realigned within half a diameter and all data runs were repeated. The recorded difference in temperatures of tube-top and bottom was now insignificant. This leads one to believe that while test section alignment is critical, the asymmetry caused by transverse gravity may not be important.

The above observation is, of course, contrary to known experimental results for 30μ particles as reported in [5]. Perhaps, even half a di-

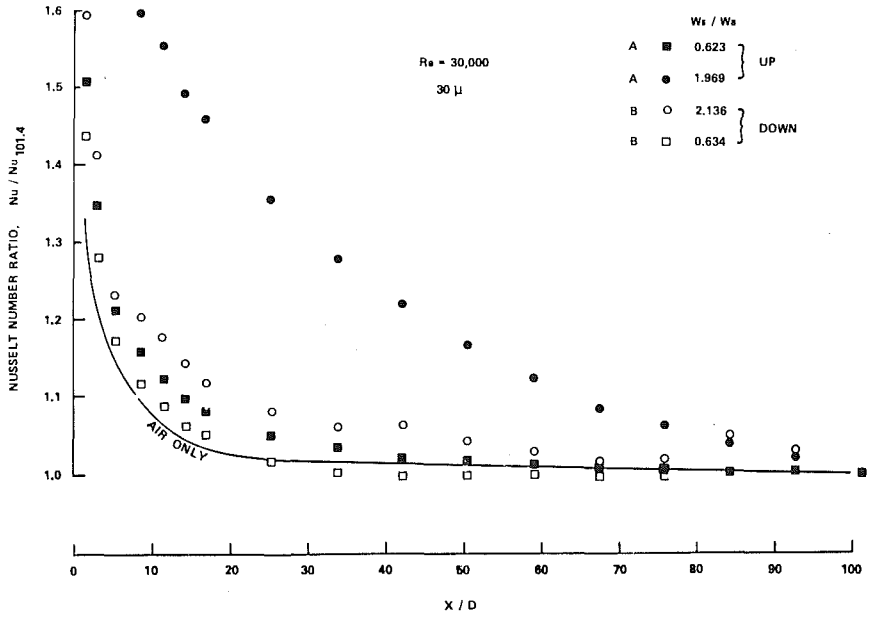

Fig. 3 Effect of solids loading ratio on thermal-entry length

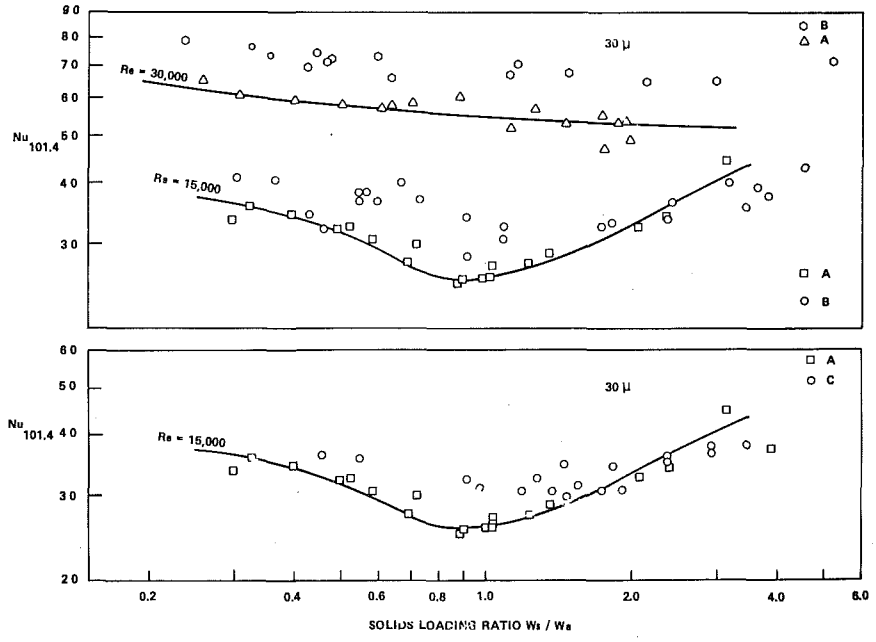

Fig. 4 Effect of test section orientation

ameter crookedness in alignment was important and should have been checked. The results for 200μ particles are, however, in agreement with those shown in [5]. The observed differences in heat transfer results between A and C configurations are close to the experimental error range (±4.5 percent), but the trend does indicate less variation in heat transfer for C than for A.

Conclusions. The subject is far from being unified and the complicated interactions between fluid and particle, particle and particle, and the mixture and the flow boundary need to be better understood. The following conclusions are based on the experimental results presented in this paper and reference [4] and are subject to verification or modification with further research.

1 The fully developed Nusselt number, after an initial decrease (as compared to the air only value) up to a loading ratio of about 1.0, shows significant increase with further solids loading, in case of 30 micron particles. The rate of increase in the Nusselt number is higher for 15,000 Reynolds number. The effect of 62μ particles is minimal, a small increase in heat transfer observed beyond a loading ratio of 3.0. Addition of 200μ particles did not affect the heat transfer.

2 The thermal entry length is substantially increased with increasing solids addition. This effect is the most profound for 30 micron size.

3 The Nusselt numbers are higher by 2–25 percent for orientation B (DOWN) than for orientation A (UP), indicating better thermal

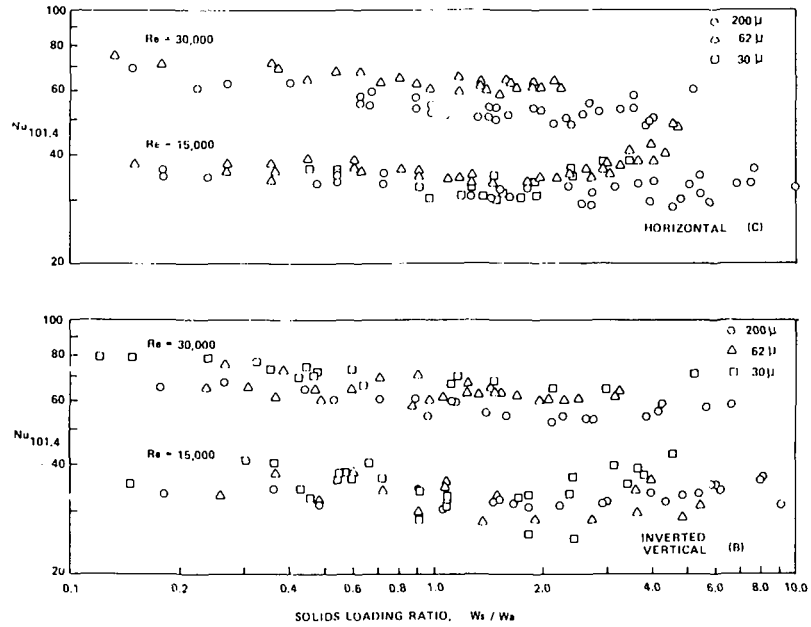

Fig. 5 Effect of solids loading ratio on asymptotic Nusselt number

equilibrium for B. Similarly, the orientation C (horizontal) results are higher than those of A by 2 to 13 percent again indicating more stable heat transfer for C.

4 The observed differences in heat transfer due to test section orientation are somewhat offset by experimental error and are therefore more of a qualitative nature.

5 Accurate test section alignment is critical.

References

1 Depew, C. A., and Farbar, L., "Heat Transfer to Pneumatically Conveyed Glass Particles of Fixes Size," JOURNAL OF HEAT TRANSFER, TRANS. ASME, Series C, Vol. 85, 1963, pp. 164–172.

2 Rajpaul, V. K., "Tube Size and Particle Size Effects on Heat Transfer to Flowing Gas-Solid Mixtures With Low Solid Loading Ratios," MS thesis in Mechanical Engineering, University of Washington, Seattle, Wash., 1963.

3 Soo, S. L., *Fluid Dynamics of Multiphase Systems*, Blaisdell Publishing Co., 1967.

4 Wahi, M. K., "Tube Size and Particle Size Effects on Heat Transfer to Flowing Gas-Solid Mixtures," MS thesis in Mechanical Engineering, University of Washington, Seattle, Wash., 1966.

5 Depew, C. A., and Kramer, T. J., "Heat Transfer to Flowing Gas-Solid Mixtures," *Advances in Heat Transfer*, Vol. 9, Academic Press, 1972, pp. 113–180.

An Analysis of Steady Fully Developed Heat Transfer in A Rotating Straight Pipe

V. Vidyanidhi,[1] V. V. S. Suryanarayana,[1] and V. C. Chenchu Raju[1]

Introduction

Barua [1][2] examined the laminar flow of an incompressible liquid through a pipe of circular cross section, when the pipe is rotated about an axis perpendicular to it with an uniform angular velocity. His analysis has been extended for the flow through an annular pipe [2]. His solution for the velocity field was based on the work of Dean [3, 4] for flow in a curved pipe. The analogy between these two flows motivated us to study the heat transfer in a thermally fully developed laminar flow in a rotating straight pipe, following the work of Tyagi and Sharma [5] for the flow in a curved pipe.

Statement of the Problem

We consider the steady laminar flow of an incompressible liquid under the action of a constant pressure gradient through a pipe of circular cross section of radius a, rotating with an uniform angular velocity Ω' about an axis perpendicular to the axis z' of the pipe. The solution of the two coupled differential equations in ϕ (stream function) and w corresponding to the secondary and primary flow is obtained as a perturbation in terms of Taylors number $T = 2\Omega' a^2/\nu$, and is given in [1, 2]. For this laminar flow, we examine the steady-state fully developed heat transfer effected by a heat source (sink) distribution in the wall material. In our analysis, we assume: (1) the velocity and temperature fields are fully developed; (2) the flow is laminar; (3) variations of physical properties are negligible; (4) secondary free convection effects are negligible; and (5) viscous dissipation is taken into account. We assume the following thermal boundary condition valid for small values of the thermal conductivity of the wall or when the wall is of very small thickness: normal temperature gradient at solid-liquid interface is constant in both the circumferential and the longitudinal direction. This condition was used by Tyagi and Sharma [5] for a similar problem in circular curved ducts.

[1] Department of Engineering Mathematics, Andhra University, Waltair, India.

[2] Numbers in brackets designate References at end of technical note.

Contributed by the Heat Transfer Division of THE AMERICAN SOCIETY OF MECHANICAL ENGINEERS. Manuscript received by the Heat Transfer Division June 9, 1976.

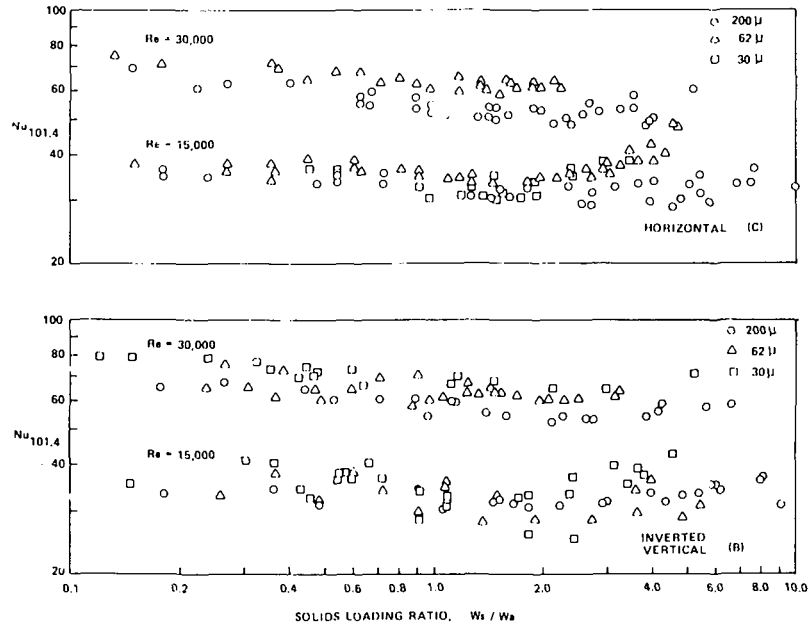

Fig. 5 Effect of solids loading ratio on asymptotic Nusselt number

equilibrium for B. Similarly, the orientation C (horizontal) results are higher than those of A by 2 to 13 percent again indicating more stable heat transfer for C.

4 The observed differences in heat transfer due to test section orientation are somewhat offset by experimental error and are therefore more of a qualitative nature.

5 Accurate test section alignment is critical.

References

1 Depew, C. A., and Farbar, L., "Heat Transfer to Pneumatically Conveyed Glass Particles of Fixes Size," JOURNAL OF HEAT TRANSFER, TRANS. ASME, Series C, Vol. 85, 1963, pp. 164–172.

2 Rajpaul, V. K., "Tube Size and Particle Size Effects on Heat Transfer to Flowing Gas-Solid Mixtures With Low Solid Loading Ratios," MS thesis in Mechanical Engineering, University of Washington, Seattle, Wash., 1963.

3 Soo, S. L., *Fluid Dynamics of Multiphase Systems*, Blaisdell Publishing Co., 1967.

4 Wahi, M. K., "Tube Size and Particle Size Effects on Heat Transfer to Flowing Gas-Solid Mixtures," MS thesis in Mechanical Engineering, University of Washington, Seattle, Wash., 1966.

5 Depew, C. A., and Kramer, T. J., "Heat Transfer to Flowing Gas-Solid Mixtures," *Advances in Heat Transfer*, Vol. 9, Academic Press, 1972, pp. 113–180.

An Analysis of Steady Fully Developed Heat Transfer in A Rotating Straight Pipe

V. Vidyanidhi,[1] V. V. S. Suryanarayana,[1] and V. C. Chenchu Raju[1]

Introduction

Barua [1][2] examined the laminar flow of an incompressible liquid through a pipe of circular cross section, when the pipe is rotated about an axis perpendicular to it with an uniform angular velocity. His analysis has been extended for the flow through an annular pipe [2]. His solution for the velocity field was based on the work of Dean [3, 4] for flow in a curved pipe. The analogy between these two flows motivated us to study the heat transfer in a thermally fully developed laminar flow in a rotating straight pipe, following the work of Tyagi and Sharma [5] for the flow in a curved pipe.

Statement of the Problem

We consider the steady laminar flow of an incompressible liquid under the action of a constant pressure gradient through a pipe of circular cross section of radius a, rotating with an uniform angular velocity Ω' about an axis perpendicular to the axis z' of the pipe. The solution of the two coupled differential equations in ϕ (stream function) and w corresponding to the secondary and primary flow is obtained as a perturbation in terms of Taylors number $T = 2\Omega' a^2/\nu$, and is given in [1, 2]. For this laminar flow, we examine the steady-state fully developed heat transfer effected by a heat source (sink) distribution in the wall material. In our analysis, we assume: (1) the velocity and temperature fields are fully developed; (2) the flow is laminar; (3) variations of physical properties are negligible; (4) secondary free convection effects are negligible; and (5) viscous dissipation is taken into account. We assume the following thermal boundary condition valid for small values of the thermal conductivity of the wall or when the wall is of very small thickness: normal temperature gradient at solid-liquid interface is constant in both the circumferential and the longitudinal direction. This condition was used by Tyagi and Sharma [5] for a similar problem in circular curved ducts.

[1] Department of Engineering Mathematics, Andhra University, Waltair, India.

[2] Numbers in brackets designate References at end of technical note.

Contributed by the Heat Transfer Division of THE AMERICAN SOCIETY OF MECHANICAL ENGINEERS. Manuscript received by the Heat Transfer Division June 9, 1976.

Analysis

The equation for the temperatue distribution t' for the flow under consideration, is

$$\rho c_p(\mathbf{v}' \cdot \nabla')t' = k\nabla'^2 t' + \mu\left[\left(\frac{\partial w'}{\partial r'}\right)^2 + \left(\frac{1}{r'}\frac{\partial w'}{\partial \theta}\right)^2\right] \tag{1}$$

The thermal boundary condition is

$$\frac{\partial t'}{\partial r'} = \beta \text{ at solid-liquid interface,} \tag{2}$$

where β is a constant and is positive or negative according as the wall of the pipe contains heat source or sink distribution.

We use the nondimensional quantities [2] defined by

$$r' = ar,\ z' = az,\ w' = \frac{ca^2}{4\rho\nu}w,\ \phi' = \frac{ca^3}{4\rho\nu}\phi \tag{3}$$

$$m\beta = \frac{\partial t'}{\partial z'} = \frac{\partial t_w'}{\partial z'} = \frac{\partial t_m'}{\partial z'}t = \frac{t' - t_m'}{a\beta} \tag{4}$$

$$\mathrm{R} = \frac{ca^3}{4\rho\nu^2} \quad \text{(Reynolds number)} \tag{5}$$

$$\mathrm{T} = \frac{2\Omega' a^2}{\nu} \quad \text{(Taylors number)} \tag{6}$$

$$\bar{B} = \frac{\mu^3}{\rho^2 a^3 k\beta},\quad \mathrm{P} = \frac{\mu c_p}{k} \quad \text{(Prandtl number)} \tag{7}$$

$$B = \bar{B}\mathrm{R}^2 \quad \text{(Dissipation number)} \tag{8}$$

Then (1) becomes,

$$\nabla^2 t = \mathrm{PR}\left[\frac{1}{r}\frac{\partial(\phi, t)}{\partial(r, \theta)} + wm\right] - B\left[\left(\frac{\partial w}{\partial r}\right)^2 + \left(\frac{1}{r}\frac{\partial w}{\partial \theta}\right)^2\right] \tag{9}$$

subject to

$$\frac{\partial t}{\partial r} = 1 \quad \text{at } r = 1,\quad t_m = 0$$

and t is finite at all points r in the tube (the suffices m and w in the foregoing equations represent the mean value over cross-sectional domain and value at solid-liquid interface, respectively). In the foregoing equations, m is the longitudinal temperature gradient and c is the modified pressure gradient along the axis of the pipe [1].

Using T as perturbation parameter in series for the temperature t and the longitudinal temperature gradient m in the form

$$t = t_0 + \mathrm{T}t_1 + \mathrm{T}^2 t_2 + \ldots$$

$$m = m_0 + \mathrm{T}m_1 + \mathrm{T}^2 m_2 + \ldots \tag{10}$$

and making use of the velocity field given in [1, 2], we obtain the solution of the equation (9).

The solutions corresponding to the straight pipe when $T = 0$, are

$$m_0 = \frac{4}{\mathrm{RP}}(1 + B) \tag{11}$$

and

$$t_0 = \frac{1}{12}(-5 + 12r^2 - 3r^4) + \frac{B}{6}(-2 + 6r^2 - 3r^4) \tag{12}$$

The solutions for the rotating pipe have been calculated to the second order of approximation in T. For our purposes, it is sufficient to note that

$$m_1 = 0,$$

$$m_2 = \frac{1}{24^2 \cdot \mathrm{PR}}\left[1 - B + \frac{\mathrm{R}^2}{16^2 \cdot 7}\right] \tag{13}$$

Also, we obtain

$$t_1 = \mathrm{R}t_{11}(r)\sin\theta \tag{14}$$

and

$$t_2 = t_{20}(r) + t_{22}(r)\cos 2\theta \tag{15}$$

The expressions for $t_{11}(r)$ and $t_{20}(r)$ are lengthy and so are not reported here. The expression for $t_{22}(r)$ is not needed in our analysis.

Heat Transfer Coefficients

The average Nusselt number Nu, defined by equation (42) of [5], gives

$$\mathrm{Nu} = \frac{2a}{k}\frac{k\left[\dfrac{\partial t'}{\partial r'}\right]_w}{(t_{wa}' - t_m')} \tag{16}$$

(the suffix a is the mean value along the cross-sectional boundary)

Under the present nondimensionalization scheme, equation (16) transforms to

$$\mathrm{Nu} = \frac{2}{t_{wa}} = 2[t_0(1) + \mathrm{T}^2 t_{20}(1)]^{-1} = \frac{6}{(1 - \mathrm{T}^2 J) + \dfrac{1}{2}B(1 - \mathrm{T}^2\bar{J})} \tag{17}$$

where

$$J = \frac{1}{24^2 \cdot 20} + \frac{11\mathrm{R}^2}{96^2 \cdot 8 \cdot 2240} + \frac{\mathrm{R}^2\mathrm{P}}{96^2 \cdot 48^2 \cdot 700}(3985 + 11310\mathrm{P}) \tag{18}$$

and

$$\bar{J} = \frac{1}{5 \cdot 24^2} + \frac{31\mathrm{R}^2}{96^2 \cdot 24^2 \cdot 560} + \frac{\mathrm{R}^2\mathrm{P}}{96^2 \cdot 48^2 \cdot 700}(-2520 + 4410\mathrm{P}) \tag{19}$$

The longitudinal temperature gradient is given by

$$m^* = \mathrm{RP}m = 4(1 + A_1 B + A_2\mathrm{T}^2) \tag{20}$$

where

$$A_1 = 1 - \frac{\mathrm{T}^2}{4 \cdot 24^2}$$

$$A_2 = \frac{1}{2304} + \frac{\mathrm{R}^2}{4128768} \tag{21}$$

If Q and Q_0 represent the mass flow rate for a rotating pipe and for straight pipe, we have from [1, 2]

$$Q = Q_0(1 - \mathrm{T}^2 A_2) \tag{22}$$

and

$$m^* = 4[1 + A_1 B + Q_0^{-1}(Q_0 - Q)] \tag{23}$$

Discussion

A qualitative picture of rotating pipe convective heat transfer is given on the basis of the analytical results (17) and (20). The results hold good for $\mathrm{T} < 33.8$ and $\mathrm{R} < 35.3$, which is apparent from the second order perturbation solution for velocity field [1].

When $B = 0$ (no viscous dissipation),

$$\mathrm{Nu} = \frac{6}{1 - \mathrm{T}^2 J} \tag{24}$$

and

$$m^* = 4(1 + A_2\mathrm{T}^2) \tag{25}$$

Since J is positive, as Prandtl number is positive, it follows that the Nusselt number is higher: (1) at greater than at smaller Taylors number and (2) at greater than at smaller Prandtl number. In general the effect of rotation is to increase the Nusselt number and the lon-

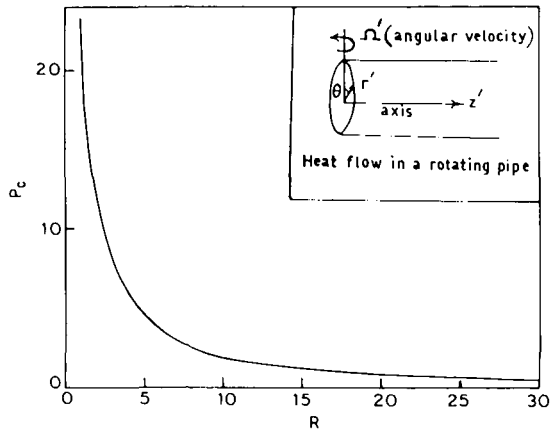

Fig. 1 Critical Prandtl number P_c versus Reynolds number R

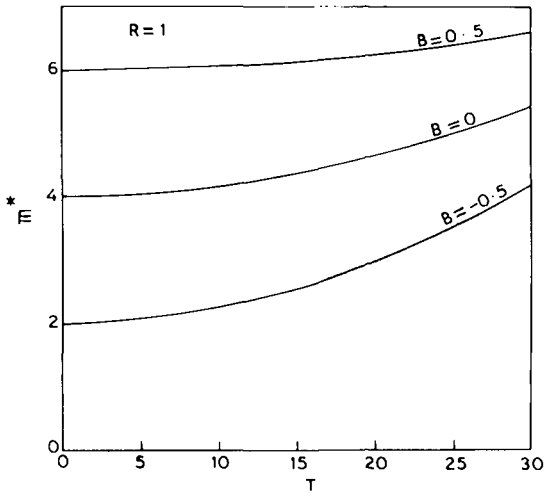

Fig. 3 m^* versus T with B as parameter

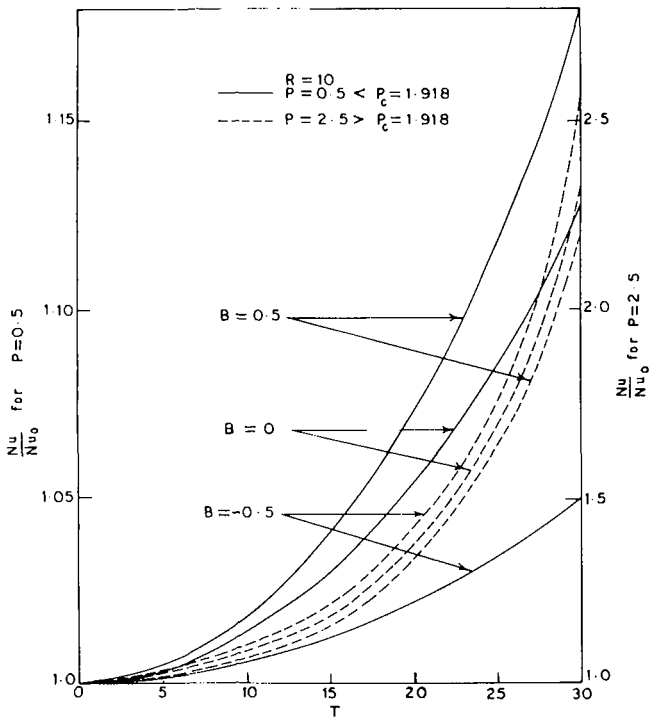

Fig. 2 (Nu/Nu_0) versus T with B as parameter

gitudinal temperature gradient for any value of the dissipation number B.

To seek the effect of viscous dissipation B, it is found more convenient to study the ratio of the Nusselt number in a rotating pipe to that in a straight pipe, i.e., Nu/Nu_0.

$$\frac{Nu}{Nu_0} = \frac{2 + B}{(1 - T^2\bar{J})(2 + T^2J')} \tag{26}$$

where

$$J' = \frac{1 - T^2\bar{J}}{1 - T^2J} \tag{27}$$

This ratio is independent of the Reynolds number, for a curved pipe [5], while it is found to be dependent on it in this case.

For a given R, there exists a critical Prandtl number $P = P_c$ (given by the positive root of the equation, $J = \bar{J}$), at which value, this ratio Nu/Nu_0 remains uneffected by viscous dissipation. Whenever,

$$P > P_c, \bar{J} < J \quad \text{and } J' > 1 \tag{28}$$

$$P = P_c, \bar{J} = J \quad \text{and } J' = 1 \tag{29}$$

$$P < P_c, \bar{J} > J \quad \text{and } J' < 1 \tag{30}$$

Fig. 1 shows that this critical Prandtl number decreases as R increases.

For a fixed R, as B increases through positive values, this ratio decreases or increases according as $P > $ or $< P_c$ for a fixed T. Fig. 2 shows the plot of this ratio Nu/Nu_0 versus the Taylors number T at the same set of values of the dissipation number B but at different fixed values of the Prandtl number. The order of the reversal of curves for $P > P_c$ and $P < P_c$ is strikingly opposite to that for a curved pipe [5]. Analytically this is because of the equations (28)–(30).

Fig. 3 shows that the effect of viscous dissipation for a fixed T, is to increase the longitudinal temperature gradient as B increases through zero.

Acknowledgment

One of the authors, V. V. Suryanarayana is grateful to the Council of Scientific and Industrial Research, New Delhi, India for the award of a Junior Research Fellowship.

References

1 Barua, S. N., "Secondary Flow in a Rotating Straight Pipe," *Proceedings of Royal Society of London*, Series A-Mathematical and Physical Sciences, Vol. 227, 1954, pp. 133–139.

2 Vidyanidhi, V., and Ramana Rao, V. V., "Secondary Flow in a Rotating Straight Annular Pipe," *Journal of the Physical Society of Japan*, Vol. 27, 1969, pp. 1027–1035.

3 Dean, W. R., "Note on the Motion of Fluid in a Curved Pipe," *Philosophical Magazine and Journal of Science*, Vol. 4, 1927, pp. 208–223.

4 Dean, W. R., "The Stream-Line Motion of Fluid in a Curved Pipe," *Philosophical Magazine and Journal of Science*, Vol. 5, 1928, pp. 673–695.

5 Tyagi, V. P., and Sharma, V. K., "An Analysis of Steady Fully Developed Heat Transfer in Laminar Flow With Viscous Dissipation in a Curved Circular Duct," *International Journal of Heat and Mass Transfer*, Vol. 18, 1975, pp. 69–78.

Prediction of Local Heat Transfer on a Rotating Disk By a Two-Equation Model of Turbulence

B. I. Sharma[1]

Nomenclature

C_μ, C_1, C_2, C_3 = constants in the turbulence model
k = turbulent kinetic energy
$\hat{h}$ = stagnation enthalpy
Nu = local Nusselt number
p = static pressure
r = radial distance from axis of symmetry
Re = $\omega r x/\nu$, spin Reynolds number
Re_t = value of Re at which transition occurs
R_t = turbulent Reynolds number, $k^2/\nu\epsilon$
U = velocity in the x-direction
W = velocity in the z-direction
V_θ = circumferential direction
x = coordinate measured along the surface
z = coordinate measured normal to the surface
ϵ = dissipation rate of turbulence energy
θ = circumferential coordinate
μ = dynamic viscosity
ν = kinematic viscosity
ρ = density
σ = Prandtl number
ω = rotational speed
Γ = thermal diffusivity

Introduction

The turbulent flow near a rotating disk in stagnant surroundings was recently computed and compared with experimental data by Launder and Sharma [1].[2] The main conclusion drawn in [1] was that the application of energy-dissipation model of turbulence generally leads to satisfactory predictions of momentum and average heat and mass transfer in the neighborhood of a rotating disk. The correct prediction of local quantities provides a more severe test of the validity of a turbulence model. The present contribution, therefore, deals with the local rather than average heat transfer computations using the energy-dissipation model of turbulence.

The availability of reliable experimental data is of major importance in the effort to develop and test universal turbulence models. The experimental data, especially of local quantities, near spinning surfaces are very scarce. Koosinlin [2] made a critical evaluation and assessment of the available experimental data for flows near rotating solid boundaries. Indeed, Koosinlin made attempts to measure local heat transfer near a rotating disk, but had to abandon efforts due to experimental difficulties. The detailed account of such matters appears in [2]. As far as the writer is aware, the only other local Nusselt number data on a rotating disk are those reported in [3] and [4]. The more recent local Nusselt number measurements of Popiel and Boguslawsky [4] are the only complete experimental data; they include laminar, transitional and turbulent regimes up to spin Reynolds number of $6.5 * 10^5$. The present paper thus compares the predictions of local heat transfer by a turbulence model based on the solution of transport equations for the turbulence kinetic energy and its local rate of dissipation with the data of Popiel and Boguslawski. Agreement with the experimental data is generally very good.

Governing Equations and the Turbulence Model

The boundary layer forms of the mass, steamwise and swirl momentum equations for a uniform-property, axisymmetric turbulent flow may be written:

$$\frac{\partial(rU)}{\partial x} + \frac{\partial(rW)}{\partial z} = 0 \tag{1}$$

$$\rho U\frac{\partial U}{\partial x} + \rho W\frac{\partial U}{\partial z} = -\frac{\partial p}{\partial x} + \frac{1}{r}\frac{\partial}{\partial z}\left[r\mu_{\text{eff}}\frac{\partial U}{\partial z}\right] + \frac{\rho V_\theta^2}{r} \tag{2}$$

$$\rho U\frac{\partial(rV_\theta)}{\partial x} + \rho W\frac{\partial(rV_\theta)}{\partial z} = \frac{1}{r}\frac{\partial}{\partial z}\left[r^3\mu_{\text{eff}}\frac{\partial(V_\theta/r)}{\partial z}\right] \tag{3}$$

Heat transfer rate from the surface is computed by solving the following equation for stagnation enthalpy $\hat{h}$:

$$\rho U\frac{\partial\hat{h}}{\partial x} + \rho W\frac{\partial\hat{h}}{\partial z} = \frac{1}{r}\frac{\partial}{\partial z}\left[r\frac{\mu_{\text{eff}}}{\sigma_{\text{eff}}}\frac{\partial h}{\partial z}\right] \tag{4}$$

The effective viscosity of the fluid μ_{eff}, is taken as the sum of the molecular and turbulent contributions, i.e.,

$$\mu_{\text{eff}} = \mu + \mu_t \tag{5}$$

The effective Prandtl number σ_{eff}, is related to the molecular and turbulent values by

$$\frac{\mu_{\text{eff}}}{\sigma_{\text{eff}}} = \frac{\mu}{\sigma} + \frac{\mu_t}{\sigma_t} \tag{6}$$

The preceding equation rests on the supposition that the effective transport coefficient for enthalpy is the sum of molecular and turbulent values.

The turbulent transport coefficients μ_t and Γ_t are obtained from the following system of differential and auxiliary equations.

$$\mu_t = C_\mu\rho k^2/\epsilon \tag{7}$$

$$\Gamma_t = \mu_t/0.9\rho \tag{8}$$

Equation (8) implies that the turbulent Prandtl number is equal to 0.9. The works of Kestin and Richardson [5] and Patankar and Spalding [6] support this hypothesis for wall boundary layers.

The two turbulence quantities k and ϵ are obtained from the following pair of transport equations that are solved simultaneously with those governing the mean flow behavior:

$$\rho U\frac{\partial k}{\partial x} + \rho W\frac{\partial k}{\partial z} = \frac{1}{r}\frac{\partial}{\partial z}\left[r\left(\frac{\mu_t}{\sigma_k} + \mu\right)\frac{\partial k}{\partial z}\right] + \mu_t\left[\left(\frac{\partial U}{\partial z}\right)^2 + \left(r\frac{\partial V_\theta/r}{\partial z}\right)^2\right] - \rho\epsilon - 2\mu\left(\frac{\partial k^{1/2}}{\partial z}\right)^2 \tag{9}$$

$$\rho U\frac{\partial\epsilon}{\partial x} + \rho W\frac{\partial\epsilon}{\partial z} = \frac{1}{r}\frac{\partial}{\partial z}\left[r\left(\frac{\mu_t}{\sigma_\epsilon} + \mu\right)\frac{\partial\epsilon}{\partial z}\right] + C_1\frac{\epsilon\mu_t}{k}\left[\left(\frac{\partial U}{\partial z}\right)^2 + \left(r\frac{\partial V_\theta/r}{\partial z}\right)^2\right] - C_2\frac{\rho\epsilon^2}{k} + C_3\nu\mu_t\left\{\frac{\partial}{\partial z}\left[\left(\frac{\partial U}{\partial z}\right)^2 + \left(r\frac{\partial V_\theta/r}{\partial z}\right)^2\right]^{1/2}\right\}^2 \tag{10}$$

where

$$C_\mu = 0.09\exp\left[-3.4/(1 + R_t/50)^2\right]$$

$$C_2 = 1.92\left[1.0 - 0.3\exp\left(-R_t^2\right)\right]$$

and $R_t = \rho k^2/\mu\epsilon$, the turbulent Reynolds number. The other empirical coefficients take the following uniform values:

$$C_1 = 1.44; \qquad \sigma_k = 1.0; \qquad \sigma_\epsilon = 1.3$$

The foregoing system of equations differ from that in [7]. Extra source terms involving the gradients of (V_θ/r) appear in the equations for k and ϵ. They are not ad hoc terms; their appearance is due to the

[1] Department of Mechanical Engineering, Imperial College of Science and Technology, London, England. Presently at Linde Division, Union Carbide Corp., Tonawanda, N. Y.

[2] Numbers in brackets designate References at end of technical note.

Contributed by The Heat Transfer Division of THE AMERICAN SOCIETY OF MECHANICAL ENGINEERS. Manuscript received by the Heat Transfer Division, September 10, 1976.

conversion of the Cartesian-tensor form of these equations to the present coordinate system. All the coefficients take the above values on the basis of extensive computer optimization as reported in [1], [8] and the author's extensive numerical experimentation with a wide variety of flow situations [9], including e.g., flow over a flat plate; high and low Reynolds number flows in pipes and rectangular channels; flow between converging plates (sink flows).

The boundary conditions to be satisfied by the foregoing equations are as follows:

$$z = 0\text{: } U = 0; \qquad V_\theta = r\omega; \qquad h = h_{\text{wall}}$$

$$k = \epsilon = 0$$

$$z = z_{\text{edge}}\text{: } U = V_\theta = k = \epsilon = 0$$

$$h = h_\infty$$

Detailed discussion about the present boundary conditions appears in [7] and [8].

The foregoing system of equations have been solved by an adapted version of the Patankar-Spalding [6] finite difference scheme as outlined in [10]. Seventy nodes were used to span the boundary layer with a substantial concentration very near the wall. The forward step used was typically 15 percent of the boundary layer thickness leading to computer times per run of about 50 S on a CDC 6600 computer.

Discussion of Predictions

The numerical predictions of local Nusselt number using the present turbulence model are compared with the experimental data of Popiel and Boguslawski [4] in Fig. 1. To make accurate predictions of Nusselt number, the Reynolds number Re_t at which the flow becomes turbulent must be prescribed. When the distance x is so small that the spin Reynolds number is less than Re_t, the flow is taken as laminar and only the mean flow equations are solved. Consistent with the previous practices of equations [8] and [10] the turbulent Reynolds number was taken as $2{\cdot}4 \times 10^5$. Agreement of predictions with the local Nusselt number data is satisfactorily close over the entire Reynolds number range explored. In the experiment with laminar boundary layer, the disk surface was maintained almost isothermal; with transition boundary layer, it was isothermal within ±1.5 percent; and with the turbulent boundary layer, it was isothermal within ±3 percent. The predictions for the turbulent regime are within this ±3 percent deviation with the present turbulence model. The small deviation of the measurements at low Reynolds numbers from the predicted values is probably due to the free convection effects having been neglected in the predictions.

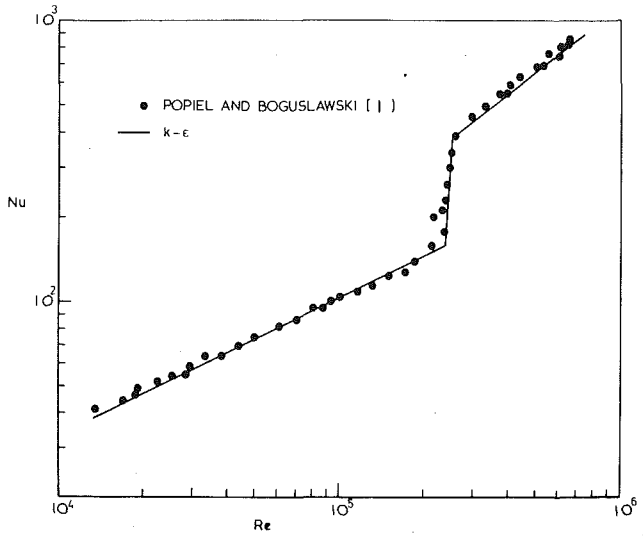

Fig. 1 Local heat transfer from a spinning disk in still air

Acknowledgment

This research has been supported by the Science Research Council through Grant No. B/RG/1863. The author is grateful to Dr. B. E. Launder for his comments.

References

1 Launder, B. E., and Sharma, B. I., "Application of the Energy-Dissipation Model of Turbulence to the Calculation of Flow Near a Spinning Disc," *Letters in Heat and Mass Transfers*, 1, 2, 1974, p. 131.

2 Koosinlin, M. L., "Turbulent Transport Properties in Swirling Tow Dimensional Boundary Layers," PhD thesis, University of London, England, 1974.

3 McComas, S. T., and Hartnett, J. P., "Temperature Profiles and Heat Transfer Associated With a Single Disc Rotating in Still Air," Fourth International Heat Transfer Conference, Paris-Versailles, III, FC7.7, 1976.

4 Popiel, Cz. O., and Boguslawski, L., "Local Heat Transfer Coefficients on the Rotating Disc in Still Air," *International Journal of Heat and Mass Transfer*, Vol. 18, 1975, p. 167.

5 Kestin, J., and Richardson, P. D., "Heat Transfer Across Turbulent, Incompressible Boundary Layers." *International Journal of Heat and Mass Transfer*, Vol. 6, 1963, p. 147.

6 Patankar, S. V., and Spalding, D. B., *Heat and Mass Transfer in Boundary Layers*, Intertext Books, London, 1970.

7 Jones, W. P., and Launder, B. E., "The Calculation of Low Reynolds Number Phenomena With a Two Equation Model of Turbulence." *International Journal of Heat and Mass Transfer*, Vol. 16, pp. 1189, 1973.

8 Launder, B. E., Priddin, C. H. and Sharma, B. I., "The Calculation of Turbulent Boundary Layers on Spinning and Curved Surfaces," Paper number 493 FMW, in Press, *Journal of Fluids Engineering*, 1976.

9 Sharma, B. I., Unpublished work, Mechanical Engineering Department. Imperial College of Science and Technology, London, 1973.

10 Koosinlin, M. L., Launder, B. E. and Sharma, B. I., "Prediction of Momentum, Heat and Mass Transfer in Swirling, Turbulent Boundary Layers." JOURNAL OF HEAT TRANSFER, TRANS. ASME Series C, Vol. 96, 1974, p. 204.

An Experimental Study of Heat Transfer to Developing Water Film Flow Over Cylinders

P. H. Oosthuizen[1] and T. Cheung[2]

Nomenclature

c = specific heat
D_h = hydraulic diameter of film, $2(R_0^2 - R_c^2)/R_c$
F_r = Froude number, u_0^2/gD_h
g = gravitational acceleration
h = local heat transfer coefficient
$\overline{h}$ = dimensionless heat transfer coefficient, $(h/k)(\nu^2/g)^{1/3}$
$\overline{h}_{\text{min}}$ = minimum value of $\overline{h}$ along surface
$\overline{h}_{fd}$ = constant value of $\overline{h}$ in fully developed flow
k = thermal conductivity
P_r = Prandtl number
q_w = local heat transfer rate at wall
R_c = radius of cylindrical surface
R_e = Reynolds number, $u_0 D_h/\nu$
R_0 = radius of outer surface of film
R_x = Reynolds number based on x
$\text{R}_{x\text{min}}$ = value of R_x at which $\overline{h}_{\text{min}}$ occurs

[1] Professor, Department of Mechanical Engineering, Queen's University, Kingston, Ontario, Canada.

[2] Research Assistant, Department of Mechanical Engineering, Queen's University, Kingston, Ontario, Canada.

Contributed by the Heat Transfer Division of THE AMERICAN SOCIETY OF MECHANICAL ENGINEERS. Manuscript received by the Heat Transfer Division June 30, 1976.

conversion of the Cartesian-tensor form of these equations to the present coordinate system. All the coefficients take the above values on the basis of extensive computer optimization as reported in [1], [8] and the author's extensive numerical experimentation with a wide variety of flow situations [9], including e.g., flow over a flat plate; high and low Reynolds number flows in pipes and rectangular channels; flow between converging plates (sink flows).

The boundary conditions to be satisfied by the foregoing equations are as follows:

$$z = 0\text{: } U = 0; \qquad V_\theta = r\omega; \qquad h = h_{\text{wall}}$$

$$k = \epsilon = 0$$

$$z = z_{\text{edge}}\text{: } U = V_\theta = k = \epsilon = 0$$

$$h = h_\infty$$

Detailed discussion about the present boundary conditions appears in [7] and [8].

The foregoing system of equations have been solved by an adapted version of the Patankar-Spalding [6] finite difference scheme as outlined in [10]. Seventy nodes were used to span the boundary layer with a substantial concentration very near the wall. The forward step used was typically 15 percent of the boundary layer thickness leading to computer times per run of about 50 S on a CDC 6600 computer.

Discussion of Predictions

The numerical predictions of local Nusselt number using the present turbulence model are compared with the experimental data of Popiel and Boguslawski [4] in Fig. 1. To make accurate predictions of Nusselt number, the Reynolds number Re_t at which the flow becomes turbulent must be prescribed. When the distance x is so small that the spin Reynolds number is less than Re_t, the flow is taken as laminar and only the mean flow equations are solved. Consistent with the previous practices of equations [8] and [10] the turbulent Reynolds number was taken as $2{\cdot}4 \times 10^5$. Agreement of predictions with the local Nusselt number data is satisfactorily close over the entire Reynolds number range explored. In the experiment with laminar boundary layer, the disk surface was maintained almost isothermal; with transition boundary layer, it was isothermal within ±1.5 percent; and with the turbulent boundary layer, it was isothermal within ±3 percent. The predictions for the turbulent regime are within this ±3 percent deviation with the present turbulence model. The small deviation of the measurements at low Reynolds numbers from the predicted values is probably due to the free convection effects having been neglected in the predictions.

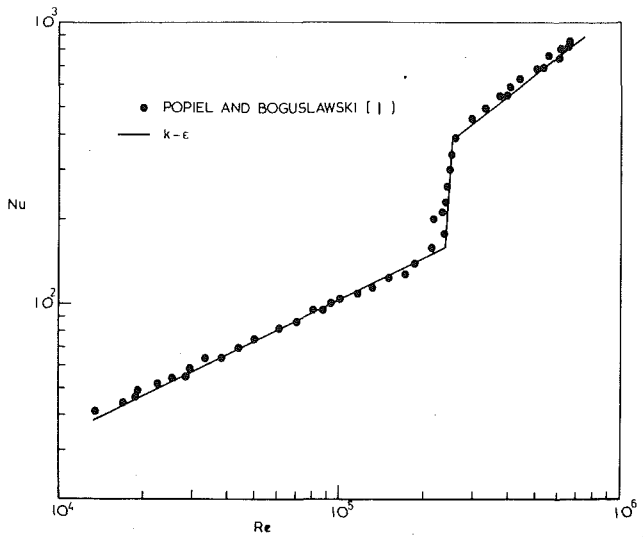

Fig. 1 Local heat transfer from a spinning disk in still air

Acknowledgment

This research has been supported by the Science Research Council through Grant No. B/RG/1863. The author is grateful to Dr. B. E. Launder for his comments.

References

1 Launder, B. E., and Sharma, B. I., "Application of the Energy-Dissipation Model of Turbulence to the Calculation of Flow Near a Spinning Disc," *Letters in Heat and Mass Transfers*, 1, 2, 1974, p. 131.

2 Koosinlin, M. L., "Turbulent Transport Properties in Swirling Tow Dimensional Boundary Layers," PhD thesis, University of London, England, 1974.

3 McComas, S. T., and Hartnett, J. P., "Temperature Profiles and Heat Transfer Associated With a Single Disc Rotating in Still Air," Fourth International Heat Transfer Conference, Paris-Versailles, III, FC7.7, 1976.

4 Popiel, Cz. O., and Boguslawski, L., "Local Heat Transfer Coefficients on the Rotating Disc in Still Air," *International Journal of Heat and Mass Transfer*, Vol. 18, 1975, p. 167.

5 Kestin, J., and Richardson, P. D., "Heat Transfer Across Turbulent, Incompressible Boundary Layers." *International Journal of Heat and Mass Transfer*, Vol. 6, 1963, p. 147.

6 Patankar, S. V., and Spalding, D. B., *Heat and Mass Transfer in Boundary Layers*, Intertext Books, London, 1970.

7 Jones, W. P., and Launder, B. E., "The Calculation of Low Reynolds Number Phenomena With a Two Equation Model of Turbulence." *International Journal of Heat and Mass Transfer*, Vol. 16, pp. 1189, 1973.

8 Launder, B. E., Priddin, C. H. and Sharma, B. I., "The Calculation of Turbulent Boundary Layers on Spinning and Curved Surfaces," Paper number 493 FMW, in Press, *Journal of Fluids Engineering*, 1976.

9 Sharma, B. I., Unpublished work, Mechanical Engineering Department. Imperial College of Science and Technology, London, 1973.

10 Koosinlin, M. L., Launder, B. E. and Sharma, B. I., "Prediction of Momentum, Heat and Mass Transfer in Swirling, Turbulent Boundary Layers." JOURNAL OF HEAT TRANSFER, TRANS. ASME Series C, Vol. 96, 1974, p. 204.

An Experimental Study of Heat Transfer to Developing Water Film Flow Over Cylinders

P. H. Oosthuizen[1] and T. Cheung[2]

Nomenclature

c = specific heat
D_h = hydraulic diameter of film, $2(R_0^2 - R_c^2)/R_c$
F_r = Froude number, u_0^2/gD_h
g = gravitational acceleration
h = local heat transfer coefficient
$\overline{h}$ = dimensionless heat transfer coefficient, $(h/k)(\nu^2/g)^{1/3}$
$\overline{h}_{\text{min}}$ = minimum value of $\overline{h}$ along surface
$\overline{h}_{fd}$ = constant value of $\overline{h}$ in fully developed flow
k = thermal conductivity
P_r = Prandtl number
q_w = local heat transfer rate at wall
R_c = radius of cylindrical surface
R_e = Reynolds number, $u_0 D_h/\nu$
R_0 = radius of outer surface of film
R_x = Reynolds number based on x
$\text{R}_{x\text{min}}$ = value of R_x at which $\overline{h}_{\text{min}}$ occurs

[1] Professor, Department of Mechanical Engineering, Queen's University, Kingston, Ontario, Canada.

[2] Research Assistant, Department of Mechanical Engineering, Queen's University, Kingston, Ontario, Canada.

Contributed by the Heat Transfer Division of THE AMERICAN SOCIETY OF MECHANICAL ENGINEERS. Manuscript received by the Heat Transfer Division June 30, 1976.

T = temperature
T_m = local mean temperature in film
T_w = wall temperature
T_0 = initial uniform temperature of film
u_0 = initial uniform velocity in film
x = coordinate down surface
$\bar{x} = x/D_h$
$\bar{x}_{min}$ = value of $\bar{x}$ at which $\bar{h}_{min}$ occurs
$\Delta\bar{x}_{tran}$ = transition length as defined in Fig. 4
μ = coefficient of viscosity
ν = kinematic viscosity

Introduction

In some industrial processes, cooling is achieved by running a liquid film over a cylindrical surface, the flow originating at a shaped nozzle so that the initial velocity distribution is essentially uniform. Local heat transfer rates in this type of flow have been investigated in the present study. Since the flow originates from a shaped nozzle, it is to be suspected that the flow near the nozzle will be laminar, that unsteady "wavy" flow will develop and transition to turbulent flow will then occur. Because of the presence of these various types of flow in the film, comparatively large variations in the local heat transfer rate along the surface are to be expected.

If the flow is assumed to be axially symmetrical, the local heat transfer coefficient at any distance x down the surface from the nozzle will be given, in general, by

$$h = \text{function}\ (\rho, u_0, D_h, \mu, k, g, c, R_c, x) \tag{1}$$

It should be noted that the local heat transfer coefficient is based on the difference between the local wall temperature, T_w, and the local mean temperature in the film, T_m. In this respect, it differs from the heat transfer coefficient as usually defined for evaporating or condensing film flow where the outer surface of the film is essentially at the boiling temperature of the liquid and the difference between the wall temperature and the boiling temperature is, therefore, used in defining h. In film flow with no phase change, which is the situation being studied in the present work, the temperature of the outer edge of the film is not, of course, known.

Applying dimensional analysis to equation (1) and rearranging the result in terms of conventionally used dimensionless parameters gives

$$\bar{h} = \text{function}\ (\mathrm{R}_c, \mathrm{P}_r, \bar{x}, \mathrm{F}_r, R_c/D_h) \tag{2}$$

Note that R_c as defined in the Nomenclature is equivalent to $4\Gamma/\mu$ where Γ is the mass flow rate per unit surface length.

Far downstream of the nozzle, the flow in the film becomes fully developed and when this state is reached $\bar{h}$ will cease to vary with distance along the surface, i.e., with $\bar{x}$, and will cease to depend on the initial conditions at the nozzle exit and thus must cease to depend on F_r.

Most previous work on heat transfer to falling films has been concerned with evaporating films, [1, 2][3] reviewing much of this work. In most of these studies the film has originated at a weir or similar device so that the nature of the flow in the development region is very different from the flow being considered in the present study. Previous work on heat transfer to nonevaporating films is reviewed in reference [3], most available measurements being for fully developed films.

Apparatus

The apparatus used in the present study is shown diagrammatically in Fig. 1. The main reservoir, S_1, contained distilled water. A cooling coil, through which tap water was circulated, in this tank kept the distilled water at a constant temperature during a test. The water from S_1 was pumped to the upper vessel S_2 from which it drained through the nozzle, N, and over the outer surface of the heated cylinder, C, into vessel S_3 and from there back into S_1. The water level in S_2 was controlled by means of valve V_1, the pump running at constant speed. The water flow rate and, hence, the initial velocity at the nozzle exit plane, could be found by closing valve V_2 and measuring the rate at which water collected in S_3. Alternatively the initial velocity could be calculated from the measured water depth, H, in S_2 by assuming that there was no losses across the nozzle. The results given by the two procedures were essentially identical.

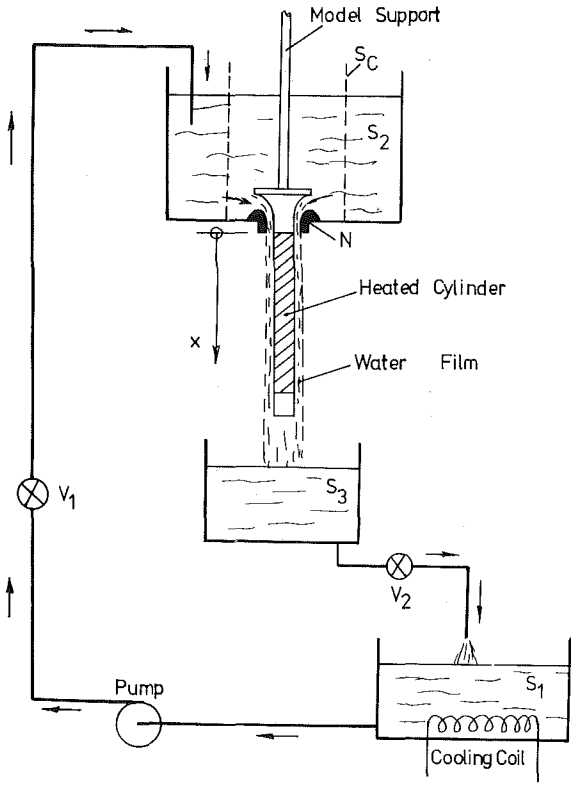

Fig. 1 Layout of apparatus

Four nozzles were used in the present study, these having diameters, D, of 38.1, 34.9, 31.8, 28.6 mm. They were made of brass and were cleaned frequently during the test program. This, together with the use of the screen, S_c, around the nozzle as shown in Fig. 1 and careful positioning of the model so that it was concentric with the nozzle, insured that the water film on the model was nonswirling and uniform around its circumference.

Two models were used, these having diameters of 25.4 and 19.1 mm. Both models were about 370-mm long. The cores of the models were made of plexiglas with copper electrode blocks near the top and bottom. A 0.025-mm thick nickel sheet was bonded to the surface of the plexiglas between the electrodes and the ends of this nickel sheet were clamped between the electrodes and the plexiglas with sufficient pressure to insure good electrical contact. Heating was then achieved by passing an electrical current through the nickel sheet, contact to the supply being made through the electrodes. A series of thermocouples were mounted in the plexiglas with their junctions at the surface beneath the nickel sheet and in contact with it, the thermocouple leads being brought out internally through the bottom of the model. The model was mounted with the top of the heated section on the nozzle exit plane. Estimates were made of the temperature drop across the nickel sheet and this was found to be negligible. It was also found that the thermocouples junctions were in sufficiently good contact with the underside of the nickel sheet for them to give a reading essentially equal to the local surface temperature of the sheet.

In order to obtain the heat transfer coefficients, the heat transfer rate was found from the measured electrical power dissipation, the

[3] Numbers in brackets designate References at end of technical note.

Table 1

TEST NO.	NOZZLE DIAMETER mm	MODEL DIAMETER mm	R_e	F_r	P_r	$\frac{D_h}{R_c}$
1	34.1	25.4	33,670	6.40	5.39	1.781
2	38.1	25.4	56,800	6.72	5.45	2.500
3	38.1	25.4	46,450	4.56	5.49	2.500
4	34.1	25.4	46,620	13.03	5.57	1.781
5	34.1	25.4	37,510	8.31	5.52	1.781
6	28.6	25.4	24,850	14.58	5.54	1.125
7	28.6	25.4	20,110	9.42	5.51	1.125
8	28.6	25.4	28,460	17.60	5.29	1.125
9	28.6	25.4	31,780	21.87	5.28	1.125
10	28.6	25.4	25,770	14.04	5.21	1.125
11	28.6	19.1	62,600	5.93	5.10	3.556
12	28.6	19.1	70,780	7.65	5.10	3.556

surface temperature was obtained from the thermocouple readings and the local mean temperature in the water film at any distance down the model was found by applying an energy balance up to that point, the initial water temperature being measured in S_2.

Experimental Results

All tests were carried out with heating currents that gave an average model surface temperature of about 5°C above the inlet water temperature, the actual local surface temperature depending, of course, on the distance from the nozzle, on the nozzle size and on the initial velocity. Although a large number of tests were carried out, attention will here be restricted to those listed in Table 1, these being typical of all the tests. In evaluating the parameters listed in this table, fluid properties have all been evaluated at the mean water temperature in the film. From Table 1, it will be seen that the results cover a Reynolds number, R_e, range of approximately 20,000–70,000, a Froude number, F_r, range of about 5–20 and a Prandtl number, P_r, range of about 5.1–5.6. Significant effects due to variations in P_r, are not, therefore to be expected.

Typical variations of dimensionless heat transfer coefficient with distance along the surface are shown in Fig. 2, the general form of this variation being the same in all cases. The heat transfer coefficient drops from a high value near the nozzle exit to a minimum value, then rises quite sharply and then levels off, rising only slowly with distance along the surface. Thus, the heat transfer coefficient distribution can be split into three regions. The first, from the nozzle exit to the point of minimum heat transfer, corresponds to laminar and wavy laminar flow in the film, the wavy flow being visually observed. The second, the region of comparatively rapid rise in the value of the heat transfer coefficient downstream of the point where it passes through a minimum, corresponds to transitional flow in the film, while the third region, that involving a comparatively slow rise in the value of heat transfer coefficient, corresponds to fully turbulent flow, the rise being due to the developing nature of this flow. The values of $\bar{h}$ tend, of course, to the constant values applicable to fully developed turbulent flow but the length of model used in the present work was not sufficient for this fully developed state to be reached.

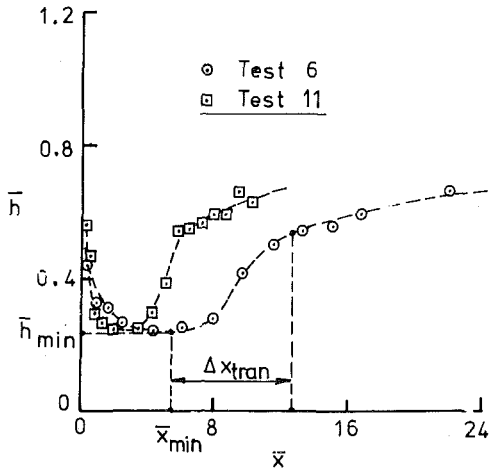

Fig. 2 Typical variations of heat transfer coefficient with distance down model

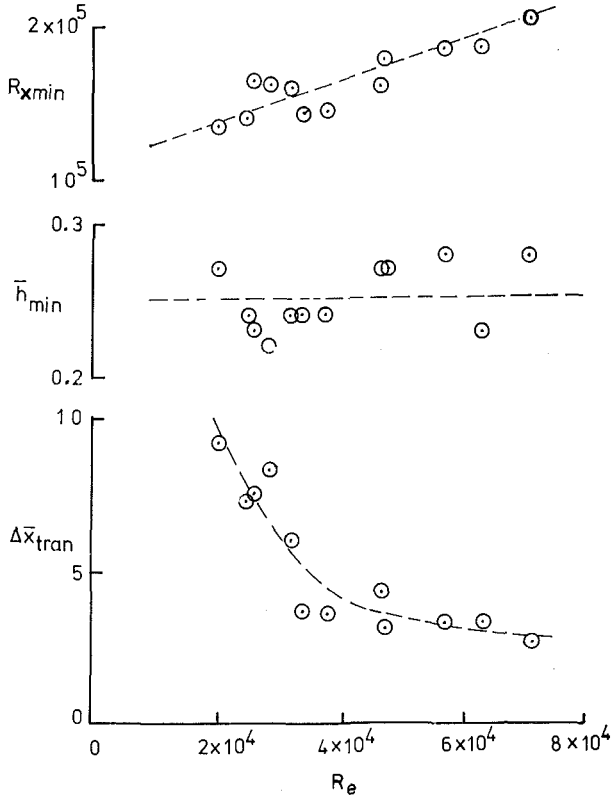

Fig. 3 Variation of derived parameters with Reynolds number

Three important parameters connected with the observed heat transfer coefficient distribution, are, therefore

(i) The minimum value of the dimensionless heat transfer coefficient, $\bar{h}_{min}$.

(ii) The distance downstream of the nozzle at which this minimum heat transfer coefficient occurs, $\bar{x}_{min}$.

(iii) The transition length, $\Delta\bar{x}_{tran}$, as defined in Fig. 2.

Values of these three parameters have been determined from the experimentally obtained variation of $\bar{h}$ with $\bar{x}$ for each test. Because this variation is comparatively flat in the region of $\bar{h}_{min}$ and towards the end of the transition region, the accuracy with which the values of the second and third parameters listed in the foregoing could be determined was not high. The variation of the three parameters with R_e is shown in Fig. 3. All three will, in general, depend on R_e, F_r, and R_c/D_h. The effects of F_r and R_c/D_h are, however, expected to be small, since changes in F_r will mainly influence the flow close to the nozzle and because R_c/D_h, which is a measure of curvature effects, is comparatively close to 1.

From Fig. 3 it will be seen that $\bar{h}_{min}$ is a constant given approximately by

$$\bar{h}_{min} = 0.25 \tag{4}$$

Now it is expected from experience with other similar flows that transition will occur when the Reynolds number based on distance down the surface from the nozzle, i.e.,

$$R_x = \frac{u_0 x}{\nu} = R_e \bar{x} \quad (5)$$

reaches a critical value. The variation of R_x at which $\bar{h}_{min}$ occurs, i.e., $R_{x\,min}$, rather than $\bar{x}_{min}$ itself is therefore shown in Fig. 3. As expected because of the difficulty in accurately locating $\bar{x}_{min}$, the scatter is quite large although there appears to be no dependency on F_r and R_c/D_h. From this figure, it will be seen that transition occurs when R_x is between 10^5 and 2×10^5 over the Reynolds number range covered by the present tests. The actual variation of $R_{x\,tran}$ with R_e is approximately linear and given by

$$R_{x\,min} = 110{,}000 + 1.25\,R_e \quad (6)$$

From the variation of the transition length, $\Delta\bar{x}_{tran}$, with R_e shown in Fig. 3, it will be seen that at the higher values of R_e, $\Delta\bar{x}_{tran}$ appears to be approximately constant but increases with decreasing R_e.

Conclusions

(1) When the cooling film originates at a shaped nozzle, large variations in the heat transfer rate along the surface arise due to changes in the type of flow within the film.

(2) Empirical equations have been developed to describe the main characteristics of the heat transfer coefficient variation.

Acknowledgments

This work was supported by the National Research Council of Canada.

References

1 Chun, K. R., and Seban, R. A. "Heat Transfer to Evaporating Liquid Films," JOURNAL OF HEAT TRANSFER, TRANS. ASME, Series C, Vol. 93, No. 4, Nov. 1971, pp. 391–396.

2 Seban, R. A., and Faghri, A., "Evaporation and Heating With Turbulent Falling Liquid Films," JOURNAL OF HEAT TRANSFER, TRANS. ASME, Series C, Vol. 98, No. 2, May 1976, pp. 315–318.

3 Pike, J. G., Smith, G. A. J., and Thompson, R. G., "Some Experimental Measurements of Heat Transfer in Thin Liquid Films," *Proceedings 4th International Heat Transfer Conference*, Paper FC1.12, 1970.

Heat Transfer in an Axisymmetric Separated and Reattached Flow Over a Longitudinal Blunt Circular Cylinder

Terukazu Ota,[1] and Nobuhiko Kon,[2]

Nomenclature

a, d = cylinder radius and diameter
C_f = skin friction coefficient
h = heat transfer coefficient, $q/(T_w - T_\infty)$
h_R = heat transfer coefficient at reattachment point
ℓ = distance from leading edge to reattachment point
Nu = Nusselt number, hd/λ
T_∞, U_∞ = temperature and velocity at upstream uniform flow
q = heat flux per unit area from wall to fluid
Re = Reynolds number, $U_\infty d/\nu$
T, T_w = temperature and wall temperature
U, U_m = x-component of local and free stream velocity
x = axial distance from leading edge
y = radial distance from cylinder surface
δ_d = displacement thickness, $\int_0^\infty (1 + y/a)(1 - U/U_m)dy$
δ_T = thermal boundary layer thickness, $\int_0^\infty (1 + y/a)(T - T_\infty)/(T_w - T_\infty)dy$
λ = thermal conductivity of air
ν = kinematic viscosity of air

Introduction

Prediction of heat transfer in the separated, reattached, and redeveloped regions of incompressible or subsonic flow is very important in relation to various engineering aspects. We have presented an experimental study of the heat transfer in the separated, reattached, and redeveloped flow over a blunt flat plate [1].[3] Seban [2] and Solntsev [3] have investigated three-dimensional flows; however, two-dimensional flows or internal flows have been the subject of study in the previous works which have been reviewed by Fletcher, et al. [4].

The purpose of the study reported in this note was to investigate the heat transfer characteristics in the separated, reattached, and redeveloped regions for longitudinal incompressible air flow along a blunt circular cylinder. The development of the flow is made clear through measurements of velocity and temperature in the separated, reattached, and redeveloped regions. The correlations of the heat transfer characteristics between the present axisymmetric flow over a longitudinal blunt circular cylinder and the two-dimensional flow over a flat plate with blunt leading edge [1] are also discussed. The flow characteristics of the present flow configuration have already been reported in an earlier paper [5]. The heat transfer characteristics are discussed in this note. The coordinate system employed is the same as that in [5].

Experimental Apparatus and Technique

The wind tunnel used in the experiments is the same as that employed in the previous work by Ota [5]. The test circular cylinder is 38 mm in diameter and 504-mm long. Two stainless steel sheets (0.05-mm thick and 59-mm wide), which cover the whole circumference of cylinder except two slits, are stuck to a polyvinyl chloride pipe of 38-mm dia and 3.8-mm thick and they are electrically connected at the leading edge through a brass circular plate 3-mm thick, and the inside of the pipe is filled with polyurethane as insulator. The leading edge of the cylinder is sharply cut at 90 deg in order that the flow always separates there over the whole circumference. The cylinder was set at the center of the working section and was supported to a strut at the most downstream section, and minute attention was paid in order not to injure the axisymmetry of the flow and not to vibrate the cylinder. The temperatures on the heating surface were measured with 0.07-mm copper-constantan thermocouples soldered on the back of the stainless steel sheet. 20 thermocouples are located in the axial direction along a generatrix of the cylinder; furthermore three thermocouples are added to the back of the polyvinyl chloride pipe in order to estimate the heat loss from the test surface to the support. The positions of thermocouples will be clear in a following figure which shows the present experimental results. The experimental procedure was almost the same as that employed in the earlier study of the two-dimensional flow [1]. The experiments were conducted under the condition of constant heat flux. The temperature differences between the wall and the free stream were at most about 40 °C which occurred at the most downstream section. These temperature differences did not materially affect the flow characteristics compared with the previous results [5]. The thermal conductivity of air and the kinematic

[1] Asst. Professor, Department of Mechanical Engineering, Akita University, Akita, Japan.

[2] Technical Assistant, Department of Mechanical Engineering, Akita University, Akita, Japan.

Contributed by the Heat Transfer Division of THE AMERICAN SOCIETY OF MECHANICAL ENGINEERS. Manuscript received by the Heat Transfer Division August 30, 1976.

[3] Numbers in brackets designate References at end of technical note.

$$R_x = \frac{u_0 x}{\nu} = R_e \bar{x} \quad (5)$$

reaches a critical value. The variation of R_x at which $\bar{h}_{min}$ occurs, i.e., $R_{x\,min}$, rather than $\bar{x}_{min}$ itself is therefore shown in Fig. 3. As expected because of the difficulty in accurately locating $\bar{x}_{min}$, the scatter is quite large although there appears to be no dependency on F_r and R_c/D_h. From this figure, it will be seen that transition occurs when R_x is between 10^5 and 2×10^5 over the Reynolds number range covered by the present tests. The actual variation of $R_{x\,tran}$ with R_e is approximately linear and given by

$$R_{x\,min} = 110{,}000 + 1.25\,R_e \quad (6)$$

From the variation of the transition length, $\Delta\bar{x}_{tran}$, with R_e shown in Fig. 3, it will be seen that at the higher values of R_e, $\Delta\bar{x}_{tran}$ appears to be approximately constant but increases with decreasing R_e.

Conclusions

(1) When the cooling film originates at a shaped nozzle, large variations in the heat transfer rate along the surface arise due to changes in the type of flow within the film.

(2) Empirical equations have been developed to describe the main characteristics of the heat transfer coefficient variation.

Acknowledgments

This work was supported by the National Research Council of Canada.

References

1 Chun, K. R., and Seban, R. A. "Heat Transfer to Evaporating Liquid Films," JOURNAL OF HEAT TRANSFER, TRANS. ASME, Series C, Vol. 93, No. 4, Nov. 1971, pp. 391–396.

2 Seban, R. A., and Faghri, A., "Evaporation and Heating With Turbulent Falling Liquid Films," JOURNAL OF HEAT TRANSFER, TRANS. ASME, Series C, Vol. 98, No. 2, May 1976, pp. 315–318.

3 Pike, J. G., Smith, G. A. J., and Thompson, R. G., "Some Experimental Measurements of Heat Transfer in Thin Liquid Films," *Proceedings 4th International Heat Transfer Conference*, Paper FC1.12, 1970.

Heat Transfer in an Axisymmetric Separated and Reattached Flow Over a Longitudinal Blunt Circular Cylinder

Terukazu Ota,[1] and Nobuhiko Kon,[2]

Nomenclature

a, d = cylinder radius and diameter
C_f = skin friction coefficient
h = heat transfer coefficient, $q/(T_w - T_\infty)$
h_R = heat transfer coefficient at reattachment point
ℓ = distance from leading edge to reattachment point
Nu = Nusselt number, hd/λ
T_∞, U_∞ = temperature and velocity at upstream uniform flow
q = heat flux per unit area from wall to fluid
Re = Reynolds number, $U_\infty d/\nu$
T, T_w = temperature and wall temperature
U, U_m = x-component of local and free stream velocity
x = axial distance from leading edge
y = radial distance from cylinder surface
δ_d = displacement thickness, $\int_0^\infty (1 + y/a)(1 - U/U_m)dy$
δ_T = thermal boundary layer thickness, $\int_0^\infty (1 + y/a)(T - T_\infty)/(T_w - T_\infty)dy$
λ = thermal conductivity of air
ν = kinematic viscosity of air

Introduction

Prediction of heat transfer in the separated, reattached, and redeveloped regions of incompressible or subsonic flow is very important in relation to various engineering aspects. We have presented an experimental study of the heat transfer in the separated, reattached, and redeveloped flow over a blunt flat plate [1].[3] Seban [2] and Solntsev [3] have investigated three-dimensional flows; however, two-dimensional flows or internal flows have been the subject of study in the previous works which have been reviewed by Fletcher, et al. [4].

The purpose of the study reported in this note was to investigate the heat transfer characteristics in the separated, reattached, and redeveloped regions for longitudinal incompressible air flow along a blunt circular cylinder. The development of the flow is made clear through measurements of velocity and temperature in the separated, reattached, and redeveloped regions. The correlations of the heat transfer characteristics between the present axisymmetric flow over a longitudinal blunt circular cylinder and the two-dimensional flow over a flat plate with blunt leading edge [1] are also discussed. The flow characteristics of the present flow configuration have already been reported in an earlier paper [5]. The heat transfer characteristics are discussed in this note. The coordinate system employed is the same as that in [5].

Experimental Apparatus and Technique

The wind tunnel used in the experiments is the same as that employed in the previous work by Ota [5]. The test circular cylinder is 38 mm in diameter and 504-mm long. Two stainless steel sheets (0.05-mm thick and 59-mm wide), which cover the whole circumference of cylinder except two slits, are stuck to a polyvinyl chloride pipe of 38-mm dia and 3.8-mm thick and they are electrically connected at the leading edge through a brass circular plate 3-mm thick, and the inside of the pipe is filled with polyurethane as insulator. The leading edge of the cylinder is sharply cut at 90 deg in order that the flow always separates there over the whole circumference. The cylinder was set at the center of the working section and was supported to a strut at the most downstream section, and minute attention was paid in order not to injure the axisymmetry of the flow and not to vibrate the cylinder. The temperatures on the heating surface were measured with 0.07-mm copper-constantan thermocouples soldered on the back of the stainless steel sheet. 20 thermocouples are located in the axial direction along a generatrix of the cylinder; furthermore three thermocouples are added to the back of the polyvinyl chloride pipe in order to estimate the heat loss from the test surface to the support. The positions of thermocouples will be clear in a following figure which shows the present experimental results. The experimental procedure was almost the same as that employed in the earlier study of the two-dimensional flow [1]. The experiments were conducted under the condition of constant heat flux. The temperature differences between the wall and the free stream were at most about 40 °C which occurred at the most downstream section. These temperature differences did not materially affect the flow characteristics compared with the previous results [5]. The thermal conductivity of air and the kinematic

[1] Asst. Professor, Department of Mechanical Engineering, Akita University, Akita, Japan.

[2] Technical Assistant, Department of Mechanical Engineering, Akita University, Akita, Japan.

Contributed by the Heat Transfer Division of THE AMERICAN SOCIETY OF MECHANICAL ENGINEERS. Manuscript received by the Heat Transfer Division August 30, 1976.

[3] Numbers in brackets designate References at end of technical note.

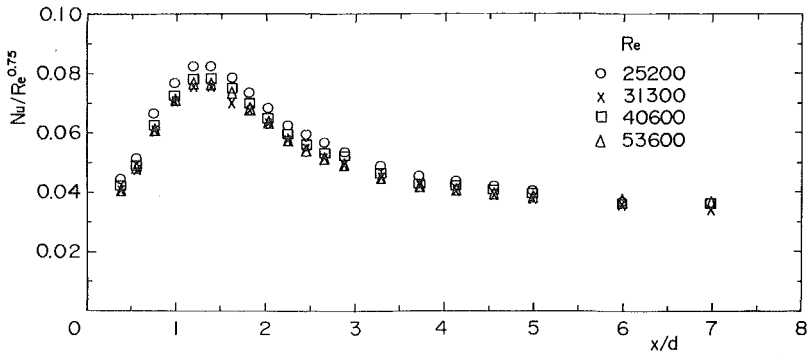

Fig. 1 Local Nusselt number distribution

viscosity are estimated at the upstream temperature. The upstream velocity U_∞ ranges from 9.7 m/s to 22.6 m/s and the corresponding Reynolds number Re from 24900 to 53600.

Before making the heat transfer study, measurements were made on the pressure distributions on the cylinder surface and the velocity and pressure profiles in the separated, reattached, and redeveloped flow regions, and these results in general confirmed the axisymmetry of the flow. In these preliminary measurements of velocity and pressure, use was made of a pitot tube having an elliptic nose (0.80 × 0.46 mm) and of a 0.80-mm static tube. The velocity and temperature measurements were made with a constant temperature hot-wire anemometer with a linearizer and a temperature probe consisting of a 0.07-mm copper-constantan thermocouple. The single wire probe used was made of 0.005-mm tungsten wire and was calibrated in the upstream uniform flow. The hot-wire was mounted at 90 deg to the flow direction in the plane parallel to the cylinder surface. Thus only the longitudinal component of velocity was determined from linearized mean voltage reading, which was corrected for temperature effects following the equation,

$$E_\infty = E_a(T_{hw} - T_\infty)^2/(T_{hw} - T_a)^2 \tag{1}$$

in which T_{hw} is the temperature of hot-wire and E_a denotes the mean voltage reading at a point of temperature T_a, and E_∞ corresponds to that at the same point but at temperature T_∞ at which the calibrations are made. No corrections were made for the tunnel wall effects in the present study.

Results and Discussion

Distributions of the heat transfer coefficient are shown in the form of $Nu/Re^{0.75}$ for various Reynolds numbers in Fig. 1. The heat transfer coefficient increases sharply to the downstream in the separated flow region and attains a maximum at about $x/d = 1.4$, and that is independent of the Reynolds number investigated in the present study. This position is confirmed with a tuft, to be the reattachment region and also is a point where the skin friction coefficient becomes zero, which will be discussed later. Therefore, the Nusselt number at $x/d = 1.4$ is hereafter called the reattachment Nusselt number. The heat transfer coefficient decreases downstream from the reattachment region and approaches a value for the turbulent boundary layer on the longitudinal circular cylinder without separation and reattachment. The correlation of the reattachment Nusselt number with Reynolds number obtained by means of the method of least square is

$$h_R d/\lambda = 0.0804\ \mathrm{Re}^{0.747} \tag{2}$$

The power of Reynolds number is almost equal to 0.75, therefore the Nusselt number distributions are shown in the form of $Nu/Re^{0.75}$ in Fig. 1. $Nu/Re^{0.75}$ is independent of the Reynolds number with some scatter and is a function of only the distance from the leading edge as seen in the figure. The power of Reynolds number 0.747 is a little larger than the value of 0.709 for a blunt flat plate [1] and of 2/3 which is found in previous works, for example [6]. This difference may partly be due to the three dimensional effects of flow, however the experimental scatters may also be a factor. When the distance from the leading edge to the reattachment point ℓ is used as the characteristic length of the Reynolds and Nusselt numbers, the following expressions of the reattachment Nusselt number are obtained,

$$h_R \ell/\lambda = 0.0875\ (U_\infty \ell/\nu)^{0.747} \tag{3}$$

for the present axisymmetric flow and

$$h_R \ell/\lambda = 0.143\ (U_\infty \ell/\nu)^{0.709} \tag{4}$$

for the flat plate flow [1]. Present results of equation (3) are smaller by 7–10 percent than those of equation (4) for the two-dimensional flow, but they are in good agreement with each other in the Reynolds number range studied. In the redeveloped flow region downstream of reattachment, a following empirical expression for the correlation of the Nusselt number with the Reynolds number is obtained by means of the method of least square,

$$hx/\lambda = 0.109\ (U_\infty x/\nu)^{0.701} \qquad (x/d \geq 3.3) \tag{5}$$

This result agrees well with that for the two-dimensional flow. However these results are about 30–50 percent larger than the well-known Colburn equation, and the present high heat transfer coefficient may be produced from the high turbulence intensity as compared with that of the normal boundary layer without separation and reattachment [5]. It could be concluded from these discussions that the strong similarity exists between the present axisymmetric flow and the two-dimensional one.

The velocity and temperature distributions were measured under a fixed upstream velocity and a fixed heat flux. The flow characteristics obtained in the present study are almost the same as those obtained under the non-heating condition in the earlier work [5]. Therefore detailed descriptions are avoided in this note. The temperature profiles in the separated and reattached flow regions are shown in Fig. 2 and those in the redeveloped region in Fig. 3. In the separated region, a large reverse flow exists [5] and the temperature profile shows a peculiar deviation from other regions, that is, the temperature decreases sharply in two regions; in the neighborhoods of the wall and the separated streamline where the strong shear layers exist. Similar behaviors are detected in the work of the downward step [7]. The temperature profile is found to become nearly similar at about 2.5–3 cylinder diameters downstream from the leading edge with some scatter near the wall. This distance is much shorter than that for the velocity profile [5]. It could be inferred from this fact that after the reattachment of flow, the thermal boundary layer develops much quicker than the flow boundary layer. In Figs. 2 and 3, the thermal and flow boundary layer characteristics are included. The thermal boundary layer thickness is much smaller than the displacement thickness, and it is relatively large in the separated and reattached regions and after reattachment, decreases in the downward direction up to about $x/d = 3$ and subsequently increases in the same direction.

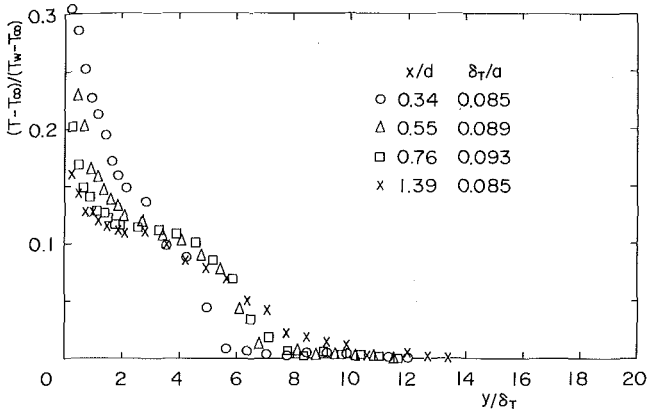

Fig. 2 Temperature profile in the separated and reattached flow regions, Re = 45000, q = 1.63 kW/m^2

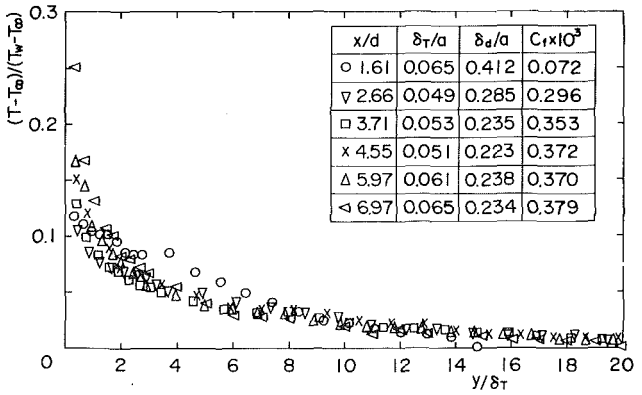

Fig. 3 Temperature profile in the redeveloped flow region, Re = 45000, q = 1.63 kW/m^2

It is interesting to note that the point at which the thermal boundary layer thickness becomes nearly minimum is quite close to that where the temperature profile attains near similarity. Present skin friction coefficients whose calculating procedure is described in [5] agree well with the data obtained under the non-heating condition. A point of zero skin friction coefficient (extrapolated) occurs at about $x/d = 1.4$ and this position is exactly the same as that of maximum heat transfer coefficient as already shown in Fig. 1. In the earlier paper [5], the reattachment point is said to occur at $x/d = 1.6$, however this value is determined as an average value of those obtained with three different methods; tuft probe exploration, zero skin friction, and nearly maximum pressure on the surface, and the value estimated with zero skin friction is about $x/d = 1.4$ as described there. It might be concluded that the heat transfer coefficient takes its maximum at the reattachment point where the skin friction attains zero, therefore it may not be acceptable to estimate the heat transfer coefficient at the reattachment point from the skin friction coefficient with existing analogies between them, as already pointed out by Spalding [8].

Acknowledgments

The authors express their sincere thanks to Mr. Tatsuo Yagi and Mr. Kenzo Watanabe for their assistance in the experiments.

References

1 Ota, T., and Kon, N., "Heat Transfer in the Separated and Reattached Flow on a Blunt Flat Plate," JOURNAL OF HEAT TRANSFER, TRANS. ASME, Series C, Vol. 96, 1974, pp. 459–462.

2 Seban, R. A., and Caldwell, G. L., "The Effect of a Spherical Protuberance on the Local Heat Transfer to a Turbulent Boundary Layer," JOURNAL OF HEAT TRANSFER, TRANS. ASME, Series C, Vol. 90, 1968, pp. 408–412.

3 Solntsev, V. P., Luzhanskii, B. E., and Kryukov, V. N., "An Investigation of Heat Transfer in the Turbulent Separation Zones in the Vicinity of Sudden Steps," *Heat Transfer-Soviet Research*, Vol. 5, 1973, pp. 122–128.

4 Fletcher, L. S., Briggs, D. C., and Page, R. H., "Heat Transfer in Separated and Reattached Flows: an Annotated Review," *Israel Journal of Technology*, Vol. 12, 1974, pp. 236–261.

5 Ota, T., "An Axisymmetric Separated and Reattached Flow on a Longitudinal Blunt Circular Cylinder," *Journal of Applied Mechanics*, TRANS. ASME, Series E, Vol. 42, 1975, pp. 311–315.

6 Krall, K. M., and Sparrow, E. M., "Turbulent Heat Transfer in the Separated, Reattached, and Redevelopment Regions of a Circular Tube," JOURNAL OF HEAT TRANSFER, TRANS. ASME, Series C, Vol. 88, 1966, pp. 131–136.

7 Aung, W., and Goldstein, R. J., "Temperature Distribution and Heat Transfer in a Transitional Separated Shear Layer," *Heat Transfer 1970*, Vol. 2, Elsevier Publishing Co., Amsterdam, 1970.

8 Spalding, D. B., "Heat Transfer From Turbulent Separated Flows," *Journal of Fluid Mechanics*, Vol. 27, 1967, pp. 97–109.

journal of heat transfer

discussion

Reduction of Heat Transfer to Gun Barrels by Wear-Reducing Additives[1]

E. G. Plett.[2] The problem of how to evaluate the heat being transferred to the walls of a vessel containing high temperature gases for a very short time period presents itself from time to time. Measurements of temperature rise within the wall together with appropriate analysis can be used for this purpose. Care must, however, be exercised to be sure that no unnecessary assumptions are made which lead to erroneous computations. One such error was made in the Brosseau-Ward paper. This note is intended to point out how the reasoning in that paper was erroneous with respect to the heat transfer computation, and to point out the correct criterion for detecting the cessation of heat input. It is only fair to add that the error mentioned probably did not change the conclusions of the paper, and that the paper is a very worthwhile contribution to the study of wear in gun barrels.

The statement under scrutiny is that when the thermocouple nearest the gun bore had reached its maximum temperature, no further heat was transferred to the barrel from the hot gases. This may be so in isolated cases, but is not generally true. This can be demonstrated by solving the one-dimensional heat conduction equations for a transient case. The point to be illustrated is that the temperature in the slab near the surface, or at the surface, could be falling with time while heat is flowing into the slab. This simply means that heat is flowing away from the surface (into the slab interior) faster than it is being introduced to the surface from the hot gases. There can, however, still be a substantial heat transfer rate to the solid while the surface temperature is falling.

Consider the one-dimensional, nonsteady heat conduction in a planar slab or cylinder,

$$\frac{1}{\alpha}\frac{\partial T}{\partial t} = \frac{\partial^2 T}{\partial x^2} \qquad \text{(slab)} \tag{1}$$

$$\frac{1}{\alpha}\frac{\partial T}{\partial t} = \frac{1}{r}\frac{\partial}{\partial r}\left(r\frac{\partial T}{\partial r}\right). \qquad \text{(cylinder)} \tag{2}$$

By simply integrating equation (1), it can be shown that for a thick slab with zero temperature gradient at some distance b from the surface, the heat flux at the surface is

$$\left.\frac{\partial T}{\partial x}\right|_{x=0} = -\left[\frac{1}{\alpha}\frac{\partial}{\partial t}\int_{x=0}^{x=b} T\,dx + \left.\frac{\partial T}{\partial x}\right|_{x=b}\right] \tag{3}$$

This equation illustrates that for $\partial T/\partial x = 0$, at $x = b$, the heat flow ends when the time derivative of the integral of the temperature over the slab thickness is zero, not when the time derivative of the surface temperature is zero. Similarly, integration of equation (2) from r_i to r_0 yields

$$\left.\frac{\partial T}{\partial r}\right|_{r=r_i} = -\frac{1}{r_i}\left[\frac{1}{\alpha}\frac{\partial}{\partial t}\int_{ri}^{r0} Tr dr + r_0\left.\frac{\partial T}{\partial r}\right|_{r=r_0}\right] \tag{4}$$

This also clearly shows that the time of peak temperature for the inner surface does not coincide with the cessation of heat flow into the cylinder, as stated by Brosseau and Ward. The time for which the temperature ceases to rise at the surface is the time for which the heat transfer into the slab (or cylindrical solid) balances the heat flow to the slab from the outside. This is a common phenomenon in shock-tube or gun-tube flows for which the initial heating rate is high, then gradually decreases as the gases cool. Heat continues to flow into the solid, however, as long as the spatial temperature gradient is such that the temperature just beneath the surface is less than the surface temperature. Therefore, the correct criterion for detecting the cessation of heat input is when the surface spatial temperature gradient is zero.

Authors' Closure

Professor Plett is correct when he asserts that a thermocouple near the bore surface reaching its maximum temperature is not a necessary and sufficient condition for cessation of all heat transfer into the gun barrel.

We merely wish to demonstrate in this reply that the assumption we made, namely, that no significant heat transfer occurred after 100-ms is valid. If the total heat transfer estimates are made with the temperature versus radius curve at 100 ms extrapolated horizontally from the thermocouple nearest the bore surface to barrel surface, then the condition of no further heat transfer from the propellant gases to the gun barrel is satisfied. When this is done, the heat transfer estimate is less than 0.5 percent of the estimate of heat transfer made in the paper. This difference is well within experimental error of our technique. The reason for this is that the thermocouple nearest the bore surface has dropped considerably at 100 ms from its maximum value, and consequently, the temperature gradient close to the surface is shallow. Hence, no significant further heat is transferred to the gun barrel after the 100 ms time interval.

---

[1] By T. L. Brosseau and J. R. Ward, published in the Nov. 1975 issue of the JOURNAL OF HEAT TRANSFER, TRANS. ASME, Series C, Vol. 97, pp. 610–614.

[2] Assoc. Professor, Department of Mechanical and Aeronautical Engineering, Carleton University, Ottawa, Ontario, Canada.